Surface Metallurgy and Rolling Contact Fatigue of Rail

Robert Ian Carroll, M.Eng.

A thesis submitted for the degree of Doctor of Philosophy in the Department of Engineering Materials at the University of Sheffield, UK.

December 2005

The
University
Of
Sheffield.

Clicketty, clacketty; clacketty, clicketty; All
should be sound and nothing ricketty.
In sound and sense we claim our share,
For what we mean is wear and tear.

Song of the Wheel and Rail - Anon.
(Railway Magazine, Volume 15, July 1904, p25)

Summary

This thesis presents the results of an investigation into the effect of surface metallurgy on the rolling contact fatigue behaviour of rail. The investigation has used laboratory based rolling/sliding twin disc testing of samples with a surface metallurgical feature simulated on them. The samples used in laboratory testing have been compared with samples of rail removed from track. Two surface metallurgical features have been investigated: decarburisation and white etching layer.

Decarburisation is the loss of carbon from the surface of the rail due to oxidation at high temperatures, resulting in a softer layer at the surface (180HV compared to 250HV bulk). The decarburised layer has been simulated in this research by heat treating discs in a laboratory furnace with an air atmosphere. The results show that by increasing the depth of decarburisation the growth rate of cracks within the sample, along with the wear rate, increases. At the maximum depth of decarburisation allowed on rail by the standard (0.5mm) there was little difference in the wear or rolling contact fatigue behaviour with or without decarburisation.

White etching layer (WEL) forms on the surface of rail due to the action of the wheels and is a very hard layer (>850HV) up to 250mm deep. White etching layer has been simulated in two ways: spot welding and gross sliding of the discs. The results have shown that cracks initiate preferentially at weak spots at the surface, such as the interface between the WEL and pearlite or along proeutectoid ferrite boundaries. It has been found that the growth of cracks below the surface depends on the strain history of the subsurface pearlite. The results indicate that white etching layer is detrimental to rail life through either the promotion of rolling contact fatigue and/or wear.

Contents

Acknowledgments

Chapter 1: Introduction

On 17th October 2000 a train travelling from London to Leeds derailed on a curve near Hatfield, Hertfordshire, with the death of 4 people and a further 70 injured. It became apparent that the rail had fractured underneath the train, this was not just a single break but the rail for 35 metres beyond had broken into over 300 pieces. The cause of this break was discovered to be "gauge corner cracking" a type of rolling contact fatigue (RCF)[1, 2]. In the days following the accident, RCF was discovered to be a widespread problem which occurred over the whole of the UK's rail network and resulted in speed restrictions, extensive delays, cancellations and in the end resulted in the financial collapse of Railtrack[3]. At the time of writing the publication of the Health and Safety Executive's final report was imminent having been delayed due to legal proceedings, which resulted in heavy fines for both companies involved.

Along with the potential for derailments, rolling contact fatigue combined with wear is a major cause of rail replacements. In the Network Rail business plan for 2004/2005, of a total renewals budget of £1.62 billion, track renewals accounted for £600 million or 37%[4]. This does not take into account the money spent on trying to alleviate the problem through track monitoring or rail grinding. Therefore, research into rolling contact fatigue and wear behaviour of rail has an important industrial application and consequently a financial impact on the railway.

Rolling contact fatigue is a form of fatigue that occurs due to repeated rolling/sliding of one surface in contact with another. This failure mechanism has been found in roller bearing, gears and, the subject of this thesis, rail. This is as a result of the unidirectional accumulation of plastic strain in the railhead, known as ratchetting, due to the repeated action of the wheels.

The investigation of rolling contact fatigue in track is hampered by the multitude of train types and axle loads running on the network; within one train there are a large number of different contact geometries possible between the wheels and rail at any point. For this reason, combined with the cost of on-track investigation, simulation in the laboratory is a cost effective and convenient research technique. A technique commonly used is twin disc rolling/sliding testing along with comparisons between the laboratory tests and rails removed from service.

Rolling contact fatigue and wear both involve the surface of the rail (less than 2mm deep), therefore the structure of this surface layer is highly important to its behaviour under the high stresses arising from the contact of the wheels on the rail. It is therefore surprising that little work has been conducted on the metallurgical structure of this surface layer and its effect on wear and rolling contact fatigue of rail. In this investigation two distinct types of surface metallurgical layers, commonly found on rail, have been investigated: namely decarburisation and white etching layer.

Decarburisation is the loss of carbon through oxidation from the surface of steel during the manufacturing process at high temperatures. This results in the surface of the rail having a lower carbon content and consequently being softer (180HV) than the bulk rail (250HV). All new rails, when placed into service, have a decarburised layer on the surface. There is some controversy as to the effect of decarburisation on the rolling contact fatigue behaviour of rail; railway operators believe it has a detrimental effect, while the manufacturers believe it has no effect. Research into the behaviour of a decarburised surface under rolling/sliding conditions is very important and it is surprising that little research has previously been carried out, particularly no laboratory tests.

White etching layer (WEL), in contrast to decarburisation, is formed on the surface of rail while it is in service by the action of the wheels. The resultant layer is much harder (>850HV) than the bulk rail, with a sharp interface between them, and is commonly present in patches on the railhead. The layer is so named because after metallographic etching it appears white and featureless. More research has been carried out on WEL in the past than on decarburisation but again there have been very few laboratory twin disc tests.

This chapter introduces the subject, giving background to the research and also outlines the content of the thesis.

- Chapter 2 is a literature review of the subject including a brief summary of rail/wheel contact mechanics, with a more developed discussion of damage mechanisms, concentrating on rolling contact fatigue and wear of rail. A comprehensive review is given of the two surface metallurgies, including their formation mechanisms and their effect on the mechanical properties.
- A description of the equipment and experimental procedures is given in chapter 3 including the materials used.
- Chapter 4 describes some investigations into the models of formation of decarburisation and white etching layer. This includes a description of the Birks decarburisation model and also details the results from initial laboratory trials. The model has been used to predict the depth of decarburisation of discs and the results from this are also given. Also discussed is a simple diffusion model, which examines a possible mechanism for the formation of white etching layer under typical rail/wheel conditions.
- The experimental results of the investigation are given in chapter 5.
- Chapter 6 discusses the results. This includes a discussion of the simulation of the two metallurgical features and comparison with samples of rail. The major part of this chapter concentrates on the rolling contact fatigue behaviour and wear of each metallurgical feature, which are discussed separately before being related to each other. As part of this discussion the laboratory results are compared with wheel/rail contact and the consequences for rail life are predicted for both decarburised and white etching layer.
- Chapter 7 presents a summary of the conclusions.

- Chapter 8 present suggestions for further work.

1.1 References

1. Train derailment at Hatfield, 17 October 2000: First interim report, Health and Safety Executive, London, Health and Safety Executive, 2000
2. Train derailment at Hatfield, 17 October 2000: Second interim report, Health and Safety Executive, London, Health and Safety Executive, 2001
3. Jack, I., The Crash that Stopped Britain, 1st Ed., Granta, London, UK, 2001
4. Anon., Network Rail Business Plan 2005, http://www.networkrail.co.uk/companyinformation/businesspublications/BusinessPlan2005.htm, Accessed on 27/05/2005

Chapter 2: Literature Review

2.1   Introduction

The novel feature of railways that makes them different to all other forms of human transport are that unsteered wheels are guided by rails. The first use of guiding rails for transport was circa 2000BC in Malta with wheels guided by ruts, which had either been cut or worn into stone[1]. Cast iron edge rails were first made in 1787 at an ironworks between Blaenavon and Merthyr Tydfil in South Wales. Over the next 30 years, with a change to wrought iron, this became the dominant form of wagon or tramway using flanged wheels running along the top surface of the rail[2]. Figure 2.1 shows a cross section of an edge rail and wheel along with the names commonly used in the industry to describe the parts of them.

This chapter introduces and reviews the contact mechanics between rail and wheel. This is followed by a literature review of the damage phenomena that arise because of the contact stresses, namely rolling contact fatigue and wear. The metallurgy and manufacture of rail are described along with a review of how wheel/rail contact is simulated in the laboratory. Previous works on the two surface metallurgical features under investigation are reviewed; with decarburisation this includes: definition, measurement and effect on rolling contact fatigue performance. With white etching layer a review of the structure, formation and effect on rolling contact fatigue is carried out.

2.2   Contact Mechanics

The study of contact mechanics was initiated by Heinrich Hertz's paper "On the contact of elastic solids" in 1882[3]. This paper showed that when two non-conformal bodies are brought into contact, the area of contact is ellipsoidal whose dimensions are much smaller than the overall dimensions of the body and are dependent on the curvature of the surfaces[4]. The contact between wheel and rail is commonly simulated by two perpendicular cylinders; a typical wheel has a radius of 0.88m and the railhead has a radius of curvature of approximately 0.3m[5]. The Hertzian contact theory, as originally developed, deals only with clean frictionless surfaces and perfectly elastic bodies; the development of the theory of contact mechanics over the last 125 years has been to remove these limitations and allow the stresses between real contact situations to be estimated. The rapid development of computing power over the last 30 years has helped immeasurably.

Wheel/rail contact is not truly Hertzian as tractive forces occur, the surfaces are never clean and the loading is frequently above the elastic limit of the materials. It is not part of this thesis to review in detail contact mechanics but only to discuss the simplified model developed by Fletcher[6] from the ESDU publications[7, 8]; for those with a greater interest in contact mechanics there have been numerous papers published by various

authors detailing the work over the years, with a good starting point being the books written by Johnson[4] and Kalker[9].

The theoretical treatment of wheel and rail contact being between two perpendicular cylinders is a simplification because rail has a constantly changing profile and the wheel has a conical cross section. It is this conical shape of the wheels that allow them to steer when the train goes around corners. Figure 2.2 shows that on tangent or straight track the wheels run in the centre of the rail, any movement from this neutral position means a change in the effective radius of the wheel, which alters the speed of rotation moving the wheel back towards the neutral position[10]. On slight curves this neutral position moves towards the outer (or high) rail of the curve, with the actual position depending on the radius of the corner and the speed of the train. On sharper curves the flange of the wheel may come into contact with the gauge corner of the rail, which results in very high contact stresses. To alleviate this problem track in curves is banked or canted so that the neutral point moves towards the centre of the rail. In the UK with a mixed traffic railway many curves are canted to give the neutral position for the average speed of trains, therefore when a high speed passenger train runs around the corner the wheels move towards the high rail and may result in flange contact. On the other hand, slower speed freight trains run towards the lower rail side of the neutral position and may come into flange contact with it. As the wheel flange moves towards the gauge corner the stresses applied by the wheel on rail increase[11].

The true contact stresses arising between rail and wheel are dependent on a wide range of parameters including[12]:

- Track curvature
- Track alignment
- Track structure e.g. ballast, sleepers and fixings
- Wheel/rail profile
- Friction/traction coefficient
- Surface roughness of wheel/rail surfaces[13]
- Train type, including bogie construction
- Speed of train

As can be seen from this list, the contact conditions even on a small piece of rail alter as every train passes over it. There have been many attempts at including just some of these features into complex computer models to allow contact stresses to be calculated under a wide range of conditions[9]. It is for these reasons that a simplified line contact model has been used to approximate contact stresses in this work.

2.2.1   Line Contact

As the curvature of the contacting surfaces is reduced the contact ellipse becomes increasingly longer and thinner, until the special case of line contact is reached once the ratio between the dimensions of the ellipse is zero, or in other words an infinitely long ellipse. Line contact occurs when two parallel cylinders are rolling against each other contacting in a strip. As no surface is infinitely long there will be some deviation from the model at the edges of the contact but this is commonly ignored. Under line contact the nominal Hertzian contact pressure can be calculated using equation 2.1 for the general case[14].

$$p_0 = \sqrt{\frac{PE^*}{\pi RL}}$$ (2.1)

where

$$\frac{1}{E^*} = \frac{1-\upsilon_1^2}{E_1} + \frac{1-\upsilon_2^2}{E_2}$$ (2.2)

$$\frac{1}{R} = \frac{1}{r_1} + \frac{1}{r_2}$$ (2.3)

and P is the load of the contact (N) while L is its length (m), E is the Young's Modulus (GPa), υ is Poisson's ratio and r is radius (m). The subscripts refer to the two separate bodies. When the two contacting bodies are elastically identical i.e.

$$E_1 = E_2 = E \text{ and } \upsilon_1 = \upsilon_2 = \upsilon \quad \text{(for steel, E = 212GPa and } \upsilon = 0.3)$$

the equation can be simplified to equation 2.4, after Timoshenko and Goodier[14].

$$p_0 = 0.418\sqrt{\frac{PE}{RL}}$$ (2.4)

The contact half width between contacting bodies is given by equation 2.5

$$b^2 = \frac{4PR}{\pi LE}$$ (2.5)

The equations given in ESDU item 85007[8], which allow the calculation of the subsurface stresses arising from the normal and tangential surfaces stresses, have been used by Fletcher to write a procedure in Maple© that allows easy simulations to be made[6].

2.2.2   Shakedown and Ratchetting

A new rail installed into track has a yield strength lower than the stresses applied during the passage of the first few wheels. This results in the plastic deformation of the surface which is readily apparent from observation of rails removed from service[15]. These high loads are accommodated, without the rail failing by plastic collapse, because of work hardening and development of residual stresses in a process known as shakedown, first developed by Johnson and Jefferis[16] and described by Kapoor and Johnson[17], figure 2.3.

If the contact stresses are lower than some critical value, related to the shear strength, of the material it will deform elastically (figure 2.3a) with the half space returning to its original state once the load has passed. The critical value is called the "elastic limit" of the material for this contact, but this rarely occurs with wheel/rail contact, as the stresses are usually greater than the elastic limit. When the load is greater than this limit the surface of the rail will deform plastically, this deformation will not proceed indefinitely because of three processes. The first is the introduction of compressive residual stresses into the material, which protects the material by making further plastic flow less likely. Second, strain hardening of the steel leads to an increase in the yield strength of the material. Finally, an increase in conformity of the contacting surface by removal of asperities and decreasing surface roughness lowering the contact stresses; initial plastic flow of the material also results in greater conformity between the wheel and rail profiles[18]. This process is called shakedown or elastic shakedown, figure 2.3b, whereby the material returns to an elastic state. It is this process that allows Hertzian contact theory to be used because subsequent plastic deformation per cycle is very small therefore approximating to elastic contact.

If the load is subsequently increased above this limit then further plastic flow will take place in two possible ways; the first (figure 2.3c) is where the load is below the plastic shakedown limit and involves closed cycles of plastic deformation where there is no net accumulation of plastic strain. This plastic strain results in the continuous movement of dislocations and possible crack initiation by low cycle fatigue[19]. If the load is greater than this limit then open cycles of plastic deformation occur that result in the accumulation of small amounts of plastic strain with each cycle; this is called ratchetting. Ratchetting leads to ductility exhaustion of the surface of the material, which is thought to be the initiation of surface rolling contact fatigue cracks[20] and is discussed further in section 2.5.

It is possible to show the effect of different contact conditions graphically on a shakedown map showing the load factor plotted against the traction coefficient, figure 2.4 for a line contact[21, 22]. The load factor is the ratio between applied Hertzian contact pressure, p_o and the yield strength of the material in shear, k. One key aspect shown on the map is that

the maximum shear stresses are subsurface when the traction coefficient (see section 2.3.3) is less than 0.3 and at the surface when greater.

Kapoor and co-workers have published several papers on the effect of an anisotropic half space on shakedown. This has included work on samples which are elastically similar but surface hardened, the results show that shakedown is proportional to the ratio of shear yield strengths and the ratio of case depth to contact radius[23]. Other work has included the effect of a stiffer and harder coating on a softer subsurface commonly used on bearings to improve fatigue life, and has shown that to be effective the coating has to be thicker than a limit that depends on the elastic and plastic properties of both materials and the roughness of the contacting surfaces[24, 25].

2.2.3   Heat Generation Arising from Wheel/Rail Contact

When two metal surfaces are in rolling and sliding contact, heat is generated by friction and by deformation of the surfaces. The resulting high temperatures are only of short durations (hence it is called a flash temperature), to a shallow depth and are rapidly cooled by the bulk of the material. There have been several theoretical treatments beginning with the work by Blok[26] which has been described by Archard[27]. This model predicts the temperature rise for a single contact sliding over a flat surface, Archard also expanded it to take into account an elastohydrodynamic lubricating layer.

Tanvir has described a simple analytical model by using a Laplace transformation technique to calculate the temperature between wheel and rail[28]. This model is designed for when a wheel is spinning against the rail either during braking or under traction, but using slip ratios commonly found during full slip conditions of 1% gives temperature rise of less than 100°C. In recent years there have been several models that have used finite element analysis to calculate the temperature between wheel and rail. One of these by Knothe and Liebelt predicted temperature rises of 70°C for a driving wheel with a slip ratio 1% and 2.8°C for a carriage (non-driven) wheel[29]. Fischer *et al.*[30] have also run a finite element model and found similar results for contact between asperities. Further discussion of the heat generated and the flash temperatures arising from wheel/rail contact is given in section 4.3.3.

2.3   Wheel/Rail Operating Conditions

The wide range of variables mentioned in section 2.2 mean that it is not easy to define the exact condition at which wheels on rail operate. This is compounded by the difficulty in measuring the conditions under real life operating conditions. Therefore there have been many simulations made to allow estimation of these conditions; these are commonly based on the Hertzian contact theory. The most important parameters with regard to wheel/rail contact are the pressure, slip and traction coefficient.

2.3.1   Contact Pressure

The maximum Hertzian contact pressure is commonly used to characterise the loading of rail wheel/contacts because it can be related to the normal load and the geometry of the contact (e.g. equation 2.1 for line contact). Oloffsson and Telliskivi[31] have used a computer simulation to model the contact conditions which depend on the position of the contact, with the results shown in figure 2.5. This figure shows that for contact between railhead and wheel tread then the maximum contact pressure will be 1500MPa, while at the gauge corner stresses of up to 3000MPa are predicted. This is in accord with the results found by Lunden of 1475MPa for an axle load of 22.5 tonne at the railhead[32]. Orringer *et al.*[33] have analysed the contact conditions in North American heavy haul service and found pressures up to 3100MPa. These are the pressure calculated for wheels under static conditions; when dynamic contact occurs arising from less than ideal conditions much higher stresses are expected, with pressures of over 7000MPa predicted by Tournay and Mulder due to hollow worn wheel treads[34]. The contact stresses also change with the age of rail and wheel; Kumar and co-workers[35, 36] found, for a laboratory simulation, that with increasing numbers of cycles the contact stresses decrease from a maximum of 950MPa to a stable contact stress of 700MPa after 45,000 cycles for an axle load of 25tonnes, because of a decrease in surface roughness and increase in conformity of the contact. The value of contact pressure used in the laboratory has commonly been 1500MPa as being representative of wheel/rail conditions[37].

Attempts have been made to measure the actual contact stresses arising between wheel and rail using ultrasonic probes[38-40]. The results have shown that the basic shape of the contact is very similar to the ellipse predicated by Hertzian contact. Marshall *et al.*[40] found that the mean pressures are similar but slightly higher than those predicted by Hertzian contact theory; the difference was that the observed values were not uniform throughout the contact, due to non-conformity and roughness of the surfaces, resulting in much higher peaks.

The maximum Hertzian contact pressures are dependent on the axle load of the train. In the UK the current maximum axle load is 25.4tonne[41] but on North American heavy haul railways then 32.7t axle load are currently being used[42]. Economics is the driving force for the increase in axle loads as the savings in maintenance by using fewer locomotives, wagons and trains can offset the increased track maintenance costs[43]. This is the reason that further increases in axle loads will occur in the future increasing the contact stresses between the rail and wheel and consequently the damage to the rail that results from them.

2.3.2   Slip

Slip or creep occurs between wheel and rail when tangential forces are being transmitted due to the wheel driving, braking and steering. Johnson describes the three components of

slip that commonly exist between the wheel and rail: longitudinal (parallel to the direction of train), lateral (perpendicular to the direction of the train) and spin (at an angle to the train direction). When no slip is present then the contact is described as pure rolling with no tractive forces present between rail and wheel.

There is very limited data in the literature on values of slip ratio found between wheel and rail, Garnham[44] gave a figure of –3% slip as being representative of typical conditions. Zakharov *et al.*[45] report that maximum slip values for freight car wheels was between 2 and 10%. Olofsson and Telliskivi have presented a diagram, figure 2.5, showing the variation of contact pressure with sliding velocity and demonstrated that there is a higher sliding velocity and hence slip at the gauge corner compared to the railhead[31].

Johnson has demonstrated that if the tangential force is below a limiting value then the contact patch is divided into stick (where there is no relative motion of the surfaces) and slip (where a small amount of motion occurs) regions[4]. Above this limiting value gross slip occurs between the two surfaces, with no stick region present. For a wheel/rail contact Greenwood has shown that this value is approximately 1% and has also shown that this is the value where the maximum adhesion occurs; therefore, in a normal operating environment wheel/rail contact occurs under full slip conditions[46]. Fletcher has also carried out experiments using twin disc testing at 1500MPa and shown that for unlubricated tests the limiting value is -1.1% and for water lubricated test it is –0.56%[6].

2.3.3   Traction Coefficient

The traction coefficient is the ratio of tangential to normal forces arising during contact and is distinct from the friction coefficient as it is also dependent on the degree of slip occurring. Under full slip condition the friction coefficient is equal to the traction coefficient[6]. Table 2.1 is taken from Stolarski and Tobe giving typical values for the traction coefficient during wheel/rail contact under different conditions[47].

2.4   Wear

Wear has been defined by the ASTM as "damage to a solid surface, generally involving the progressive loss of material, due to relative motion between that surface and a contacting substance or substances"[48]. Wear is of major economic importance, it has been estimated that in 1988 it cost the British economy £2,000,000,000[49]. There are several different types of wear mechanisms that occur depending on the contact loading, materials and environmental conditions; it is also common for more than one mechanism to occur at the same time. The common wear mechanisms that occur in metal contacts are described below; further details are given in any textbook on Tribology, e.g. [49, 50].

2.4.1   Wear Mechanisms
2.4.1.1   Adhesive wear

Adhesive wear is the cold welding of asperities between surfaces under normal pressure with material being transferred from one surface to another. This is usually removal from the softer surface and transfer to the harder surface but it can also occur in reverse; Archard has proposed a semi empirical model to describe how this occurs[51]. Severe damage of this type is known as galling and can lead to macroscopic chunks being removed from a surface; this is a particular problem when both surfaces are of the same material and sliding speeds are high[50]. Adhesive wear only occurs where there is good contact between the surfaces, when lubricant or other interfacial (such as oxide) layers are present then adhesion and the wear rate is low.

2.4.1.2   Abrasive wear

Abrasive wear is where a surface is worn by the action of hard asperities in the counter face (two body abrasive wear) or where hard particles are trapped between the contact (three body abrasive wear). These third body particles can consist of bits of the surface that have already worn away and oxidised or may involve hard contaminants such as silica or quartz[50]. The wear is by the hard particles ploughing the soft surface resulting in debris being detached.

2.4.1.3   Oxidative wear

Oxidative wear is where the temperature of the contact is sufficiently high for oxidation of the surface to occur. If an oxide film occurs under one contact cycle then as long as it remains intact further cycles will have a lower wear rate because it prevents metal to metal contact and adhesive wear. However if the contact load is high the oxide film may be broken down with the oxide particles subsequently acting as third body particles. Related to oxidative wear is corrosive wear; this is where a surface corrodes due to the action of the environment with no contact occurring but with the corrosion product breaking up when the next contact cycle occurs[52]. The formation of an oxide film removes metal from the surface resulting in a loss of material.

2.4.1.4   Delamination wear

When a surface is plastically deformed under repeated cyclic conditions thin sheets of wear debris are detached from the surface; this is known as delamination wear[50]. Suh proposed that it occurred by the formation of subsurface voids which under continued deformation join up to form cracks resulting in the detachment of the surface[53]. Kapoor and co-workers have shown that this method of producing delamination is invalid as it assumes linear elastic fracture mechanics in a heavily plastically deformed layer[17, 54, 55] and have proposed that the slivers are produced by ratchetting of the surface layers and reaching a critical plastic strain; hence the term "ratchetting wear". Liu *et al.*[56] also found that, along with ratchetting of the surface, low cycle fatigue was involved with the

production of wear debris. This wear mechanism is related to the formation of RCF cracks and is described further in section 2.5.

2.4.2   Wheel Wear

Wheels undergo many millions of cycles during their lifetime, each of which is different due to the wide variety of conditions making it difficult to determine the processes occurring during wheel/rail contact[57]; therefore the wear of wheels occur in several ways. The wear of wheels occurs during every cycle; if this occurs evenly around the wheel it will eventually require the wheel to be changed. Uneven wear is more common and can result in the wheel becoming out of round, increasing the dynamic forces that occur between the wheel and rail. Hollow worn wheels are another wear problem where the profile changes during service resulting in unstable running which can lead to derailment of the train[58]. These phenomena require the wheel to be turned to allow a safe wheel profile to be reintroduced to limit the contact stresses[59]. This machining results in an artificial wear rate that is much higher than the natural wear rate[60].

2.4.3   Rail Wear

There have been several observations made of the wear of rail in track that have found a difference in wear mechanisms and rate depending on the location it is measured. The two types of wear that are commonly described are lateral (side) wear and vertical (railhead) wear.

An investigation by Dearden in the 1950's measuring the vertical wear of rail in a variety of different environmental conditions found that wear was greater in urban areas and tunnels compared to rural areas[61]. He also discovered that wear was greater with lower traffic levels; this is due to the repeated formation of a layer of oxide on the surface of the railhead when no traffic is passing with the action of the wheels removing it; typical values of railhead wear are 1mm of wear for every 50million gross tonnes (MGT) for BS11 rail[62]. On high speed track in the UK a depth of 9mm of vertical wear is allowed; loss of depth has been found to be greater on curved track due to creepage especially on the low rail of high speed curves[63]. Clayton and Allery, re-examining railhead wear in the early 1980's, found that corrosion was no longer the dominant mechanism but had been replaced by plastic deformation and fracture of pearlite, combined with the formation and fracture of the white etching layer (see section 2.9)[64].

Side wear occurs on curves because of the lateral force of the wheels on rail and its severity is dependent on the radius of the curve. The effect of side wear is to limit the life of rail in curves because of the increased angle between the gauge face and the crown of the rail leading to a widened gauge and greater risk of derailment[62]. Side wear can be limited by the use of harder rails or by rail lubricators.

Rail lipping is not a true wear mechanism in that the surface is not removed as wear debris but is nevertheless a mechanism that removes material from useful service. This is where gross plastic deformation of the rail occurs leading to lip formation because of the high contact stresses common on the low rail of curves[62].

Bolton and Clayton have performed laboratory tests using an Amsler test rig and defined three modes of wear that occur with rail steel[65]. Type I wear is a combination of corrosive wear and the formation of slivers due to the deformation of the surface of the disc; these are especially related to manganese sulphide inclusions. Type II wear is due to plastic deformation and fracture creating a flake like particle, combined with adhesive wear. Type III is a similar fatigue process where large particles are removed from the surface because of cracks that run parallel with the surface before turning back to it. Bolton and Clayton also examined side worn rails and found that wear at the gauge corner was type II but further down the gauge face it became type III. Similar results were found by Steele and Devine who found that side wear of rail was a fatigue mechanism that has some similarities to Suh's delamination wear[66].

2.4.4   Rail and Wheel Wear Interaction

The wear of the wheel/rail is complicated by the interaction of the wear of one component with that of the other. Kalousek has commented that an increase in the hardness of rail results in a decrease in the wear rate of the wheel and vice versa, because there is less third body wear debris to increase the rate[67]. In adhesive wear this has been found to be the case but Steele and Devine have found that for the fatigue mechanism this is less certain and depends on the magnitude of the hardness change and on relative wear rates[66].

2.5   Rolling Contact Fatigue

Rolling contact fatigue is the formation of cracks through repeated rolling/sliding contact between two metal surfaces. Far from being a recent problem the first reference found in the literature dates from 1899 where incipient cracks at the surface of rail are described by Kirkaldy; the discussion to the paper indicates that it was a widespread problem at the time[68]. This work resulted from a broken rail at St Neots, Hertfordshire (not far from Hatfield!) which led to a government inquiry on the "the loss of strength in steel rails through use on railways"[69]. Developments in rail metallurgy had eliminated this problem in the UK until the proliferation of high speed trains and increased axle loads in the 1970's led to it resurfacing. British Rail Research and Cambridge University carried out significant amounts of work on the study of RCF during the 1970's and 80's[70], culminating in the European research project D173 in the 1990's[71]. Research on RCF has been of heightened interest especially in the UK following the Hatfield accident in 2000[72]. This is only a brief literature review of RCF, several comprehensive ones have been undertaken in previous years[73-76].

The European project on rolling contact fatigue reviewed rail defects and classified them into two categories: subsurface and surface initiated[73]. Subsurface initiated fatigue, sometimes called tache ovals or shells, are commonly associated with manufacturing defects within the steel such as hydrogen shatter cracks or oxide inclusions. These types of defect have largely been removed over the last thirty years through the introduction of improved steel making techniques, such as vacuum degassing and argon blowing, allowing cleaner steels to be manufactured.

Surface initiated cracks are much more important in modern railroads. There are at least two distinct types of defect that are initiated at the surface; the first is the "squat" and is characterised by a dark spot which forms on the surface of the railhead due to the growth of cracks in all directions and subsequent collapse of the surrounding material. Squats can be a serious problem if the cracks branch downward resulting in the transverse failure of the rail. An example of a squat can be found in figures 2.6 and 2.7[77]. The second type are called "head checks", which are characterised by fine surface cracks on the railhead (figure 2.8). Head checks within 10mm of the gauge corner are classified as gauge corner cracking[78].

Rolling contact fatigue does not only affect rails; a similar failure mechanism is found on bearings[79], gears[80] and back up rolls[81]. RCF on bearings is often called micropitting and instead of complete failure, particles separate from the surface increasing wear and uneven running leading to noise and vibration[82]. Several reviews of RCF in machine components have been carried out including Scot[83] and Barrois[84]. The difference between bearings and rail are that bearings are made from much harder steels, typically up to 850HV[85], compared to standard rail of 250HV. Bearings operate under well lubricated conditions where there is an elastohydrodynamic lubrication (EHL) layer separating the metal components, reducing the shear stresses at the surface[86]. This is in contrast to rail where the contact is either dry or water lubricated; resulting in much higher stresses at the surface than is common with bearings.

2.5.1   Crack Initiation

The initiation of RCF cracks is less understood than propagation but is believed to involve the accumulation of strain at the surface due to the high contact stresses[87]. One theory is that the high stresses arising from asperity contact result in the folding over of them leading to cracks initiating[64]. Another theory is that the strain increase of the bulk material initiates cracks either by low cycle fatigue in the plastic shakedown region or ductility exhaustion by ratchetting[76]. In recent years there have been many models developed to further the understanding of crack initiation. Kapoor[88] has developed a model for ratchetting failure that simulated the initiation of cracks based on a model by Kapoor and Johnson[17] for the wear of rail material. Jiang and Sehitoglu have modeled multi-axial fatigue and ratchetting with bainitic and Hadfield steels. They found that

ratchetting occurred initially but initiation was then dominated by low cycle fatigue[89]. Ringsberg has compared these models and found that in the majority of cases cracks are predicted to initiate by low cycle fatigue but the ratchetting model also predicated similar results[90]. It is therefore unclear from the models whether RCF cracks initiate by ductility exhaustion (ratchetting) or by a fatigue mechanism (plastic shakedown). Ringsberg has further developed the models so that both damage mechanisms are taken into account to simulate crack initiation[91]. During twin disc testing it is found that cracks initiate due to a ratchetting process demonstrated by the accumulation of plastic strain with increasing numbers of cycles[6, 92].

2.5.2   Crack Propagation

Once cracks have initiated at the surface, it has been found by Way[93] that a lubricant is required to allow them to propagate through the region of residual compressive stresses at the surface of the material[94]. Bower[95] has proposed several possible mechanism by developing the work of Way[93].

1) Cracks may propagate in mode II driven by cyclic shear stresses with the fluid lubricating the faces.
2) Fluid may be forced into the crack prising the faces apart and driving the crack by transferring the stress by hydraulic action creating mode I stress intensities at the tip.
3) Fluid may be trapped inside the crack and then pressurised by being pushed towards the crack tip allowing movement of the lubricated faces.

Results by Bower from mathematical modelling found that the first mechanism was theoretically possible but was discounted by the difficulty of cracks growing under mode II conditions. The second mechanism could not take account of the direction of the motion of the load or of the tractive force. Therefore the most likely mechanism is fluid entrapment where the crack propagates under mixed mode I and II cycles[95]. This work has been reinforced by recent modelling carried out by Bogdanski who found that mode II stress intensity factors were higher than mode I[96]. The resulting mechanism is generally known by the name of the fluid pressure mechanism. This mechanism is shown in figure 2.9; as the wheel approaches the crack it opens the mouth allowing water to penetrate the tip. When the wheel has passed above the crack, the mouth closes pressurising the fluid within the crack allowing the two faces to remain apart allowing movement laterally and provide the required shear stresses at the crack tip for it to grow. The fluid pressure also allows mode I stress intensities to be developed at the crack tip. The mechanism is complicated and has led to substantial quantities of research trying to model it in recent years[96, 97].

Cracks growing by the fluid pressure mechanism propagate at a shallow angle 15-20° to the surface of the railhead. Individual cracks can join up to create a network with debris spalling from the railhead, this is not dangerous in itself as the rail underneath is still intact and can take the load but it will give an uncomfortable ride and increase the dynamic load on the rail[98]. The problem arises when the cracks have grown to a length of 5mm because they can branch, with the most dangerous being downwards at an angle of 55-65°, as seen in figure 2.8[77]. Once a crack has branched it can keep growing until it passes into the bulk rail, which contain tensile residual stresses that allow the crack to grow at a much faster rate. Figure 2.10 shows how the growth rate of a crack alters with crack length, different mechanisms control crack growth at different steps[97]. In region A the crack is initiated by ratchetting or low cycle fatigue, region B is where the fluid entrapment mechanism dominates crack growth but the rate slows down as the crack is further away from the contact stress field (C). The crack then enters the region of bulk tensile residual stresses (D) which arise from manufacture and welding, increasing the rate of crack growth until the rail breaks once it reaches a critical length.

2.6   The Interaction of Rolling Contact Fatigue and Wear

Rolling contact fatigue and wear occur on the railhead at the same time because both are a result of the contact stresses[99]. If the wear rate is higher than the crack initiation and growth rate, rolling contact fatigue can be eliminated as the surface is worn away before ductility exhaustion occurs, demonstrated by wear rate 1 in figure 2.10[97]. If the wear rate of the material is lower, i.e. at point 2, cracks are removed after initiation but before they can propagate, whereas wear rate 3 is very low and will not affect the growth of cracks. The use of higher strength/hardness grades of rail has resulted in lower natural wear rates, therefore for RCF to be removed the wear has to be artificially increased by the use of rail grinding[100]. The idea behind the grinding strategy of a railway is to find the balance of wear and crack growth, the so called "magic wear rate", that removes the crack after they have initiated but not so soon that the wear rate is so high that it leads to rail replacement; this should be around wear rate 2 in figure 2.10[101].

2.7   Experimental Investigation of Rolling Contact Fatigue

The complexity of the wheel/rail contact with its wide range of conditions, as described in section 2.2, make the investigation of rolling contact fatigue on track difficult, although track tests are still conducted[102]. The main problem is the quantification of results to find which of the wide range of variables is affecting the results combined with the time required for tests. Because of these problems there have been many methods developed to simulate rolling contact fatigue and wear of the wheel/rail contact under controlled conditions.

The simplest method for simulating wheel/rail contact in the laboratory is twin disc testing, this involves one disc (wheel) driving a second disc (rail) while a normal load is applied between them. The most widely used twin disc machine is the "Amsler" developed by Amsler[103] and used more recently by Clayton and Hill[94]. This machine uses a single motor that is geared so that a tractive force is present between the discs with the slip ratio controlled by the diameter of the discs, with the normal load provided by a spring. To allow the high contact pressures, experienced by the wheel/rail, to be simulated, narrow discs are required; which result in a greater proportion of the disc being affected by edge effects and not under true line contact conditions. To overcome these problems several purpose built tests rigs have been developed[104]. One of these was developed by Garnham and Beynon[105] with further development by Fletcher and Beynon[106], which used a hydraulic ram to apply a load between the discs allowing contact pressures as high as 3000MPa. A more detailed description and the procedures for using this machine are presented in chapter 3.

The size advantage of twin disc testing is also one of its problems because scaling is required to allow comparison with real contact conditions. A common way to do this is using a simple Hertzian contact program that allows comparison between the shear stresses below both twin disc and wheel/rail contact such as the one used by Fletcher[6]. To overcome some of these scaling difficulties several tests rigs have been designed that use a full scale wheel on rail. One of these has been developed by DB (German Railways) which consists of a wheel-set running against a roller made from an original rail, the loading conditions allow skewing of the wheel to create spin creep forces to simulate curving[107]. The advantage of tests rigs such as this over twin disc testing are that they simulate conditions similar to the real world, but the main problem is the cost required to build the equipment and to run tests. A further development from this has been to build a dedicated test track that allows many different components to be assessed at the same time. This is the approach used by the Transportation Technology Centre, Inc.(TTCI) in the USA which has 48 miles of test tracks allowing rates of 1MGT per day to be simulated with axle loads of up to 37 tonnes[108].

2.8   Rail Steel

Before the development of cheap and plentiful steel by the Bessemer converter and the Siemens open hearth furnace the only material used for rail was wrought iron. In 1857 the first steel rails were installed on a trial basis at Derby station on the Midland Railway to overcome the problem of wear but it was not until 1878 that the majority of rail in the UK had been laid in steel[109]. After initial development the composition of the most common rail steel, given by the BS11 standard of 1922, is similar to the modern grade used today but with less control on the hydrogen, aluminium and oxygen content[110].

2.8.1   Rail Steel Grades

The majority of rail in the UK is made to the new European standard BS EN13674-1(2003) grade 220 which is the equivalent of the old BS11(1985) normal grade rail. This has a pearlitic microstructure, with an ultimate tensile strength (UTS) of 700MPa and a chemical composition of 0.5-0.6 weight%C, 0.2-0.6%Si and 1-1.25%Mn[111, 112]. The typical features of a pearlitic microstructure are shown in figure 2.11[6]. Other grades of rail used in the UK include grade 260 (formally BS11 grade A) which has a eutectoid composition, is stronger than grade 220 with a UTS of 900MPa and is used where increased wear resistance is required. An even harder rail is also used which is classified as 350HT grade and is known as "mill heat treated" (MHT) or head hardened rail with a UTS of 1300MPa and is used where severe wear occurs, commonly on high speed curves[113]. For switches and crossings, where wear is severe, Hadfield's austenitic manganese steel is used.

2.8.2   Rail Steel Metallurgy

The metallurgy of rail steel is dependent on both its composition and the conditions under which it is formed as shown by the iron – carbon phase diagram, figure 2.12. This diagram is only for pure steels with no other alloying elements, whereas rail steel contains over 1wt%Mn which result in a slight change in the temperature and composition of the different positions shown[114]. When steel is heated above the A_3 temperature, for a 0.6wt%C steel it is 760°C, it is called austenite (γ) with a maximum solubility of 2%C it is therefore single phase and has a face centred cubic (fcc) structure. When a hypoeutectoid steel is cooled from the austenite phase field it starts transforming to ferrite once the A_3 temperature is reached. This occurs along the prior austenite grain boundaries, which are preferential sites for nucleation. Ferrite (α) is a single phase structure but has a maximum solubility of only 0.02%C and a body centred cubic structure (bcc). The transition from austenite to ferrite results in volume expansion of the material as the fcc structure has closer packing than the bcc one but this is compensated by volume thermal contraction on cooling. The low solubility of ferrite results in a carbon-enriched austenite surrounding the solid ferrite, which on cooling below the eutectoid temperature (A_1) transforms to pearlite. Pearlite has a lamellar structure of ferrite and cementite which grows from the austenite grain boundary or proeutectoid ferrite, this growth is diffusion controlled with the transport of carbon in austenite being the rate controlling step, therefore the interlamellar spacing is dependent on the cooling rate with a finer spacing produced by a faster cooling rate. Cementite or iron carbide is a compound of iron and carbon (Fe_3C) which is hard and strong but is also brittle with a carbon content of 6.67wt%. An example of pearlitic steel with 0.6wt%C is shown in figure 2.13 showing proeutectoid ferrite and pearlite colonies.

Ferritic/pearlitic steels are only produced if the cooling from austenite are close to equilibrium conditions; if the cooling rate is faster, then other phases are produced which are metastable, these are demonstrated by the continuous cooling transformation (CCT)

diagram, figure 2.14. The curves show different cooling rates: 1 is a slow cooling rate and gives a steel with a ferrite/pearlite structure as explained above, 2 is a medium cooling rate and produces bainite (figure 2.15) and 3 is quenched producing martensite (figure 2.16)[115]. Bainite consists of fine aggregates of ferrite laths together with cementite particles with hardness of around 400HV[114]; martensite is ferrite supersaturated with carbon and has a body centred tetragonal structure (the unit cell distortion is to accommodate the carbon in solution) and a very high hardness of 800HV but it is also very brittle.

2.8.3   Manufacture of Rails

The production of rail is carried out through several processes that starts with iron ore and finishes with a heat-treated rail[12]. Iron is produced in a continuous process in the blast furnace from iron ore, coke and limestone as raw ingredients; the pig iron is tapped from the bottom of the furnace into a torpedo ladle to transfer the hot metal to the steel making plant. Iron is converted to steel through the Basic Oxygen Steel making process (BOS), this involves blowing the molten metal, which has been combined with scrap and limestone, with oxygen removing the carbon and other impurities as gas and slag. During blowing, the chemical composition is adjusted by the addition of elements. Modern rail steel undergoes secondary steel-making processes to improve the quality, this includes argon flushing and vacuum degassing to reduce the gas content of the steel, particularly hydrogen. The steel is then cast into blooms in a continuous process and cut to the required length.

After casting the bloom is transferred to the rolling mill, rolling usually requires it to be reheated to 1200°C; this is carried out in several ways depending on the manufacturing route. Before rolling the oxide scale is removed by water jets, the bloom is then rolled initially in a roughing stand to reduce the size and increase the length, this also breaks up the as cast structure; the roughed bloom then passes to the finishing stands where between 8 and 10 passes are carried out with the section being developed progressively at each stage. Hot rolling of steel allows dynamic recovery and recrystallisation of the austenitic structure so that the grains, which have grown during reheating, are refined to a smaller size. The production of 220 and 260 grade rail is performed by allowing it to cool naturally in air to room temperature giving a pearlitic microstructure with an interlamellar spacing of approximately 200nm[116]. In contrast 350HT grade is cooled with water sprays to give a much finer interlamellar spacing of 80nm this may occur by an on or off line process after reheating. After cooling, the rail is straightened in the vertical and lateral directions; this roller straightening introduces residual stresses into the rail, which are tensile at the surface and compressive in the web. Rails can be rolled in lengths up to 120m and after rolling are inspected with various techniques including ultrasonic and eddy current equipment looking for defects combined with laser monitoring for surface flatness[110].

2.8.4   Pearlitic Rail Steels

Pearlite is a constituent of steel that is strong and tough as well as resistant to wear. This is because of its lamellar structure; the hardness of the cementite gives pearlite its strength while the ferrite gives it ductility and toughness. The properties of pearlite are proportional to the interlamellar spacing, with refinement the strength and hardness of the material is increased while toughness decreases[117]. As the interlamellar spacing is reduced the thickness of the lamellae is also reduced increasing the relative amounts of cementite in the pearlite[114]. The wear resistance of pearlite is also inversely proportional to the interlamellar spacing; this is the reason for the use of head hardened rails.

When rails are in service refinement takes place due to the plastic deformation of the surface resulting from the high contact stresses[15]. Therefore even normal grade rail at the surface has a finer interlamellar spacing when in service than the bulk of the same rail. The initial surface has a random orientation of pearlite lamella but they become parallel with the surface by plastic deformation; the softer ferrite is deformed more than the cementite resulting in the effective interlamellar spacing of the cementite reducing and therefore a higher proportion of cementite lamellae at the surface compared to the bulk. The surface becomes harder and this self-optimising structure results in a lower wear rate of the surface than the initial structure[116].

The role of pearlite on crack initiation is harder to qualify under the complex stress field involved with wheel/rail contact; but during tensile testing, ductile failure of steels is by the cracking of cementite plates forming voids which coalesce and create cracks which result in failure of the material[118]. Gray *et al.*[119] have investigated the metallurgical variables of pearlitic steel and found that the interlamellar spacing has the largest effect on initiation with the endurance limit increasing with refinement of the spacing. This has been confirmed by Beynon *et al.*[120] with twin disc testing of rail steels who found head hardened rail resisted RCF more than BS11. As part of their investigation Gray *et al.*[119] found that the majority of cracks initiated at dislocation pile ups near inclusions, this is in accordance with the data reported by ERRI D173[73] for subsurface initiated fatigue with the presence of inclusions being detrimental to rail life. Allery and Hodgson[110] report that due to the increasing cleanliness of steel there are fewer inclusions present to initiate cracks. Therefore it is much more likely that RCF crack initiation from the surface of rail is due to the ductility exhaustion brought about by ratchetting or low cycle fatigue[90].

2.9   Decarburisation

Decarburisation is defined as the loss of carbon from the surface of a steel sample as a result of a heating operation[121]. Molten steel after vacuum degassing is continuously cast into blooms, which have to be reheated to temperatures of over 1200°C to allow

rolling to the rail profile to take place[122]. Therefore all new rails have decarburisation present on their surface when they enter service.

2.9.1   Definitions of Depth of Decarburisation

There are several definitions of the depth of decarburisation that are used within industry for assessment of steel components. These are given in the relevant national standards for each country; in the UK this is BS EN ISO 3887(2003[123]) and in the United States ASTM E1077-01-E1[124]. The depth of decarburisation can be shown on a graph of carbon content versus depth, figure 2.17, and can also be seen on a micrograph of the sample, figure 2.18. There are three commonly used definitions for the depth of decarburisation; which are the same in both standards plus a functional definition only given in the international standard these are marked on figure 2.17 and 2.18 by d_1-d_4.

2.9.1.1   Complete decarburisation, d_1
Complete decarburisation is the loss of carbon at the surface below a limiting level. The ASTM standard[124] defines this limiting level as the solubility limit of carbon in ferrite; the solubility of carbon at room temperature in ferrite is found, from figure 2.12, to be 0.008wt%C. This depth of decarburisation is observed by the presence of a complete surface layer of ferrite at the surface with no other transformation products present; it is also called the free ferrite layer in the ASTM standard.

2.9.1.2   Functional decarburisation, d_2
Functional decarburisation is defined as the depth at which the carbon content is acceptable for the intended application; commonly carried out by specifying a fraction of the bulk carbon content. This allows the effect of the depth of decarburisation to be related to the performance of the component when in use.

2.9.1.3   Partial decarburisation, d_3
Partial decarburisation is the loss of carbon at the surface compared to the unaffected steel but to a lesser extent than if it were completely decarburised. The ASTM standard[124] defines it as a lower carbon content than the unaffected interior but greater than the solubility of carbon in ferrite. Partial decarburisation can be observed by the presence of ferrite as well as other transformation products, typically pearlite, but with more ferrite than the unaffected region. If complete decarburisation is present at the surface there will be a region of partial decarburisation between it and the core material.

2.9.1.4   Total decarburisation, d_4
This leads to the third definition, which is the total depth of decarburisation. This is the perpendicular distance from the surface of the metal to the point where the carbon content is the same as that of the unaffected core, i.e. it is the sum of both partial and complete decarburisation. This depth of decarburisation can be seen in figure 2.17 to be where the

carbon concentration reaches an asymptote. The problem with finding this value is compounded by the range of carbon concentration allowed in the standards; for grade 220 rail steel then 0.5-0.6wt%C is allowed. This depth of decarburisation is called, a continuously closed ferrite network in the European standard for rail steel[111]. With hyper-eutectoid steel (>0.8wt%C) it is easy to find the total depth of decarburisation, as there is no pro-eutectoid ferrite present on the grain boundaries of the core material. With hypo-eutectoid steel (<0.8wt%C) then the definition is more complicated as the presence of ferrite on the grain boundaries of the bulk material makes it harder to accurately place the depth of total decarburisation.

2.9.1.5   Use of different definitions

These definitions give the depth of decarburisation at one point but it is also necessary to define the variance across a larger area, therefore maximum and average values are used. The maximum depth of decarburisation is the largest measurement of total decarburisation that can be found in the sample; the average depth of decarburisation is the mean of 5 or more measurements of decarburisation across the sample[124].

For research all the definitions have been used by different people; for industry then total decarburisation is the definition commonly used. In the European project on decarburisation and oxidation use has been made of complete, total and functional decarburisation[125]. The criterion for the functional decarburisation depended on the carbon content, for steel with 0.7wt%C then a definition was of continuous grain boundary ferrite. With lower carbon contents, 0.4wt%, then the definition was taken as a distinct change in appearance. This shows the problem with measuring the functional depth of decarburisation as it is rather a vague definition and the criterion used allows no direct comparison between different alloys.

The four definitions of the depth of decarburisation have all been used by for research purposes. Birks and co-workers used a functional decarburisation with a criterion of 92.5% of the bulk carbon composition[126, 127], whereas Baggerly and Drollinger used a criterion of 99% of the bulk values[128]. The depth of total decarburisation has been used by Baud *et al.*[129]; whereas the depth of complete decarburisation has been used by Nomura *et al.*[130].

The reason for choosing the definition for depth of decarburisation is due to the ease and reliability of measurement, which depends on the method of measurement as well as the alloy content and structure of the steel. For a rail steel the European standard (BS EN13674-1) states that total decarburisation is not to exceed a depth of 0.5mm anywhere on the railhead[111]. The micrograph, figure 2.19, shows that there is no layer of complete decarburisation present for grade 220 only partial decarburisation. This rail steel contains between 0.5 and 0.6wt% carbon and consequently ferrite will be present on the grain boundaries of the bulk material, making measurement of decarburisation difficult.

2.9.2   Measurement of decarburisation

There is a vast array of methods for measuring the extent of decarburisation within a steel sample. The techniques that are commonly used are described in both the British and ASTM standards[123, 124]. The requirements for a method of measurement of decarburisation are set out by Sachs[131]:

1) Ability to measure a clearly defined depth of decarburisation
2) Reproducibility of measurement
3) Ease and convenience of measurement

The most important of these depends on the purpose of the measurement; for industrial use it is ease of measurement, while for research and quality control reproducibility of results is the most important.

2.9.2.1   Metallography

This uses a sample that is sectioned normal to the surface, which is polished and etched using standard metallographic techniques. The measurement can be carried out using a calibrated microscope or on a photomicrograph. For quality control purposes the assessment is made by measuring the distance from the surface to the specified decarburisation depth with several measurements taken and a mean calculated. The magnification recommended is between 100 to 200 times to allow a large surface area to be examined, although higher magnifications may be required to fully resolve the features for a measurement to be made[123, 124]. The ASTM standard also gives a technique for research purposes where traverses are taken, either with a calibrated microscope or on micrographs, at known depths from the surface with the amount of each phase present being determined by measurement[124]. Optical methods of measuring the depth of decarburisation have been reported in numerous papers. Some workers use the optical technique to find the depth of total decarburisation including Litvinov *et al.*[132]. Others have reported the use of optical microscopy to measure the layer of complete decarburisation including Nomura et al.[130]. Optical microscopy is able to be automated by use of quantitative television microscopy, it was found however that a trained technician could give the same results at a faster speed[125].

Various other techniques have been developed using the optical microscope. The first of these is colour etching of high alloy steels, etching is carried out in 4% nital with the colour of the steel depending on the carbon content; this etching helps to distinguish between the core structure and the decarburised layer[131]. This technique has been used on high tungsten steel by Smolyakov and Mininzon[133].

The second technique that has been used is the arrest quench method as described by Turpin *et al.*[134]. This involves a sample being austenitised and quenched with the

quench being arrested immediately above the martensite start temperature of the core material. The reduction in carbon content of the decarburised surface means that it will transform while the core is still austenitic, the hold results in the martensite at the surface being tempered. After holding for a short time the sample is quenched with the remaining austenite transforming to un-tempered martensite. The specimen is then polished and etched showing a sharp contrast between regions of tempered and un-tempered martensite corresponding to areas of high and low carbon concentration respectively; this technique has been used by Sachs and Jay[135] for low carbon steel. This depth of decarburisation is a functional one with the boundary being fixed at a certain carbon concentration as opposed to the total or complete depth of decarburisation but does give reproducible results for a single alloy composition. The results from this method of measurement have been analysed and show that they are more accurate than from conventional structures[131].

2.9.2.2   Microhardness

The relationship between the carbon content and the hardness of a steel is well documented[121, 136]. As the carbon content of the steel is increased then the hardness increases, for ferrite-pearlite structures this is an almost linear relationship as shown in figure 2.20. The reason for the increase in hardness is due to increasing amounts of iron carbide (Fe_3C) present, which has a higher hardness than ferrite[121]. When a sample is decarburised the carbon content of the surface decreases and therefore the hardness of the surface also decreases. Thus the depth of decarburisation can be measured by finding how the hardness varies with depth from the surface and comparison with the bulk hardness allows an estimation of the depth of decarburisation to be made. Decarburised layers are sometimes very thin so it is more accurate to use a microhardness test with a small load (<500g) rather than a full-scale hardness test. Microhardness testers are also commonly fitted with a platen that can measure the distance moved across a sample to ±0.01mm, which allows the depth of the hardness indentation from the surface to be accurately measured. There are two types of microhardness indenter in common use, Knoop and Vickers; the difference between the two is in the geometry of the indentation. The ASTM standard recommends the use of Knoop hardness as the Vickers indentation can be deformed by the hardness gradient of the sample[124]. Although the geometry of the Vickers indentation results in any difference being averaged out between the two diagonal measurements as long as the difference between the two values is less than 5%[137]. A single hardness traverse measures only a small area of the sample, therefore several traverses have to be carried out to give an average depth. In the case of steels the difference in hardness between ferrite and cementite mean that the indentations give widely varying results; the results are more accurate if the microhardness tests are carried out in a single phase structure, such as martensite[131].36

Microhardness has been used by Baggerly and Drollinger[128] in the determination of decarburisation depth. Microhardness cannot be used to measure complete decarburisation, as it is impossible to differentiate between the hardness of a complete ferrite layer and the

hardness of the layer when a small amount of some other constituent is present. Another problem with this technique is that hardness measurement cannot be taken close (<0.05mm) to the surface due to deformation of it. A method to overcome this problem has been proposed by Gassner called the chord evaluation method using a disc specimen which through use of geometry allows magnification of the surface layer[138].

2.9.2.3 Chemical analysis

Chemical analysis has been used to measure decarburisation by the removal of successive layers from the surface and measuring the carbon content of each by various techniques. Using a lathe or milling machine a sample is machined to remove a specific depth of steel (at least 0.05mm) with the turnings collected together and chemical analysis performed to find the carbon content[123]. This is repeated until the core carbon concentration is reached; a graph of depth versus carbon concentration can then be drawn. The problem with this method is that there must be sufficient turnings for chemical analysis to be carried out but the depth removed each time must be small enough to allow enough points to be plotted on the graph; this problem is compounded if the depth of the decarburised layer is only very thin. This technique is slow as well as expensive but does give an accurate graph of carbon concentration and is therefore commonly used for research [139-141]. The depth of decarburisation is given as a percentage of the bulk value and is therefore a functional definition.

2.9.2.4 Spectrographic analysis

This technique is similar to chemical analysis and is described in detail by Bramhall *et al.*[142] as the BISRA technique. The main difference is that instead of using chemical analysis the profile of carbon concentration is carried out using an electrical discharge in an argon atmosphere with the analysis by optical methods. The benefit of this technique means that the distance between measurements is much smaller as the depth of the spark is only 0.03mm with grinding being carried out to remove the spark and the next spark being carried. This technique has been used by Birks *et al.*[127, 143].

A development of this technique is called glow discharge optical emission spectroscopy (GDOES). This involves sputtering of the sample by an argon plasma to erase the surface, the sputtered material from the sample is then identified through atomic emission. The sputtering removes material from the surface allowing measurements to be made at greater depths into the sample[144]. This technique can be used for all elements and has been used for a wide range of uses as reviewed by Payling[145]. Work has been carried out on decarburisation using this technique at depths of up to 50μm at Sheffield Hallam University[146].

2.9.2.5 Electron probe microanalysis (EPMA)

This technique uses a probe that projects a small diameter beam of electrons into a sample, with analysis of the X-rays produced giving the concentration of the sample. This

technique can be used for any element but requires calibration with samples of known concentration[147]. It has been found that the use of a single-phase structure is required as two components of varying composition, such as ferrite and pearlite, give unreliable results[125]. This technique was used by Kao and Wan for measuring decarburisation using a voltage of 25kV and a probe current of 30nA[148].

2.9.2.6   Other techniques

Several other techniques have also been used to look at decarburisation but these do not measure the depth but look at the amount of carbon lost from the samples. These methods have been used to study the kinetics of decarburisation especially in methane and hydrogen atmospheres.

The first technique is measuring the carbon concentration before and after heat treatment using chemical analysis giving an average carbon concentration of the whole sample. This has been used for examination of thin (0.64mm) hot band samples by Marder *et al.* [149]. The measurement of the rate of decarburisation has been carried out by thermo-gravimetric analysis (TGA). This continually measures the mass of the sample while it is being heated up. The problem with this technique is that only atmospheres that are non-oxidising can be used because of the weight gain due to oxidation of the steel masking the weight loss due to decarburisation. Another problem with TGA is that only very small samples can be used. This technique has been used to study the decarburisation kinetics of several different steels in different atmospheres. Turkdogan and Martonik[150] used an atmosphere of hydrogen, while Grieveson[151] as well as Fruehan and Martonik used a CO_2-CO atmosphere[152].

In similar experiments to those with TGA an alternative technique to measure the decarburisation is gas chromatography, which measures the chemical composition of the gas as it is exhausted from the furnace. This technique is used for measuring decarburisation when heated in different atmospheres and allows oxidising atmospheres to be used. Hajduga and Kucera[141] used an oxygen containing atmosphere; Marini and Abbruzzese[153] used a H_2O-H_2 atmosphere while Billings *et al.*[154] used a CO_2 atmosphere. This technique requires a sealed furnace but this would be the case anyway with these atmospheres. The amount of carbon liberated during decarburisation is small but measurable with Yamazaki reporting an increase in the carbon monoxide content of 1500ppm.[155]

Resistance measurements have also been used for measuring the decarburisation of thin foils (<28µm thick). This technique is utilised because the resistance of steel is proportional to the carbon content; a galvanometer measures the change in the resistance of the sample while it is being heated. This technique has been used by Grabke *et al.*[156, 157] for studying the kinetics of decarburisation in hydrogen containing atmospheres.

2.9.2.7   Comparison of techniques

Several people have compared different measurement techniques with the most comprehensive work being carried out by Marston et al.[125], who looked at the depth of decarburisation measured using EPMA, chemical analysis and hardness testing. The work showed that EPMA and chemical analysis give results that are in good agreement with one another with the chemical analysis giving the more consistent results due to a larger volume being sampled. The hardness measurements depended on the load that was used, with lower loads giving slightly lower hardness values. Hardness and EPMA results show considerable scatter due to the small volume that is sampled with each measurement; the hardness values were not related to the carbon content of the metal.

Other workers have also tried to compare different methods of measurement including Baud et al.[129] who used spectrographic and micrographic techniques to measure the total depth of decarburisation for samples heated at 700°C. Their results show some agreement at the shortest time but the microscopy results are lower at longer times. Smolyakov and Mininzon[133] used colour etching, arrest quench and chemical analysis on tool steels. The results show that there is very good correlation between the colour etching and chemical analysis results but the arrest quench method gives widely varying results. Kucera et al. have compared chemical analysis and hardness and found that hardness varies with carbon concentration but not uniformly, the data shows that below 0.4wt%C the relationship is linear[158]. Baggerly and Drollinger have also used an empirical relationship between hardness and carbon content[128].

2.9.3   Mechanism of Decarburisation

When steel is heated to high temperatures there are two competing surface reactions; the first is decarburisation giving a surface layer depleted in carbon, while the second is oxidation of the iron resulting in the loss of metal from the surface. To get a decarburised surface the rate of formation has to be greater than the rate of oxidation. This section includes a brief summary of the oxidation of steel and the possible mechanisms for the decarburisation of steel.

2.9.3.1   Oxidation of steel

Steel at high temperatures reacts with atmospheric oxygen creating an iron oxide scale on the surface of the sample. There are several forms of iron oxide whose formation depends on the temperature of the steel and the amount of oxygen available to react; the reactions formed can be summarised on a iron oxide phase diagram as shown in figure 2.21[159]. It can be seen that for atmospheric conditions of 21wt% oxygen with a temperature below 570°C the thermodynamically stable oxide is magnetite (Fe_3O_4), whereas above 570°C it is wüstite (FeO). This can be seen graphically on the Ellingham diagram where the most negative value of free energy is the most stable phase, figure 2.22[160]. In reality oxidation is rarely under equilibrium conditions therefore the oxide scale is multi layered comprising

the three forms of iron oxide as shown in figure 2.23[159]. Also shown is the mechanism of oxidation with iron ions diffusing through the scale outwards and oxygen ions diffusing inwards with electrons moving to retain charge neutrality. The oxide is formed at the interface between the magnetite and the haematite (Fe_2O_3) and because the reactions are diffusion controlled the oxidation rate obeys a parabolic rate law. The importance of the oxidation of steel to engineering is demonstrated by the quantity of work carried out; reviews of this work have been carried out by Pilling and Bedworth[161], Birks and Meier[126] and more recently by Chang and Wei[159] among others.

2.9.3.2   Possible mechanisms of decarburisation

Decarburisation at high temperatures (above A_3) occurs by transport of carbon through austenite from the bulk metal to the surface where it reacts with oxygen to form CO and CO_2[129]. This mechanism is complicated by the formation of the oxide scale at the surface of the metal; at the temperatures involved in heating and rolling steel the thermodynamically stable oxide formed will be wüstite. Webb *et al.*[162] have described two possible reaction mechanisms to which a third can be added.

a)   Gas penetration through the oxide, reacting at the metal/oxide interface

This involves gaseous oxygen moving through the oxide to the interface where it reacts with carbon, forming carbon monoxide, which then has to move away from the surface for the reaction to continue, therefore this requires the presence of pores and cracks in the oxide. Thus the formation of a compact oxide scale would act as a barrier to decarburisation, but due to the strain caused by the oxide growing and residual stresses form the bulk materials this is rarely the case for wüstite[163]. The addition of up to 2wt% silicon in the steel creates a more compact oxide which is less porous, retards diffusion and is therefore a barrier to decarburisation and oxidation[159].

b)   Carbon diffusion through the scale to react at the oxide/gas interface

Carbon transfers from the metal to the oxide and then diffuses through the oxide to the surface where it could react with gaseous oxygen to form CO or CO_2. This would require the oxide to be closely adherent to the metal to allow transfer of carbon from one to the other and the dissociation of carbon at the metal/oxide interface.

c)   Oxygen diffusion through the scale to metal oxide/interface

Another alternative would be for oxygen ions to diffuse through the scale reacting with carbon forming gases, which then escape by rupture of the scale.

The evidence found in the literature show that the most probable reaction is mechanism a). Reeves and Smeltzer found 2-3% porosity in wüstite which allowed gas transport as long as the scale thickness was less than 100μm[164]. It is unlikely that b) is the dominant mechanism because the solubility of carbon in wüstite is very low therefore decarburisation would be at a very slow rate and may be removed by the oxidation

reaction[154]. Mechanism c) may occur initially but is unlikely at longer times because the reaction would involve the release of gaseous carbon monoxide which would rupture the scale allowing mechanism a) to proceed; this has been found to be the case by Engell and co-workers[165, 166]. The diffusion of oxygen ions inwards in wüstite is also thought to be unlikely because the oxidation of iron involves the outward diffusion of iron ions via vacancies on the iron lattice sites, as shown in figure 2.23[167].

Whichever mechanism decarburisation follows it is also dependent on the transport of carbon through the steel to the metal/oxide interface. This is the classic diffusion controlled transport in metals, which is valid for substitutional diffusion but may not be so for interstitial diffusion. This is commonly modelled using Fick's laws of diffusion with the depth of decarburisation depending, among other things, on temperature and time[168].

The rate controlling step will depend on the conditions of the heat treatment (temperature, time, atmosphere) and also on the composition of the steel. Birks and co-workers[126] found that for reheat furnace atmospheres then diffusion of carbon is the rate determining step, this was confirmed by Baggerly and Drollinger[128]; this mechanism was also confirmed for oxidation in ambient air by Kucera and Hajduga [141, 169]. In other atmospheres this is not the case Smeltzer and co-workers have found that in CO-CO_2 atmospheres then the reaction is controlled by slow surface reactions coupled with gaseous transport; Turkdogan and Martonik[150] also found this was the case for H_2/H_2O atmospheres.

It is therefore likely that in the oxidising conditions present in the reheating furnace and also in the air atmosphere that is easier to utilise in the laboratory, the rate controlling step will be the diffusion of carbon through the metal to the oxide/metal interface. For this reason the model derived by Birks and co-workers will be used to model decarburisation; a further description is given in section 4.2[126].

2.9.4   Decarburisation and Mechanical Properties

The effect of decarburisation on the surface properties of rail steel is vitally important to the lifetime of components therefore a review of the effect on rolling contact fatigue, wear mechanical fatigue and fretting fatigue is presented.

2.9.4.1   Rolling contact fatigue and wear

There has been only one paper written on the effects of decarburisation on rolling contact fatigue and wear of rails, with two others that briefly mention it; because of this a review of the effect of other surface treatments on bearings and gears will be carried out. Rotthäuser, Muders and Grohman reported their observations carried out on track over 2 years[170]. It involved two grades of steel UIC 900A (BS EN13674 grade 260) and 900 head hardened (grade 350HT) with varying levels of decarburisation, which were installed

into curves of different radii. The wear of the rail, measured by the change in cross section, and the length of surface crack were measured every six months. The results found that with 900A rail, increasing the level of decarburisation delayed the initiation of head checks; with 0.5mm depth of decarburisation initiation was delayed by 12 months compared to no decarburisation for an average traffic of 23 million gross tonnes (MGt) per year. This was due to an increase in the wear rate but no quantitative data was provided. With the head hardened grade it was impossible to attain the correct hardness due to the reduction in carbon at the surface. The second paper to mention decarburisation is by Boulanger who reports that track trials conducted by SNCF on rails with decarburisation greater than 1mm in depth showed no notable difference from standard rails[171]. The effect of decarburisation was found by Dearden during track trials to increase the initial wear rate of rail until the subsurface pearlite developed a work hardened layer but no effects on RCF were reported[60].

To prevent rolling contact fatigue in bearings they commonly are given surface treatments, the simplest of these is carburisation, which is the opposite of decarburisation, and involves increasing the amount of carbon at the surface. The bulk structure of is martensite with a hardness of 450HV which carburisation increases to 680HV[172]. The effect of carburisation is to increase by an order of magnitude the RCF life of the bearing as long as no oxide impurities are introduced into the surface during treatment[173]. The effect of increasing the hardness (related to shear strength) of the surface is to make it more resistant to initiation of cracks by reducing the amount of deformation that occurs on application of contact stresses combined with a reduction in the wear rate[24]. Another way of reducing the rate of initiation of cracks is to introduce compressive residual stresses into the surface of the sample by shot preening; this has been carried out by Xiao *et al.*[172] on carburised steel bearings and showed an increase in 30% RCF life on just the carburised samples.

A further improvement in life has been brought about through the use of surface coatings; these may have a higher hardness combined with a higher stiffness than the bulk material. Hard coatings have been used including diamond like carbon coatings[174] and tungsten carbide with hardness of up to 1200HV. A review of surface coatings and rolling contact fatigue have been carried out by Stewart and Ahmed[175] and also by Maurer[176]. It has been found that the thicker the surface layer; the greater the resistance to RCF damage due to the maximum shear stress being moved away from the interface[175].

The use of coatings on bearings and the rise in RCF failures and wear rates of rail have lead to the development of a two-material rail under a European research project called "Infrastar"[177]. This is rail coated using laser cladding with a layer of high hardness (370HV) material which reduces the friction coefficient[178]. Experiments have been carried out using twin disc testing (SUROS) and field trials. The field trials show that the coating gives an increase in life with 10 months of testing no cracks had developed unlike a standard 260 grade rail[179]. The SUROS tests under standard conditions of −1% slip

and contact pressure of 1500MPa with 1000 dry cycles showed a life of 4000 cycles for the untreated rail, compared to at least 200000 cycles without cracks forming for the coated rail[180].

2.9.4.2   Mechanical fatigue

The effect of decarburisation on mechanical fatigue under a cyclic load is an area that has generated much more research than rolling contact fatigue. Papers written by Hankins and co-workers in the 1920's and 30's on spring steel report that decarburisation reduces the fatigue limit by half[181-183]. Work in similar areas has served to confirm these results, Spiegler *et al.*[184] found that for a pearlitic microstructure with 0.6wt%C there is a reduction in the fatigue limit of 30% due to an increased rate of initiation of cracks but the depth of decarburisation (between 0.08-0.58mm) does not have an effect on propagation. Arieli and Mukherjee found that the presence of a decarburised layer increased the fatigue life of the specimen and increasing the applied maximum stress resulted in a greater improvement in fatigue life[185]. This was despite an increase in the initiation rate of the ferrite layer and was due to a decrease in the propagation rate of the fatigue crack. One effect of decarburisation is to introduce residual tensile stresses into the surface because of the volumetric change due to a loss of carbon this would allow fatigue cracks to initiatie more readily at the surface[184, 186].

2.9.4.3   Fretting fatigue

Fretting fatigue is a form of contact fatigue due to high frequency, low amplitude oscillatory sliding between the two surfaces. This action promotes debris formation, which can lead to earlier nucleation of fatigue cracks[19]. Decarburisation was found by Waterhouse and Taylor[187] to give a reduction in the fretting fatigue strength compared to those without.

2.10   White Etching Layers (WEL)

White etching layer is formed on the surface of the rail while it is in service, it is so called because of its resistance to etching and therefore appearing white under the microscope. It has also been called several other names including white layer, white phase, nanostructured layer and adiabatic shear bands (ASB). Typical features of white etching layer on rail are the distinct interface with the bulk material and hardness greater than 1000HV. The structure and mechanism of formation are controversial and will be reviewed along with comparison of similar layers found during wear and machining operations. The behaviour of white etching layers on rail and how they are simulated in the laboratory will also be explored.

2.10.1   Structure and Properties of White Etching Layer

White etching layer is found on the railhead and is commonly associated with corrugations[188]. Corrugations are ripples that appear on the surface of the rail and are formed by a fixed frequency excitation of the wheel on rail. The excitation causes a damage mechanism such as wear or plastic deformation to develop the ripples to a greater extent[189]. It is not clear as to whether the white etching layer is a cause or consequence of the corrugation but it can commonly be found on the high point or crest of the corrugation with none in the valley[190]. Several reviews of corrugations have been carried out with the most comprehensive by Nielsen et al[191]. Several authors have reported the Young's modulus of white etching layer measured using hardness indentations and a technique described by Moylan et al.[192]. Lojkowski et al. reported a value of 245GPa for WEL on railhead compared with a bulk of 212GPa[193]; Akcan et al. reported values of 235GPa, the same as the bulk material, on a WEL produced during machining[194]. Moylan found values of 233GPa for a white etching layer produced during machining compared to 218GPa for the bulk material[192].

The structure of WEL is contentious. The first report of a non-etching product on the surface of rails was written at the turn of the 20th century during an investigation by the House of Commons committee on rail steels and was found to be martensitic because of its high hardness and its similarity to quenched samples[69]. The evidence that WEL is martensitic was backed up through the use of transmission electron microscopy by Newcomb and Stobbs[195]; who found that the white etching layer was a heavily deformed martensite with no carbides present but were unable to determine the lattice parameters. Later papers have questioned whether it could be martensite because the hardness of WEL for a 0.24%C steel is 1100HV compared to martensite produced in the conventional way of heating and quenching which has a maximum of 500HV[196]. Another difference between white etching layer and conventional martensite is its tempering behaviour, Kuznetsov et al.[197] found that WEL preserved its high hardness up to tempering temperatures of 800°C compared to standard martensite which is tempered at temperatures of less than 500°C.

These results from experimentation have lead to the conclusion that white etching layer is not a conventional martensite but a nanocrystalline structure of either martensite or supersaturated ferrite. The evidence for a nanocrystalline structure is the grain size of less than 25nm by Lojkowski et al.[198] using TEM and less than 10nm by Pyzalla et al.[199]. Akcan et al.[194] attribute the nanocrystalline structure for the white appearance of WEL because of the scattering of light from the small crystals and not due to the chemical resistance to etching.

The evidence for a martensitic structure has been found by Pyzalla et al.[199] using synchrotron X-ray scattering who characterised the WEL as martensitic with a maximum

The evidence for a martensitic structure has been found by Pyzalla *et al.*[199] using synchrotron X-ray scattering who characterised the WEL as martensitic with a maximum c/a ratio of 1.01[199]. Wild *et al.*[200] also found that some cementite particles remained in the white etching layer with a maximum size of 4nm. In contrast Lojkowski *et al.*[198] found that white etching layer is a nanocrystalline ferrite with an average grain size of 25nm with irregular grain boundaries surround by clouds of dislocations and no cementite platelets. They also found that lattice was strained compared to the bulk material due to carbon dissolution but couldn't determine if it was in one or all directions. Bauman *et al.*[201] also found that WEL was constituted of supersaturated ferrite.

This use of the term "supersaturated ferrite" is an unnecessary complication as it is the same structure as martensite; the definition given by Honeycombe and Bhadeshia is "martensite is a supersaturated solid solution of carbon in ferrite"[114]. Martensite has the same body centred structure as ferrite but with the lattice distorted in the c-direction to accommodate the carbon in solution resulting in a tetragonal not cubic structure[202]. The fact that martensite and supersaturated ferrite are the same structure is compounded by the shift in the XRD peaks attributed to martensite by Wild *et al.*[200] this is the same as that attributed to nanostructured ferrite by Lojowski *et al.*[198]. The distinction is made because of the difficulty in determining whether the lattice strain is in one or all directions. In this thesis WEL will be classified as a martensitic structure unless evidence proves that it is cubic and not tetragonal.

Baumann *et al.*[201] have investigated the possible mechanisms responsible for the high hardness of the white etching layer and concluded that the most important mechanism, based on the Hall-Petch relationship, is due to the reduction in grain size and the consequent grain boundary hardening. Precipitation hardening from broken cementite particles and work hardening of the surface may also play a part but both mechanisms cannot explain the hardness on their own. Hardening from reduced interlamellar spacing was discounted due to no lamellae being found in white etching layer and metallurgical transformation was discounted because the temperature rise would be insufficient. An estimation was made for the possible increase in hardness for DIN50 150 steel of hardness 338HV from each mechanism and found that grain boundary hardening could give a rise of 1000-1250HV, particle hardening 560-740HV and work hardening 580HV[201].

One other aspect that is occasionally found in WEL on rails is ferrite grains on the prior austenite grain boundaries that are continuous from the bulk material into the white etching layer which have not transformed[64, 200].

2.10.2   Mechanism of Formation

The mechanism of formation of white etching layers is even more controversial than their structure. The classic way of producing martensite is by heating the steel above the

eutectoid temperature, A_1, and above the A_3, into the austenite phase field before cooling rapidly by quenching(see section 2.8)[202]. Mitao *et al.*[203] assume that the surface of the rail is heated by friction with the sharp interface being at the depth at which the sample reaches the A_3 temperature. Similarly Clayton and Allery[64] believed in a thermal cycle but the presence of ferrite in the WEL means that the temperature is only just high enough (above the A_1 but not the A_3) to cause austenisation or the duration of the cycle is very short. The problem with this theory, first pointed out by Newcomb and Stobbs[195], is that all theoretical considerations of wheel/rail contact temperatures are substantially below the austenite transformation temperature, A_3.

The transformation from pearlite and ferrite to austenite is controlled by diffusion and both heating and cooling have to be considered[114]. The cooling cycle is not regarded as being critical because only a small area at the surface will be heated up with the rest of the rail acting as a heat sink with a fast cooling rate[195]. Newcomb and Stobbs[195] applied Archard's[27] equation for rubbing contact and found that for a wheel load of 10tonne (axle load 20t) with 1% slip at $50ms^{-1}$ a temperature rise of 66°C would be expected. They also applied Tanvir's[28] theory for rolling/sliding contact using the same conditions and found a temperature rise of 72°C if the surface deformation was elastic and 151°C if plastic. Newcomb and Stobbs also adapted this model to take into account the deformation of the rail and found that under a slip of 1% at full speed than a temperature rise would never exceed 400°C; they also found that for austenisation to occur at $50ms^{-1}$ in a contact time 0.3 milliseconds (typical for wheel/rail contact) then a slip of 5% was required. Knothe and Liebelt found that to give a temperature rise of 600°C at $75ms^{-1}$ then a slip of 6% was required. The values given in section 2.3.2 show that this is unlikely to occur on the railhead and white etching layers are not found at the gauge corner.

The common calculations of temperature rise have been made for the bulk of the rail and do not take into account the deformation of the asperity contacts. Nakkail[204] has proposed a mechanism involving plastic deformation of the asperities giving a temperature increase that is well in excess of the austenisation temperature in the surface layer of rails. The passage of one set of wheel leads to localised white etching layer formation which coalesce and are tempered during subsequent wheel passage due to deformation and localised heating. With increasing traffic the white etching layer covers the entire railhead and looks homogenous due to the tempering process. This mechanism is in agreement with Clayton and Allery's examination of white etching layer of individual overlapping areas, which were semi elliptical in shape which first appear as streaks but with time develop into continuous surface layers[64]. The provisional European standard on in-service rail grinding prEN13231-3:2000[205] gives a maximum average surface roughness, R_a, of 10μm therefore asperities will not be significantly deeper than twice this value and this mechanism is unlikely to produce white etching layers with a depth of up to 100μm. Some evidence that austenisation does occur on rail has been found by Osterle *at al.*[206] with retained austenite being present in WEL on rails indicating that at least part of the rail has

been heated above the A_1. In contrast Fischer *et al.*[30] modelled asperity contact with deformation and found that for contact pressures of 1500MPa and slip of 1% then the temperature rise will still not be greater than 100°C and temperature rises high enough for transformation, arise only under conditions that are unlikely to occur on the railhead.

One other possibility exists that the transformation occurs at a lower temperature due to the effect of the contact pressure. Austenite has a higher density and consequently smaller volume than ferrite so the effect of the hydrostatic pressure results in a reduction in the transformation temperature. Ahlström and Karlsson[207] calculated that with a hydrostatic pressure of 400MPa the A_1 was lowered by 4°C while the A_3 was lowered by 17°C, Hillard found experimentally a similar reduction and a linear relationship between them[208]. Therefore a reduction in the eutectic temperature of over 300°C to below 400°C by hydrostatic pressure is unlikely to occur. A second aspect is the time required for diffusion of carbon to occur, Archard and Rowntree using an order of magnitude calculation found that for sufficient diffusion to occur for the austenisation process; a contact time of 10ms is required at 910°C whereas at higher temperatures (>1500°C) a time of 0.3ms is required[209]. These results show that transformation to austenite is unlikely to take place by the rolling and sliding of the wheel on rail.

For these reasons the mechanism proposed by Newcomb and Stobbs[195] are much more likely to occur: this involves the breaking and dissolution of the cementite plates into ferrite at temperatures of up to 100°C. Plastic deformation of the rail surface, especially at the surface due to asperities, introduces large numbers of dislocations on which the carbon atoms sit preferentially in the ferrite structure to relieve the strain on the lattice. Under several processes of severe plastic deformation a true strain of at least 7-8 is required for WEL formation[210]. For complete dissolution in a 0.6wt% carbon steel, a dislocation density of $1 \times 10^{17} m^{-2}$ was required which is common in martensite but unknown in ferrite (which has a maximum of $10^{15} m^{-2}$)[211]. The presence of carbon increases the number of dislocations that can be accommodated within the structure of iron[212]. This, combined with the dislocations being repeatedly moved by the contact stresses result in a higher probability of them interacting with the carbon atoms[195]. This mechanism would lead to greater depths of white etching layer with increased traffic volumes although a limiting depth will occur as the contact stresses decrease; further evidence is found by the breaking up of cementite lamella in the region below the white etching layer[195, 201]. This mechanism has been developed by Lojkowski *et al.*[198, 213] who established it was analogous to mechanical alloying which occurs during severe plastic deformation. They found that temperatures could not rise above 150°C or the dislocations would recover and annihilate themselves leading to lower hardness[198]. A similar process is the fracture and dissolution of cementite found under severe deformation during ball milling of steel powders[214, 215].

2.10.3   White Etching Layer, Rolling Contact Fatigue and Wear

The effect of white etching layer on rolling contact fatigue has been observed both on rail as well as during twin disc testing in the laboratory. Clayton and Allery made some of the first observations on rail and found that cracks were present within the white etching layer but didn't penetrate beyond the interface [64]. They also found that cracks developed at the surface and propagated along the interface between the WEL and the pearlite bulk material but did not penetrate more than 0.17mm deep; both types of cracks gave rise to wear particles. Dikshit et al.[216] studied white etching layer on a head hardened rail and found that the number of cracks associated with it was greater than in track without. Eyre, using pin on disc wear tests, found that WEL reduced the wear rate of the steel substantially due to the prevention of adhesive metallic wear[217], but this was only the case if the load was insufficient to crack the white etching layer. Milman et al.[218] have conducted tribological tests on white etching layer found on railhead and found that it displays high wear resistance as long as it remains continuous and does not crack, if it does then the wear rate is greater than the bulk materials. Nishida et al.[219] found that cracks initiated at the surface and propagated through the white etching layers into the bulk material with no change in direction at the interface. The initial growth of some cracks was in the opposite direction to the wheel motion but then turned 90° at 0.1mm below the surface and propagated in the opposite direction.

2.10.4   Laboratory Simulation of White Etching Layers

One common way of producing white etching layers is using spot welding, the technique is described by Welsh[220], using two electrodes and discharging an electric current across the sample. This leads to localised heating and quenching of the surface producing a martensitic structure. Mitao et al.[203, 221] used this technique and found that cracks propagate along the WEL/matrix interface and also along the ferrite on the prior austenite grain boundaries close to the white etching layer. Aw has also used this technique and found that cracks initiate at the surface of the white etching layer and propagate at steeper angles to the surface than for pearlite. He also found that cracks can initiate at the WEL/matrix interface but propagation is in the bulk pearlite[222]. A technique using a laser has been used to simulate the structure of white etching layer; this technique, like spot welding locally heats a thin surface layer which is quenched by the bulk metal underneath forming a martensite type white etching layer [206].

Another method for introducing white etching layer is using a pin on disc test to give the required deformation combined with heating for white etching layer formation. This technique was used by Shur et al.[223] who found that cracks initiated on the interface at the surface and propagated along them; leading to flaking of the surface and forming pits on the surface with complete removal of the white etching layer.

2.10.5   Other White Etching Layers

White etching layers have been found in a wide range of different circumstances involving deformation and/or heating. Many machining operations have produced white etching layers including cutting[224], reaming[225], deep drilling[226] and grinding[227, 228]. The white etching layers that are produced are different depending on the material and formation conditions the common feature being that on etching they appear white and the majority show high hardness.

White etching layers are also found on worn surfaces such as gun barrels [229, 230], rope[231] and earth moving equipment[232, 233]. As with machined white etching layers these are formed under widely differing circumstance and it is hard to draw comparisons with rail. The main differences between other white etching layers and those on rail are the temperature at which they form; machining and unlubricated sliding wear usually occur at temperatures high enough to cause austenisation. Impact tests, using balls dropped on to a sample, have created white etching layers by severe plastic deformation; these white etching layers crack under repeated impacts[234, 235]. Several reviews have been made on various aspects of white etching layers produced by machining and wear[196, 236]. Griffiths has also tried to draw comparison between white etching layers produced by the two methods[237].

2.11 References

1.   Lewis, M., 'Dinosaur' tracks from the dawn of civilisation, The Railway Magazine, 150, (1235), p4-6, March 2004
2.   Pigott, N. and Lewis, M., The prehistory of Britain's railways, The Railway Magazine, 150, (1235), p7-13, March 2004
3.   Hertz, H., Über die Berührung fester elastischer Körper (On the contact of elastic solids), J. reine und angewandte Mathematik, 92, p156-171 (for English translation see "Miscellaneous Papers by H. Hertz", Eds. Jones and Schott, Macmillan, London, 1986.), 1982
4.   Johnson, K. L., Contact Mechanics, 1st Ed., Cambridge University Press, UK, 1985
5.   Ekberg, A., Bjarnehed, H. and Lunden, R., A fatigue life model for general rolling contact with application to wheel/rail damage, Fatigue and Fracture of Engineering Materials and Structures, 18, (10), p1189-1199, 1995
6.   Fletcher, D. I., The influence of lubrication on the fatigue of pearlitic rail steel, PhD Thesis, Department of Mechanical Engineering, University of Sheffield, UK, 1999
7.   Anon., 84017 Contact Phenomena II: Stress fields and failure criterion in concentrated elastic contacts under combined normal and tangential loading, Engineering Science Data Unit (ESDU), Institute of Mechanical Engineers, London, UK, 1984
8.   Anon., 85007 Contact Phenomena III: Calculation of individual stress components in concentrated elastic contacts under combined normal and tangential loading, Engineering Science Data Unit (ESDU), Institute of Mechanical Engineers, London, UK, 1994
9.   Kalker, J. J., Three-dimensional elastic bodies in rolling contact, 1st Ed., Kluwer Academic Publishers, Dordrecht, The Netherlands, 1990
10.   Wickens, A. H., Steering and stability of the bogie: vehicle dynamics and suspension design, Proceedings of the I.Mech.E.: Part F, Railway and Rapid Transit, 205, (2), p109-122, 1991

11.   Smallwood, R., Sinclair, J. C. and Sawley, K., An optimisation technique to minimise rail contact stresses, Wear, 144, (1-2), p373-384, 1991

12.   Esveld, C., Modern Railway Track, 2nd Ed., MRT Productions, Delft, The Netherlands, 2001

13.   Kapoor, A., Franklin, F. J., Wong, S. K. and Ishida, M., Surface roughness and plastic flow in rail wheel contact, Wear, 253, (2-3), p257-264, 2002

14.   Timoshenko, E. A. and Goodier, J. N., Theory of Elasticity, 3rd Ed., McGraw Hill Kogakusha, Tokyo, Japan, 1970

15.   Alwahdi, F., Kapoor, A. and Fletcher, D. I., The metallurgy of pearlitic rail steel following service, in: The World Congress on Railway Research, WCRR 2003, Edinburgh, Scotland, UK, Immediate Proceedings, Beccles, Suffolk, UK, p932-939, 2003

16.   Johnson, K. L. and Jefferis, J. A., Plastic flow and residual stresses in rolling and sliding contact, in: Proceedings of the Symposium on Fatigue in Rolling Contact, Institution of Mechanical Engineers, London, p54-65, 1963

17.   Kapoor, A. and Johnson, K. L., Plastic ratchetting as a mechanism of metallic wear, Proceedings of the Royal Society, A445, p367-381, 1994

18.   Kapoor, A., Effect of changes in contact geometry on shakedown of surfaces in rolling/sliding contact, International Journal of Mechanical Sciences, 34, (3), p223-239, 1992

19.   Suresh, S., Fatigue of Materials, 2nd Ed., Cambridge University Press, UK, 2003

20.   Beynon, J. H. and Kapoor, A., The interaction of wear and rolling contact fatigue, in: Reliability Assessment of Cyclically Loaded Engineering Structures, Smith, R. A.(Ed), Kluwer Academic Publishers, Dordrecht, The Netherlands, p1-26, 1997

21.   Bower, A. F. and Johnson, K. L., Shakedown, residual stress and plastic flow in repeated wheel/rail contact, in: Rail Quality and Maintenance for Modern Railway Operation, Delft, The Netherlands, Kalker, J. J., Cannon, D. F. and Orringer, O.(Ed's), Kluwer Academic Publishers, Dordrecht, The Netherlands, p239-249, 1992

22.   Ponter, A. R. S., Hearle, A. D. and Johnson, K. L., Application of the kinematical shakedown theorem to rolling and sliding point contacts, Journal of the Mechanics and Physics of Solids, 33, p339-362, 1985

23.   Kapoor, A. and Williams, J. A., Shakedown limits in rolling/sliding contact on an anisotropic half space, Wear, 191, p256-260, 1996

24.   Wong, S. L. and Kapoor, A., Effect of hard and stiff overlay coatings on the strength of surfaces in repeated sliding, Tribology International, 29, (8), p695-702, 1996

25.   Wong, S. L. and Kapoor, A., Shakedown limits on coated surfaces, Thin Solid Films, 292, (1-2), p156-163, 1997

26.   Blok, H., Measurement of temperature flashes on gear teeth under extreme pressure conditions, in: Proceedings of the General Discussion on Lubrication and Wear, Institution of Mechanical Engineers, London, UK, p222-235, 1937

27.   Archard, J. F., The temperature of rubbing surfaces, Wear, 2, (6), p438-455, 1958/1959

28.   Tanvir, M. A., The temperature rise due to slip between wheel and rail: an analytical solution for Hertzian contact, Wear, 61, (2), p295-308, 1980

29.   Knothe, K. and Liebelt, S., Determination of temperatures for sliding contact with application to wheel rail systems, Wear, 189, p91-99, 1995

30.   Fischer, F. D., Davies, W. and Werner, E. A., On the temperature in the wheel-rail rolling contact, Fatigue and Fracture of Engineering Materials and Structures, 26, (10), p999-1006, 2003

31.   Olofsson, U. and Telliskivi, T., Wear, plastic deformation and friction of two rail steels: a full-scale test and a laboratory study, Wear, 254, (1-2), p80-93, 2003

32.   Lunden, R., Contact region fatigue of railway wheels under combined mechanical rolling pressure and thermal brake loading, Wear, 144, (1-2), p57-70, 1991

33.   Orringer, O., Paxton, W. R., Gray, D. E. and Raj, P. K., Residual stress and its consequences on both sides of the wheel-rail interface, Wear, 191, (1-2), p25-34, 1996

34.   Tournay, H. M. and Mulder, J. M., The transition from wear to the stress regime, Wear, 191, p107-112, 1996

35.   Kumar, S. and Rajkumar, B. R., Experimental investigation of contact stresses between a US locomotive wheel and rail, Transactions of the ASME: Journal of Engineering for Industry, 105, p64-70, 1983

36.   Kumar, S. and Rajkumar, B. R., Laboratory investigation of wheel/rail contact stresses for US freight cars, Transactions of the ASME: Journal of Engineering for Industry, 103, p246-255, 1981

37.   Hill, D. N. and Clayton, P., The development of a laboratory rolling contact fatigue testing procedure, Report No: TM MF 32 / 263-384-32, British Rail Research, Derby, UK, 1982

38.   Pau, M., Aymerich, F. and Ginesu, F., Ultrasonic measurement of nominal contact area and contact pressure in a wheel/rail system, Proceedings of the I.Mech E: Part F Journal of Rail and Rapid Transit, 214, (4), p231-243, 2000

39.   Pau, M., Aymerich, F. and Ginesu, F., Distribution of contact pressure in wheel–rail contact area, Wear, 253, (1-2), p265-274, 2002

40.   Marshall, M. B., Lewis, R., Dwyer-Joyce, R. S., Olofsson, U. and Björklund, S., Ultrasonic characterisation of a wheel/rail contact, in: Proceedings of the 30th Leeds-Lyon Symposium on Tribology, INSA da Lyon, France, Elsevier Tribology Series No. 43, p151-158, 2003

41.   Anon.,   Axle   Loads,   Network   Rail, www.networkrail.co.uk/freight/general/infrastructure/axleloads.htm,   Accessed   on 07/04/2005

42.   LoPresti, J. A., Davies, D. and Kristan, J., Development and implementation of track technology for heavy axle loads, in: The World Congress on Railway Research, WCRR 2003, Edinburgh, Scotland, UK, Immediate Proceedings, Beccles, Suffolk, UK, p1370-1378, 2003

43.   Kumpfmuller, N. and Ripke, B., The technical and economical effects of increasing axle load on track, in: The World Congress on Railway Research, WCRR 2003, Edinburgh, Scotland, UK, Immediate Proceedings, Beccles, Suffolk, UK, p1379-1393, 2003

44.   Garnham, J. E., The wear of bainitic and pearlitic steels, Ph.D Thesis, University of Leicester, UK, 1995

45.   Zakharov, S. M., Komarovsky, I. and Zharov, I., Wheel flange/rail head wear simulation, Wear, 215, p18-24, 1998

46.   Greenwood, J., The contact of real surfaces, in: Proceedings of the 1st International Conference on Contact Mechanics and Wear of Rail/Wheel Systems, Vancouver, BC, Canada, p21-37, 1982

47.   Stolarski, T. A. and Tobe, S., Rolling Contacts, 1st Ed., Professional Engineering Publishing Limited, Bury St Edmunds, UK, 2000

48.   ASTM, G40-99 Standard terminology relating to wear and erosion, 2000

49.   Hutchings, I. M., Tribology: Friction and Wear of Engineering Materials, 1st Ed., Butterworth-Heineman, Oxford, UK, 1992

50.   Williams, J. A., Engineering Tribology, 1st Ed., Oxford University Press, Oxford, UK, 1994

51.   Archard, J. F., Contact and rubbing of flat surfaces, Journal of Applied Physics, 24, (8), p981-988, 1953

52.   Rabinowicz, E., Friction and Wear of Materials, 2nd Ed., John Wiley and Sons Inc., New York, USA, 1995

53.   Suh, N. P., The delamination theory of wear, Wear, 25, (1), p111-124, 1973

54.   Kapoor, A., Johnson, K. L. and Williams, J. A., A model for the mild ratchetting wear of metals, Wear, 200, (1-2), p38-44, 1996

55.   Kapoor, A. and Franklin, F. J., Tribological layers and the wear of ductile materials, Wear, 245, p204-25, 2000

56.   Liu, J., Kopalinsky, E. M. and Oxley, P. L. B., An investigation of the role of crack initiation, propagation and ratchetting in producing wear in metallic sliding contacts, Proceedings of the I.Mech.E., Part C - Journal of Mechanical Engineering, 214, (1), p63-74, 2000

57.   Kalker, J. J., Simulation of the development of a railway wheel profile through wear, Wear, 150, (1-2), p355-365, 1991

58.   Sawley, K., Urban, C. and Walker, R. M., The effect of hollow worn wheels on vehicle stability in straight track, in: Proceedings of the 6th International Conference on Contact Mechanics and Wear of Rail/Wheel Systems, Gothenburg, Sweden, Ekberg, A., Kabo, E. and Ringsberg, J. W.(Ed's), Chalmers University of Technology, Sweden, p49-48, 2003

59.   Sawley, K. and Wu, H., The formation of hollow worn wheels and their effect on wheel/rail interaction, in: Proceedings of the 6th International Conference on Contact Mechanics and Wear of Rail/Wheel Systems, Gothenburg, Sweden, Ekberg, A., Kabo, E. and Ringsberg, J. W.(Ed's), Chalmers University of Technology, Sweden, p469-477, 2003

60.   Dearden, J., The wear of steel rails and tyres in railway service, Wear, 3, (1), p43-59, 1960

61.   Dearden, J., The wear of steel rails: a review of the factors involved, Proceedings of the Institute of Civil Engineers: Part II, Research and Theory, 3, (2), p456-505, 1954

62.   Tolley, K. H., Rail wear and associated problems, in: Fourth R.I.A. Track Sector Course, p4.6.4/1-4.6.4/11, 1992

63.   Purbrick, M. C., The use of rails on British Railways, in: 2nd International Heavy Haul Conference, Colorado Springs, USA, International Heavy Haul Association, Virginia Beech, Virginia, USA, p380-387, 1982

64.   Clayton, P. and Allery, M. B. P., Metallurgical aspects of surface damage problems in rails, Canadian Metallurgical Quarterly, 21, (1), p31-46, 1982

65.   Bolton, P. J. and Clayton, P., Rolling-sliding wear damage in rail and tyre steels, Wear, 93, (2), p145-165, 1984

66.   Steele, R. K. and Devine, T. J., Wear of rail/wheel systems, in: Proceedings of the 1st International Conference on Contact Mechanics and Wear of Rail/Wheel Systems, Vancouver, BC, Canada, p293-315, 1982

67.   Kalousek, J., Wheel/rail damage and its relationship to track curvature, in: Proceedings of the 6th International Conference on Contact Mechanics and Wear of Rail/Wheel Systems, Gothenburg, Sweden, Ekberg, A., Kabo, E. and Ringsberg, J. W.(Ed's), Chalmers University of Technology, Sweden, p1-16, 2003

68.   Kirkaldy, W. G., The effects of wear upon steel rails, Minutes of the Proceedings of the Institution of Civil Engineers, LXXXVI, (2), p141-250, 1898/9

69.   The loss of strength in steel rails through use on railways, House of Commons Committee, Sessional Papers, LXXVI part 1, (Cd174), p553-718, 1900

70.   Grassie, S. L., Preventive grinding controls RCF defects, International Railway Journal, January 2001

71.   Cannon, D. F. and Pradier, H., Rail rolling contact fatigue: research by the European Rail Research Institute, Wear, 191, (1-2), p1-13, 1996

72.   Smith, R. A., Rolling Contact Fatigue of Rails - What Remains to be Done?, in: World Conference on Railway Research 2001, Koln, Germany, 2001

73.   D173, Report No. 1: Review of rolling contact fatigue in rails, Office for Research and Experiments of the International Union of Railways, Utrecht, The Netherlands, 1990

74.   Clayton, P., Tribological aspects of wheel/rail contact: a review of recent experimental research, Wear, 191, (1-2), p170-183, 1996

75.   Ekberg, A. and Kabo, E., Rolling contact fatigue of railway wheels and rails: an overview, in: Proceedings of the 6th International Conference on Contact Mechanics and Wear of Rail/Wheel Systems, Gothenburg, Sweden, Ekberg, A., Kabo, E. and Ringsberg, J. W.(Ed's), Chalmers University of Technology, Sweden, p11-24, 2003

76.   Cannon, D. F., Edel, K.-O., Grassie, S. and Sawley, K., Rail defects: an overview, Fatigue and Fracture of Engineering Materials and Structures, 26, (10), p865-886, 2003

77.   Rolling contact fatigue in rails: a guide to current understanding and practice, RT/PWG/001, Railtrack, London, UK, 2001

78.   Anon., PWSI No. 4, Issue 3 (Revised). Instruction on the management of rails to control RCF (GCC & HC), Network Rail, London, UK, 2003

79.   Tsushima, N., Crack propagation of rolling contact fatigue in ball bearing steel due to tensile strain, Tribology Transactions, 47, p567-575, 2004

80.   Bull, S. J., Evans, J. T., Shaw, B. A. and Hofmann, D. A., The effect of the white layer on micro pitting and surface contact fatigue failure of nitrided gears, Proceedings of the I.Mech.E: Part J, Journal of Engineering Tribology, 213, (4), p305-313, 1999

81.   Frolish, M. F. and Beynon, J. H., Design criteria for rolling contact fatigue resistance in back up rolls, Ironmaking and Steelmaking, 31, (4), p300-304, 2004

82.   Oila, A. and Bull, S. J., Assessment of the factors influencing micropitting in rolling/sliding contacts, Wear, 258, (10), p1510-1524, 2005

83.   Scott, D., Rolling Contact Fatigue, in: Wear of Materials, Scott, D.(Ed), Academic Press, Inc., New York, USA, p321-361, 1979

84.   Barrois, W., Repeated Plastic Deformation as a Cause of Mechanical Surface Damage in Fatigue, Wear, Fretting-Fatigue and Rolling Fatigue. A Review, International Journal of Fatigue, 1, (4), p167-189, 1979

85.   Voskamp, A. P., Osterlund, R., Becker, P. C. and Vingsbo, O., Gradual changes in residual stress and microstructure during contact fatigue in ball bearings, Metals Technology, 7, p14-21, 1980

86.   Nelias, D. and Ville, F., Detrimental effects of debris dents on rolling contact fatigue, Transactions of the ASME: Series F, Journal of Tribology:, 122, (1), p55-64, 2000

87.   Beynon, J. H., Brown, M. W. and Kapoor, A., Initiation, growth and branching of cracks in railway track, in: Engineering Against Fatigue, Sheffield, UK, Beynon, J. H., Brown, M. W., Smith, R. A., Lindley, T. C. and Tomkins, B.(Ed's), Balkema, Rotterdam, The Netherlands, p461-472, 1997

88.   Kapoor, A., A re-evaluation of the life to rupture of ductile metals by cyclic plastic strain, Fatigue and Fracture of Engineering Materials and Structures, 17, (2), p201-219, 1994

89.   Jiang, Y. and Sehitoglu, H., A model for rolling contact fatigue, Wear, 224, (1-2), p38-49, 1999

90.   Ringsberg, J. W., Cyclic ratchetting and failure of a pearlitic rail steel, Fatigue and Fracture of Engineering Materials and Structures, 23, (9), p747-758, 2000

91.   Ringsberg, J. W., Life prediction of rolling contact fatigue crack initiation, International Journal of Fatigue, 23, (7), p575-586, 2001

92.   Tyfour, W. R., Interaction between wear and rolling contact fatigue in pearlitic rail steels, PhD Thesis, Department of Engineering, University of Leicester, 1995

93.   Way, S., Pitting due to rolling contact, Journal Applied Mechanics, 57, pA49, 1935

94.   Clayton, P. and Hill, D. N., Rolling contact fatigue of a rail steel, Wear, 117, (3), p319-334, 1987

95.   Bower, A. F., The influence of crack face friction and trapped fluid on surface initiated rolling contact fatigue cracks, Transactions of the ASME: Series F, Journal of Tribology:, 110, (10), p704-711, 1988

96.   Bogdanski, S., Lewicki, P. and Szymaniak, M., Experimental and theoretical investigation of the phenomenon of filling the RCF Crack with liquid, in: Proceedings of the 6th International Conference on Contact Mechanics and Wear of Rail/Wheel Systems, Gothenburg, Sweden, Ekberg, A., Kabo, E. and Ringsberg, J. W.(Ed's), Chalmers University of Technology, Sweden, p377-383, 2003

97.   Ringsberg, J. W., Shear mode growth of short surface-breaking RCF cracks, Wear, 258, (7-8), p955-963, 2005

98.   Grohmann, H. D., Schnitzer, T. and Edel, K.-O., Head checks and further damage, in: Proceedings of the 6th International Conference on Contact Mechanics and Wear of Rail/Wheel Systems, Gothenburg, Sweden, Ekberg, A., Kabo, E. and Ringsberg, J. W.(Ed's), Chalmers University of Technology, Sweden, p99-104, 2003

99.   Donzella, G., Faccoli, M., Ghidini, A., Mazzù, A. and Roberti, R., The competitive role of wear and RCF in a rail steel, Engineering Fracture Mechanics, 72, (2), p287-308, 2005

100.   Grassie, S. L., Rolling contact fatigue on the British railway system, in: Proceedings of the 6th International Conference on Contact Mechanics and Wear of Rail/Wheel Systems, Gothenburg, Sweden, Ekberg, A., Kabo, E. and Ringsberg, J. W.(Ed's), Chalmers University of Technology, Sweden, p1-10, 2003

101.   Kalousek, J. and Magel, E., Achieving a balance: the "magic" wear rate, Railway Track and Structures, p50-52, March 1997

102.   Griffin, K. J. and Rosval, G. W., In -track assessment of premium and intermediate grade rail steels, Canadian Mining and Metallurgical Bulletin, 81, (914), p117-124, 1988

103.   Amsler, A. J., Abnützungsmaschine für metalle (Wear machine for metals), Zeitschrift - Verein Deutscher Ingenieure, 66, (15), p377-378, 1922

104. Kalousek, J., Development of a 1/8th scale dual disc-on-disc rail/wheel wear testing facility, Canadian Metallurgical Quarterly, 21, (1), p67-72, 1982

105. Garnham, J. E. and Beynon, J. H., The early detection of rolling - sliding contact fatigue cracks, Wear, 144, (1-2), p103-116, 1991

106. Fletcher, D. I. and Beynon, J. H., Development of a machine for closely controlled rolling contact fatigue and wear testing, Journal of Testing and Evaluation, 28, (4), p267-275, 2000

107. Meadler, K., Ullrich, D. and Luke, M., Rolling contact phenomena at wheels and rails observed at DB's full scale simulation test rig, in: Proceedings of the 6th International Conference on Contact Mechanics and Wear of Rail/Wheel Systems, Gothenburg, Sweden, Ekberg, A., Kabo, E. and Ringsberg, J. W.(Ed's), Chalmers University of Technology, Sweden, p17-22, 2003

108. Hargrove, M. B., Mitchell, F. S., Steele, R. K. and Young, R. E., Evaluation of rail behaviour at the facility for accelerated service testing, Transportation Research Record, 744, p6-15, 1980

109. Brooke, D., The advent of the steel rail 1857-1914, Journal of Transport History, 7, (1), p18-31, 1986

110. Allery, M. B. P. and Hodgson, W. H., Improvements in rail maintenance techniques and manufacturing processes, Proceedings of the Institution of Civil Engineers: Transport, 100, (11), p227-230, 1993

111. BS EN 13674-1, Railway Track Applications - Rail - Part 1: Flat Bottom Symmetrical Rails 46kg/m and Above, British Standards Institution, London, UK, 2003

112. BS11, Specification for Railway Rails, British Standards Institute, 1985

113. D173, Report No. 8: Rolling Contact Fatigue, Review of the development and use of high strength rail steels, Office for Research and Experiments of the International Union of Railways, Utrecht, The Netherlands, 1995

114. Honeycombe, R. W. K. and Bhadeshia, H. K. D. H., Steels: Microstructure and Properties, 2nd Ed., Edward Arnold, London, UK, 1995

115. Micrograph Library, http://www.doitpoms.ac.uk/miclib/index.php, Department of Materials Science and Metallurgy, University of Cambridge, UK, Accessed on 16/05/05

116. Perez-Unzueta, A. J. and Beynon, J. H., Microstructure and wear resistance of pearlitic rail steel, Wear, 162-164, (1), p173-182, 1993

117. Kavishe, F. P. L. and Baker, T. J., Effect of prior austenite grain size and pearlite interlamellar spacing on strength and fracture toughness of a eutectoid rail steel, Materials Science and Technology, 2, (8), p816-822, 1986

118. Park, Y. J. and Bernstein, I. M., The process of crack initiation and effective grain size for cleavage fracture in pearlitic eutectoid steel, Metallurgical Transactions, 10A, (11), p1653-1664, 1979

119. Gray, G. T., Thompson, A. W. and Williams, J. C., Influence of microstructure on fatigue crack initiation in fully pearlitic steels, Metallurgical Transactions, 16A, (5), p753-760, 1985

120. Beynon, J. H., Garnham, J. E. and Sawley, K. J., Rolling contact fatigue of three pearlitic rail steels, Wear, 192, (1-2), p94-111, 1996

121. Krauss, G., Microstructure, processing and properties of steels, in: Vol 1: Properties and Selection: Iron, Steel and High Performance Alloys, Metals Handbook, American Society of Metals, USA, p126-139, 1996

122. The Track Handbook, 2nd ed., Corus Rail, 2002

123. BS EN ISO 3887, Steels. Determination of Depth of Decarburization, British Standards Institution, London, UK, 2003

124. E1077-01-E1, Measurement of Decarburization, American Society for Testing Materials, USA, 1997

125. Marston, H. F., Ratcliffe, R., Bolt, P. H., van Lankveld , M., Lanteri, V., Leprince, G., Jarl, M., Niska, J., Klima, R. and Roder, M., Oxidation and decarburisation of high carbon: special and general steels, European Commission - Science Research Development, 2002

126. Birks, N. and Meier, G. H., Introduction to High Temperature Oxidation of Metals, 1st Ed., 1983

127.   Birks, N. and Jackson, W., A quantitative treatment of simultaneous scaling and decarburization of steels, Journal of the Iron and Steel Institute, 280, (1), p81-85, 1970

128.   Baggerly, R. G. and Drollinger, R. A., Determination of decarburization in steel, Journal of Materials Engineering and Performance, 2, (1), p47-50, 1993

129.   Baud, J., Ferrier, A., Manenc, J. and Benard, J., The oxidation and decarburizing of Fe-C alloys in air and the influence of relative humidity, Oxidation of Metals, 9, (1), p69-97, 1975

130.   Nomura, M., Morimoto, H. and Toyama, M., Calculation of ferrite decarburizing depth, considering chemical composition of steel and heating condition, ISIJ International, 40, (6), p619-623, 2000

131.   Sachs, K., Decarburization - definition and measurement, in: Conference on Decarburization, Sheffield, UK, Birks, N.(Ed), Iron and Steel Institute, London, UK, p13-39, 1970

132.   Litvinov, B. M., Odinokov, Y. I., Krym, O. Y. and Lashin, V. V., Tool steels heated by induction for decarburization, Stal in English, 5, (5), p424-426, 1968

133.   Smolyakov, V. F. and Mininzon, R. D., Investigation of decarburization and scaling in R6M5 and R18 steels, Steel in the USSR, 3, (8), p684-686, 1973

134.   Turpin, R. J. B., Jay, G. T. F., Ray, M. J. and Sachs, K., Measurement of decarburization, Journal of the Iron and Steel Institute, 205, p1252-1260, 1967

135.   Sachs, K. and Jay, G. T. F., Variation of decarburization in billets, in: Reheating for Hot Working, Iron and Steel Institute, Publication 111, London, p36-45, 1968

136.   The Metals Black Book: Volume 1 Ferrous Metals, Ed., CASTI Publishing Inc.,

137.   BS EN ISO 6507-1, Metallic Materials - Vickers Hardness Test: Part 1 - Test Method, British Standards Institution, London, UK, 1998

138.   Gassner, R. H., Decarburization and its evaluation by the chord method, Metal Progress, 113, (3), p59-63, 1978

139.   Belchenko, G. I., Bugaets, M. P., Bunin, K. P. and Movchan, V. I., Some features of the decarburization kinetics of low carbon steel in austenitic ferritic condition, Steel in the USSR, 6, (4), p220, 1976

140.   Block, W. F. and Jayaraman, N., Reactions during decarburization annealing of electrical steel, Material Science and Technology, 2, (1), p22-27, 1986

141.   Hajduga, M. and Kucera, J., Decarburization of Fe-Cr-C steels during high temperature oxidation, Oxidation of Metals, 29, (5-6), p419-433, 1988

142.   Bramhall, P. S., Haynes, R. G. and Willingham, R. C., A Spectrographic Method for Measuring Decarburisation of Steel, Metallurgia, 76, (453), p43-46, 1967

143.   Birks, N. and Nicholson, A., Calculation of decarburization depth in steels reheated under practical conditions, in: Mathematical Models in Metallurgical Process Development, London, UK, The Iron and Steel Institute, London, UK, p219-224, 1969

144.   Weiss, Z., Quantitative evaluation of depth profiles analysed by glow discharge optical emission spectroscopy: analysis of diffusion processes, Spectrochimica Acta, 47B, (7), p859-876, 1992

145.   Payling, R., Glow discharge optical emission spectrometry, Materials Forum, 18, p195-213, 1994

146.   Keeping on the right track, Glow discharge spectrometry at the materials research institute, Sheffield Hallam University, Sheffield, UK, 1995

147.   Runnsjo, G., On the accuracy of carbon determination in steels by electron probe microanalysis, Scandinavian Journal of Metallurgy, 9, p205-210, 1980

148.   Kao, C. H. and Wan, C. M., Oxidation and decarburization of an Fe-Al-C alloy, Journal of Materials Science, 23, (3), p894-899, 1988

149.   Marder, A. R., Perpetua, S. M., Kowalik, J. A. and Stephenson, E. T., The Effect of carbon content on the kinetics of decarburization in Fe-C alloys, Metallurgical Transactions A, 16A, (6), p1160-1163, 1985

150.   Turkdogan, E. T. and Martonik, L. J., Kinetics of decarburization of austenite in hydrogen, High Temperature Science, 2, (2), p154-168, 1970

151.   Grieveson, P., Kinetics of decarburization of gamma-iron-carbon alloys in oxygen potential atmospheres, Scandinavian Journal of Metallurgy, 1, (5), p231-234, 1972

152. Fruehan, R. J. and Martonik, L. J., Rate of decarburization of austenite in CO-CO_2, High Temperature Science, 3, (3), p244-256, 1971

153. Marini, P. and Abbruzzese, G., Decarburization rate related to surface oxidation of grain oriented silicon steel, Journal of Magnetism and Magnetic Materials, 26, (1-3), p15-21, 1982

154. Billings, G. J., Smeltzer, W. W. and Kirkaldy, J. S., Oxidation and decarburization kinetics of iron-carbon alloys, Journal of the Electrochemical Society, 117, (1), p111-117, 1970

155. Yamazaki, T., On the decarburization of silicon steel sheet, Transactions of the Iron and Steel Institute of Japan, 9, (1), p66-75, 1969

156. Grabke, H. J., Muller, E. M. and Konczos, G., Kinetics of carburization and decarburization of iron and iron-10% nickel in CH_4-H_2 mixtures, Scripta Metallurgica, 14, (1), p159-162, 1980

157. Grabke, H. J., Muller, E. M., Speck, H. V. and Konczos, G., Kinetics of the carburization of iron alloys in methane-hydrogen mixtures and of the decarburization in hydrogen, Steel Research, 56, (5), p275-282, 1985

158. Kucera, J., Hajduga, M., Glowacki, J. and Broz, P., Decarburization and hardness changes of Fe-C-Cr-Mn-Si steels caused by high temperature oxidation in ambient air, Zeitschrift fur Metallkunde, 90, (7), p514-521, 1999

159. Chang, Y. N. and Wei, F. I., High temperature oxidation of low alloy steels, Journal of Materials Science, 24, p14-12, 1989

160. Gaskell, D. R., Introduction to Metallurgical Thermodynamics, 1st Ed., 1981

161. Pilling, N. B. and Bedworth, R. E., The oxidation of metals at high temperatures, Journal of the Institute of Metals, 29, p529-582, 1923

162. Webb, W. W., Norton, J. T. and Wagner, C., Oxidation studies of metal/carbon systems, Journal of the Electrochemical Society, 103, (2), p112-117, 1956

163. Evans, U. R., The Corrosion and Oxidation of Metals, 1st Ed., Edward Arnold, London, UK, 1960

164. Reeves, A. S. and Smeltzer, W. W., Decarburization of an iron-0.8wt% carbon alloy in the presence of a wüstite scale, Journal of the Electrochemical Society, 117, (1), p117-121, 1970

165. Bohnenkamp, K. and Engell, H. J., Ablauf der Oxydation von Eisen and Kohlenstoff bei der Verunderung von Eise Kohlenstoff Begrugen, Arch. Eisenhuttenwes, 33, p359, 1962

166. Engell, H. J. and Peters, F. K., Unterschungen über den Aufbau und die Hartfestegkeit von zanerschiften auf Grobblechen aus antergreten Stahl, Arch. Eisenhuttenwes, 28, p567, 1957

167. Kubaschewski, O. and Hopkins, B. E., Oxidation of Metals and Alloys, 1st Ed., Butterworths, UK, 1962

168. Wilkinson, D. S., Mass Transport in Solids and Fluids, 2nd Ed., Cambridge University Press, UK, 2000

169. Kucera, J. and Adamaszek, K., The initial stage of oxidation of iron and steels heated at high temperatures in ambient air, Metallic Materials (Kovove Materialy), 39, (5), p289-301, 2001

170. Rotthauser, N., Muders, L. and Grohmann, H.-D., Influence of surface-decarburisation area of the rail on rolling contact fatigue, Eisenbahningenieur, 52, (3), p62-65, 2001

171. Boulanger, D., Rail metallurgical developments to address the changing needs of railway, in: The World Congress on Railway Research, WCRR 2003, Edinburgh, Scotland, UK, Immediate Proceedings, Beccles, Suffolk, UK, p932-939, 2003

172. Xiao, H. B., Chen, Q., Shao, E., Wu, D. Z., Chen, Z. H. and Wang, Z. G., The effect of shot peening on rolling contact fatigue behaviour and its crack initiation and propagation in carburized steel, Wear, 151, (1), p77-86, 1991

173. Queeney, R. A., Lange, J. H., Amateau, M. F. and Sonti, N., Rolling contact fatigue resistance in ausrolled 1% C 9310 steel, International Journal of Fatigue, 16, (4), p281-286, 1994

174. Rosado, L., Jain, V. K. and Trivedi, H. K., The effect of diamond like carbon coatings on the rolling fatigue and wear of M50 steel, Wear, 212, (1), p1-6, 1997

175. Stewart, S. and Ahmed, R., Rolling contact fatigue of surface coatings: a review, Wear, 253, (11-12), p1132-1144, 2002

176.   Maurer, R. E., Friction, wear and corrosion control in rolling bearings through coatings and surface modification: A review, Journal of Vacuum Science Technology, 4, (6), p3002-3006, 1986

177.   Hiensch, E. J. M., Two material rail combats rolling contact fatigue, Railway Gazette International, 159, (9), p587-590, 2003

178.   Hiensch, E. J. M., Kapoor, A., Josefson, L., Ringsberg, J. and Nielsen, J., Two material rail development to prevent rolling contact fatigue and reduce noise emissions in curved rail track, in: World Conference on Railway Research 2001, Koln, Germany, 2001

179.   Hiensch, E. J. M., Larson, P. O., Nilsson, O., Levy, D., Kapoor, A., Franklin, F. J., Nielsen, J., Ringsberg, J. and Josefson, B. L., Two material rail development: Field test results regarding rolling contact fatigue and squeal noise behaviour, in: Proceedings of the 6th International Conference on Contact Mechanics and Wear of Rail/Wheel Systems, Gothenburg, Sweden, Ekberg, A., Kabo, E. and Ringsberg, J. W.(Ed's), Chalmers University of Technology, Sweden, 2003

180.   Franklin, F. J., Weeda, G. J., Kapoor, A. and Hiensch, E. J. M., Rolling contact fatigue and wear behaviour of the Infrastar two material rail, in: Proceedings of the 6th International Conference on Contact Mechanics and Wear of Rail/Wheel Systems, Gothenburg, Sweden, Ekberg, A., Kabo, E. and Ringsberg, J. W.(Ed's), Chalmers University of Technology, Sweden, p559-566, 2003

181.   Hankins, G. A. and Ford, G. W., The mechanical and metallurgical properties of spring steels as revealed by laboratory tests, Journal of the Iron and Steel Institute, 119, p217-253, 1929

182.   Hankins, G. A., Becker, M. L. and Mills, H. R., Further experiments on the effect of surface conditions on the fatigue resistance of steels, Journal of the Iron and Steel Institute, 133, p399-426, 1936

183.   Hankins, G. A. and Becker, M. L., The effect of surface conditions produced by heat treatment on the fatigue resistance of spring steels, Journal of the Iron and Steel Institute, 124, p387-460, 1931

184.   Spiegler, B., Wieiss, B. Z. and Taub, A., Influence of decarburization on the fatigue properties and the propagation of cracks in silicon steels, Journal of the Iron and Steel Institute, 202, (6), p509-517, 1964

185.   Arieli, A. and Mukherjee, A. K., Decarburization and fatigue: a fresh look, in: The Enigma of the Eighties: Environment, Economics, Energy: 24th National SAMPE Symposium and Exhibition, San Francisco, California, USA, Society for the Advancement of Material and Process Engineering, USA, p103-111, 1979

186.   Gildersleeve, M. J., Relationship between decarburisation and fatigue strength of through hardened and carburising steels, Materials Science and Technology, 7, (4), p307-310, 1991

187.   Waterhouse, R. B. and Taylor, D. E., The effect of heat treatment and decarburization on the fretting fatigue behaviour of a 0.7% carbon steel, Proceedings of the I.Mech.E., 185, (46), p691-695, 1971

188.   Frederick, C. O. and Jones, E. G., Review of rail research on British Rail, Transportation Research Record, 744, p26-37, 1980

189.   Grassie, S. L. and Kalousek, J., Rail corrugation, characteristics, cause and treatments, Proceedings of the I.Mech.E: Part F, Journal of Rail and Rapid Transit, 207, p57-68, 1993

190.   Hiensch, E. J. M., Nielsen, J. and Verheijen, E., Rail corrugation in the Netherlands: Measurements and simulations, Wear, 253, p140-149, 2002

191.   Nielsen, J. C. O., Lunden, R., Johansson, A. and Vernersson, T., Train/track interaction and mechanisms of irregular wear on wheel and rail surfaces, Vehicle System Dynamics, 40, (1-3), p3-54, 2003

192.   Moylan, S. P., Kompella, S., Chandrasekar, S. and Farris, T. N., A new approach for studying mechanical properties of thin surface layers affected by manufacturing processes, Journal of Manufacturing Science and Engineering: Series B, Transactions of the A.S.M.E., 125, (2), p310-315, 2003

193.   Lojkowski, W., Millman, Y., Chugunova, S. I., Goncharova, I. V., Djahanbakhsh, M., Burkle, G. and Fecht, H. J., The mechanical properties of the nanocrystalline layer on the surface of railway tracks, Materials Science and Engineering A, 303, (1-2), p209-215, 2001

194. Akcan, S., Shah, S., Moylan, S. P., Chhabra, P. N., Chandrasekar, S. and Yang, H. T. Y., Formation of white layers in steels by machining and their characteristics, Metallurgical and Materials Transactions, 33A, p1245-1254, 2002

195. Newcomb, S. B. and Stobbs, W. M., A transmission electron microscopy study of the white etching layer on a railhead, Materials Science and Engineering, 66, (2), p195-204, 1984

196. Eyre, T. S. and Baxter, A., The formation of white layers at rubbing surfaces, Tribology, 5, (6), p256-261, 1972

197. Kuznetsov, V. D., Savitskiy, K. V. and Sukahrina, N. N., Some features of the structure of white layers, Physics of Metals and Metallography (Fizika Metallov I Metallovedenie), 15, (1), p135-137, 1963

198. Lojkowski, W., Djahanbakhsh, M., Burkle, G., Gierlotka, S., Zielinski, W. and Fecht, H. J., Nanostructure formation on the surface of railway tracks, Materials Science and Engineering, 303A, (1-2), p197-208, 2001

199. Pyzalla, A., Wang, L., Wild, E. and Wroblewski, T., Changes in microstructure, texture and residual stresses on the surface of a rail resulting from friction and wear, Wear, 251, (1-12), p901-907, 2001

200. Wild, E., Wang, L., Hasse, B., Wroblewski, T., Goerigk, G. and Pyzalla, A., Microstructure alterations at the surface of a heavily corrugated rail with strong ripple formation, Wear, 254, (9), p876-883, 2003

201. Baumann, G., Fecht, H. J. and Liebelt, S., Formation of white etching layers on rail treads, Wear, 191, (1-2), p133-140, 1996

202. Nishiyama, Z., Martensitic Transformation, 1st Ed., Academic Press, 1978

203. Mitao, S., Yokoyama, H., Yamamoto, S., Kataoka, Y. and Sugiyama, T., High strength bainitic steel rails for heavy haul railways with superior damage resistance, in: IHHA STS Conference on Wheel/Rail Interface, Moscow, Russia, p489-496, 1999

204. Nakkalil, R., Formation of Adiabatic Shear Bands in Eutectoid Steels in High Strain Rate Compression, Acta Metallurgica et Materialia, 39, (11), p2553-2563, 1991

205. prEN 13231-3, Acceptance of Rail Grinding, Milling and Plaining Work in Track, British Standards Institution, London, UK, 2000

206. Osterle, W., Rooch, H., Pyzalla, A. and Wang, L., Investigation of white etching layers on rails by optical microscopy, electron microscopy, x-ray and synchrotron x-ray diffraction, Materials Science and Engineering A, 303, (1-2), p150-157, 2001

207. Ahlstrom, J. and Karlsson, B., Microstructural evaluation and interpretation of the mechanically and thermally affected zone under railway wheel flats, Wear, 232, p1-14, 1999

208. Hilliard, J. E., Iron carbon phase diagram: isobaric sections of the eutectoid region at 35, 50 and 65 kilobars, Transactions of the Metallurgical Society of the AIME, 227, (4), p429-438, 1963

209. Archard, J. F. and Rowntree, R. A., Metallurgical phase changes in the wear of steels: a critical reassessment, in: 6th Leeds-Lyon Symposium: Thermal Effects in Tribology, Lyon, France, Dowson, D.(Ed), Mechanical Engineering Publications, Ltd., UK, 1979

210. Umemoto, M., Nanocrystallization of steels by severe plastic deformation, Materials Transactions, 44, (10), p1900-1911, 2003

211. Kalish, D. and Cohen, M., Structural changes and strengthening in the strain tempering of martensite, Material Science and Engineering, 6, p156-166, 1970

212. Hidaka, H., Kawasaki, K., Tsuchiyama, T. and Takaki, S., Effect of carbon on nanocrystallisation in steel during mechanical milling treatment, Materials Transactions, 44, (10), p1912-1918, 2003

213. Djahanbakhsh, M., Lojkowski, W., Burkle, G., Baumann, G., Ivanisenko, Y. V., Valiev, R. Z. and Fecht, H. J., Nanostructure formation and mechanical alloying in the wheel/rail contact area of high speed trains in comparison with other synthesis routes, Materials Science Forum, 360-362, p175-182, 2000

214. Korznikov, A. V., Ivanisenko, Y. V., Laptionok, D. V., Safarov, I. M., Pilyugin, V. P. and Valiev, R. Z., Influence of severe plastic deformation on structure and phase composition of carbon steels, Nanostructured Materials, 4, p159, 1994

215.   Fecht, H. J., Nanostructure formation by mechanical attrition, Nanostructured Materials, 6, p33, 1995

216.   Dikshit, V., Clayton, P. and Christensen, D., Investigation of rolling contact fatigue in a head hardened rail, Wear, 144, (1-2), p89-102, 1991

217.   Eyre, T. S., Wear of pearlitic steel, in: 2nd International Heavy Haul Conference, Colorado Springs, International Heavy Haul Association, Virginia Beech, Virginia, USA, p277-281, 1982

218.   Millman, Y. V., Grinkevych, K. E., Chugunova, S. I., Lojkowski, W., Djahanbakhsh, M. and Fecht, H. J., Tribological properties of the surface of railway tracks, studied by indentation technique, Wear, 258, (1-4), p77-82, 2005

219.   Nishida, S. I., Sugino, K., Urashima, C. and Masumoto, H., Study on contact rolling fatigue of rails: II. Analysis by high speed rail testing machine, Bulletin Japanese Society of Mechanical Engineers, 28, (243), p1819-1824, 1985

220.   Welsh, N. C., Spark hardening of metals, Journal of the Institute of Metals, 88, p103-111, 1959/60

221.   Yokoyama, H., Mitao, S., Yamamoto, S., Kataoka, Y. and Sugiyama, T., High strength bainitic steel rails for heavy haul railways with superior damage resistance, NKK Technical Review, 84, p44-51, 2001

222.   Aw, P. K., Effect of white layer on rolling contact fatigue, 3rd Year Undergraduate Project, Engineering Department, University of Leicester, UK, 1992

223.   Shur, E. A. and Trushevsky, S. M., Physical metallurgy aspects of rolling contact fatigue of rail steel, Wear, 258, (7-8), p1165-1171, 2005

224.   Okusa, K., Takahashi, H. and Nishizawa, M., Behaviour of white layer during cutting of iron and steels, Bulletin Japanese Society of Precision Engineering, 12, (4), p171-176, 1978

225.   Turley, D. M., The nature of white layers produced during reaming ultra-high strength steel, Material Science and Engineering, 19, p76-86, 1975

226.   Griffiths, B. J., White layer formation at machined surfaces and their relationship to white layer formations at worn surfaces, Transactions of the ASME: Series F, Journal of Tribology:, 107, (2), p165-171, 1985

227.   Tomlinson, W. J., Blunt, L. A. and Spraggett, S., Running-in wear of white layers formed on EN24 steel by centreless grinding, Wear, 128, (1), p83-93, 1988

228.   Eda, H., Kishi, K. and Hashimoto, S., The formation mechanism of ground white layers, Bulletin Japanese Society of Mechanical Engineers, 24, (190), p743-747, 1981

229.   Snair, W. H. and Wood, W. P., The white layer structure in the erosion of machine gun barrels, Transactions of the ASM, 27, p608-624, 1939

230.   Botstein, O. and Arone, R., The microstructural changes in the surface layer of gun barrels, Wear, 142, (1), p87-95, 1991

231.   Trent, E. M., The formation and properties of martensite on the surface of rope wire, Journal of the Iron and Steel Institute, 143, (1), p401, 1941

232.   Bulpett, R., Eyre, T. S. and Ralph, B., The characterization of white layers formed on digger teeth, Wear, 162-164, p1059-1065, 1993

233.   Mashloosh, K. M. and Eyre, T. S., Abrasive wear and its applications to digger teeth, Tribology International, 18, (5), p259-266, 1985

234.   Zhang, B., Liu, Y., Shen, W., Wang, Y., Tang, X. and Wang, Y., A study on the behaviour of adiabatic shear bands in impact wear, Wear, 198, (1-2), p287-292, 1996

235.   Yang, Y. Y., Fang, H. S., Zheng, Y. K., Yang, Z. G. and Jiang, Z. L., The failure models induced by white layers during impact wear, Wear, 185, (1-2), p17-22, 1995

236.   Scott, D., Smith, A. I., Tait, J. and Tremain, G. R., Materials & metallurgical aspects of piston ring scuffing - A literature survey, Wear, 33, (2), p293-315, 1975

237.   Griffiths, B. J., Mechanisms of white layer generation with reference to machining and deformation processes, Transactions of the ASME: Series F, Journal of Tribology:, 109, (3), p525-530, 1987

2.12   Tables

Condition of Rail Surface	Traction Coefficient
Dry Rail (Clean)	0.25-0.30
Dry Rail (with Sand)	0.25-0.33
Wet Rail (Clean)	0.18-0.2
Wet Rail (with Sand)	0.22-0.25
Greasy Rail	0.15-0.18
Moisture on Rail	0.09-0.15
Sleet on Rail	0.15
Sleet on Rail (with sand)	0.2
Light Snow on Rail	0.1
Light Snow on Rail (with Sand)	0.15
Wet Leaves on Rail	0.07

Table 2.1: Values of traction coefficient for wheel/rail contact (after Stolarski and Tobe[47])

2.13   Figures
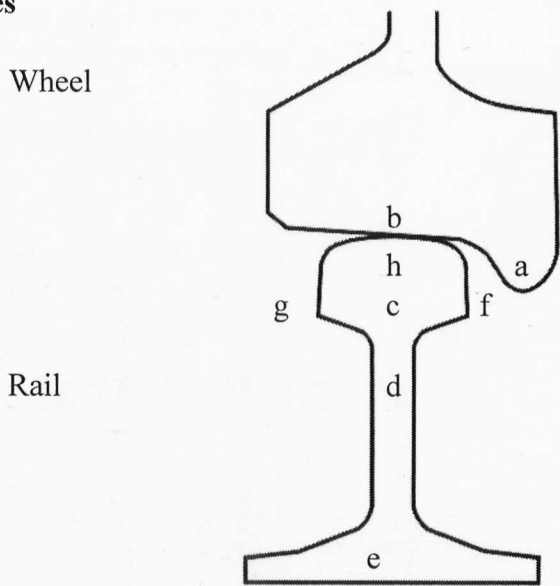
Wheel

Rail

Figure 2.1: Wheel and rail profiles showing nomenclature to describe the parts of each. a) Wheel flange, b) wheel tread c) head of rail, d) web, e) foot, f) gauge corner/side, g) field or cess corner/side, h) crown.

Tangent Track

Shallow Left
Hand Curve

Sharp Curve
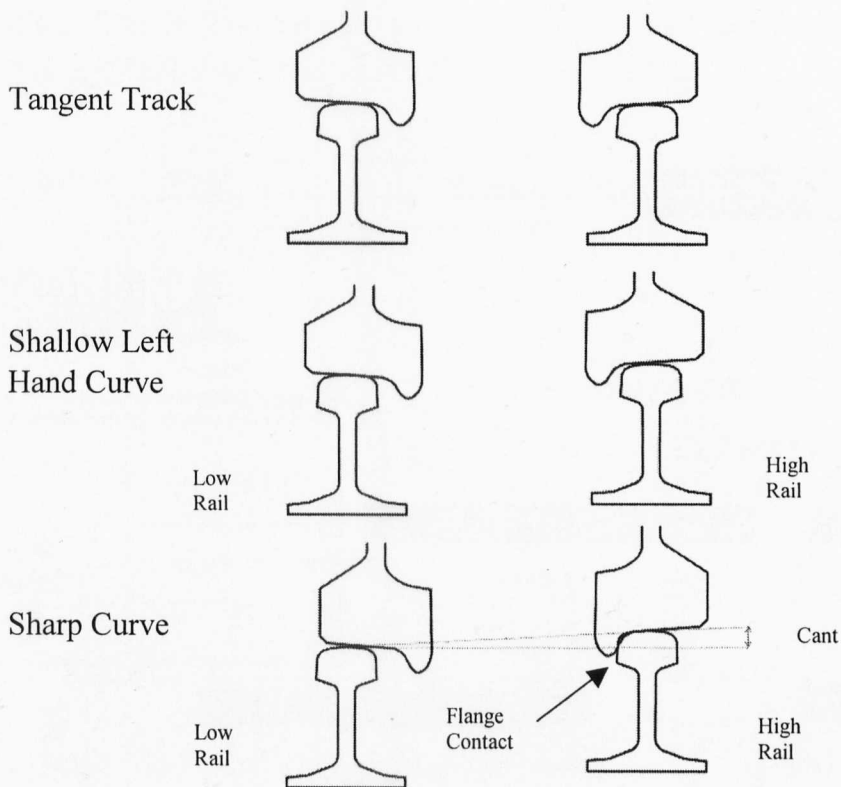
Figure 2.2: Steering of conical wheels on tangent and curved track (after Wickens[10])
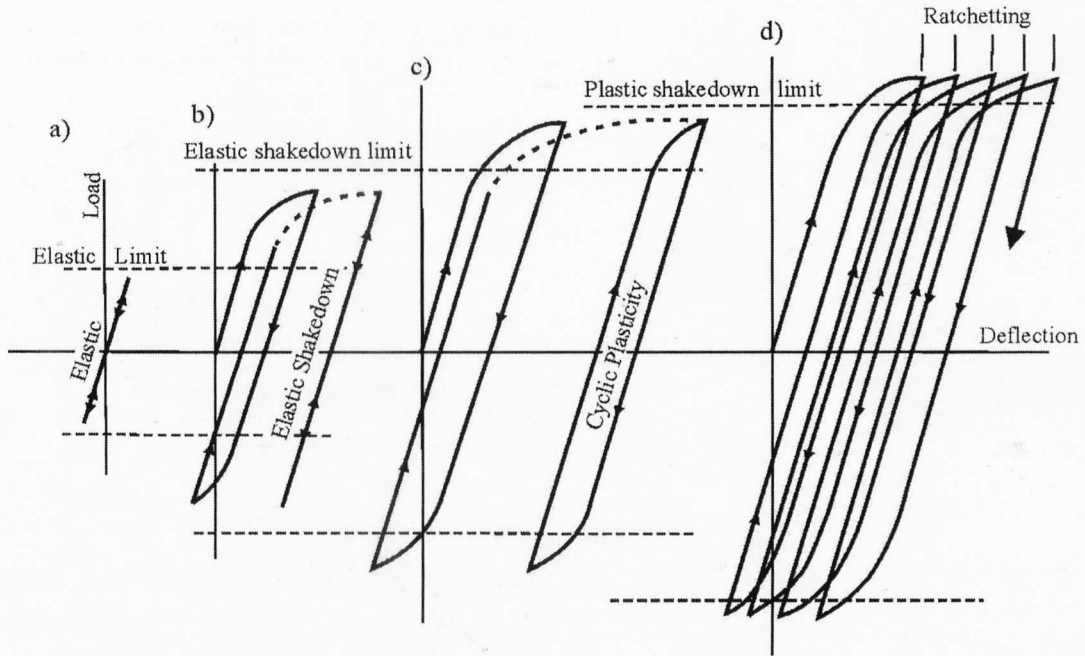
Figure 2.3: The response of a material to cyclic loading. a) Elastic response up to elastic limit. b) Elastic Shakedown. Plastic response above elastic limit but residual stresses develop giving shakedown to an elastic state. c) Plastic Shakedown. If the load is above elastic shakedown limit deformation occurs as closed cycles of plastic strain d) Ratchetting. If the load is above the plastic shakedown limit then accumulation of uniaxial plastic strain or ratchetting. (after Kapoor and Johnson[17])
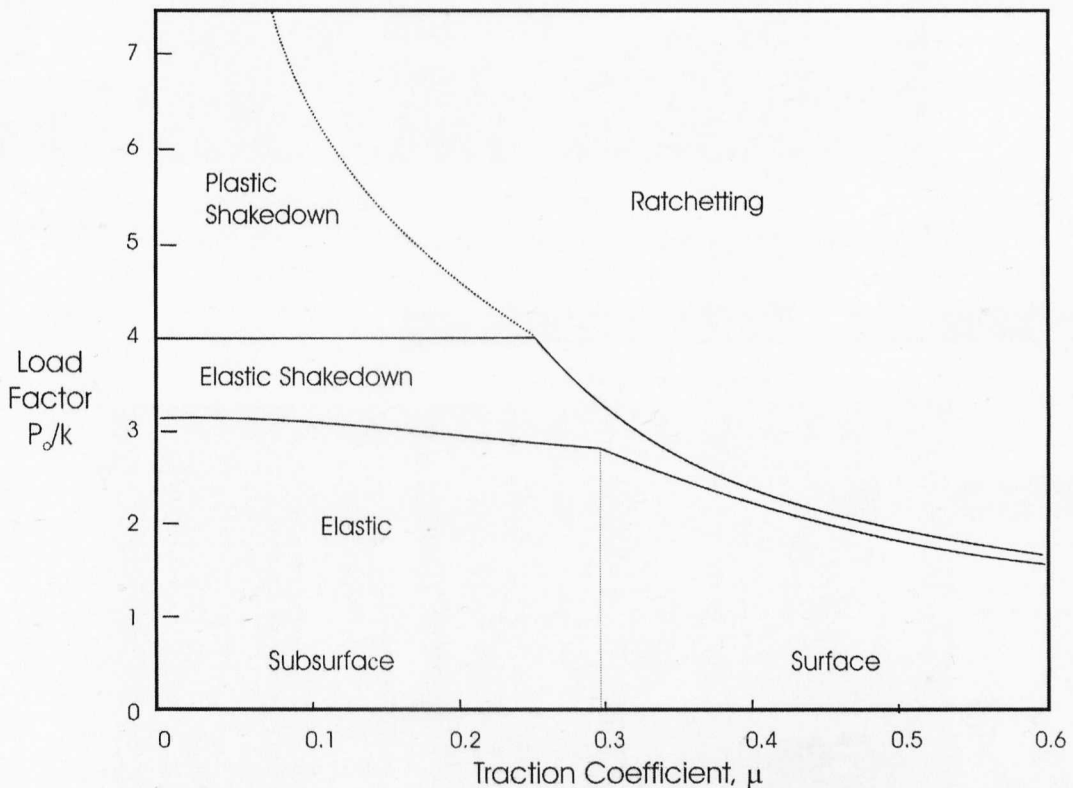
Figure 2.4: Shakedown map for a rail steel under line contact (after Bower and Johnson[21])
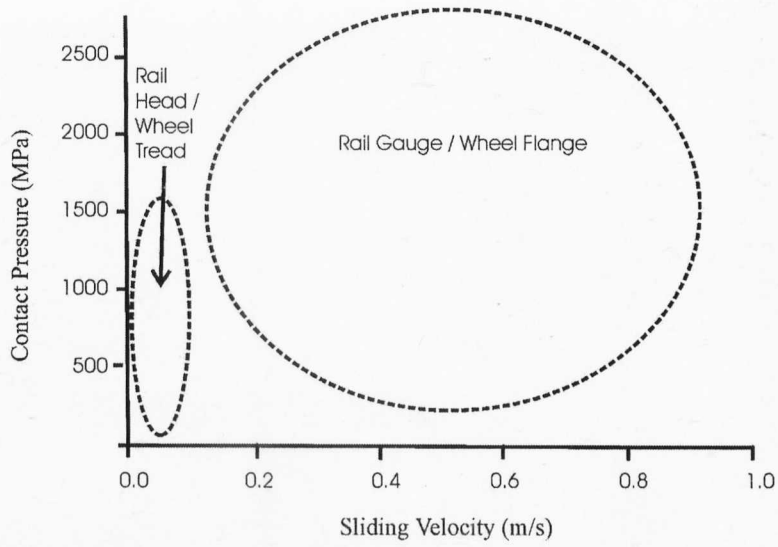
Figure 2.5: Typical operating conditions of wheel on rail (after Olofsson and Telliskivi[31])
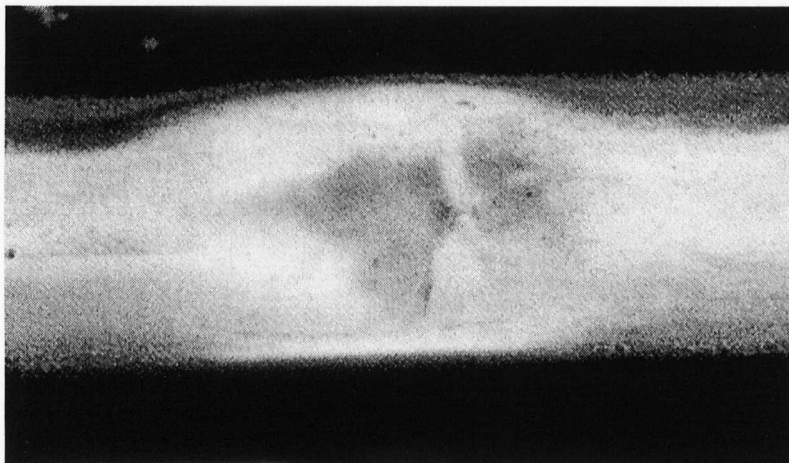
Figure 2.6: Surface view of a squat on a railhead (after Railtrack[77])
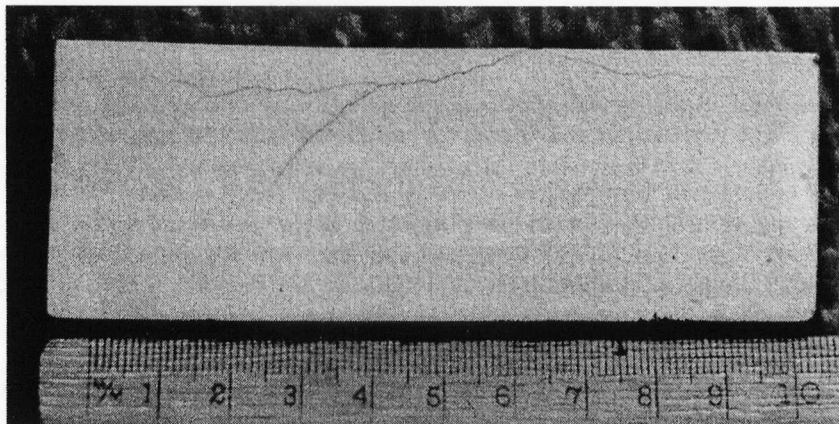
Figure 2.7: transverse section of a squat (after Railtrack[77])
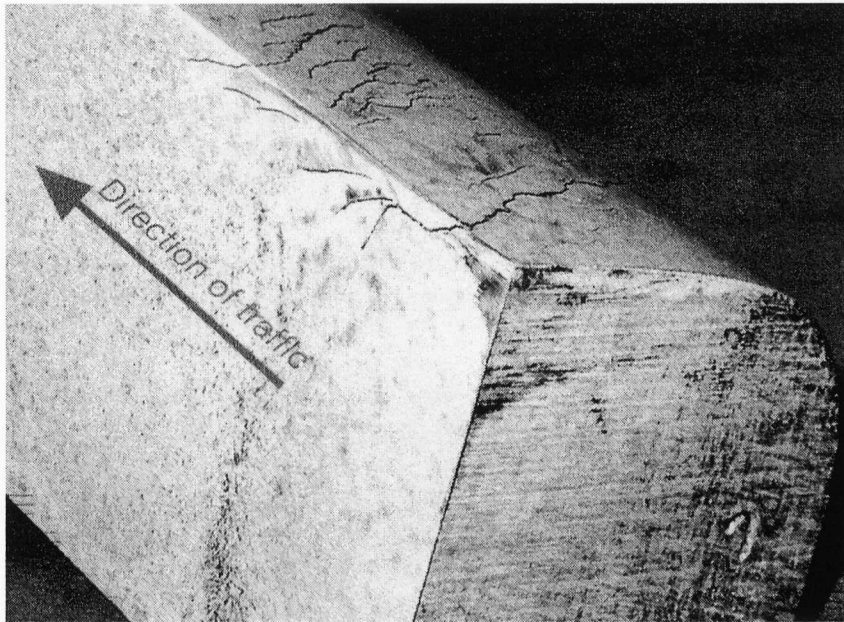
Figure 2.8: Longitudinal section of a head check (after Railtrack[77])
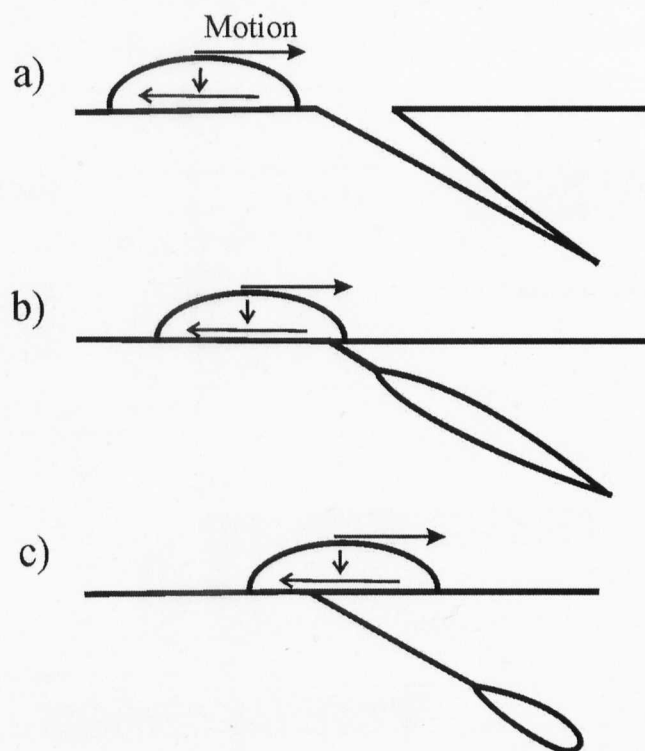
Figure 2.9: Fluid pressure mechanism. a) as contact approaches the crack opens allowing fluid to fill it. b) as contact moves above crack it seals the mouth trapping fluid. c) fluid forced towards the crack tip where pressure transmits tensile stress and allows crack faces to move against each other (after Bower[95]).
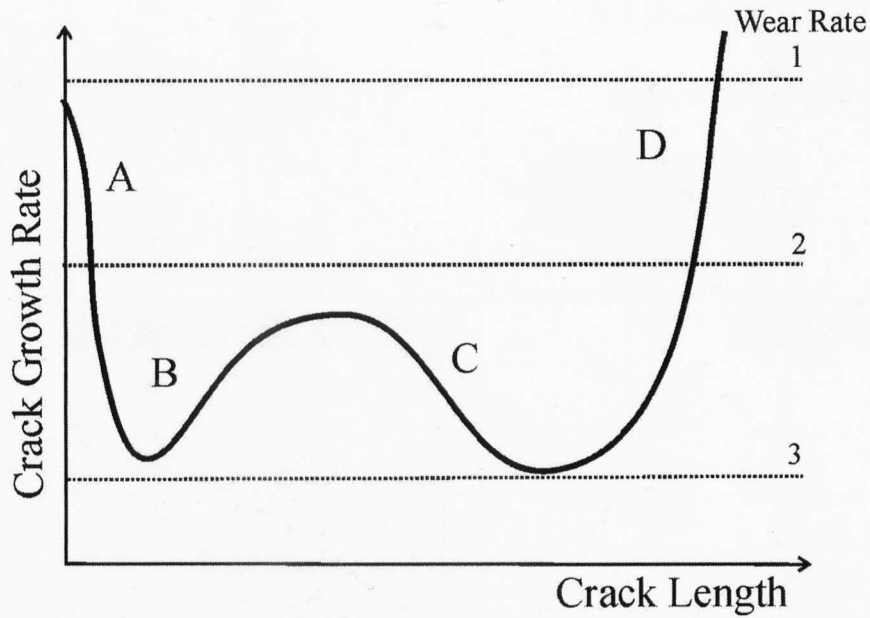
Figure 2.10: Crack growth rate and wear (after Ringsberg[97]). Growth by ratchetting/LCF (A), Fluid entrapment (B), crack away remote from contact stress field (C), tensile bulk stresses (D). Wear rate: 1 is high to remove cracks before they initiate, 2 is medium and removes them before propagation and 3 is to low to have any effect on crack formation.
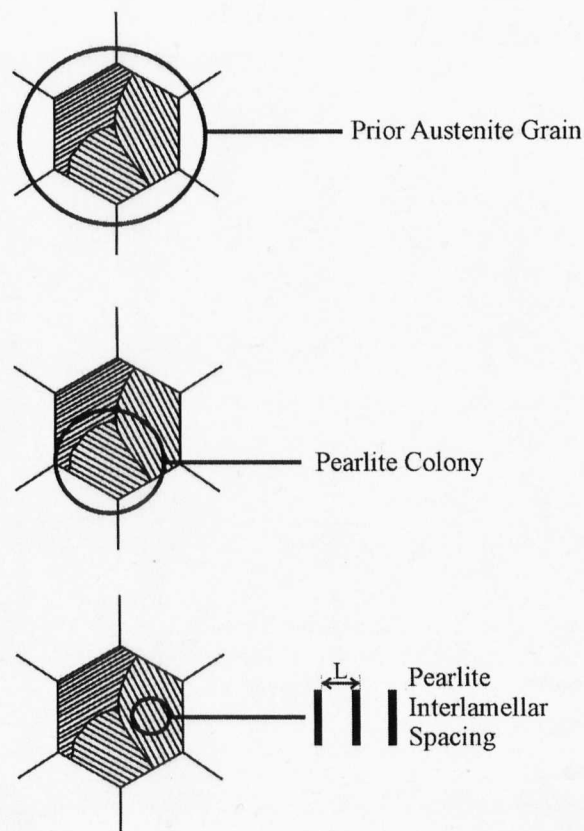
Figure 2.11: Features of a pearlitic microstructure. a) Prior austenite grain size. b) Pearlite colony size. c) Pearlite interlamellar spacing (after Fletcher[6]).
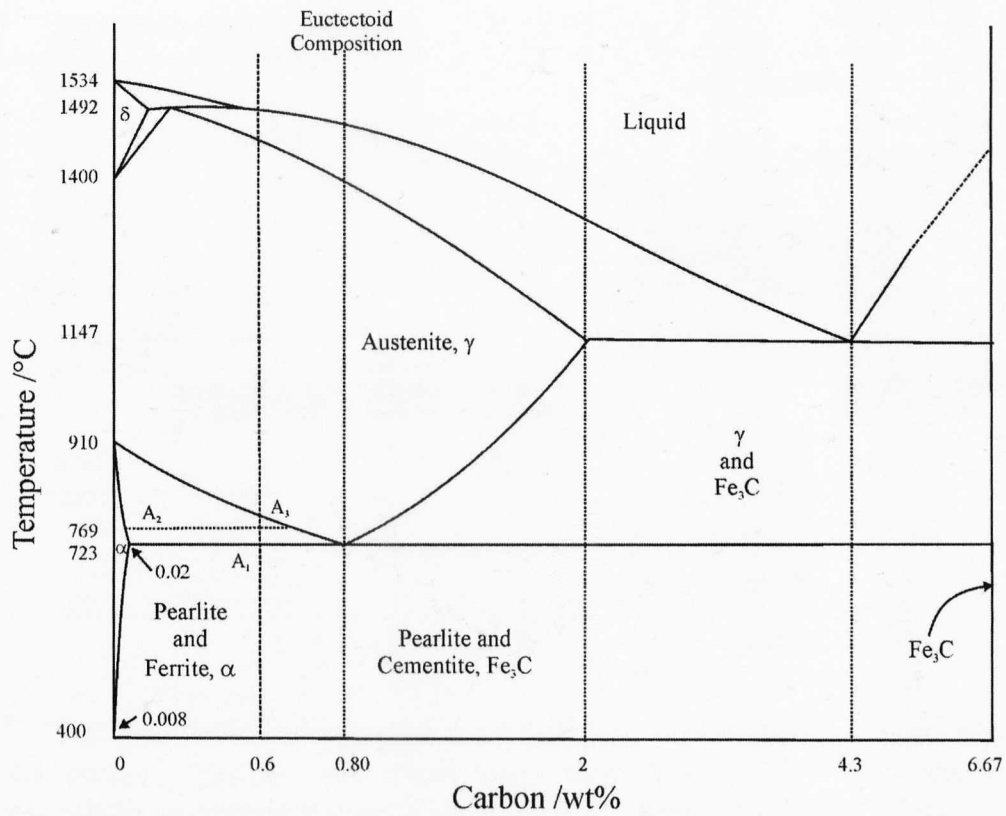
Figure 2.12: Iron - Iron carbide phase diagram (after Honeycombe and Bhadeshia[114])

Proeutectoid Ferrite   Pearlite
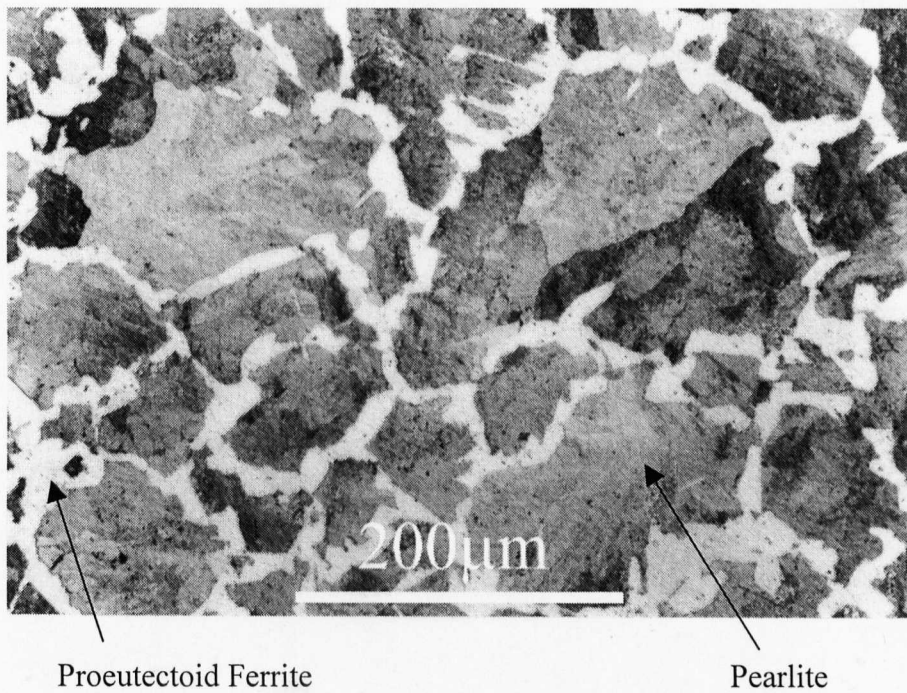
Figure 2.13: Typical pearlitic structure of 220 grade rail (after Cambridge University[115])
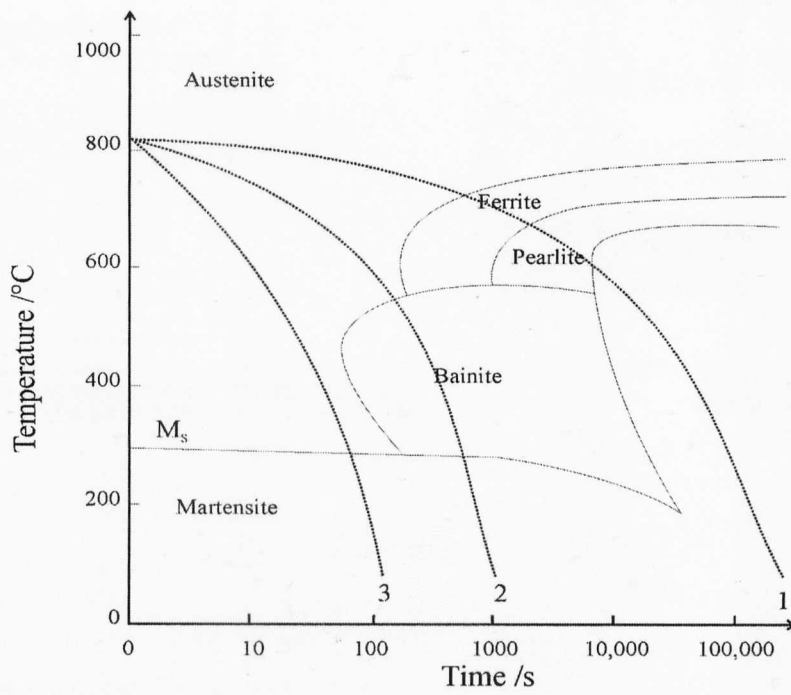
Figure 2.14: Schematic CCT diagram for a rail steel. 1 slow cooling rate (air) resulting in pearlite/ferrite. 2. Medium cooling rate (oil) results in bainite. 2. Fast cooling rate (water quench) results in martensite (after Honeycombe and Bhadeshia[114]).

Figure 2.15: Bainitic steel (after Cambridge University[115])

Figure 2.16: Martensitic steel (after Cambridge University[115])
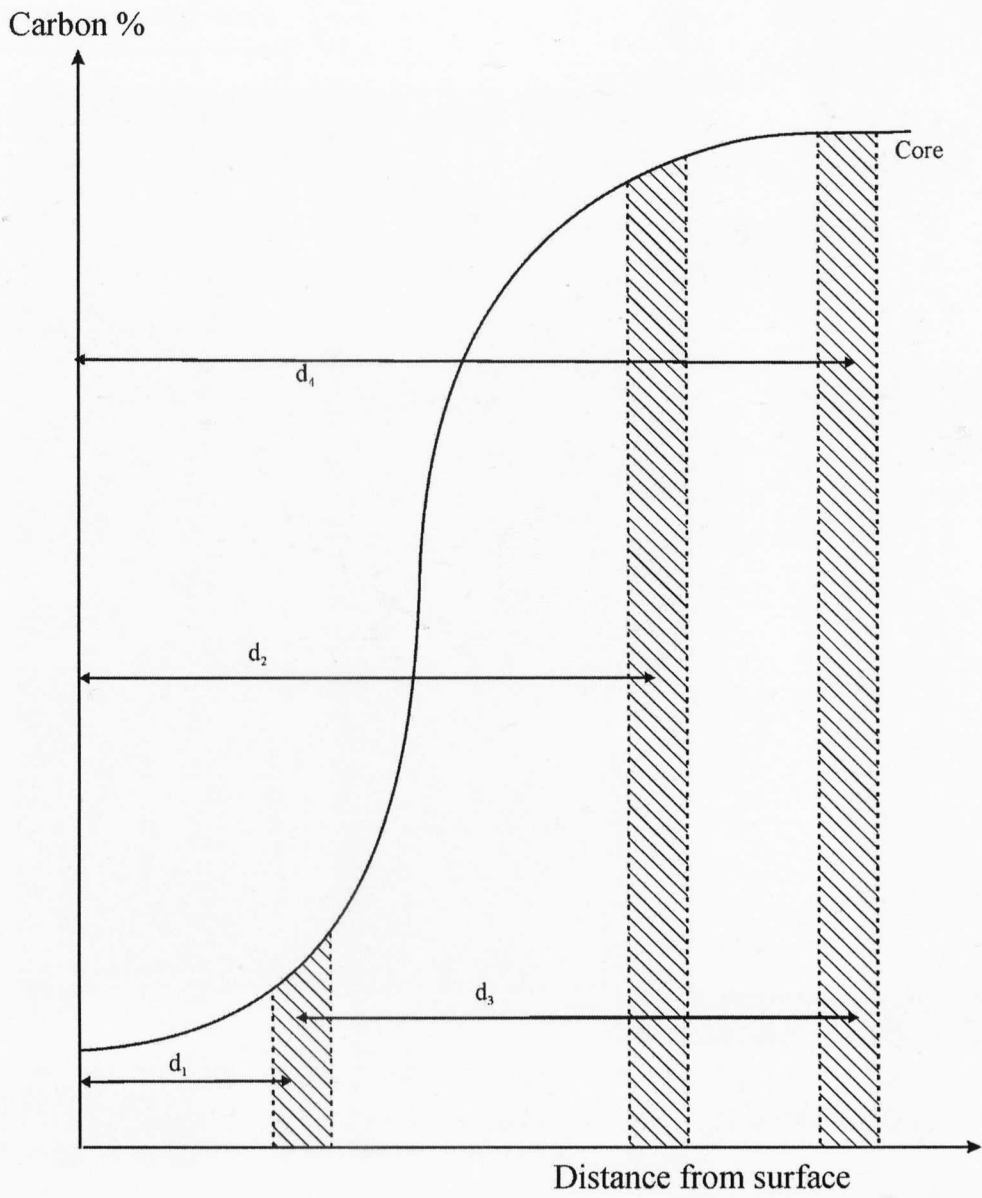
Figure 2.17: Graph of Carbon Content against Depth d_1 = complete, d_2 = functional, d_3 = partial and d_4 = total decarburisation (after BS EN ISO3887[123]).
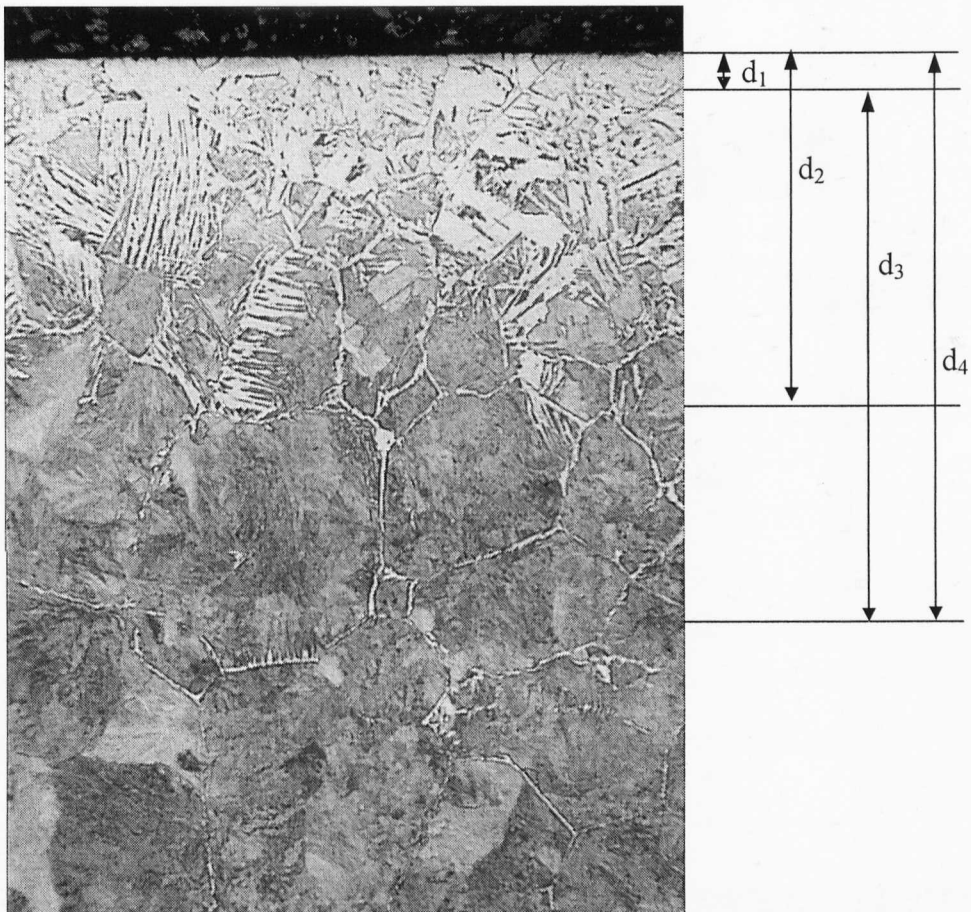
Figure 2.18: Micrographs showing definition of decarburisation: d_1 = complete, d_2 = functional, d_3 = partial and d_1 = total decarburisation (after BS EN ISO3887[123]).
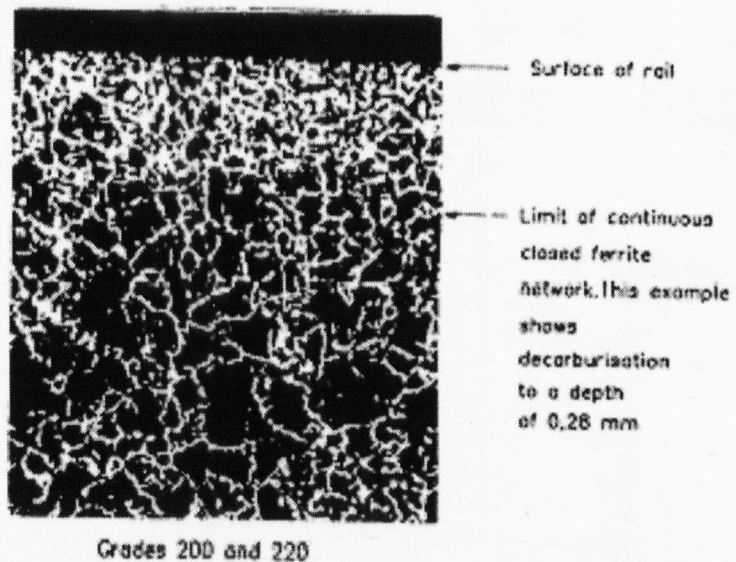
Figure 2.19: Decarburisation on rail steel grades 220 and 240 (after BS EN13674-1[111])
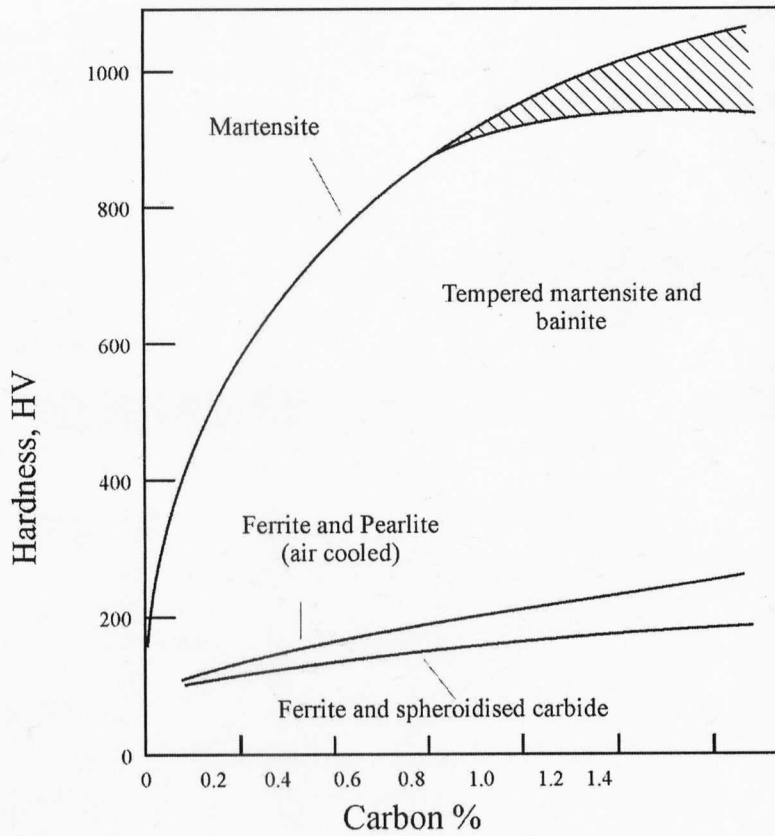
Figure 2.20: Carbon content versus hardness (after Krauss[121])
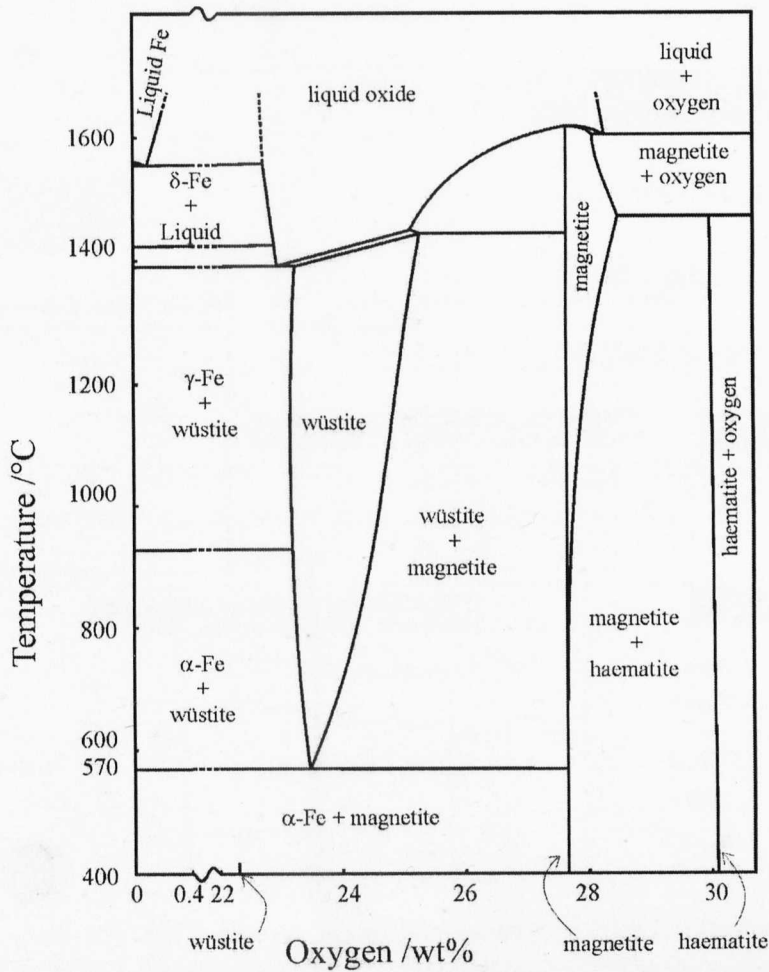
Figure 2.21: Iron - Oxygen Phase Diagram (after Chang and Wei[159])
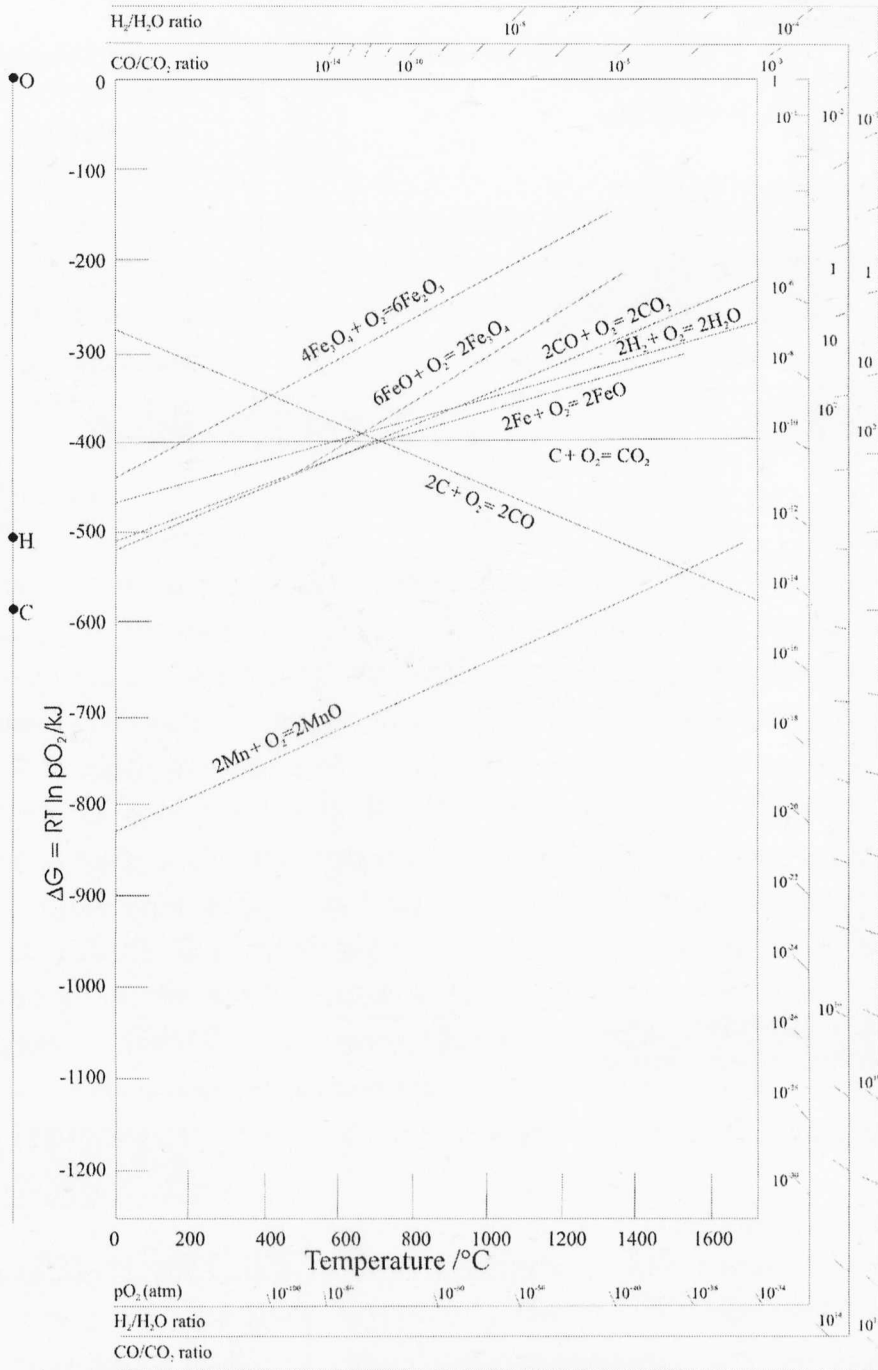
Figure 2.22: Ellingham Diagram, showing Gibbs's free energy of different reactions depending on temperature and partial pressure (After Gaskell[160]).
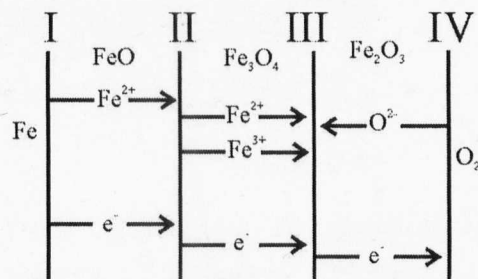
Figure 2.23: Mechanism of Oxidation showing movement of iron ions and electrons from the oxide/metal interface towards the atmosphere and oxygen ions from the surface into the oxide. (after Chang and Wei[159])

Chapter 3: Experimental Procedure

3.1   Introduction

This chapter describes the experimental procedures used in this investigation. This includes the procedure used during rolling/sliding twin disc testing along with other subsidiary techniques such as metallography and surface measurements. A further section is the simulation of the two surface metallurgical features in the laboratory. This chapter begins with details of the materials used in this investigation.

3.2   Materials

The chemical compositions along with the mechanical properties of the materials used in this investigation are given in table 3.1. Several of the ultimate tensile strength (UTS) figures have been calculated from the hardness values using the conversion tables in the Metals Handbook[1]; this is only an approximation not a measurement of the UTS. The rail steel, RA, which was machined into rail discs and used in this investigation, has been manufactured in accordance with BS EN 13674-1[2] grade 220 by Corus Rail at Workington, Cumbria, UK; the method of production has been described in section 2.8.3. An optical micrograph is given in figure 3.1 with the light phase being ferrite and the darker phase pearlite. The contrast between the pearlite colonies is due to the difference in the orientation of the pearlite lamellae in relation to the sectioning plane; this is demonstrated by the SEM micrograph, figure 3.2 showing the lamellar structure of pearlite. In this micrograph the light phase is cementite while the dark phase is ferrite. The method of measurement of the prior austenite grain size and pearlite interlamellar spacing are described in section 3.4.

Two wheel steels were used in this investigation; their chemical composition and mechanical properties are given in table 3.1. The first was WA which was used in a previous investigation by Fletcher[3] and was cut from a new wheel that had not been in service; the microstructure is illustrated in figure 3.3. This wheel steel was used for the two initial twin disc tests due to problems with the supply and machining of the second wheel steel which was used for all other tests. This second wheel steel, WB, was provided in the form of hot rolled bar but has the same composition and properties as wheels made to BS 5892-3 grade R3[4]; a micrograph is provided in figure 3.4. The only significant difference between these two steels is in the prior austenite grain size, which is much greater for WB than WA.

To see if Birks' model was applicable to the decarburisation of rail, initial tests were carried out on small samples of rail steel. The material used for these preliminary experiments was a section of spare rail found in the laboratory and produced in accordance with British Standard BS11 normal grade[5]; this is the predecessor of the European standard BS EN 13674-1 grade 220 rail[2]. The chemical composition and mechanical

properties of the two rail materials were almost identical and in accordance with the relevant specifications.

The final material, whose data is given in table 3.1, is BU9 which was a bainitic back up roll steel used in a previous investigation[6]. This material was used to investigate the formation of white etching layer because of the high content of Cr, Mo and V which are not present in grade 220 steel (RA); this test is discussed further in section 6.3.2.

The samples used in twin disc testing were machined into the correct disc profile, a schematic of which is given in figure 3.5a. The discs had an external diameter of 47mm and a contact width of 10mm; the central bore was 19mm with a keyway cut into one face of the disc to allow mounting on the twin disc testing machine. The running surface was ground so that it had an average roughness, R_a, of less than 1μm. The rail disc samples were cut from the railhead in the manner shown in figure 3.5b so that the axis of rotation of the disc was parallel to the longitudinal axes of the rail.

3.3   SUROS Testing

Rolling contact fatigue has been tested in the laboratory using the Sheffield University rolling sliding (SUROS) test machine. The heart of the machine is a Colchester Mascot 1600 lathe modified by Garnham and Beynon[7] with further development by Fletcher and Beynon[8]. The main modification is a second AC motor fixed to the lathe bed allowing two discs to be rolled against each other, with the lathe providing the drive mechanism for the upper sample. A normal load of up to 29kN can be applied between the discs by a hydraulic piston; a schematic of the machine is shown in figure 3.6, while a picture is given in figure 3.7. The two discs were mounted and bolted on to the end of the shafts from the motors; the AC motor shaft has a universal joint to allow the discs to be brought into contact. The central axes of the shafts and hence the discs were parallel to each other, thus ensuring a line contact between them.

The machine is controlled using a National Instruments[®] Labview[®] version 4 program on a Pentium[®] 100MHz computer, which also data logs the speed, number of revolutions and torque of each shaft, along with the load applied between the discs. The required conditions of the test along with dimensions of the disc were programmed into the computer; which also calculates the contact load, using equation 2.4, which was controlled manually during the test. For all tests the maximum Hertzian contact pressure used was 1500MPa and was maintained within 2% of the mean value. The rail disc was rotated at a nominal speed of 400rpm with the wheel disc rotating slightly faster to give the required slip that is programmed into the computer. Instantaneous slip (S_i) is calculated as a percentage using equation 3.1[8] and is a measure of the relative movement of one disc in relation to the other. The value used during this investigation was −1% where the negative sign indicates that the wheel disc is driving the rail disc. The computer typically maintains

this value so that 75% of the total number of cycles were within ±0.08 of its nominal percentage value but over a test these are cancelled out resulting in a range of ±0.02 for the cumulative slip.

$$S_i(\%) = 200 \left(\frac{R_{Top}V_{Top} - R_{Bottom}V_{Bottom}}{R_{Top}V_{Top} + R_{Bottom}V_{Bottom}} \right) \qquad (3.1)$$

where R_{Top} and R_{Bottom} are the radius of the discs in millimetres and V_{Top}, V_{Bottom} are the speed of the discs in rpm. The computer and AC motor control alters the speed of the wheel disc to maintain the required percentage slip.

The screw in figure 3.8 was used to prevent the discs contacting while a steady speed was attained. Once the discs reached a constant speed the torque and load settings were calibrated to zero. The discs were then brought together by loosening the screw with subsequent application of the load. The computer recorded the conditions of the test (torque, contact load) against the number of cycles.

Water lubrication was commonly used during the test because of the requirement of a fluid for cracks to grow by fluid assistance, as discussed in section 2.5. This fluid was distilled water applied to the discs at 1 drip per second from the nozzle shown in figure 3.8 by gravity. Several tests were carried out without lubrication, with both discs being cooled using compressed air.

Detection of cracks on the rail discs was carried out using an Elotest® B1 eddy current detector, with a probe scanned across the contact width of the disc using a servomotor controlled by the computer. This crack detector was used in two ways: the first was during the test while the rail disc was rotating at 400rpm, the second was with the rail disc being rotated by hand to locate the cracks after the test. The eddy current probe was fixed in a cradle at the front of machine, figure 3.8, and positioned using a feeler gauge so that it was 0.2mm away from the rail disc. For detection during the test the lateral position of the probe was zeroed to the left edge of the rail disc using a micrometer gauge; movement was controlled by the computer in 1mm steps every second. The results from the probe were displayed on an oscilloscope, figure 3.9, with a time base such that the position of the cracks was in the same position on the display every cycle. The eddy current probe was calibrated using disc R1(45) to set the gain required on the detector. This was a disc machined with a slot at 45° to the surface, the length of the crack is unknown but remained constant so that every time the machine was set up, the detector was calibrated to monitor cracks with the same sensitivity. The eddy current detector did not allow accurate lengths of cracks to be monitored but gave an indication of their length and rate of growth.

The initial series of tests on decarburised and normal samples used the eddy current detector so that they were stopped once cracks had grown large enough to trigger a gate.

Subsequent tests were continued until the number of cycles was the same as a disc without decarburisation that was run until the gate was triggered. The test series on WEL was conducted in a similar manner, with several short tests carried out to examine the behaviour of cracks at short times.

Before the tests both wheel and rail discs were measured using a digital Vernier calliper (±0.01mm) to give a diameter and contact width. The discs were then cleaned in methanol using an ultrasonic bath for 5 minutes, dried using hot air and weighed on a self calibrating top pan balance (±0.0001g). They were then held using a paper tissue and placed on to the appropriate shaft on SUROS. After the test the discs were again cleaned, weighed and measured to allow calculation of the wear of the discs. The rail disc was then replaced on the lathe shaft, rotated by hand and examined using the eddy current probe to find the location of the longest crack, which was then marked to allow sectioning to occur. This required the detector to be changed to a higher sensitivity.

The machining of the discs resulted in a surface that had a surface roughness, R_a, that was nominally less than 1 micron though this was checked using a Taylor Hobson Surtronic® 3. This is a surface profilometer which uses a stylus to trace the surface of the disc; because of the curvature of the disc this was only possible perpendicular to the circumference. The results of the Surtronic are plotted on a graph with depth of the surface in microns against the distance scanned in millimetres, which was typically 4mm. The results were data logged to a computer using a software package, Taylor Hobson Talyprofile for Windows 2.0®, which also calculated the R_a value. The discs were measured again after the test with at least 12 profiles being taken of each disc and a mean calculated.

Before the test the discs were also checked using a Taylor Hobson Talyrond® 100 for accuracy of the circumference of the disc and also concentricity with the inner bore. This equipment consists of a turntable with a stylus used to measure the deviation of the surface with the results being plotted on carbon paper. Figure 3.10a shows the surface profile of a disc alongside the circle, which it would follow if it were perfectly round; this trace shows that the disc was slightly oval. The graduations on the carbon paper allow the deviation to be measured using equation 3.2[9].

$$\text{True measurement (µm)} = \frac{\text{measurement on paper (mm)} \times \text{magnification}}{1000} \quad (3.2)$$

The deviation in figure 3.10a from the circle taken with a magnification of ×1000 is measured on the carbon paper as ±1.5mm, resulting in the disc varying in real life by 1.5µm. The surface profile was also measured after the SUROS test to see the changes occurring during it.

Concentricity was measured by setting the machine up to give the surface profile on the outer running surface, then moving the stylus on to the bore with the equipment measuring the difference giving a plot illustrated in figure 3.10b. This figure shows that the inner and outer diameters were concentric; this trace was carried out with a magnification of ×200. If either parameter was markedly different from the ideal then the disc was rejected because it may have caused damage to the SUROS machine.

3.4   Metallography

After the test the rail and wheel discs had their surface examined optically with photographs of interesting features taken using the macro function on a digital camera and also using an optical microscope at low magnification. The disc was then sectioned either side of the feature of interest using a Buehler Abrasimet 3, with the segment then being cut using a Buehler Accutom. This allowed accurate cutting at a measured distance (±0.1mm) so that discs were sectioned just in front of the location of the greatest depth of the crack.

After sectioning the samples were mounted in conducting Bakelite with the sample number engraved on the back. The samples were then ground using SiC papers starting with 120 grit and working progressively through 240, 400, 800 and 1200, each paper having a finer grit. After each grinding paper the samples were cleaned with running water to remove any particles before proceeding on to the next paper. Once the samples had been ground using 1200 paper they were cleaned using a soap called Teepol and cotton wool, then washed in propan-1-ol and dried using hot air. The samples were then polished using diamond paste starting with 6µm and progressing to 1µm and finally ¼µm; the samples were cleaned between each stage. After polishing the samples were etched using 1% Nital (nitric acid diluted in methanol) for 5 seconds and washed with copious amounts of water, dried and rinsed in propan-1-ol.

The etched samples were observed in the optical microscope with photomicrographs being taken of features of interest. Several different microscopes have been used but the magnification is always recorded allowing scale bars to be drawn on all photomicrographs. Several of the samples have also been examined using a scanning electron microscope (SEM), usually a Cambridge Instruments Camscan 100 but use was also made of a JEOL 6400. Both SEMs allow images to be taken and both incorporate an energy dispersive spectroscopy (EDS) instrument that determines the composition of phases to be found. This has not been used for quantitative analysis, instead qualitatively to find which elements were present. The EDS in the JEOL was used without a filter to allow the detection of elements with low atomic numbers, especially oxygen.

The effect of the heat treatment on the microstructure of the rail disc was studied by examining the prior austenite grain size and the interlamellar spacing of the pearlite. The prior austenite grain size was measured using an optical micrograph to obtain the mean

linear intercept of proeutectoid ferrite that formed on the prior austenite grain boundaries. Lines were drawn randomly on each micrograph so that at least 100 intersections were measured for each sample. The mean true interlamellar spacing was determined from the mean random spacing by the method proposed by Underwood[10]. The mean true spacing, $\bar{S}_t$, is related to the mean random spacing, $\bar{S}_r$, by equation 3.3 which was found from experimental results[11].

$$\bar{S}_t = \frac{\bar{S}_r}{2} \tag{3.3}$$

The mean random spacing was measured by using the number of intersections of cementite on a circle drawn randomly on a photomicrograph, figure 3.2. With the length of the line known, dividing it by the number of intersections gives the mean random interlamellar spacing.

The depth of decarburisation was measured on the photomicrograph using lineal analysis (section 2.9.2.1). This involved traverses drawn on the micrographs (figure 3.11) of the sample at increasing depth with the relative amounts of ferrite and pearlite measured on each line using a ruler (±0.5mm). Knowing how much carbon is in the bulk steel by chemical analysis, wt%C = 0.57%, it is possible to find how much carbon is present in the pearlite by studying the relative amounts of pearlite and ferrite in the bulk of the steel. Ferrite has a maximum solubility of 0.008wt%C at room temperature; a factor Z can be calculated using equation 3.4 relating the amount of carbon in cementite to the amount in pearlite.

$$Z = \frac{\%Pearlite \times 6.67}{100 \times wt\%C - \%\alpha \times 0.008} \tag{3.4}$$

Examination of the photomicrographs from the bulk of the initial heat treated samples has been found to give a Z factor of between 11.52 and 11.73. This variation gives an error in the carbon content of ±0.01% of each sample. Using the value of Z found for each individual sample allows the carbon content at each depth to be calculated using equation 3.5.

$$wt\%C = \frac{\%Pearlite \times 6.67}{100Z} + \frac{\%\alpha \times 0.008}{100} \tag{3.5}$$

The depth of decarburisation used has been defined as 98% of the bulk carbon content of the disc or 0.549wt%C for grade 220. This was found to be the average carbon content, ±1%, at the depth of the continuous ferrite network as determined by observation, which is the depth defined in BS EN13674-1 for rail[2].

The shear strain of the deformed surface, γ, was measured using the angle, δ, between the flow lines of the sample and a line drawn perpendicular to the surface, figure 3.12, using a protractor ($\pm0.5°$) on the photomicrograph and calculated using equation 3.6[12].

$$\gamma = \tan \delta \qquad\qquad\qquad\qquad (3.6)$$

This equation is only valid if the original microstructure is perpendicular to the surface[13, 14]. The ferrite of the original surface can be seen to be randomly orientated, figure 3.11. After deformation the flow lines of the material are orientated to the surface, figure 3.12; most noticeably with the ferrite being at a similar angle whatever the original orientation, the error therefore from using this equation will be minimal. The strain was measured on micrographs at different depths below the surface with at least five measurements taken at each depth using at least four micrographs for each sample with an average taken.

The macrohardness of the samples was measured using a Vickers hardness tester with a load of 100kg and at least 12 values taken per sample with a mean calculated. The bulk hardness of the samples was also measured using microhardness to allow the effect of the heat treatment on the mechanical properties of the sample to be examined. The equipment used was a Mitutoyo HM microhardness tester with a load of 100g and a Vickers diamond pyramid indenter. Microhardness traverses of the surface of the discs were carried out to measure the hardness of the surface to assess how much strain hardening had occurred during the test; these were spaced at least five times the length of the diagonal of the indentation[15]. The depth of the traverse depended on the number of cycles and depth of deformation of the sample but was to a sufficient extent that all of the deformation was measured, with several readings of the bulk values being recorded at the end of each traverse. The depth of decarburisation was also measured using micro hardness traverses from the surface of the sample into the bulk and defined as 98% of the bulk value.

3.5   Decarburisation Heat Treatments

To examine the Birks model of decarburisation a series of initial experiments were carried out. The initial samples were approximately 15mm square and were polished using 800 grit SiC paper so that the sides were smooth and parallel. Before heat treatment the samples were measured using a digital Vernier calliper (±0.01mm) and cleaned in alcohol, with any subsequent handling being carried out using rubber gloves. Heat treatment was carried out in the centre of a chamber furnace; a chamber furnace was used because the heat treatment of discs for rolling/sliding testing requires more space than would have been available in a tube furnace. This allowed knowledge of the furnace to be gained, including mapping the variation of temperature with position. After the samples were placed within the furnace it was programmed to heat up to the hold temperature at its maximum rate; once this was attained the samples were held for the required length of time. After the desired time the samples were removed with tongs and placed on a furnace brick on the laboratory floor

and left to air cool to room temperature. The temperature of the furnace was measured using a K type thermocouple embedded within a hole drilled in a reference sample heated at the same time as the other samples. The temperature was recorded manually every minute during the heat up, every 30 minutes once the hold temperature had been attained and every 20 seconds during cooling. The thermocouple was calibrated using a thermal bath held at a temperature of 750°C, which had been previously calibrated with an error of ±4°C; the temperature profile results were corrected accordingly.

After cooling, the thick oxide scale was removed from the sample by mechanical means, including grinding, with the dimensions of the samples measured to allow the oxidation constant to be determined. The samples were sectioned through the centre and prepared for metallographic investigation. The etched samples were observed under an optical microscope with images taken of the microstructure. The depth of decarburisation was measured using the technique described in section 3.4.

After the initial series of tests, rail discs were heat treated to create a decarburised layer using the same furnace for various times at 1000°C. The oxidation and depth of decarburisation results are discussed in chapter 4 in relation to the Birks model. The central bore and keyway had to be protected from oxidation otherwise the fit on the shafts could be slack and result in uneven running on SUROS. For the majority of tests with short heat treatment durations the central bore was filled with silica wool and then sealed with a refractory cement called Sairset®. After heat treatment this was removed by soaking in water and removed by hand. The discs were machined to remove the oxide layer from the running surface and to ensure that the internal and external diameters were concentric. The sample with the greatest heat treatment time also had the internal diameter opened out with a collar fitted because of excessive oxidation giving a loose fit on the shaft. At the same time as the discs, small reference samples were also heat treated for the same time to allow the depth of decarburisation to be determined because the running surface of the disc would be altered by twin disc testing along with the loss of diameter due to grinding before subsurface examination could take place. The diameter of the discs was measured before and after the heat treatment and also after machining. This allowed the diameter loss during machining to be measured with the appropriate depth subtracted from the depth of decarburisation. The variation in oxidation means that errors of ±0.01mm on the diameter resulted in ±5μm on the depth of decarburisation. The temperature of the furnace during the heat treatment of the discs was measured in similar way to that during the initial tests with a thermocouple embedded within a spare disc.

3.6   Simulation of White Etching Layer

The simulation of white etching layer has been carried out in two different ways, the first used a spot welder to locally heat the surface of the disc, while the second used the SUROS machine in a novel way to deform the surface of the rail disc

3.6.1.1   Spot Welding

A schematic of the spot welder is given in figure 3.13; this is a transformer with an on/off switch that applies a potential difference across two copper electrodes. For initial tests these electrodes were two copper bars of 25mm diameter with a hole in the end of each in which a thinner bar of diameter 6.3mm was fastened with a screw; the end of these bars were ground to a point. A sample approximately 11mm thick was fastened using the mole grips between the electrodes. Welding times of between 1 and 4 seconds were used; several samples had overlapping spot welds to create a larger area of WEL. Tests have also been carried out using a steel plate 1.5mm thick placed between the top electrode and the sample to prevent damage to the surface of the sample. The initial samples were sectioned for metallographic examination to be carried out.

The spot welding of discs required a new electrode that allowed the discs to be positioned accurately below the top electrode such that the spot weld was in the centre of the running surface. This electrode was a copper bar machined down to 18.75mm on to which the disc was slid; a plate was clamped between the disc and the top electrode. Spot weld durations of between 0.5s and 2 seconds have been used. The longer test durations resulted in the plate being welded to the surface of the disc and hence the disc required machining to give a smooth surface before the SUROS test. The discs were visually examined after machining along with surface roughness measurements and showed no obvious marks of spot welding before the SUROS rolling/sliding test was carried out.

3.6.2   Sliding White Etching Layer

The twin disc testing machine was used to create the second white etching layer by sliding one disc against another. The rail and wheel discs were measured, cleaned and mounted in the usual way, as described in section 3.3. The disc on the lathe was then rotated in the opposite direction to that during a rolling/sliding test, i.e. clockwise rather than anticlockwise, so that it was in the same direction as the AC motor. The sliding was conducted for 5 seconds for the majority of the tests; one test was conducted for 30 seconds to examine the formation mechanism of the WEL. The settings used for the test were the same as those programmed into the computer and AC motor controller for a rolling/sliding tests, with a contact pressure of 1500MPa and a slip ratio of −1%. In the majority of cases the wheel disc used to create the WEL had been used in a previous investigation and machined down to give a fresh running surface. The rolling/sliding SUROS test was conducted with a new wheel disc. In contrast the rail disc was not ground but used with the surface created by sliding. To reverse the plastic deformation of the rail disc several tests were conducted with the rail disc on the AC motor shaft and the wheel disc on the lathe shaft.

3.7   References

1.   Krauss, G., Microstructure, processing and properties of steels, in: Vol 1: Properties and Selection: Iron, Steel and High Performance Alloys, Metals Handbook, American Society of Metals, USA, p126-139, 1996

2.   BS EN 13674-1, Railway Track Applications - Rail - Part 1: Flat Bottom Symmetrical Rails 46kg/m and Above, British Standards Institution, London, UK, 2003

3.   Fletcher, D. I., The influence of lubrication on the fatigue of pearlitic rail steel, PhD Thesis, Department of Mechanical Engineering, University of Sheffield, UK, 1999

4.   BS 5892-3, Railway Rolling Stock Material - Specification for Monobloc Wheels for Traction and Trailing Stock, British Standards Institution, London, UK, 1992

5.   BS11, Specification for Railway Rails, British Standards Institute, London, 1985

6.   Frolish, M. F. and Beynon, J. H., Design criteria for rolling contact fatigue resistance in back up rolls, Ironmaking and Steelmaking, 31, (4), p300-304, 2004

7.   Garnham, J. E. and Beynon, J. H., The early detection of rolling - sliding contact fatigue cracks, Wear, 144, (1-2), p103-116, 1991

8.   Fletcher, D. I. and Beynon, J. H., Development of a machine for closely controlled rolling contact fatigue and wear testing, Journal of Testing and Evaluation, 28, (4), p267-275, 2000

9.   Dagnall, H., Let's Talk Roundness, 2nd Ed., Rank Taylor Hobson Limited, Leicester, UK, 1984

10.   Underwood, E. E., Quantitative Stereology, 1st Ed., Addison-Wesley Publishing Company, Reading, Massachusetts, 1970

11.   Gensamer, M., Pearsall, E. B. and Pellini, W. S., The tensile properties of pearlite, bainite and spheroidite, Transactions of American Society for Metals, 30, p983, 1942

12.   Tyfour, W. R., Interaction between wear and rolling contact fatigue in pearlitic rail steels, PhD Thesis, Department of Engineering, University of Leicester, 1995

13.   Moore, M. A. and Douthwaite, R. M., Plastic deformation below worn surfaces, Metallurgical Transactions, 7A, p1833, 1976

14.   Hill, R., The Mathematical Theory of Plasticity, 1st Ed., Clarendon Press, Oxford, UK, 1950

15.   BS EN ISO 6507-1, Metallic Materials - Vickers Hardness Test: Part 1 - Test Method, British Standards Institution, London, UK, 1998

3.8 Tables

	RA	BS11	WA[1]	WB	BU9
Chemical Composition /wt%					
C	0.56	0.57	0.55	0.53	0.42
Si	0.16	0.17	0.27	0.31	0.36
Mn	1.10	1.08	0.75	0.83	0.61
Cr	0.03	0.03	0.26	0.25	2.95
V	<0.01	<0.01	<0.01	<0.01	0.10
Ni	<0.01	<0.01	0.20	0.05	0.17
Mo	<0.01	<0.01	0.08	<0.02	0.35
S	0.025	0.036	0.018	0.010	0.024
P	0.019	0.029	0.011	0.019	0.024
Fe	Remainder	Remainder	Remainder	Remainder	Remainder
Mechanical Properties					
UTS /MPa	863[2]	869[2]	906	910[2]	
Yield Strength /MPa		442[1]	573[3]		
Hardness /HV(100kg)	245	237	272[5]	257[5]	444
Elongation/%		17.8[1]	14		

Table 3.1: Composition and mechanical properties of materials used. 1. Data from D.I. Fletcher (WA =WH268)[3], 2. UTS values from Vickers hardness testing values using comparison chart in Metals Handbook[1], 3. 0.2% Proof Stress. RA=BSEN13674-1(2003) grade 220[2], BS11(1985)[5], WB = BS5892-3(1992) grade R3[4].

3.9 Figures

Figure 3.1: Rail disc material RA
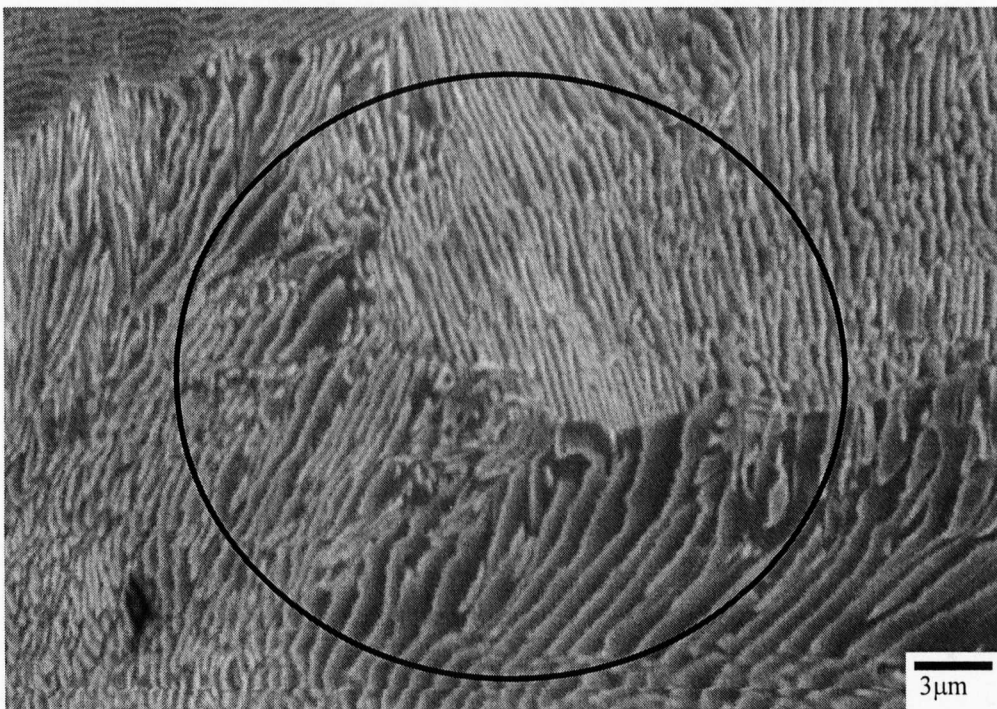
Figure 3.2: Scanning electron microscopy of rail material RA, demonstrating pearlite interlamellar spacing, The circle is used to measure the random interlamellar spacing.
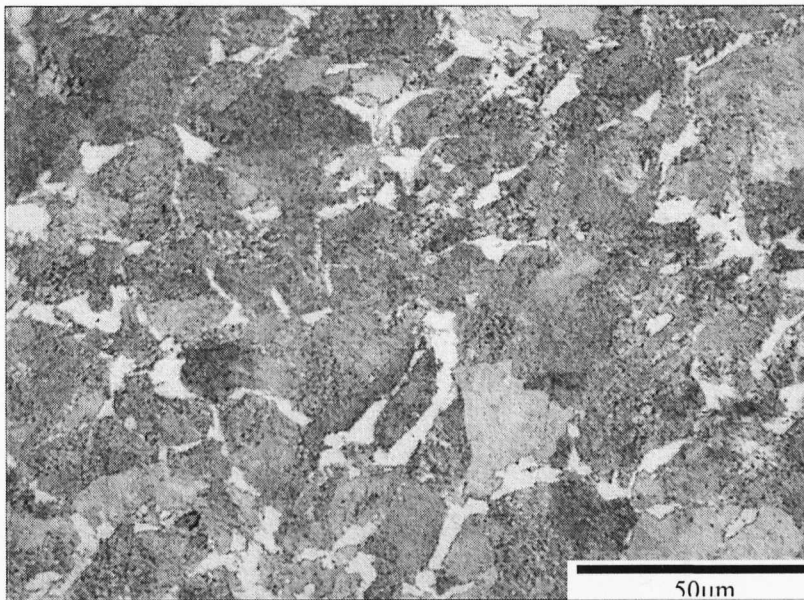
Figure 3.3: Wheel disc WA
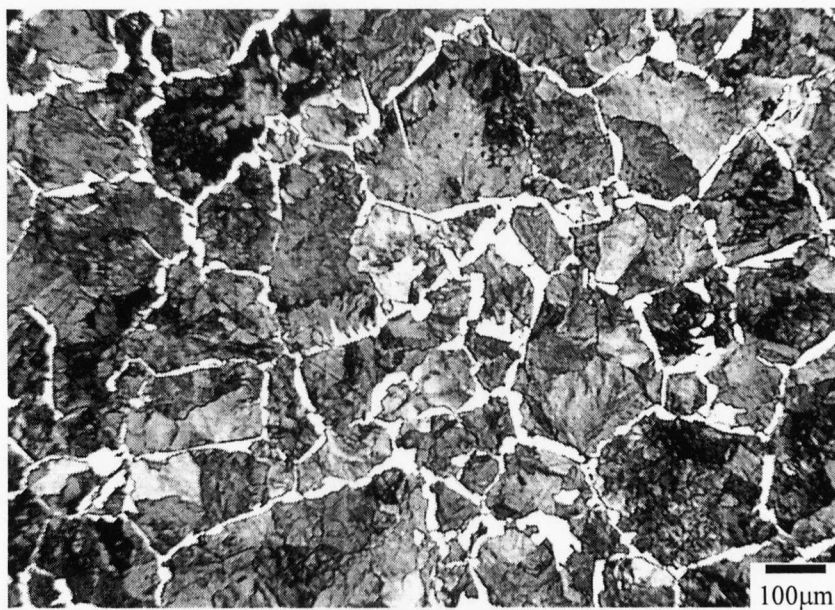
Figure 3.4: Wheel disc material WB

a)   b)
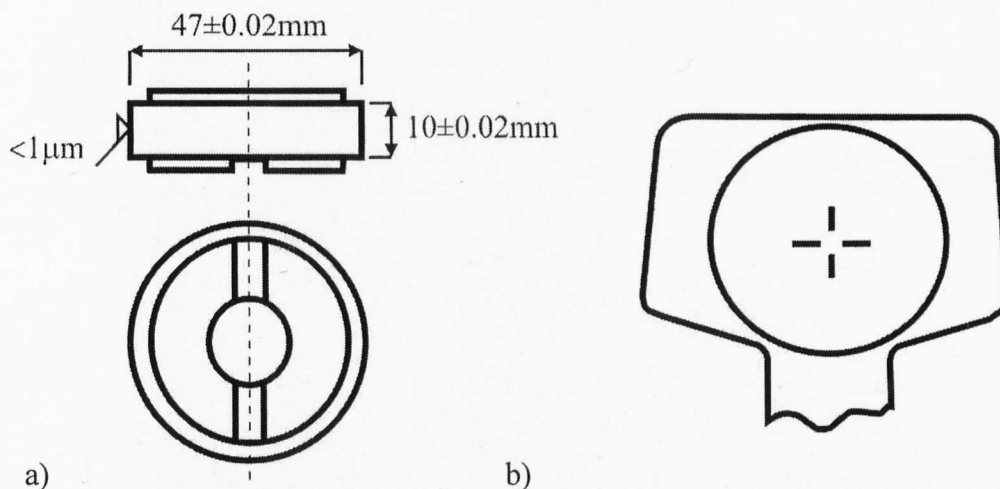
Figure 3.5: Diagram of discs. a) Discs cut from railhead. b) Dimensions of discs. (after Fletcher [3])
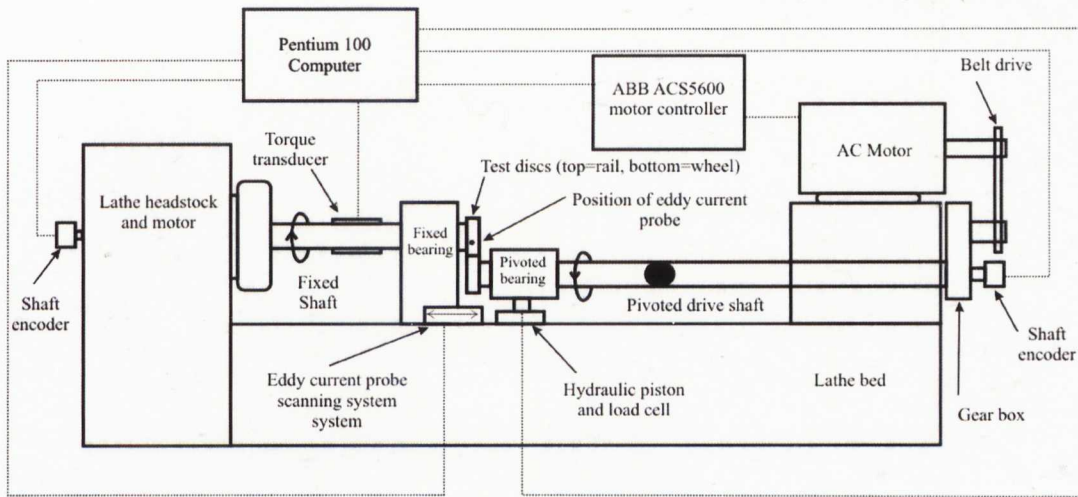
Figure 3.6: Schematic of the SUROS testing machine (after Fletcher [3])
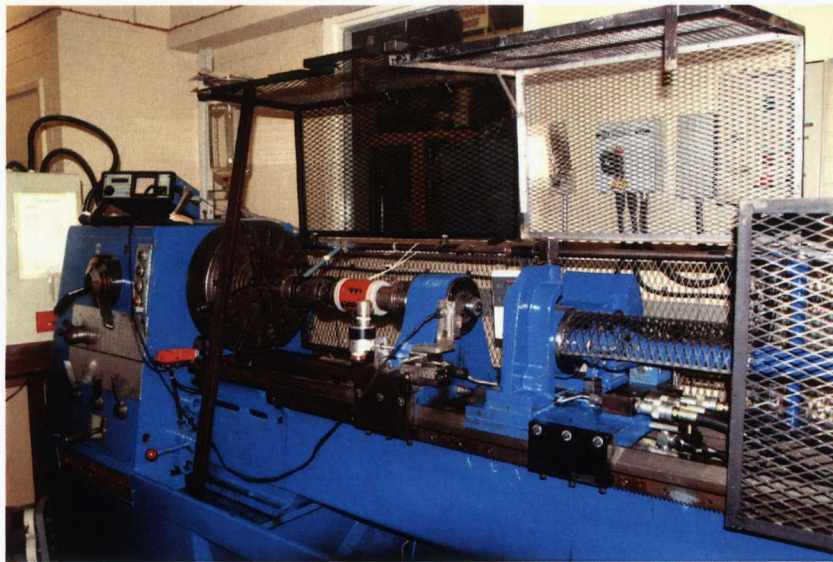
Figure 3.7 : SUROS twin disc testing machine
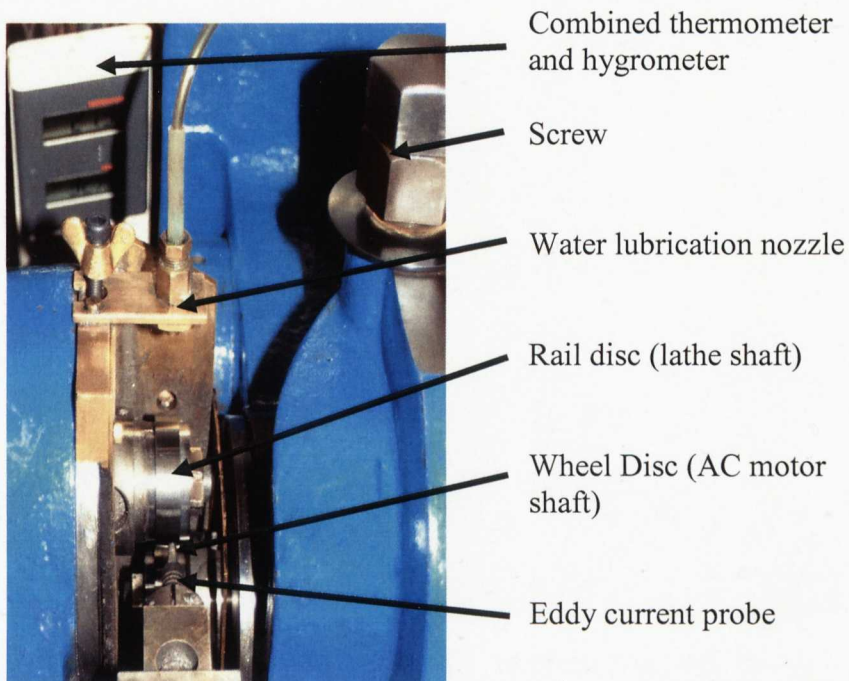
Figure 3.8: Photograph of discs mounted on SUROS machine

Figure 3.9: Eddy current analyser, The peak indicates the presence of the machined slot in the calibration disc.

a)   b)

Figure 3.10: a) Surface profile of rail disc RA01 before test, b) Concentricity profile of rail disc RA08 before test

100μm
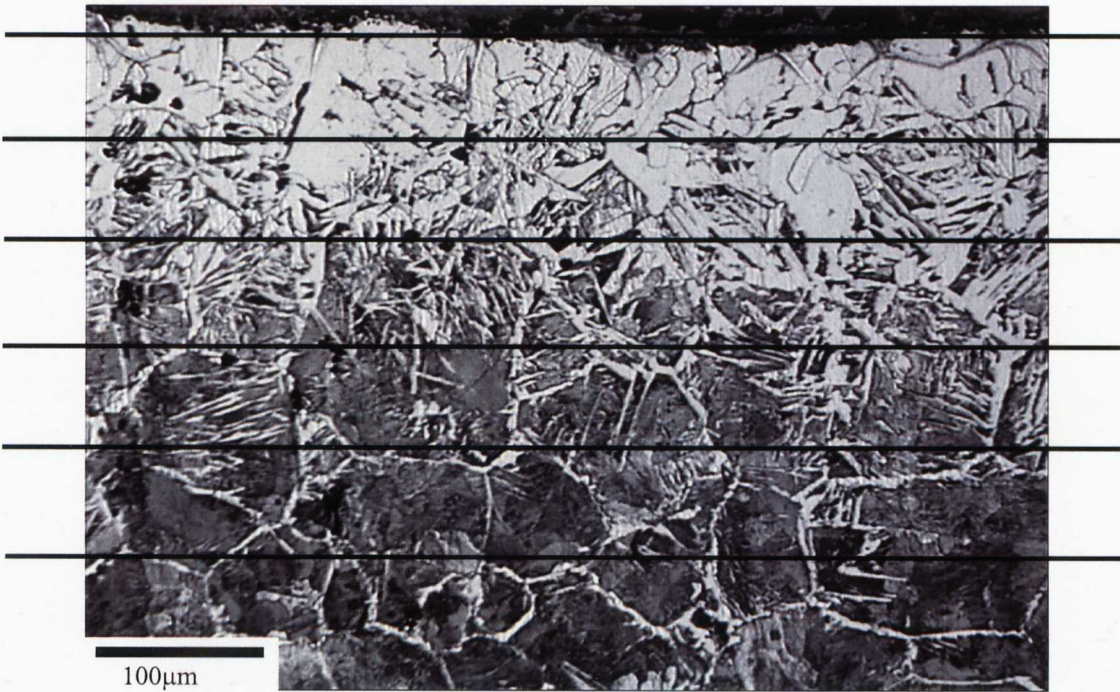
Figure 3.11: Decarburised surface of sample DE03 showing traverses used to measure the depth of decarburisation. The white phase is ferrite and the dark constituent is pearlite.
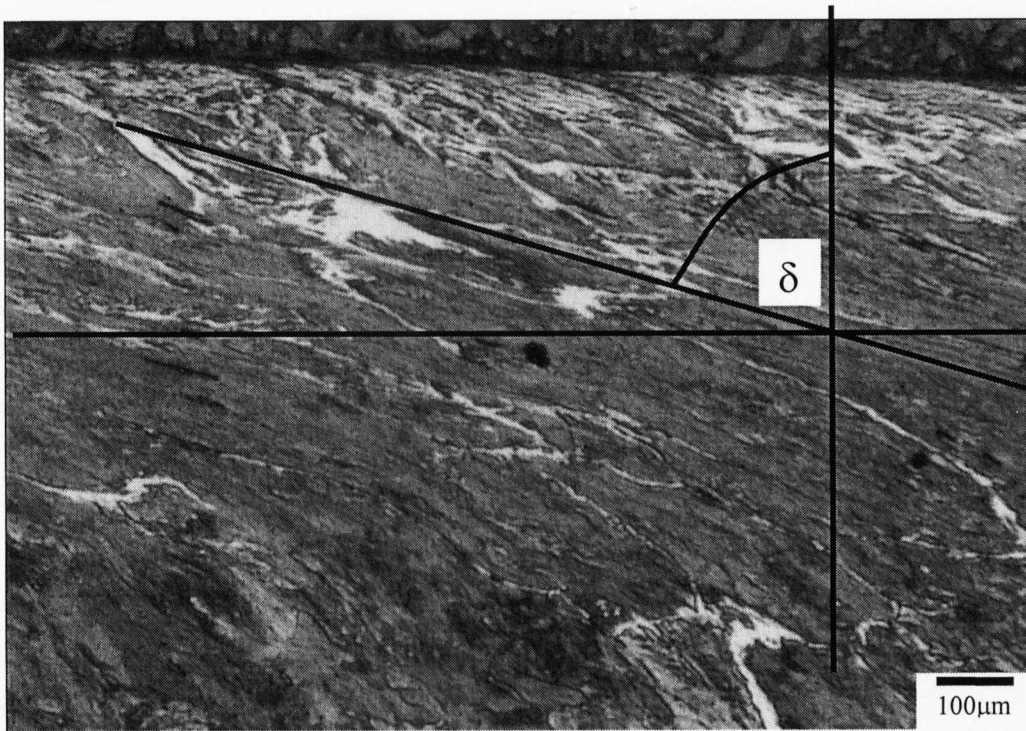
Figure 3.12: Measurement of shear strain by measuring the angle between (after Tyfour [12])
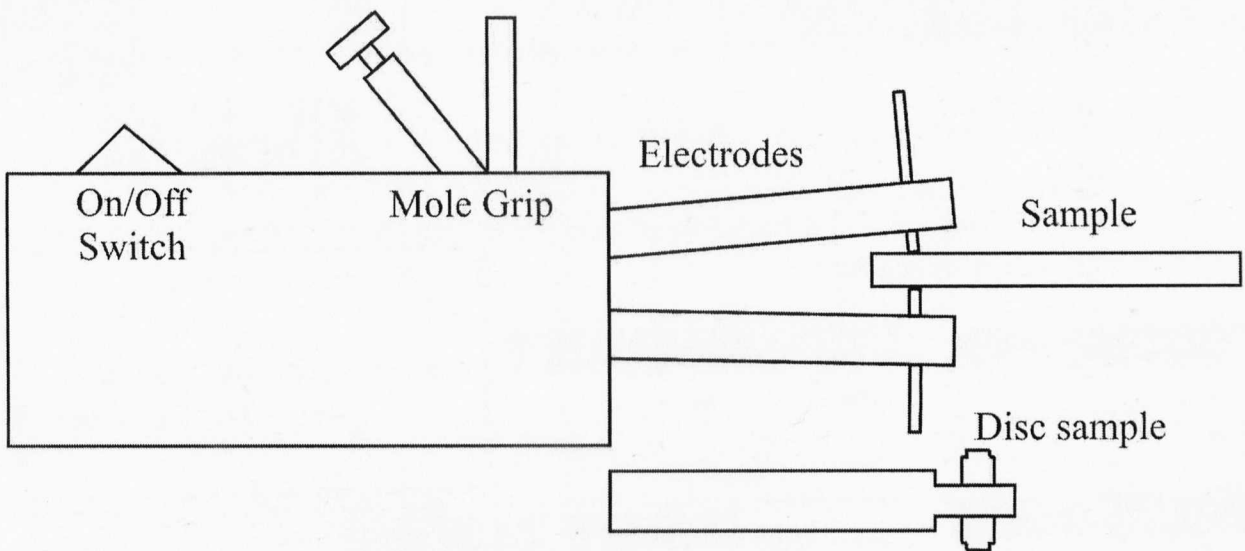
Figure 3.13: Schematic of the spot welder used to create WEL on rail discs

Chapter 4: Decarburisation and White Etching Layer Models

4.1   Introduction

This section describes an investigation into the formation mechanisms of the surface metallurgical features. With regard to decarburisation this chapter discusses the diffusion model developed by Birks and presents results from the initial work on the heat treatment of rail steel. The second section is a simple diffusion model for the formation of white etching layer on the surface of rail. This has been carried out to study whether it is possible to create WEL while the rail is in service through diffusion of carbon.

4.2   Diffusion Modelling of Decarburisation
4.2.1   Birks Model

As discussed in the literature survey, chapter 2, the most likely rate determining step in the formation of a decarburised layer is the diffusion of carbon through the steel to the surface. A model of decarburisation has been developed by Birks and co-workers[1-4] for the bulk diffusion of carbon (of concentration C) in austenite based on Fick's second law of diffusion, equation 4.1, for a semi-infinite slab:

$$\frac{\partial C}{\partial t} = D\frac{\partial^2 C}{\partial x^2} \qquad \text{for } x > X \qquad (4.1)$$

when solved for the following boundary conditions, shown schematically in figure 4.1:

1) Initial (time, t=0) uniform carbon concentration (C_O) through the thickness (x)
   i.e. $C = C_o$ for $x > 0$; $t = 0$
2) The carbon concentration at the metal/scale interface (C_S) is constant
   i.e. $C = C_s$ for $x = 0$; $t > 0$

With these conditions and at constant temperature Fick's second law can be solved as equation 4.2[5].

$$\frac{C_O - C}{C_O - C_S} = \frac{\text{erfc}\left[x/2\sqrt{Dt}\right]}{\text{erfc}\left[\sqrt{k_C/2D}\right]} \qquad (4.2)$$

where k_C is the parabolic oxidation constant, see below (equation 4.4) and D is the diffusion coefficient from the Arrhenius relationship, see below (equation 4.7).

The function "erfc" is the complementary error function, which is related to the error function by equation 4.3. The error function is an integration of an exponential with the values commonly tabulated, see Stroud[6].

$$\text{erfc}(x) = 1 - \text{erf}(x) \tag{4.3}$$

The parabolic oxidation constant, k_c, is derived from the thickness of metal loss, M, after time t by equation 4.4:

$$k_c = \frac{M^2}{2t} \tag{4.4}$$

To correct the decarburisation equation for removal of metal from the surface by oxidation, the depth of decarburisation, d, is modified to give equation 4.5.

$$d = x - M = x - \sqrt{2k_c t} \tag{4.5}$$

Rearranging equation 4.2 and combining with equation 4.5 allows the depth of decarburisation from the final metal surface to be calculated using equation 4.6.

$$d = 2\sqrt{Dt} \cdot \text{erfc}^{-1}\left[\left(\frac{C_O - C}{C_O - C_S}\right)\text{erfc}\sqrt{\frac{k_c}{2D}}\right] - \sqrt{2k_c t} \tag{4.6}$$

This model assumes that decarburisation only occurs in the austenite phase. Even though diffusion of carbon in ferrite is faster than in austenite, the amount transported is negligible due to its very low solubility (0.008wt%C at room temperature). Therefore during heat treatment the majority of decarburisation occurs when the steel is in the austenite phase field. The pearlite constituent transforms to austenite at the A_1 temperature (723°C) but ferrite transforms only on reaching the A_3 temperature. For pure iron A_3 is at 910°C but for steel the temperature varies with alloying content, especially carbon as seen in the iron-carbon phase diagram, figure 2.12[7]. The diffusion model (equation 4.6) assumes that carbon reacts with gaseous oxygen, which is readily available, at the surface to form carbon monoxide; which escapes through a porous scale. The model only considers bulk diffusion and takes no account of diffusion shortcuts such as grain boundaries; it also takes no account of the oxygen potential of the atmosphere.

A similar model for decarburisation of austenite in air has been developed by Kucera *et al.*[8] from the same solution to Fick's second law that does not incorporate the oxidation term found in Birks model. Other diffusion models have also been developed for decarburisation in ferrite by Nomura *et al.*[9] and by Pyyry and Kettunen[10] for a mixture of ferrite and austenite.

The Arrhenius equation, equation 4.7, describes the diffusion behaviour of materials at any temperature, T, where D_o is the pre-exponential term of the diffusion coefficient and Q is the activation energy; both of these are constant for a given composition of material, R is the molar gas constant and equal to 8.314J.mol^{-1}K^{-1} [5].

$$D = D_o \exp\left(\frac{-Q}{RT}\right) \tag{4.7}$$

One factor not taken into account in the Arrhenius equation is that both D_o and Q vary with alloying content. A set of data that has been widely used is quoted by Kucera and Stransky[11] but originally reported by Wells[12] for carbon in austenite is given in equations 4.8 and 4.9; where N_1 is the carbon concentration in atomic percent.

$$\ln D_o = -\left(0.7407 + 0.2680 N_1 + 0.008758 N_1^2\right) \tag{4.8}$$

$$Q = 155.5 - 4.848 N_1 - 0.1944 N_1^2 \quad \text{kJ/mol} \tag{4.9}$$

The effect of other alloying elements on diffusion of carbon in steel has also been studied. One method considers the effect of alloying elements on the activity of carbon, but the effect is not always the same as on diffusion. Roy *et al.*[13] found that increasing the amount of silicon increased the activity but reduced the diffusivity of carbon in steel. It was for this reason that the diffusion interaction coefficient, which is similar to the activity interaction coefficient, was developed by Kucera *et al.*[11, 14], equation 4.10.

$$D_C\left(N_i\right) = D_C\left(Fe\right)\exp\left[\sum_i \beta_C^i N_i\right] \tag{4.10}$$

where $D_C(Fe)$ is the diffusion coefficient of pure iron, N_i is the atomic fraction of the different elements, β_C^i is the diffusion interaction parameter of the element on carbon given by equation 4.11.

$$\beta_C^i = \beta_C^i(1) + \beta_C^i(2)\frac{10^4}{T} \tag{4.11}$$

β_C^i *(1)* and β_C^i *(2)* are constant for each element and found using experimental methods; values are given from several references in table 4.1[8, 11, 15, 16] and T is the temperature in Kelvin.

Decarburisation reduces the carbon content at the surface resulting in a concentration gradient present within the steel, which affects the diffusion coefficient of carbon. In the literature no solution to this problem has been presented. Birks used extrapolated values of diffusion coefficient for 0%C as this value gave the best fit to the observed data[4].

A problem not incorporated into any model is the effect of the thermal cycle to and from the hold temperature, T_a. This can be corrected for by using the Scheil or equivalent time analysis, equation 4.12, which calculates the equivalent length of time that the sample would be at the hold temperature when the sample is actually at a lower temperature[5].

$$t_e = \Delta t \sum_{i=1}^{N} \exp\left[-\frac{Q}{R}\left(\frac{1}{T_i} - \frac{1}{T_a} \right) \right]$$ (4.12)

The heating cycle (up or down) is split into small equal intervals Δt, with each interval at the mean temperature T_i, as shown in figure 4.2. The activation energy, Q, is the same as that used in the Arrhenius equation for diffusion coefficient, which means that the rate controlling mechanism is assumed not to change over this temperature range.

4.2.2   Experimental Procedure

To examine the model a series of heat treatment tests have been carried out on small samples of BS11 rail; the experimental procedure and materials used are given in chapter 3.

4.2.3   Results

The oxidation results, showing the metal loss as depth from the initial surface, of both the initial experiments and the rail discs are shown in table 4.2. The results for the initial tests are plotted in figure 4.3 and for the oxidation of discs figure 4.4 (the initial tests at 1010°C are given for comparison). The oxidation constants were calculated from the gradients of the best-fit lines using equation 4.4 and presented in table 4.2.

The carbon profile for sample 1 (1920s, 1010°C) and sample 5 (20760s, 1010°C) are given in figures 4.5 and 4.6 respectively, these are measured using optical metallography and calculated using equation 3.5. The complex nature of the Birks model meant that the software (Sigma Plot) was unable to fit a curve to the data, therefore a best fit line was drawn by eye and used to find the depth of decarburisation. The higher horizontal line is the bulk carbon content, while the lower one is the definition at 98% of the bulk carbon concentration. Along with the data are two solid lines showing Birks model, equation 4.6; the difference is in the diffusion coefficient used and is discussed later.

The depth of decarburisation results for the preliminary experiments are summarised in table 4.3 for the three temperatures used. Shown on this table is the equivalent time for each temperature from the Scheil analysis. The results for the depth of decarburisation measured by both optical microscopy and micro hardness are shown. The depth of decarburisation is plotted against total time in figures 4.7, 4.8 and 4.9 for temperatures of 910°C, 1010°C and 1125°C respectively. Figure 4.8 shows several results from the model comparing the effect of carbon content and that of the interaction parameter in relation to the alloying content. Figures 4.7 and 4.9 only show the model calculated using a carbon content of 0% and no effect from alloying elements. The depths of decarburisation measured using a micro hardness tester are plotted against time in figure 4.10 for all three temperatures. The results from the decarburisation of the reference samples heat treated at

the same time as the discs are given in table 4.4. Also shown is the slight variation in hold temperature and consequently that in the equivalent time analysis.

Using the experimental data it is possible to calculate the diffusion coefficient by rearranging equation 4.6 to give equation 4.15.

$$D = \frac{\left(d + \sqrt{2k_c t}\right)^2}{4t.\mathrm{erfc}^{-1}\left[\left(\dfrac{C_O - C}{C_O - C_S}\right)\mathrm{erfc}\sqrt{\dfrac{k_c}{2D}}\right]} \tag{4.15}$$

This equation has a diffusion term, D, inside the error function therefore an iterative technique has been used to calculate the diffusion coefficient for each tests result. The average value is then taken for each temperature with the results plotted on an Arrhenius plot, figure 4.11. The line of best fit through the data point gives an Arrhenius equation for the measured diffusion coefficient, equation 4.16. Also plotted are the results for the diffusion coefficient taken from Kucera and Stransky[11] with 0% carbon.

$$D = 4.9 \times 10^{-6} \mathrm{m^2 s^{-1}} \exp\left(\frac{-147864 J}{RT}\right) \tag{4.16}$$

The diffusion coefficient calculated at 1010°C using equation 4.16 is 4.2×10^{-12} $\mathrm{m^2 s^{-1}}$ and was used in equation 4.6 to predict the depth of decarburisation for the heat treatment of the discs. The initial experimental results for all three temperatures, along with those from the heat treatment of the discs are plotted in figure 4.12. The lines in this figure are the adjusted Birks model with the diffusion coefficient calculated using equation 4.16.

4.2.4   Discussion

The results from the Scheil analysis show that the equivalent time is less than 15 minutes for all temperatures. The results for the experiments at 1010°C show a greater equivalent time due to a problem with the furnace during the heat up. This demonstrated how the equivalent time analysis allowed the variation in the thermal cycle between experiments to be accounted for.

The oxidation of the samples, figure 4.3, shows a trend close to that expected under a Wagner law of parabolic oxidation[4]. As the temperature is increased there is an increasing gradient and consequently an increase in the parabolic rate constant (k_c), table 4.2; this fits well with an Arrhenius equation for oxidation, as reported by Birks and Nicholson[2]. The data is in accordance with results quoted in the literature for oxidation of iron alloys; Kubaschewski and Hopkins[17] give a value of $1.7 \times 10^{-11} \mathrm{m^2 s^{-1}}$ for pure iron, whereas for eutectoid steel a value of $2.4 \times 10^{-12} \mathrm{m^2 s^{-1}}$ has been given by Birks and

Nicholson[2]. The calculated value for 1010°C lies in between these results, as would be expected for steel with 0.57% carbon.

The lines of best fit for 1010°C and 1125°C cross at a time of 7000s; the samples at less than this time for the higher temperature show they oxidise less than those at the lower temperature. This is possibly because a different oxide is formed at the higher temperatures; the iron oxygen phase diagram, figure 2.21, does not show a change in the phase formed at this temperature but oxidation at the surface is highly unlikely to be under equilibrium conditions. One possible reason is the presence of silicon within the steel which is likely to alter the oxide formed, resulting in a more protective oxide scale[18]. This may also be the cause of the data not being an exact fit to the straight lines shown in figure 4.3 with a curve to the data that is especially pronounced for the results at 1125°C; this shows that oxidation of steel is a more complex function than the Wagner law predicts[19].

The oxidation of discs at approximately 1000°C, figure 4.4, exhibit a similar trend to the initial samples at 1010°C with a slightly higher gradient that is closer to the 1125°C than the results for 1010°C. Although if the circled result for a disc sample is ignored, the other disc results lie close to the trend line for the initial samples. The results in figures 4.3 and 4.4 show a spread; the reason for this is the method of measuring metal loss of samples. Oxidation is an inhomogeneous process with a large variation in the loss of metal across the surface of the sample this can be seen in the uneven surface of the decarburised sample, figure 4.3. There are many reasons for this, including the microstructure of the steel and the localised atmospheric conditions. After oxidation the surface was ground until it was estimated that half of the oxidised layer had been removed leaving a surface of bare metal and oxide, therefore there is a large possible error. This method is therefore not an accurate determination of oxidation rate constant, for oxidation experiments the mass loss is a more accurate measurement[4]; but for these decarburisation experiments the measurement requires the actual depth lost from the surface therefore this technique was deemed as being sufficiently accurate as well as appropriate.

Figures 4.5 and 4.6 show an increase in the carbon concentration with increasing depth from the surface. The difference in between the graphs is that as the time is increased, at constant temperature, the curve shifts towards greater depths. It can also be seen in figure 4.6 that with increasing time the concentration profile becomes increasingly sigmoidal, indicating that there is a limiting concentration at the surface. This would be expected to be at the maximum solubility of carbon in ferrite resulting in an almost carbon free layer at the surface. The model does not show this behaviour but displays inverted exponential behaviour that starts at zero and reaches a limiting value at the bulk carbon concentration.

The definition of the depth of decarburisation used by Birks[3] was at 92.5% of the bulk carbon content; found by metallography to be where a distinct change in the microstructure

occurred. He conducted experiments on eutectoid steel, which exhibits a distinct change close to where the bulk carbon concentration is reached with no proeutectoid ferrite present within the bulk of the sample. This definition is similar to that given in BS EN13674-1[20] for rail steel but is defined as the depth of the continuous ferrite network at the surface. With hypoeutectoid steels it is a much harder definition to use because proeutectoid ferrite is formed within the bulk of the sample. The observations by metallography on heat treated rail disc samples found that the change occurred at 98% of the bulk carbon concentration within ±1%, therefore this definition has been used for all experiments. The surface of the oxidised sample is not flat, as seen in figure 3.11, with the depth calculated from a straight line, therefore there is an error in the depth of each result of ±20μm. There will also be errors resulting from the measurement using a ruler; this error will be the order of ±0.03%C.

The three figures of depth of decarburisation against time for the different temperatures show that the model predicts higher values than the experimental results. A possible reason for this is the composition of the furnace atmosphere. The experiments were carried out in air whereas the model was originally developed using data from experiments conducted in industrial gases; these gases are by products of industrial processes, with coke oven or blast furnace gas being common. A decarburisation model used by Corus has also been found to predict much greater depths of decarburisation than the results found here; this model also used an industrial atmosphere[21]. The composition of gases used in industry is variable with one composition of the oxidising gases given by Marston *et al.*[19] of 1.5wt%O_2, 23%CO_2 and 3%H_2O; this has a lower oxygen content than air but a much greater carbon dioxide content. The paper also demonstrated that the oxidation potential of the atmosphere depended on composition and oxidising ability of the individual gasses; the results show that for furnace gases and air the oxidation potential and therefore rate are similar. The model used by Kucera *et al.*[8] without the oxidation term has also been examined and found to predict a greater depth of decarburisation than those by the Birks model.

One possible reason for the difference between measurements and models is the effect of alloying composition, figure 4.8. The lower three curves on this graph are the model using the diffusion coefficient from Kucera and Stransky[11], equations 4.8 and 4.9. This has varied the carbon content between zero and the eutectoid composition, the lowest curve nearest to the data is with no carbon present, i.e. pure iron. The effect of the other alloying elements has also been studied using the values in table 4.1 with the diffusion coefficient calculated using equation 4.8 and 4.9 with no carbon present. The highest line in figure 4.8 gives the maximum effect, whereas the minimum is described by a line that is almost the same as the model without any carbon present. It is likely that this minimum line is the most likely as the effect of 0.2% Si and 1% Mn have previously been found to cancel each other out[18].

The depth of decarburisation measured by microhardness has shown similar results to those observed by metallography but at greater depths for all three temperatures. It is difficult to compare the results between the two methods of measurement directly, even though figure 2.20 shows a linear relationship for air-cooled samples[22]. This is because the relationship depends on the heat treatment and cooling rates of the samples which control the microstructural features and hence mechanical properties of the steel. Therefore, for this investigation into modelling the depth of decarburisation, these results are not very useful, but when twin disc testing is carried out it will allow the effect of decarburisation on the mechanical properties of the surface to be examined.

The determination of the diffusion coefficient from the results of the initial samples have shown that it is much lower than values given in the literature for bulk diffusion of interstitial carbon in austenitic (fcc) steel, figure 4.11[11]. The diffusion coefficient has also been calculated for the samples heat treated at the same time as the discs with the average value plotted in figure 4.11; this is very close to the best fit line of the initial samples. The diffusion coefficients for all three temperatures determined from the experiments have been substituted into the decarburisation model and plotted in figure 4.12 along with the experimental data. This has shown very good correlation with the results at 1000°C and 1010°C; the fit for 910°C is also reasonably good, while at 1125°C the fit is good at the lower times but at the longer times the model predicts greater depths of decarburisation. The adjusted model has also been plotted on the graphs of carbon content versus depth of the samples, figures 4.5 and 4.6. These have shown that the model can predict the depth of decarburisation with reasonable accuracy, but the trend of the model is somewhat different to the trend in the data.

The results from the diffusion coefficient and the depth of decarburisation have shown that the use of diffusion data found in the literature does not fit the experimental results. The most likely reason is that the rate-controlling step of decarburisation of rail steel in air is not diffusion controlled and therefore the boundary conditions selected are not appropriate. Section 2.9.3.2 has shown that it is possible that the rate determining step are the reactions occurring at the surface or possibly the transport of oxygen through the oxide scale. There are several possible reasons for this including the presence of silicon in the steel, which may form a more protective oxide scale that does not rupture allowing oxidising species in and the resultant gasses away from the oxide/metal interface. Another alternative is that the depth of decarburisation is lower because of higher oxidation of the surface; Birks and Meier found that any reduction in the oxidation rate by reducing the oxygen potential of the atmosphere results in a greater observed depth of decarburisation[4]. One reason for this is the humidity (typically 40% in the laboratory) of the atmosphere, which has been found to increase the rate of oxidation[23].

These results have shown that Birks model, using the diffusion coefficient determined from the initial results, can be used to predict the decarburisation of rail discs that will be

used for rolling/sliding testing. The results from the reference samples heat treated at the same time as the discs have confirmed this.

4.3   Modelling of the Formation of White Etching Layer

This section is involved with modelling flash temperatures arising from wheel/rail contact and its effect on the diffusion of carbon in steel to make a martensitic white etching layer. Also studied is the effect on diffusion and solubility of carbon when dislocations are present in the railhead due to severe plastic deformation of the surface. The aim is to find out whether it is possible to create WEL under the typical conditions found between wheel and rail.

4.3.1   Diffusion Modelling of Transformation

If white etching layer is a classic martensitic, body centred tetragonal (bct), structure (see section 2) then conventional metallurgy dictates that it has to be created by a heat cycle above the eutectoid temperature followed by rapid cooling[24]. The formation of austenite by heating is controlled by diffusion, therefore it is possible to calculate the time required to form austenite with a homogenous distribution of carbon from the lamella pearlite present before the contact. The cooling process is disregarded from this analysis because the area that is heated will be much smaller than the bulk rail, which will quickly quench the surface. Some evidence for this are the experiments carried out with the spot welder, which heated a much larger area with a smaller cooling bulk but still created martensite, see section 3.6.1.

When the temperature of a steel sample is raised above the eutectoid temperature, A_1, there is an isothermal transformation of the pearlite to austenite. This austenite is in two forms: high carbon (6.67wt%), which was formerly cementite, and low carbon (0.02wt%) which was formally ferrite; see figure 4.13. As the solubility of carbon in austenite is only 2wt% there is a high driving force for carbon redistribution towards the ferrite to create a homogenous austenite with an average concentration of 0.57wt%.

Examination of the deformed surface of a railhead sample by scanning electron microscopy shows that the interlamellar spacing 5μm below the white etching layer, is 185nm, figure 4.14. The width of the cementite lamellae is measured to be 70nm and the ferrite lamellae 110nm. Perez-Unzeuta and Beynon have reported values of deformed interlamellar spacing at a depth of 25μm from the surface for a BS11HT grade rail of 63nm after twin disc testing[25]. Also observed in figure 4.14 is the presence of proeutectoid ferrite within the WEL indicating that the transformation has occurred with a heat cycle above the eutectoid temperature, A_1, but not above the A_3. The presence of proeutectoid ferrite is ignored in this analysis because its fraction is small compared to pearlite and also because it remains untransformed. Grade 220 rail steel has a eutectoid

temperature of 723°C and an A_3 of 770°C, therefore the heat cycle must lie between these two temperatures if the formation of white etching layer is performed by an increase in temperature alone[7].

Using the solution to Fick's second law for long time, transient diffusion for a semi-infinite solid, it is possible to obtain an equation similar to that used in section 4.2 to give an average concentration through the sample[5].

$$\frac{C_\alpha - C}{C_\alpha - C_{Fe_3C}} = 2\sqrt{\frac{Dt}{L^2}}\left\{\frac{1}{\sqrt{\pi}} + 2\sum_{n=1}^{\infty}(-1)^n\,\mathrm{ierfc}\left(\frac{nL}{\sqrt{Dt}}\right)\right\} \qquad (4.17)$$

where C_α is the initial carbon concentration of the ferrite, 0.02wt%, C_{Fe3C} is the initial concentration of the cementite (6.67wt%C), C is the concentration at position L (from figure 4.14, L=87.5nm) after time, t, in this case 0.57%. "ierfc" is the integral error function given by equation 4.18, where z is a mathematical function:

$$\mathrm{ierfc}(z) = \int_z^\infty \mathrm{erfc}(\eta)d\eta = \frac{1}{\sqrt{\pi}}e^{-z^2} - z\,\mathrm{erfc}(z) \qquad (4.18)$$

Combining equations 4.17 and 4.18 and using only one strip to represent half the ferrite lamellae (n =1), results in equation 4.19.

$$\frac{C_\alpha - C}{C_\alpha - C_{Fe_3C}} = 2\sqrt{\frac{Dt}{L^2}}\left\{\frac{1}{\sqrt{\pi}} - \frac{2}{\sqrt{\pi}}e^{-\left(\frac{L}{\sqrt{Dt}}\right)^2} + \frac{2L}{\sqrt{Dt}}\,\mathrm{erfc}\left(\frac{L}{\sqrt{Dt}}\right)\right\} \qquad (4.19)$$

The diffusion coefficient varies with carbon concentration but to simplify the calculation this is ignored and only the variation with temperature by the Arrhenius relationship, equation 4.7, is used. The diffusion coefficient can be found for carbon in austenite with D_o of $1.50\times10^{-5}\mathrm{m^2s^{-1}}$ and activation energy, Q, of 175kJ.mol^{-1}[5].

The error function in equation 4.19 makes it difficult to rearrange with respect to time. Analysis has shown that for the short times involved with carbon diffusion over nanometre scale distances, the relationship 4.20 tends to zero and it is possible to use equation 4.21.

$$\frac{2}{\sqrt{\pi}}e^{-\left(\frac{L}{\sqrt{Dt}}\right)^2} + \frac{2L}{\sqrt{Dt}}\,\mathrm{erfc}\left(\frac{L}{\sqrt{Dt}}\right) \to 0 \qquad (4.20)$$

$$\frac{C_\alpha - C}{C_\alpha - C_{Fe_3C}} = 2\sqrt{\frac{Dt}{\pi L^2}} \qquad (4.21)$$

Rearranging for time gives equation 4.22.

$$t = \frac{\pi L^2}{4D} \left(\frac{C_\alpha - C}{C_\alpha - C_{Fe_3C}} \right)^2 \tag{4.22}$$

Therefore using the data above, the time required for carbon to diffuse from the edge of the former cementite lamella to the centre of the former ferrite lamella can be found at different temperatures to give a homogenous carbon concentration within the austenite.

4.3.2   Time of Contact Between Wheel and Rail

A simple model can be used to give the time of contact between a wheel and rail with the terms defined in figure 4.15. A train moving at speed, V_1, has a wheel of radius, r, which moves against the rail with a peripheral velocity, V_2 and a contact half width of length a. Slip, S (as a positive fraction), is the ratio between the velocities of the wheel and rail and is given by equation 4.23[26].

$$S = \frac{V_2 - V_1}{V_1} \tag{4.23}$$

Rearranging equation 4.23 and solving for contact half width gives equation 4.24 for time of contact, θ, between the wheel and rail at any point on the rail.

$$V_2 = V_1(1+S) = \frac{2a}{\theta}$$
$$\theta = \frac{2a}{V_1(1+S)} \tag{4.24}$$

Therefore if the train is moving at 56ms^{-1}(125mph) with a contact half width of 5mm[27] then the time of contact for different slip ratios will be as follows.

$$S = 1\% => \theta = (2 \times 5 \times 10^{-3})/56(1+0.01) = 177 \mu s$$

$$S = 9\% => \theta = (2 \times 5 \times 10^{-3})/56(1+0.09) = 164 \mu s$$

This is the time for the total elliptical area of contact across its widest part; the rail at any one point will not see this total time but only part of it due to the true area of contact being much smaller than the apparent area of contact due to surface roughness.

4.3.3   Temperature of Contact Between Wheel and Rail

The difficulties in measuring the temperatures arising from the contact between rail and wheel have meant there have been several theoretical treatments reported in the literature. A finite element method was used by Fischer et al.[27] who modelled asperity contact with a rod rubbing against a flat surface with heat generated by both friction and plastic deformation. The model is very complicated with the results presented as a graph of temperature against train speed; the data is presented in figure 4.16 with train speed converted to time of contact using equation 4.24.

A second model has been developed by Tanvir[28] using a Laplace transform method for an elliptical contact giving equation 4.25 for flash temperatures of rail.

$$\Theta_R = \frac{2.26 P_m \mu}{K} \left(\frac{aKV_1}{\pi \rho C} \right)^{1/2} \left\{ (1+S)^{1/2} - 1 \right\} \tag{4.25}$$

where P_m is the maximum contact pressure, μ is the coefficient of adhesion, V_1 is the forward velocity of the wheel, K is the thermal conductivity, ρ is the density of the material, C is the specific heat, a is the contact half width and S is the slip ratio. This is for when the slip ratio is less than infinity and the forward speed, V_1, is less than the peripheral speed of the wheel, V_2, i.e. when the wheel is slipping on the rail.

A comparison of the two models is shown in figure 4.16 for various slip values with the following values used: $P_m = 1500MPa$, $\mu = 0.3$, $a = 5mm$, $K = 45W.s^{-1}.K^{-1}$, $\rho = 7.85kg.m^{-3}$, $C = 637kJ.kg^{-1}K^{-1}$ all taken from the paper by Fischer et al.[27] as typical values at the rail head. Figure 4.16 shows that the Tanvir model is higher than the Fischer et al.[27] model for all slip values with a difference of 10°C for 1% slip and 50°C for slip of 9%. This would be expected as Tanvir's model is for when the wheel is spinning on rail and therefore creating more heat. The simple nature of the Tanvir model and its similarity to the results of the Fischer model mean that it will be used for calculations of the flash temperature arising from the contact between wheel and rail.

4.3.4   Dislocations and Diffusion of Carbon in Ferrite

The effect of randomly orientated dislocations on diffusivity is important to thermal processes that occur at less than half the melting temperature of the material[29]. The prediction of the temperature rise occurring during wheel/rail contact, for slip values of less than 7%, is less than half the melting point of steel. The dislocation density of the surface of the railhead is dependent on the amount of plastic deformation it has undergone. Annealed iron has a dislocation density of $10^{13}m^{-2}$[30] compared to samples deformed to 40% plastic work with $10^{17}m^{-2}$[31]. With greater amounts of cold work, such as those on railheads with strains greater than 5, then a high dislocation density will be present and

consequently pipe diffusion will be important in the transport of carbon atoms. The dislocation core acts as a pipe by which solute atoms can move with a higher average jump frequency than in the lattice due to a lower activation energy. Therefore the effective diffusion for the sample, D_{eff}, can be related to diffusion within the lattice, D_L, and pipe diffusion, D_p, by a simple law of mixtures, equation 4.26[32].

$$D_{eff} = fD_p + D_L(1-f)$$ (4.26)

where f is the fraction of time spent by the diffusing species in the dislocation core. It is possible to relate f to the dislocation density by equation 4.27 given by Cowan et al.[30].

$$f = A_p\rho$$ (4.27)

where ρ is the dislocation density of the crystal and A_p is the pipe diffusion cross sectional area approximated by $A_p \approx 4a^2$, where a is the lattice parameter of iron, 287Å. For the diffusion densities mentioned above the following values of f have been calculated:

$$\rho = 10^{13}\text{m}^{-2} \therefore f = 4\times(2.87\times10^{-10})^2 \times 10^{13} = 3.3\times10^{-5}$$
$$\rho = 10^{17}\text{m}^{-2} \therefore f = 4\times(2.87\times10^{-10})^2 \times 10^{17} = 3.3\times10^{-2}$$

There is a limited amount of data on the diffusion of carbon along dislocation cores or grain boundaries in austenitic iron. One set of data is given by Demel[33] for carbon in a high nickel (35wt%) austenitic stainless steel (15wt%Cr). The diffusion data for the lattice and grain boundary is given by equation 4.28 and 4.29 respectively.

$$D_L = 3.8\times10^{-5}\text{m}^2\text{s}^{-1} \exp\left(\frac{-401\text{kJ}}{RT}\right)$$ (4.28)

$$D_P = 9.0\times10^{-6}\text{m}^2\text{s}^{-1} \exp\left(\frac{-152\text{kJ}}{RT}\right)$$ (4.29)

These diffusion coefficients are plotted, along with that used in section 4.3.1, in figure 4.17 with the natural logarithm of D versus 10^4T^{-1}. It shows that below 950°C grain boundary diffusion dominates, whereas above lattice diffusion dominates. It can be seen that diffusion using the values given by Wilkinson are faster than those for the austenitic stainless steel[33] at temperatures of less than 1200°C. This is due to the effect of the alloying elements on the activity and diffusion of carbon; therefore, it is not possible to provide a direct comparison for the effect of dislocations on diffusion.

The temperature and time required for diffusion of carbon as a function of dislocation density for one thermal cycle is plotted in figure 4.18 while that for 50×10^6 cycles is shown in figure 4.19. The effect of the increase in dislocation density for a deformed crystal is a reduction in temperature required for diffusion by 10°C to 850°C at contact times of 200μs

(100mph). If the dislocation density is further increased, say by an order of magnitude, which is possible for rail with strains greater than 40%, the reduction in temperature will be approximately 75°C to 780°C; a further increase in the dislocation density to $10^{19} m^{-2}$ leads to a reduction of the required temperature to 635°C. If WEL is formed over 50×10^6 cycles and not one, the temperature required for diffusion to take place in an annealed crystal is 500°C, whereas a plastically deformed crystal ($\rho = 10^{17} m^{-2}$) requires a temperature of 290°C, with a further decrease to 250°C for an increase in the dislocation density by a further order of magnitude.

4.3.5   Discussion

The measurement of the deformed pearlite spacing below the surface may not be representative of the sample because the surface of the railhead is deformed in two directions, along the rail as seen in figure 4.14, as well as towards the gauge corner of the rail. This measurement is taken immediately below the white etching layer; before the WEL is formed the pearlite at the surface will have a finer spacing. The results found by Perez-Unzueta after twin disc testing has therefore been used which are thought to be nearer to the actual values encountered at the surface of the railhead[25].

The temperatures arising from the wheel/rail contact, plotted in figure 4.16, are the maximum temperatures attained for the time of contact depending on the speed of the train. This analysis is related to the UK's historic main lines where the maximum speed is $56 ms^{-1}$ (125mph); speeds greater than this only occur, within the UK, on the dedicated high-speed lines of the Channel Tunnel Rail Link.

The diffusion model predicts the minimum time required for transformation of pearlite into austenite at each temperature. The values are similar to those found by Archard and Rowntree[34] using a different diffusion equation for sliding contact with no rolling who found a temperature of 1440°C is required for 200µs to transform eutectoid steel for a diffusion distance of 883nm. Using this data in the model gives a diffusion time of 60µs required for transformation, but this uses a different diffusion coefficient on which the model is highly dependent. The effect of plastic strain and consequent increase in dislocation density, figures 4.18 and 4.19, result in a decrease in the time required for diffusion of carbon at the same temperature. However, this would have little effect on the transformation of ferrite to austenite because the temperature is less than the eutectoid temperature and therefore no transformation can occur.

The diffusion model has been plotted for temperature against time for several different conditions including both measurements of pearlite interlamellar spacing of 65nm and 180nm, figure 4.20. Also plotted are modifications to the model which take into account that the formation of white etching layer is unlikely to occur within one cycle, therefore the diffusion distance has been divided by the number of cycles with the time for each

individual step being summed together. This has been calculated for 0.1, 5 and 50 million cycles which are estimated as the typical number of cycles for a high speed main line in the UK for a lifetime of 2 weeks, 2 and 20 years respectively.

The plot of both the diffusion and flash temperature models are shown in figure 4.20 and display the conditions required to transform the pearlitic steel present at the surface of rail to austenite by diffusion alone. The diffusion model shows that when the number of cycles is greater than 100,000 cycles then the temperature required for diffusion at all train speeds of less than 56ms^{-1} is less than 300°C. The choice of 100,000 cycles relates to two weeks in service after which Clayton and Allery report that new rails may exhibit white etching layers[35]. This shows that if it were possible to form austenite at temperatures below the A_1, then for trains speeds of greater than 13ms^{-1} a slip ratio of 5% would be sufficient to form WEL. But as mentioned earlier, a temperature rise to greater than the eutectoid temperature is required to form austenite because even though the diffusivity in ferrite is higher, the solubility of carbon is very low (0.02% at 723°C). Therefore the creation of the homogenous carbon content required to form martensite will not occur. To form a martensitic white etching layer by diffusion, a slip ratio of 9% is required to create temperatures of greater than 700°C as shown by the hatched areas in figure 4.20.

The temperatures given by the phase diagram for the transformation of ferrite to austenite are only true under equilibrium conditions, which are far removed from those at the surface of rail. Two factors that affect the transformation include the hydrostatic pressure under which the transformation occurs and the dislocation density near the surface. Austenite has a higher density and consequently smaller volume than the same mass of ferrite so the effect of the compressive hydrostatic pressure is to reduce the transformation temperature. Ahlström and Karlsson[36] calculated that with a hydrostatic pressure of 400MPa there was a linear reduction in the A_1 by 4°C and the A_3 by 17°C, similar to what Hilliard has found experimentally[37]. Therefore with a hydrostatic pressure of 1500MPa there could be a reduction in the A_1 from 723°C to 708°C.

The effect of dislocations is to decrease the eutectoid transformation temperature to 680°C with a strain of 40%. This is due to an increase in the solubility of carbon within the ferrite by a factor of 5[31]. With a strain of 90%, austenite nucleation could be expected to begin in the range 635-655°C [38]. This is only for moderately fast heating rates of less than 200°C/minute; for faster heating rates then the temperature rises above 723°C[31]. It is therefore likely that this will have little effect on the transformation of a railhead because the heating rates are much greater than 200°C/minute.

By combining the effect of hydrostatic pressure and the maximum effect possible by dislocation density, it is possible that the A_1 temperature is lowered to near 620°C. Therefore, to form austenite a flash temperature rise of 620°C is required which, from figure 4.20, means that a slip of 7% is required at a speed of 50ms^{-1}. The problem with this

conclusion is that this value is only rarely found on the surface of a railhead where WEL is found. This value of slip is only found on the gauge face of rail when flange contact occurs during cornering where the normal contact load is much lower. The slip values found on railhead rarely exceed 1% even at high speed on curves as reported by Beynon *et al.*[39]. The only times when a railhead experiences higher slip values are either when a driving wheel is slipping when the train is starting, resulting in isolated patches of martensitic wheel burn material, or when a wheel is locked, sliding along the surface of the rail. The former is unlikely to be a factor because WEL appears on rail under a wide range of contact conditions not just in areas associated with trains starting. The use of modern disc brakes and anti-skid devices mean that locked wheels are much less common than in the past, therefore it is unlikely to account for all cases of white etching layer.

It is clear from this that some other mechanism must be present to account for formation of white etching layer on the railhead. The conclusions of this simple model, in accordance with both Newcomb and Stobbs[40] and Lojowski *et al.*[41], are that white etching layers are unlikely to form due to temperature rise alone because they are not high enough to cause transformation of the steel to austenite. They have proposed models where the high dislocation density resulting from the severe plastic deformation of the surface leads to the dissolution of cementite particles combined with dynamic recrystallisation, resulting in the formation of nanocrystalline martensite (see chapter 2). Further investigation of the mechanism of formation of WEL is beyond the scope of this thesis, since effort is focussed on the consequence of WEL however it is formed, on rail performance.

4.4   Conclusions
4.4.1   Diffusion Modelling of Decarburisation

The diffusion modelling has allowed the prediction of the depth of decarburisation to be carried out for the rail discs, but only when the diffusion coefficient calculated from the initial experiments was used.

The results have indicated that for the decarburisation of rail steel in air, the rate-determining step is not controlled by the diffusion of carbon through the steel to the surface but by some other mechanism.

4.4.2   Modelling of the Formation of White Etching Layer

A simple diffusion model has been developed that tries to explain the formation of white etching layer on the surface of rail. This has included an analysis of the effect of dislocations on the diffusion coefficient.

The results have shown that white etching layer is highly unlikely to form due to diffusion alone because the temperature rise occurring during wheel/rail contact is insufficient for

transformation from pearlite to austenite to occur. Consequently some other mechanism is required for the formation of white etching layer on rail suppoting the work of Newcomb and Stobbs[40].

4.5   References

1.   Birks, N. and Jackson, W., A quantitative treatment of simultaneous scaling and decarburization of steels, Journal of the Iron and Steel Institute, 280, (1), p81-85, 1970

2.   Birks, N. and Nicholson, A., Calculation of decarburization depth in steels reheated under practical conditions, in: Mathematical Models in Metallurgical Process Development, London, UK, The Iron and Steel Institute, London, UK, p219-224, 1969

3.   Birks, N., Mechanisms of decarburization, in: Conference on Decarburization, Sheffield, UK, Iron and Steel Institute, London, UK, p1-12, 1970

4.   Birks, N. and Meier, G. H., Introduction to High Temperature Oxidation of Metals, 1st Ed., 1983

5.   Wilkinson, D. S., Mass Transport in Solids and Fluids, 2nd Ed., Cambridge University Press, UK, 2000

6.   Stroud, K. A., Further Engineering Mathematics, 4th Ed., MacMillan Press Ltd., London, UK, 1995

7.   Honeycombe, R. W. K. and Bhadeshia, H. K. D. H., Steels: Microstructure and Properties, 2nd Ed., Edward Arnold, London, UK, 1995

8.   Kucera, J., Hajduga, M., Glowacki, J. and Broz, P., Decarburization and hardness changes of Fe-C-Cr-Mn-Si steels caused by high temperature oxidation in ambient air, Zeitschrift fur Metallkunde, 90, (7), p514-521, 1999

9.   Nomura, M., Morimoto, H. and Toyama, M., Calculation of ferrite decarburizing depth, considering chemical composition of steel and heating condition, ISIJ International, 40, (6), p619-623, 2000

10.   Pyyry, I. and Kettunen, P., Decarburization in plain carbon steels, Scandinavian Journal of Metallurgy, 2, (5), p265-268, 1973

11.   Kucera, J. and Stransky, K., Diffusion in iron, iron solid solutions and steels. A review, Materials Science and Engineering A, 52, (1), p1-38, 1982

12.   Wells, C., Batz, W. and Mehl, R. F., Diffusion coefficient of carbon in austenite, Transactions of the American Institute of Mining and Metallurgical Engineers, 188, (3), p553, 1950

13.   Roy, S. K., Grabke, H. J. and Wepner, W., Diffusivity of carbon in austenitic Fe-Si-C alloys, Archiv fur das Eisenhuttenwesen, 51, p91, 1980

14.   Kucera, J., Stransky, K. and Dojiva, R., Diffusion interaction coefficients and thermodynamic interaction coefficients of carbon in alloyed austenite, Material Science and Engineering A, 125A, (5), p75, 1990

15.   Million, B., Kucera, J. and Michalicka, P., The influence of silicon on carbon redistribution in steel weldments, Material Science and Engineering A, 190A, (1-2), p247-252, 1995

16.   Liu, W. J., Brimacombe, J. K. and Hawbolt, E. B., Influence of Composition on the Diffusivity of Carbon in Steels. I. Non-Alloyed Austenite, Acta Metallurgica et Materialia, 39, (10), p2373-2380, 1991

17.   Kubaschewski, O. and Hopkins, B. E., Oxidation of Metals and Alloys, 1st Ed., Butterworths, UK, 1962

18.   Marston, H. F., Ratcliffe, R., Bolt, P. H., van Lankveld , M., Lanteri, V., Leprince, G., Jarl, M., Niska, J., Klima, R. and Roder, M., Oxidation and decarburisation of high carbon: special and general steels, European Commission - Science Research Development, 2002

19.   Marston, H. F., Bolt, P. H., Leprince, G., Roder, M., Klima, R., Niska, J. and Jarl, M., Challenges in the modelling of scale formation and decarburisation of high carbon, special and general steels., Ironmaking and Steelmaking., 31, (1), p57-65, 2004

20.   BS EN 13674-1, Railway Track Applications - Rail - Part 1: Flat Bottom Symmetrical Rails 46kg/m and Above, British Standards Institution, London, UK, 2003

21.   Marston, H. F., Private Communication with Author, 2003

22. Krauss, G., Microstructure, processing and properties of steels, in: Vol 1: Properties and Selection: Iron, Steel and High Performance Alloys, Metals Handbook, American Society of Metals, USA, p126-139, 1996

23. Kofstad, P., High Temperature Corrosion of Metals, in: Microscopy of Oxidation, Cambridge; UK, p2-9, 1990

24. Nishiyama, Z., Martensitic Transformation, 1st Ed., Academic Press, New York, USA, 1978

25. Perez-Unzueta, A. J. and Beynon, J. H., Microstructure and wear resistance of pearlitic rail steel, Wear, 162-164, (1), p173-182, 1993

26. Johnson, K. L., Contact Mechanics, 1st Ed., Cambridge University Press, UK, 1985

27. Fischer, F. D., Davies, W. and Werner, E. A., On the temperature in the wheel-rail rolling contact, Fatigue and Fracture of Engineering Materials and Structures, 26, (10), p999-1006, 2003

28. Tanvir, M. A., The temperature rise due to slip between wheel and rail: an analytical solution for Hertzian contact, Wear, 61, (2), p295-308, 1980

29. Shewman, P., Diffusion in Solids, 2nd Ed., The Minerals, Metals and Materials Society, Pennsylvania, USA, 1989

30. Cowan, J. R., Evans, H. E., Jones, R. B. and Bowen, P., Role of dislocation density and structure in grain boundary segregation of phosphorus and carbon in model Fe-P-C alloy, Materials Science and Technology, 18, (11), p1305-1313, 2002

31. Barabash, R. I., Gridnev, V. N., Krivoglaz, M. A., Meshkov, Y. U. A. and Ryaboshapka, K. P., Influence of dislocations on solubility and the phase transformation curves in deformed alloys, Physics of metals and metallography (Fizika Metallov I Metallovedenie), 37, (6), p64-75, 1974

32. Hart, E., On the role of dislocations in bulk diffusion, Acta Metallurgica, 5, (10), p597, 1957

33. Demel, O., Iron-nickel-chromium/carbon, in: Handbook of Grain and Interphase Boundary Diffusion Data, Kaur, I.(Ed), p786, 1989

34. Archard, J. F. and Rowntree, R. A., Metallurgical phase changes in the wear of steels: a critical reassessment, in: 6th Leeds-Lyon Symposium: Thermal Effects in Tribology, Lyon, France, Dowson, D.(Ed), Mechanical Engineering Publications, Ltd., UK, 1979

35. Clayton, P. and Allery, M. B. P., Metallurgical aspects of surface damage problems in rails, Canadian Metallurgical Quarterly, 21, (1), p31-46, 1982

36. Ahlstrom, J. and Karlsson, B., Microstructural evaluation and interpretation of the mechanically and thermally affected zone under railway wheel flats, Wear, 232, p1-14, 1999

37. Hilliard, J. E., Iron carbon phase diagram: isobaric sections of the eutectoid region at 35, 50 and 65 kilobars, Transactions of the Metallurgical Society of the AIME, 227, (4), p429-438, 1963

38. Gridnev, V. N., Ivasishin, O. M., Meshkov, Y. U. A. and Oshkaderov, S. B., Conditions of formation of metastable austenite in steel with an imperfect structure during heating, Physics of metals and metallography (Fizika Metallov I Metallovedenie), 35, (3), p562-566, 1973

39. Beynon, J. H., Garnham, J. E. and Sawley, K. J., Rolling contact fatigue of three pearlitic rail steels, Wear, 192, (1-2), p94-111, 1996

40. Newcomb, S. B. and Stobbs, W. M., A transmission electron microscopy study of the white etching layer on a railhead, Materials Science and Engineering, 66, (2), p195-204, 1984

41. Lojkowski, W., Djahanbakhsh, M., Burkle, G., Gierlotka, S., Zielinski, W. and Fecht, H. J., Nanostructure formation on the surface of railway tracks, Materials Science and Engineering A, 303A, (1-2), p197-208, 2001

4.6   Tables

x	$\beta^i{}_{C}(1)$ /at.frac.$^{-1}$	$\beta^i{}_{C}(2)$ /at.frac.$^{-1}$	$\beta^i{}_{C}$ at 900°C /at.frac.$^{-1}$	$\beta^i{}_{C}$ at 1100°C /at.frac.$^{-1}$	Reference
C	-9.8	2.32	9.98	7.10	[11]
C	-17.52	3.44	11.82	7.55	[16]
C	-32.17	4.81	8.87	2.89	[11]
C	-101.6	16.5	39.06	18.57	[8]
C	-25.9	5.63	22.10	15.11	[11]
Mn	-671.5	97.73	161.66	40.30	[8]
Mn	2.7	-0.87	-4.72	-3.64	[15]
Si	20.8	-4.2	-15.01	-9.79	[15]
Si	194.4	-27.75	-42.17	-7.71	[8]
Si	23.3	-4.46	-14.72	-9.18	[11]

Table 4.1: Values of interaction parameter for element x in an fcc γ-iron matrix

Sample	Total Time /s	Metal Loss/μm
910°C, $k_c = 1.70 \times 10^{-13} \, \mathrm{m^2 s^{-1}}$		
DE06	143	13
DE07	1103	29
DE08	2183	44
DE09	6743	56
DE10	14663	73
1010°C, $k_c = 2.95 \times 10^{-12} \, \mathrm{m^2 s^{-1}}$		
DE01	2646	228
DE02	4446	175
DE03	8046	312
DE04	15246	313
DE05	21486	402
1125°C, $k_c = 5.51 \times 10^{-12} \, \mathrm{m^2 s^{-1}}$		
DE11	2225	95
DE12	4025	153
DE13	7625	295
DE14	14825	405
DE15	21425	464
Discs, 1000°C, $k_c = 4.99 \times 10^{-12} \, \mathrm{m^2 s^{-1}}$		
DE37	2390	227
DE35	4184	204
DE28	7986	203
DE33	6023	251
DE31	8951	226
DE29	12831	299
DE32	15191	311
DE36	15884	373
DE34	15923	388
DE30	18831	401
DE38	27170	550

Table 4.2: Metal loss of samples due to oxidation for both initial and disc samples

Sample No.	Hold Time /s	Depth of Decarburisation (98% of bulk values) /μm		
		Metallography	Microhardness	Model (0%C)
910°C, t_e = 438s				
6	0	106	302	166
7	960	111	364	297
8	2040	0	178	395
9	6600	255	323	666
10	14520	321	341	970
1010°C, t_e = 726s				
1	1920	545	350	711
2	3720	542	663	921
3	7320	639	788	1240
4	14520	765	815	1706
5	20760	846	1259	2026
1125°C, t_e = 620s				
11	1620	597	825	1224
12	3420	631	1240	1644
13	7020	880	1755	2261
14	14220	952	1809	3152
15	20820	1274	2567	3788

Table 4.3: Results of depth of decarburisation for initial samples

Sample	Temperature /°C	Equivalent Time, t_e /s	Hold Time /s	Total Time /s	Depth of Decarburisation (98%C_o) /μm
DE37	1003	590	1800	2390	220
DE35	999	584	3600	4184	389
DE33	1006	623	5400	6023	476
DE28	1000	606	7380	7986	538
DE31	1000	611	8340	8951	500
DE29	1003	711	12120	12831	590
DE32	1000	611	14580	15191	606
DE36	999	584	15300	15884	733
DE34	1006	623	15300	15923	645
DE30	1003	711	18120	18831	771
DE38	1003	590	26580	27170	991

Table 4.4: Results of depth of decarburisation for samples heated with discs measured by optical microscopy

4.7   Figures
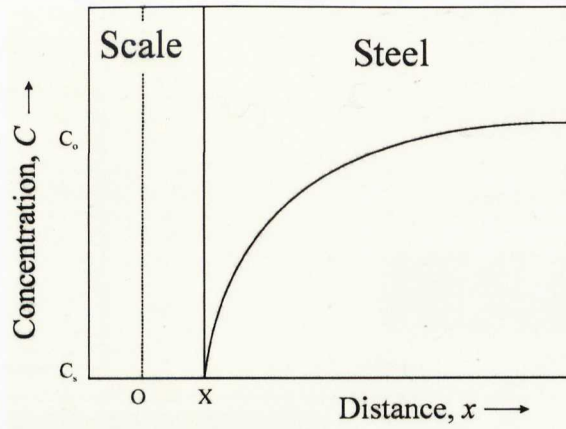
Figure 4.1: Boundary conditions of Birks model [1-4]. C_s is the surface concentration at the oxide/metal interface, X and C_o is the bulk concentration of the metal.
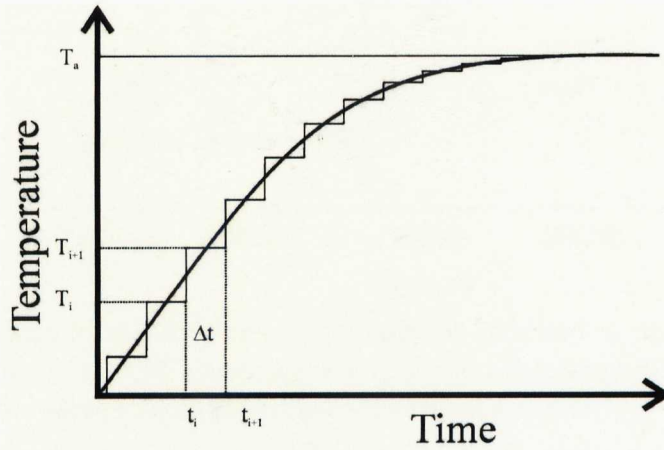
Figure 4.2: Scheil analysis of variation of temperature, T, with time, t, for a fixed time interval of Δt[5].
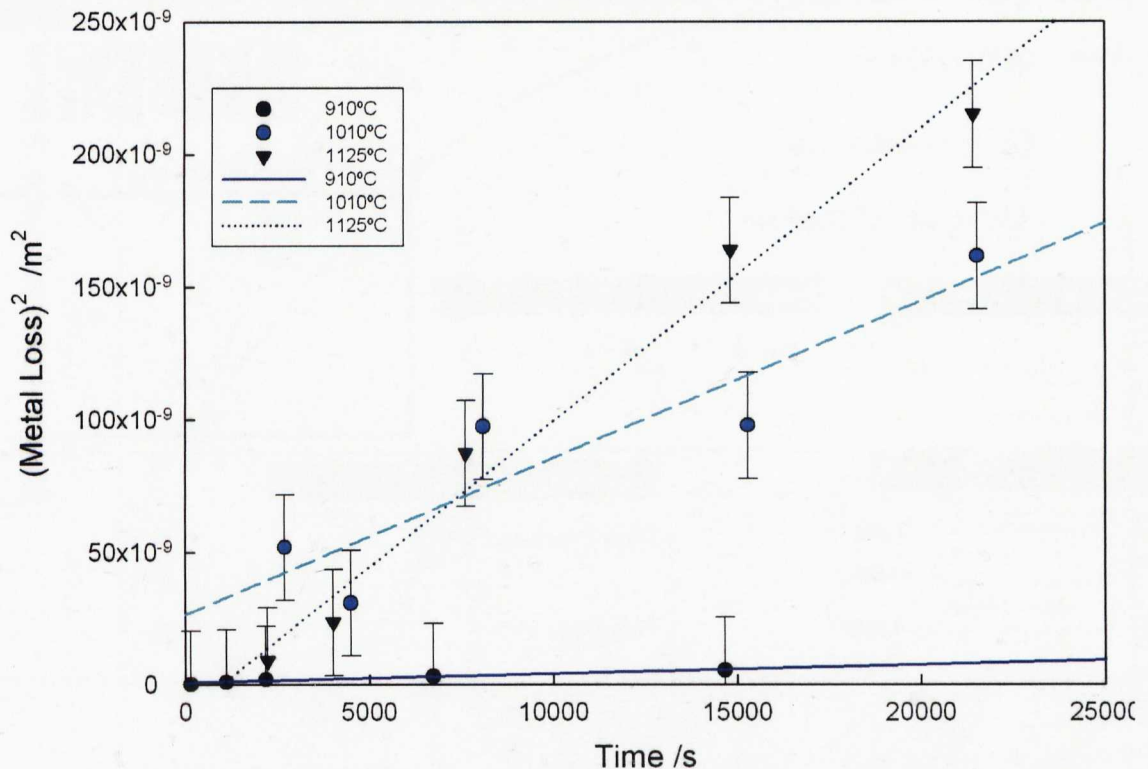
Figure 4.3: Metal loss of samples during oxidation squared, plotted against time allowing the parabolic oxidation constant to be calculated from the gradient for initial tests.
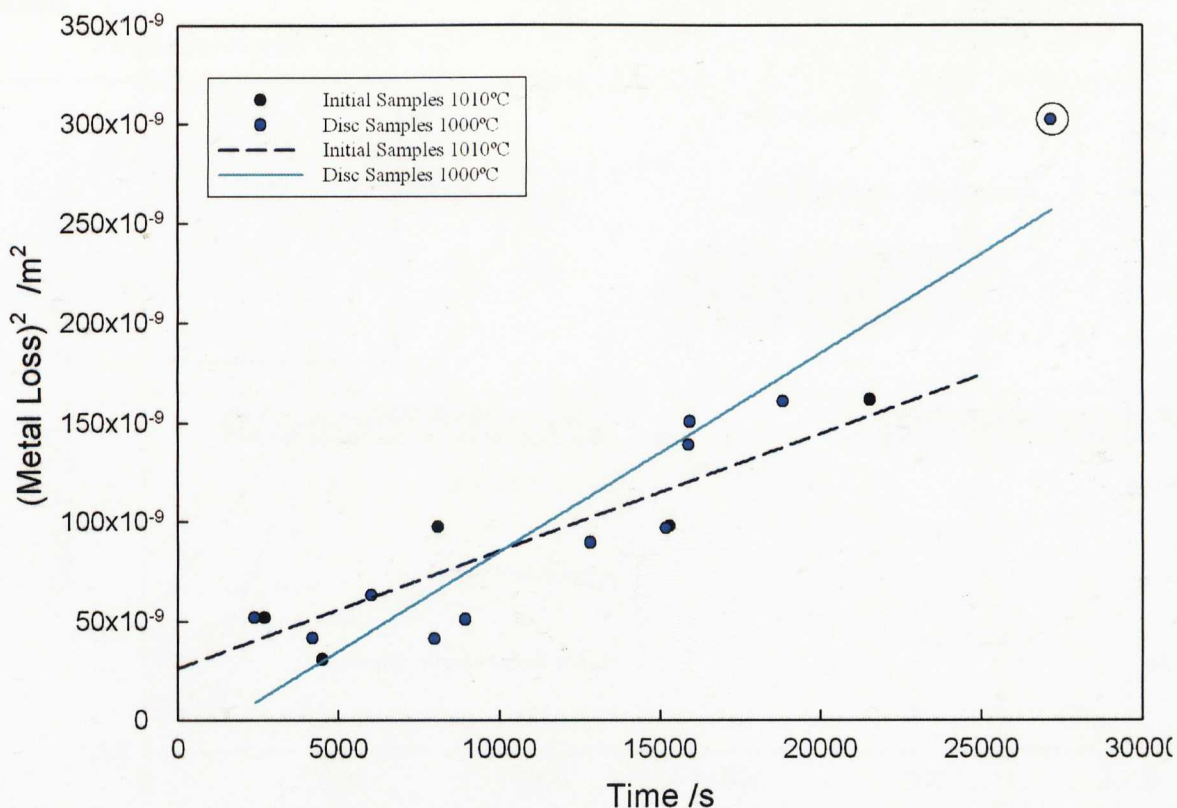
Figure 4.4: Metal loss of rail disc reference samples oxidised at approximately 1000°C with initial results from 1010°C for comparison. If the circled sample is ignored then the other disc samples lie close to the trend line of the initial samples.
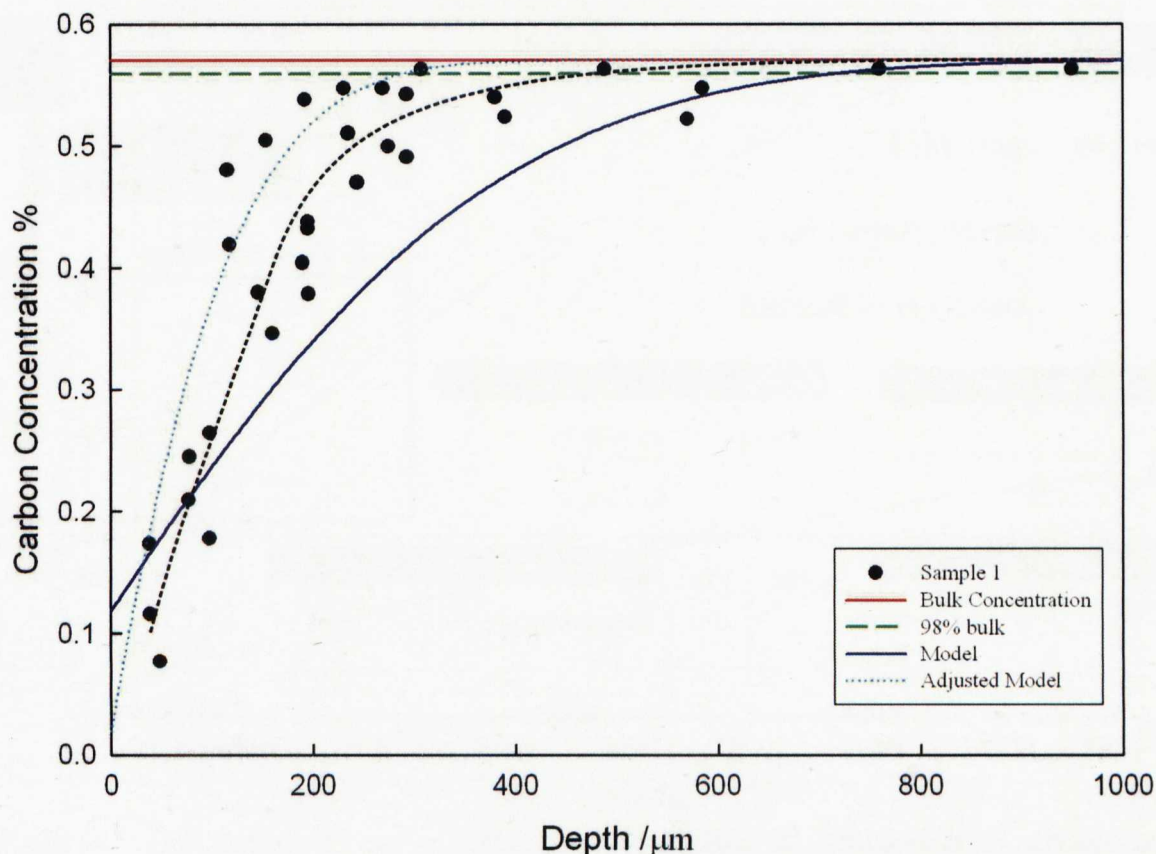
Figure 4.5: Carbon profile for sample 1 after 1920 seconds at 1010°C, measured by metallography
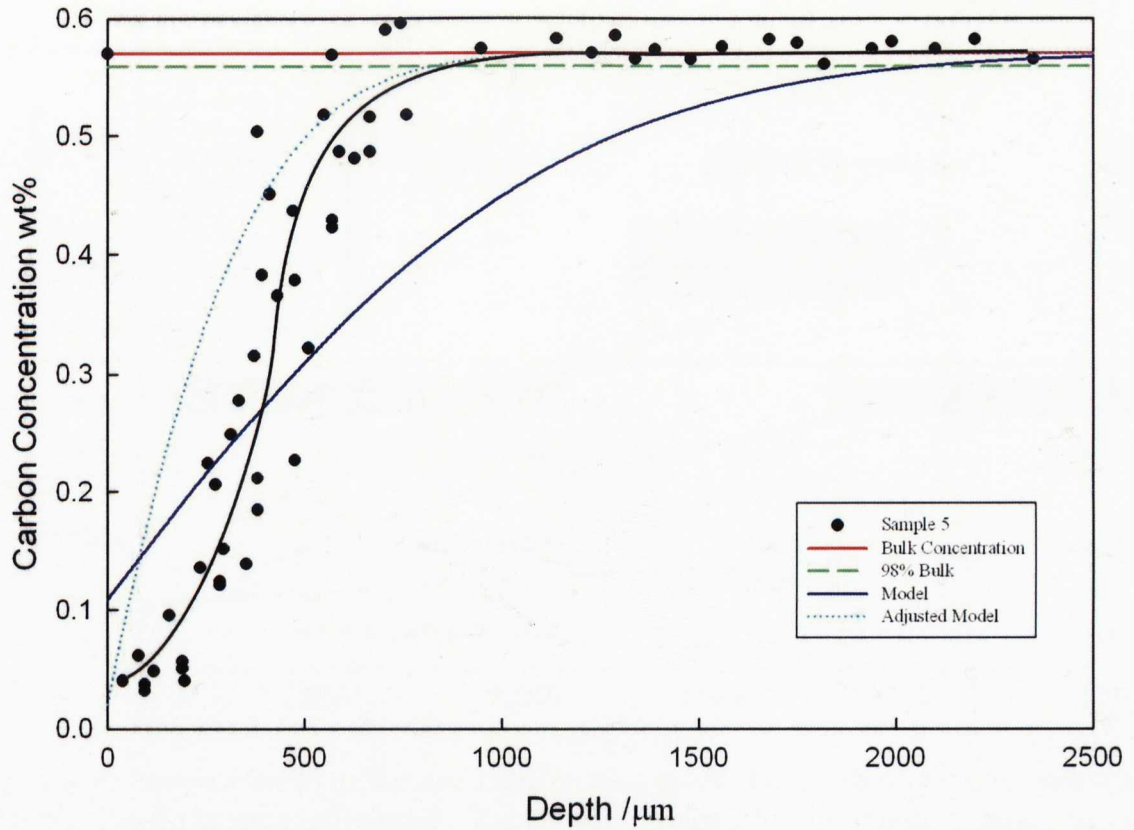
Figure 4.6: Carbon profile for sample 5 after 20760 seconds at 1010°C, measured using metallography.
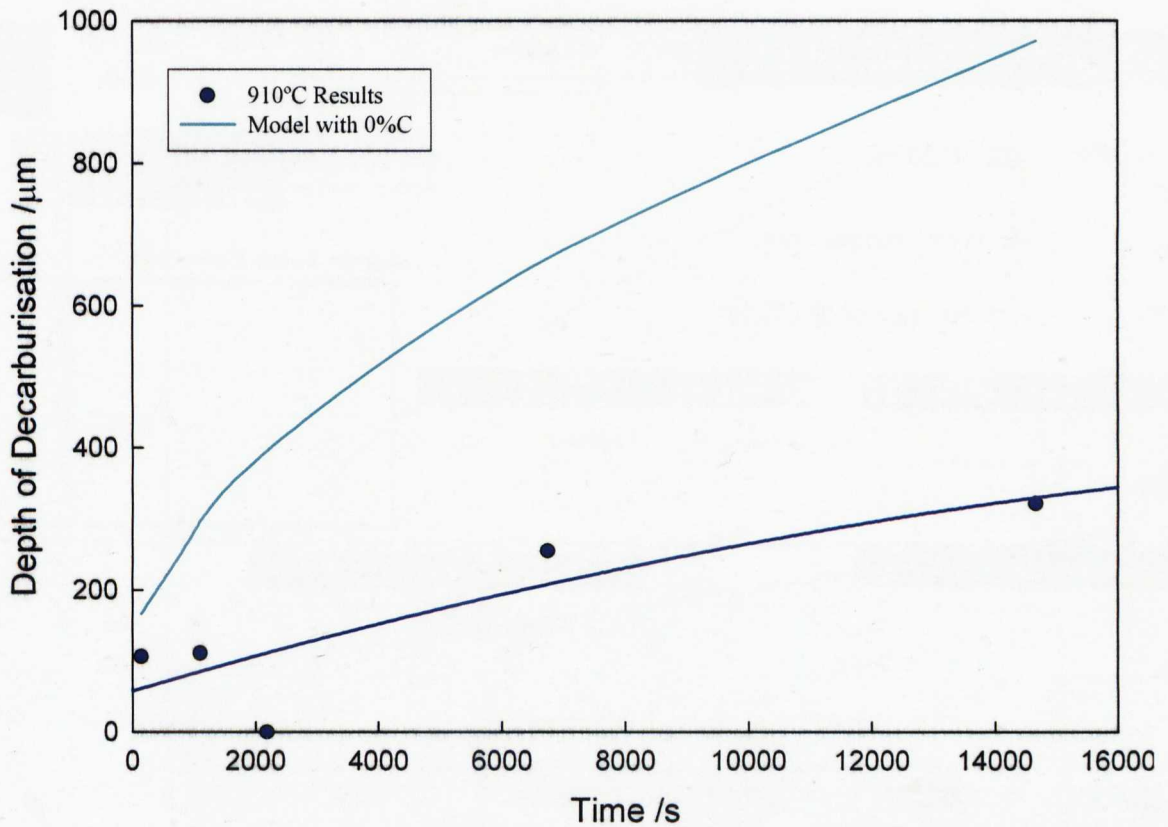
Figure 4.7: Comparison of experimental results for depth of decarburisation, defined as 98% of the bulk concentration, with the Birks model at 910°C using the diffusion coefficient given by Kucera and Stransky with 0% carbon[11].
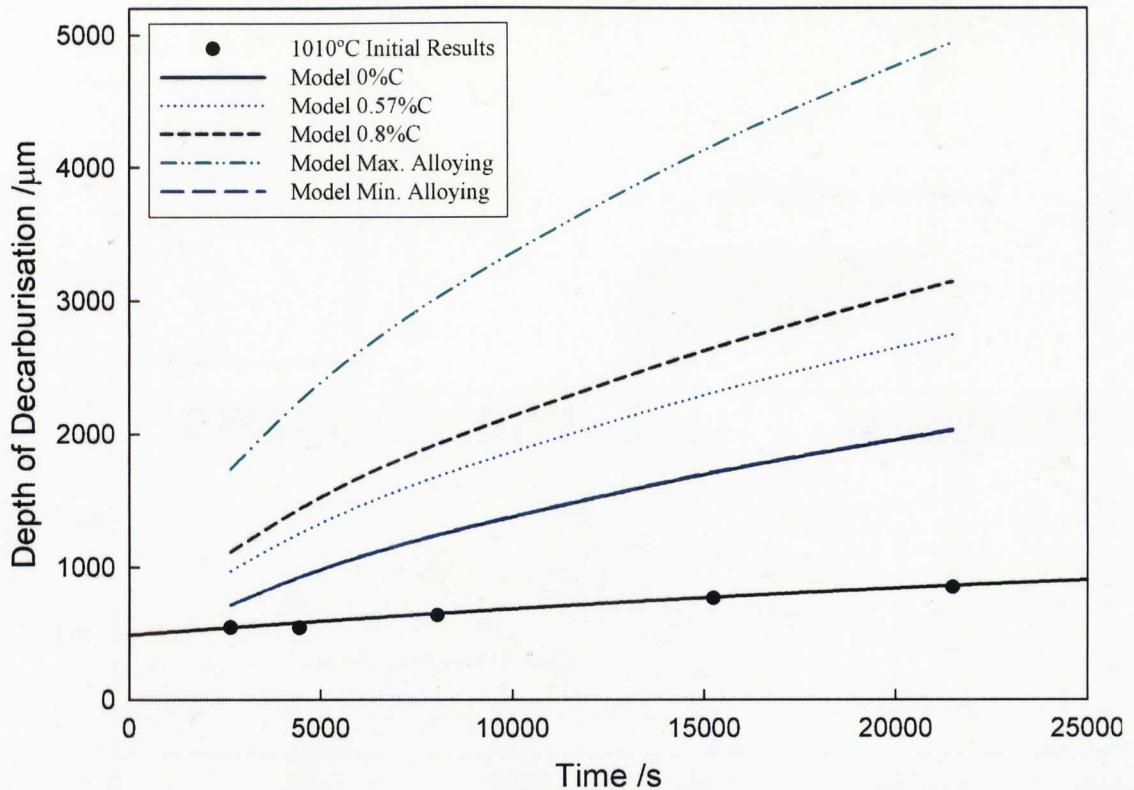
Figure 4.8: Comparison of model and experimental results for depth of decarburisation at 1010°C. The diffusion coefficient by Kucera and Stransky has been used to examine the effect of carbon content at 0, 0.57 and 0.8%[11]. The interaction parameter has been used to examine the effect of the other alloying elements; the minimum alloying line is identical to the 0%C line[11,14].
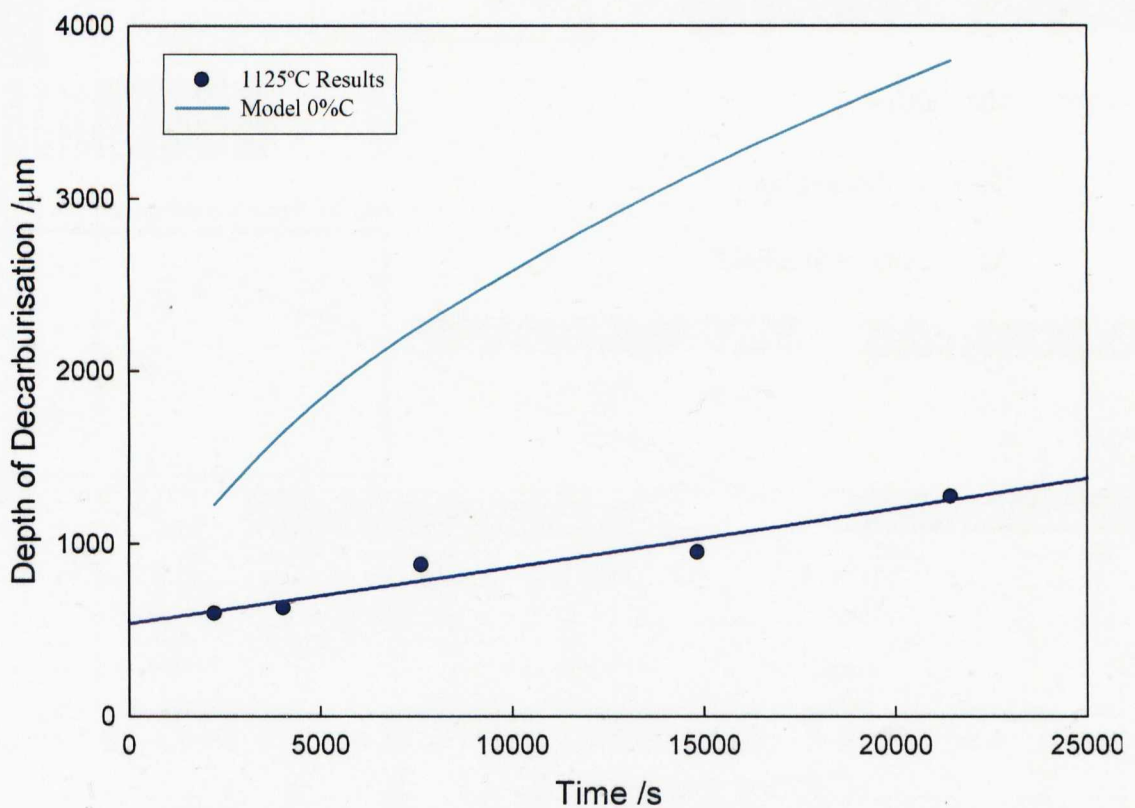
Figure 4.9: Comparison of Birks model and experimental results for depth of decarburisation at 1125°C.
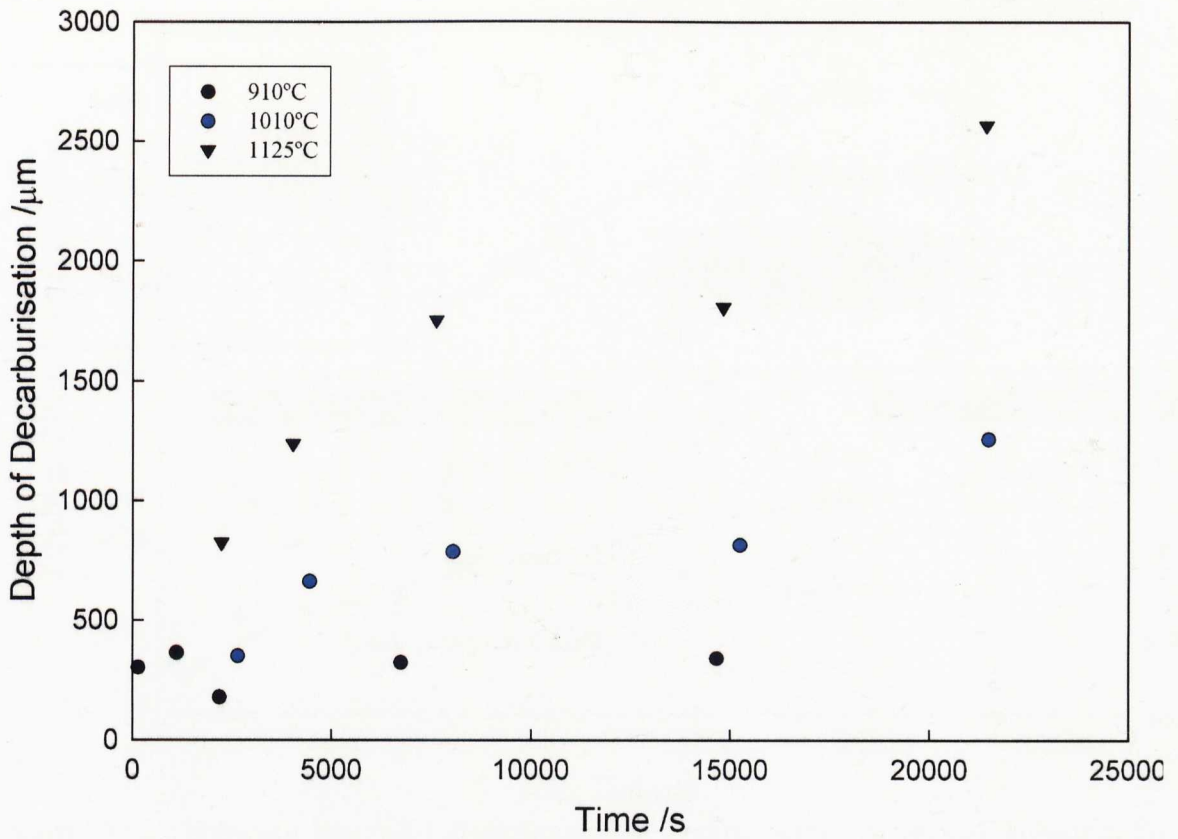
Figure 4.10: Depth of decarburisation measured using micro hardness traverses of samples defined as 98% of the bulk hardness values.
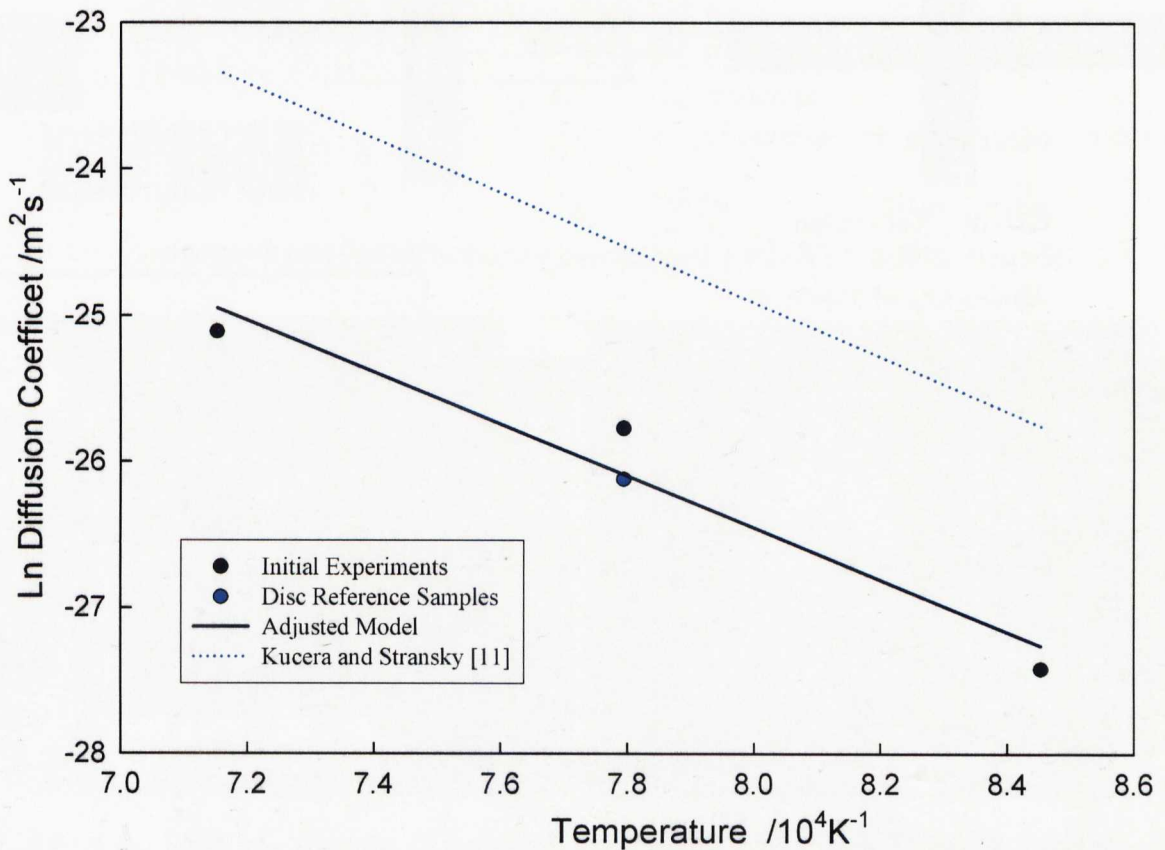
Figure 4.11: Arrhenius plot of the experimental results of diffusion coefficients calculated from depth of decarburisation, including results from rail disc reference samples[11].
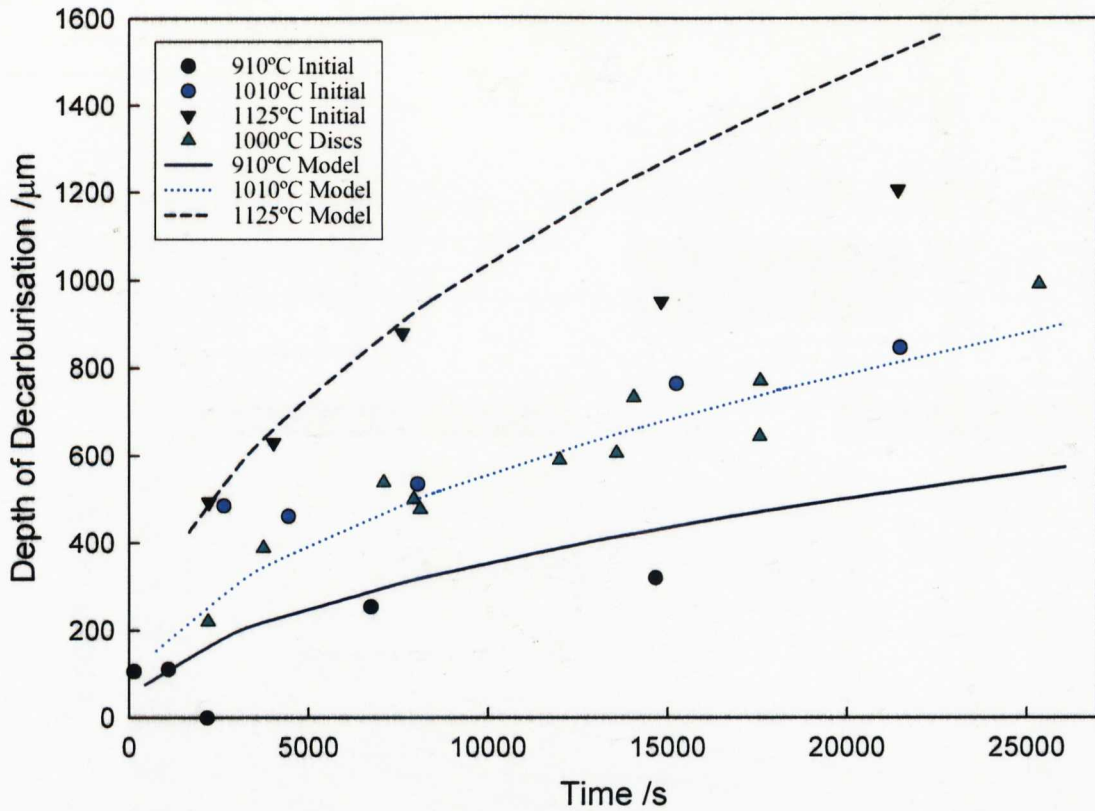
Figure 4.12: Showing depth of decarburisation results with the model adjusted for diffusion coefficient measured from initial experiments.
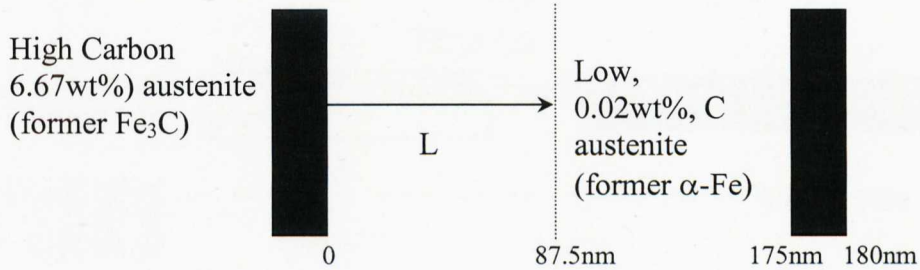
Figure 4.13: Schematic of boundary conditions for the WEL diffusion model
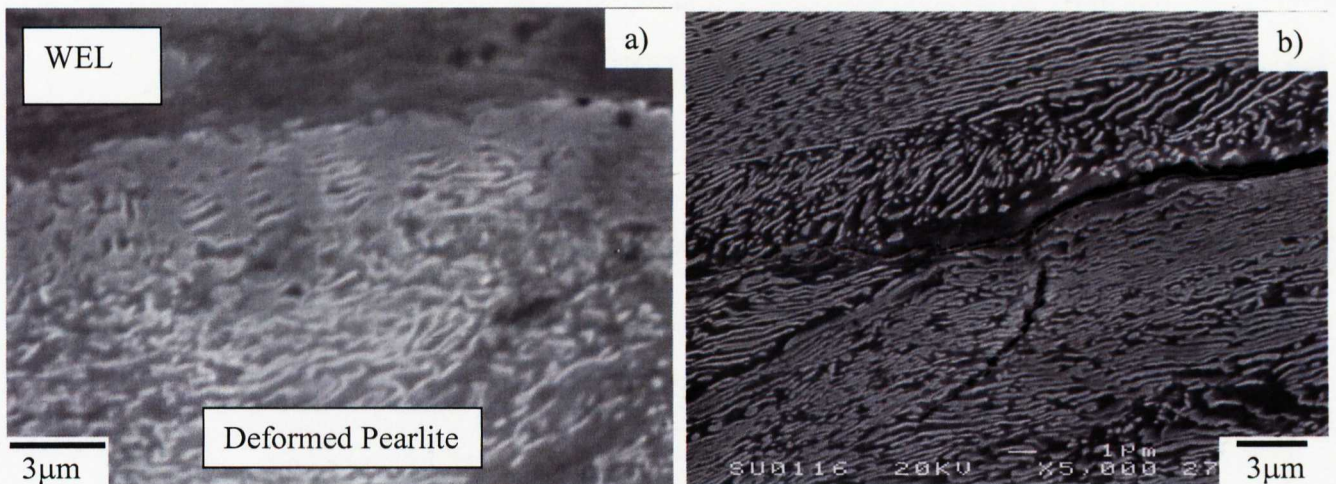
Figure 4.14: SEM micrographs of deformed layer below white layer found on a section of railhead removed from track. a) Showing WEL and the deformed pearlite, b) 20μm below WEL – lamella spacing of 185nm.
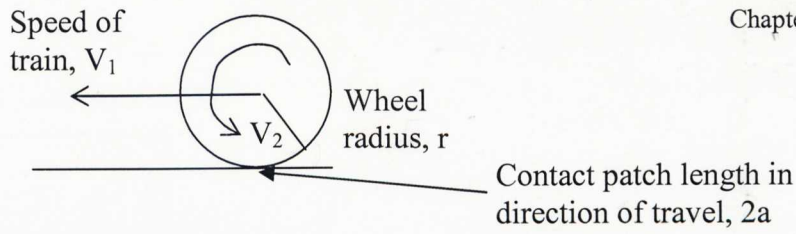
Figure 4.15: Definitions used in train speed/slip model, where V_1 is the velocity of the train and V_2 is the peripheral velocity of the wheel
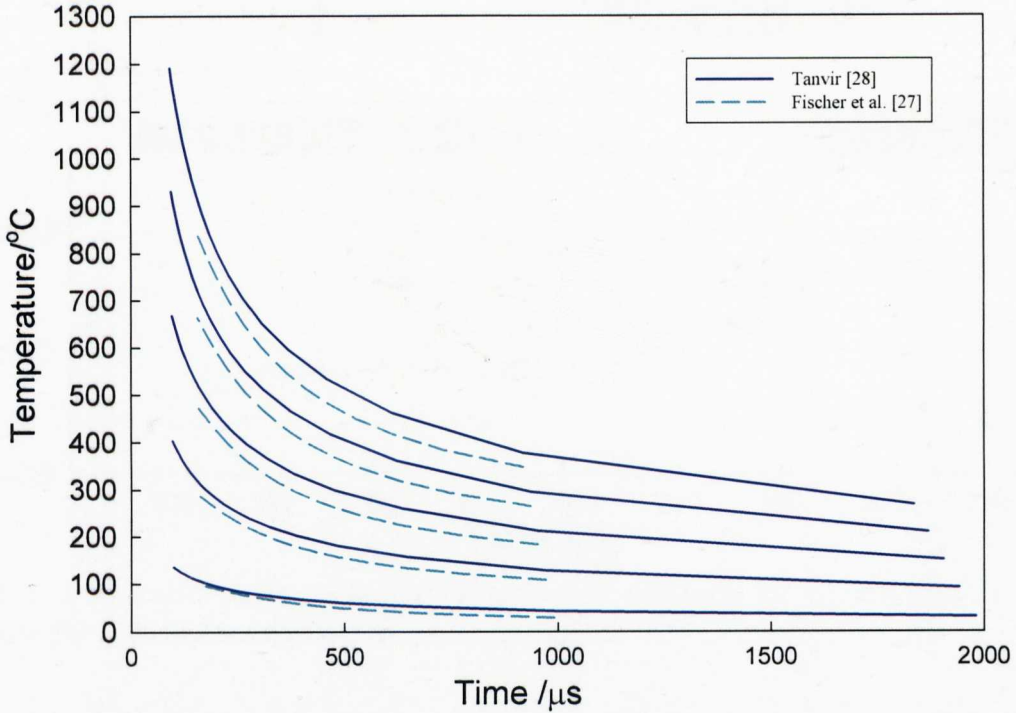
Figure 4.16: Comparison of flash temperature models of Fischer *et al.* [27] and Tanvir[28] for different slip values.
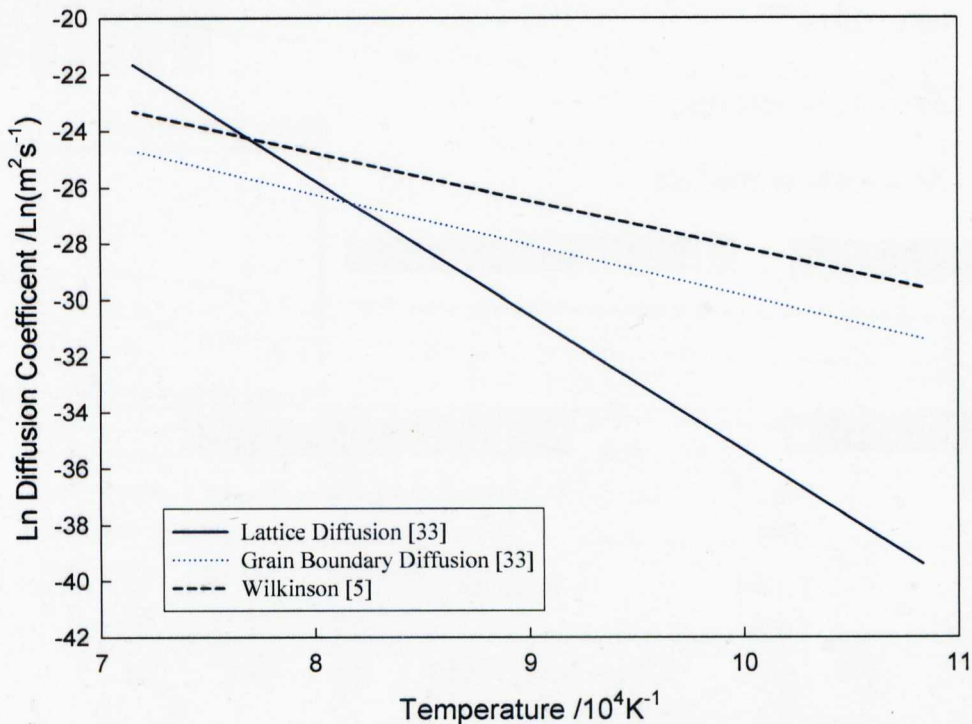
Figure 4.17: Arrhenius plot comparing lattice and grain boundary diffusion in a stainless steel and the values given by Wilkinson for carbon in austenite[5,33].
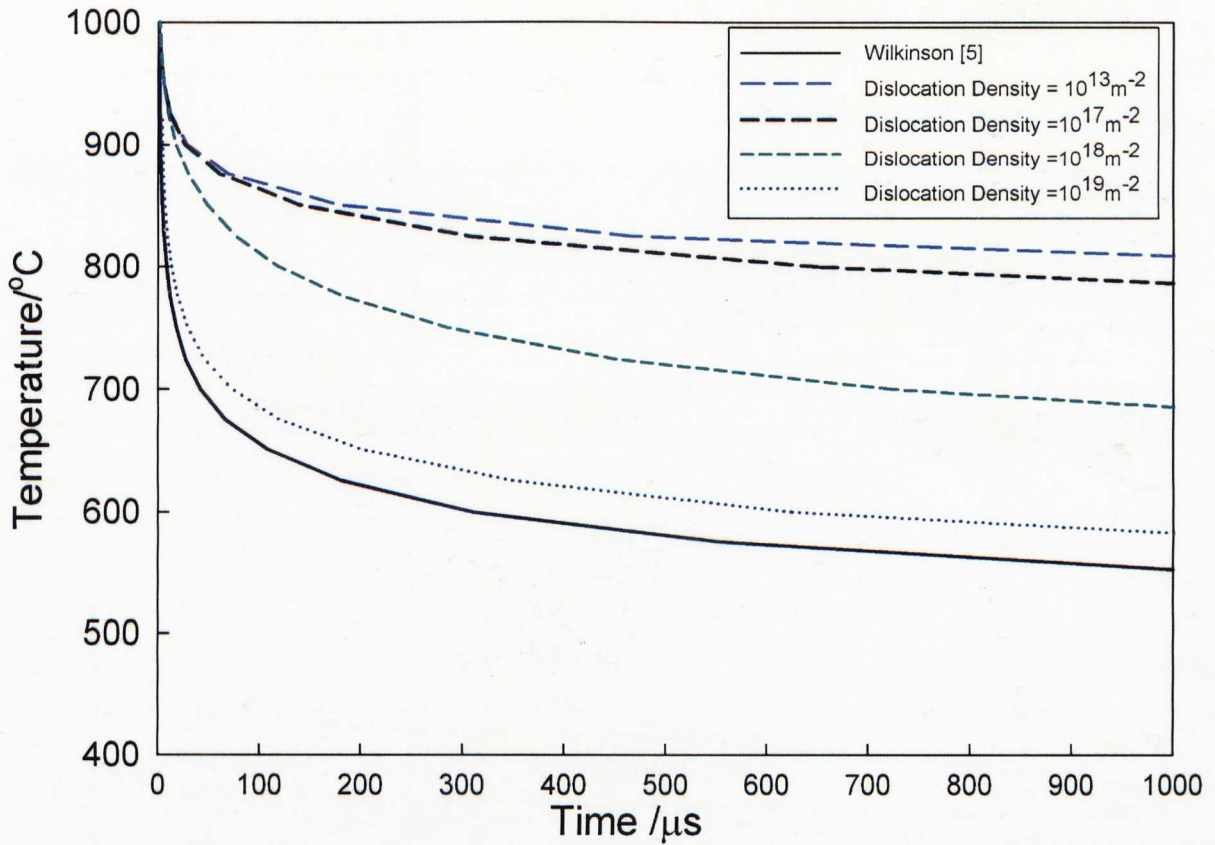
Figure 4.18: Effect of dislocation density on time of diffusion for 1 thermal cycle with a diffusion distance of 24nm[5].
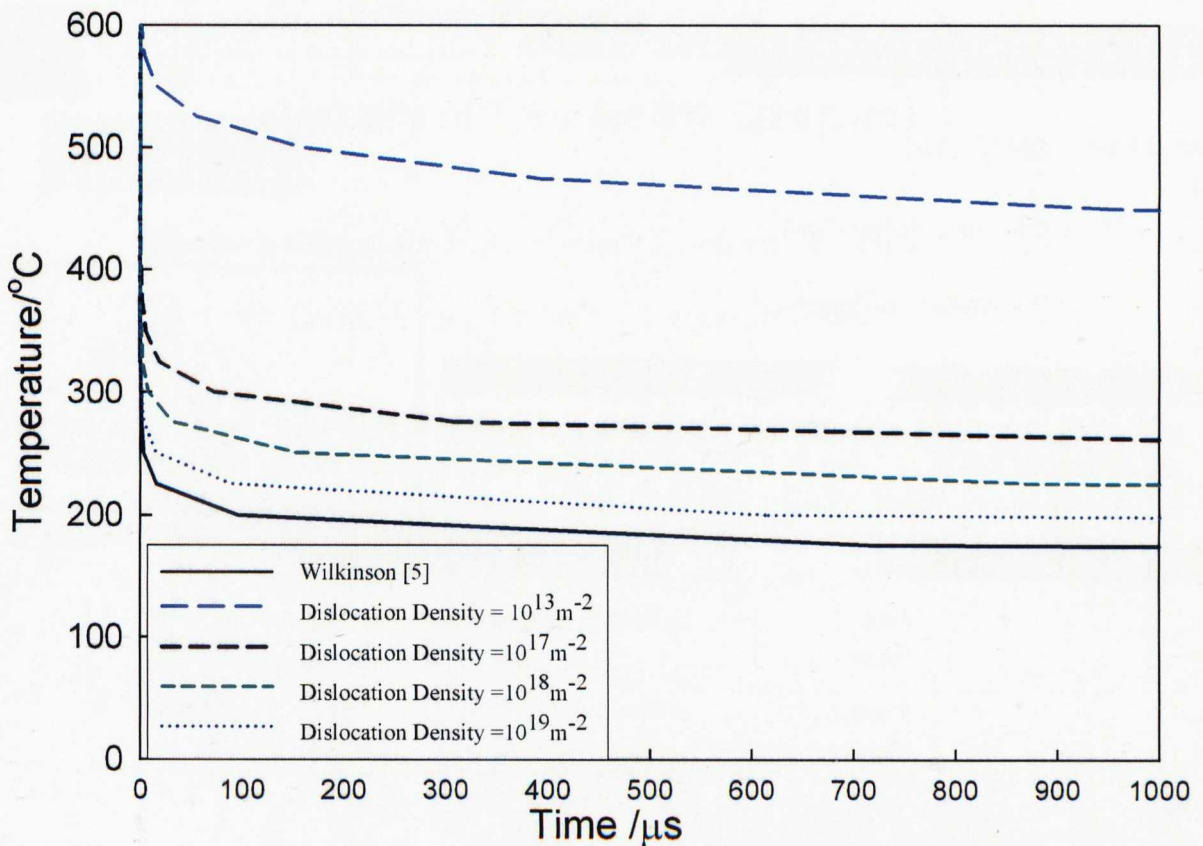
Figure 4.19: Effect of dislocation density on time of diffusion for 50×10^{6} thermal cycles with a diffusion distance of 24nm[5].
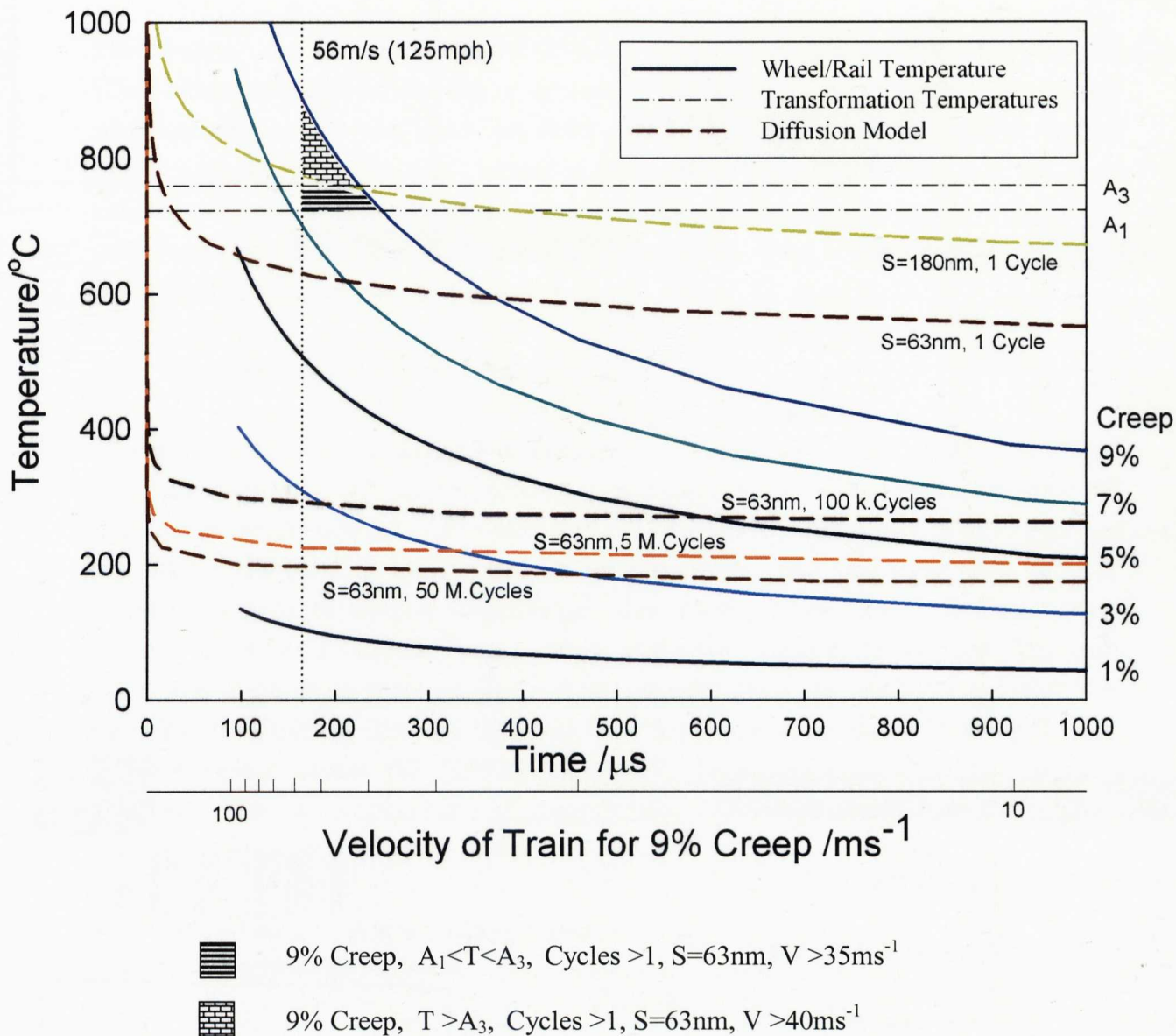
Figure 4.20: Flash temperature and diffusion model as a function of contact time, the vertical dotted line shows the maximum speed in the UK, 125mph. As speed decreases the time of contact increases. The horizontal lines show the transformation temperatures, for transformation to austenite to occur then the A_1 temperature has to be reached.

Chapter 5: Experimental Results

5.1   Introduction

This chapter describes the experimental results from the investigation: this includes the effect of heat treatment on the bulk microstructural features of rail, experiments to simulate white etching layer on rail discs and observations of decarburisation and white etching layer on rail. The majority of this section is given to the rolling/sliding twin disc testing of rail samples containing a simulated surface metallurgical feature. The results include tests on normal samples without any treatment of the surface along with the decarburised and white etching layer samples.

5.2   Heat Treatment of Rail Discs

The heat treatment of the rail discs, to create a decarburised layer at the surface, has altered their bulk microstructure; the parameters of heat treatment, including temperature and total time, are given in table 5.2.1. The effects of the heat treatment is shown in table 5.2.2 on the pearlite interlamellar spacing and the prior austenite grain size along with the bulk micro hardness of the samples. The average values for the unheat-treated rail disc samples are also given along with the average values of the two wheel materials used. The main difference in the wheel materials is the prior austenite grain size with that for steel WA being less than half the size of WB; wheel steel WB is also softer than WA being close to the bulk values of the rail samples of 250HV. The standard deviation is given to demonstrate the variation within each measurement. The results from the measurement of decarburisation have been given in chapter 4.

5.3   Simulation of White Etching Layer
5.3.1   Spot Welds

The results of the three initial spot weld tests, carried out on small samples of rail steel, are given in table 5.3.1. This includes the time of the pulse, the dimension of the resulting spot weld and whether a plate was present between the bottom electrode and the sample. The effect of the plate is to reduce the size of the spot weld by approximately 1mm; it also prevents any contamination of the spot weld by copper from the electrode. A photomicrograph of the interface between the brown martensitic spot weld material and the bulk ferrite/pearlite is shown in figure 5.3.1. On sample SW4, figure 5.3.2, several spot welds have been carried out so that they result in overlapping martensite. A noticeable interface is seen within the martensitic material at the surface with a lighter appearance on the side of the initial weld and a darker appearance on the second and third welds. The micro hardness values are also displayed in this figure and show that the initial weld is softer than the subsequent spot-welds. A hardness gradient is also seen in the last spot weld

with a hardness of 700HV at the surface falling to 550HV at the interface with the bulk steel, which has a hardness of 250HV.

Three rail discs have had white etching layers simulated on them by spot welding, each disc has four spot welds evenly spaced. The duration of the electrical pulse is given in table 5.3.2 along with the dimensions of the resulting spot weld. Spot-weld C in disc RA22 was carried out using a sheet of steel sheet that had been folded so its thickness was doubled; the thickness of the plate was 1.5mm. The depth of the weld is measured in the centre of the spot weld after the disc had been sectioned and was found to vary between 1 and 2mm. This sectioning was usually in the centre of the disc where the weld was the widest but RA19B was a transverse section; no micrographs were taken of spot welds in discs before twin disc testing, but there appearance after grinding was similar to the surrounding pearlite.

5.3.2   White Etching Layer Created by Sliding

All experiments, which have been carried out on discs where the white etching layer had been created by sliding, are given in table 5.3.3. The majority of rail discs have been subjected to subsequent rolling/sliding experiments but other tests have also been carried out to investigate the formation of the WEL and also to study whether it is possible to create a patch of WEL on the surface. The change in dimensions and mass of the discs is shown in table 5.3.4 for all tests. This shows that the mass gain of the rail disc is almost exactly the same as that lost by the wheel discs. The diameter and track width of the rail disc is also increased for the majority of the tests, while the wheel disc diameter is reduced.

The wheel disc, WB01, from the initial sliding WEL test, DP03, has been sectioned and is shown in figure 5.3.3 where the subsurface deformation of the pearlite can be seen; figure 5.3.4 shows the presence of proeutectoid ferrite within the WEL. The rail disc, RA07, from test DP03 was subjected to a further period of sliding for 30 seconds against wheel disc WB04 which had been ground after a previous test; this resulted in both discs turning blue, figure 5.3.5. Figure 5.3.6 shows RA07 sectioned with the WEL exhibiting a brown colour with a hardness of 491HV.

Test WE13A was carried out to allow examination of the WEL after it has been created without a subsequent rolling/sliding test. Figures 5.3.7 and 5.3.8 show this WEL on the surface of rail disc RA31. The microhardness of RA31 is plotted against depth in figures 5.3.9 while the shear strain, calculated using equation 3.6, is shown in figure 5.3.10. Also shown on these figures are the results from the initial test, DP03, for the wheel disc WB01. The shear strain shows that the maximum values are at the surface for both discs but a secondary maximum also occurs for RA31 at a depth of 200μm.

Test WE14A has been carried out to study whether material was transferred from the wheel disc to the rail disc during sliding. This involved using a back up roll disc that has a different composition to rail steel and also a bainitic microstructure, seen in figure 5.3.11 post-test. The test was initially carried out for 5 seconds but observation of the surface indicated that a WEL had not formed so a further 5 seconds of sliding was carried out. The WEL created is shown in figures 5.3.12 and 5.3.13. The transverse section shows that the WEL is not even across the disc but has a variable thickness. Chemical analysis of a slice from the surface of RA34 has shown a higher chromium content by 600% than the bulk rail disc. Also present within the WEL is molybdenum and vanadium which are not present in the rail steel, table 5.3.5. The EDS results have shown that the WEL present on rail disc RA34 has chromium and vanadium present along with iron, manganese and silicon, figure 5.3.14; whereas the pearlite below contains only the last three elements, figure 5.3.15.

The experiments to create patches of WEL on the rail have been conducted in two ways. The first, WI01, involved holding the rail disc, RA32, stationary while sliding the wheel disc, WB05, against it. The grooves formed can be seen in figure 5.3.16, a cross section of one of these is given in figure 5.3.17, deformed pearlite can be seen along with a patch of WEL, with a crack present within it. The second method, WI02, involved the discs rotating at their slowest rate, approximately 12rpm, with the load cycled so it was turned on for 1/3 of a rotation and off for 2/3; only 3 load cycles were able to be completed due to a problem with the testing equipment. Observation of the surface of the two discs after sliding show that the surface has been altered for about ¼ of the circumference of the wheel disc, WB06, and for 2/3 of the rail disc, RA33. The wheel disc exhibits grooves in the surface (figure 5.3.18), while the rail disc shows a build up of material (figure 5.3.19) indicating that cold welding has occurred between the two discs with material transferred from the wheel to the rail disc. A cross section of the rail disc is shown in figure 5.3.20 and shows heavily deformed pearlite welded to the surface but the presence of no WEL.

The final test DW01 has been carried out to investigate whether white etching layer can be formed on the surface of a disc, which has been previously decarburised. Rail disc RA03 has been heat treated to form a depth of decarburisation of 772μm. Figure 5.3.21 shows that a WEL has been formed with the presence of more proeutectoid ferrite than would be normal in the deformed material below the WEL. The soft decarburised surface results in a loss of mass of the rail disc and a gain in mass of the wheel disc during sliding.

5.4   Observations of Rail
5.4.1   Decarburisation

The observation of decarburisation on the surface of the rail has shown that it alters around the railhead. Figure 5.4.1 shows a typical micrograph at the crown of the rail disc surface, while figure 5.4.2 shows a section of the rail near to the gauge corner, which exhibits a greater amount of ferrite at the surface. This figure also shows some oxide that has been

deformed into the railhead during manufacturing. Two samples of rail 30mm apart have been sectioned and examined with the depth of decarburisation measured, figure 5.4.3. The depth of decarburisation is greatest at the gauge corners; the horizontal line on figure 5.4.3 shows the maximum depth of decarburisation allowed by the European standard BS EN 13674-1. At the gauge corners the depth of decarburisation is greater than the maximum standard by 200μm, whereas around the rest of the railhead the average is 450μm.

5.4.2   White Etching Layer

A sample of rail has been removed from service because of a rail break, this has been found to exhibit two different white etching layers; a photograph of the rail with the location of the WEL's is shown in figure 5.4.4. The first form of WEL is at the initiation point of the RCF crack, which resulted in the rail breaking, figure 5.4.5. This WEL has a depth of almost 200μm and exhibits several other cracks within it, which propagate to the interface with the pearlite. These cracks have pearlite deformed up into them, figure 5.4.6. The second WEL is found approximately 10mm away from the first, with a depth of 25μm and can be seen in figure 5.4.7, parallel to, and figure 5.4.8, perpendicular to, the running direction of the rail. Cracks have been found in this WEL initiating at the interface between the WEL and the pearlite (figure 5.4.9) and also at proeutectoid ferrite present within the WEL, figure 5.4.10; the maximum crack length within the WEL is 50μm. Microhardness traverses of the WEL have been carried out (figure 5.4.11) and show that both white etching layers have an average hardness of 780HV at the surface, WEL 1 shows a range of hardness values within it of between 730 and 950HV before a gradual fall to 350HV at the interface. WEL 2 on the other hand has a sharper interface but a similar hardness within the deformed pearlite as in WEL 1. The shear strain of the pearlite has also been measured on WEL 2, figure 5.4.12, showing higher values near the surface when a section of rail has a WEL than one without.

5.5   SUROS Testing of Discs

The conditions of the rolling/sliding SUROS tests are given in table's 5.5.1, 5.5.2 and 5.5.3 for untreated, decarburised and WEL samples respectively.

5.5.1   Data Logging Results

The results described in this section are those data logged during twin disc testing. The data logging allows the calculation of the contact pressure and the traction coefficient. Two examples of the contact pressure graph are shown in figures 5.5.1.1 and 5.5.1.2. These graphs show that the contact pressure of 1500MPa is maintained within ±15MPa or ±1% of the nominal value.

The results of traction coefficient are shown in figures 5.5.1.3 to 5.5.1.13 for all tests graphically against the number of rail disc cycles. Table 5.5.1.1 shows the maximum values for the dry and wet cycles, the end of test values and the average values for the test. The standard samples that have had no heat treatment are shown in figure 5.5.1.3 for those with an initial 200 dry cycles and show a traction coefficient of between 0.28 and 0.4 for the dry cycles. With water lubrication the samples rise to a maximum and then decrease until the end of the test as can be seen in figures 5.5.1.3 and 5.5.1.4 for normal samples and figures 5.5.1.5 – 5.5.1.8 for decarburised samples. The normal samples show an average traction coefficient of 0.17-0.18, while the decarburised samples have values between 0.12-0.15.

The two water lubricated spot welded samples, figure 5.5.1.9, show an initial rise to over 0.2 followed by a sudden decrease to 0.17 after 1000 cycles, with the values then remaining reasonably constant (within 0.15-0.17) until the end of the test. In contrast the traction coefficient of the dry tests rises to a maximum of 0.37 before decreasing to 0.35 at the end of the test.

The trend of the traction coefficient for the unidirectional sliding WEL samples display a similar trend to the standard samples and the decarburised samples, although the average values are higher, figure 5.5.1.10. Figure 5.5.1.11 shows the results for the reversed tests. A problem with the data logging equipment resulted in data being recorded once every five minutes initially during the test of RA24 and shows a rise to a maximum followed by a gradual decrease with a sudden decrease from 0.18 to 0.16 after 26000 cycles. The other two tests were similar and show sudden changes in the traction coefficient. Figure 5.5.1.12 for the test under pure rolling shows a gradual increases from the start to the end of the test; the values are much lower than any other tests with a maximum value of 0.08. The two dry tests, figure 5.5.1.13 show much higher values than the water lubricated tests; with RA36 displaying a similar trend to the unidirectional water lubricated samples. In contrast RA35 shows a drop after 5000 cycles from 0.30 to 0.24 followed by an increase to 0.27 with the values then being similar until the end of the test.

5.5.2   Strain and Hardness

Table 5.5.2.1 shows the Vickers microhardness and shear strain results of the normal and decarburised samples while table 5.5.2.2 gives the results for the WEL tests. The results for the variation of the shear strain with depth are given graphically in figure 5.5.2.1 for the normal samples, figures 5.5.2.2 and 5.5.2.3 for the decarburised samples, for all tests the maximum is at a depth close to 200μm. The shear strain of the spot welded samples in the pearlite away from the spot welds is shown in figure 5.5.2.4. The contour plot, figure 5.5.2.5 shows how the shear strain varies around a spot weld in sample RA19; the black lines indicate where the interface between the pearlite and the spot welds is. The shear strain in the WEL samples is given in figures 5.5.2.6 – 5.5.2.9. The unidirectional tests

show a maximum at the surface but also one at a depth of approximately 200μm. Figure 5.5.2.7 show the results from a reversed test, RA23, with the shear strain measured away from the spot-welds at four separate points; two of the traverses shows a negative strain because the flow lines are in the opposite direction. The shear strain of pure rolling samples are given in figure 5.5.2.8 and the dry samples are given in figure 5.5.2.9.

The shear strain is shown for the decarburised samples in figure 5.5.2.10 divided by the number of cycles against the depth of decarburisation. The results show an increase in the amount of strain at 200μm below the surface with increasing depth of decarburisation. The shear strain is plotted against the number of cycles for the spot welded samples away from the spot welds, along with the values for the normal samples in figure 5.5.2.11. The shear strain of the white etching layer produced by sliding is shown in figure 5.5.2.12, the dotted line on this graph is the trend for all samples without white etching layer. The general trend for all unidirectional tests is an increase in the shear strain with the number of cycles, while the reversed test shows the opposite trend.

An example of the microhardness traverse of a standard samples is shown in figure 5.5.2.13 with a maximum at a depth of 200μm. The results for the decarburised tests (figures 5.5.2.14 and 5.5.2.15) show the results for the rail disc after the test, along with that for the reference sample. The results from the reference sample are adjusted so that the average bulk values are equal; the depth of the reference samples is also adjusted for the material removed by grinding from the surface of the rail disc. This results in an error in the depth of hardness values of ±0.1mm.

The results from the hardness of the pearlite of spot welded sample, RA21, is given in figure 5.5.2.16 away from the spot welds; the distance each measurement is taken from the spot weld is also shown. The hardness around a spot weld of sample RA19 is given in figure 5.5.2.17. The hardness of the pearlite below a WEL produced by sliding is shown in figure 5.5.2.18, the horizontal lines show where the two interfaces: between the WEL and the brown layer of deformed pearlite and between the brown layer and the bulk pearlite. The vertical lines in this figure are the average values of hardness for the bulk pearlite, the WEL and the deformed brown layer.

The percentage hardening of the decarburised samples is the difference between the reference sample and the rail disc after the test, measured at a depth of 200μm; while that for the normal samples and the WEL samples are measured from the average bulk values. The rate of percentage hardening is used to eliminate the effect of the different number of cycles on the results. Figure 5.5.2.19 show that as the depth of decarburisation is increased then the rail steel is deformed more resulting in a greater percentage hardening. The results for depth of decarburisation of less than 200μm show similar results to normal samples. The results for the white etching layer are plotted as the percentage hardening against the number of rail disc cycles in figure 5.5.2.20. With the exception of the two dry tests the

percentage hardening is similar for all samples, including those without WEL; a trend can be seen that the hardness increases with number of cycles. The two dry tests had a much greater hardness than the samples with a white etching layer.

The results of strain and hardness of selected wheel discs is shown in table 5.5.2.3. The values depend on the conditions of the test so these are also given in the table.

5.5.3   Surface Roughness and Roundness of Discs

The surface roughness measured using the Surtronic has resulted in profiles of the surface, an example of which is given in figure 5.5.3.1 for a normal disc before the test, while 5.5.3.2 shows the same disc after the SUROS test. The results of surface roughness are the average of at least 10 separate traces taken at random intervals around the disc. Table 5.5.3.1 show the results for the normal and decarburised samples while those for the spot welded samples are given in table 5.5.3.2. Shown in these tables are the roughness of both discs before and after the SUROS test; included in the latter table are the values for the spot welds and the surrounding pearlite. The white etching layers created by sliding are shown in table 5.5.3.3 for the rail disc after machining, after sliding and at the end of the rolling/sliding test; values are also given for the wheel used during the sliding to create the WEL and for the wheel during the rolling/sliding test.

The Talyrond profiles of the rail discs after the rolling/sliding tests are shown in figure 5.5.3.3 for a normal, a decarburised and a sliding white etching layer sample. Shown on these figures are the areas of the disc which have spalled or cracked. This is especially clear with trace c) for the WEL sample where the rail surface has collapsed in the spalled area. A trace of a spot welded sample is given in figure 5.5.3.4 and shows the location of the spot welds and the uneven wear that occurs during the SUROS test. The spot welds are higher than the average of the disc with a dip in the surface before the spot weld and a peak after the weld.

5.5.4   Wear

The dimensions of the wheel and rail discs before and after the tests are shown in table 5.5.4.1; while the total wear and the wear rate of the samples measured by the change in mass of the samples during the rolling sliding test are shown in table 5.5.4.2. The total wear of the rail disc samples measured by loss of radius for the decarburised tests are shown in figure 5.5.4.1 plotted against the depth of decarburisation and show a general trend of increasing wear with increasing depth of decarburisation. The results for the samples without decarburisation show the spread in results when the test conditions were the same.

The wear rate is the total wear measured by mass change divided by the number of rail disc cycles. This is not an accurate measure of wear rate but an average for the whole test and allows tests with different number of cycles to be compared. Figures 5.5.4.2 and 5.5.4.3 show the results for rail and wheel respectively of the decarburised samples. Figure 5.5.4.2 shows that as the depth of decarburisation is increased then the wear rate of the rail disc also increases; for samples with depths of less than 200μm the wear is similar to those without decarburisation. The wear of wheels is lower for all samples run against rail discs with decarburisation than those without; this also includes a result where material has been picked up by the wheel disc giving a negative wear rate. The results have shown there is little difference in the samples, which were run dry for 200 cycles and those run wet from the start.

The total wear of the spot welded rail samples is shown in figure 5.5.4.4. The results for the water lubricated tests show that after 4000 cycles the wear is similar to samples without spot-welds but as the number of cycles is increased then the wear of the rail is higher. The wear of the rail disc, RA21, under unlubricated condition is higher than samples with water lubrication for the same number of cycles. The wear of the wheel discs is shown in figure 5.5.4.5 and shows for all three tests the wear is higher than for samples without spot-welds.

The wear rate of the rail discs with a white etching layer produced by sliding are plotted against the depth of the WEL in figure 5.5.4.6. Also shown is the equivalent depth of the WEL that would be present on rail using the contact dimensions to scale the results. It can be seen in this figure that the thickness of the WEL only varies by 15μm and there is no correlation between the results.

The wear results for the sliding WEL test are best plotted as total wear against the number of rail disc cycles and is plotted in figure 5.5.4.7 for rail discs and figure 5.5.4.8 for wheel discs. The rail wear shows for the majority of tests it is lower for samples with a WEL than without; the only exception to this are for the unidirectional tests at long times that have resulted in spalling of the surface, RA25 and RA26. A dry sample, RA35, has a much higher wear than other samples because of uneven running on the machine and is therefore not shown in figure 5.5.4.7. In contrast the wear of the wheel discs run against WEL sample is much greater than of the wheel samples run against rail discs without WEL; in the case of the longer test duration this is by an order of magnitude.

5.5.5   Rolling Contact Fatigue Cracks

The numerical results of cracks present within sectioned samples are shown in table 5.5.5.1 for all tests. The results for the decarburised samples are shown in figures 5.5.5.1 – 5.5.5.4, the spot welded samples are in figures 5.5.5.5 and 5.5.5.6 and the sliding WEL tests are shown in figures 5.5.5.7 - 5.5.5.11. The crack growth rate is given for the figures of decarburisation to allow the elimination of the number of cycles and show the wide depth

of decarburisation; whereas for the WEL samples the narrow range in the depth means that the crack lengths are plotted against the number of cycles.

Figures 5.5.5.1, 5.5.5.2 and 5.5.5.3 show that for samples without decarburisation there is a large spread in the results of all three measures of crack growth. The trend of the decarburised samples shows that with increasing depth there is an increase in the crack length growth rate, figure 5.5.5.1; for the two samples with 6600 cycles the rate is much lower than for samples with greater numbers of cycles. The depth crack growth rate (figure 5.5.5.2) shows that there is a possible maximum at a depth of 250μm. The average crack growth rate (figure 5.5.5.3) shows a considerable spread in results but the general trend is increasing rate with increasing depth of decarburisation. The length/depth ratio (figure 5.5.5.4) shows an increase with depth of decarburisation; with the correlation to a straight line being quite good for the wet samples but not for those with 200 dry cycles.

The crack lengths and depths of the spot welded samples are shown in figures 5.5.5.5 and 5.5.5.6 respectively. The maximum length and depth of the cracks within the spot welds are similar for all three samples whatever the test conditions or number of cycles, with the greatest being for the dry test after 4000 cycles. The cracks within the pearlite on the other hand show a dependence on the number of cycles and the test conditions. After 4000 cycles of water lubricated running no cracks were found, but after the same number of cycles with no lubrication small cracks, less than 150μm in length were found. Once the number of cycles is increased to 23000 with water lubrication the length of the maximum crack is increased to 2.3mm. The length and depth of cracks was much greater than for samples without any spot welds for the same number of cycles.

For WEL created by sliding the maximum crack length and depth plotted against the number of cycles of each test are shown in figures 5.5.5.7 and 5.5.5.8 respectively. The maximum crack length and depth show that for the majority of samples the values are similar for all test durations and conditions, whereas the samples without show a gradual increase. The significant difference is in the three unidirectional samples with greater than 10000 cycles which have much longer cracks. The average crack length is shown in figure 5.5.5.9; this is estimated from all cracks present within the sectioned area with a mean of crack lengths being calculated. It is hard to draw any conclusions from figure 5.5.5.9 because of the great spread in the results but the general trend is increasing length with number of cycles as would be expected for cracks that grow with increasing numbers of cycles.

Figure 5.5.5.10 shows the length over depth ratio (L/D) of the largest crack against the duration of the test; a high L/D represents a long and shallow crack, which indicates a high degree of deformation because the cracks follow the flow lines of the material. The trend for samples without WEL is a decrease with increasing number of cycles whereas for samples with a WEL an increase occurs with the number of cycles. The reversed tests

show no trend but are much higher than the other results. The density of cracks is shown in figure 5.5.5.11 around the disc for all samples; for the samples with many cracks the value is dependent on the location that the density is taken. If the measure is taken in a spalled area the number of cracks is much greater than on discs away from them. For most discs the crack densities are similar whatever the test conditions; for samples with test durations of greater then 15000 cycles the density is much lower than for samples without a WEL.

5.6   Photographs of Samples

This section describes the physical appearance of the sample. This includes macro photographs of discs taken after testing of the running surface. Also included are micrographs of discs taken using the optical and electron microscope once the disc have been sectioned in the vicinity of the longest crack found using the eddy current director. Other features of interest have also been sectioned.

5.6.1   Normal

The surface of a rail disc, RA01, which is a standard disc with no alteration of the microstructure is shown in figure 5.6.1.1 and exhibits small dark patches. A section of the disc has been examined after polishing and etching in the optical microscope. Figure 5.6.1.2 shows several cracks at the surface while figure 5.6.1.3 shows a higher magnification of a single crack.

5.6.2   Decarburisation

The surface of a decarburised rail disc is shown in figure 5.6.2.1; the higher magnification photograph shows that the surface has small dark patches along with scratches. A sectioned sample of decarburised disc RA17 showing more ferrite present at the surface than in the bulk of the material is given in figure 5.6.2.2. Typical pictures of cracks present in decarburised samples are shown in figures 5.6.2.3 and 5.6.2.4. A lower magnification micrograph is given in figure 5.6.2.5 and shows many cracks present at the surface of the disc. Much higher magnification micrographs taken using the scanning electron microscope are shown in figure 5.6.2.6 of cracks at the surface. Rail disc RA09, which spalled during testing, is shown in figure 5.6.2.7 with a series of interconnected cracks. A picture showing the deformation of the wheel disc after running against a decarburised sample is shown in figure 5.6.2.8.

5.6.3   White Etching Layer
5.6.3.1   Spot welds
An example of a spot weld after twin disc testing is displayed in figure 5.6.3.1; the higher magnification image shows there are distinct wear grooves within the harder spot welded material which are not present within the pearlite. Also seen close to the interface with the

bulk material, but within the spot welds, are several cracks. Close inspection of the low magnification image shows that a plate of material is covering part of the spot weld. A cross section through this spot weld is shown in figure 5.6.3.2 where several cracks can be seen near the right edge of the spot weld. A higher magnification of similar cracks in another spot weld on the same disc is shown in figure 5.6.3.3; whereas figure 5.6.3.4 shows the opposite side of the spot weld where the pearlite has been deformed and is piling up against the harder spot weld. Figure 5.6.3.4 is for 4000 cycles with water lubrication whereas after 23000 cycles cracks have grown within the samples, figure 5.6.3.5.

5.6.3.2   Sliding WEL

The surface of the white etching layer samples after twin disc testing for all tests with a traction force exhibit a characteristic chevron pattern near the centre of the disc, figures 5.6.3.6 and 5.6.3.7. Also seen on figure 5.6.3.6 are several small cracks inclined to the edge of the discs. Figure 5.6.3.8 shows that for a disc under pure rolling conditions no chevron cracks appear but a series of circumferential cracks are present near the edge of the discs. The higher magnification images show that these cracks are not parallel with the wear grooves but inclined at an angle of approximately 10° to them. A cross section of rail disc RA30 after 30000 cycles with no slip present shows the transverse deformation that occurs during twin disc testing, figure 5.6.3.9.

The cross sectioning of discs has shown that there are several crack morphologies below the surface depending on the conditions and duration of the twin disc test. Cracks have been found that initiate within the WEL, these can be vertical or aligned at 45° the surface. Vertical cracks are most likely to initiate at the surface, figures 5.6.3.10 and 5.6.3.12 but may possibly initiate at the interface between the WEL and pearlite, figure 5.6.3.11. Angled cracks are seen in figures 5.6.3.13 and 5.6.3.14; in the latter figure the WEL has the appearance of being forced backwards and under the adjacent section of WEL, also seen are small cracks initiating at the surface but which have not grown deeper than 15μm. Along with these single cracks seen in the WEL there are several double cracks as seen in figures 5.6.3.15, 5.6.3.16 and 5.6.17. A further development of these cracks is the formation within the WEL of gaps as seen in figures 5.6.3.12.

The formation of gaps, figures 5.6.3.18 and 5.6.3.19, means that if the WEL has remained intact then it has had to move elsewhere on the disc this can be demonstrated by several pictures showing how this overlapping may occur. Figure 5.6.3.20 shows how two cracks close together allow the WEL to be deformed down into the pearlite. Figures 5.6.3.21 and 5.6.3.22 shows how with high plastic strain during dry testing the pearlite is deformed over the top of the WEL. It has also been seen that the WEL can be deformed backwards into itself resulting in it cracking, figure 5.6.3.23

After gaps have formed within the WEL they have been found to fill with an unknown substance. The unknown substance, figure 5.6.3.24, has had EDS performed on it with the

results summarised in figure 5.6.3.25; for simplicity this material will be known hereafter as wear debris. The EDS trace of dark material within the gap, figure 5.6.3.26, shows that oxygen is present for a trace taken in the dark phase of the wear debris near the surface. In contrast, figure 5.6.3.27, shows that the only elements present are iron, manganese and carbon as is the case for the bulk pearlite. The results for other sections have shown that no oxygen is present within the Bakelite mounting material but silicon and calcium are.

Cracks that have propagated through the WEL can propagate into the bulk in several ways. Figure 5.6.3.28 shows a single crack passing through the WEL with a slight angle at the surface. Once cracks have propagated through the WEL these single cracks usually follow the flow lines of the deformed pearlite, figure 5.6.3.29. Like the normal and decarburised samples these cracks have also been found to branch. It is also possible that they propagate along the interface for a short distance before turning down into the pearlite and propagating along the flow lines, figure 5.6.3.30.

Instead of a single crack in the WEL propagating into the pearlite, cracks can also propagate from the gaps within it; figure 5.6.3.31 shows two cracks propagating, wear debris can also be seen in the bottom of the gap. These cracks like the single ones propagate along the flow lines of the material. With an increase in the test duration the pearlite between the cracks is deformed towards the surface, figure 5.6.3.32, until it appears as an extrusion above the WEL, figure 5.6.3.33. To accommodate this plastic strain the two original cracks extend into the bulk of the material; also the white etching layer in front of the crack is deformed down into the bulk pearlite resulting in it breaking. With a further increase in cycles the pearlite is further deformed towards the surface until the wheel disc cuts it, figure 5.6.3.34, resulting in cracks initiating in the pearlite between the original pair; the breaking of the WEL has also resulted in further cracks initiating in the pearlite. The result of all these cracks has resulted in the formation of a step on the surface of the disc. Figure 5.6.3.35 shows several cracks on the surface of RA25 after 26000 water lubricated cycles, it can be seen that the initial twin cracks result in only one propagating to great lengths; the maximum crack length is 2.5mm after 26,000 cycles and grows to 4.5mm after 37,000 cycles. Within the WEL on the right hand side of the step in figure 5.6.3.34, an example can be seen of cracks propagating in two directions, as described above.

A further type of cracks has been found propagating into the pearlite. Once a gap has formed then the deformation of pearlite up into it can be seen to being in figure 5.6.3.12 and continue in figures 5.6.3.18 and 5.6.3.19. These micrographs show that as deformation occurs cracks initiate within the pearlite and propagate below the WEL close to the interface. This deformation continues until the pearlite reaches the surface, figures 5.6.3.16 and 5.6.3.36 by which time the cracks have propagated to over 0.5mm. If there are several of these cracks close together they can be seen to start joining up in figure 5.6.3.37, they have also been found to grow in three dimensions in the transverse section, figure 5.6.3.38,

when the number of cycles is increased to 37000 cycles these cracks join up and result in the WEL spalling off, figure 5.6.3.39. The heavy deformation of the surface results in many cracks appearing once the WEL has fallen off and results in slivers of pearlite as wear debris. These types of crack have been found in both the reversed and unidirectional tests when water lubrication was present.

Tests with no lubrication show different types of cracks than those with water lubrication. Figure 5.6.3.40 shows that after 11000 cycles a gap has formed within the WEL, the heavy deformation of the sample has resulted in pearlite being deformed up into it resulting in a crack growing into the pearlite along the flow lines. The WEL on the right of this has also been deformed towards the surface. After 31000 cycles the surface of the rail disc has spalled in patches like RA26 but this is due to the heavy deformation of the subsurface pearlite and the formation of cracks that turn towards the surface, figure 5.6.3.41. The maximum crack length has only reached 650μm when no water lubricant is present. The heavy deformation of the surface has resulted in some of the WEL not spalling off but being deformed into the pearlite, figures 5.6.3.21 and 5.6.3.22. The arrows in figure 5.6.3.22 show the movement of the WEL.

Figure 5.6.3.42 displays a standard gap in the surface which has been filled with pearlite, while cracks have grown from the surface into the bulk material. Also seen is a second crack that is three legged and appears to have initiated subsurface with no connection to the crack at the surface.

The wheel discs that have run against the WEL disc have shown that with water lubrication and 1% slip after 37000 cycles the surface of the disc has cracks in it as shown in figure 5.6.3.43. With pure rolling then the cracks have grown to a much greater extent with plates of materials falling off from the surface, figure 5.6.3.44. The sectioned samples of the wheel discs show that the surface is deformed to a depth of less than 700μm, figures 5.6.3.45-5.6.3.47. After 4000 unlubricated cycles there is a high level of deformation in comparison to water lubricated tests. Figure 5.6.3.46 shows that cracks have initiated at the surface; under conditions of 0% slip and 34000 cycles the cracks can be seen to have propagated to a greater extent, figure 5.6.3.47.

5.7   Tables

Rail Disc	Reference Sample	Temperature /°C	Equivalent Time, t_e /s	Hold Time /minutes	Total Time /minutes
RA04	DE28	1000	606	123	133
RA05	DE29	1003	711	202	214
RA06	DE30	1003	711	302	314
RA09	DE31	1000	611	139	149
RA10	DE32	1000	611	243	253
RA12	DE33	1006	623	90	100
RA13	DE34	1006	623	255	265
RA14	DE35	999	584	60	70
RA15	DE36	999	584	255	265
RA16	DE37	1003	590	30	40
RA17	DE38	1003	590	443	453

Table 5.2.1: Heat treatment parameters of rail disc samples

Rail disc	Interlamellar Spacing /nm		Prior Austenite Grain Size /μm		Micro-Hardness (HV100g)	
	Average	SD	Average/um	SD	Average	SD
Un-Heat Treated Rail Discs						
RA01	268	23	184	21	224	11
RA08	369	81	185	29	240	16
RA11	231	33	200	31	248	19
RA18	267	50	197	54	234	19
Average	284	47	191	34	236	16
Decarburised Rail Discs						
RA04	227	89	292	72	242	8
RA05	221	71	298	68	241	8
RA06	211	35	290	86	272	12
RA09	190	31	289	58	249	17
RA10	205	25	276	52	260	20
RA12	245	51	256	65	272	12
RA13	245	52	326	96	266	18
RA14	227	58	331	104	254	14
RA15	230	66	310	85	257	12
RA16	201	40	329	91	256	15
RA17	239	42	352	115	256	13
Wheel Discs						
WA	223	64	107	18	274	19
WB	248	80	239	61	247	15

Table 5.2.2: Microstructural parameters of rail and wheel disc samples for both unheat treated and heat treated samples.

Sample	Pulse /s	Plate	Top Electrode		Bottom Electrode	
			Maximum Depth /mm	Surface Width /mm	Maximum Depth /mm	Surface Width /mm
SW1	1	Y	0.97	4.09	0	0
SW2	2	Y -Weld	1.45	3.58	0.47	1.74
SW3	3	N	2.04	5.02	1.95	4.75

Table 5.3.1: Results of initial spot welded samples

	Spot Weld	Time /s	Width /mm	Depth /mm
RA19	A	0.5	8.35	1.95
	B (transverse)	1	10.27	1.84
	C	2	7.52	1.93
	D	2.5	7.63	2.08
RA21	A	1		
	B	0.5-1	6.47	1.55
	C	1	8.71	1.97
	D	1.5		
RA22	A	1		
	B	0.5		1.47
	C	1 Double sheet	5.74	1.32
	D	<0.5	4.77	1.14

Table 5.3.2: Dimensions of spot welds in rail disc samples

Test	Disc on Lathe Shaft	Disc on AC Motor Shaft	Time of Sliding /s	Hardness of WEL /HV100g	Comments
DP03	RA07	WB01	3	782W	Initial Test
WMO1	RA07	WB04	30	491	Discs turned blue
WE01A	WB06	RA20	5	789	SUROS
WE03A	WB07	RA23	5	846	SUROS
WE04A	WB08	RA24	5	845	SUROS
WE07A	RA25	WB05	4	898	SUROS
WE08A	RA26	WB09	4	826	SUROS
WE09A	RA27	WB10	4	829	SUROS
WE10A	RA28	WB12	5	863	SUROS
WE11A	RA29	WB13	5	872	SUROS
WE12A	RA30	WB14	5	830	SUROS
WE13A	RA31	WB25	5	804	No SUROS Test
WE14A	RA34	BU9	5+5	648	High Cr Disc
WE15A	RA35	WB09	5	876	SUROS
WE16A	RA36	WB10G	5	852	SUROS
WI01	RA32	WB05G		767	Rail Stationary
WI02	RA33	WB06G		461	Intermittent Load
DW01	RA03	WB02	5	662	Decarburised Disc

Table 5.3.3: Creation of WEL tests (G = wheel disc that has been ground back to bulk pearlite after a previous test)

Disc	Mass change /g		Rail Diameter /mm		Wheel Diameter /mm		Rail Track Width /mm	
	Rail	Wheel	Before	After	Before	After	Before	After
RA20	0.15	-0.15	46.99	46.97	46.98	46.89	10.00	10.46
RA23	0.23	-0.23	46.98	47.00	46.75	46.64	10.19	10.57
RA24	0.32	-0.32	46.98	47.04	46.77		10.06	
RA25	0.35	-0.36	46.96	47.03	46.68	46.56	10.17	10.46
RA26	0.24	-0.25	46.97	47.00	46.46	46.41	10.57	10.76
RA27	0.41	-0.41	46.97	47.06	46.78	46.62	10.14	10.36
RA28	0.24	-0.24	46.99	47.04	46.83	46.76	10.12	10.28
RA29	0.30	-0.30	46.98	47.03	46.75	46.67	10.19	10.48
RA30	0.24	-0.24	46.99	47.01	46.65	46.59	10.12	10.35
RA31	0.08	-0.08	46.99	46.95	46.97	46.90	10.02	10.51
RA34	1.74	-1.74	46.97	47.23	49.40	49.20	10.14	10.23
RA35	0.20	-0.20	46.97	46.96	45.98	45.91	10.64	10.91
RA36	0.22	-0.22	46.98	46.99	46.40	46.34	10.35	10.74
RA33	0.08	-0.09	46.99	47.07	46.42	46.44	10.30	10.33
RA03	-0.27	0.19	46.46	46.40	46.78	46.82	10.16	10.37

Table 5.3.4: The change in the dimensions and mass of discs during sliding

wt%	C	Mn	Si	S	P	Cr	Ni	Mo	V
RA	0.56	1.10	0.16	0.025	0.019	0.03			
BU9	0.42	0.61	0.36	0.024	0.024	2.95	0.17	0.35	0.1
RA34	0.55	0.95	0.22	0.022	0.021	0.18	0.02	0.03	<0.01
% RA34 / RA	98	86	138			600			

Table 5.3.5: Composition of surface layer of RA34 compared to rail steel RA and back up roll disc, BU9.

Test	Rail Disc	Wheel Disc	Number of Rail Disc Cycles		Wheel Disc Cycles
			Dry	Total	
DP01	RA01	WA01	212	20232	20434
DP06	RA08	WB04	212	27840	28106
DP07	RA11	WB05	0	30869	31172
DP14	RA18	WB12	207	6645	6710

Table 5.5.1 Conditions of SUROS tests on normal samples at 1% creep and 1500MPa

Test Number	Rail Disc	Wheel Disc	Number of Rail Disc Cycles		Wheel Disc Cycles	Depth of Decarburisation on Grain Boundaries /μm	Depth of Decarburisation 98% /μm
			Dry	Total			
DP02	RA04	WA02	207	10512	10592	270	311
DP04	RA05	WB02	213	13736	13767	402	394
DP05	RA06	WB03	219	6619	6565	480	552
DP08	RA09	WB07	213	20227	20032	216	266
DP09	RA10	WB06	0	20014	19272	287	327
DP10	RA12	WB08	215	20486	20542	193	189
DP11	RA13	WB09	0	20079	19518	189	134
DP12	RA14	WB10	0	30237	30001	184	179
DP13	RA15	WB11	0	30086	29373	326	306
DP16	RA16	WB13	0	31231	31089	87	93
DP15	RA17	WB14	0	20001	19411	596	621

Table 5.5.2 Conditions of SUROS tests on decarburised samples at 1% creep and 1500MPa

Test	Rail Disc	Wheel Disc	Rail Cycles	Wheel Cycles	Conditions	Lubrication	% Slip	Depth of WEL /μm
WE01	RA20	WB06	2163	2196	Reversed	Wet	1	41
WS02	RA19	WB15	4005	3915	Spot Welds	Wet	1	1987
WE03	RA23	WB17	8187	8273	Reversed	Wet	1	31
WE04	RA24	WB18	30027	30308	Reversed	Wet	1	37
WS05	RA21	WB19	4022	3921	Spot Welds	Dry	1	1552
WS06	RA22	WB20	24012	23313	Spot Welds	Wet	1	1467
WE07	RA25	WB21	25789	25854	Unidirectional	Wet	1	36
WE08	RA26	WB22	37014	37410	Unidirectional	Wet	1	39
WE09	RA27	WB23	2000	2100	Unidirectional	Wet	0	46
WE10	RA28	WB24	8013	8101	Unidirectional	Wet	1	34
WE11	RA29	WB26	16024	16203	Unidirectional	Wet	1	37
WE12	RA30	WB27	23468	23484	Unidirectional	Wet	0	35
WE15	RA35	WB28	10904	11010	Unidirectional	Dry	1	30
WE16	RA36	WB29	31498	31808	Unidirectional	Dry	1	39

Table 5.5.3 Conditions of SUROS tests on white etching layer samples at 1500MPa

Rail Disc	Traction Coefficient			
	Maximum Dry Cycles	Maximum Wet Cycles	End of Test	Average
Normal Samples				
RA01	0.38	0.22	0.11	0.18
RA08	0.36	0.20	0.17	0.18
RA18	0.28	0.19	0.17	0.17
RA11		0.22	0.15	0.17
Decarburised Samples, 200 Dry - Wet				
RA04	0.35	0.16	0.15	0.14
RA05	0.32	0.16	0.16	0.15
RA06	0.25	0.15	0.14	0.14
RA09	0.33	0.17	0.14	0.15
RA12	0.34	0.17	0.13	0.15
Decarburised Samples, Wet				
RA10		0.17	0.12	0.14
RA13		0.16	0.10	0.13
RA14		0.17	0.13	0.15
RA15		0.15	0.13	0.14
RA16		0.17	0.12	0.14
RA17		0.16	0.10	0.12
WEL - Spot Welds				
RA19		0.19	0.19	0.16
RA21	0.37		0.35	0.35
RA22		0.21	0.14	0.17
WEL - Unidirectional				
RA25		0.20	0.16	0.19
RA26		0.21	0.14	0.18
RA28		0.22	0.20	0.20
RA29		0.20	0.18	0.19
WEL - Reversed				
RA20		0.22	0.16	0.16
RA23		0.18	0.18	0.15
RA24		0.20	0.17	0.18
WEL – 0% Slip				
RA30		0.08	0.08	0.06
WEL - Dry				
RA35	0.31		0.26	0.28
RA36	0.37		0.33	0.37

Table 5.5.1.1: Traction coefficient values for all tests

Rail Disc	Vickers Microhardness (100g)						% Hardening	% Hardening /cycle	Strain at 200µm	Strain Rate (strain /cycle)
	Disc Bulk	Sample Bulk	Surface Disc	Surface Sample	Disc at 200µm	Sample at 200µm				
Normal Samples										
RA01	224		267		316		41	2.0	2.22	11.0
RA08	240		289		329		37	1.3	2.21	7.9
RA18	234		246		315		35	5.2	1.76	26.5
RA11	248		294		357		44	1.4	3.05	9.9
Decarburised Samples, 200 Dry - Wet										
RA04	242	290	236	221	314	251	54	5.1	2.25	21.3
RA05	248	282	216	198	324	226	68	5.0	3.12	22.7
RA06	272	267	214	175	321	191	63	9.6	2.85	43.0
RA09	246	286	287	213	346	227	85	4.2	2.26	11.2
RA12	263	272	256	229	364	247	53	2.6	3.00	14.6
Decarburised Samples, Wet										
RA10	260	288	246	227	359	233	75	3.7	6.07	30.3
RA13	262	266	257	234	372	246	53	2.7	2.93	14.6
RA14	254	282	230	254	363	273	49	1.6	2.95	9.8
RA15	257	296	260	226	335	249	60	2.0	4.52	15.0
RA16	256	269	266	229	352	257	44	1.4	1.73	5.5
RA17	256	269	233	196	360	199	93	4.7	5.45	27.2

Table 5.5.2.1: The microhardness and strain of decarburised samples

Rail Disc	Vickers Microhardness (100g)				% Hardening	% Hardening /cycle	Strain at 200µm	Strain Rate (strain /cycle)
	WEL	Deformed Pearlite	Bulk	200µm				
WEL – No SUROS								
RA31	804		251	311	24		1.76	
WB01	782		242	284	17		1.23	
RA34	648		253	642				
WEL – Spot Welds								
RA19	717	242	242	327	35	8.8	1.44	36.0
RA21	701	247	247	343	39	9.7	2.33	57.9
RA22	688	241	244	351	44	1.8	1.67	7.0
WEL - Unidirectional								
RA25	898	566	244	346	42	1.6	2.99	11.6
RA26	826	528	238	355	49	1.3	4.12	11.1
RA28	863	581	249	333	34	4.2	2.85	35.6
RA29	872	531	245	341	40	2.5	2.61	16.3
WEL - Reversed								
RA20	789		240	314	31	14.4	1.92	88.7
RA23	846		247	326	32	3.9	1.01	12.3
RA24	845	519	243	352	45	1.5	-1.43	-4.8
WEL – 0% Slip								
RA27	829	561	245	319	30	15.0	1.22	61.2
RA30	830		248	330	33	1.4	1.78	7.6
WEL - Dry								
RA35	876		251	381	52	4.8	4.63	42.4
RA36	852		240	388	61	1.9	4.78	15.2

Table 5.5.2.2: The microhardness and shear strain of white etching layer samples

Wheel Disc	Rail Disc	Cycles	Conditions	Shear Strain at 200µm	Strain rate	Hardness /HV100g			% Hardening
						Rail Disc Surface	Wheel Bulk	Wheel 200µm	
WA01	RA01	20222	200 Dry - Wet	0.78	3.84	224	281	334	19
WA02	RA04	10592	200 Dry - Wet, Decarb. - 270µm	0.00	0.00	177	292	325	11
WB11	RA15	30086	Decarb. - 326µm	1.40	4.66	160	254	343	35
WB18	RA24	30027	Sliding WEL	1.27	4.22	845	254	454	79
WB19	RA21	4022	Unlubricated, Spot Welds	3.61	89.86	247/700*	244	390	60
WB23	RA27	2000	Sliding WEL, 0% Slip	0.97	48.58	829	242	330	36

Table 5.5.2.3: The microhardness and shear strain of wheel disc samples (*Spot weld has hardness of 700HV while pearlite is 247HV)

Rail Disc	Wheel Disc	Rail Disc Surface Roughness, R_a /μm		Wheel Disc Surface Roughness, R_a /μm	
		Before Test	After Test	Before Test	After Test
Normal Samples					
RA01	WA01		0.92		0.43
RA08	WB04		0.34		0.31
RA18	WB12	0.63	0.21	0.70	0.43
RA11	WB05		0.49		0.26
Decarburised Samples, 200 Dry - Wet					
RA04	WA02		0.57	0.21	0.44
RA05	WB02		0.29		0.27
RA06	WB03		0.24		0.21
RA09	WB07	0.66	0.50	0.77	0.47
RA12	WB08	0.84	0.42	0.75	0.16
Decarburised Samples, Wet					
RA10	WB06	0.78	0.59	0.67	0.27
RA13	WB09	0.92	0.31	0.75	0.14
RA14	WB10	0.71	0.47	0.72	0.25
RA15	WB11	0.93	0.66	0.56	0.26
RA16	WB13	1.17	0.52	0.67	0.45
RA17	WB14	0.75	1.03	0.63	0.72
Average		0.82		0.64	

Table 5.5.3.1: The surface roughness before and after SUROS test for normal and decarburised samples

Rail Disc	Wheel Disc	Rail Disc Surface Roughness, R_a /μm				Wheel Disc Surface Roughness, R_a /μm	
		Spot Welds		Pearlite		Before Test	After Test
		Before Test	After Test	Before Test	After Test		
RA19	WB15		0.46	0.89	0.17	0.80	0.28
RA21	WB19		0.38	0.42	0.36	0.57	0.44
RA22	WB20	0.71	0.32	0.55	0.35	0.60	0.45

Table 5.5.3.2: The surface roughness of before and after of spot welded samples

Rail Disc	Sliding Wheel Disc	SUROS Wheel Disc	Surface Roughness Ra						
			Rail Disc			Sliding Wheel Disc		SUROS Wheel	
			Turned	Sliding	After Test	Turned	After Test	Turned	After Test
WEL - Reversed									
RA20	WB16	WB06G		1.43	1.04	0.79	1.00	0.64	0.67
RA23	WB07G	WB17	0.71	1.4	1.26	0.55	2.11	0.68	1.37
RA24	WB08G	WB18	0.72	1.19	0.74	0.73	1.30	0.63	0.66
WEL - Unidirectional									
RA25	WB05G	WB21	0.80	1.57	0.85	0.71	1.43	0.58	1.77
RA26	WB09G	WB22	0.96	1.20	0.81	0.78	1.36	0.61	1.65
RA28	WB12G	WB24	0.85	1.23	0.73	0.70	1.03	0.59	0.57
RA29	WB13G	WB26	0.63	1.71	1.15	0.67	1.81	0.61	2.38
WEL – 0% Slip									
RA27	WB10G	WB23	0.57	1.15	1.00	0.63	1.24	0.67	1.53
RA30	WB14G	WB27	0.59	1.35	1.02	0.63	1.21	0.60	4.83
WEL - Dry									
RA35	WB09G2	WB28	0.61	1.76	0.79			0.51	0.61
RA36	WB10G2	WB30							
WEL – No rolling/sliding test									
RA07	WB01			1.92			1.95		
RA31	WB25		0.81	2.40			2.30		
Average			0.73			0.69		0.61	

Table 5.5.3.3: The surface roughness of white etching layer samples created by sliding.

Rail Disc	Wheel Disc	Diameter of discs /mm				Track Width /mm			
		Wheel		Rail		Wheel		Rail	
		Before	After	Before	After	Before	After	Before	After
Normal Samples									
RA01	WA01	47.00	46.98	47.00	46.97	10.02		10.05	
RA08	WB04	46.99	46.96	46.98	46.96	9.98		10.04	
RA18	WB05	46.99	46.94	46.98	46.94	10.03	10.06	10.01	10.04
RA11	WB12	46.99	46.95	46.98	46.95	10.01	10.24	10.05	10.19
Decarburised Samples, 200 Dry – Wet									
RA04	WA02	46.98	46.99	46.13	46.11	10.00		9.50	
RA05	WB02	46.98	46.93	45.99	45.96	9.99	10.19	9.94	
RA06	WB03	46.99	46.95	45.75	45.70	10.01		9.94	
RA09	WB09	46.98	46.94	46.06	46.03	10.00	10.21	9.24	9.79
RA12	WB08	46.98	46.96	45.91	45.89	9.99	10.09	9.04	9.21
Decarburised Samples, 200 Dry – Wet									
RA10	WB06	46.98	46.97	45.81	45.78	9.99	10.07	9.97	9.34
RA13	WB09	46.99	46.91	45.22	45.18	10.02	10.67	8.78	9.57
RA14	WB10	46.98	46.94	46.15	46.13	10.01	10.18	8.95	9.13
RA15	WB11	46.97	46.93	45.40	45.39	10.01	10.19	8.87	9.11
RA16	WB13	46.96	46.94	46.28	46.27	9.99	10.13	9.42	9.51
RA17	WB14	46.98	46.95	45.14	45.08	9.97	10.09	8.56	9.39
WEL - Spot Welds									
RA19	WB15	46.98	46.94	45.47	45.46	10.01	10.32	10.01	10.17
RA21	WB19	46.95	46.85	45.31	45.31	10.02	10.64	10.00	10.18
RA22	WB20	46.97	46.87	45.15	45.13	10.02	10.61	10.02	10.25
WEL – Unidirectional									
RA25	WB21	46.98	46.70	47.03	47.02	10.02	10.99	10.36	10.81
RA26	WB22	46.99	46.64	47.02	46.98	10.00	11.34	10.39	10.91
RA28	WB24	46.99	46.87	47.03	47.02	10.01	10.48	10.20	10.40
RA29	WB26	46.98	46.76	47.03	47.01	10.00	10.78	10.37	10.63
WEL – Reversed									
RA20	WB06G	46.74	46.71	46.97	46.95	10.05	10.32	10.04	10.50
RA23	WB17	46.98	46.74	47.00	46.96	10.00	10.75	10.43	10.59
RA24	WB18	46.98	46.68	47.04	47.02	10.04	10.82	10.33	10.71
WEL – 0% Slip									
RA27	WB23	46.98	46.92	47.08	47.07	9.99	10.26	10.36	10.40
RA30	WB27	46.98	46.81	47.01	46.99	10.01	11.08	10.37	10.93
WEL – Dry									
RA35	WB28	46.98	46.75	46.96	46.88	10.02	11.10	10.60	11.30
RA36	WB30	46.96	46.76	46.95	46.95	10.01	10.92	10.50	10.68

Table 5.5.4.1: Dimensions of wheel and rail discs before and after SUROS test

Rail Disc	Wheel		Rail		
	Wear /mg	Wear rate /µg. cycle^{-1}	Wear /mg	Wear rate /µg. cycle^{-1}	Wear /um
Normal Samples					
RA01	6.1	0.3	29.1	1.4	14
RA08	16.3	0.6	39.2	1.4	12
RA18	6.2	0.9	6.2	0.9	20
RA11	27.7	0.9	47.1	1.5	15
Decarburised Samples, 200 Dry - Wet					
RA04	-1.1	-0.1	31.8	3.0	10
RA05	0.7	0.1	49.4	3.6	12
RA06	1.5	0.2	67.0	10.1	23
RA09	1.6	0.1	102.2	5.1	15
RA12	2.9	0.1	27.5	1.3	8
Decarburised Samples, Wet					
RA10	5.5	0.3	31.2	1.6	15
RA13	2.4	0.1	132.6	6.6	19
RA14	26.0	0.9	37.6	1.2	11
RA15	7.1	0.2	32.3	1.1	4
RA16	5.6	0.2	62.5	2.0	5
RA17	1.1	0.1	113.4	5.7	31
WEL - Spot Welds					
RA19	7.5	1.9	3.2	0.8	5
RA21	21.8	5.6	10.9	2.7	-2
RA22	35.8	1.5	56.5	2.4	9
WEL - Unidirectional					
RA25	945.0	36.6	58.6	2.3	5
RA26	1116.6	29.8	281.4	7.6	23
RA28	291.3	36.0	-2.9	-0.4	5
RA29	777.9	48.0	-1.3	-0.1	7
WEL - Reversed					
RA20	68.6	31.2	1.0	0.5	11
RA23	401.3	48.5	0.5	0.1	20
RA24	937.0	30.9	2.1	0.1	10
WEL – 0% Slip					
RA27	18.3	8.7	0.6	0.3	4
RA30	1075.2	45.8	0.7	0.0	11
WEL - Dry					
RA35	204.1	18.5	52.3	4.8	38
RA36	358.9	11.3	18.3	0.6	2

Table 5.5.4.2: Total wear and wear rate of all rail and wheel disc samples

| Rail Disc | Maximum Crack | | | | Average Crack | | Crack Density /cracks.mm⁻¹ | Length Depth Ratio | Angle of Crack at Surface /° |
	Length /μm	Length Growth Rate /nm.cycle⁻¹	Depth /μm	Depth Growth Rate /nm.cycle⁻¹	Length /μm	Rate /nm.cycle⁻¹			
Normal Samples									
RA01	1189	59	613	30	315	16	15.0	1.0	17
RA08	651	23	366	13	163	6	11.5	0.5	26
RA18	10	2	3	0	50	8	1.3	5.8	17
RA11	883	29	473	15	257	8	13.0	0.6	13
Decarburised Samples, 200 Dry - Wet									
RA04	533	50	214	20	207	20	9.5	2.1	14
RA05	800	58	100	7	156	11	2.5	4.6	14
RA06	26	4	5	1	50	8	1.6	4.8	22
RA09	4436	219	920	45	359	18	11.6	1.5	11
RA12	937	46	469	23	227	11	10.3	1.1	29
Decarburised Samples, Wet									
RA10	1803	90	534	27	443	22	9.4	2.3	14
RA13	1012	50	376	19	100	5	22.7	0.2	26
RA14	1654	55	679	22	367	12	14.7	0.8	20
RA15	1764	59	657	22	325	11	17.6	0.6	11
RA16	791	25	462	15	233	7	18.0	0.4	11
RA17	1408	70	346	17	353	18	16.1	1.1	10
WEL - Unidirectional									
RA25	2390	93	700	27	301	12	1.7	3.4	
RA26	5290	143	1090	29	450	12	2.5	4.9	
RA28	266	33	115	14	112	14	0.3	2.3	
RA29	2786	174	1033	64	339	21	0.9	2.7	
WEL - Reversed									
RA20	403	186	51	24	104	48	1.3	7.9	89
RA23	407	50	81	10	96	12	1.1	5.0	71
RA24	521	17	66	2	135	5	1.1	7.9	84
WEL – 0% Slip									
RA27	0	0	0	0	0	0	0	0	
RA30	230	10	36	2	157	7	0.3	6.4	
WEL - Dry									
RA35	329	30	74	7	239	22	1.2	4.4	
RA36	673	21	140	4	218	7	2.3	4.8	
Spot Welded Samples - Spot welds									
RA19	762	190	582	145	425	106	0.1	1.3	92
RA21	917	228	771	192	157	39	1.3	1.2	82
RA22	805	34	699	29	0	0	0.0	1.2	68
Spot Welded Samples - Pearlite									
RA19	0	0	0	0	NA	NA	NA	0.0	
RA21	109	27	11	3	NA	NA	NA	9.7	
RA22	2300	96	873	37	NA	NA	NA	2.6	

Table 5.5.5.1: Crack length and depth data for all rail disc samples

5.8   Figures
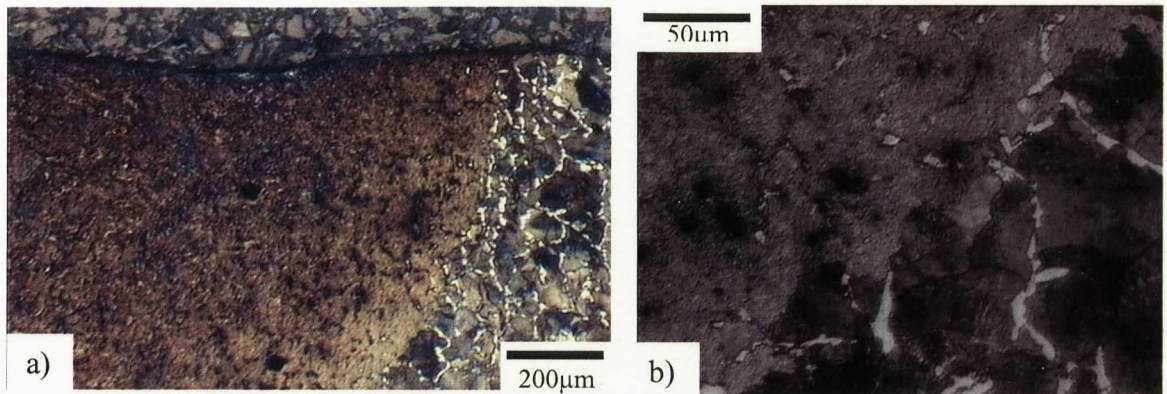
Figure 5.3.1: The interface between a single spot weld and the bulk pearlite, SW1
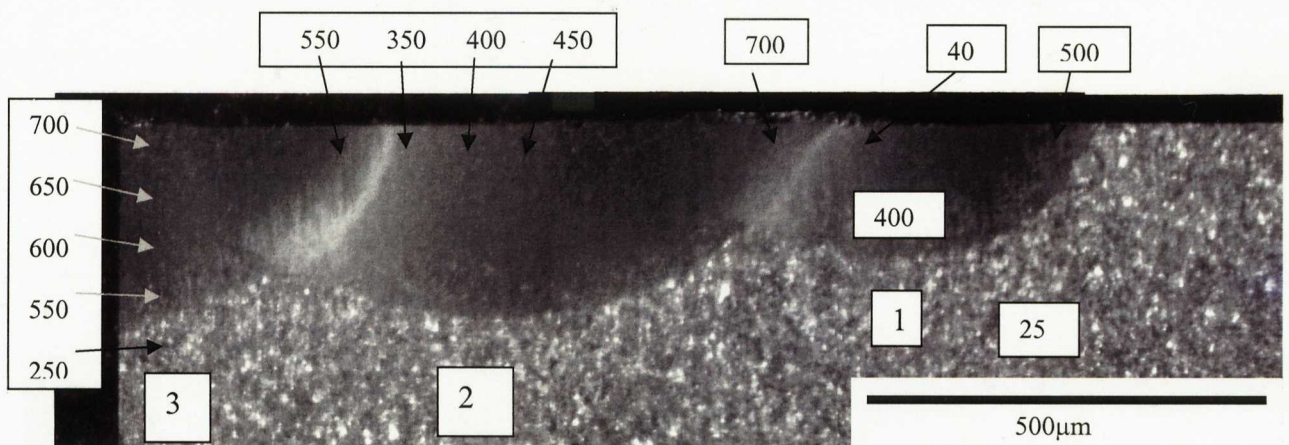
Figure 5.3.2: Three overlapping spot welds in rail sample, SW4, showing the Vickers micro hardness results.

Figure 5.3.3: White etching layer formed on WB01

130
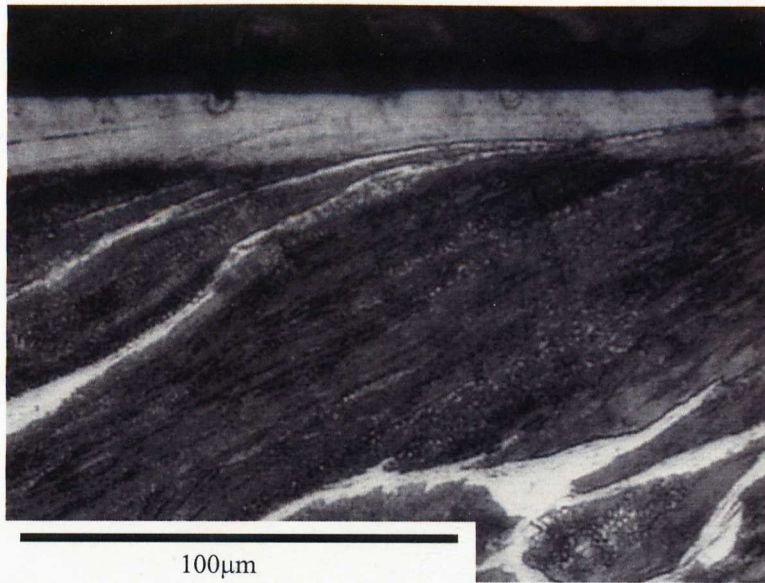
Figure 5.3.4: WEL on WB01 showing proeutectoid ferrite present within it.

Figure 5.3.5: Wheel disc WB04 after sliding for 30 seconds
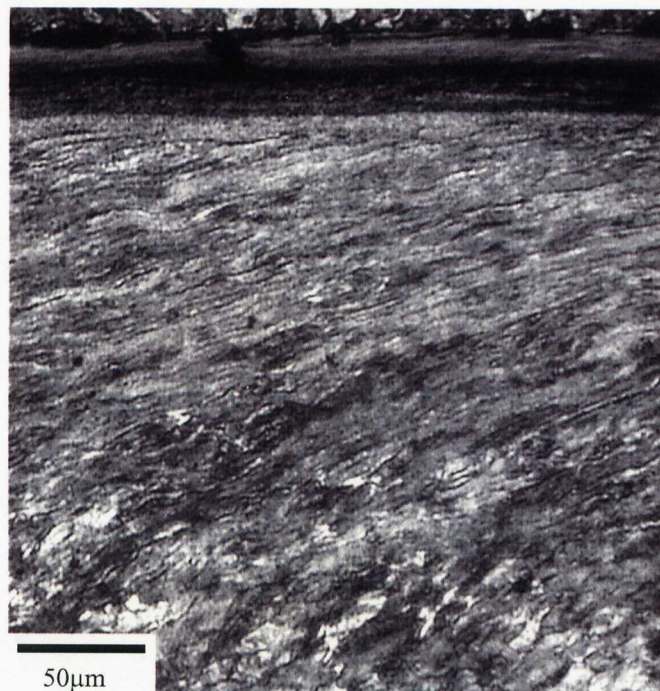
Figure 5.3.6: Rail disc RA07 after 30seconds sliding
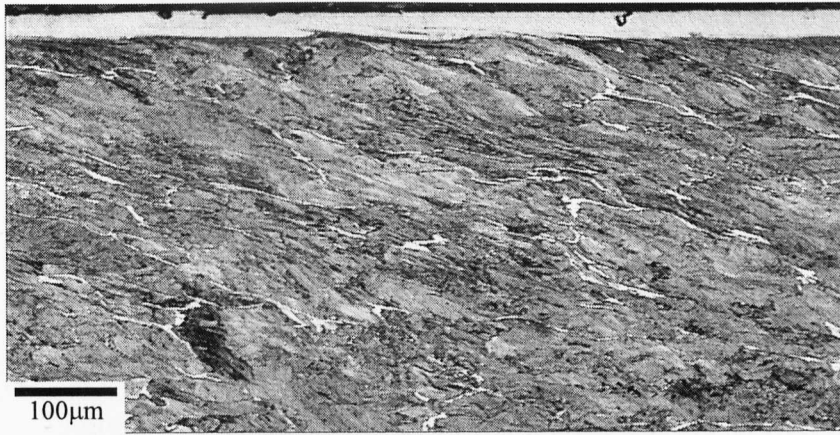
Figure 5.3.7: Rail disc RA31 after 5 seconds sliding
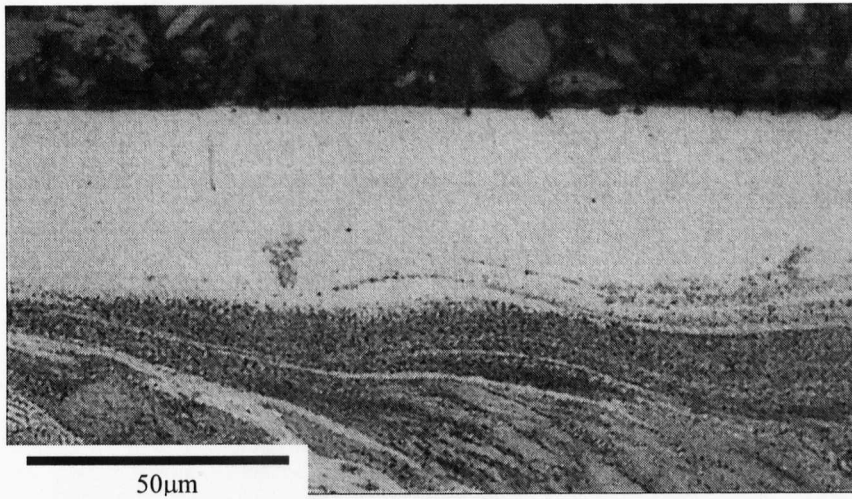
Figure 5.3.8: WEL on surface of RA31
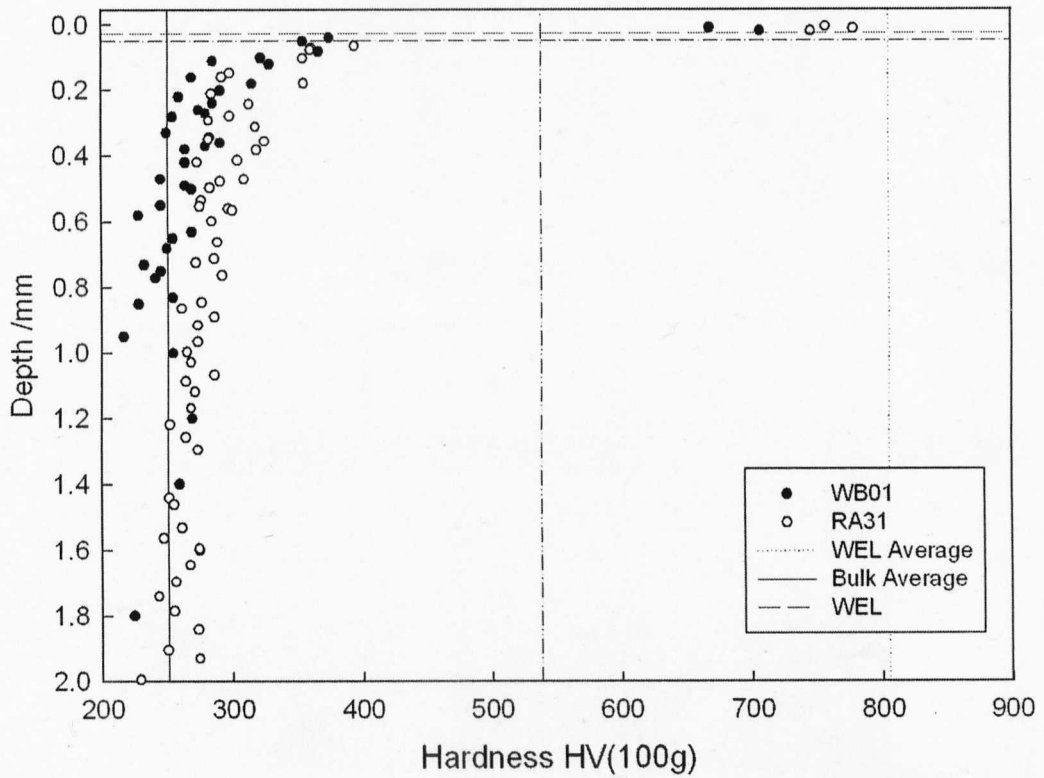
Figure 5.3.9: Microhardness of pearlite with WEL created by 5s sliding
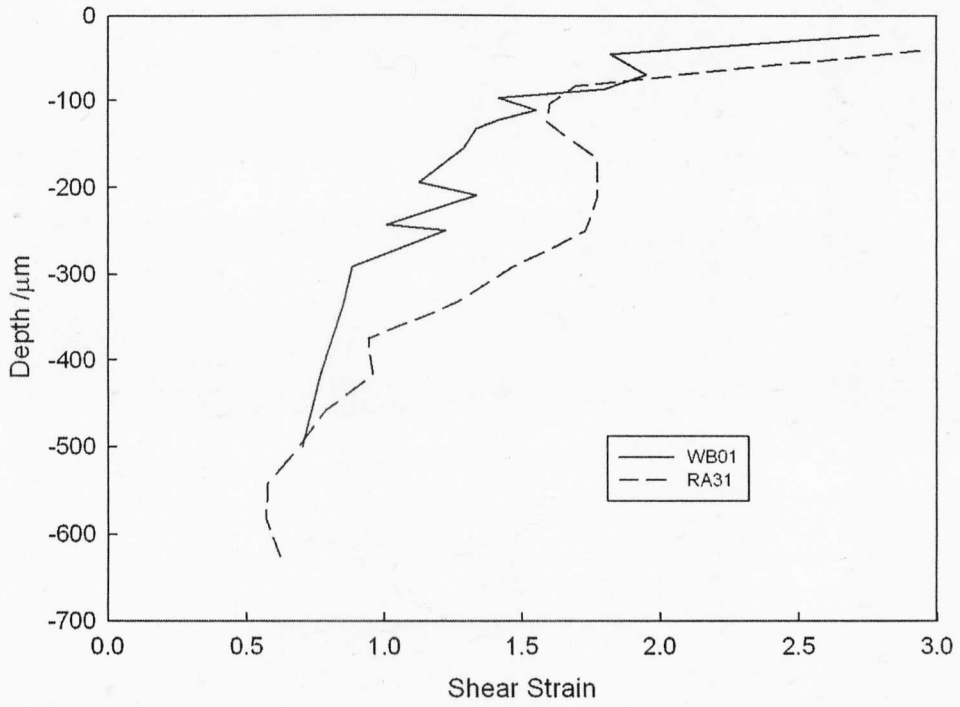
Figure 5.3.10: Shear strain of pearlite with WEL created by 5s sliding

Figure 5.3.11: Microstructure of bainitic back up roll, BU9, after sliding against RA34
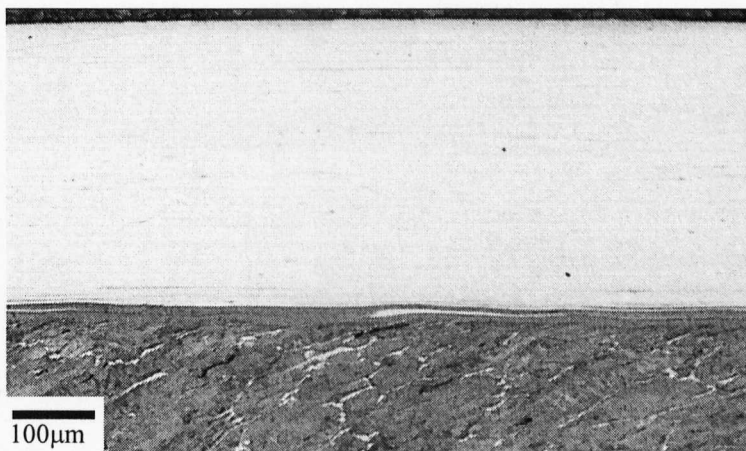
Figure 5.3.12: White etching layer formed on RA34 after 10 seconds sliding
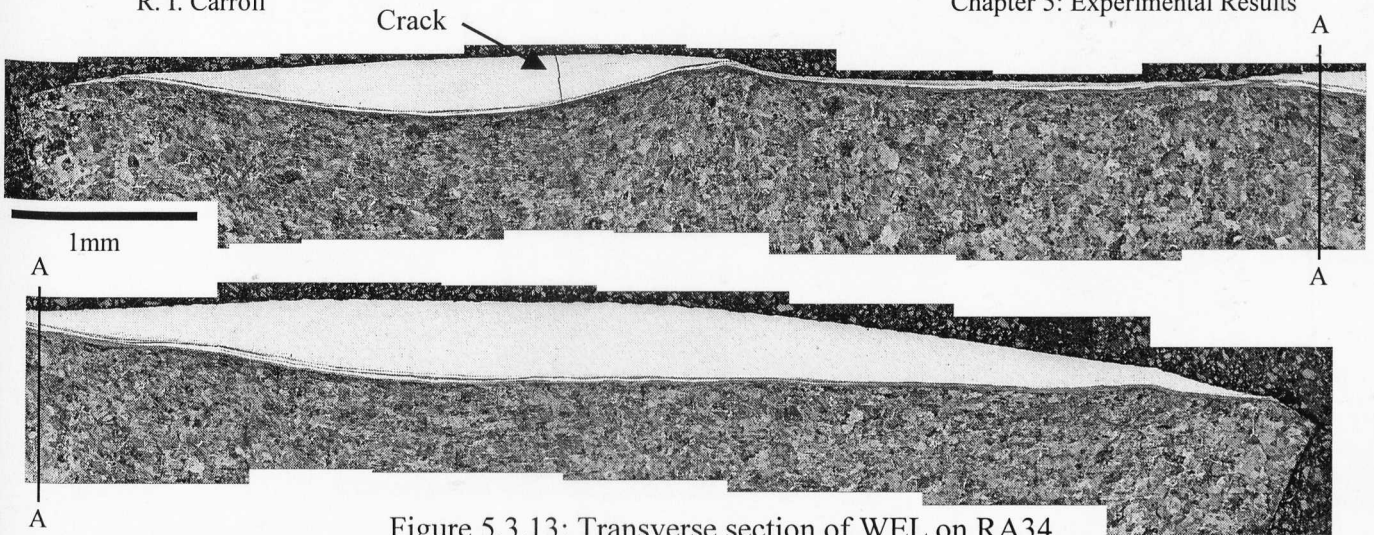
Figure 5.3.13: Transverse section of WEL on RA34
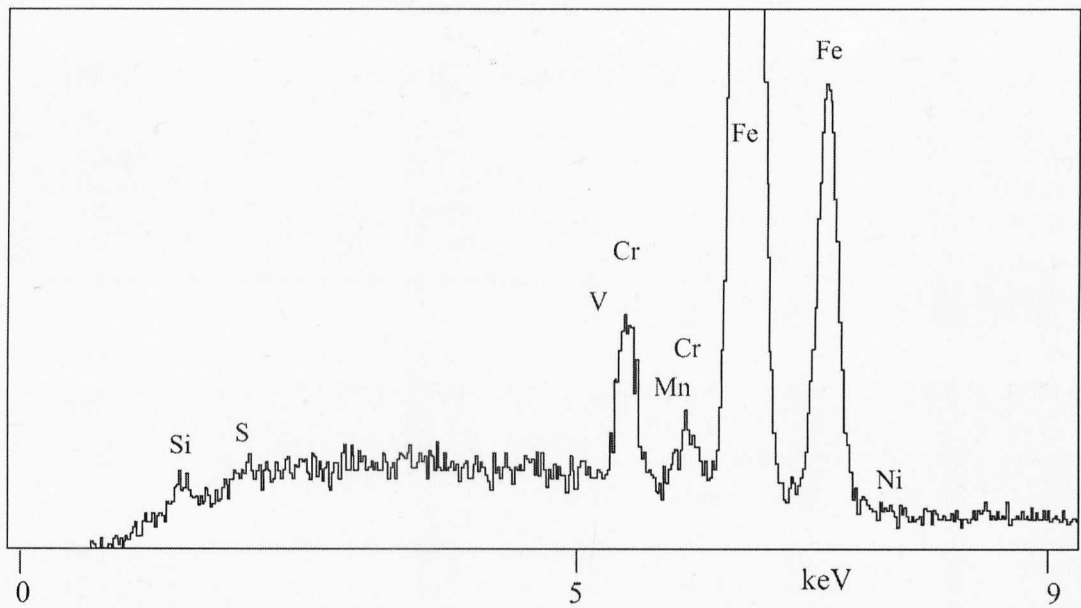
Figure 5.3.14: EDS trace, using Camscan SEM, of WEL on sample RA34 created by sliding.
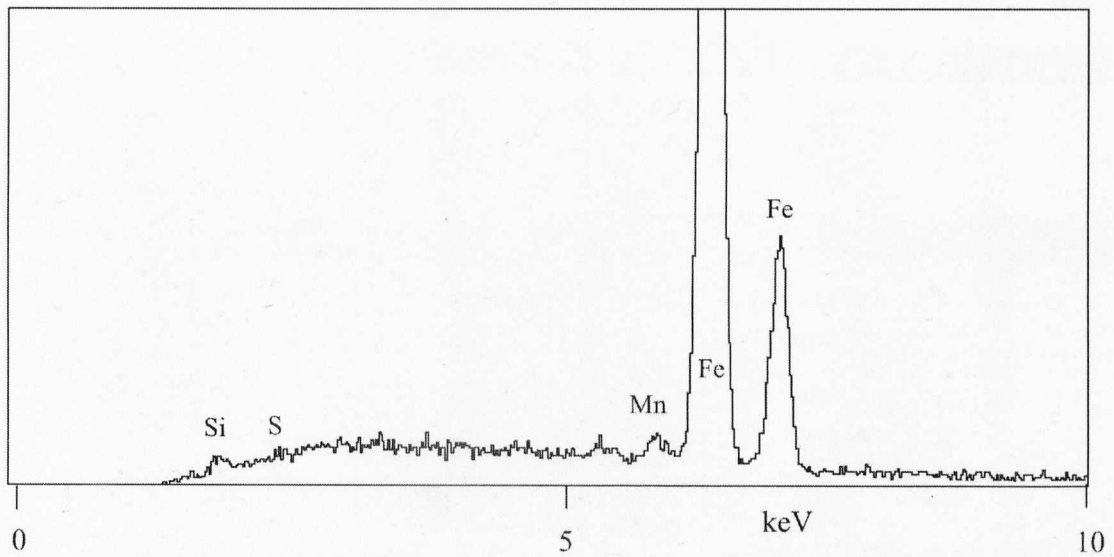
Figure 5.3.15: EDS trace of Pearlite using Camscan SEM
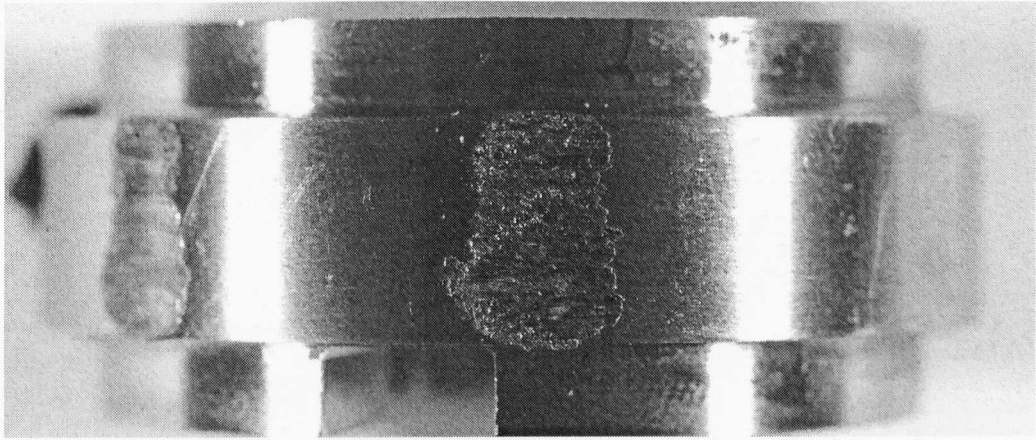
Figure 5.3.16: Groove worn in rail disc RA32 held stationary while wheel is slid against it.
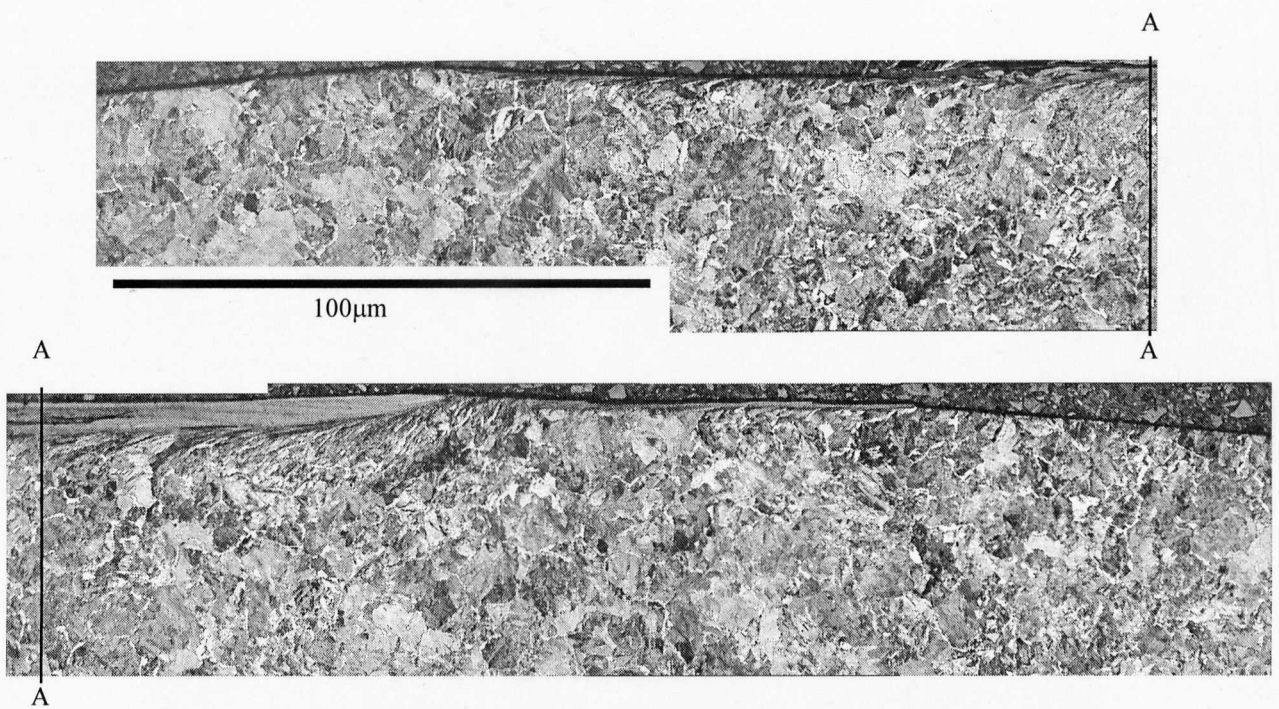
Figure 5.3.17: Section of grove in rail disc RA32
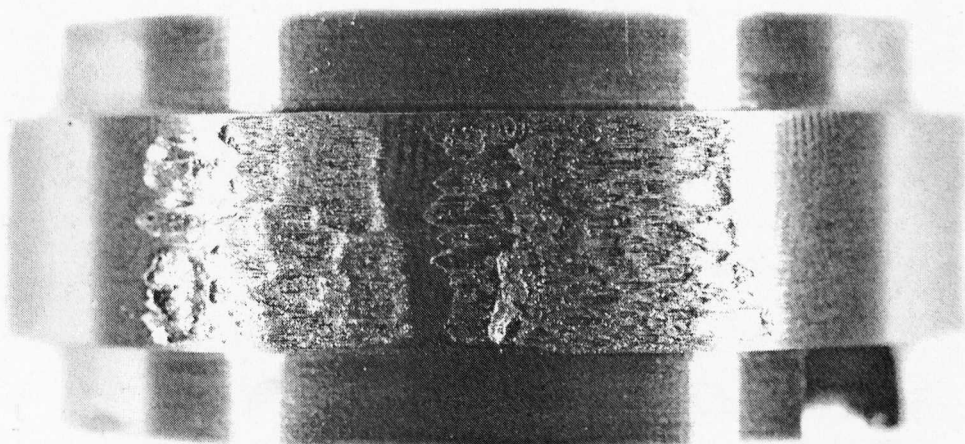
Figure 5.3.18: Wheel disc, WB06, after pulsed loading to create a spot of WEL
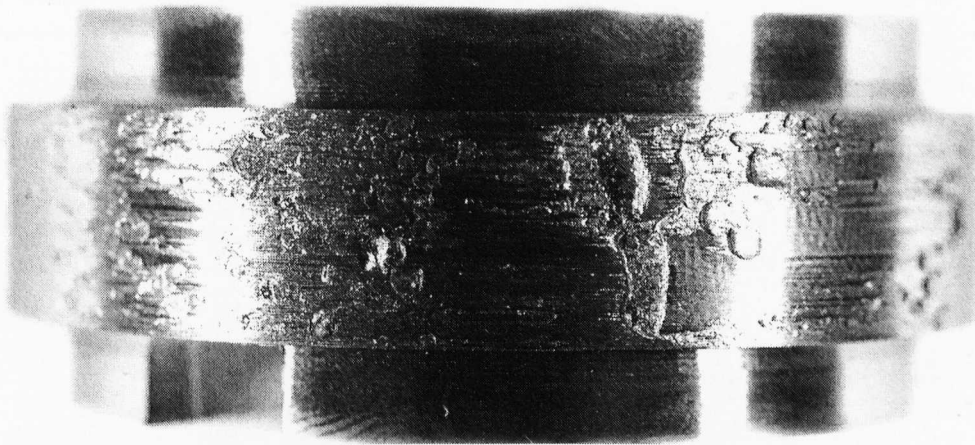
Figure 5.3.19: RA33 after sliding against WB06, with material on surface
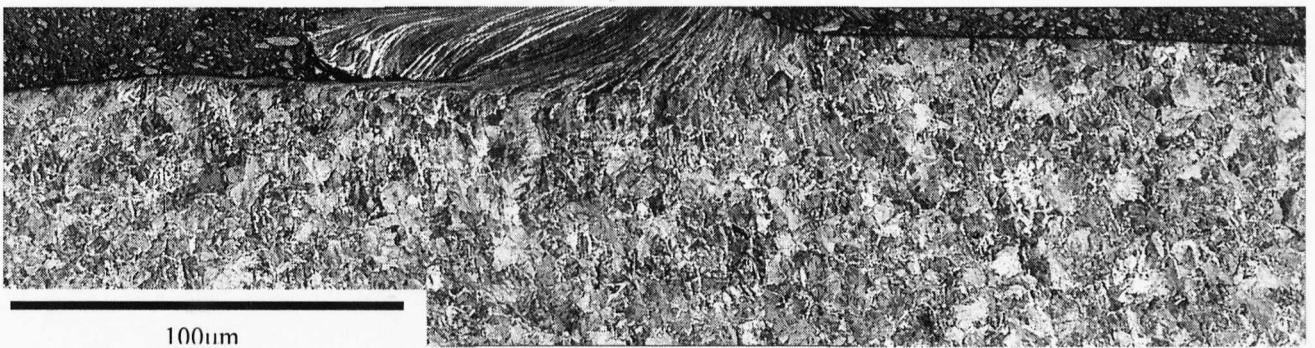
Figure 5.3.20: Cross section of RA33 showing build up on surface
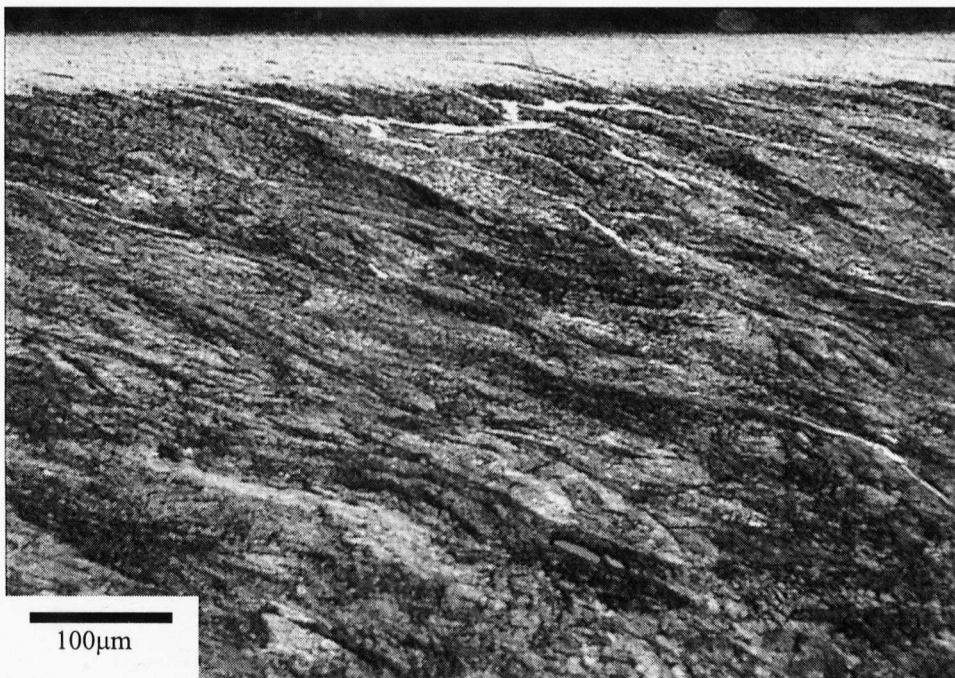
Figure 5.3.21: White etching layer created on decarburised disc showing more ferrite at surface than is present in normal samples.
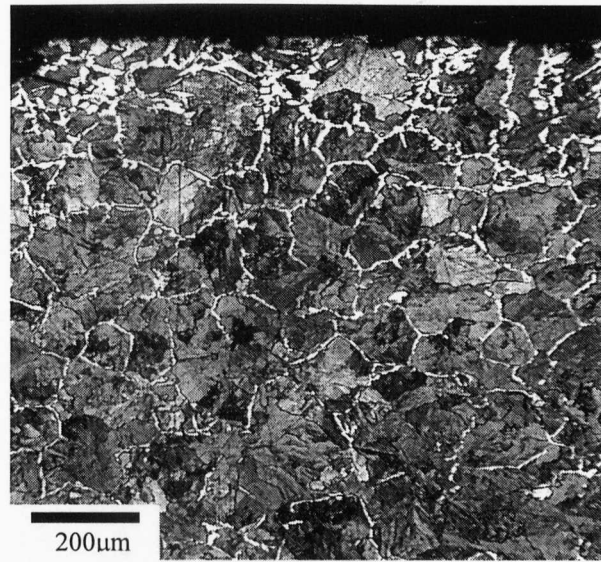
Figure 5.4.1: Decarburised surface on crown of rail after manufacture.
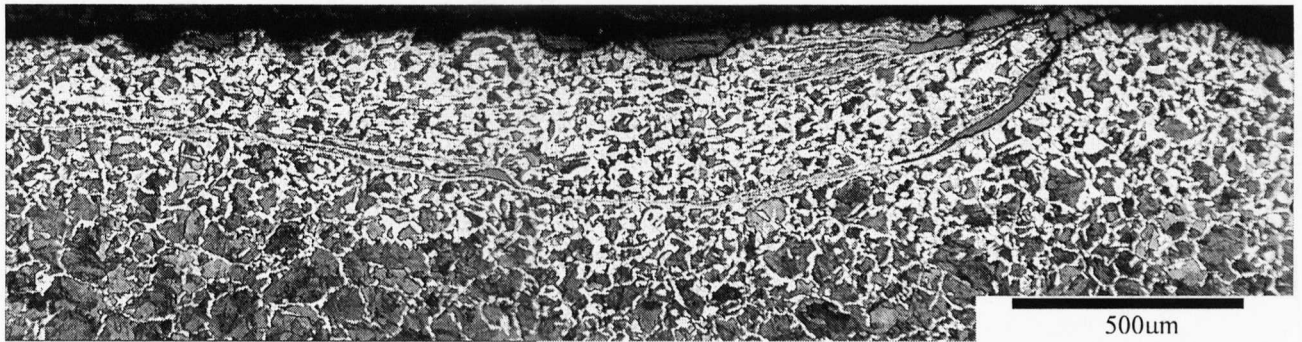
Figure 5.4.2: Decarburised surface of rail including manufacturing defect near the gauge corner.
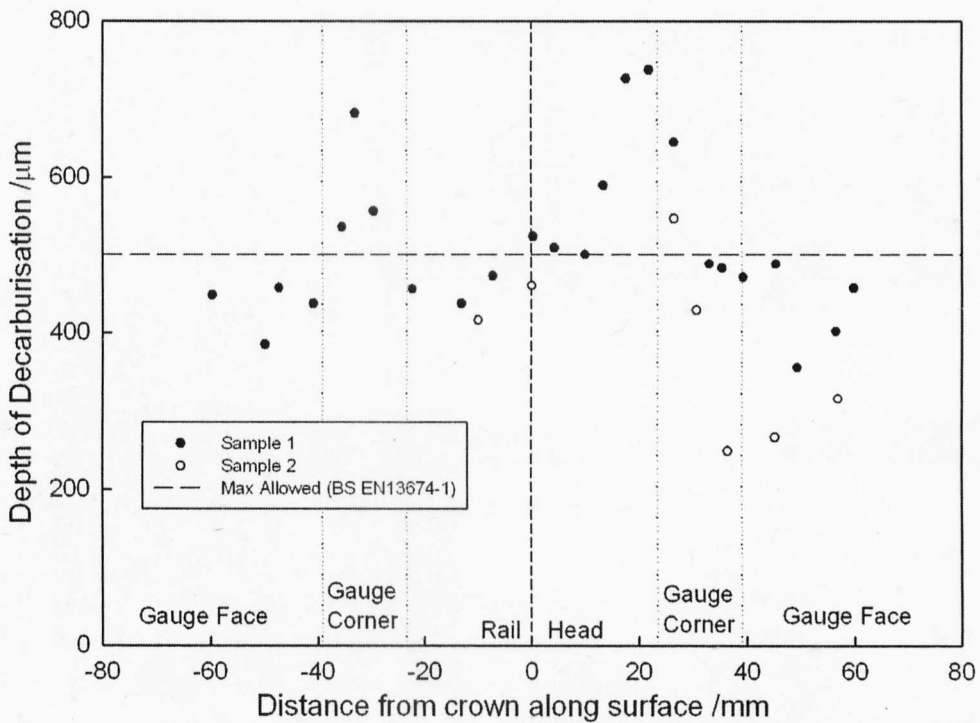
Figure 5.4.3: Depth of decarburisation around railhead measured using metallography at 98% bulk content.
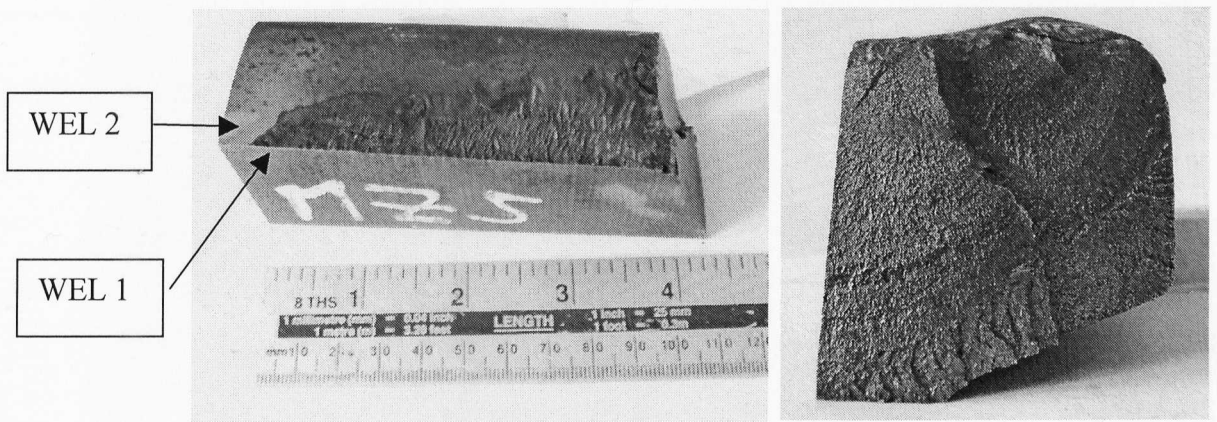
Figure 5.4.4: RCF crack in rail sample where the WEL was found
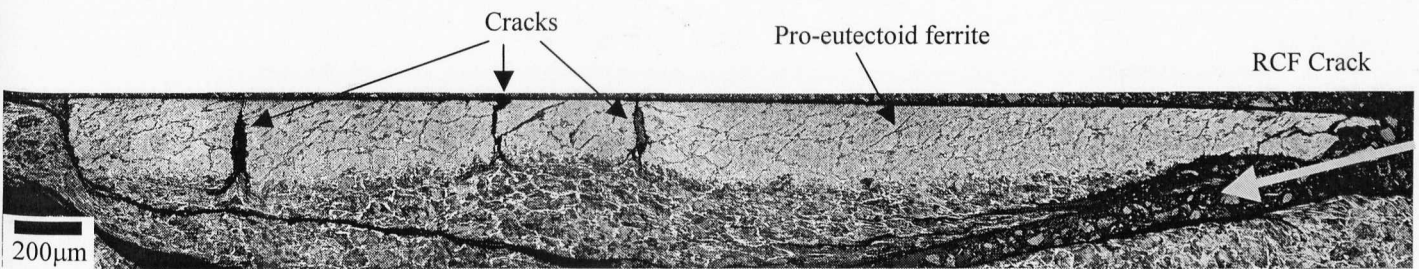
Figure 5.4.5: WEL 1 on section of rail removed from service. RCF crack observed has resulted in failure of rail.
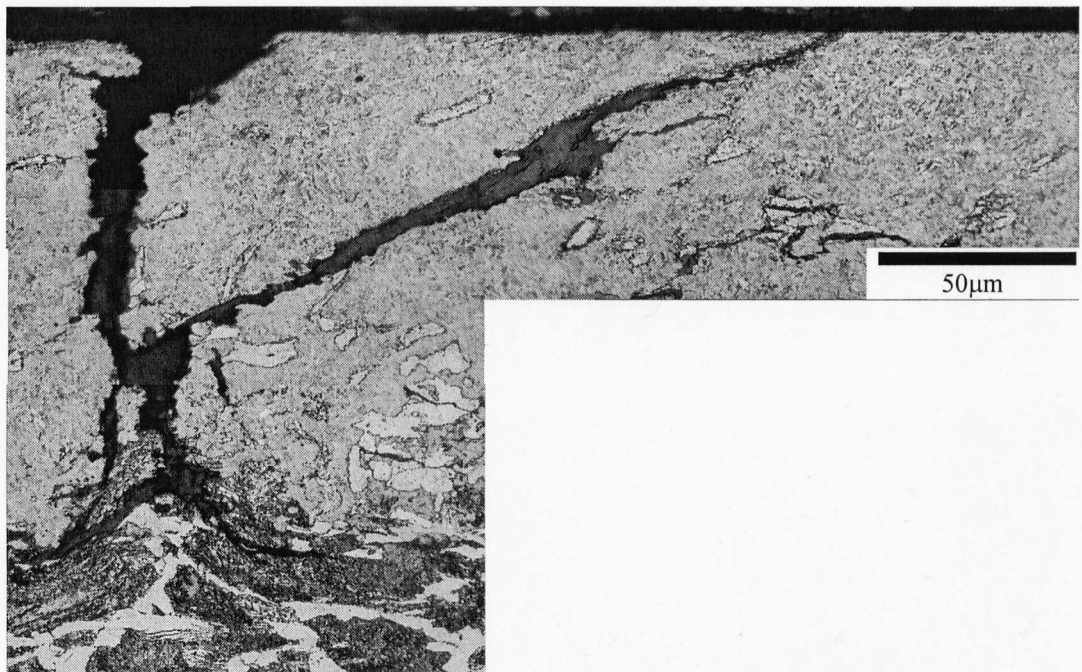
Figure 5.4.6: Crack in WEL 1 demonstrating deformation of pearlite into gap.
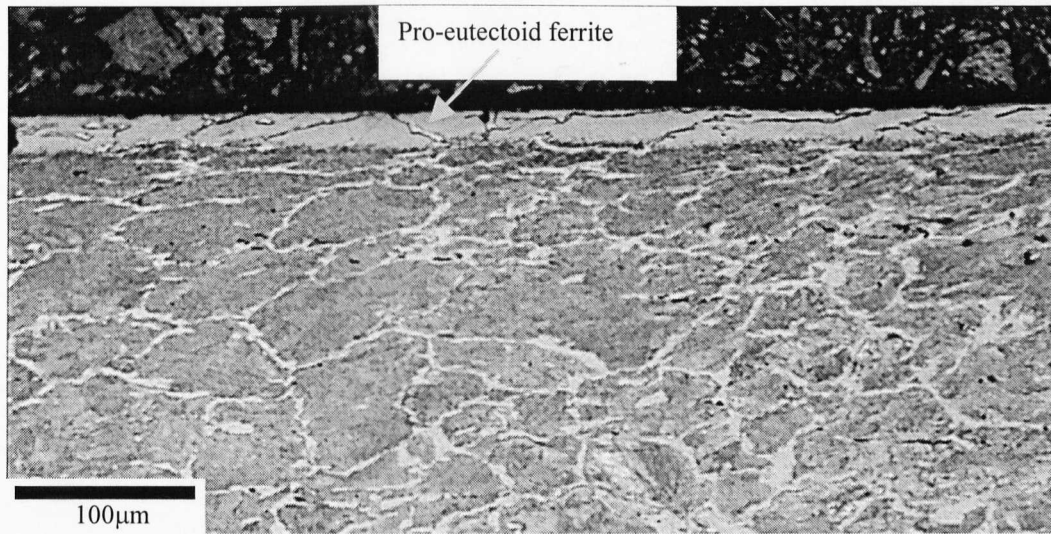
Figure 5.4.7: WEL 2 on section of rail away from large RCF crack
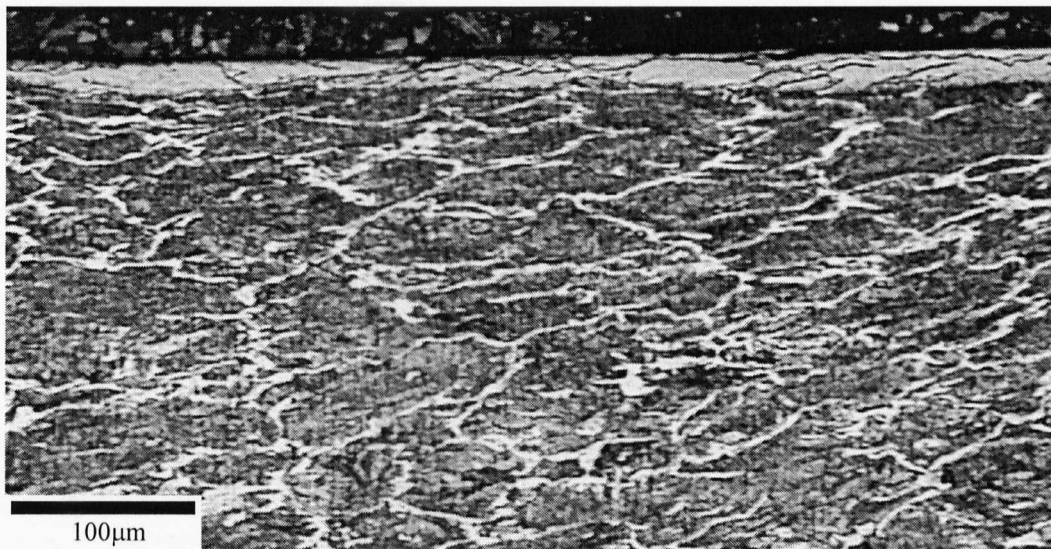
Figure 5.4.8: Transverse section of WEL 2 on rail away from large RCF crack
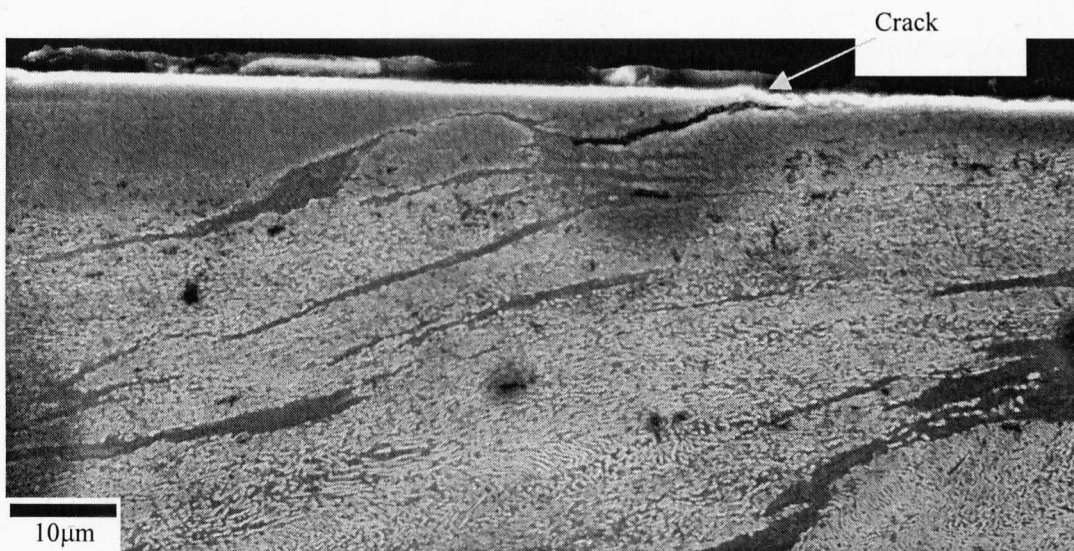
Figure 5.4.9: Crack at the interface of pearlite and WEL.
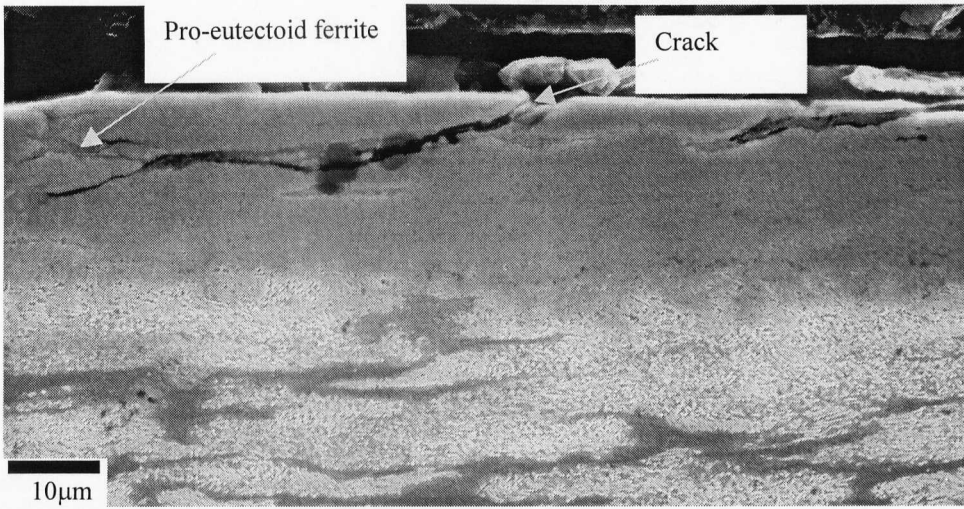
Figure 5.4.10: Crack in WEL 2 along proeutectoid ferrite.
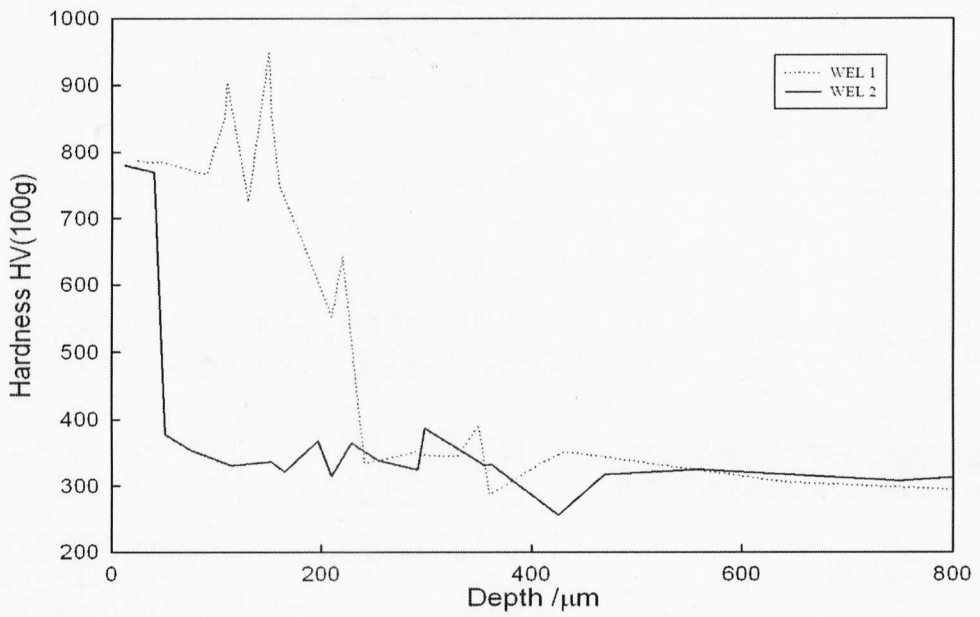
Figure 5.4.11: Hardness traverse of WEL found on rail sample
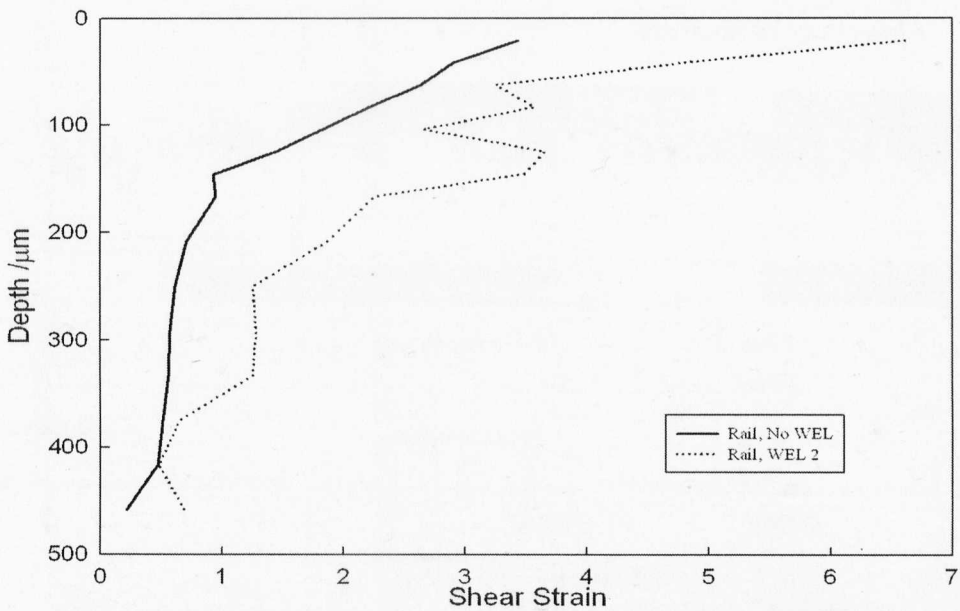
Figure 5.4.12: Strain of rail below WEL 2 and rail without WEL
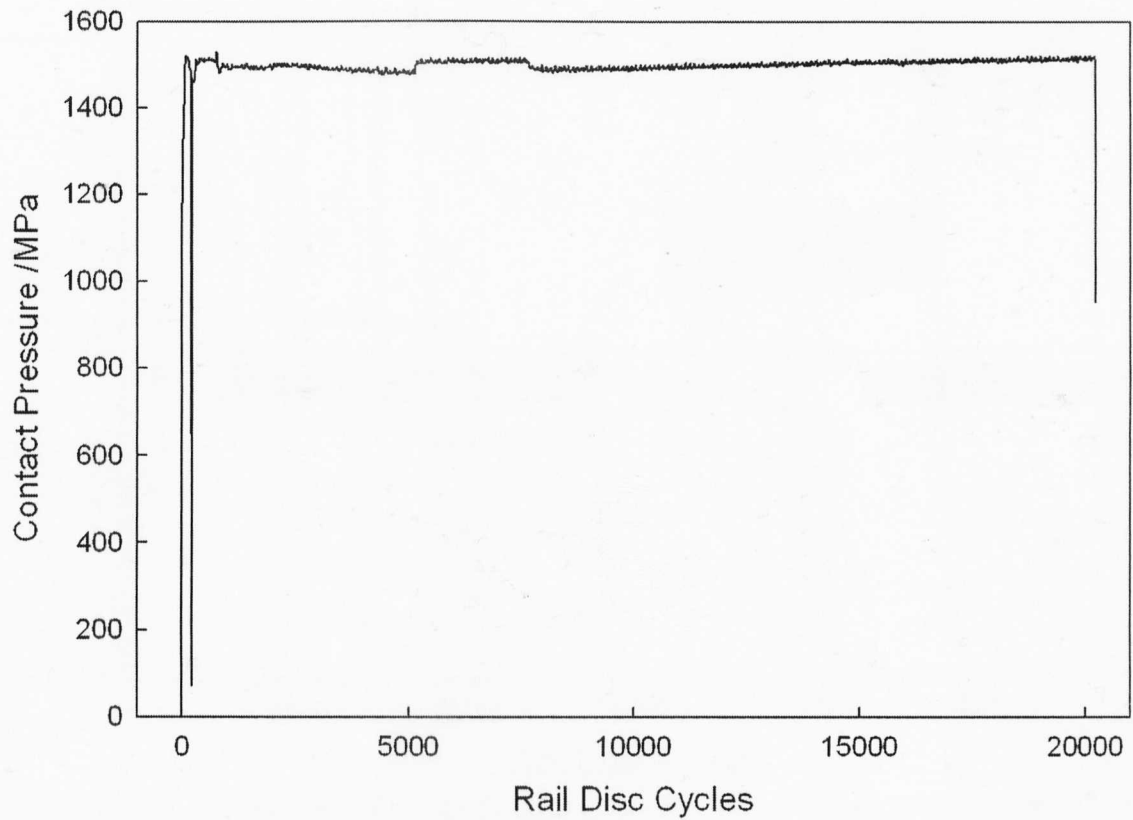
Figure 5.5.1.1: Contact pressure for test DP01 from data logged results, the dip at 200 cycles is where the test was restarted with water lubrication.
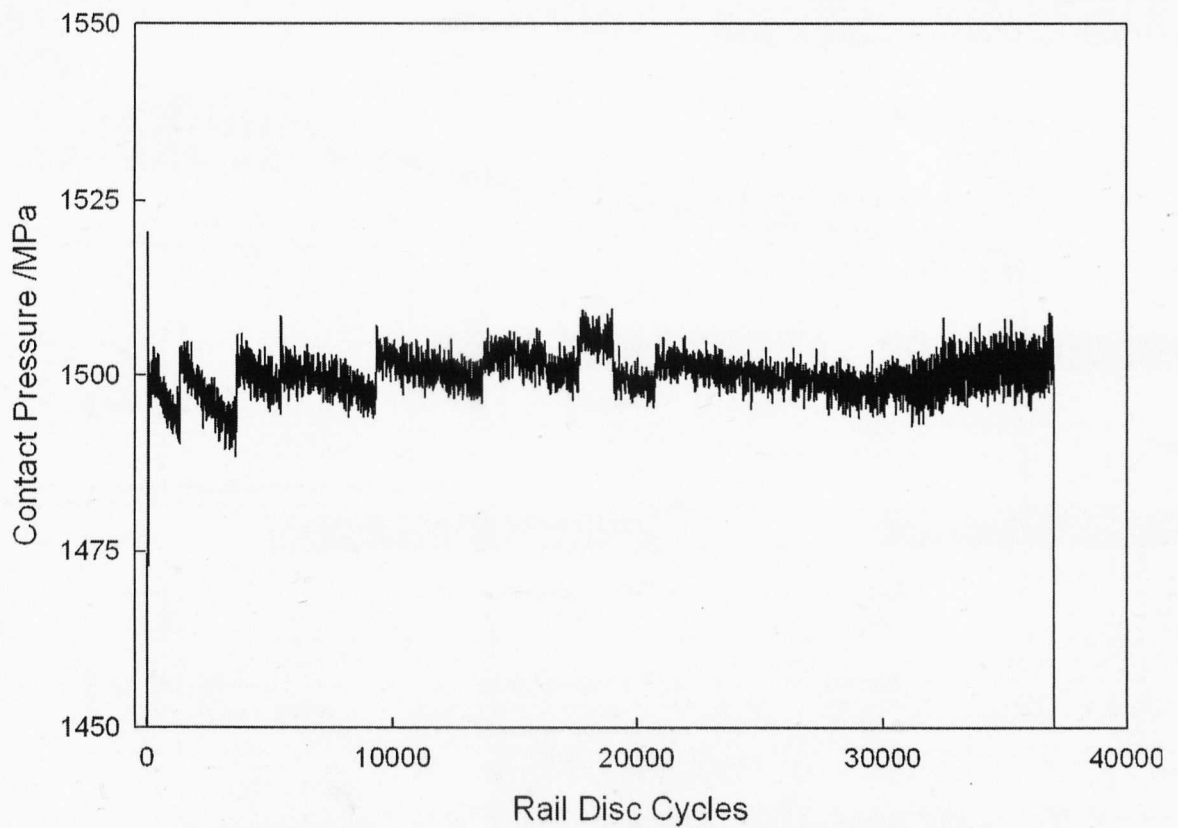
Figure 5.5.1.2: Contact pressures from test WE08.
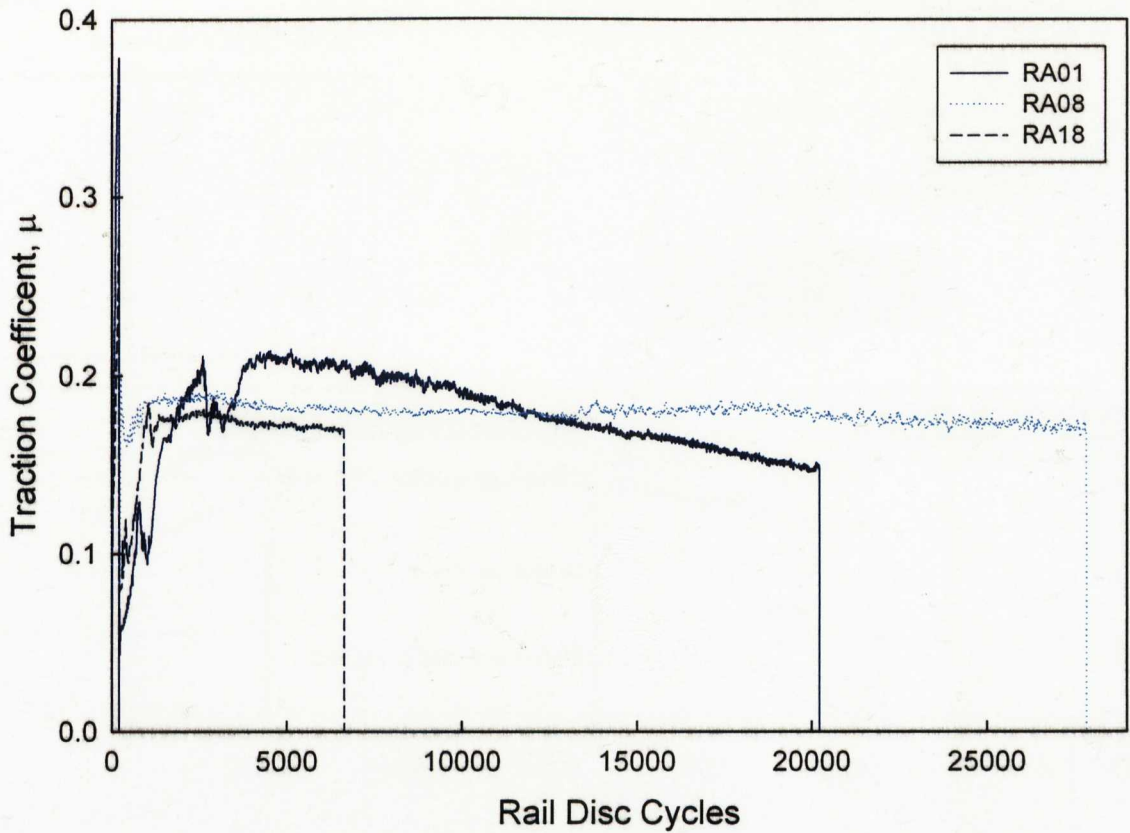
Figure 5.5.1.3: Traction coefficient of normal samples with 200 dry cycles. (RA01, RA08 and RA18)
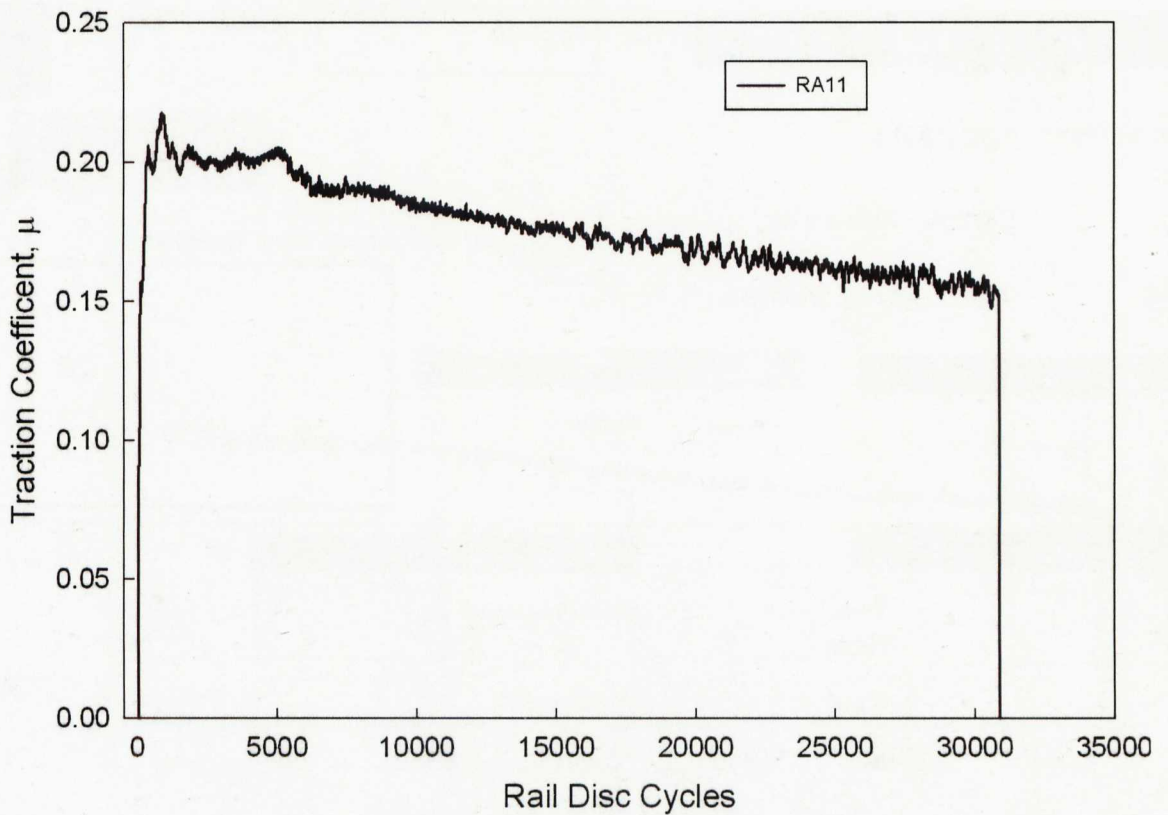
Figure 5.5.1.4: Traction coefficient of normal sample, RA11, water lubricated from the start of the test
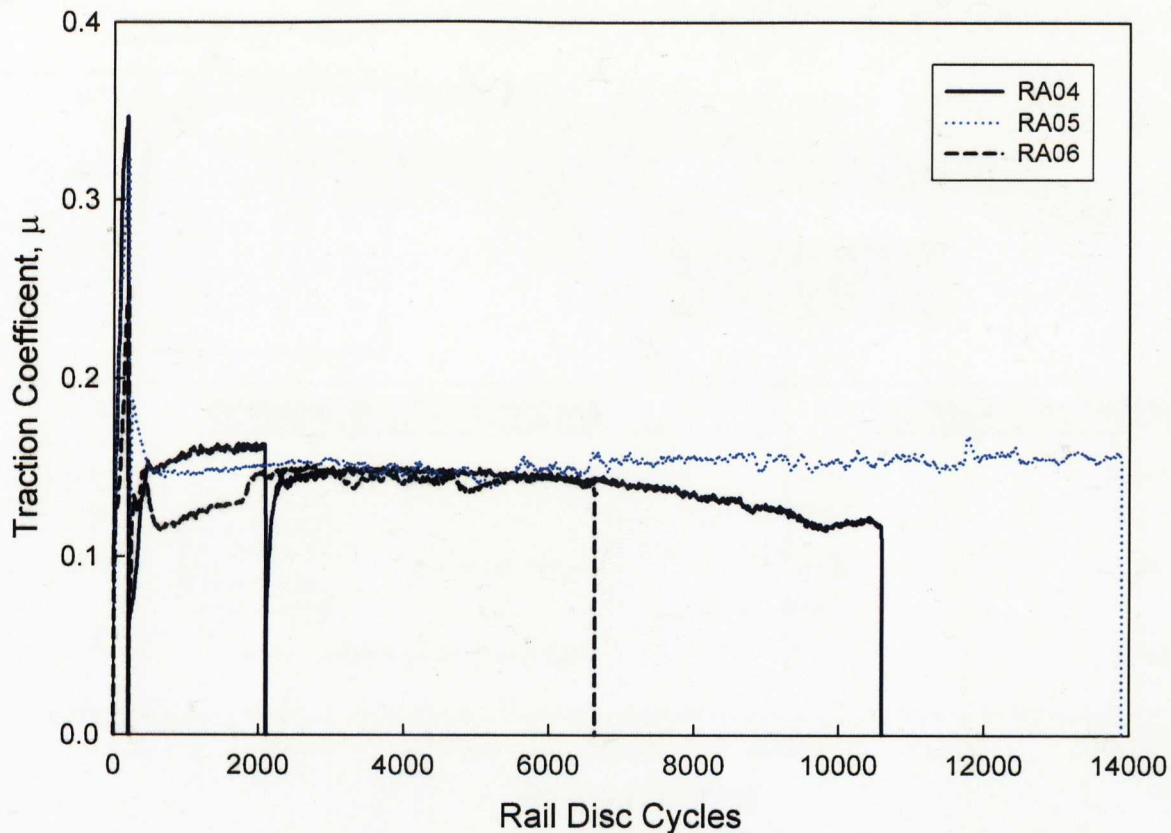
Figure 5.5.1.5: Traction coefficient of water lubricated decarburised samples with 200 dry cycles, RA04, RA05 and RA06
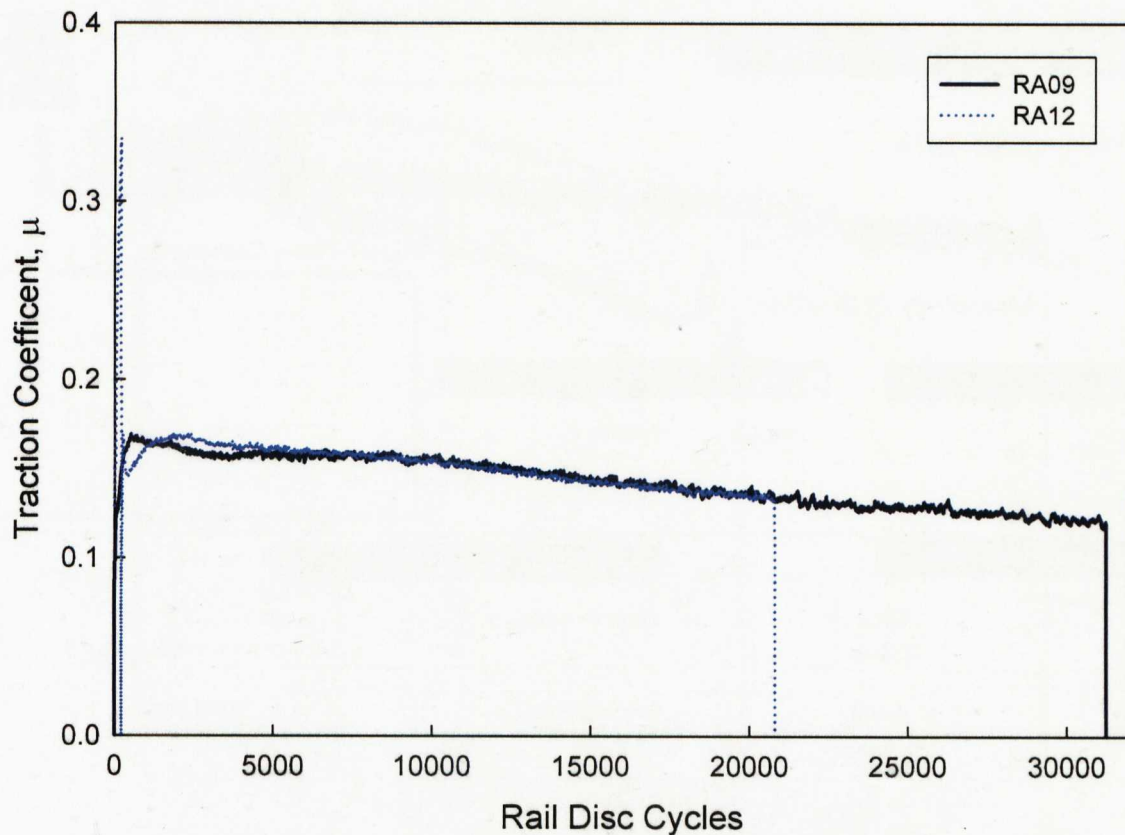
Figure 5.5.1.6: Traction coefficient of water lubricated decarburised samples with 200 dry cycles, RA09 and RA12

143
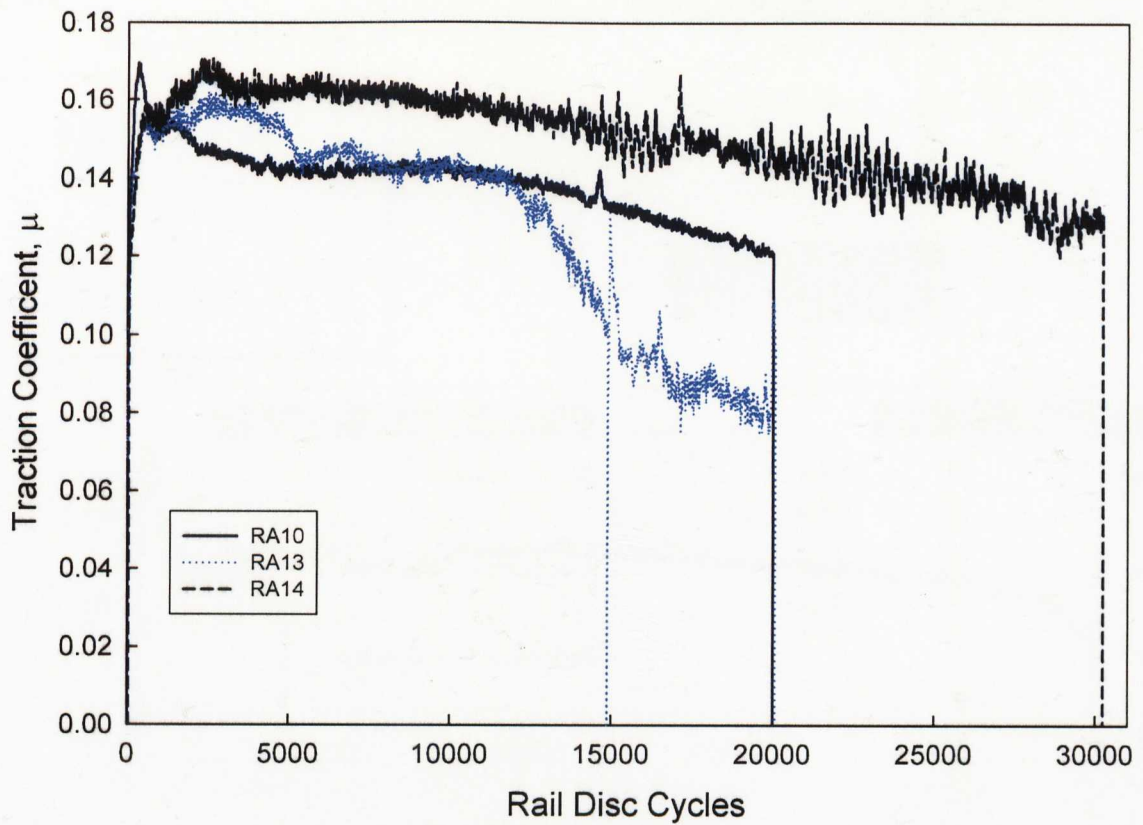
Figure 5.5.1.7: Traction coefficient of water lubricated decarburised samples, RA10, RA13 and RA14.
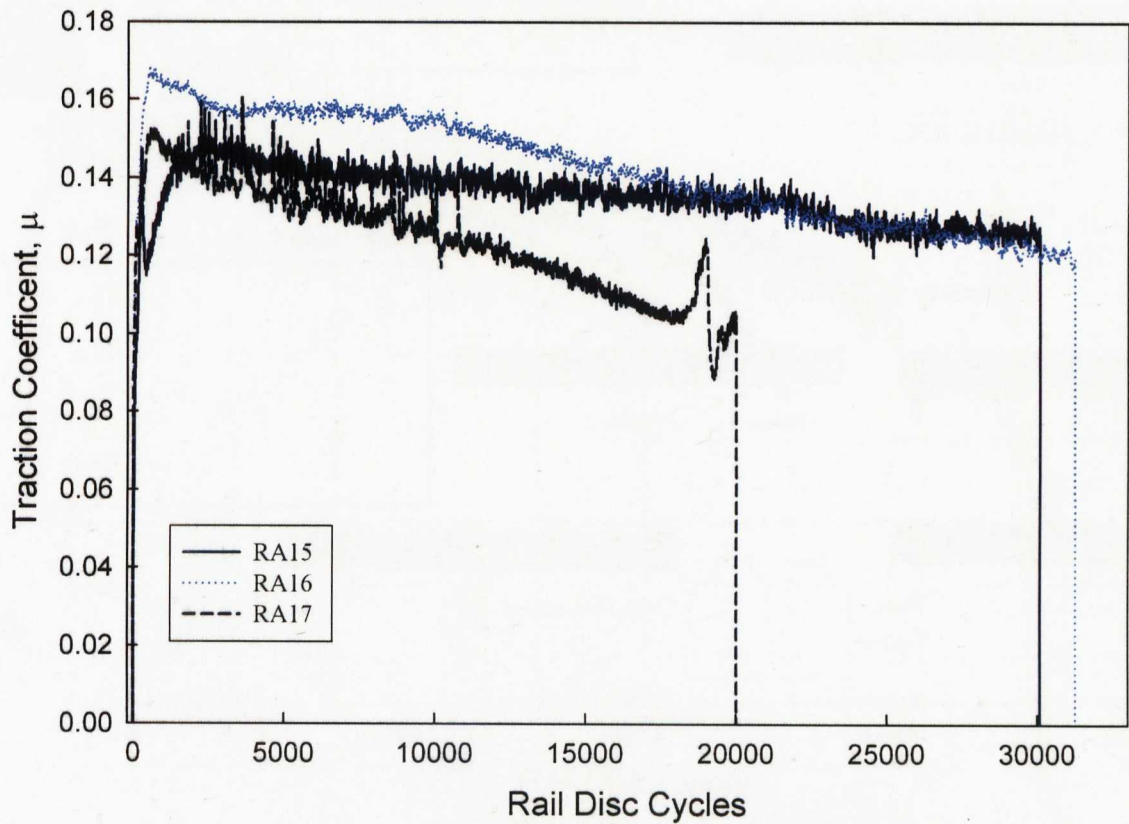
Figure 5.5.1.8: Traction coefficient of water lubricated decarburised samples, RA15, RA16 and RA17.
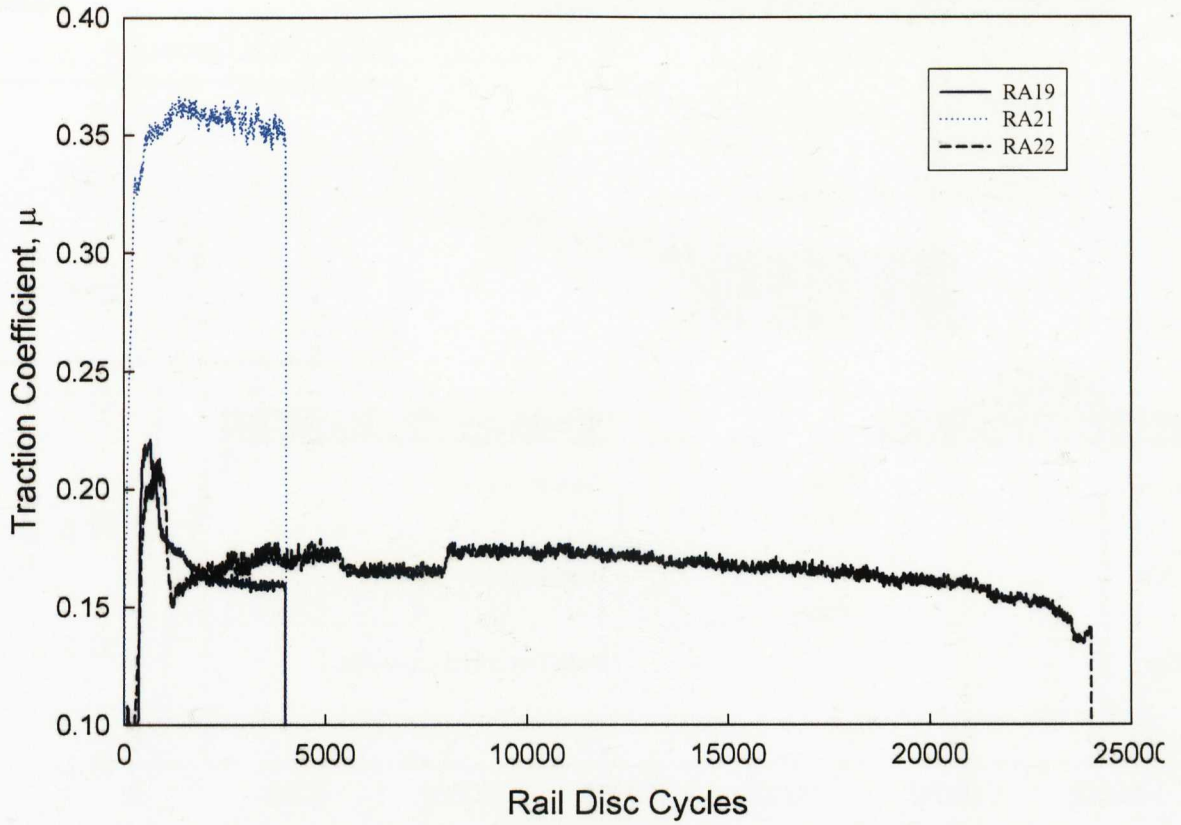
Figure 5.5.1.9: Traction coefficient of spot welded WEL samples. (RA19, RA21 and RA22)
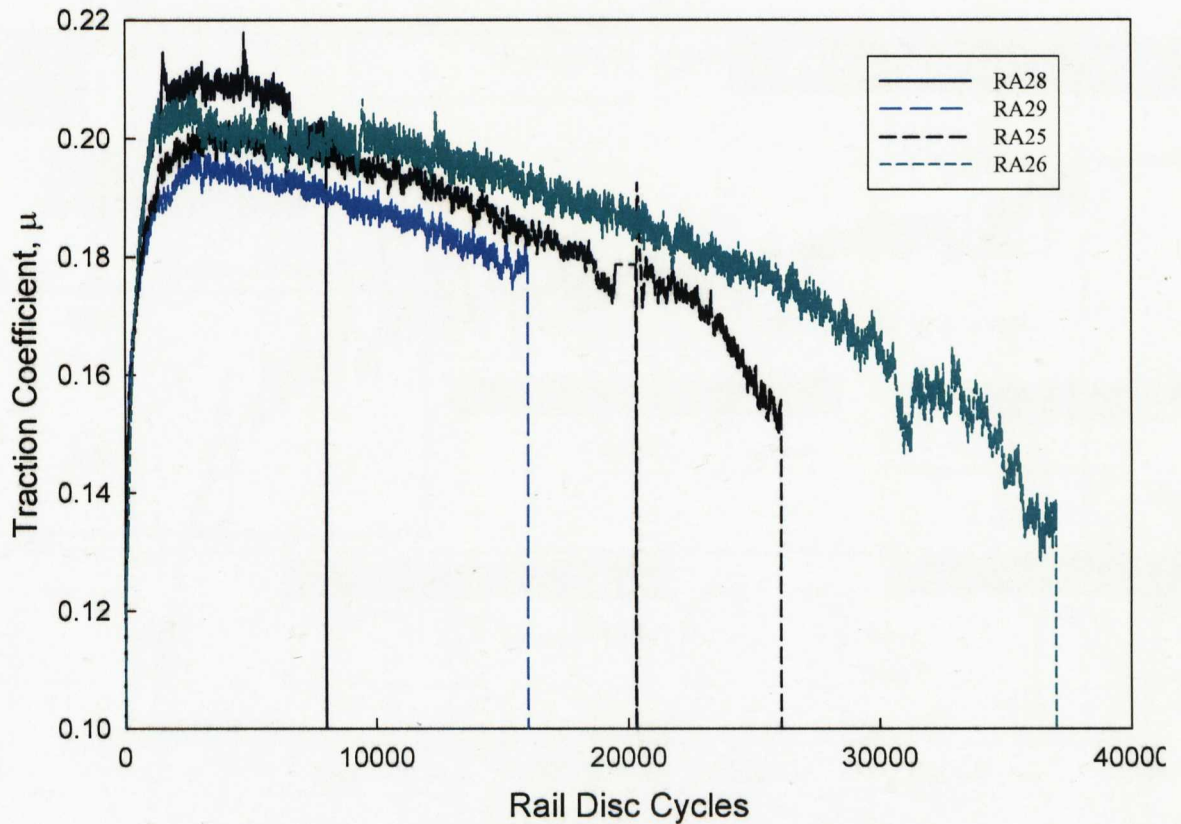
Figure 5.5.1.10: Traction coefficient of water lubricated unidirectional WEL samples. (RA25, RA26, RA28 and RA29)
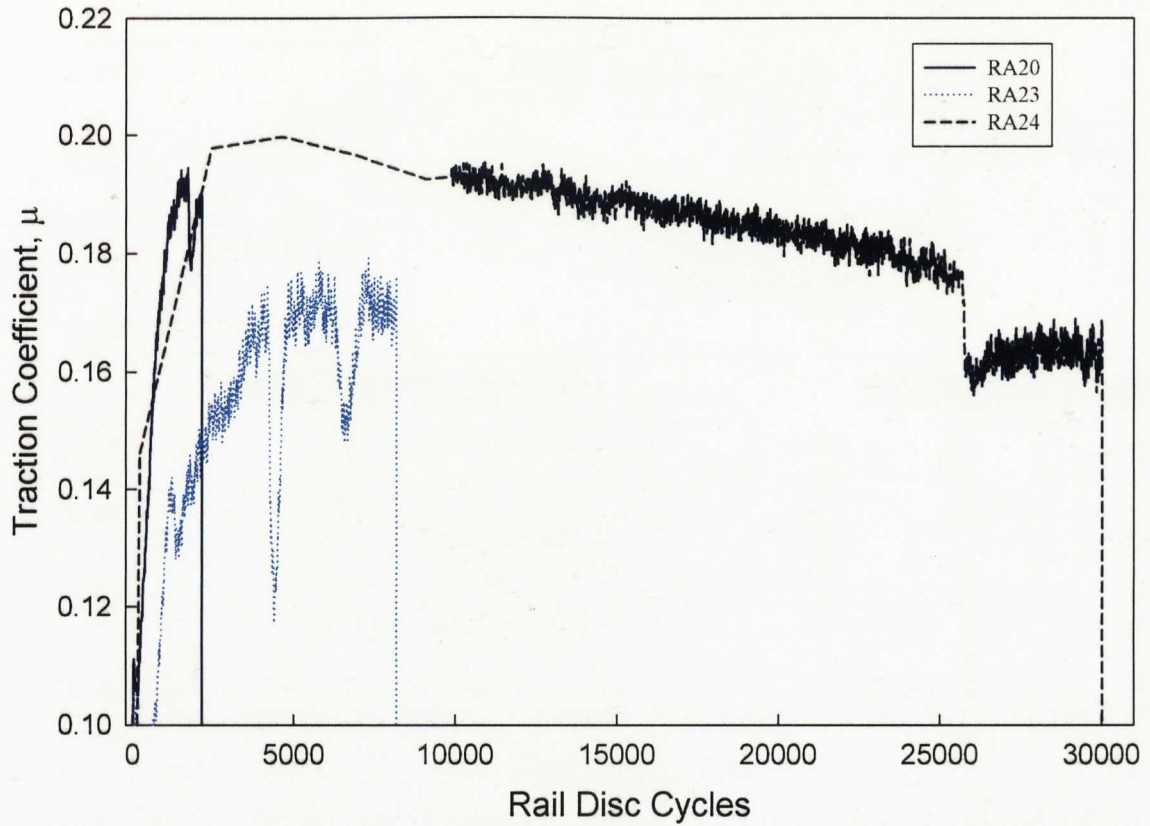
Figure 5.5.1.11: Traction coefficient of water lubricated reversed WEL samples. (RA20, RA23 and RA24)
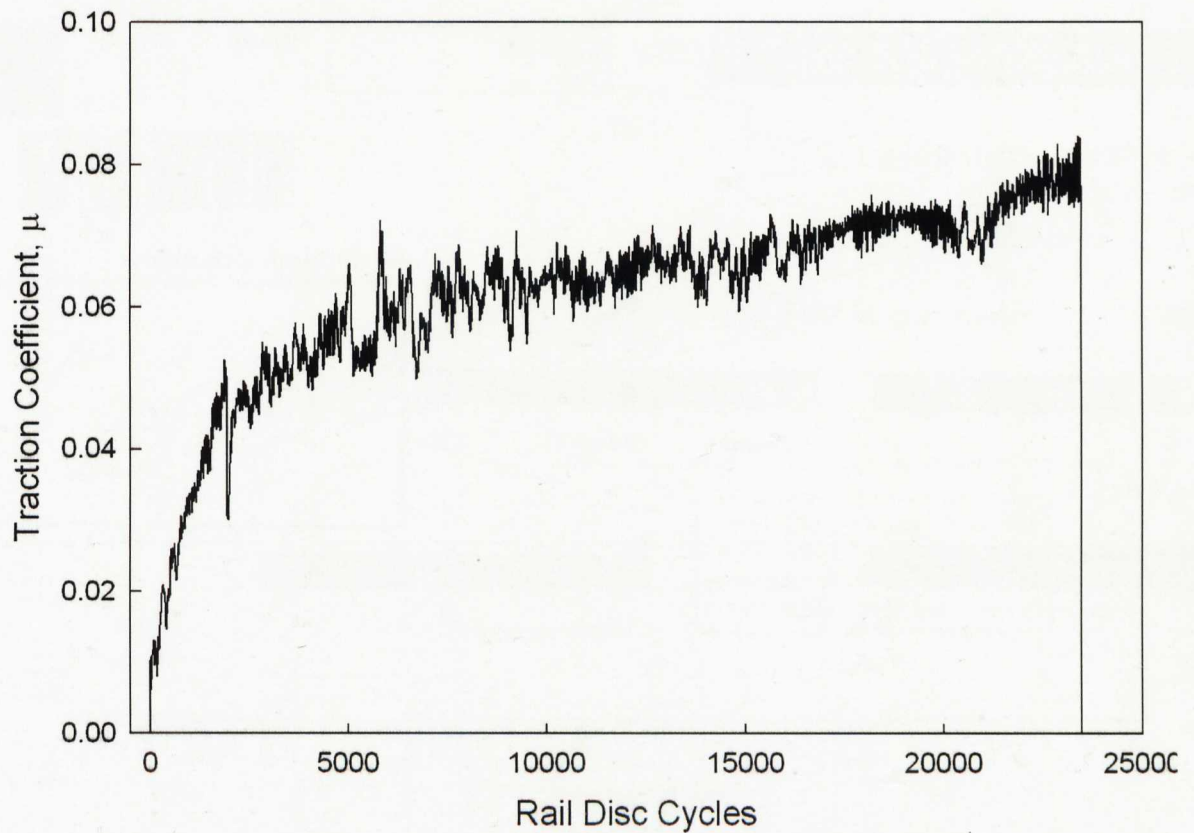
Figure 5.5.1.12: Traction coefficient of water lubricated WEL samples with 0% slip, RA30.
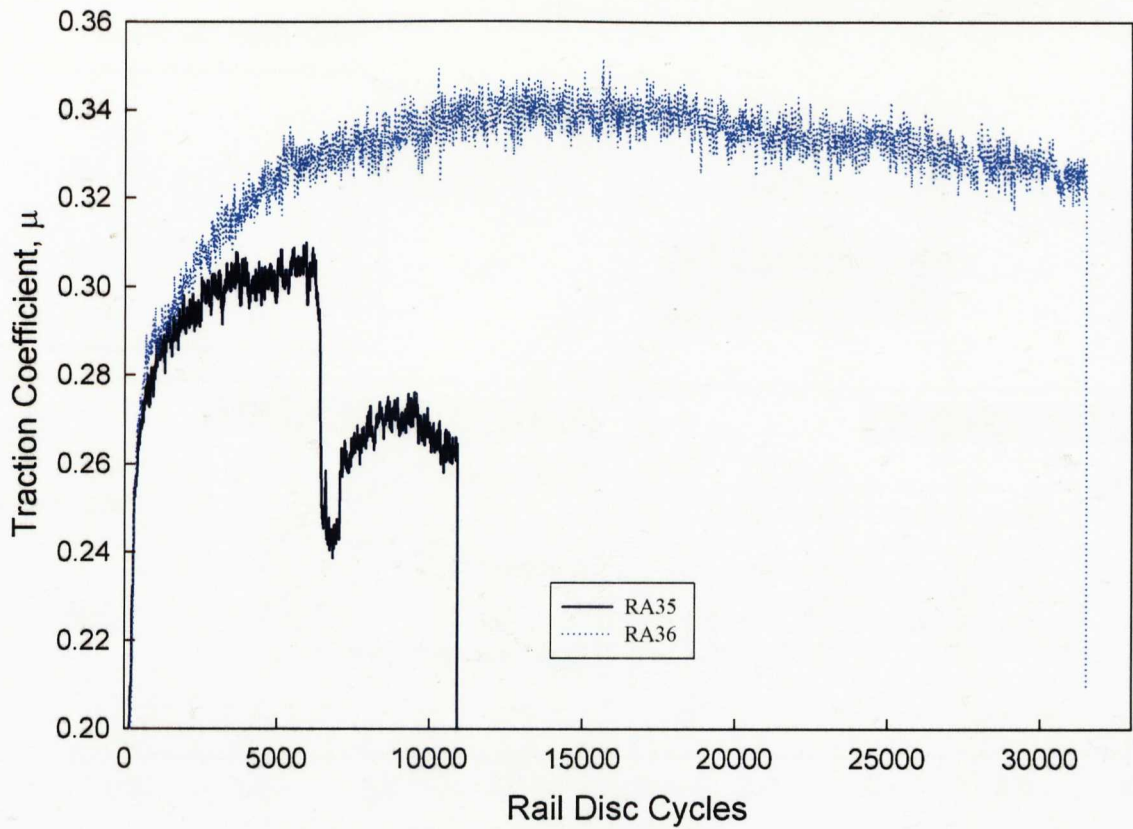
Figure 5.5.1.13: Traction coefficient of unlubricated WEL samples. (RA35 and RA36)
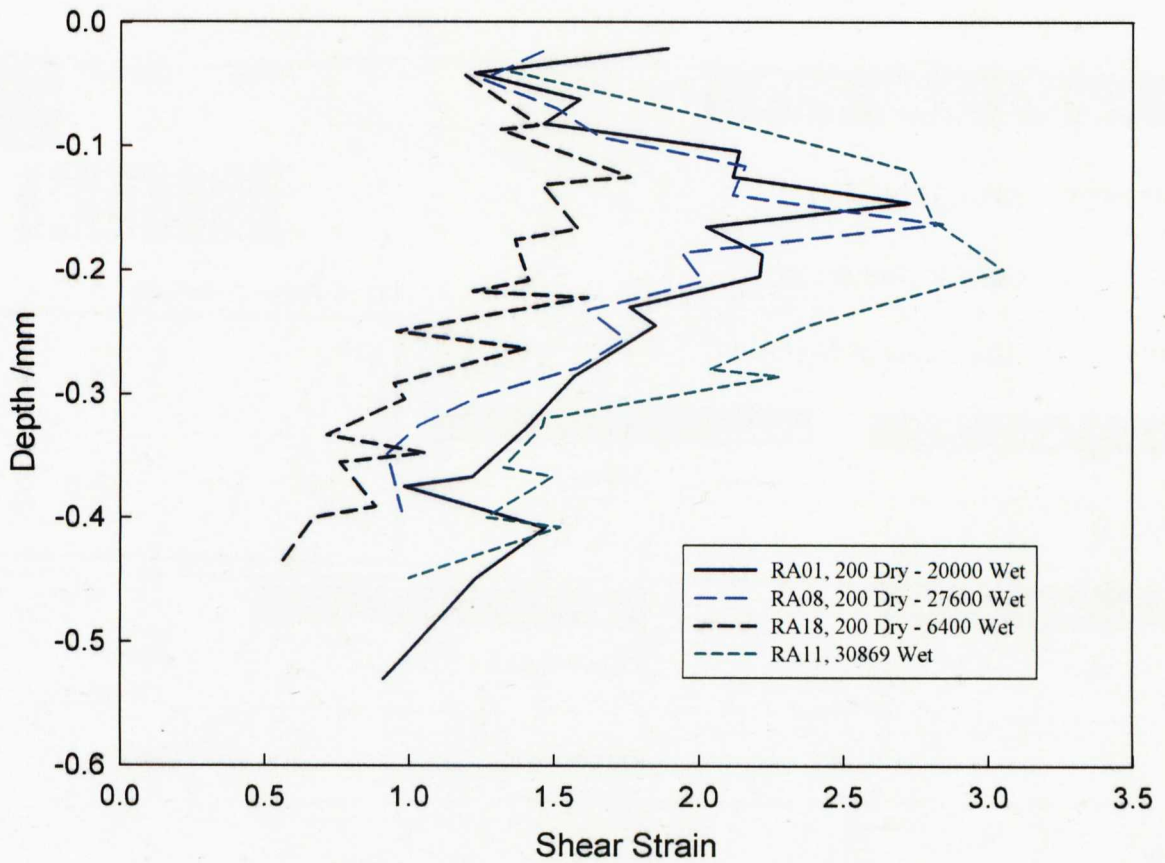
Figure 5.5.2.1: Shear strain of normal samples after twin disc testing. (RA01, RA08, RA11 and RA18)
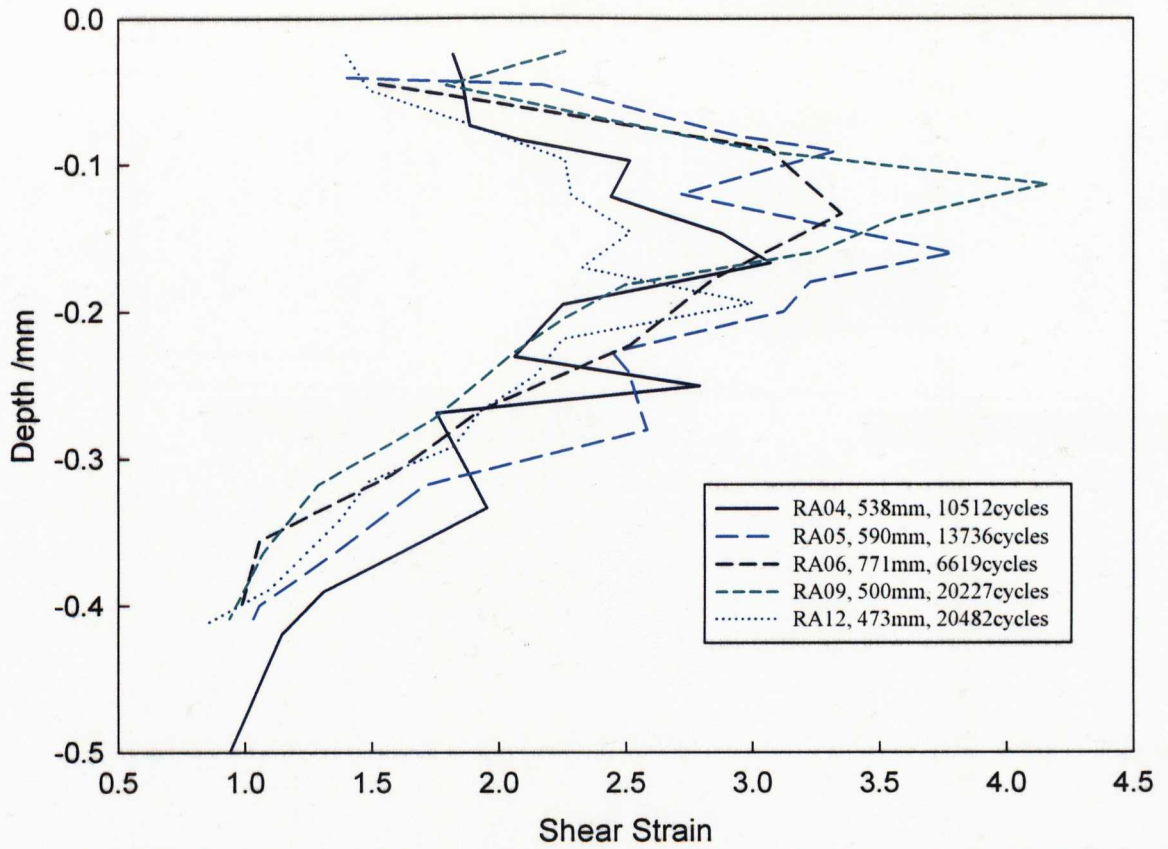
Figure 5.5.2.2: Shear strain of decarburised samples after twin disc testing with 200 dry cycles. (RA04, RA05, RA06, RA09 and RA12)
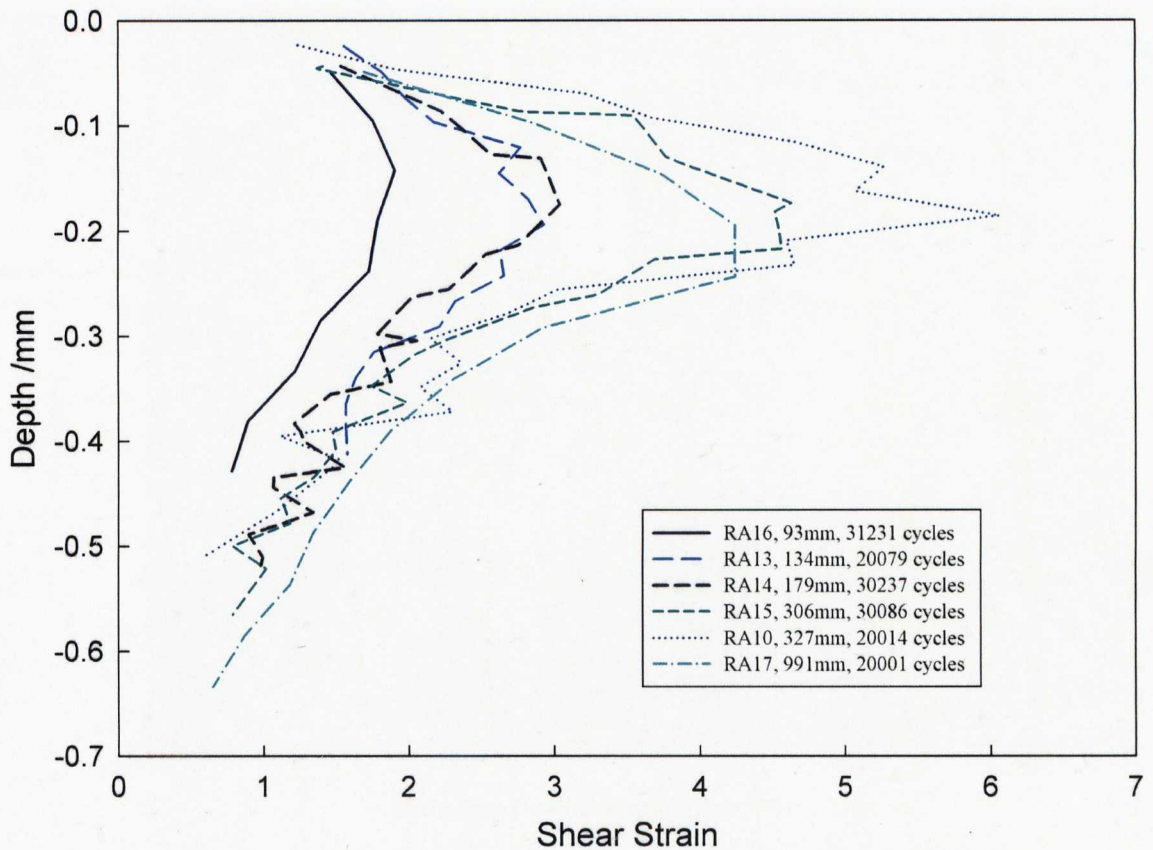
Figure 5.5.2.3: Shear strain of decarburised samples after twin disc testing. (RA10, RA13, RA14, RA15, RA16 and RA17)
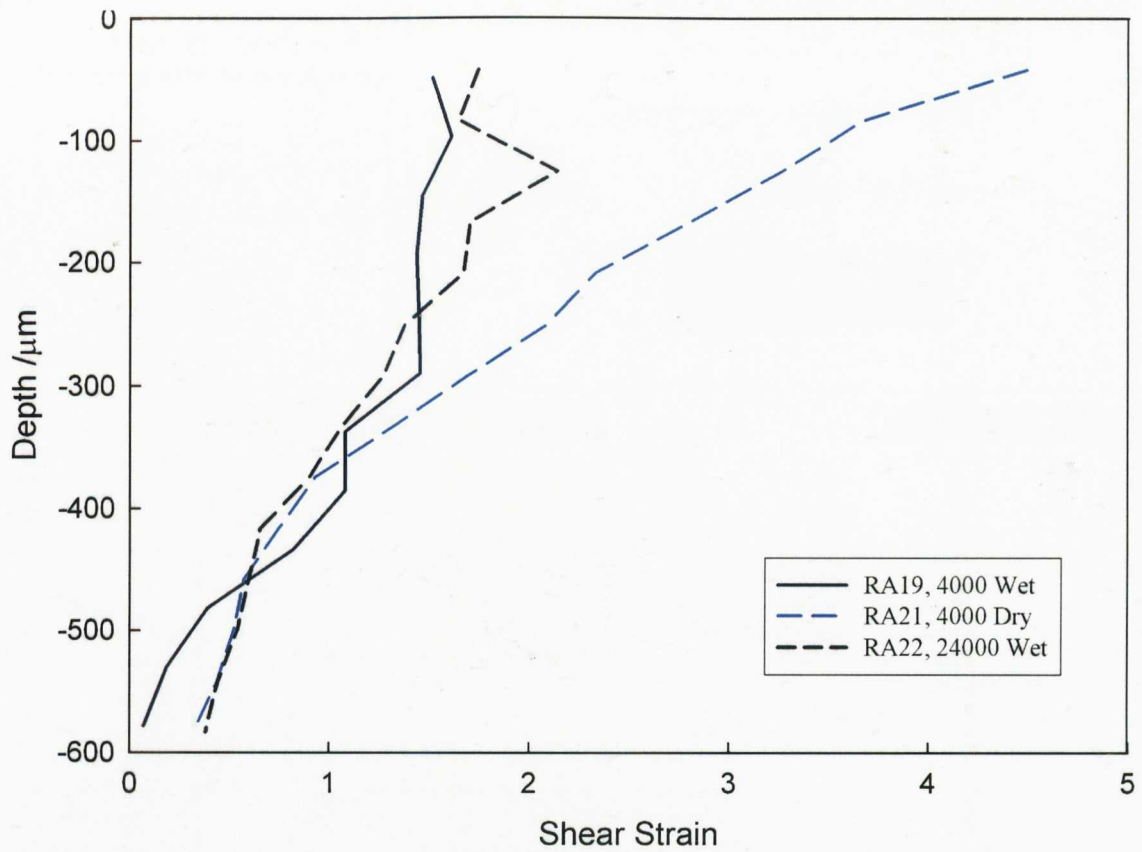
Figure 5.5.2.4: Shear strain of spot welded samples measured in the pearlite away from spot weld. (RA19, RA21 and RA22)
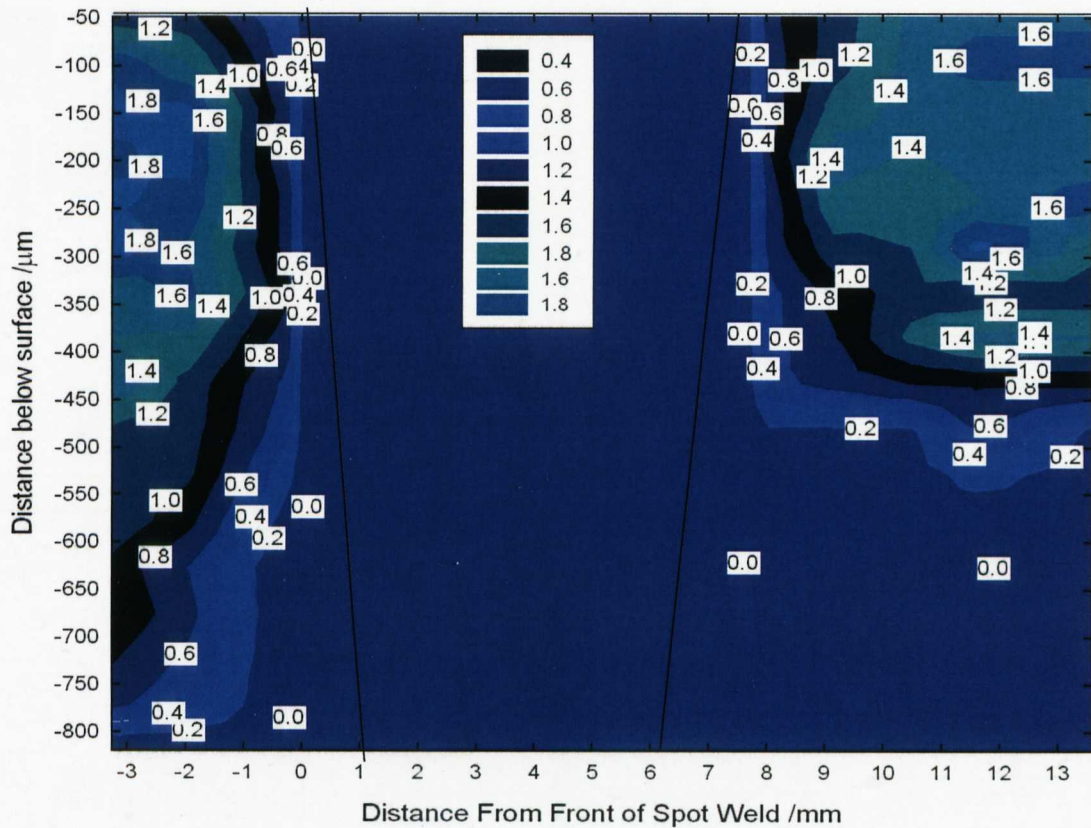
Figure 5.5.2.5: Shear strain of spot welded sample RA19 measured around a spot weld
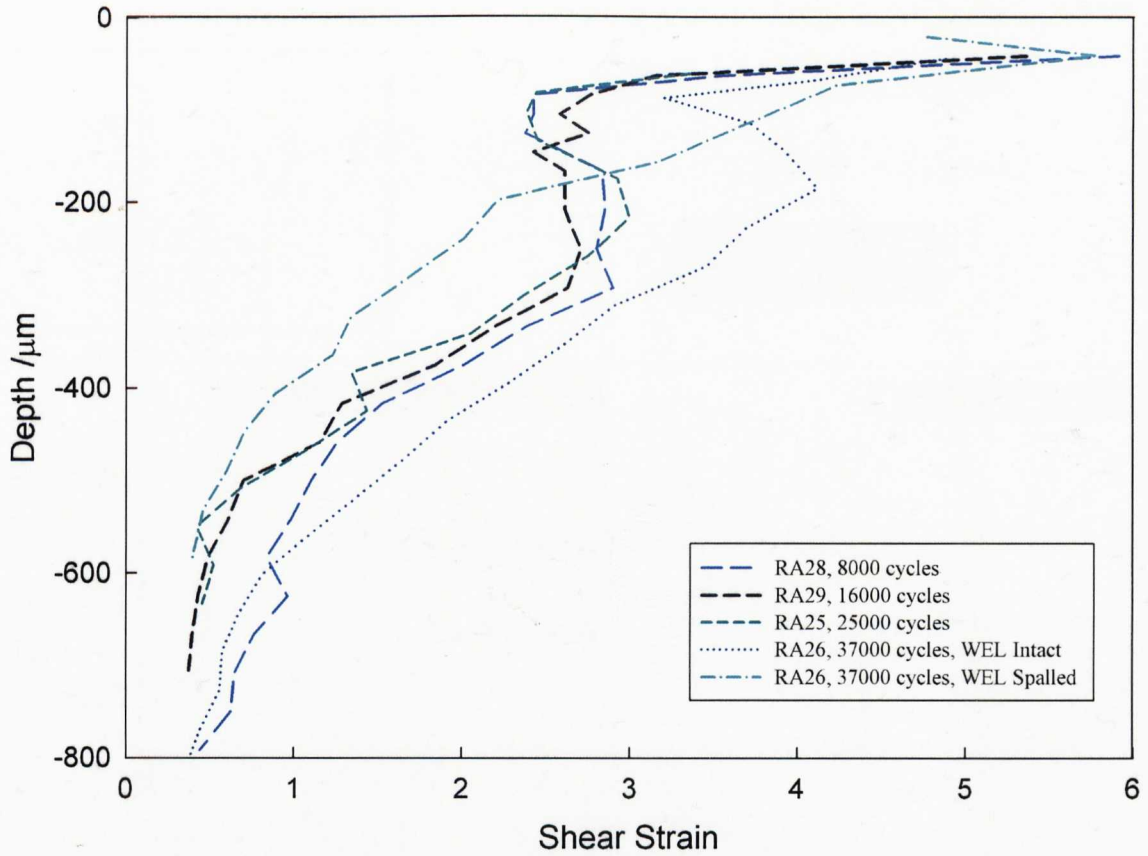
Figure 5.5.2.6: Shear strain of unidirectional WEL samples. (RA25, RA26, RA28 and RA29)
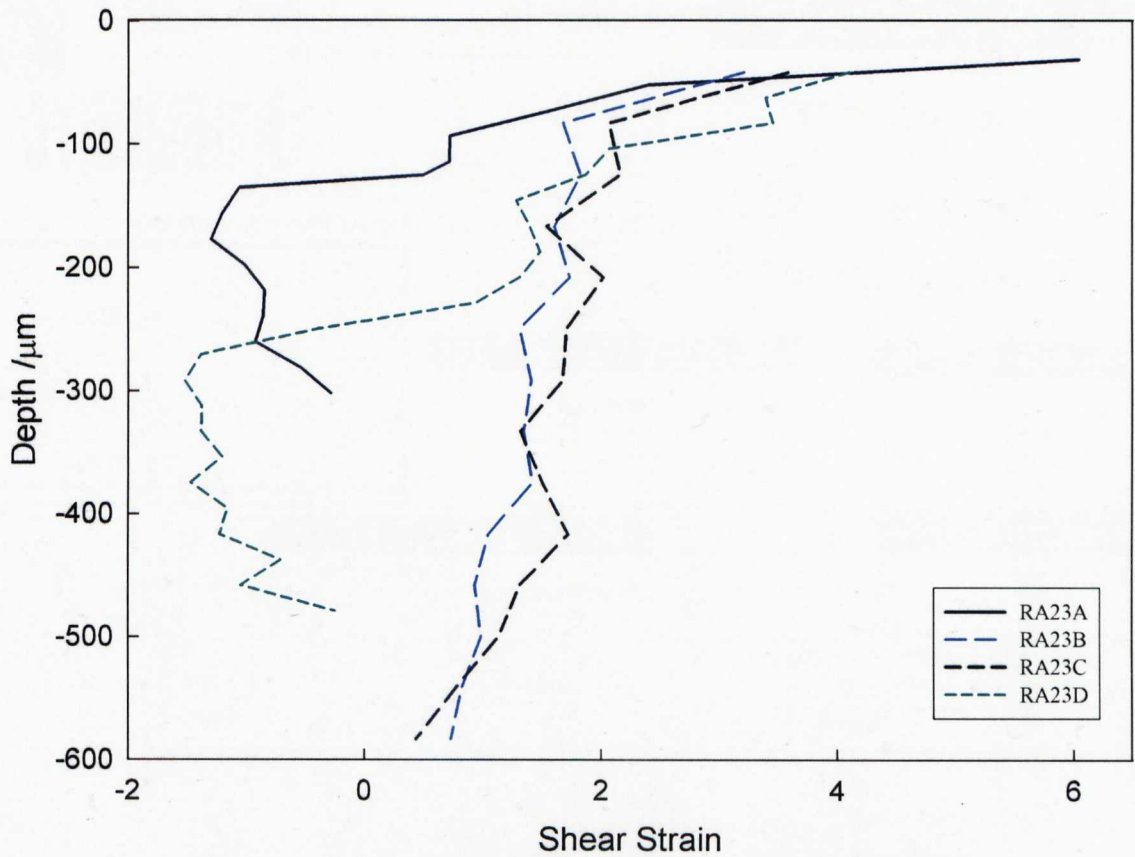
Figure 5.5.2.7: Shear strain of reversed test, RA23.
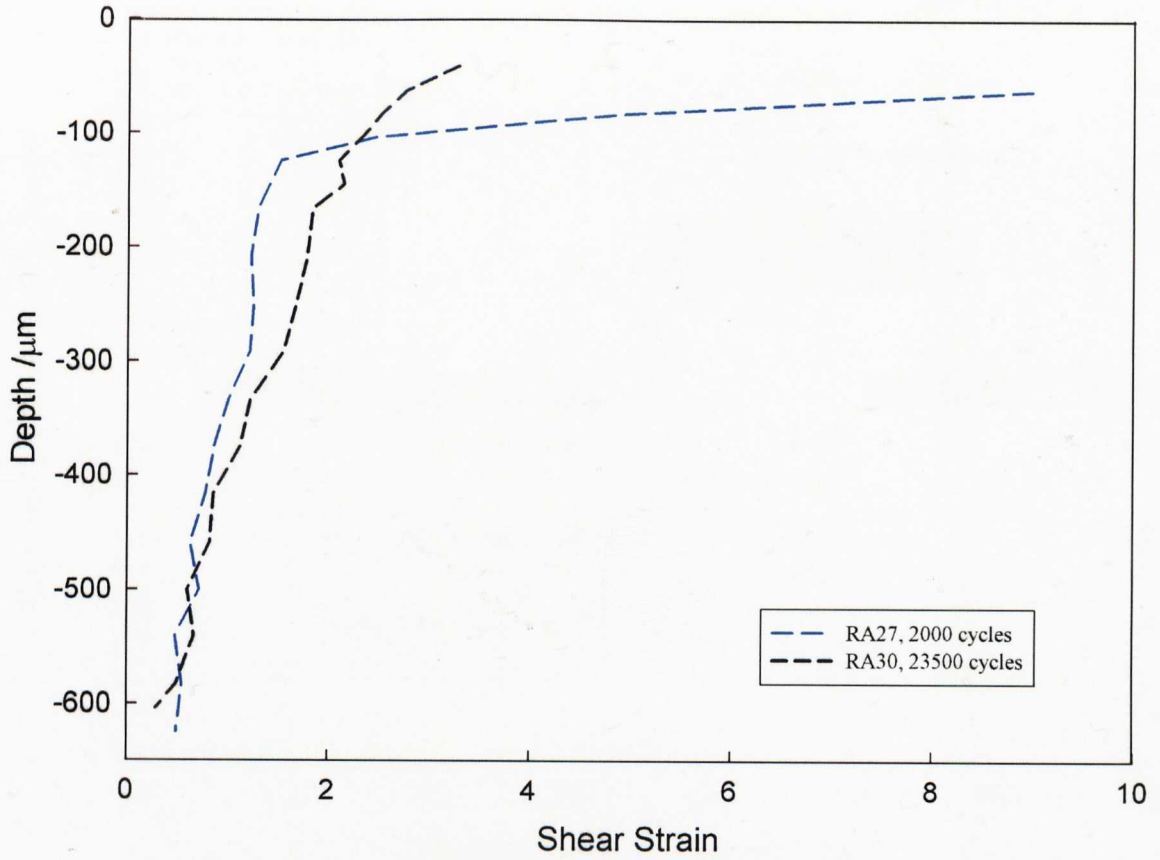
Figure 5.5.2.8: Shear strain of 0% slip WEL tests. (RA27 and RA30)
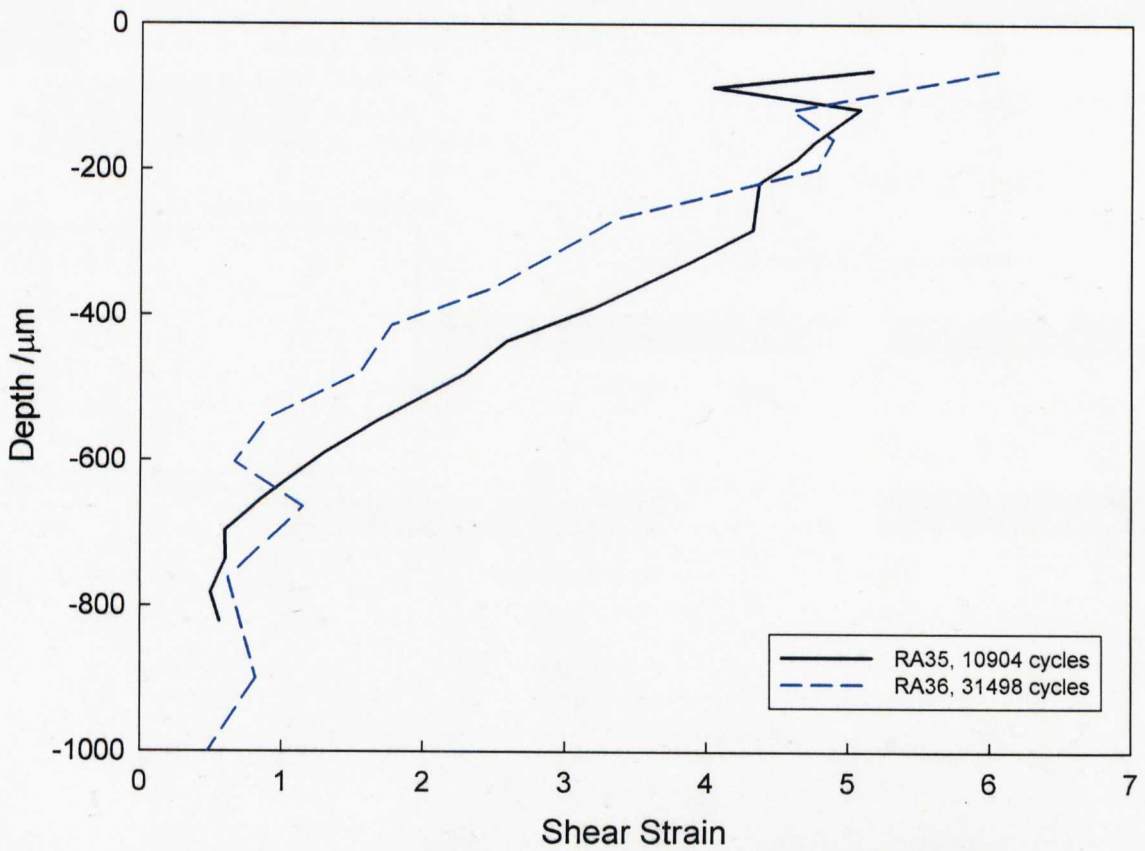
Figure 5.5.2.9: Shear strain of dry WEL tests. (RA35 and RA36)
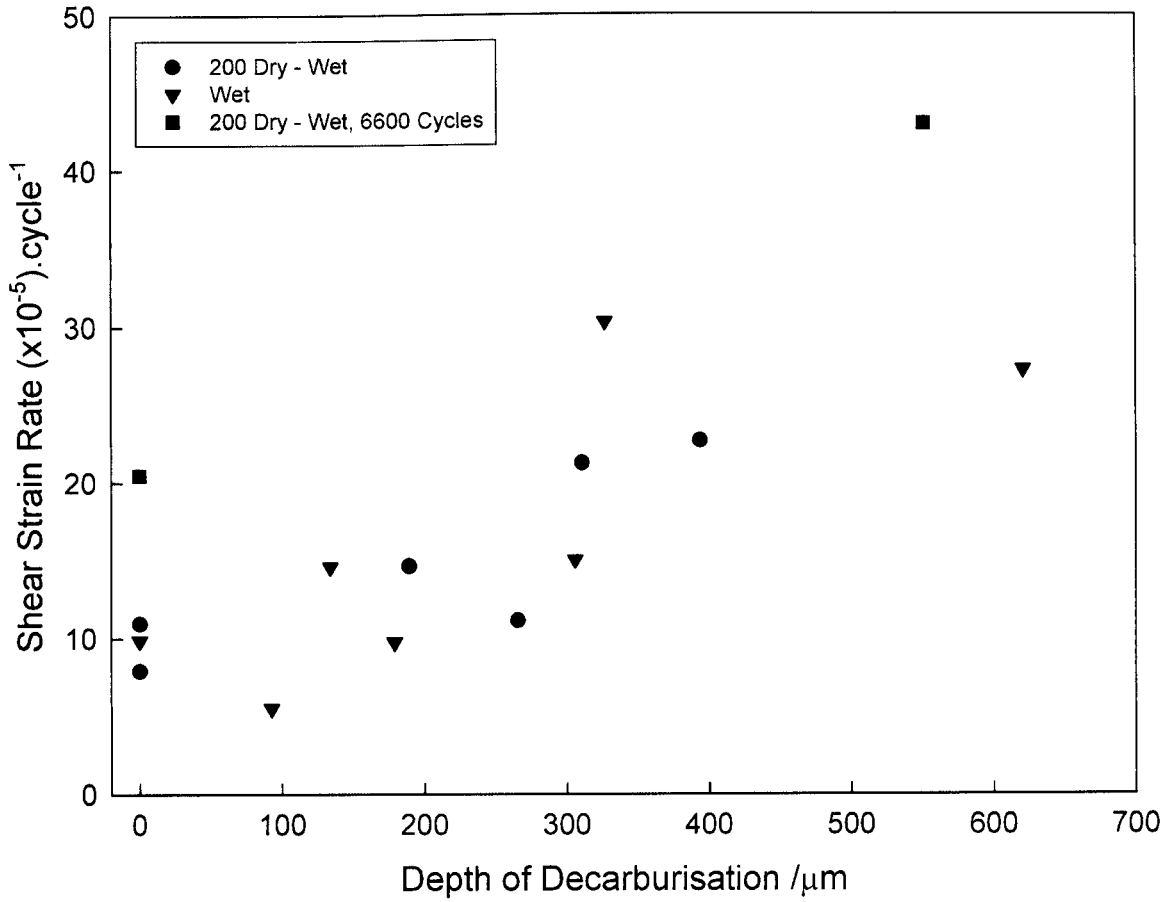
Figure 5.5.2.10: Shear strain rate of decarburised samples at a depth of 200μm
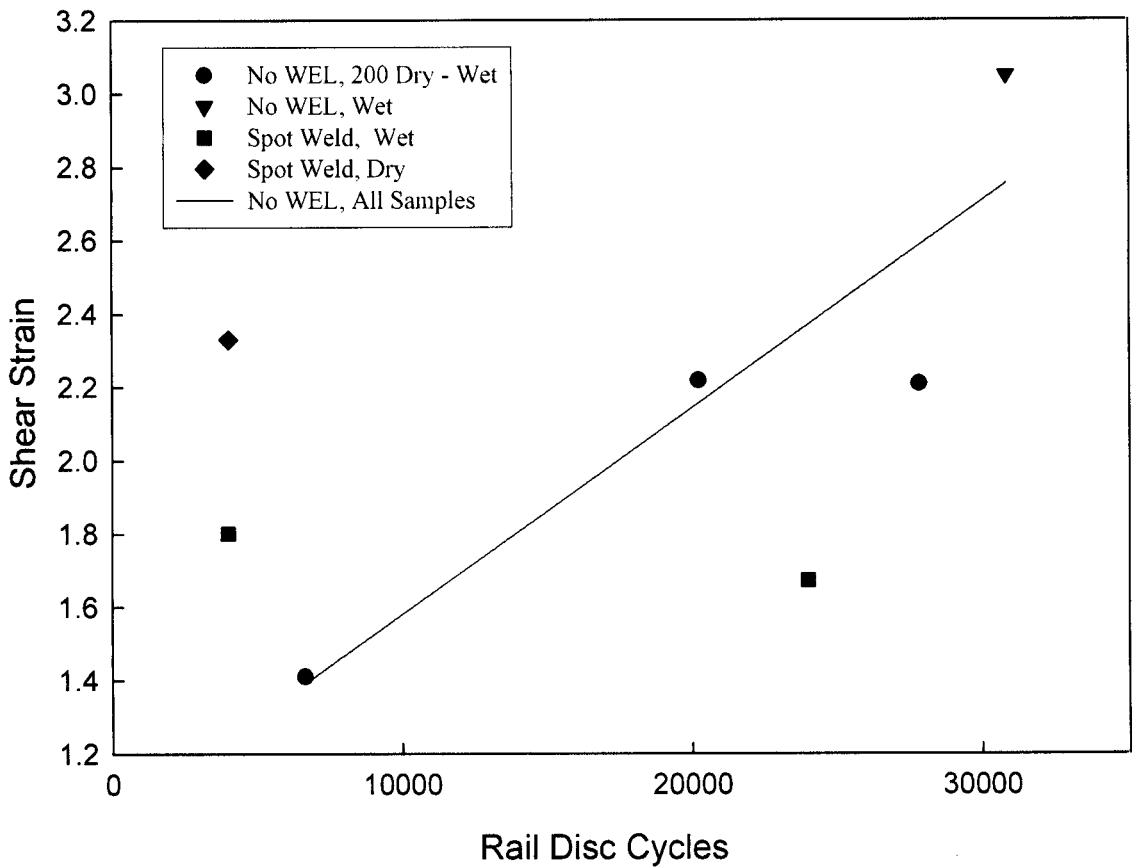
Figure 5.5.2.11: Shear strain of spot welded samples at 200μm for samples away from spot weld
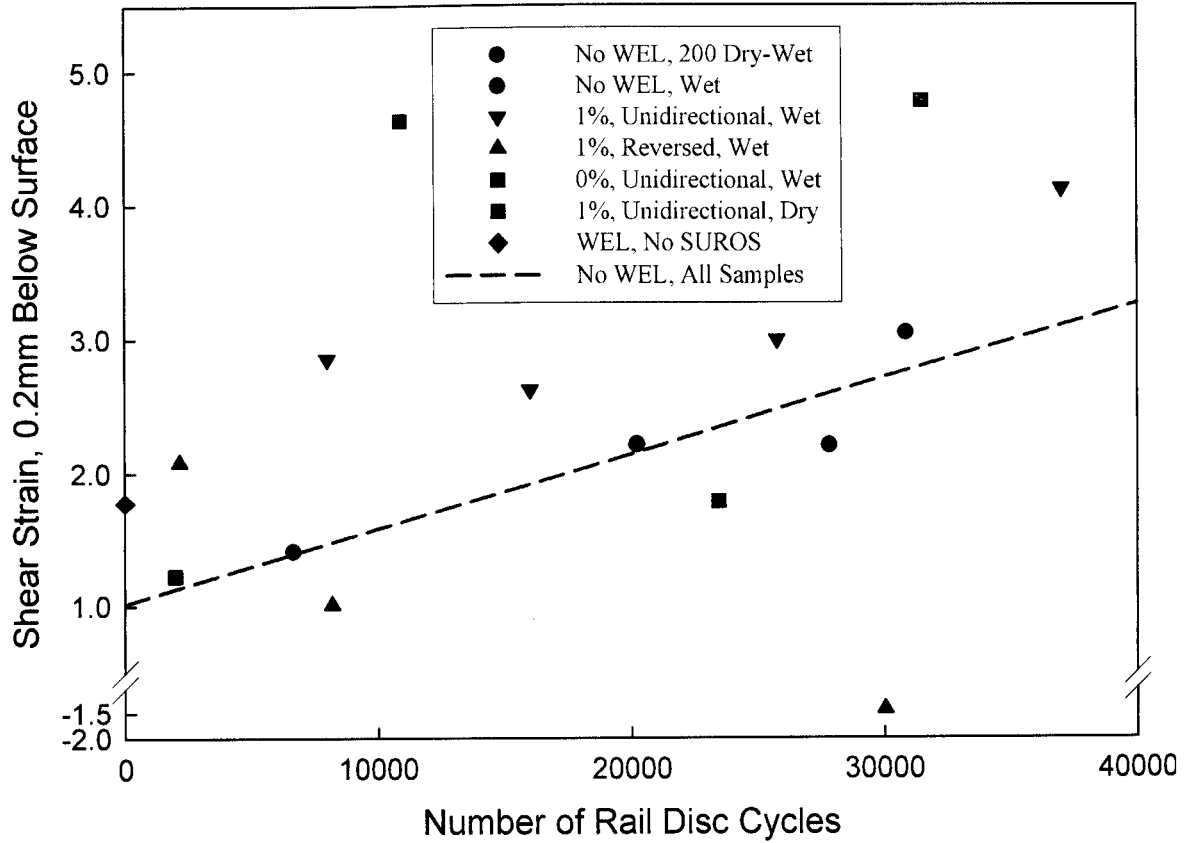
Figure 5.5.2.12: Shear strain of WEL samples at 200μm
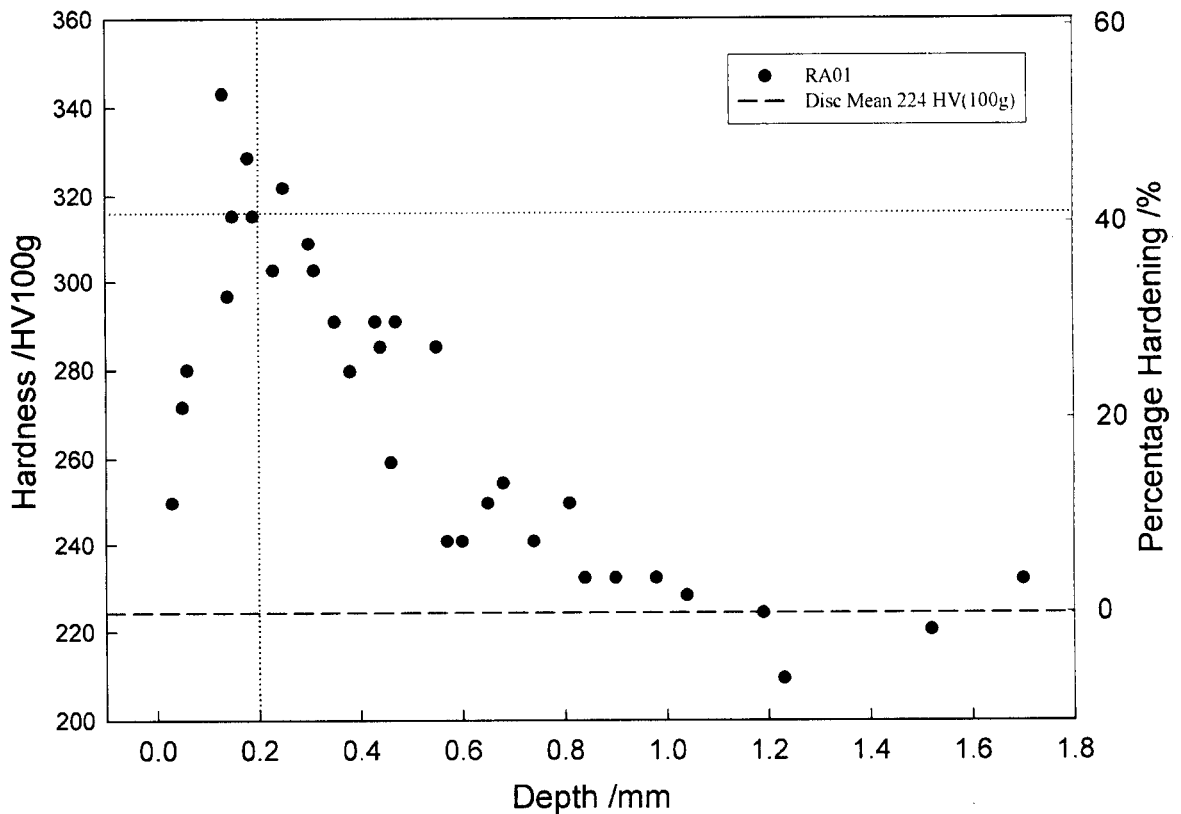
Figure 5.5.2.13: Vickers microhardness of RA01 with no decarburisation
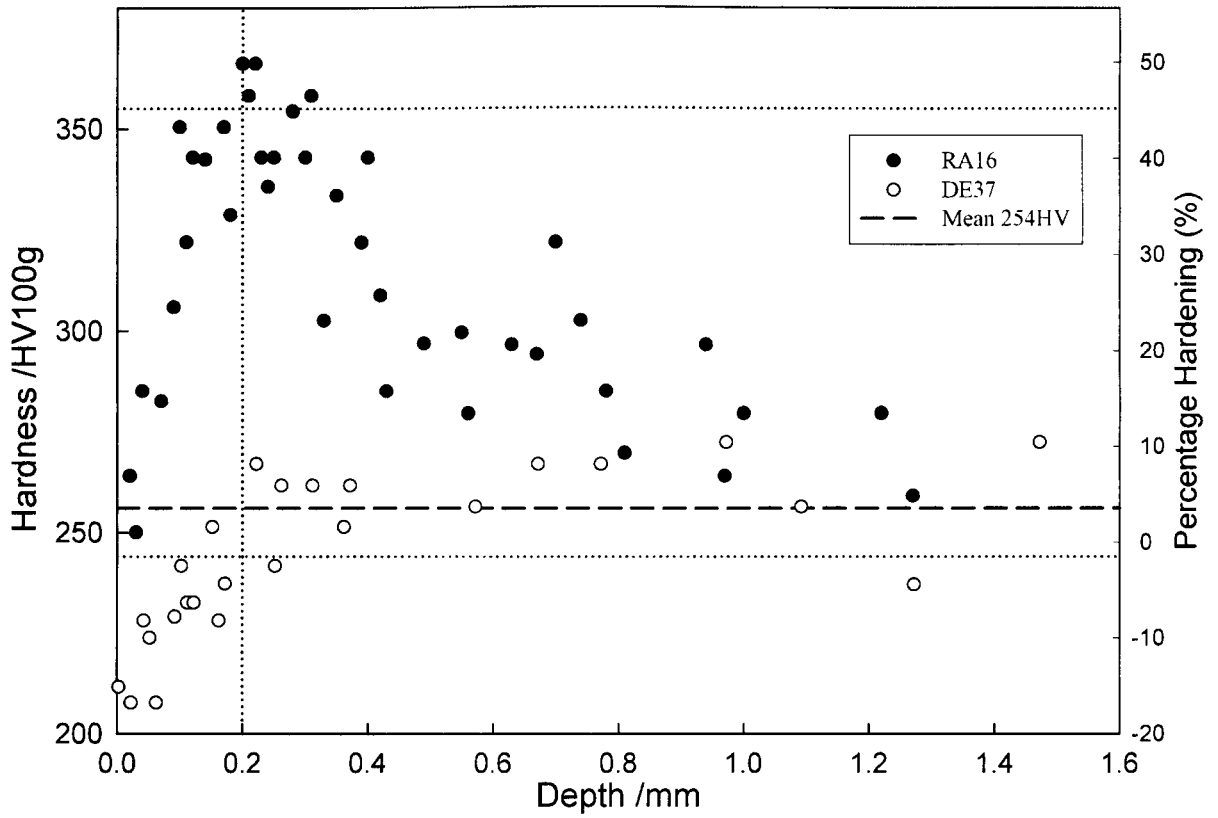
Figure 5.5.2.14: Vickers microhardness of RA16 and DE37 with a depth of decarburisation of 93μm
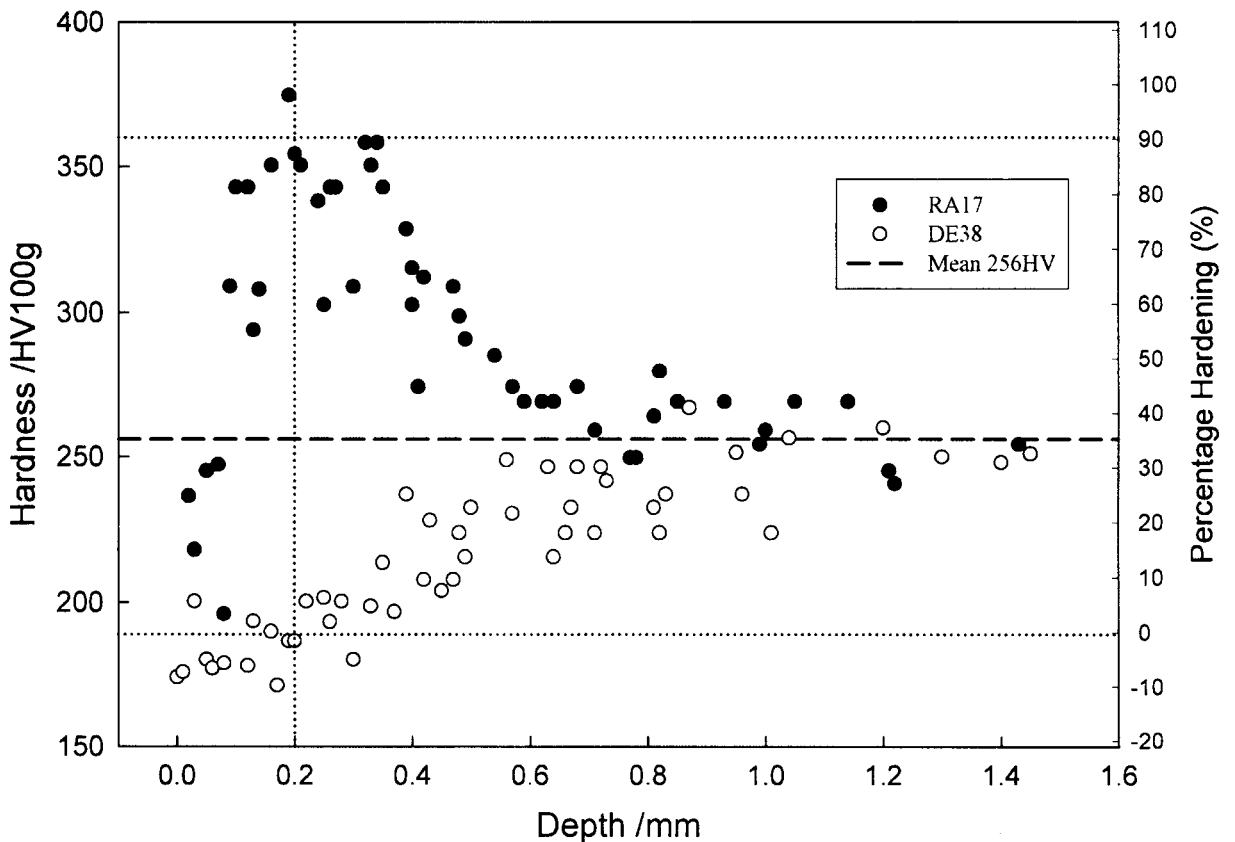
Figure 5.5.2.15: Vickers microhardness of RA17 and DE38 with a depth of decarburisation of 621μm
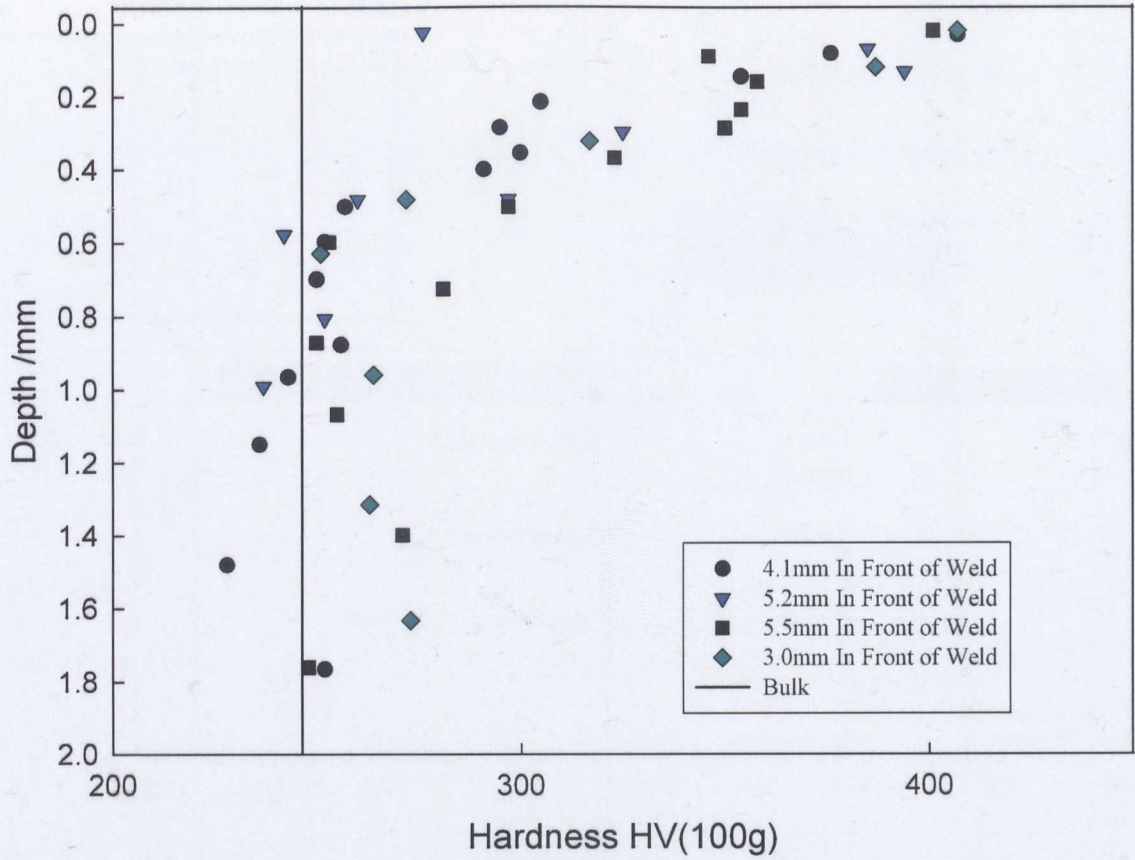
Figure 5.5.2.16: Vickers microhardness of spot welded sample RA21 away from weld
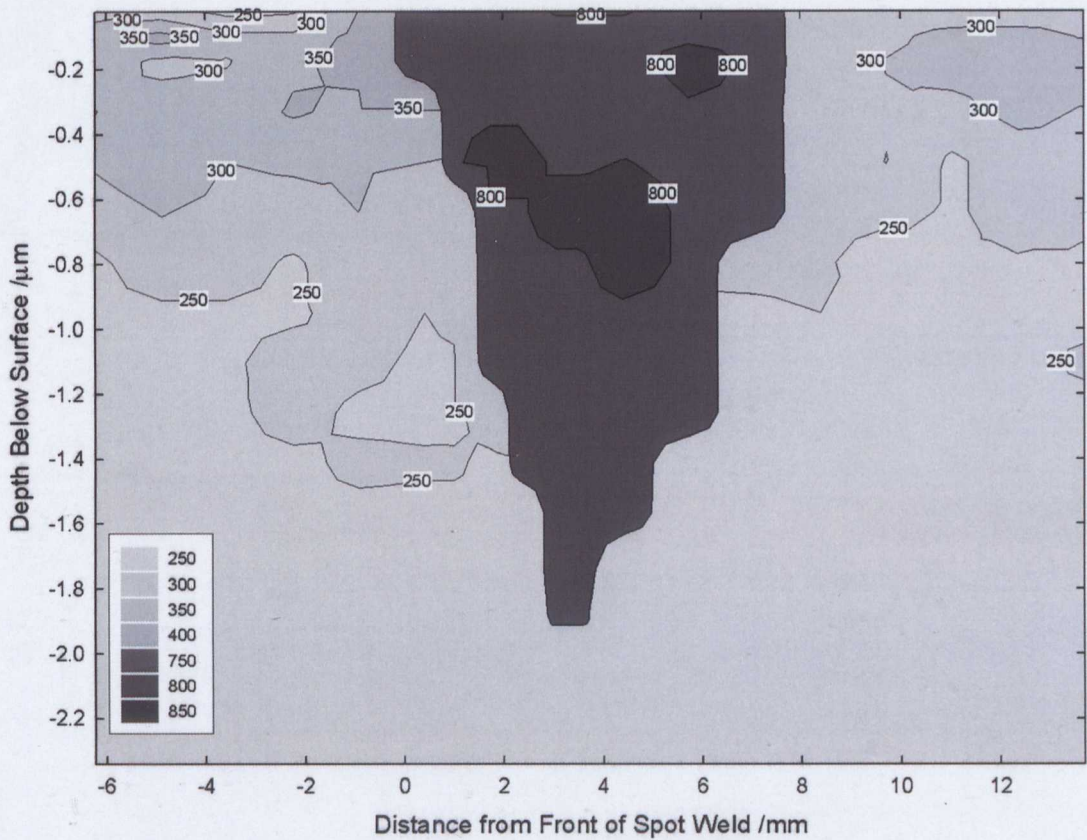
Figure 5.5.2.17: Vickers microhardness around a spot weld in RA19
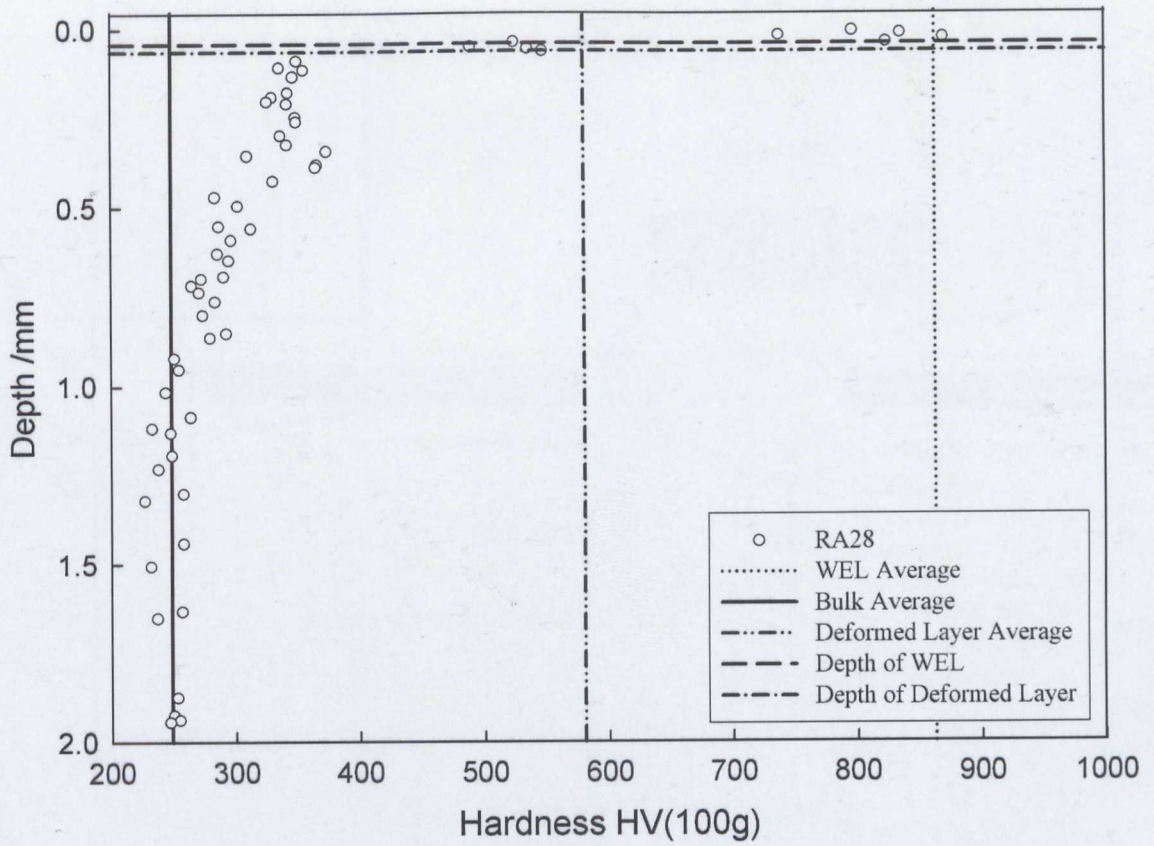
Figure 5.5.2.18: Vickers microhardness of WEL sample RA28
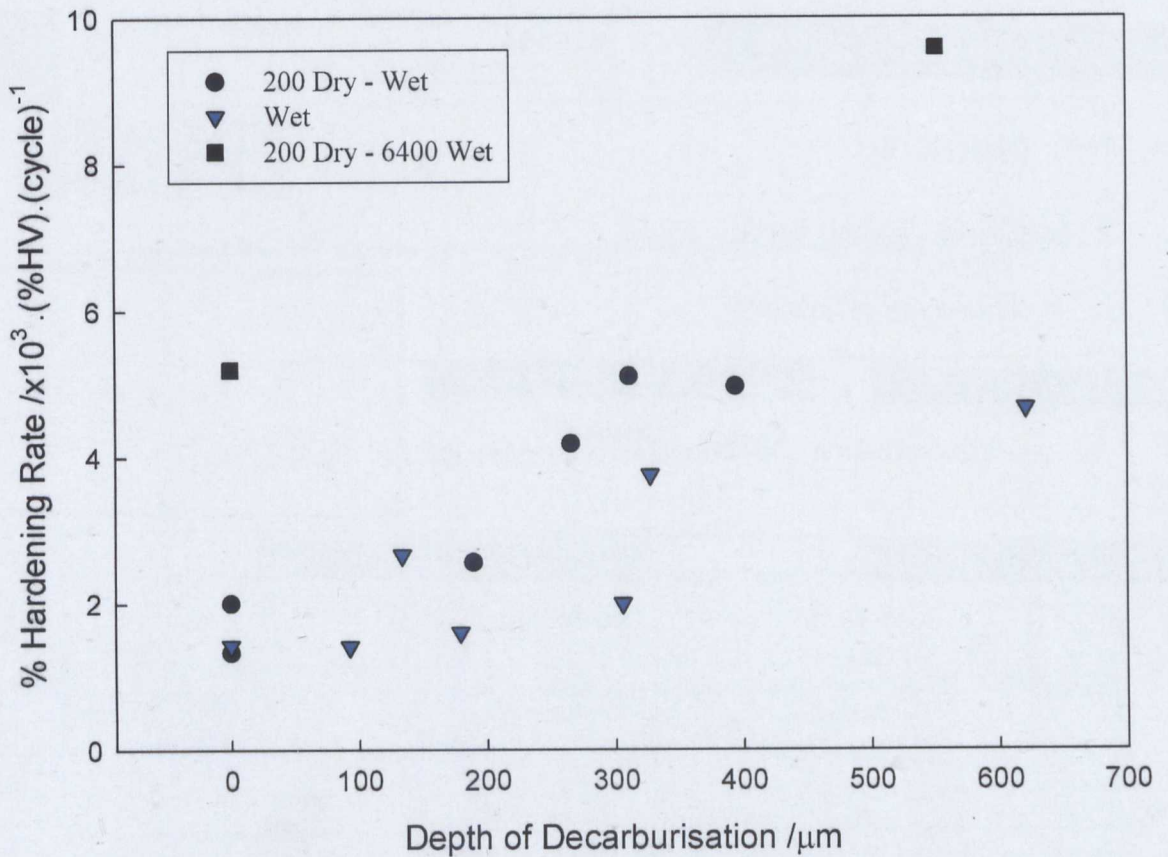
Figure 5.5.2.19: Percentage hardening rate of decarburised samples
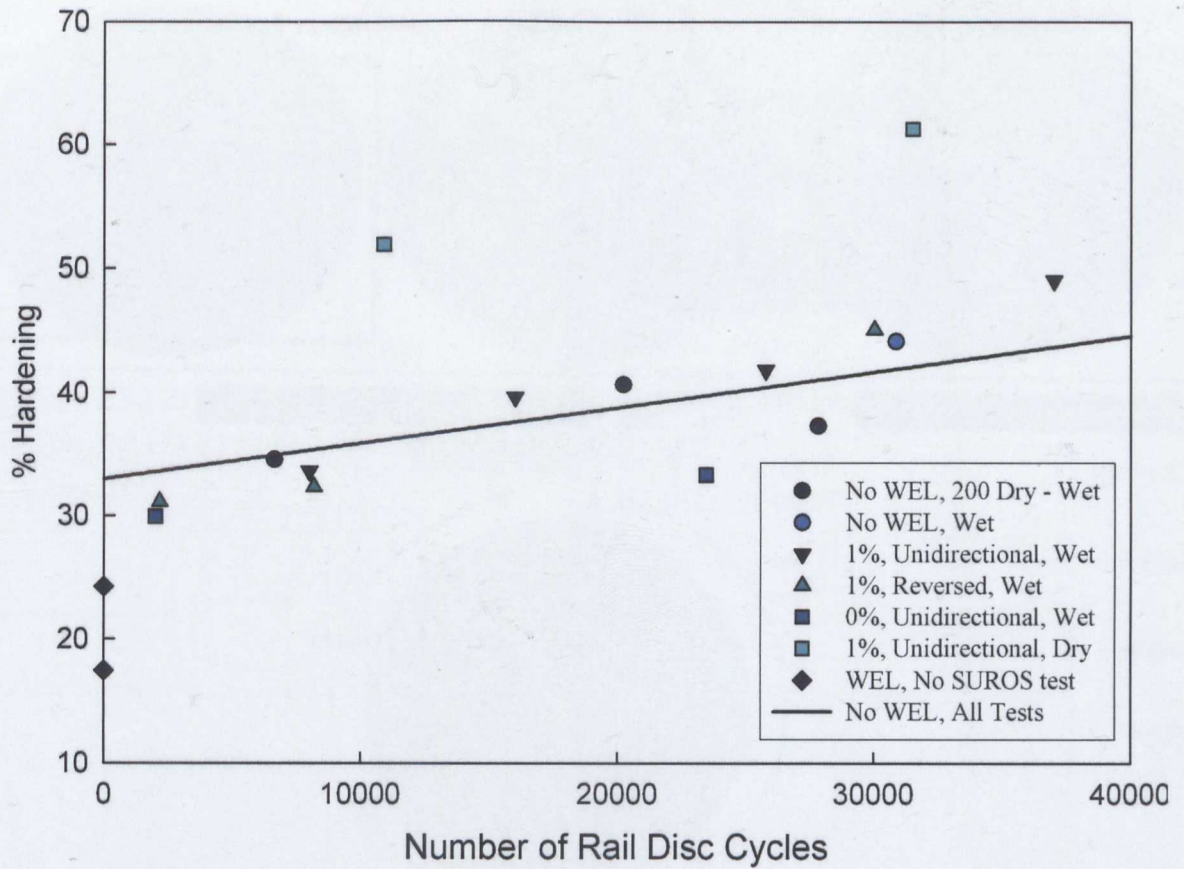
Figure 5.5.2.20: Percentage hardening of WEL samples against the number of rail disc cycles
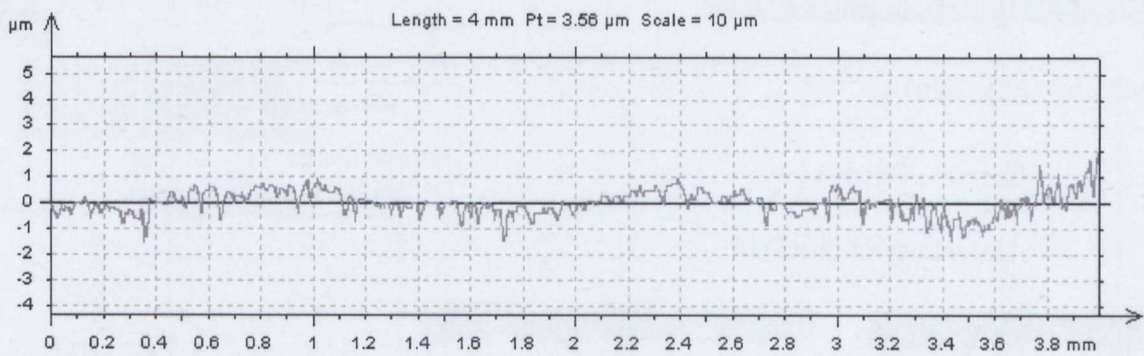
Figure 5.5.3.1: Surface roughness before test of a normal sample
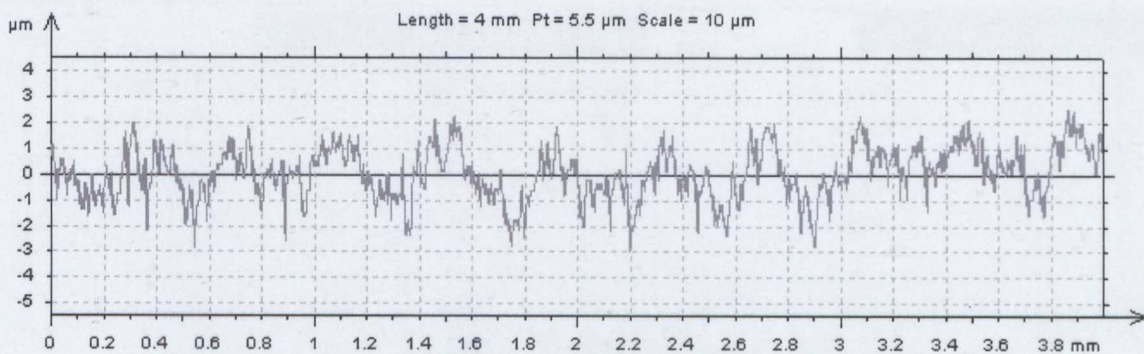
Figure 5.5.3.2: Surface roughness after test of a normal sample
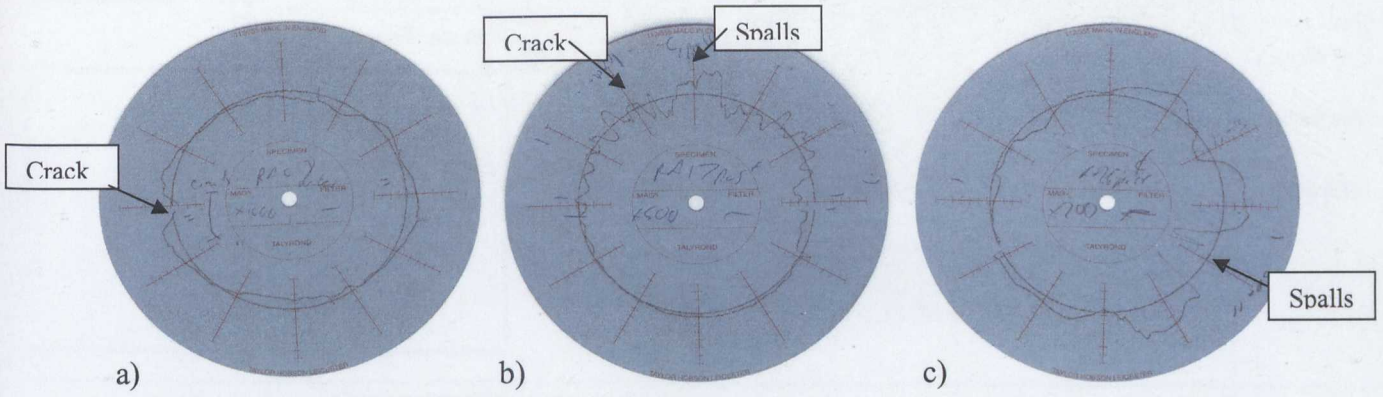
Figure 5.5.3.3: Talyrond profile for rail discs. a) normal sample(RA08), b) decarburised sample(RA17), c) sliding WEL samples (RA26).
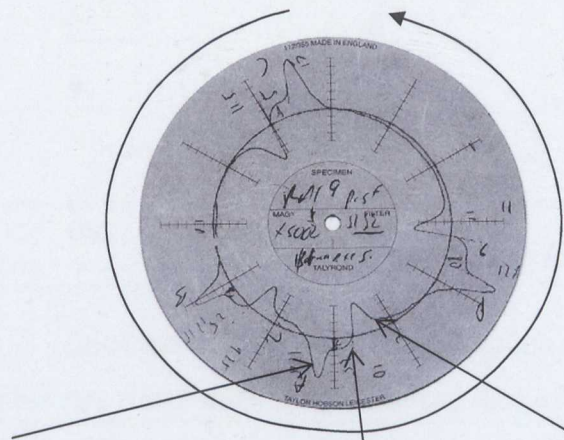
Figure 5.5.3.4: Talyrond profile for rail disc RA19 with four spot welds (4000 cycles, water lubrication)
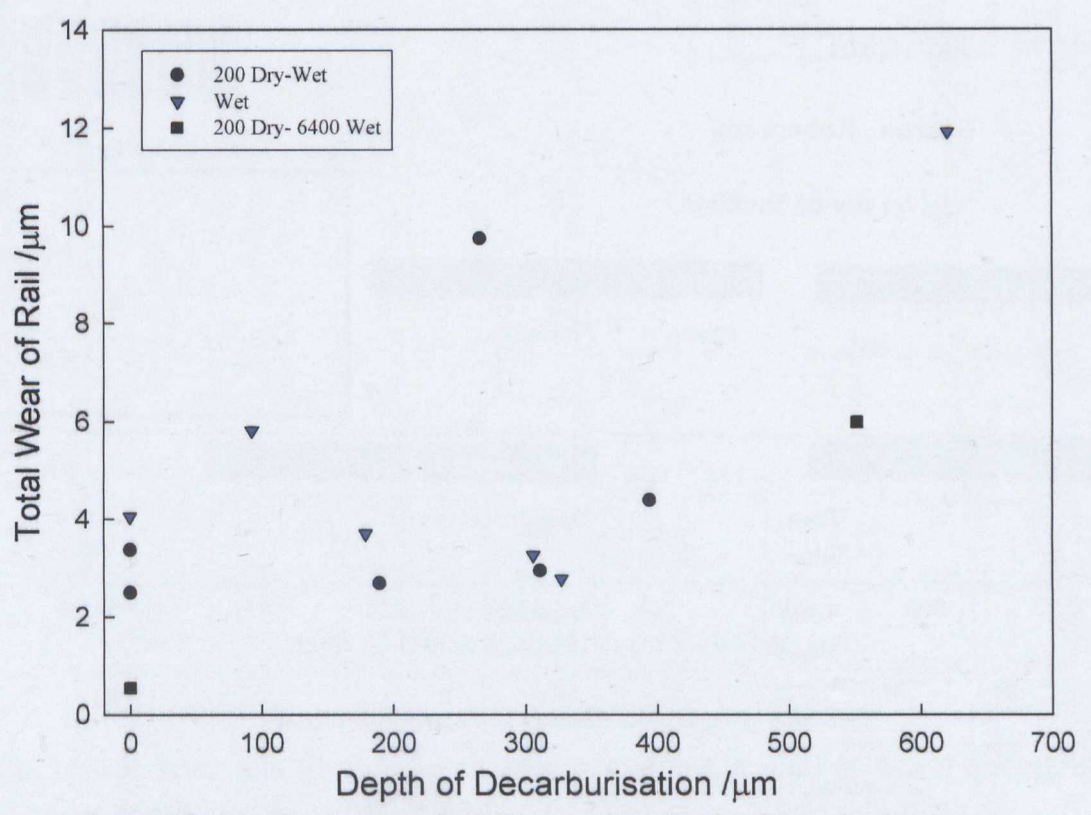
Figure 5.5.4.1: Total wear of rail disc against depth of decarburisation
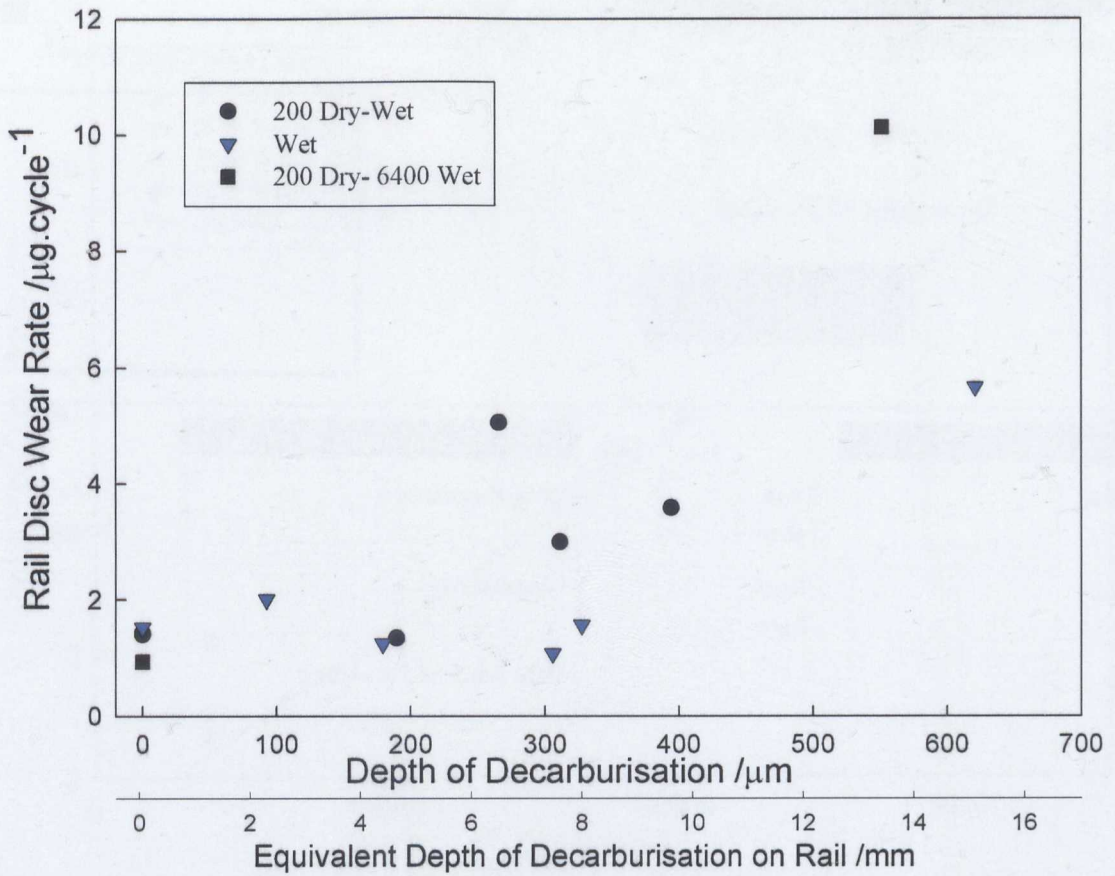
Figure 5.5.4.2: Wear rate (total wear/ number of rail disc cycles) of rail disc against depth of decarburisation
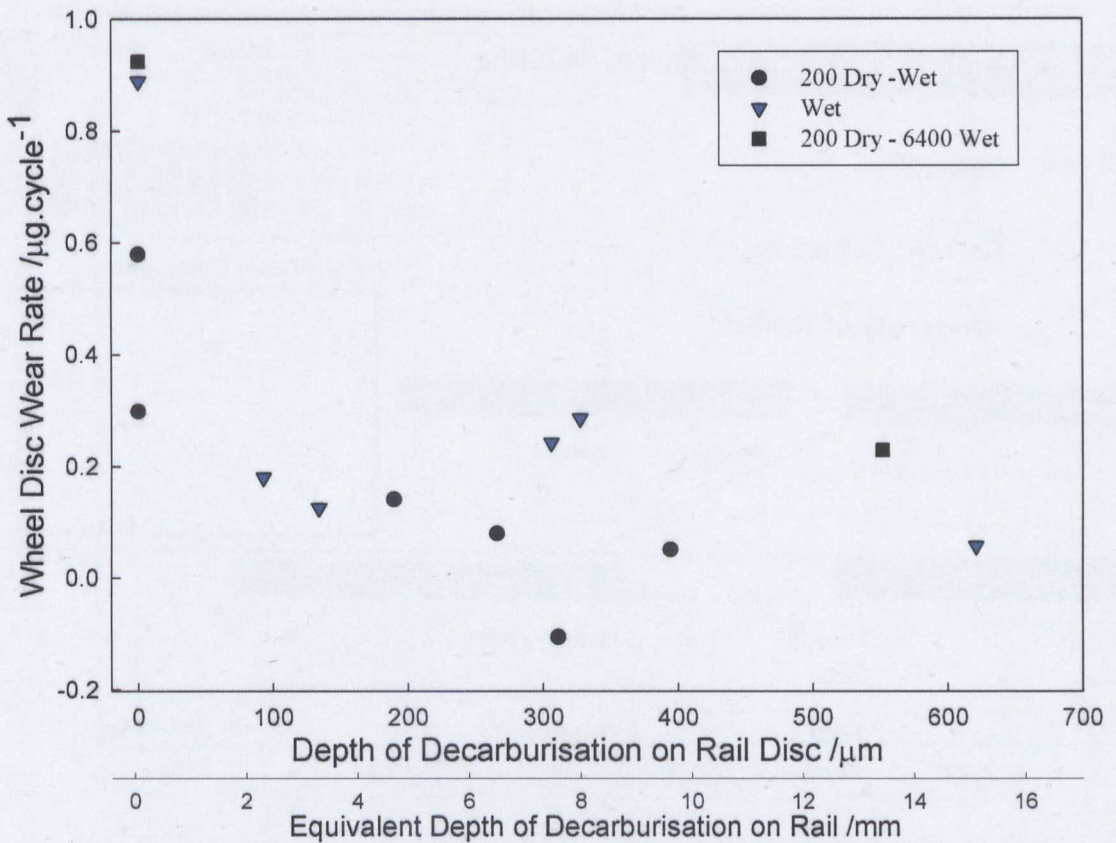
Figure 5.5.4.3: Wear rate (total wear/ number of rail disc cycles) of wheel disc against depth of decarburisation on rail disc
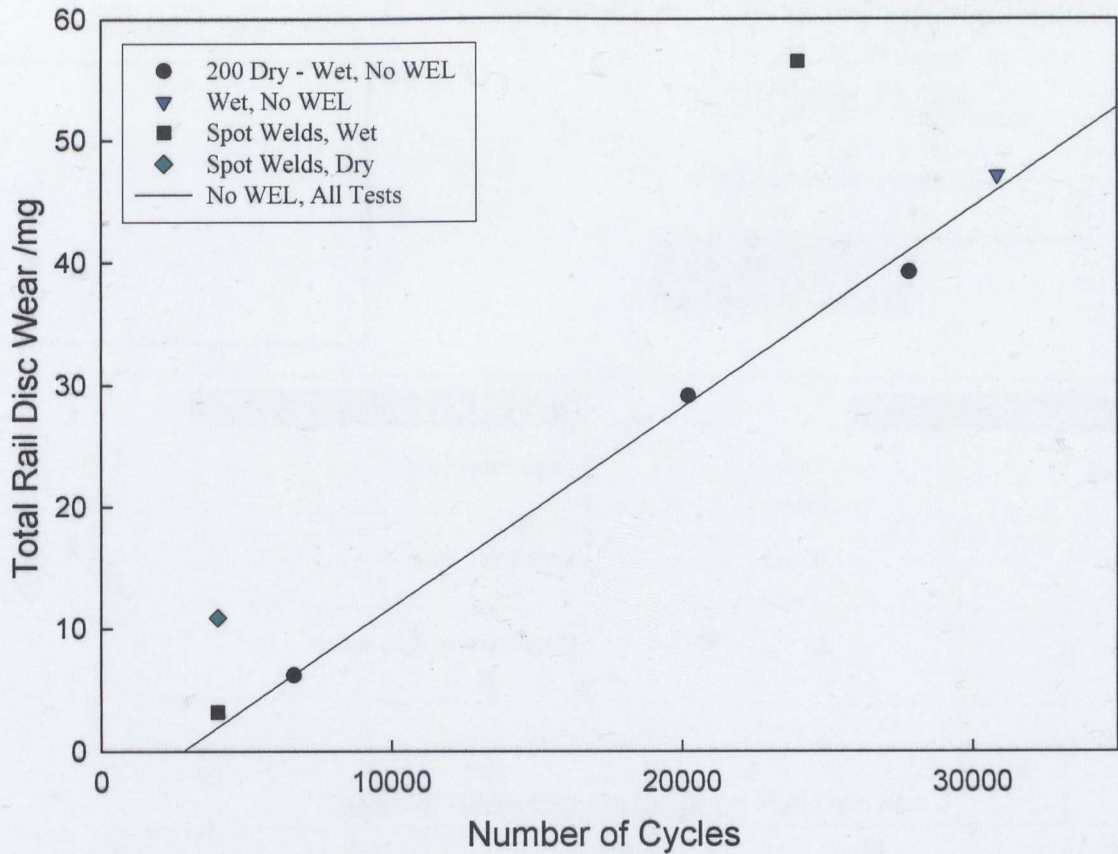
Figure 5.5.4.4: Total wear of rail disc against number of rail disc cycles for spot welded samples
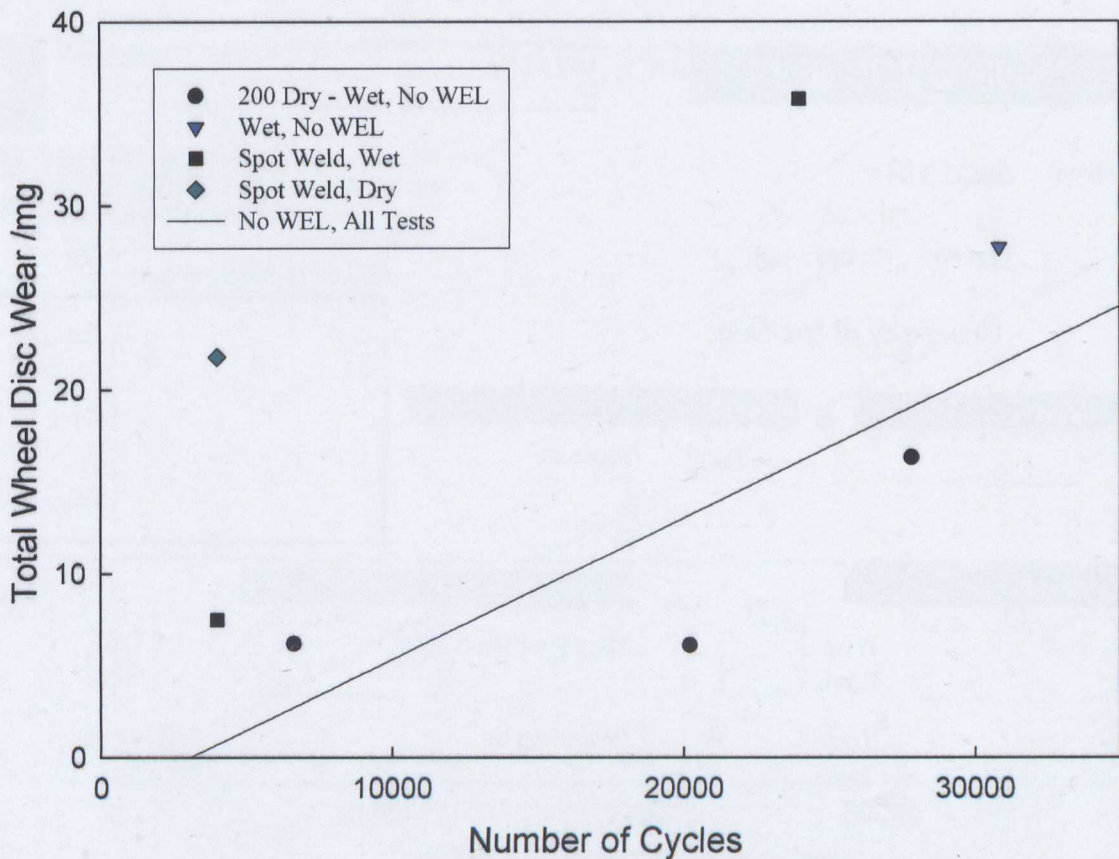
Figure 5.5.4.5: Total wear of wheel disc against number of rail disc cycles for spot welded samples
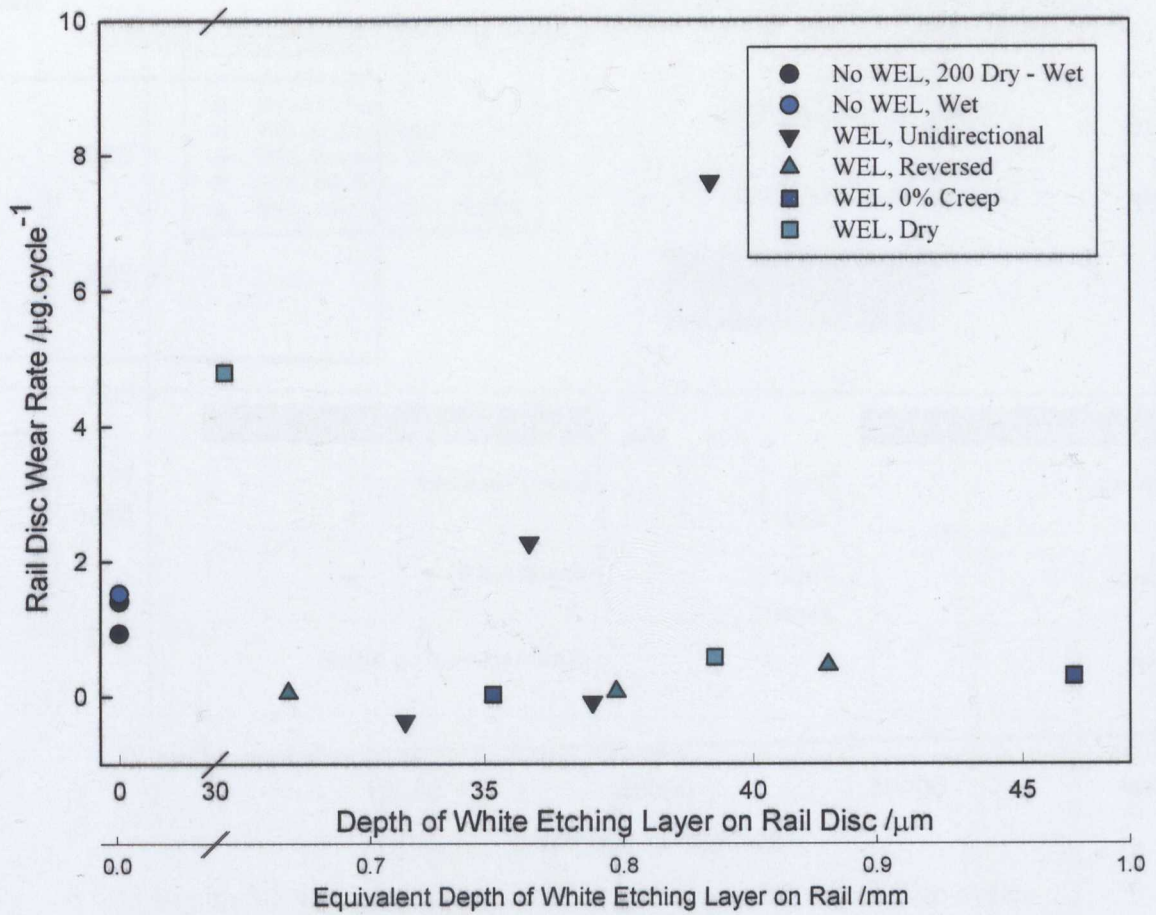
Figure 5.5.4.6: Wear rate of rail disc against depth of WEL for sliding samples
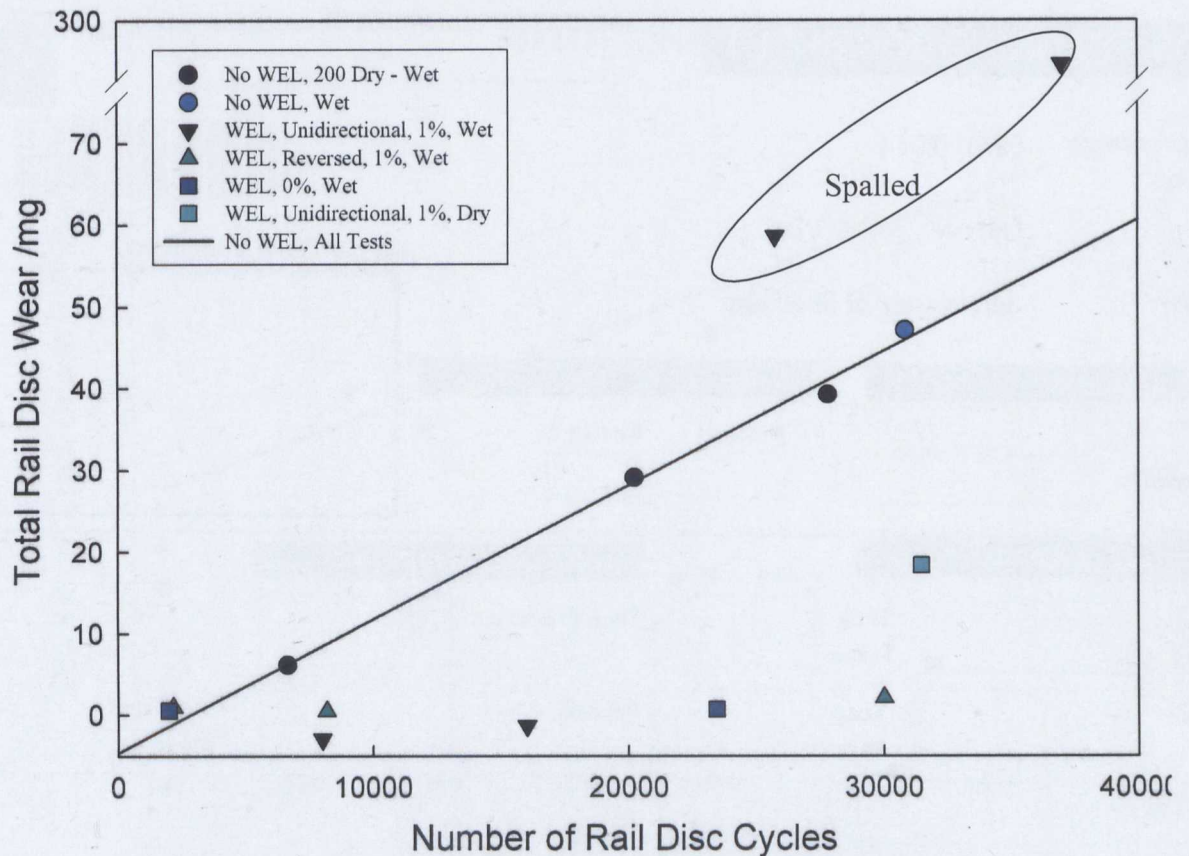
Figure 5.5.4.7: Wear of rail disc against number of rail disc cycles
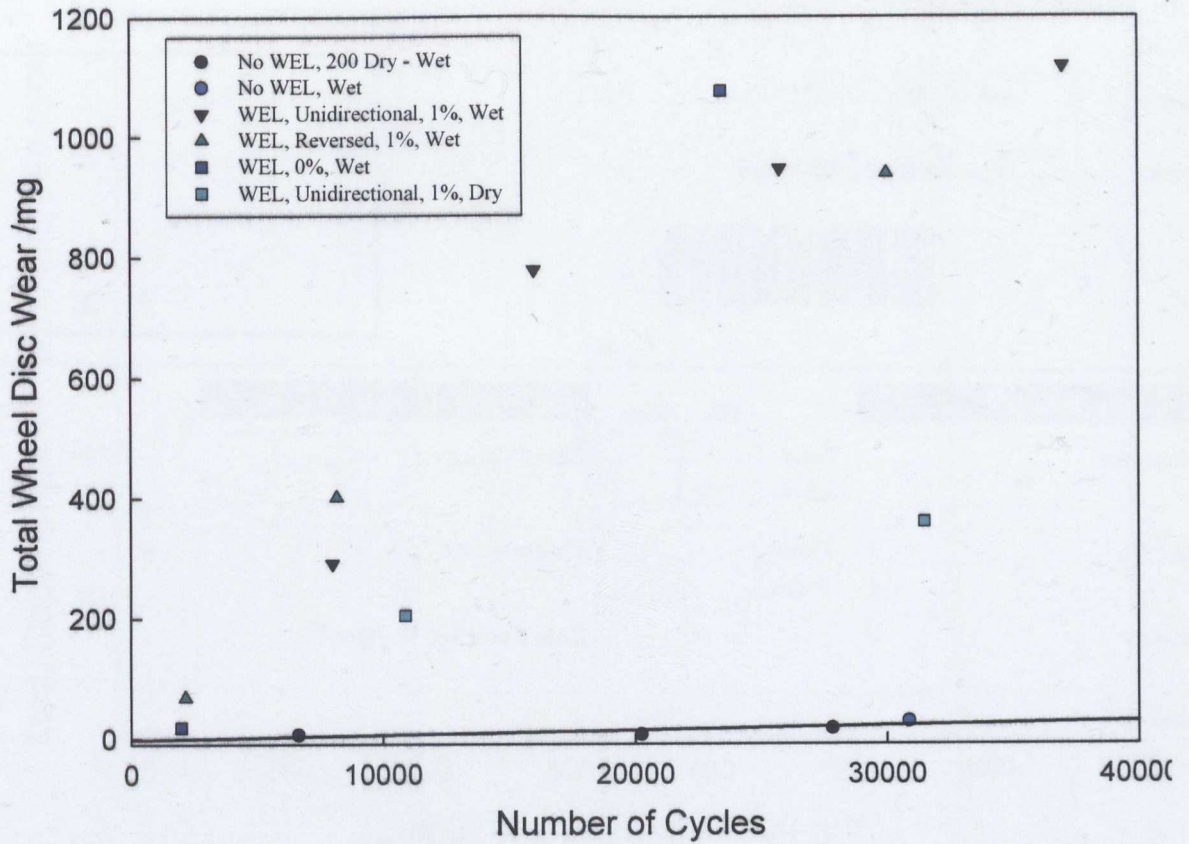
Figure 5.5.4.8: Wear of wheel disc against number of rail disc cycles
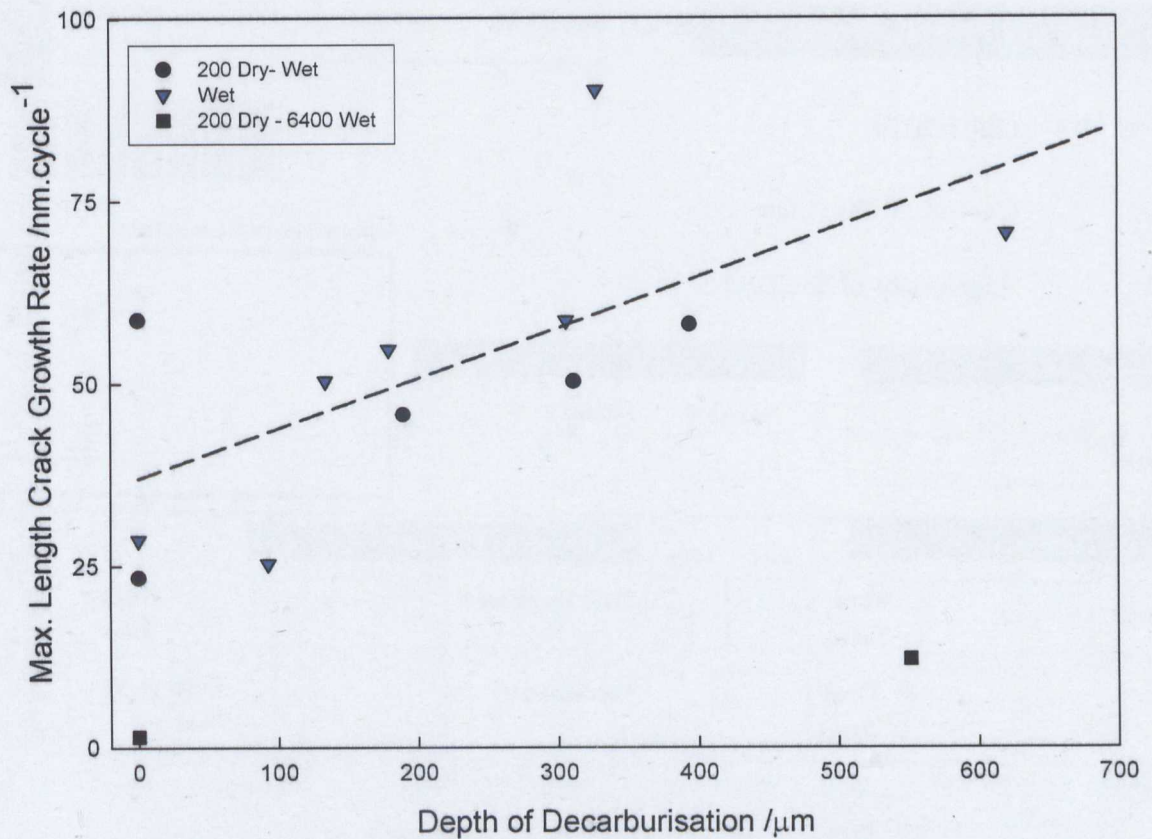
Figure 5.5.5.1: Maximum length crack growth rate of decarburised samples
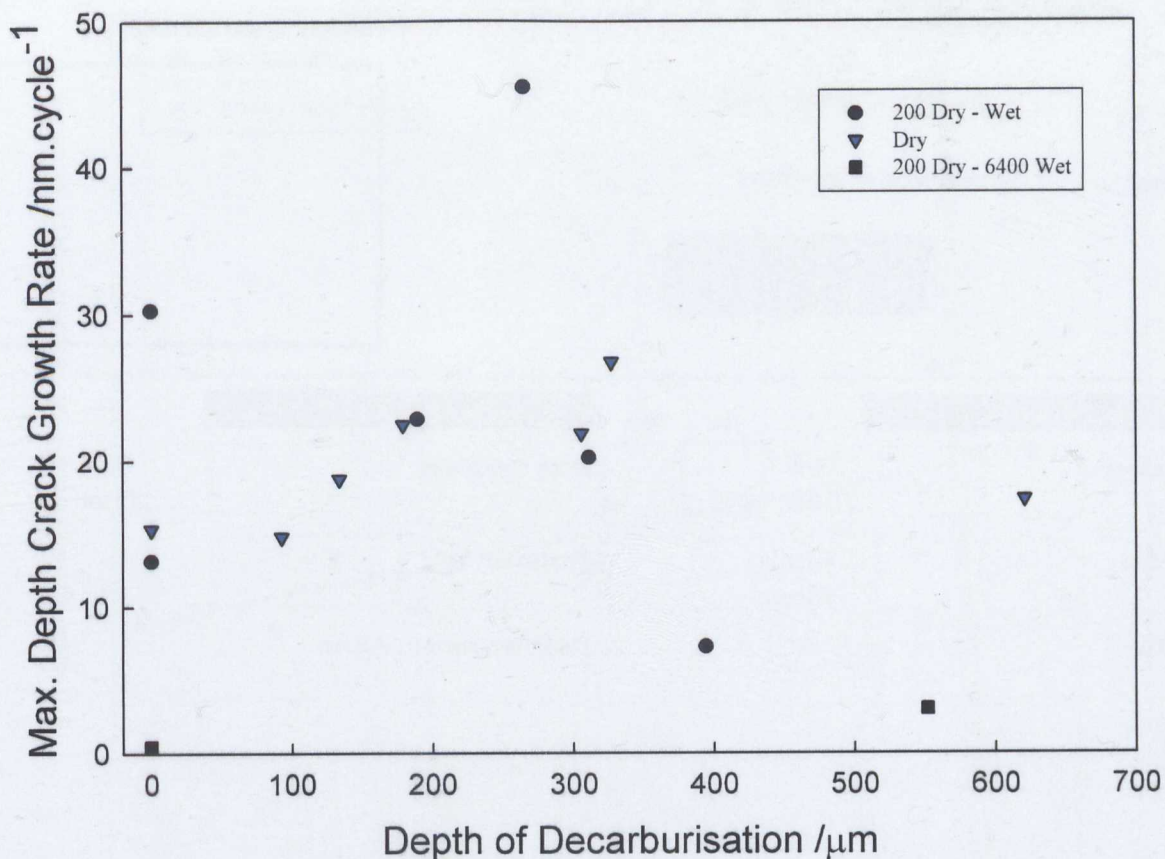
Figure 5.5.5.2: Maximum depth crack growth rate of decarburised samples
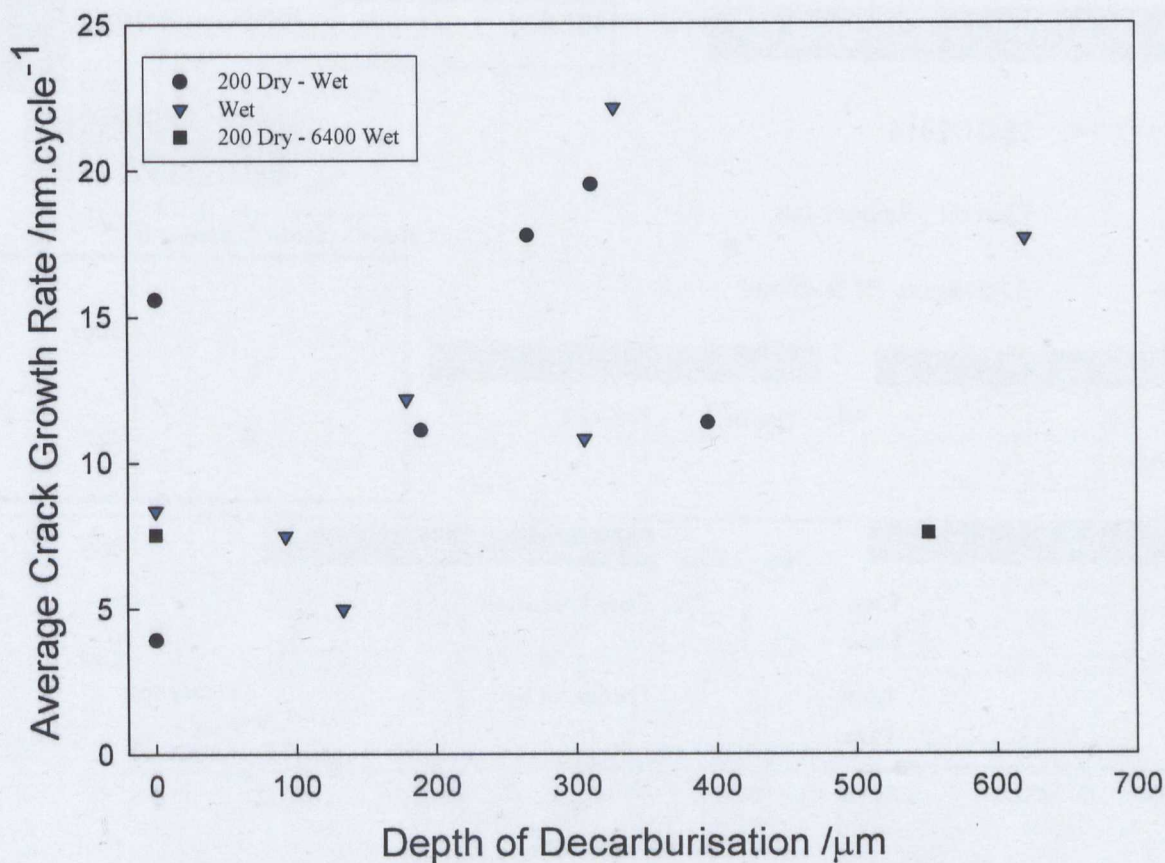
Figure 5.5.5.3: Average length crack growth rate of decarburised samples
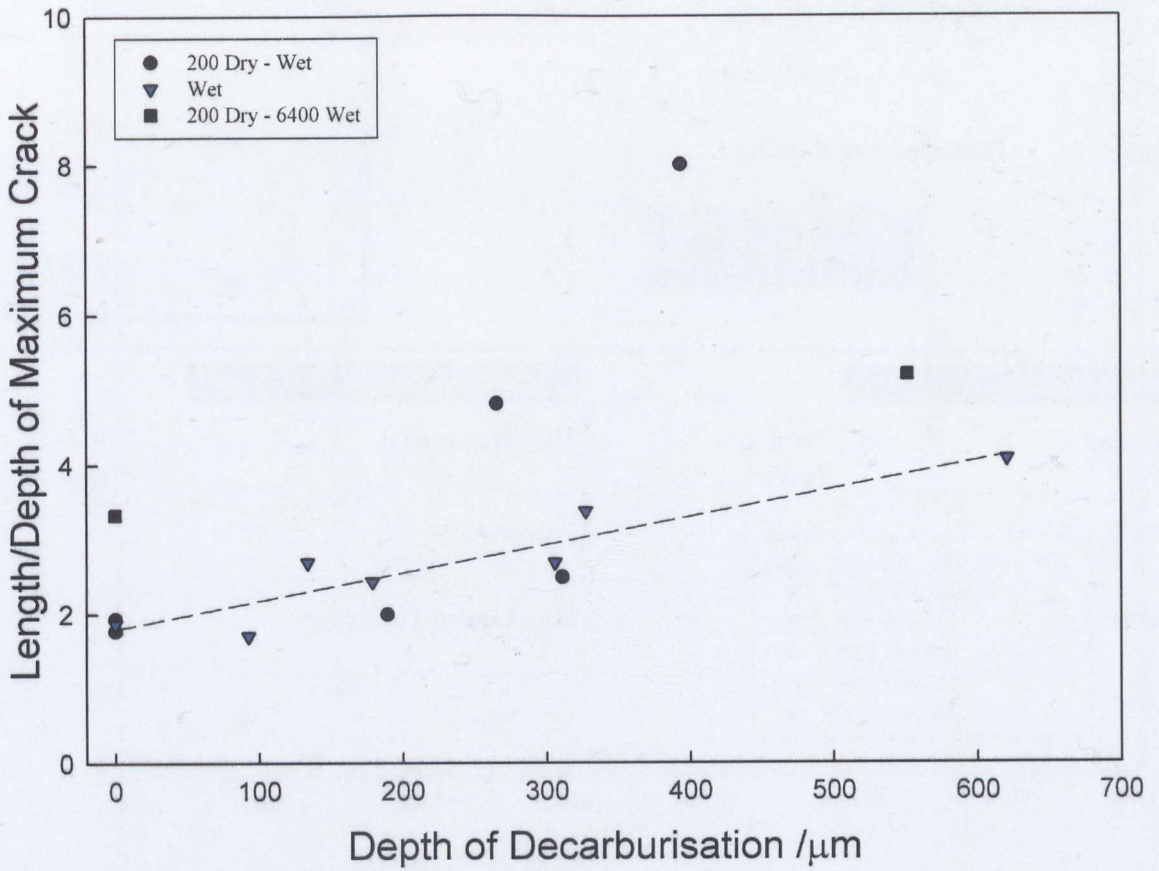
Figure 5.5.5.4: Length/depth of maximum crack of decarburised samples
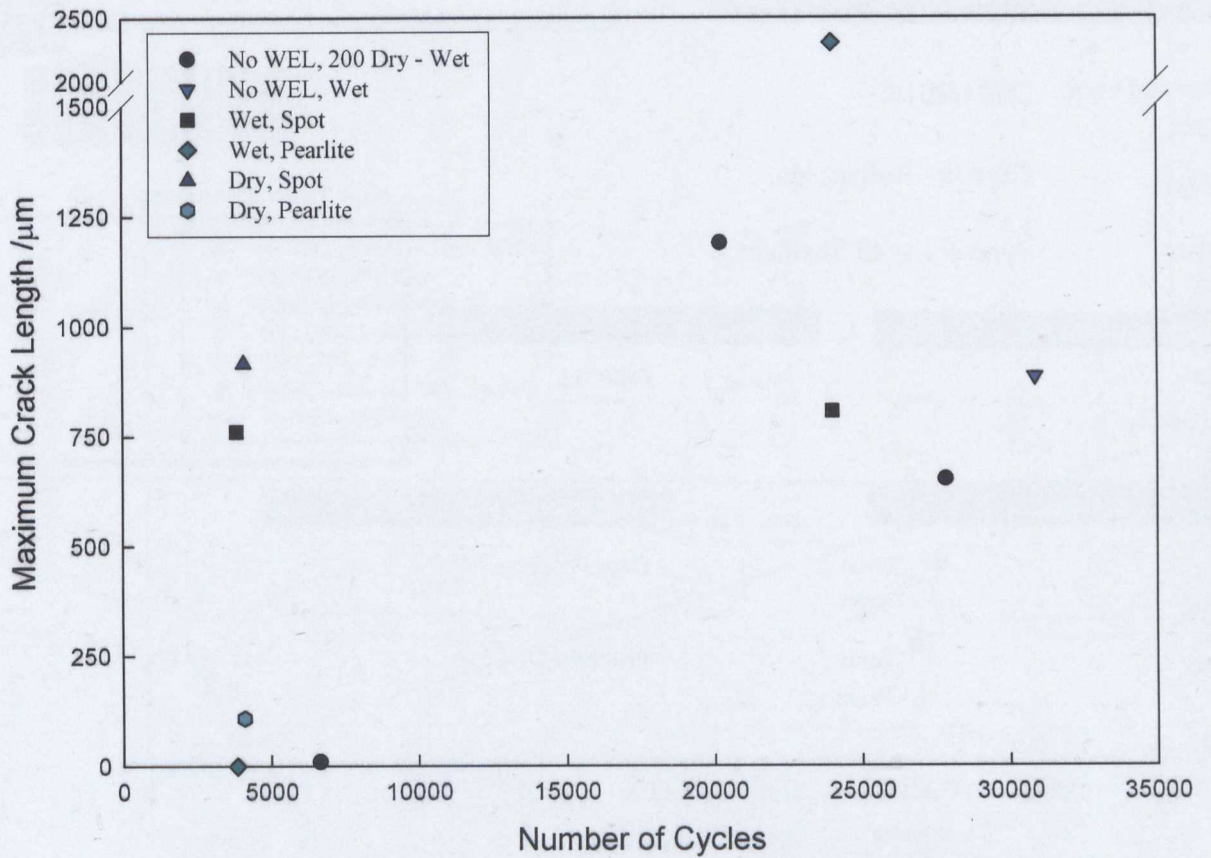
Figure 5.5.5.5: Maximum crack length of spot-welded samples
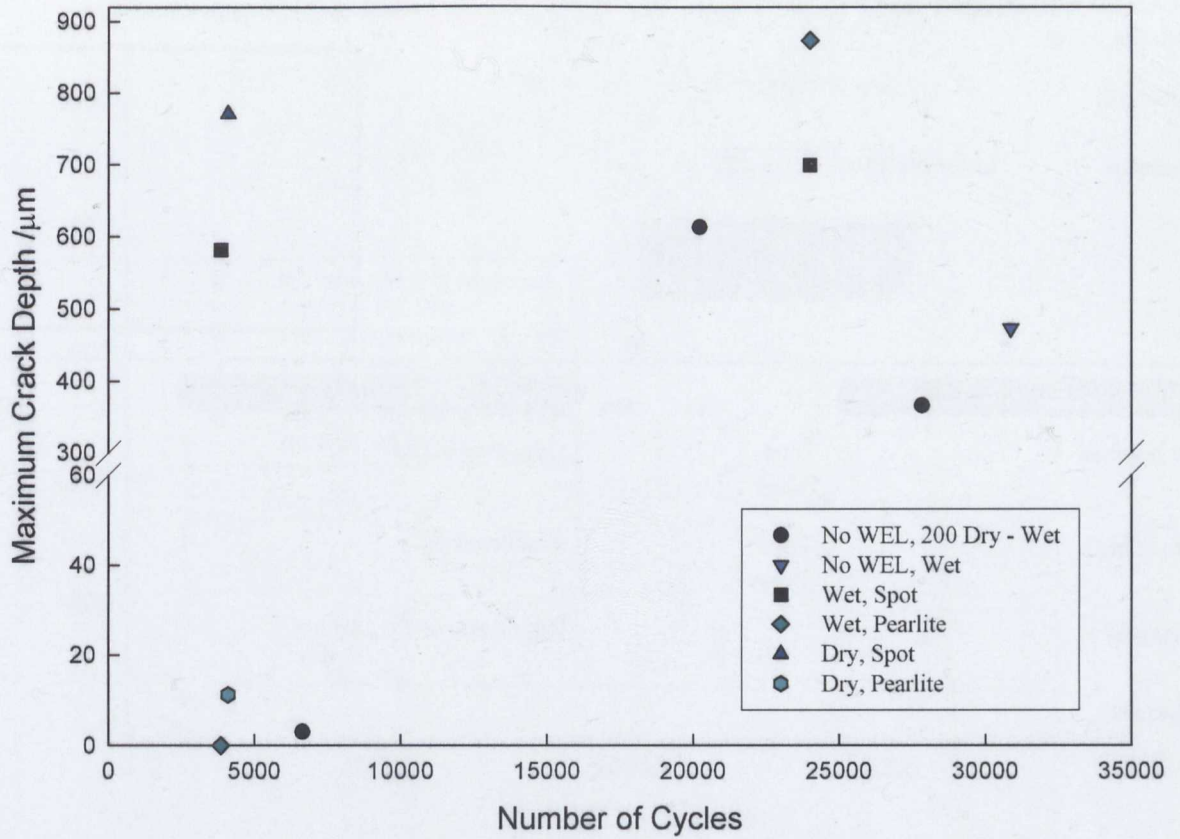
Figure 5.5.5.6: Maximum crack depth of spot-welded samples
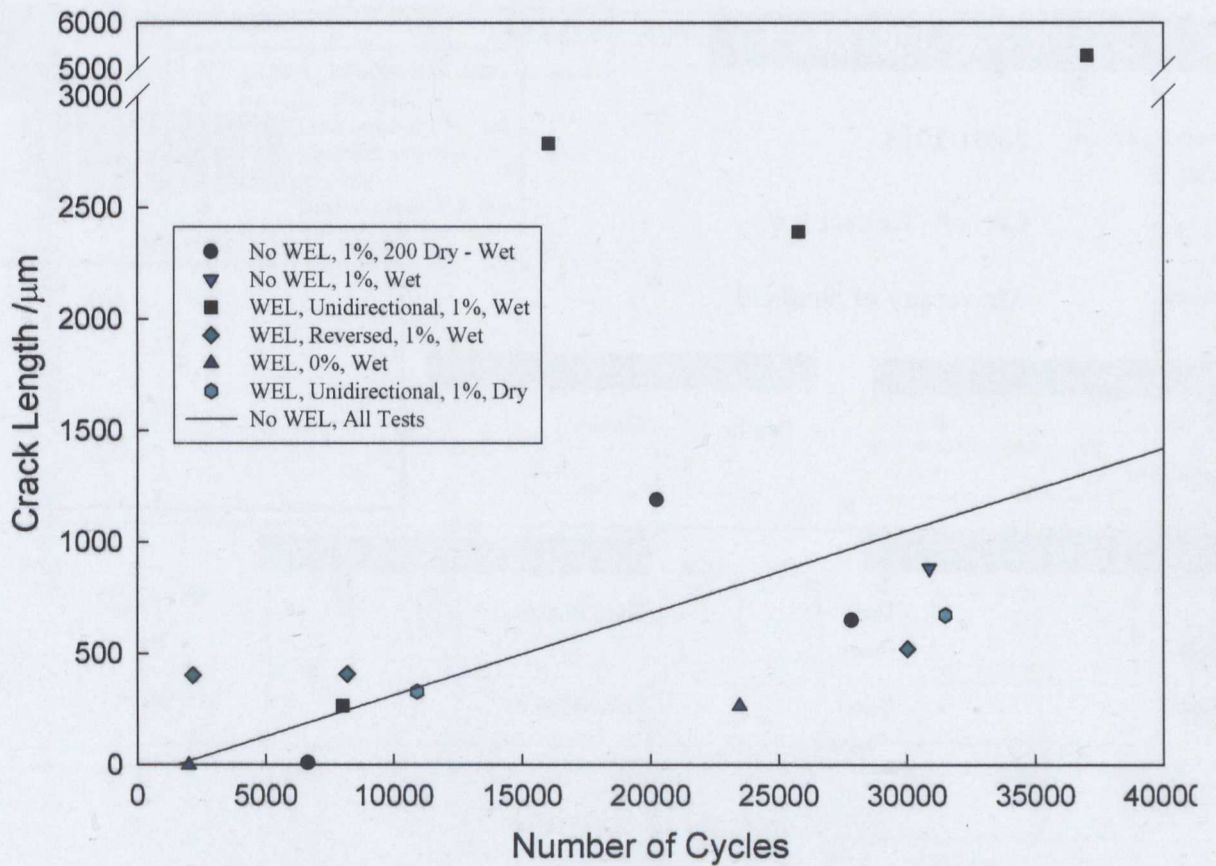
Figure 5.5.5.7: Maximum crack length of sliding WEL samples
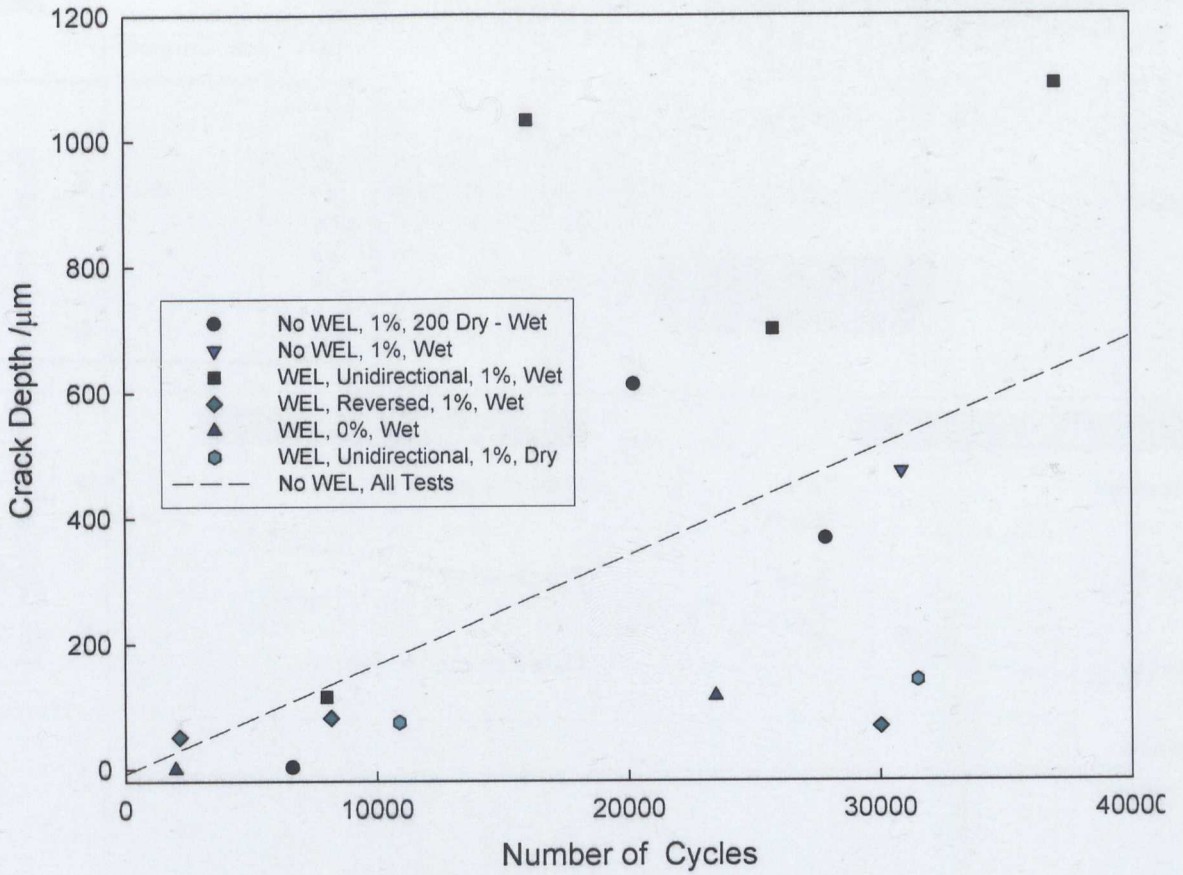
Figure 5.5.5.8: Maximum crack depth of sliding WEL samples
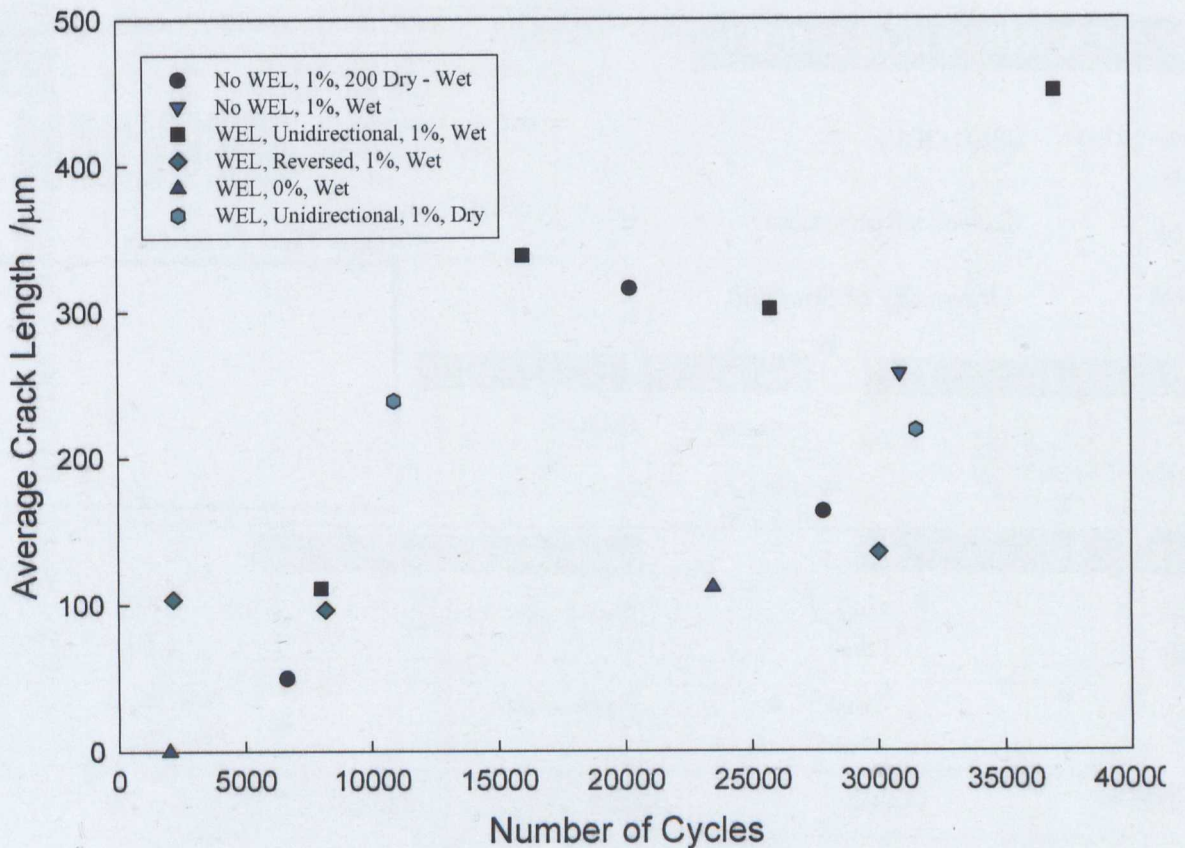
Figure 5.5.5.9: Average crack length of sliding WEL samples
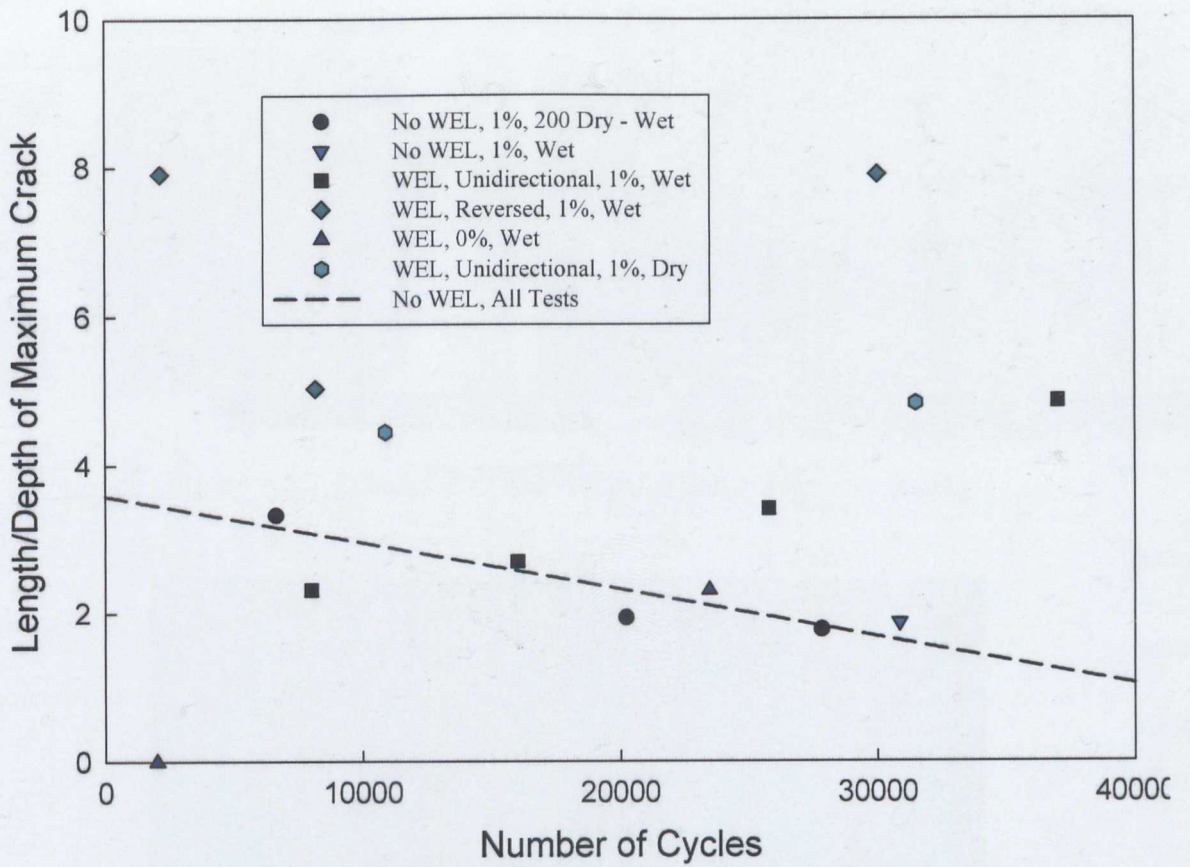
Figure 5.5.5.10: Length/depth ratio of cracks present in sliding samples
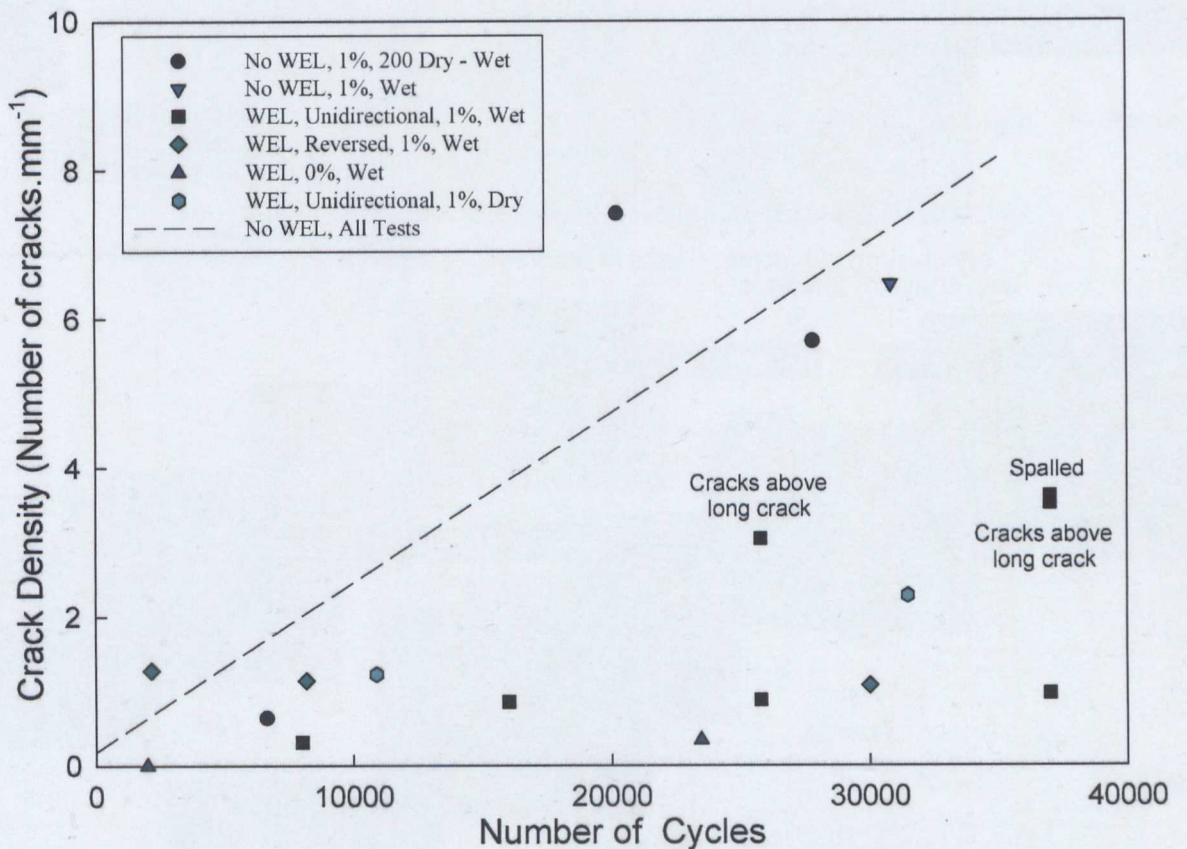
Figure 5.5.5.11: Density of cracks in WEL produced by sliding
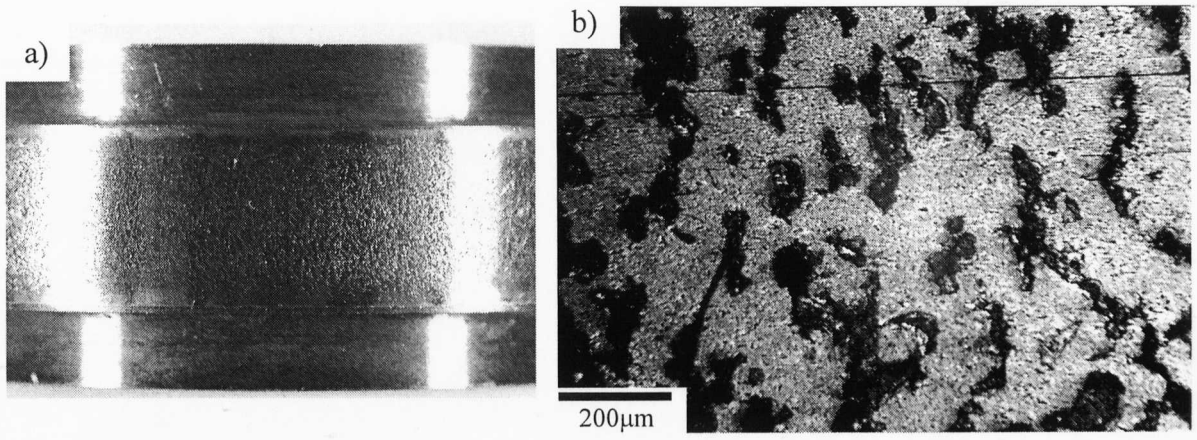
Figure 5.6.1.1: Surface of rail disc RA01 after twin disc testing
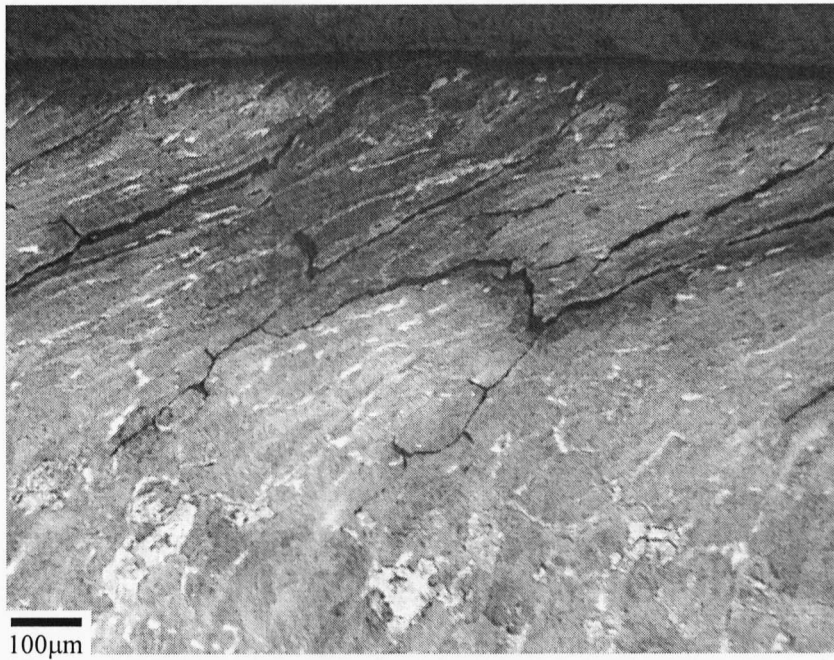
Figure 5.6.1.2: Micrograph of several cracks in normal sample RA01
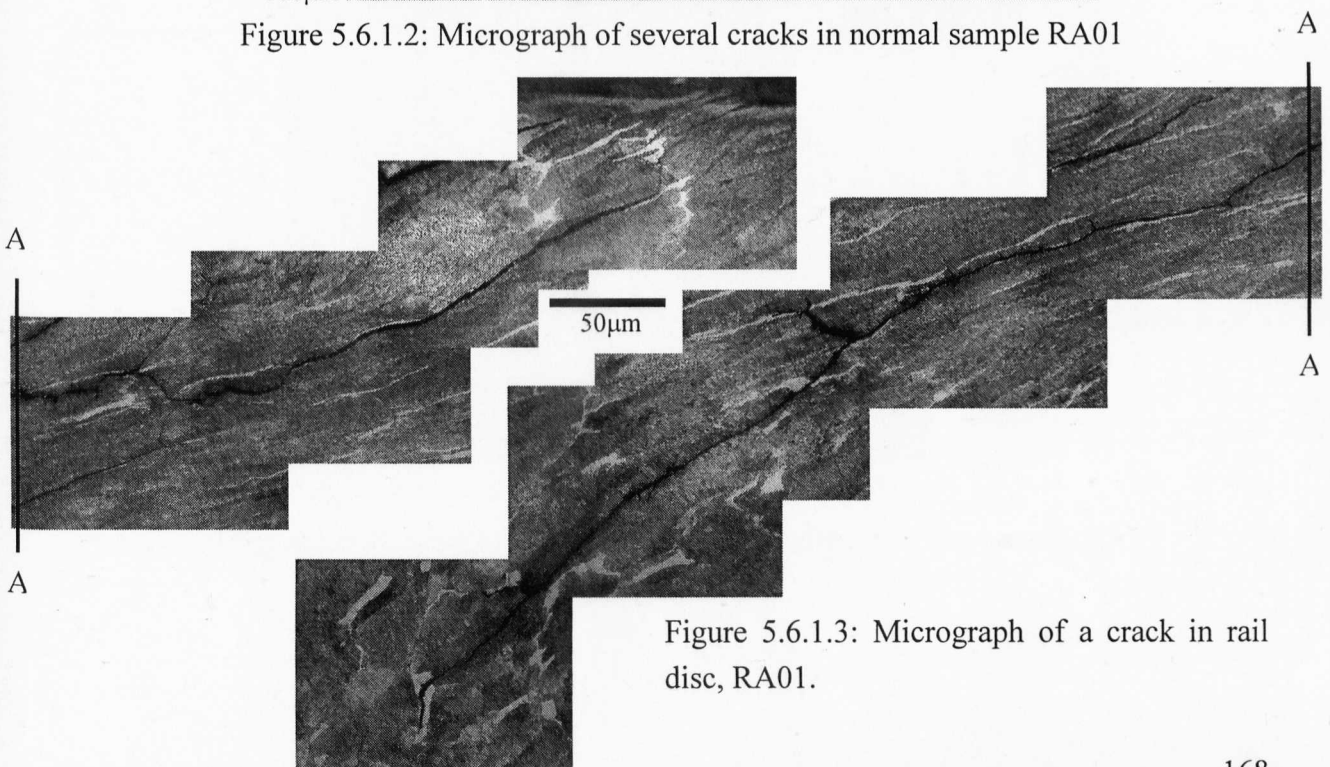
Figure 5.6.1.3: Micrograph of a crack in rail disc, RA01.
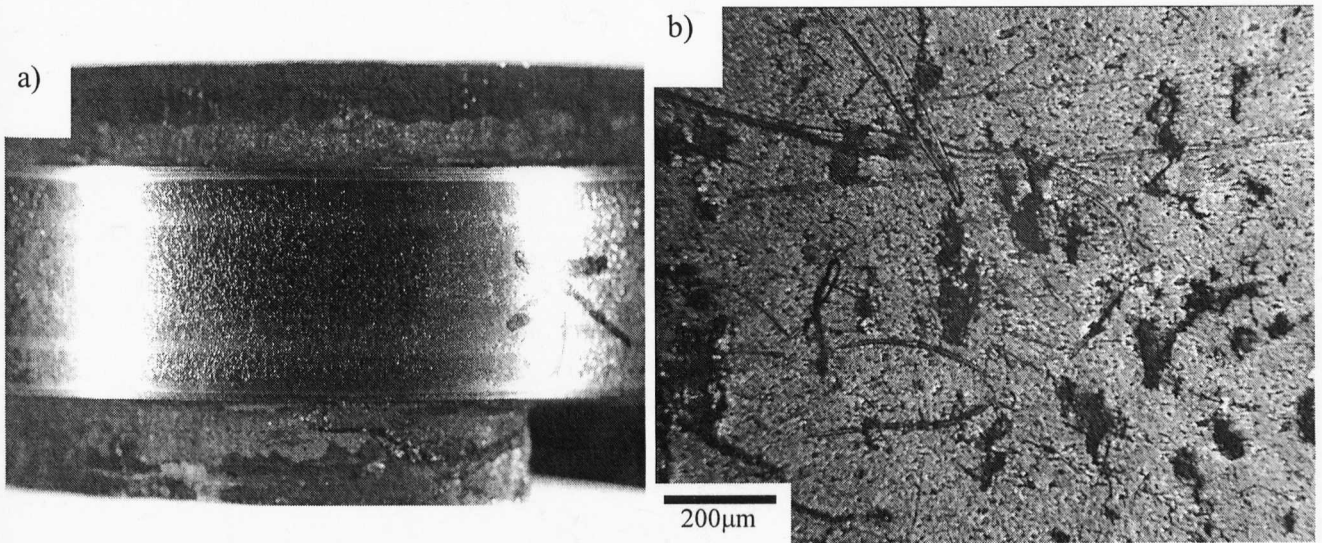
Figure 5.6.2.1: Surface of a decarburised sample, a)RA04, b) RA06
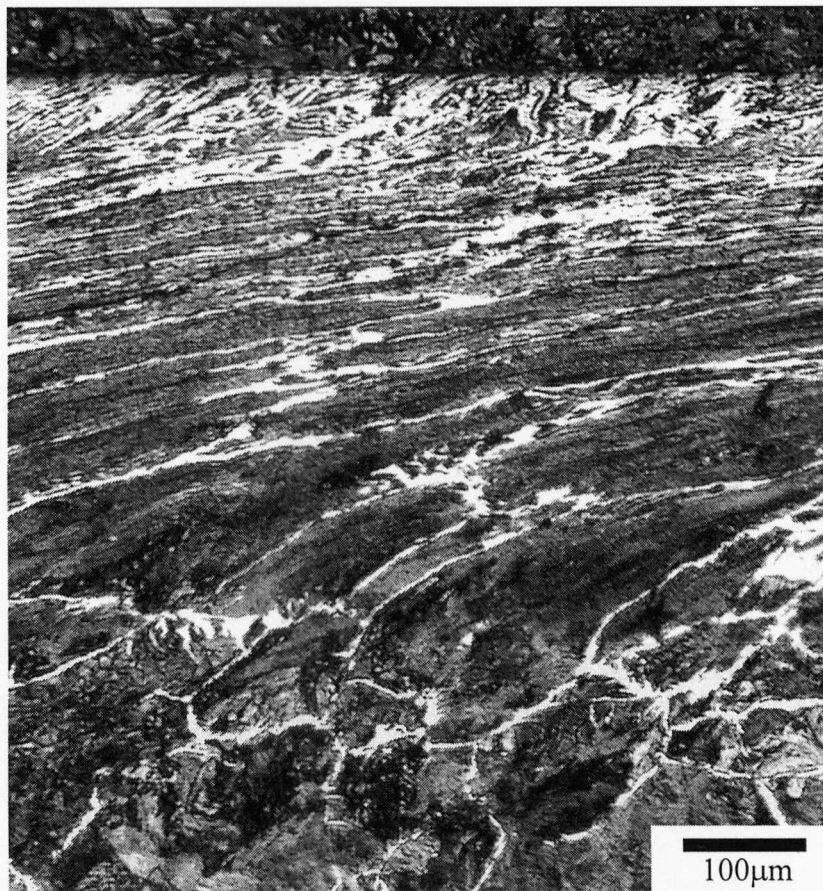
Figure 5.6.2.2: Surface of decarburised disc after twin disc testing, RA17
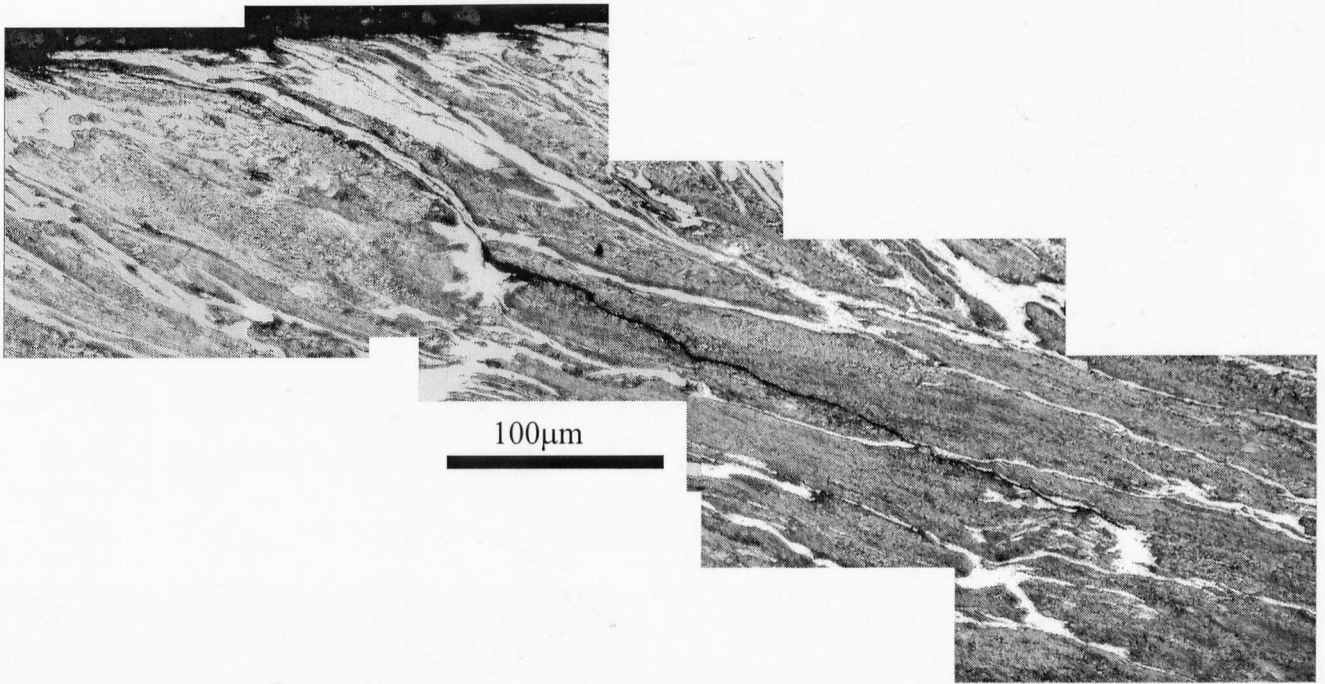
Figure 5.6.2.3: Optical micrograph of a decarburised sample, RA04, after test (light phase ferrite and dark constituent pearlite)
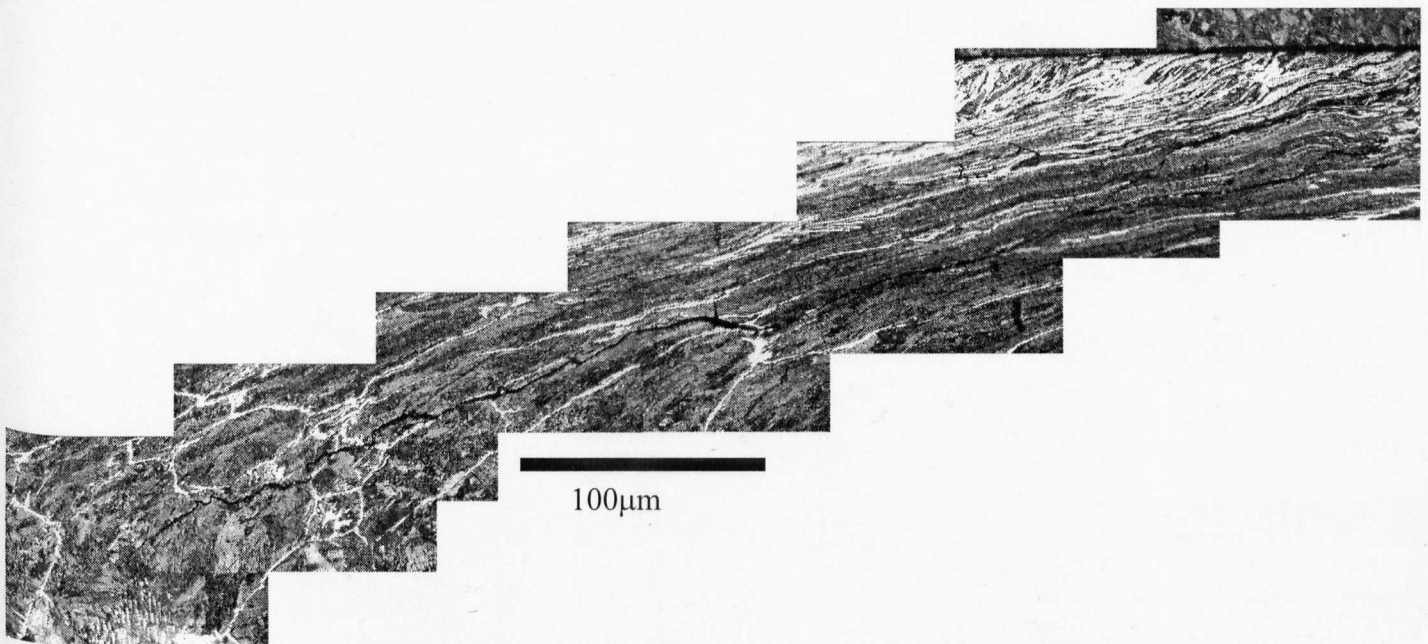
Figure 5.6.2.4: Optical micrograph of a decarburised sample, RA10, after test (light phase ferrite and dark constituent pearlite)
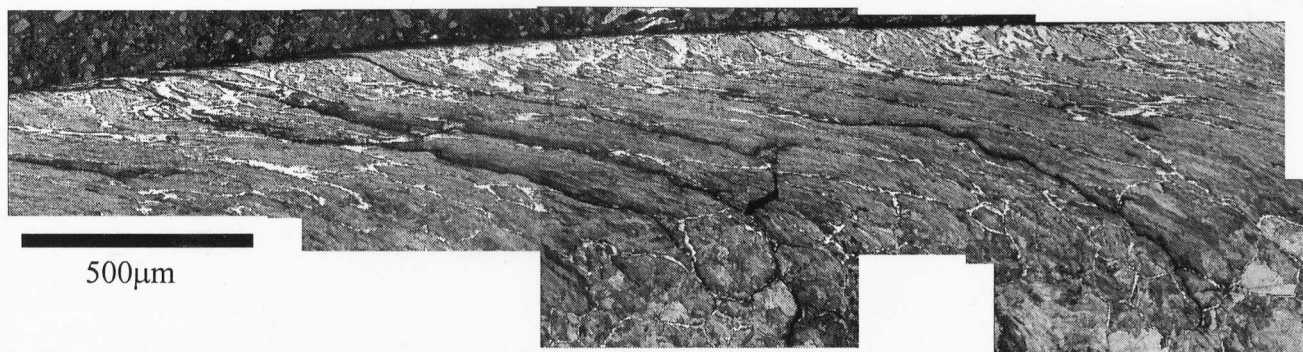
Figure 5.6.2.5: Optical micrograph of a decarburised sample, RA14, after test (light phase ferrite and dark constituent pearlite)
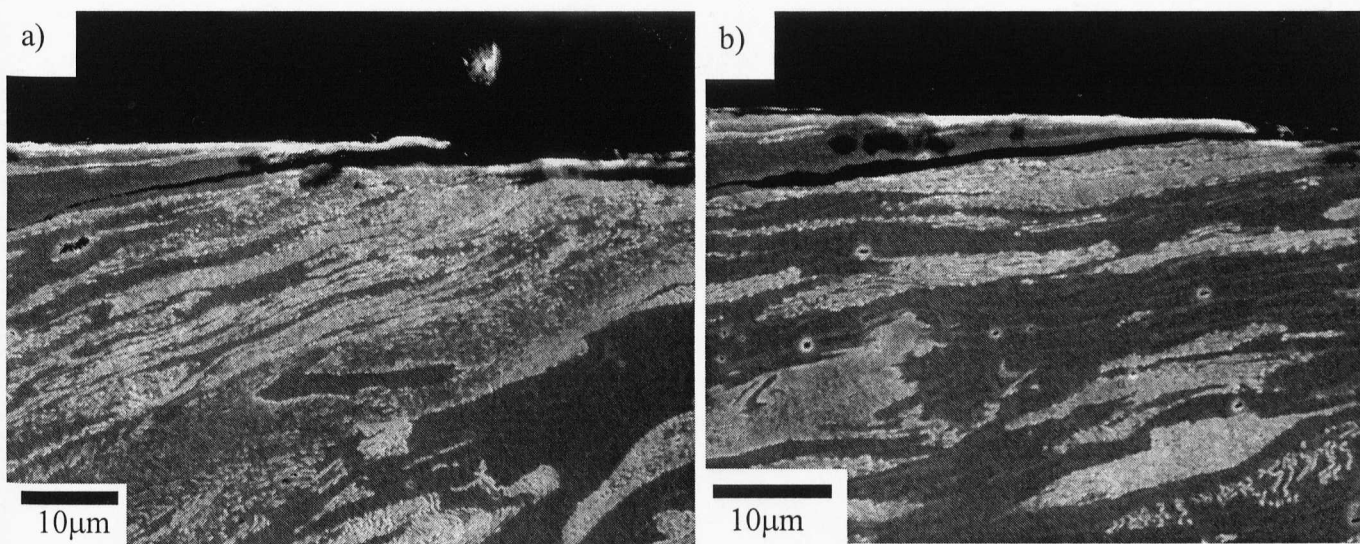
Figure 5.6.2.6: SEM micrographs of cracks at the surface of the decarburised sample RA05 (light phase cementite and dark phase ferrite)
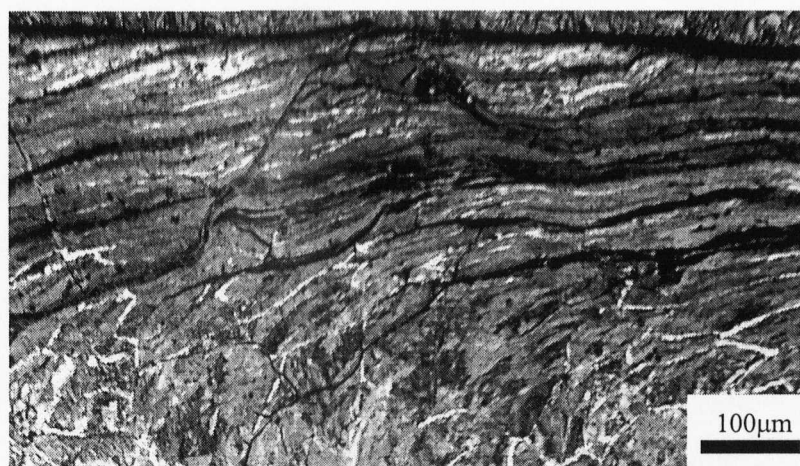
Figure 5.6.2.7: Severe crack growth at surface of rail disc, RA09
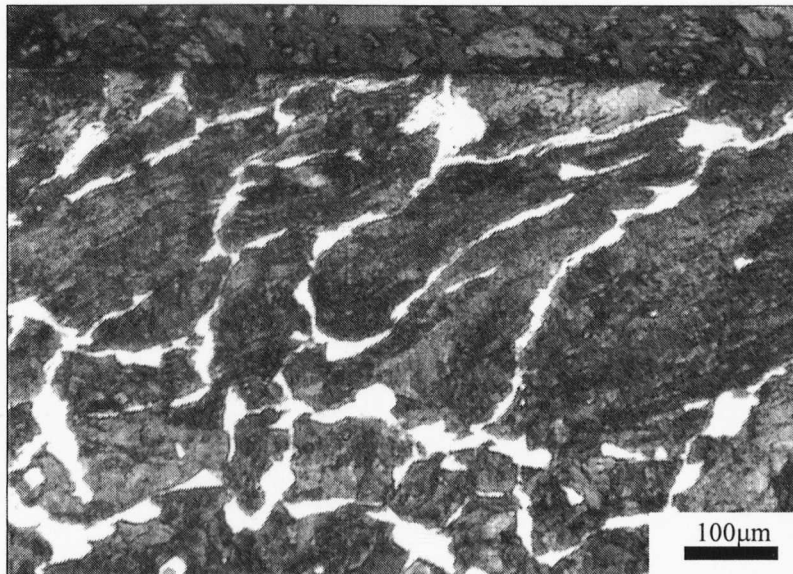
Figure 5.6.2.8: Micrograph of deformation of surface wheel disc WA02 after test against decarburised disc RA04
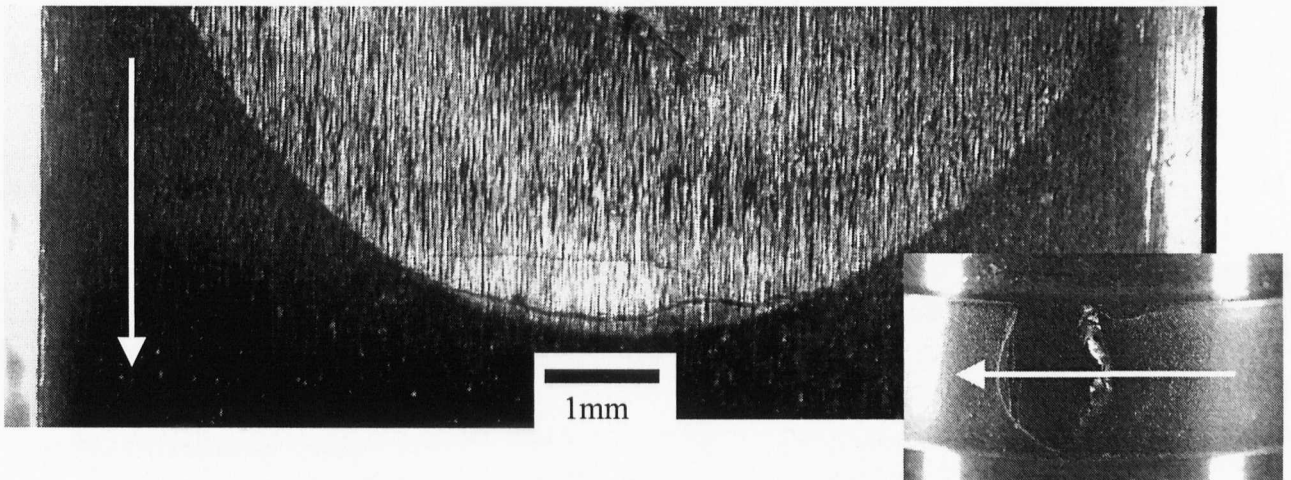
Figure 5.6.3.1: Photograph of spot weld on surface RA21 (4000 Cycles, no lubrication), the arrows show the direction of the traction force.
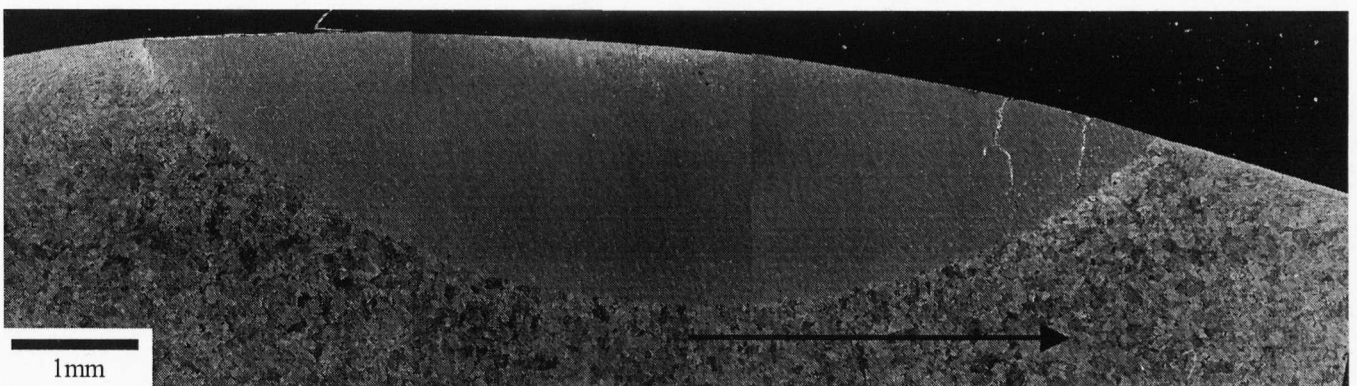
Figure 5.6.3.2: Spot Weld on RA21 (4000 Cycles, no lubrication), the arrow shows the direction of the traction force.
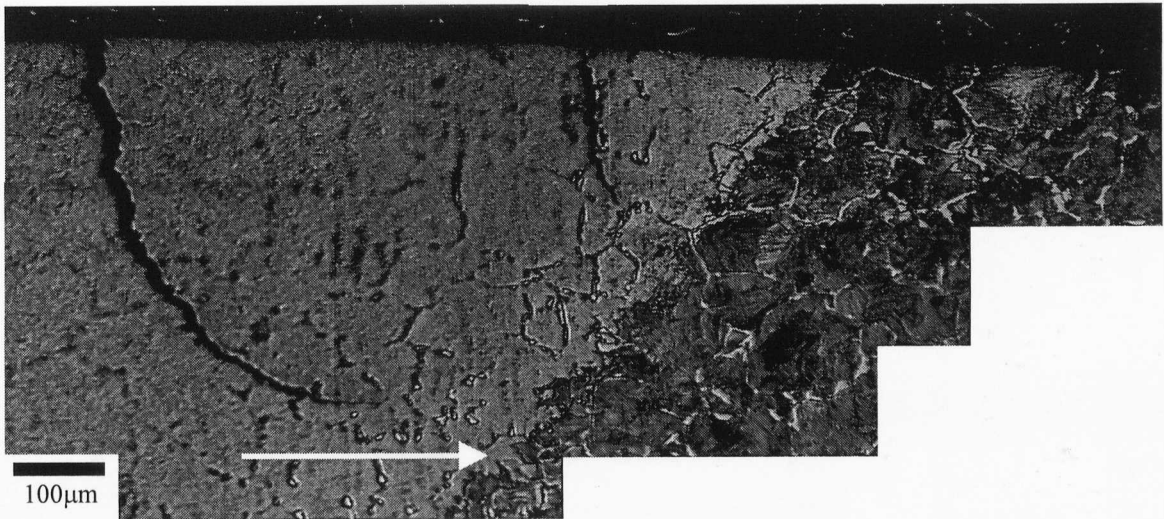
Figure 5.6.3.3: Cracks at leading edges of spot weld, RA21 (4000 Cycles, no lubrication) the arrow shows the direction of the traction force.
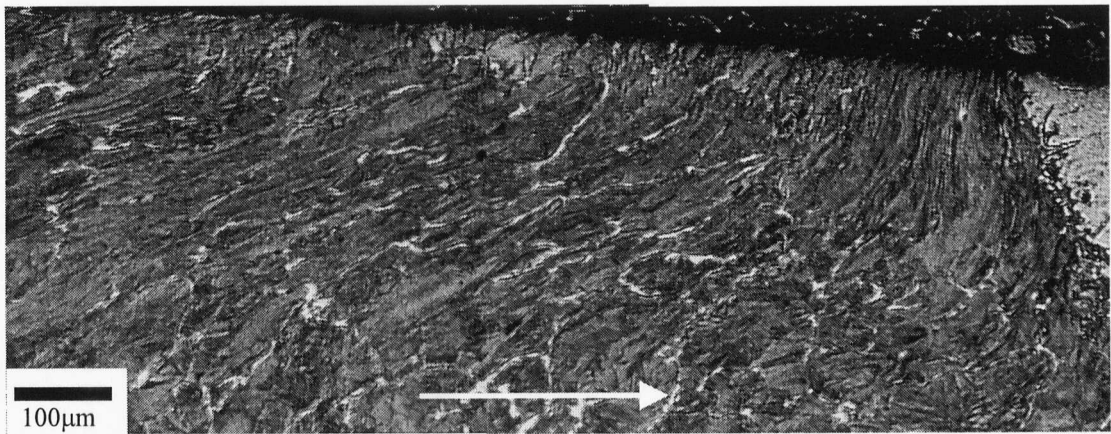
Figure 5.6.3.4: Plastic deformation at trailing edge of spot weld, RA19 (4000 Cycles, water lubrication) the arrow shows the direction of the traction force.
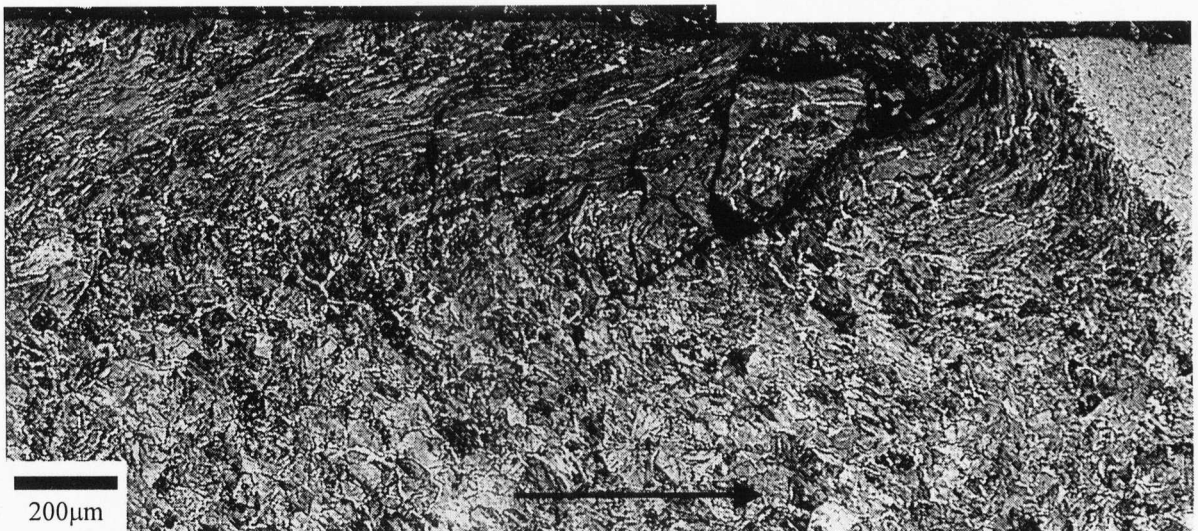
Figure 5.6.3.5: Cracks in pearlite at trailing edge of spot weld, RA22 (24000 cycles, water lubrication) the arrow shows the direction of the traction force.
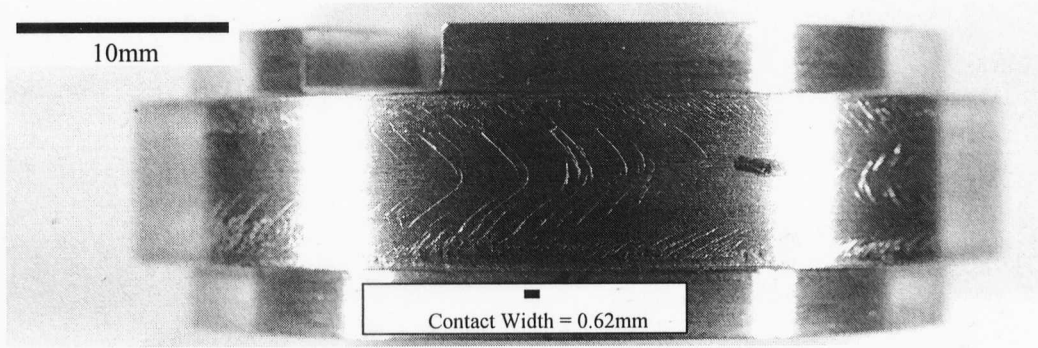
Figure 5.6.3.6: Photograph of RA23 displaying "chevron" cracks (8190 reversed cycles)
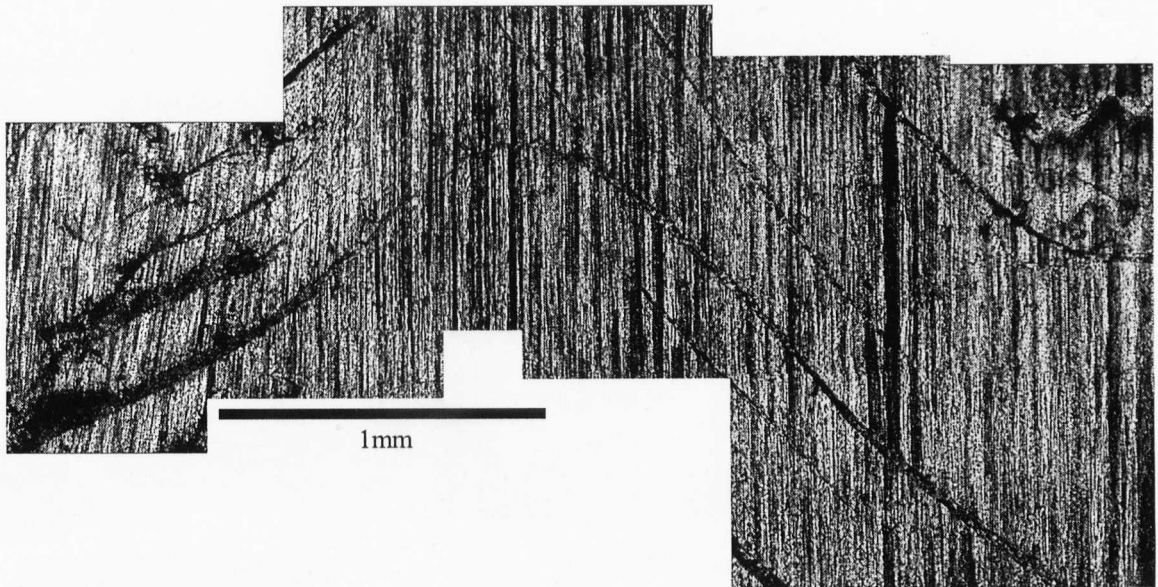
Figure 5.6.3.7: Photomicrograph of "chevron" cracks in RA23 (8190 reversed cycles)
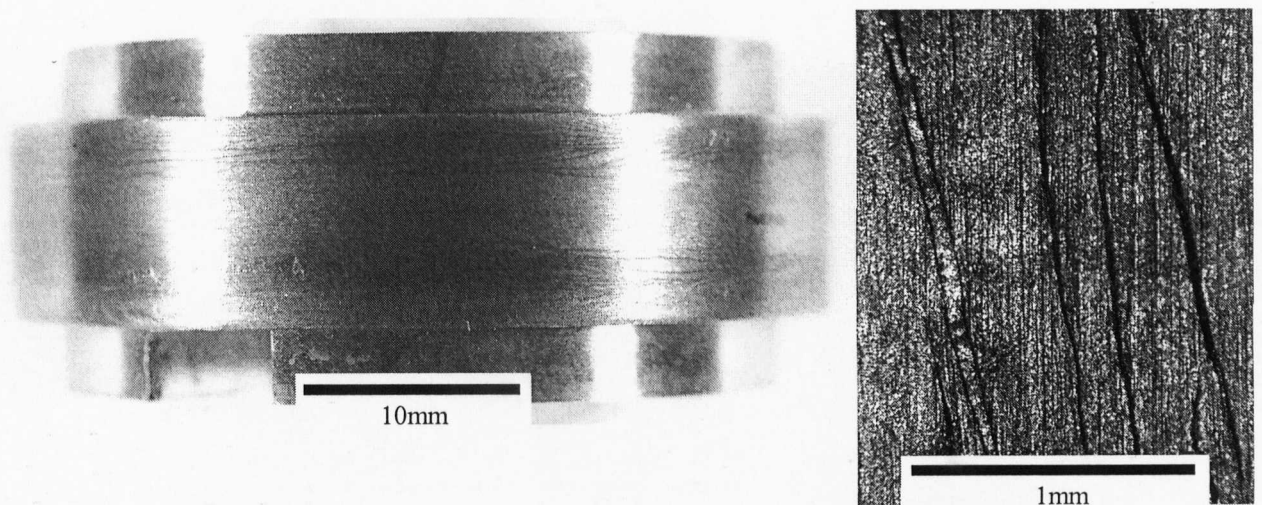
Figure 5.6.3.8: Circumferential cracking of RA30 (23470 cycles, pure rolling water lubricated)
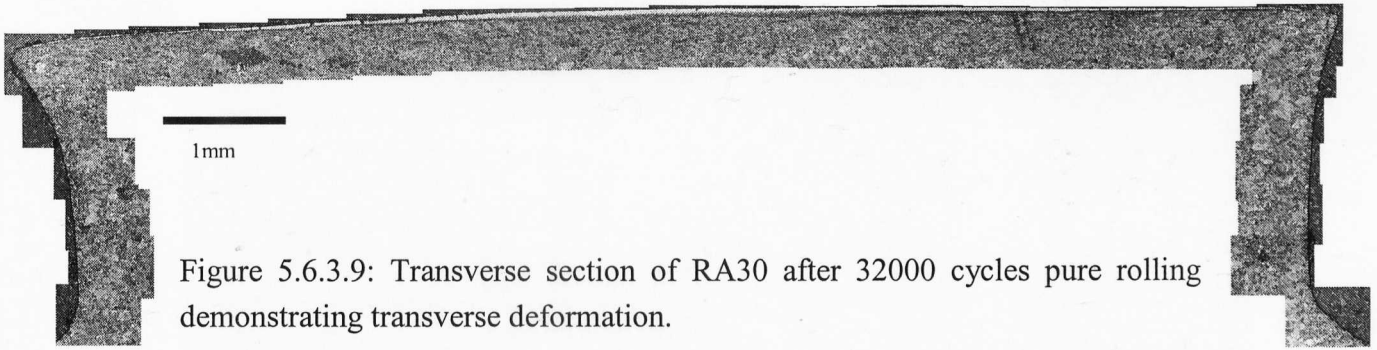
Figure 5.6.3.9: Transverse section of RA30 after 32000 cycles pure rolling demonstrating transverse deformation.
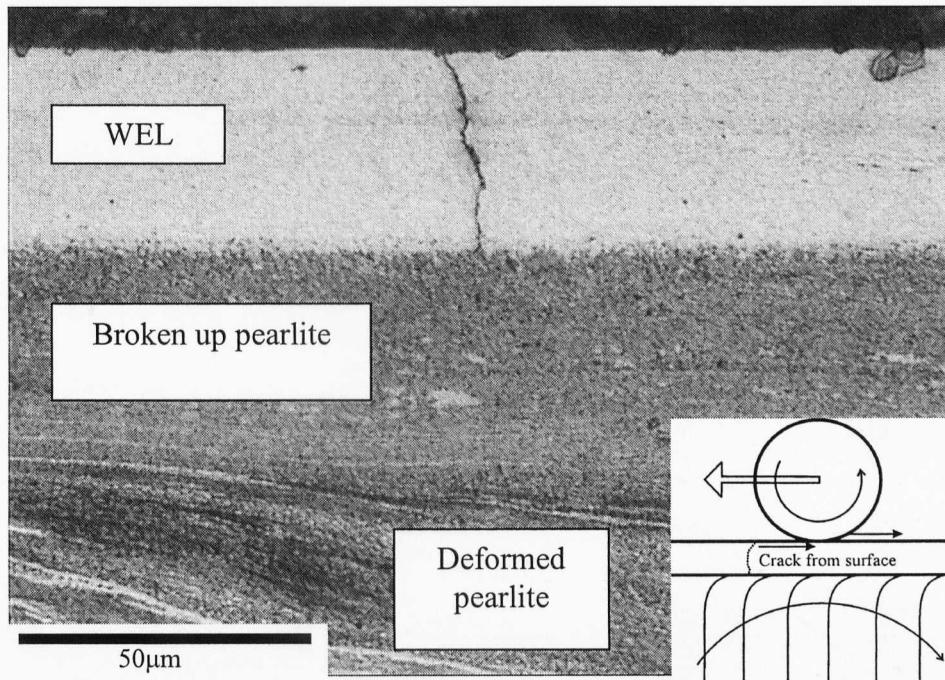
Figure 5.6.3.10: The growth of vertical cracks in the WEL, RA25 (25790 cycles, water lubricated, unidirectional)
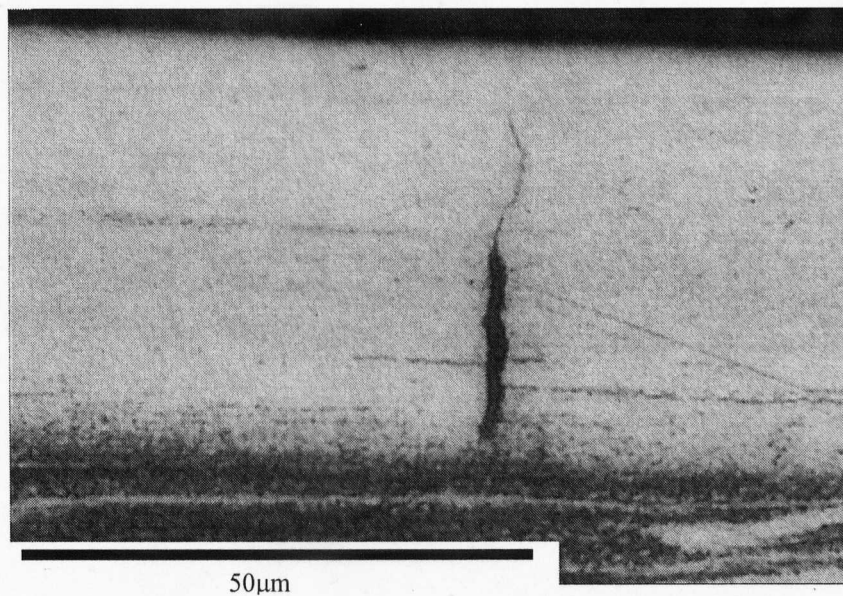
Figure 5.6.3.11: Crack within WEL that does not break the surface, RA36 (31500 unidirectional dry cycles)
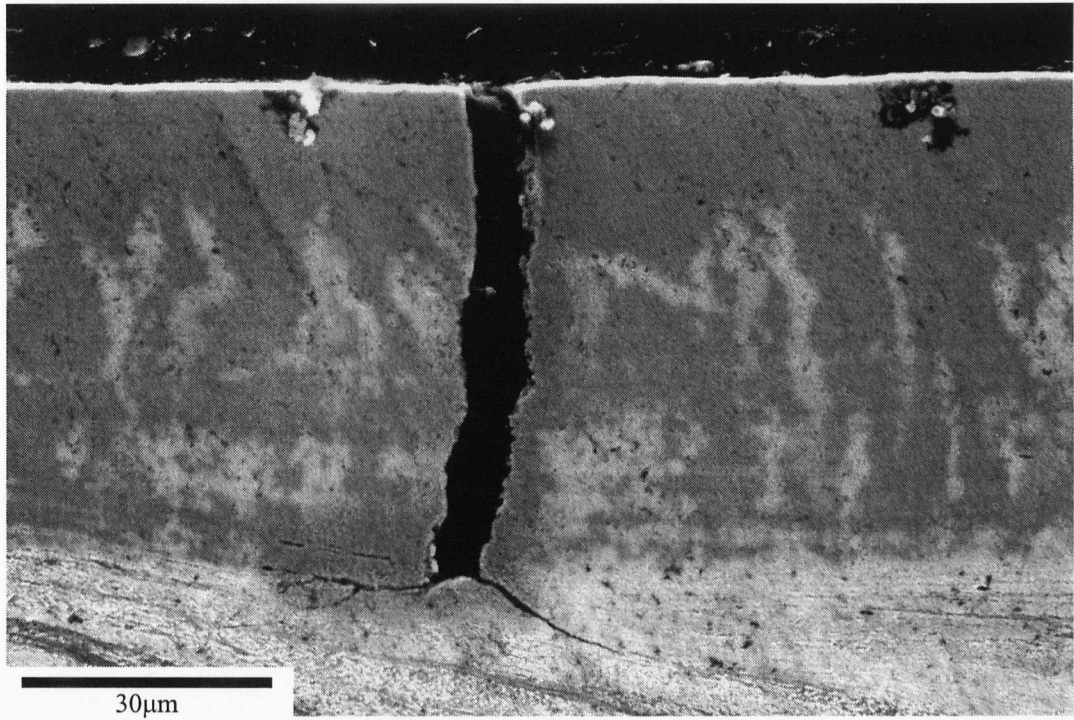
Figure 5.6.3.12: Cracks propagating from gap in two directions, RA20 (2160 reversed cycles)
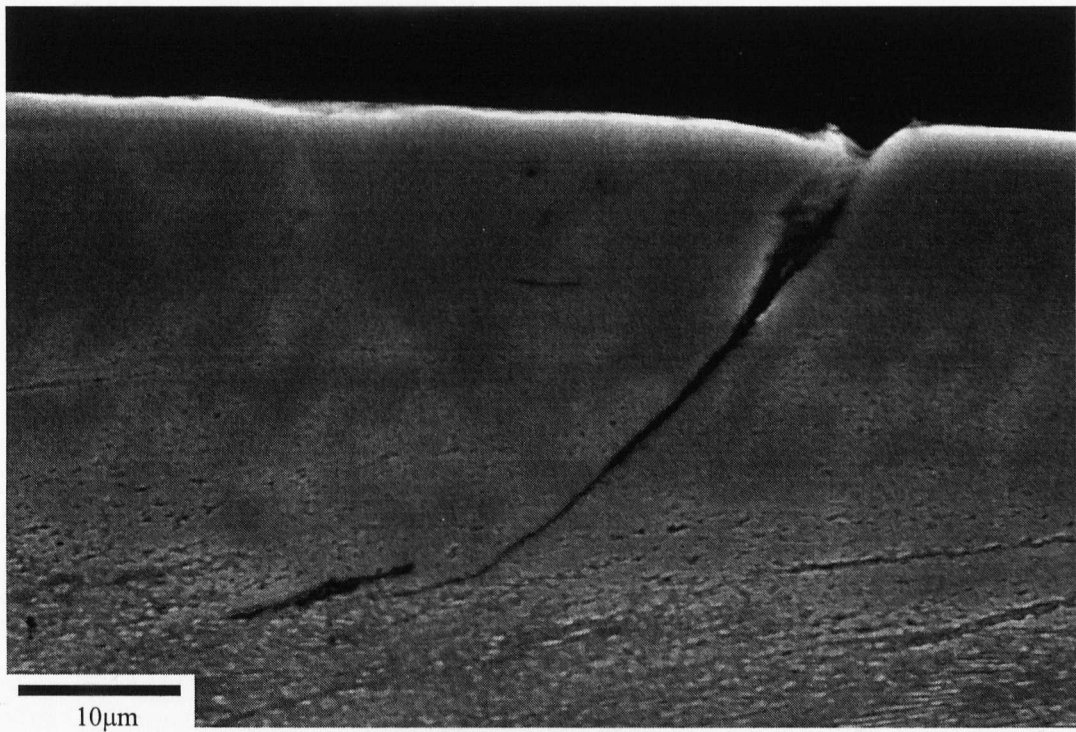
Figure 5.6.3.13: An angled crack within the WEL, RA26 (37000 unidirectional cycles)
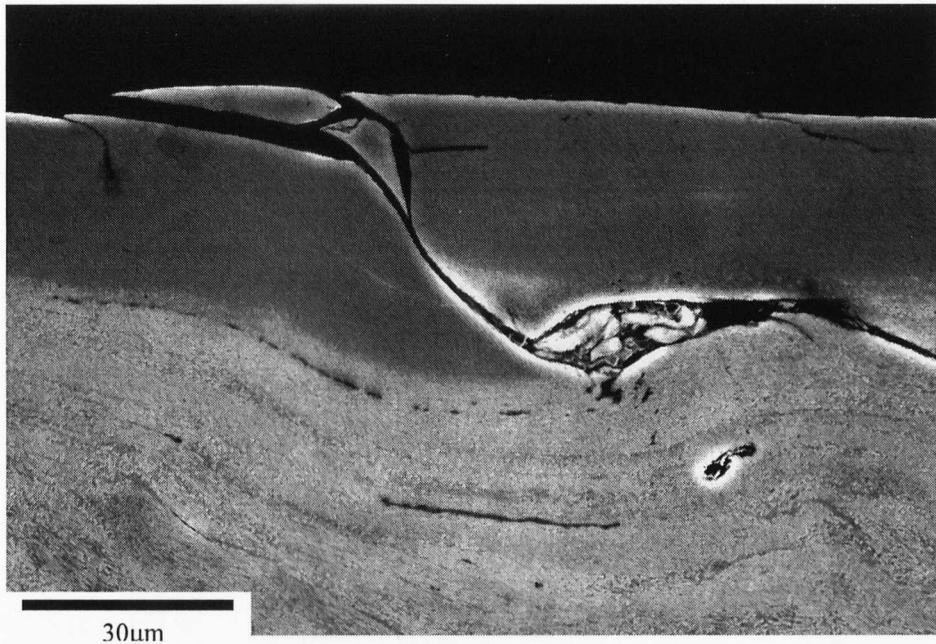
Figure 5.6.3.14: Breaking of edges of angled crack, RA29 (16000 unidirectional cycles)
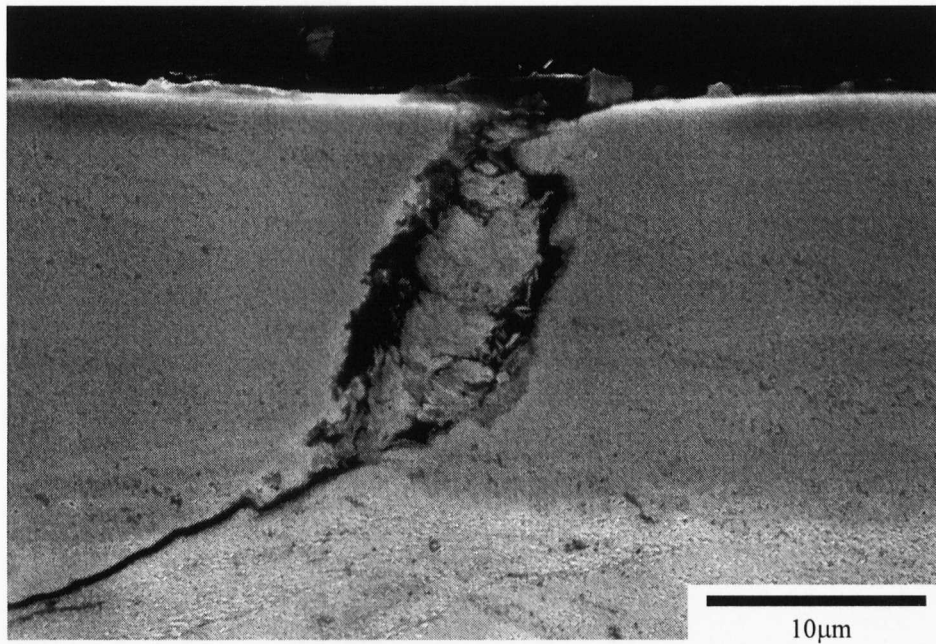
Figure 5.6.3.15: Debris remaining in gap after it has broken up, RA23 (8190 reversed cycles)
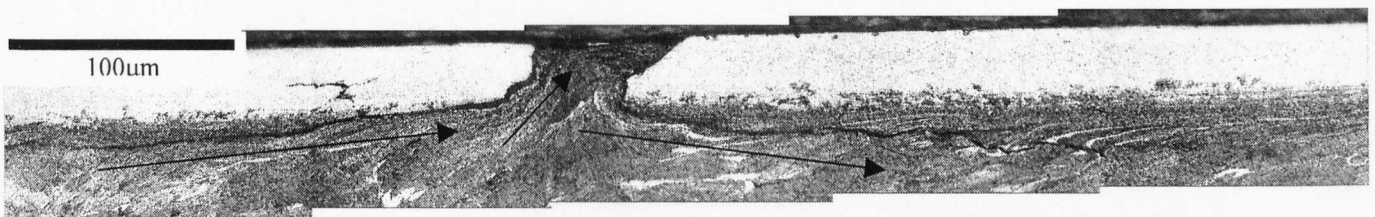
Figure 5.6.3.16: Deformation of the pearlite into gap in WEL, RA24 (30000 reversed cycles)
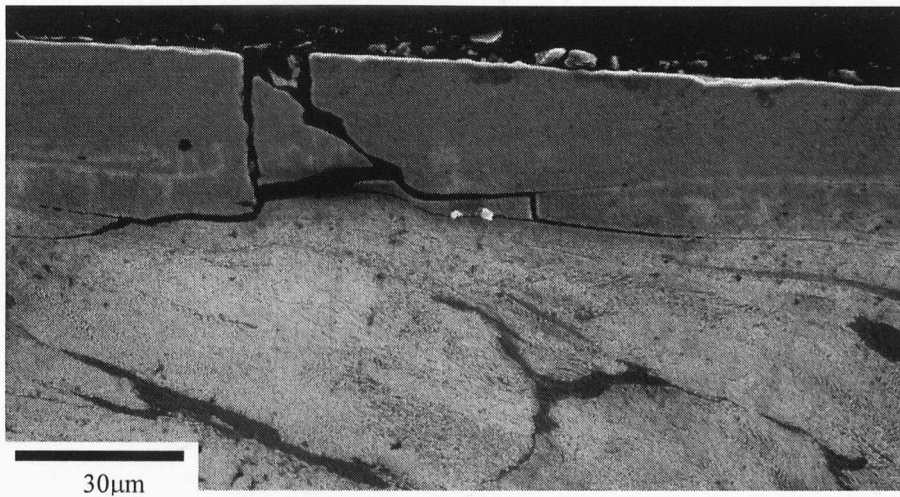
Figure 5.6.3.17: Formation of gap in WEL, RA20 (2160 reversed cycles)
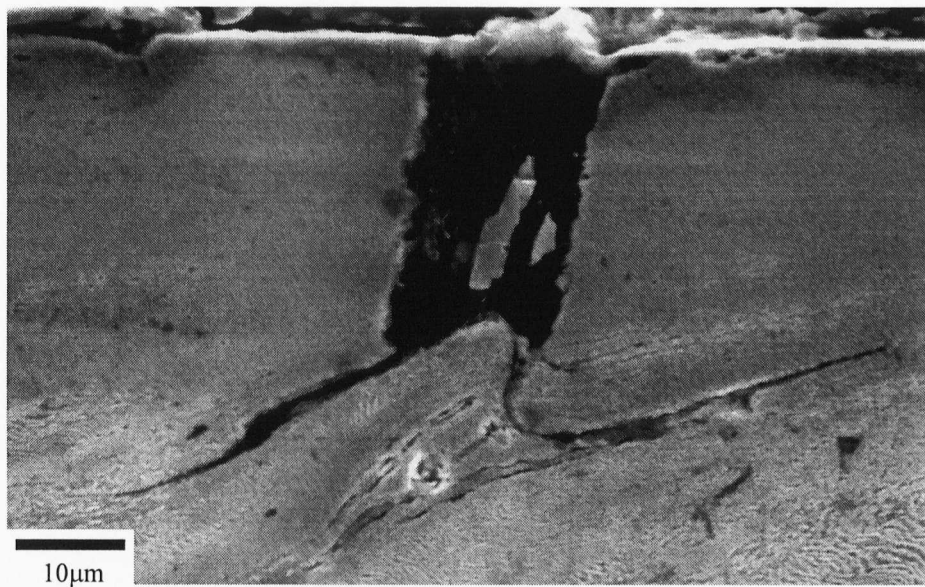
Figure 5.6.3.18: SEM micrograph of gap in WEL, RA23 (8190 reversed cycles)
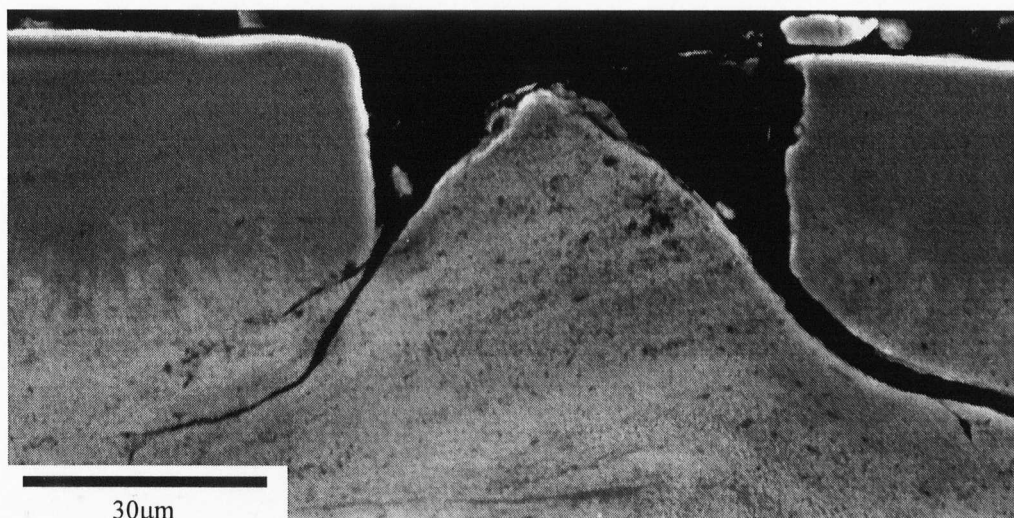
Figure 5.6.3.19: Deformation of pearlite up into gap in WEL, RA26 (37000 unidirectional cycles)
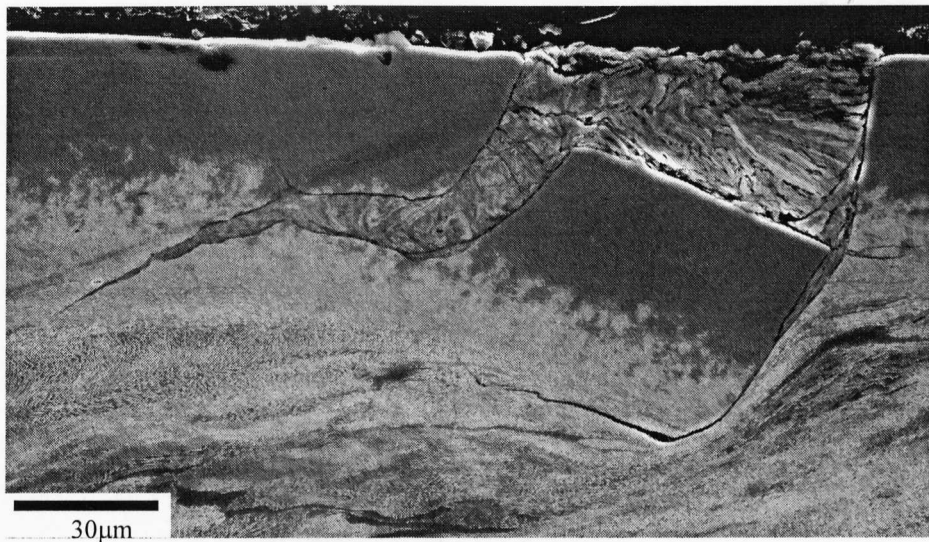
Figure 5.6.3.20: Deformation of WEL down into pearlite, RA26 (37000 unidirectional cycles)
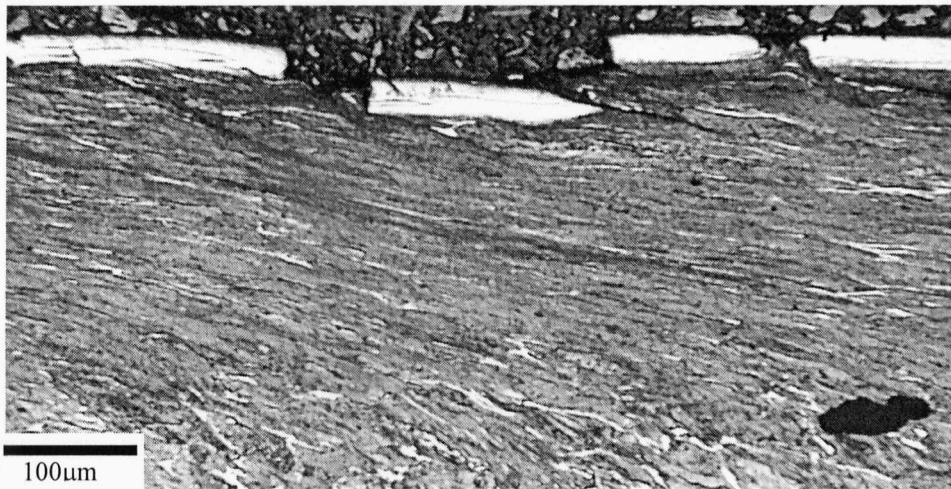
Figure 5.6.3.21: Overlapping of white etching layer over its self due to plastic deformation RA36, (31500 unidirectional dry cycles)
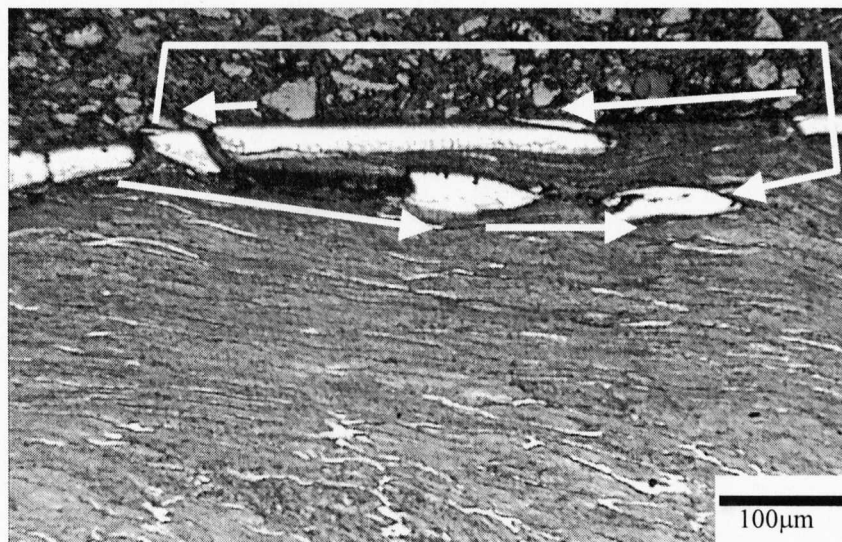
Figure 5.6.3.22: The deformation of pearlite above WEL at surface, RA36 (31500 dry cycles). The arrows indicate the movement of the WEL around the surface.

179
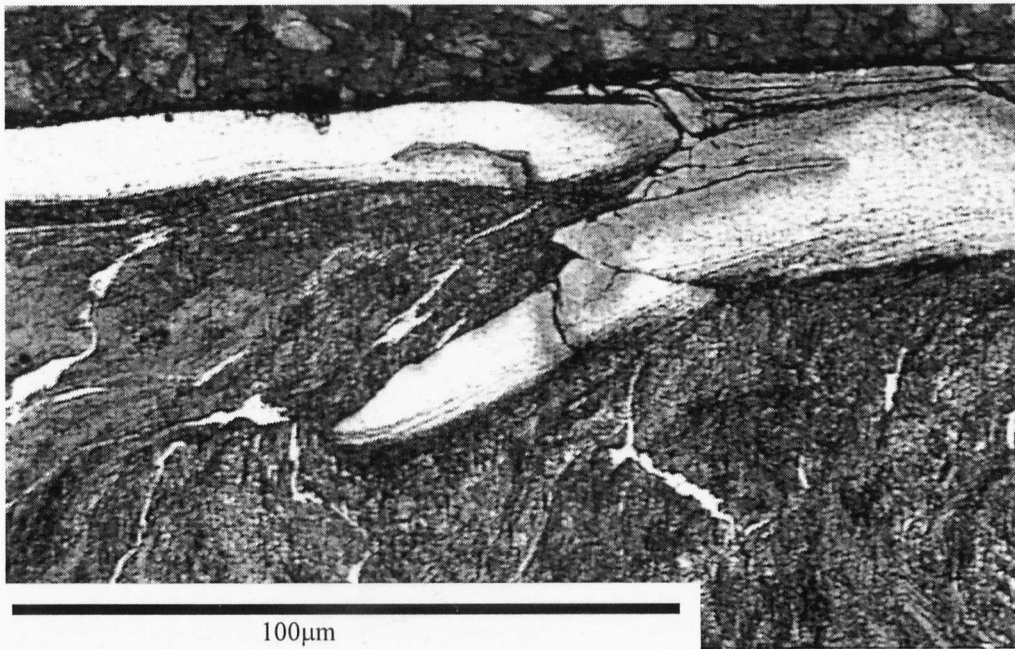
Figure 5.6.3.23: WEL being deformed backwards into it self, RA23 (8190 reversed cycles)
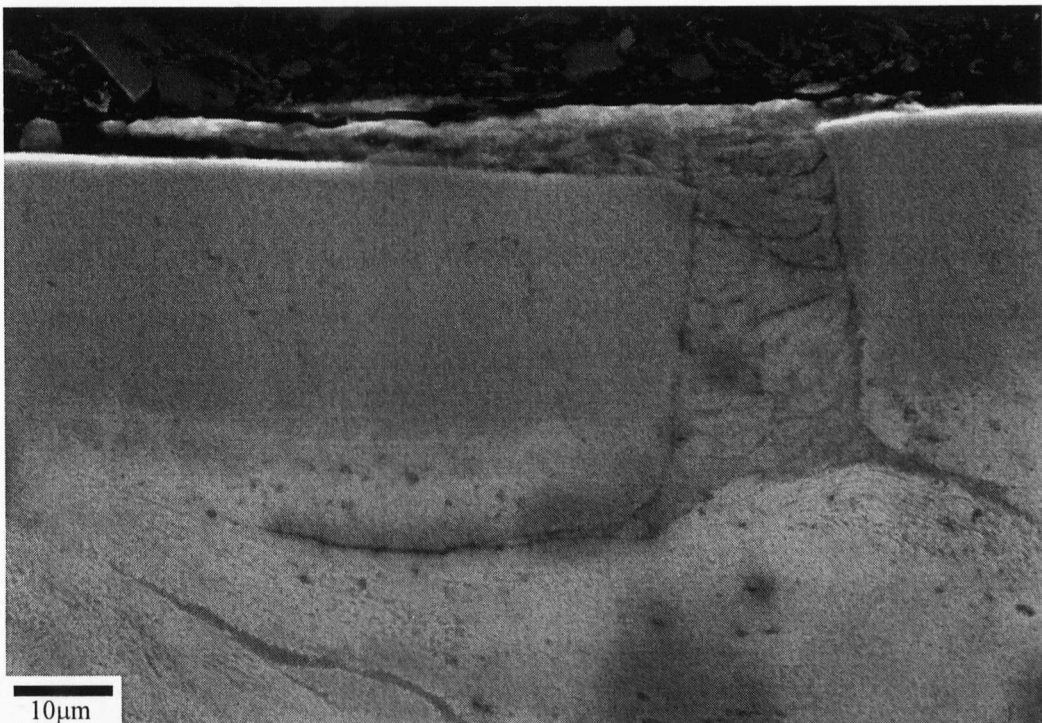
Figure 5.6.3.24: Wear debris in crack being extruded by pearlite, RA23 (8190 reversed cycles)
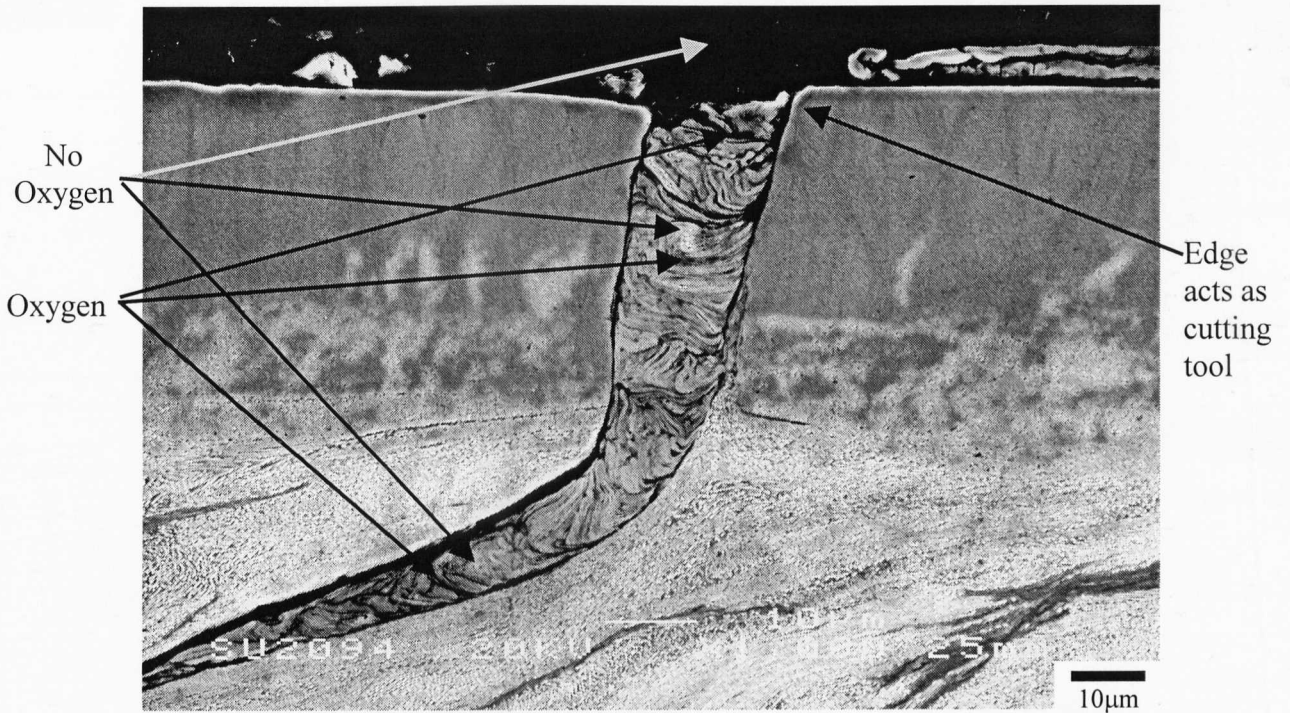
Figure 5.6.3.25: Wear debris filling gap in WEL, RA29 (16000 unidirectional cycles), with the results from the EDS indicated.
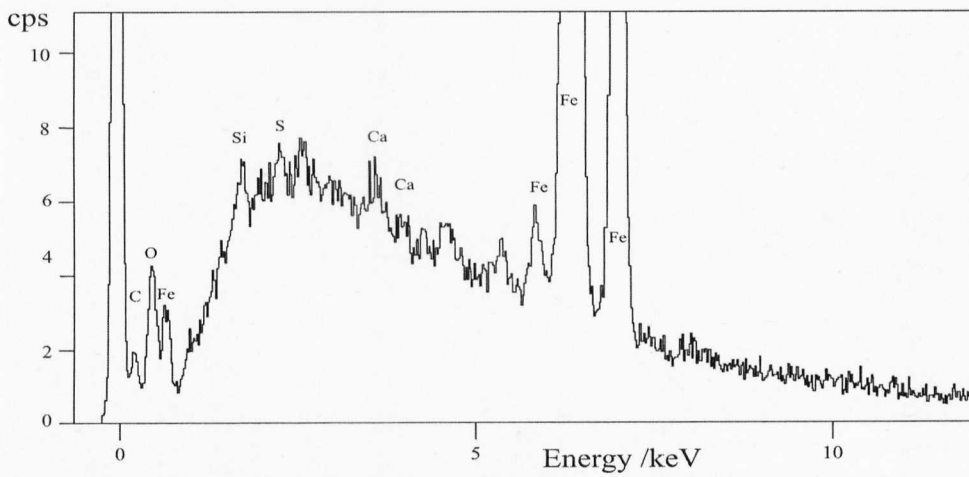
Figure 5.6.3.26: EDS trace of the light phase of wear debris in gap in WEL near surface; trace taken using JEOL 6400 SEM
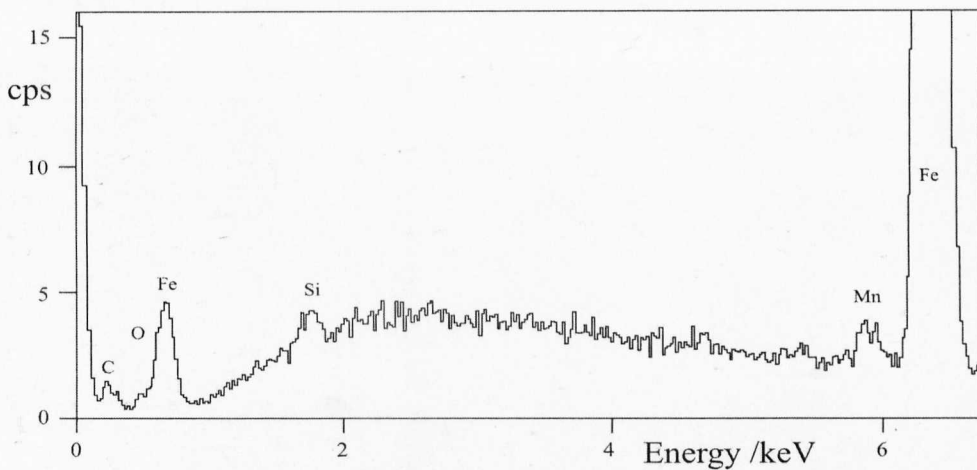
Figure 5.6.3.27: EDS trace of WEL using JEOL 6400 SEM

181
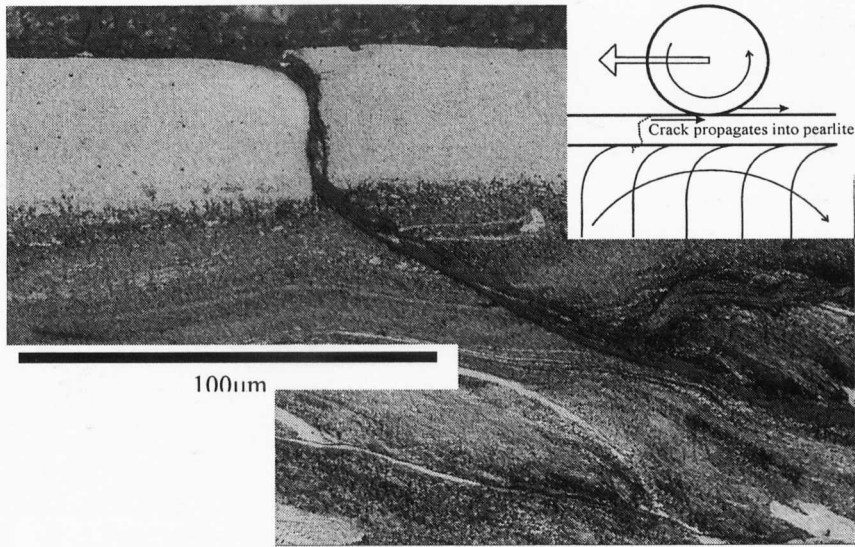
Figure 5.6.3.28: Crack propagating into pearlite, RA25(25790 unidirectional cycles)
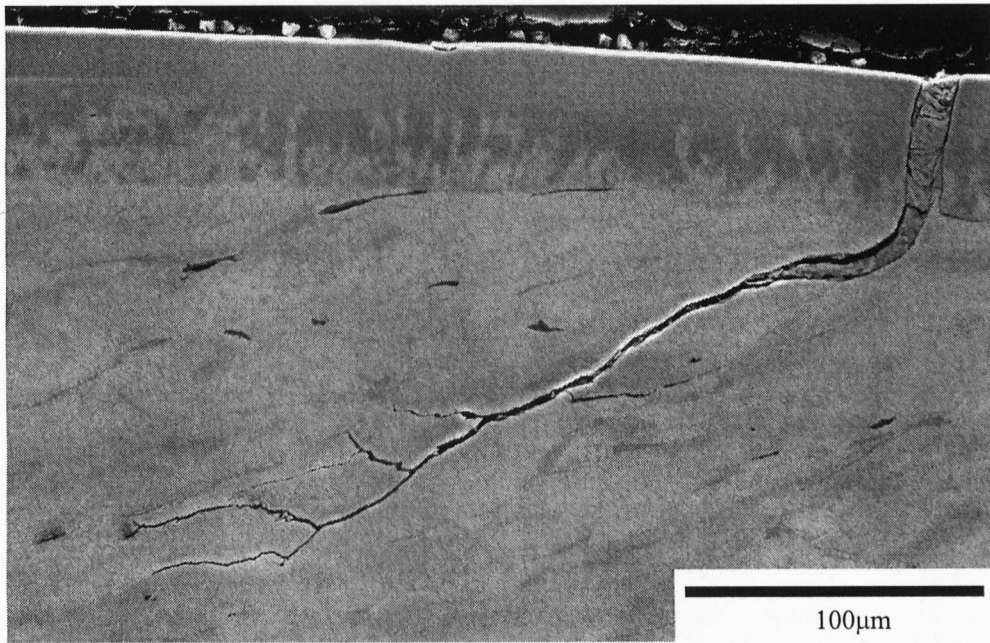
Figure 5.6.3.29: SEM micrograph of crack propagating along flow lines, RA29 (16000 unidirectional cycles)
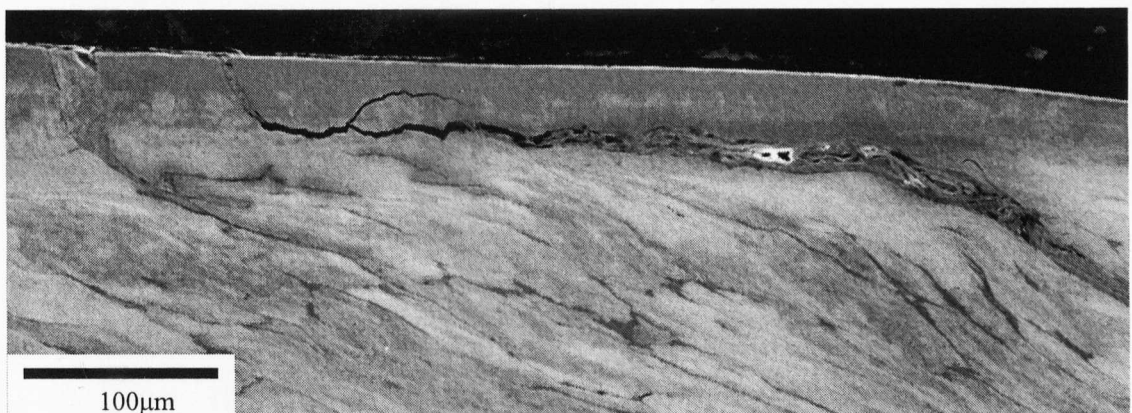
Figure 5.6.3.30: Crack propagating along interface, RA25 (25790 unidirectional cycles)
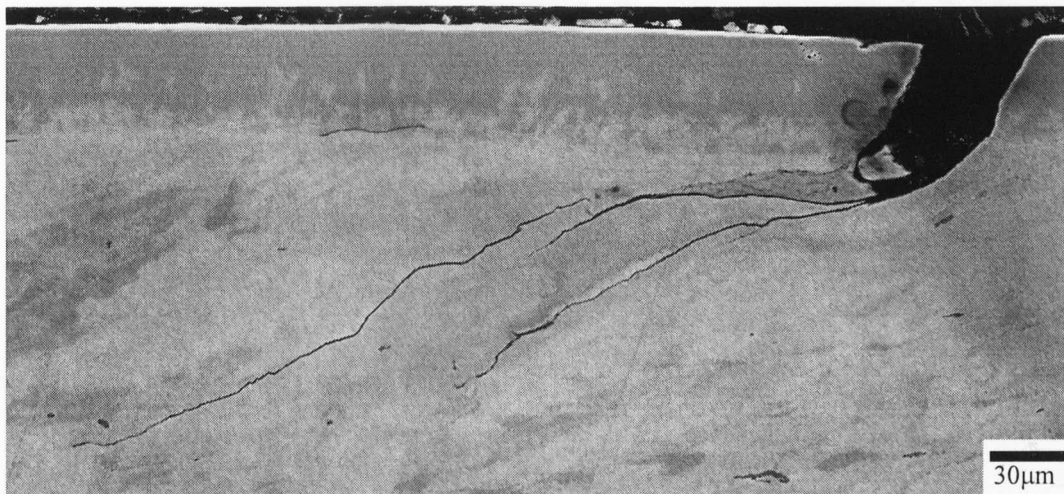
Figure 5.6.3.31: Two cracks growing from the same gap in WEL along flow lines, RA29 (16000 unidirectional cycles)
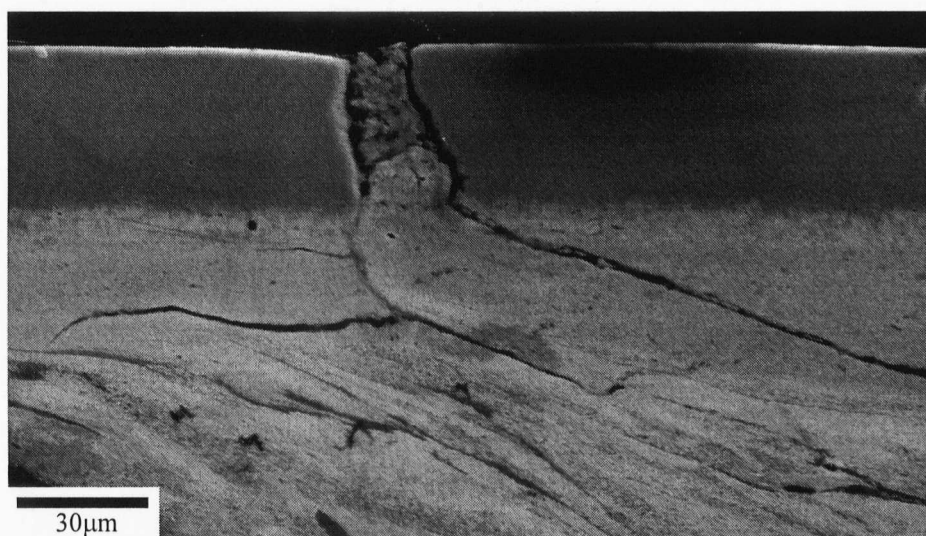
Figure 5.6.3.32: Pearlite deformed up into gap in white layer, RA25 (25790 unidirectional cycles)
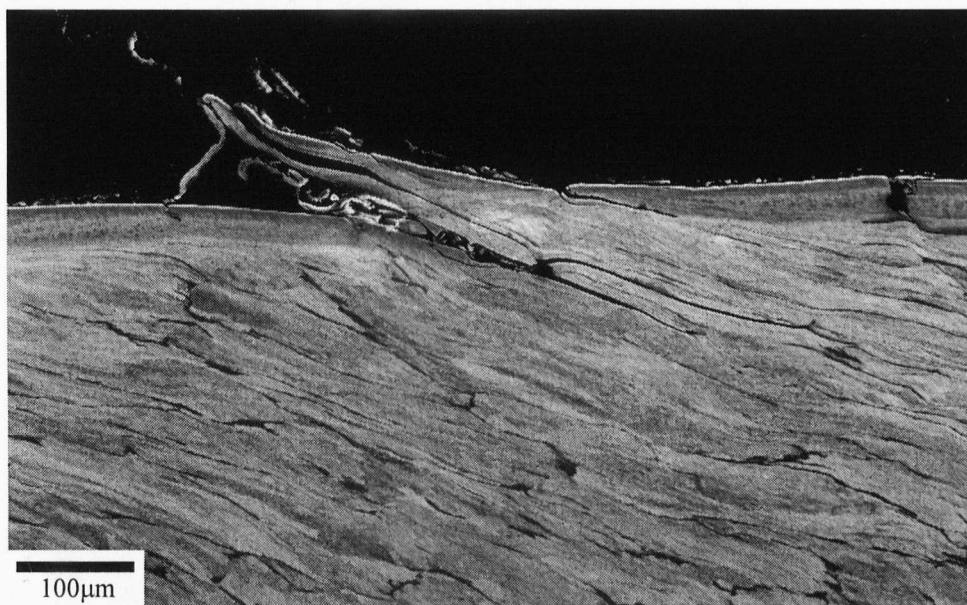
Figure 5.6.3.33: Pearlite extruded through white layer, RA25 (25790 unidirectional cycles)
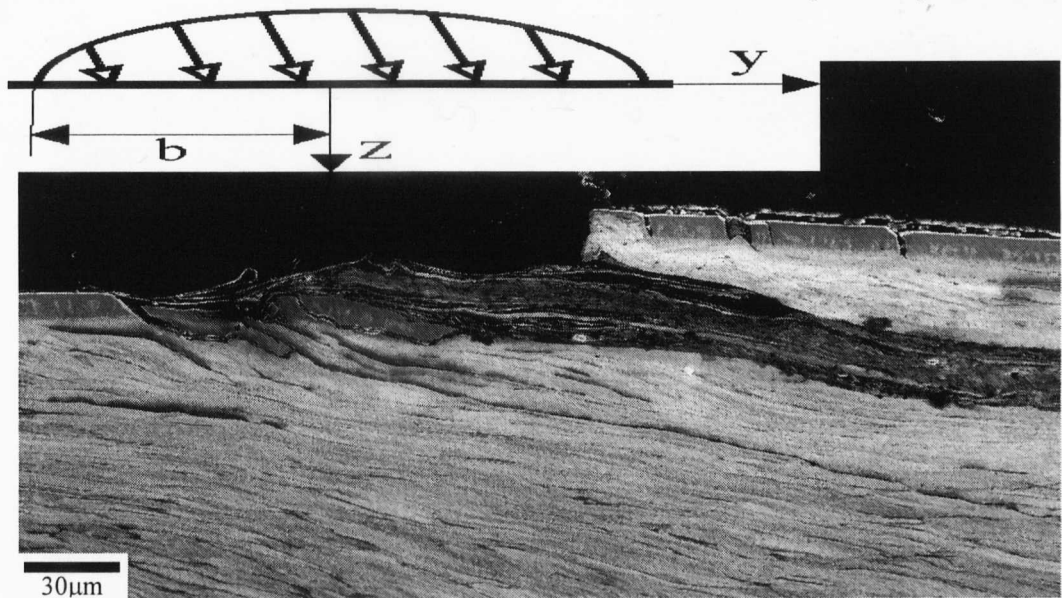
Figure 5.6.3.34: Pearlite being chopped off at surface, RA26 (37000 unidirectional cycles). The insert shows the nominal pressure profile of the contact patch (half width = b, y and z are spatial coordinates)

More cracks in WEL above steps than at a distance
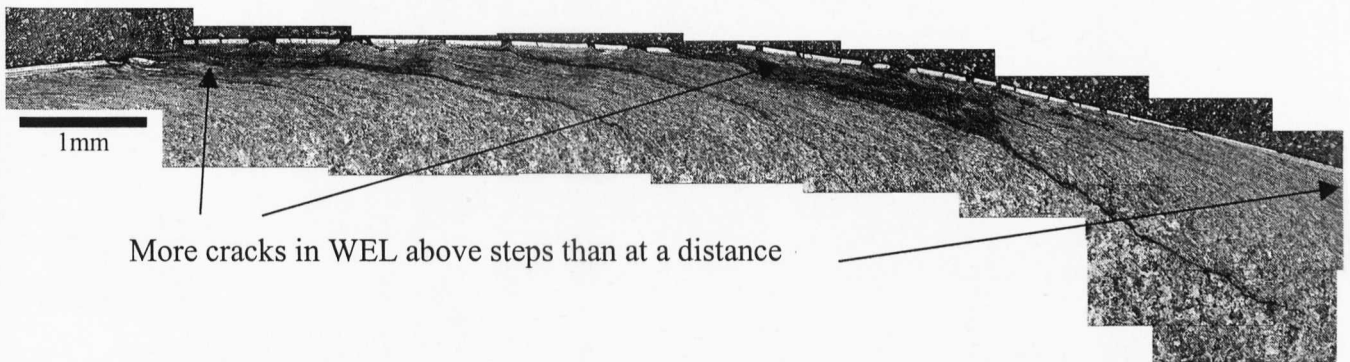
Figure 5.6.3.35: Long cracks present within WEL sample, RA25 (25790 unidirectional cycles)
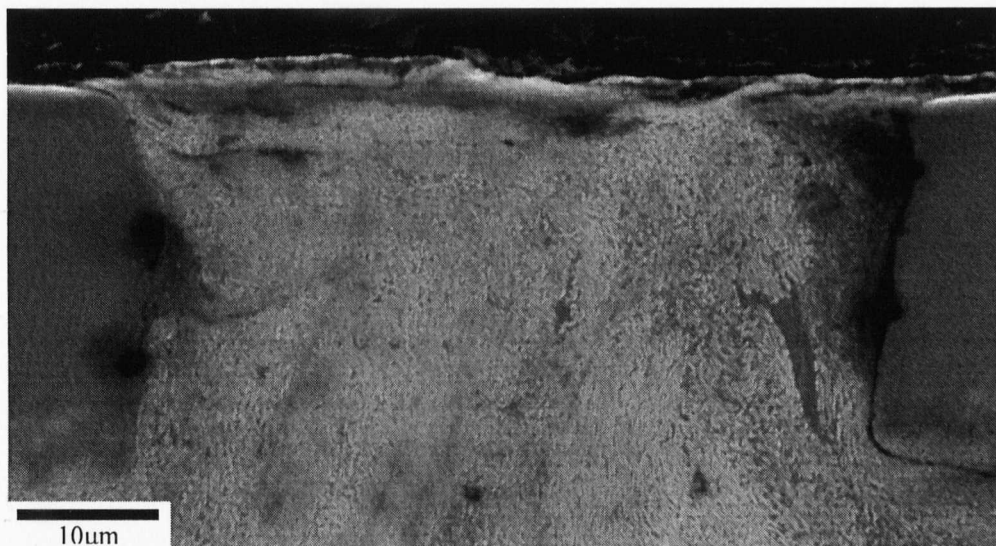
Figure 5.6.3.36: Pearlite sealing gap up to surface, RA24 (30000 reversed cycles)
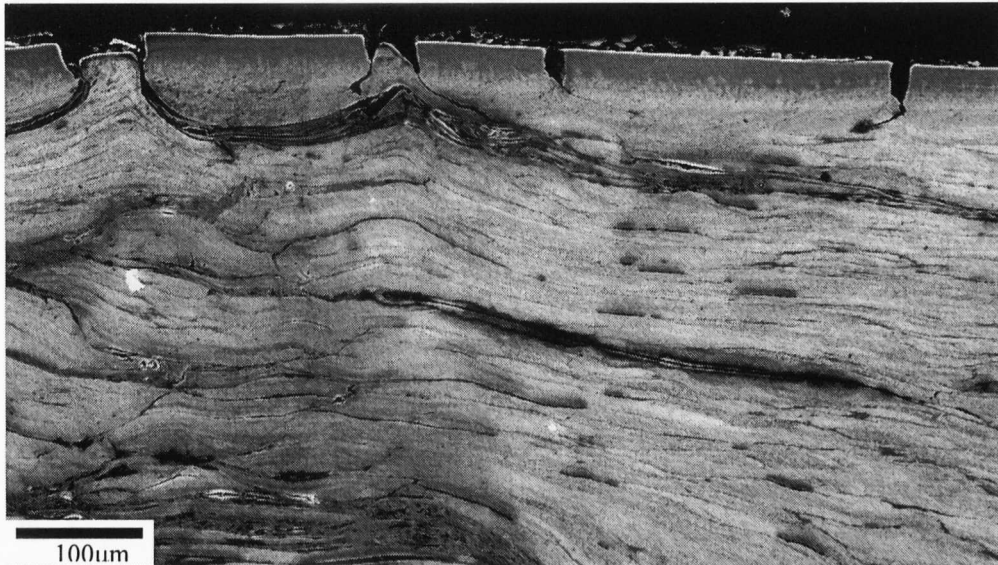
Figure 5.6.3.37: Cracks joining up below WEL, RA26 (37000 unidirectional cycles)
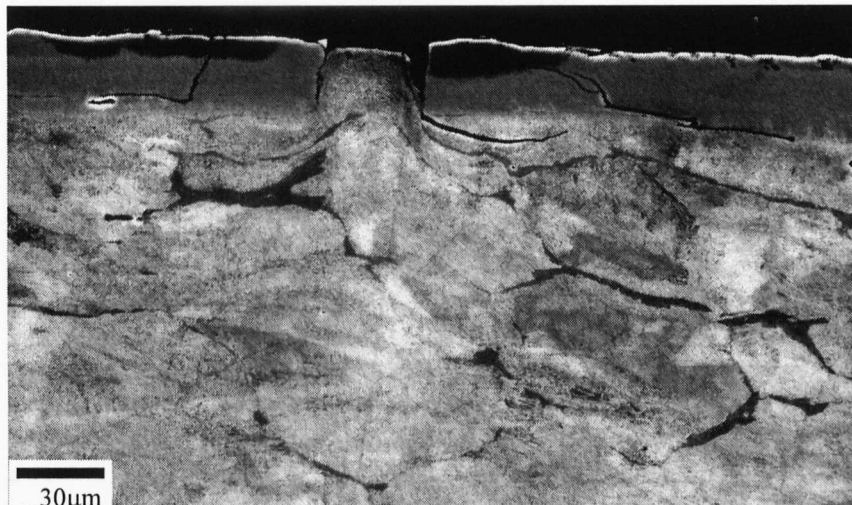
Figure 5.6.3.38: Transverse section of RA30 (23470 cycles, pure rolling water lubricated)
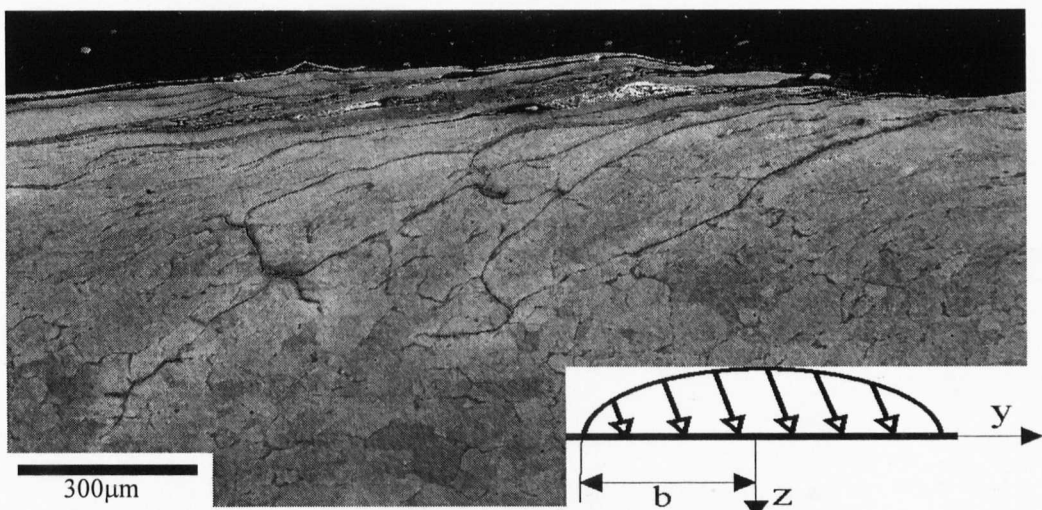
Figure 5.6.3.39: Spallation of WEL, RA26 (37000 unidirectional cycles) The insert shows the nominal pressure profile of the contact patch (half width = b, y and z are spatial coordinates)
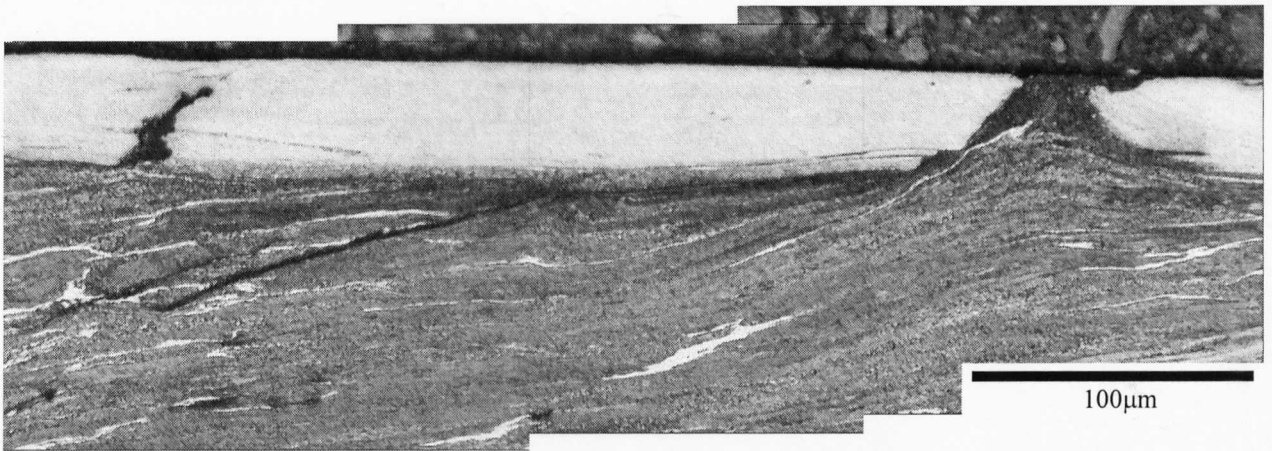
Figure 5.6.3.40: Cracks growing without water lubrication, RA35 (10900 dry cycles)

Figure 5.6.3.41: Spallation of WEL under unlubricated conditions, RA36 (31500 dry cycles)
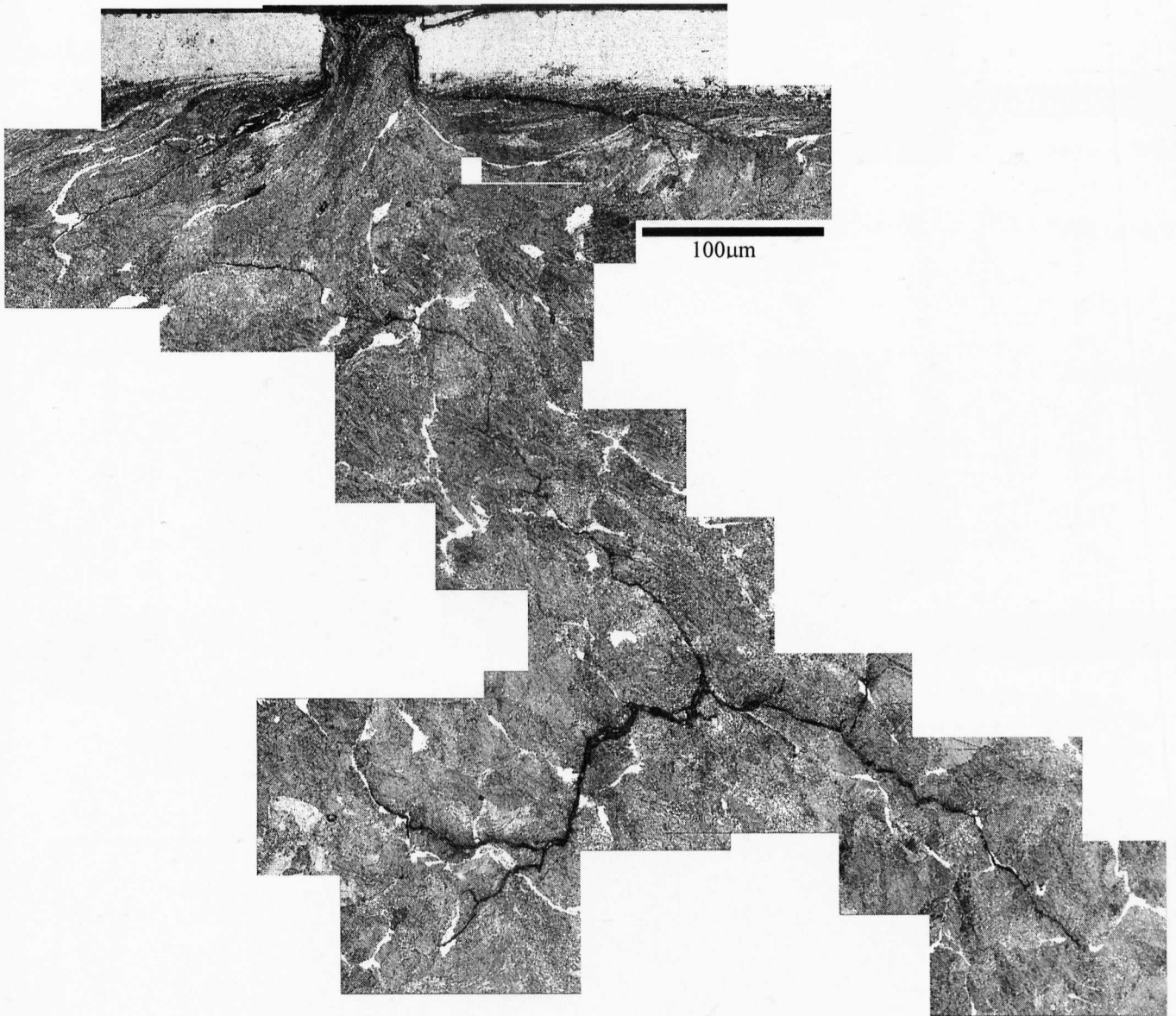
Figure 5.6.3.42: Three legged crack below a gap in WEL
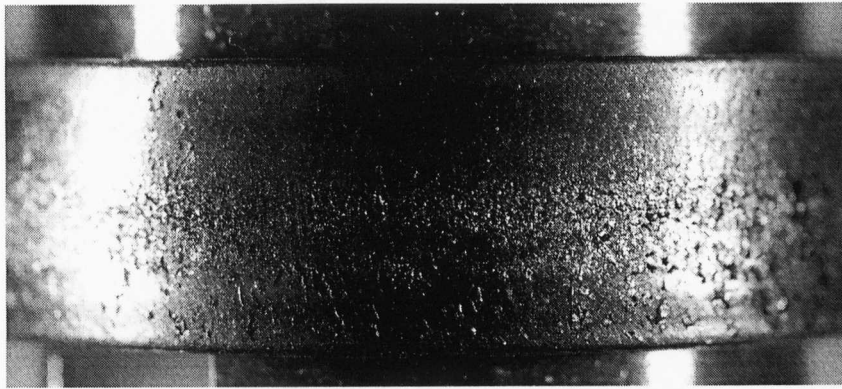
Figure 5.6.3.43: Wheel disc WB22 after rolling/sliding test against RA26 for 37000 water lubricated cycles
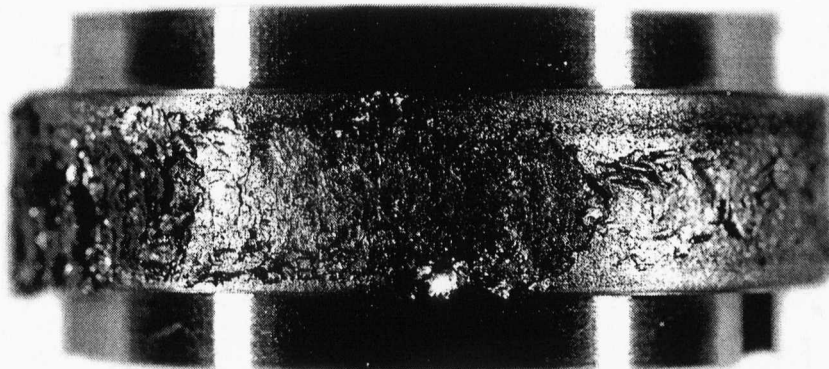
Figure 5.6.3.44: Wheel disc WB27 after rolling/sliding test against RA30 for 23400 cycles with 0% creep
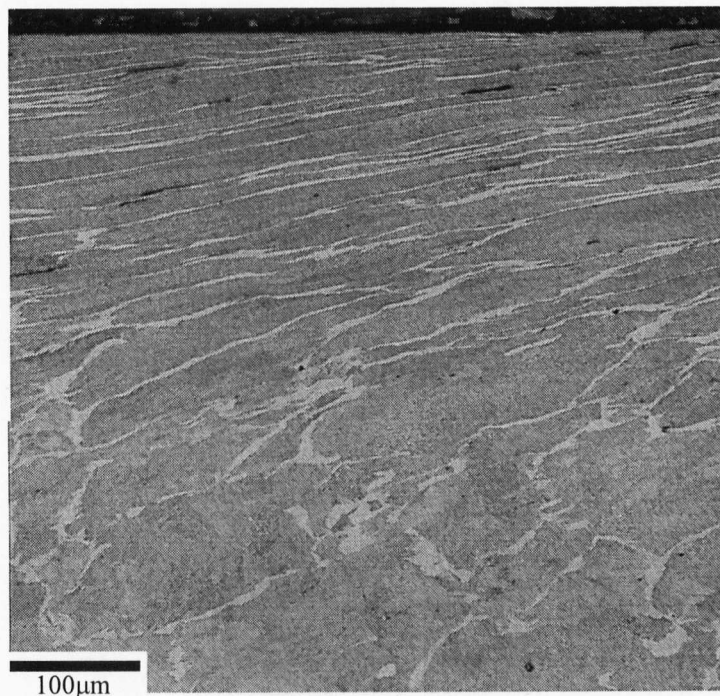
Figure 5.6.3.45: Wheel disc WB19, 4000 unlubricated cycles against RA21.

Figure 5.6.3.46: Wheel disc WB18, 30000 water lubricated cycles against RA24
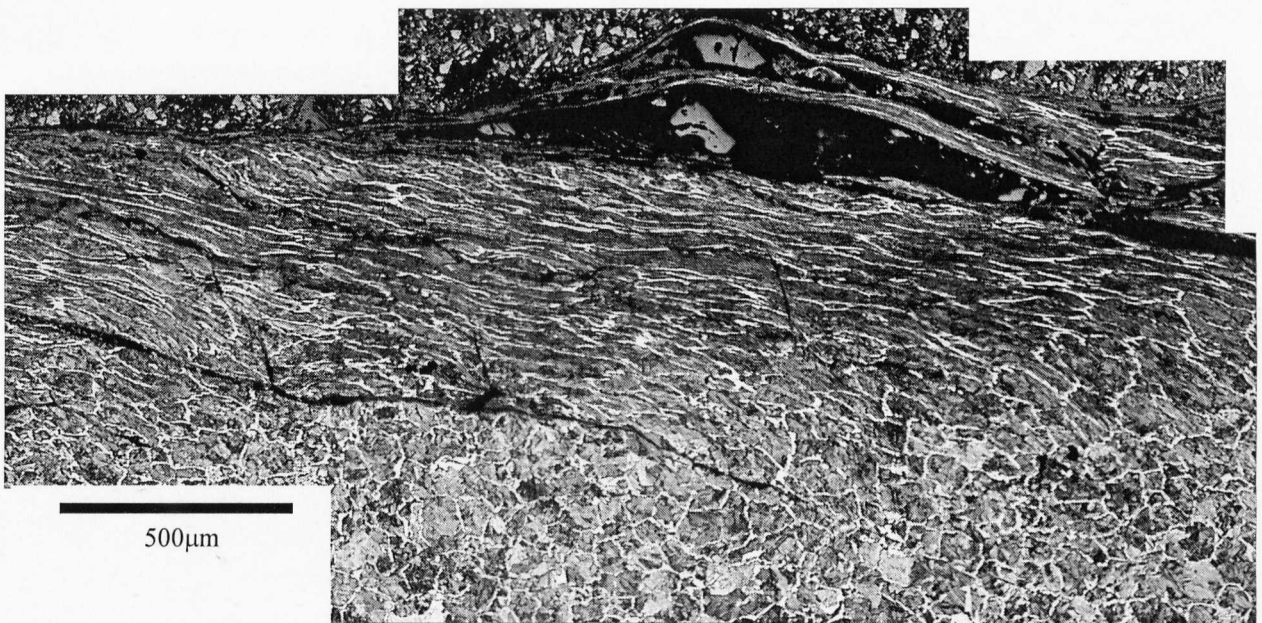
Figure 5.6.3.47: Wheel disc WB27 after rolling/sliding test against RA30 for 23400 cycles with 0% slip

Chapter 6: Discussion

6.1   Introduction

This chapter discusses the experimental results. This includes the effect of heat treatment on the bulk microstructural features and properties of the rail steel. The most important section is concerned with the results from twin disc testing; a part of this is a comparison between the two types of surface metallurgy. An important part of the discussion is the relation of the laboratory results to actual wheel/rail contact, which was made by examining samples of rail after manufacturing and also some that have been removed from service.

6.2   Heat Treatment of Rail Discs

The effect of the heat treatment, to create a decarburised layer, on discs has resulted in changes to the microstructural features of the bulk. This is reflected in a larger prior austenite grain size, 250-300μm, compared to 180-200μm for the as supplied material, table 5.2.2. This is due to the extended time at high temperatures that these samples undergo to create the decarburised layer. When steel is heated above the A_1 temperature the pearlite structure is dissolved into austenite in the transition range which, for this rail steel (0.52wt%C), is between 732°C and 760°C[1]. Once the steel has transformed to austenite, there is a thermodynamic driving force for grain growth to reduce the grain boundary area and energy. The prior austenite grain size is found by measuring the number of intersections of ferrite on a line; this is the first phase to transform on cooling. Diffusion during this second heat treatment, combined with a faster cooling rate, means that this grain boundary ferrite is harder to see than in the as supplied rail. The increase in the prior austenite grain size with heat treatment may have an effect on the initiation of cracks by having fewer boundaries of proeutectoid ferrite and pearlite intersecting the surface[2], but the effect will be overshadowed by decarburisation. The larger grain size of the heat-treated samples means there is less proeutectoid ferrite and consequently it would be expected that crack growth would be slower; this was found to be the case by Gray *et al.*[3, 4], but again the effect of decarburisation will dominate any effect of changes to the bulk microstructure. The prior austenite grain size has little or no effect on the hardness of the samples because the size of the grains (>190μm) is much larger than the microhardness indentation (20μm). The prior austenite grain size has also been found to have little influence on the strength of steel, whereas fracture toughness and fatigue crack growth have been found to be influenced by the austenite grain size [4, 5]. Ductility of pearlite decreases with an increase in the prior austenite grain size therefore, for the heat treated samples, less plastic deformation will be required to initiate cracks in comparison to the as supplied material[6].

The second microstructural parameter measured, the interlamellar spacing of pearlite, is thought to have a much stronger influence on the mechanical properties than prior austenite grain size. The interlamellar spacing is reduced for the heat-treated samples, 190-245nm, compared to those cut from untreated rail, 284nm, but there is a large spread in the results with a standard deviation of up to ±90nm (±35%). The refinement of the interlamellar spacing increases the yield strength of the steel according to a Hall-Petch type relationship[5]; this is reflected by the increase in hardness to 240-270HV for the heat treated samples from 224-247HV for the un-treated. This will mean that the steel acts more like head hardened (HH) rail, typified by an interlamellar spacing of 126nm and hardness greater than 350HV[7], which has been found to be more resistant to rolling contact fatigue and wear than grade 220[8]. The interlamellar spacing is strongly dependent on the cooling rate of the steel; the fine interlamellar spacing of head hardened rail is created by increasing the rate through the use of water cooling. The reason for the spread in results is that there is a considerable variance in the measured interlamellar spacing, the main reason being the orientation of the pearlite plates under the plane of examination. There is also some variation in the interlamellar spacing because of the variation in cooling rates within the sample with a faster rate at the surface than in the bulk. There is also the effect of the inhomogeneous concentration of alloying elements; the lower carbon content at the surface of decarburised samples results in a greater interlamellar spacing than in the bulk of the sample. The problem is eliminated from these results by only measuring the spacing in the bulk of the sample; but it will have some effect on the strength of the surface layer as reflected in the hardness measurements, which were usually taken within pearlite colonies.

There is a considerable difference in the prior austenite grain size of the two wheel materials. Wheel steel WA used for tests DP01 and DP02 can be seen in table 5.2.2 to have a much smaller grain size (107μm) compared to that for steel WB (239μm) used for all the other tests. This is probably due to the different heat treatments and manufacturing techniques between WA, which has been machined from a wheel, and WB, machined from a hot rolled bar. As mentioned above the effect of this on RCF of the rail steel is slight because it has little effect on the hardness or strength of the steel. The interlamellar spacing of the two materials is similar; WA is slightly less than WB, with a corresponding difference in the hardness of the two materials, table 5.2.2.

The overall effect of the heat treatment to create a decarburised layer is to refine the interlamellar spacing and increase the prior austenite grain size. In terms of mechanical properties this increases the hardness and hence yield strength of the heat treated samples over the as supplied material. The effect of this on the rolling/sliding behaviour of the samples, if no decarburised layer were present, would be to lower the wear rate because of the higher hardness and refined interlamellar spacing[7]. The refined interlamellar spacing also means that the initiation and propagation of cracks from the surface will also be more difficult[3]. This, combined with the increase in prior austenite grain size, resulting in less ferrite at the surface, means that it will be harder for rolling contact fatigue cracks to

initiate. The effect of the decarburised layer will overshadow any effect from the change in the bulk microstructural properties[2] until the cracks have passed through it. But by the time the cracks have propagated through the decarburised layer, the plastic deformation of the subsurface will result in the material no longer behaving like the initial bulk material. Therefore, the effect of the heat treatment of the bulk steel on the rolling/sliding behaviour of the steel will have little effect, first being dominated by the decarburised layer and subsequently by the plastically deformed material below. It is possible that once a crack has propagated to such a length as to be out of the deformed material then the heat treatment will affect the growth, but under twin disc testing conditions this is unlikely to occur.

The decarburisation model, developed by Birks and co-workers[9], described in chapter 4, has been used to allow the time of heat treatment of the discs to be predicted for a certain depth of decarburisation, using the calculated value for the diffusion coefficient from the initial tests. This has allowed twin disc testing over a range of decarburisation depths to be investigated, but has not been completely accurate because the discs were ground after heat treatment to give a smooth surface with the depth of machining being varied depending on the oxidation of the discs.

6.3   Simulation of White Etching Layer
6.3.1   Spot Welds

The initial spot weld tests have shown that it is possible to create a hard layer at the surface with a different microstructure to the bulk rail. This layer can be seen in figure 5.3.1 and it has a hardness of 700HV which is typical of martensite in a 0.57wt% carbon steel, figure 2.20[10]; comparison with the martensitic microstructure in figure 2.16 shows that they are similar and therefore this spot welded area can be regarded as martensite. The micrograph, figure 5.3.1, demonstrates a distinct interface between the pearlite and the martensite but proeutectoid ferrite is also present within the spot weld for approximately 100μm inside the interface. The structure of the spot welds allows some knowledge of the heat cycle to be determined. The interface between martensite and pearlite shows where the temperature has been above the eutectoid temperature, $A_1 = 723°C$; elsewhere the temperature was lower, therefore transformation to martensite has not occurred. The presence of ferrite within the spot weld indicates where the temperature did not reach A_3 (for this steel, approximately 790°C); ferrite only transforms to austenite at or above this temperature[1].

The overlapping spot welds, figure 5.3.2, were produced to see if it was possible to create a greater area of martensite than just a single spot. The change in colour of the initial spot weld with subsequent ones indicates that the heat cycle tempers the initial welds. This is confirmed by the microhardness measurements, showing values of 400-500HV for the initial welds; these are typical values for tempered martensite. There is no evidence in the

literature that WEL on rail is tempered during service therefore these tests were discontinued as the surface of the disc would not be representative of rail.

The twin disc experiments on spot welded samples have allowed the effect of a small hard phase surrounded by a much softer phase on the rolling/sliding behaviour of rail. A key part of this is the interface between the phases being present at the surface.

6.3.2   Sliding White Etching Layer

The sliding of one disc against another has resulted in the formation of a layer at the surface of both discs which does not etch but remains colourless, as can be seen in figures 5.3.3 and 5.3.4 for the wheel and figures 5.3.7 and 5.3.8 for the rail. This "white etching layer" has a hardness that varies between discs 782-898HV with an average of 840HV compared to the bulk hardness of approximately 250HV. Examination of this layer shows that near the interface, proeutectoid ferrite is present within it but not present at the surface of the disc, figure 5.3.8. This is because the white etching layer formed by sliding is a composite layer; near the interface it is formed by heavy deformation of the original surface of the disc, but at the new WEL surface it is a result of material transfer from the wheel disc which is then deformed into a continuous layer. This has been demonstrated by test WI02 with disc WB06 to create a spot of white etching layer on the surface of RA33 using a pulsed loading. Grooves can be seen on the wheel disc from which material has been removed, figure 5.3.18, and deposited on the rail disc, figures 5.3.19 and 5.3.20. The build up of material on the surface can be seen in figure 5.3.20, where it has not created a white etching layer but has resulted in heavily deformed pearlite. This is because the deformation was insufficient due to the short test duration. The WEL on the wheel discs during sliding is a result of the high material around the grooves being deformed into a continuous layer; further evidence for this is the presence of proeutectoid ferrite to much nearer the surface than on the rail disc, figure 5.3.4.

Further evidence for the transfer of material from the wheel to the rail disc is found by the results of weighing the discs before and after the sliding tests, which show a decrease in the mass of the wheel and an increase in the rail disc for all tests, table 5.3.4. It is possible to relate this mass change of the rail disc to the thickness gain of the rail disc via density, which shows that the calculated increase in thickness is between 15 and 84% of the measured average thickness, as seen in figure 6.1. This reinforces the conclusion that not all of the WEL is created from material transferred to the rail disc but some of it is created from the deformation of the original surface. The change in the mass of the wheel discs shows that less than 0.5% of the mass loss is not transferred to the rail disc but lost as wear debris. Confirmation for this material transfer is the test carried out for 10s of sliding against the high Cr back up roll disc, RA34. The white etching layer formed on this disc is continuous but also contains a much thicker band (400μm) that weaves across the disc, figures 5.3.12 and 5.3.13. The average value for this sample is therefore much more

difficult to calculate with the values in figure 6.1 being taken from one transverse cross section of the disc, but, even so, the calculated value is 98% of the measured values. The reason the thickness of the white etching layer is thicker than standard WEL samples is because the wear resistance of bainite is lower than pearlite of the same hardness[11], but the wear of bainitic steel is highly dependent on the contact pressures and its ability to work harden before being removed[12]. The short duration of the sliding means that the material is transferred before the surface has had time to work harden.

The chemical analysis of a surface section of RA34 has shown that the Cr content is 600% higher than in grade 220 rail along with a higher Ni and Mo content and a lower Mn content. These results for RA34 are between the composition of rail steel RA and the back up roll disc. Energy dispersive spectroscopy (EDS) of the surface has also shown that considerable amounts of Cr, with smaller amounts of Ni and V are present in the WEL, figure 5.3.14, which are not present in the bulk pearlite, figure 5.3.15.

The test WM01 was carried out to see if it was possible to create a thicker layer on the surface than that created during 5 seconds of sliding. The results have shown that this was not possible because heating of the discs has resulted in it turning blue, figure 5.3.5. This tempering of the WEL is demonstrated by its dark brown colour in figure 5.3.6 and also a hardness of 491HV, which is similar to the hardness of the tempered spot welds reported in section 6.3.1. The thickness of the white etching layer of 40μm is similar to the samples which were slid for 5 seconds. Therefore it was felt that increasing the time of sliding to create a WEL would not alter the depth but would its hardness.

The test to create a WEL on the decarburised sample has shown that it is possible after sliding for 10 seconds, figure 5.3.21. After sliding against a standard wheel disc for 5 seconds; observation and hardness tests showed that no white etching layer had been formed, therefore a further 5 seconds sliding was carried out which resulted in a white etching layer on the surface. The reason no WEL was present after 5 seconds sliding is because the surface of the decarburised sample is softer (180HV) than a standard disc; this means that it is not able to remove material from the surface of the wheel disc. Therefore, the first 5 seconds sliding work harden the surface to a sufficient level for it to remove material from the wheel disc, which occurs during the final 5 seconds combined with deformation into the white etching layer.

The transfer of material is due to adhesive wear, which is common under the severe wear conditions of two clean, like materials sliding against each other[13]. The mechanism is by cold welding of asperities and the pull out of material from one surface. Material transfer is always from the wheel to rail whatever the position of the discs with the exception of the decarburised disc, indicating that it is a material property of the discs, table 5.3.4, and not due to the relative sliding speeds.

The experiments to create spots of sliding white etching layer to examine the effect of the interface at the surface on the rolling/sliding behaviour have failed. The first method of holding the rail disc still and sliding the wheel disc against it created a partial WEL, figure 5.3.17, but cracks can also be seen to be present. It also resulted in the formation of a groove, figure 5.3.16, meaning that the disc was no longer round and would result in vibration, which may cause damage to the test equipment. The second method of intermittent load also failed because the safety mechanism turned SUROS off after only 3 cycles, which were insufficient to form a WEL, as detailed above.

Measurement of the strain and hardness below the simulated WEL for two discs, which did not have a subsequent rolling/sliding test, has been carried out and show slightly different results. RA31 shows a subsurface peak in the graph of shear strain, figure 5.3.9, that WB01 does not; the graphs of hardness for both samples show no subsurface peak, figure 5.3.10. This may be due to the effect of the different positions during the sliding. RA31 was on the lathe shaft while WB01 was on the AC motor shaft. The maximum shear strain for both is at the interface with the WEL and is between 2.8 and 2.9. The measurement of both strain and hardness allows a starting point to be determined for tests, which are subjected to a subsequent period of rolling/sliding contact.

The featureless appearance of the white etching layer is a result of the dissolution of the carbides within it. This is because the plastic deformation of the surface introduces large numbers of dislocations into the metal. Dislocations increase the solubility of carbon within the ferrite matrix as they provide low energy sites at their core, on which the carbon atoms can sit preferentially. For the carbon to be dissolved, the cementite lamellae have first to be broken up, which occurs because of the high plastic deformation resulting in high strains at the interface between ferrite and cementite lamellae[14]. The continued plastic strain by repeated cycles will help move the dislocations so they continually come into contact with carbide particles, increasing the rate at which the carbon goes into solution[15]. This dissolution results in the supersaturation of the ferrite into what has been called "ferritic martensite" by Newcomb and Stobbs; this may have a BCC structure because it is formed by deformation rather than the BCT expected by quenching from austenite[15]. Baumann *et al.*[16] discovered a refinement in the ferrite/martensite grain size from 5-10μm to 50nm within the WEL. The network of dislocations may act as nucleation points for recrystallisation of the martensite grains. This grain refinement, combined with the dissolution of carbides, is responsible for the white "featureless" appearance of the layer which is not resolvable in the optical microscope. The small grain size combined with the high dislocation density and the supersaturation of the ferrite produces the high hardness of the layer.

6.4   Surface Features on Rail and Comparison with Laboratory Simulation

6.4.1   Decarburisation

The manufacture of rail is primarily involved with creating the rail profile during hot rolling from bloom. The majority of decarburisation occurs during the reheating of the bloom to temperatures in excess of 1000°C, with little occurring during the rolling process. The geometry of the bloom means that the greatest depth of decarburisation occurs at the corners. This is demonstrated in figure 6.2, which is a photomicrograph of the corner of initial sample 10 showing the greater depth of decarburisation. During the rolling process the corners of the bloom are rolled such that their final position is at or near the gauge corner, demonstrated by the difference in figures 5.4.1 and 5.4.2 along with peaks in figure 5.4.3. The depth of decarburisation shows that apart from the two peaks up to a depth of 750μm the majority of the rail is between 450 and 500μm and therefore in accordance with BS EN 13674-1.

The presence of oxide that has been rolled into the surface of the rail, figure 5.4.2, is likely to be detrimental to rail life. The main achievement in the making of rail steel over the last 30 years has been to produce cleaner steels with fewer oxide inclusions[17]. Oxide inclusions have been found to initiate rolling contact fatigue cracks, these are commonly much smaller than the oxide present in figure 5.4.2[18]. It is for these reasons that the decarburised samples after heat treatment are machined to give a smooth surface and remove any oxide present on the surface. A further consequence of grinding is that it removes the totally decarburised layer at the surface which is not present on the railhead, as seen in figure 5.4.1 or 5.4.2. This is demonstrated in figure 6.3 for DE38 where the rail disc RA17 was ground back by 370μm. Therefore the simulated decarburisation shows a similar microstructure to the decarburisation found on new rail when it enters service.

The contact conditions between the wheel and rail, as described in the literature review, are commonly described as an elliptical contact; twin disc testing on the other hand is a line contact. For simplification, line contact will be used for scaling between twin disc testing and full scale wheel/rail contact with the difference being the contact half width used in the model. The maximum orthogonal shear stresses are plotted against the depth of the contact for twin disc testing, with a half width of 0.31mm, in figure 6.4 and for wheel/rail contact, with a half width of 6.6mm, in figure 6.5[19]. Several different traction coefficients are plotted on each graph and demonstrate that for less than 0.3, a maximum in shear stress is subsurface, close to 200μm deep for twin disc testing and 4mm for wheel rail contact; for a traction coefficient greater than 0.3, the maximum is at the surface. These figures are for perfectly smooth surfaces; under real contact the stresses at the surfaces will be higher due to surface roughness[20]. It can be seen that the stresses are higher to greater depths for wheel/rail than for twin disc testing because of the higher normal load.

The consequence of the difference in the contact situations for decarburisation is that a maximum of 0.5mm on rail is equivalent to 23μm on a disc. Therefore to examine the effect of decarburisation on rail using twin disc testing the depth of the simulated decarburised layer had to be adjusted accordingly. Due to limitations with the heat treatment and the machining of the discs this depth of 23μm was not achieved, with the nearest depth of decarburisation of 93μm being equivalent to 2mm on rail.

6.4.2   White Etching Layer

The rail removed from service has exhibited two different types of white etching layer on the same section. WEL 1 has a depth of 200μm and can be seen to be present close to an RCF crack but it is difficult to know whether it forms before or after the crack has grown; if it were present before the crack then the interface would seem to have initiated the crack that has led to the broken rail. There are several cracks within this white etching layer, figure 5.4.5; the pearlite below has been deformed up into these initial cracks with two cracks growing into the pearlite from the bottom. These cracks do not propagate for any great distance because the RCF crack limits the amount of pearlite available for deformation

The second type of white etching layer, WEL2, is only 25μm thick and for the majority remains well bonded to the pearlite below it, which is plastically deformed like the twin disc samples. The rail samples show the presence of proeutectoid ferrite up to the surface, with the crack in figure 5.4.10 initiating along it. The presence of ferrite at the surface has been found to initiate cracks in ferritic/pearlitic steels[2] therefore it is also likely to be a crack initiation site in WEL. Cracks have also been found to initiate at the interface between the white etching layer and the pearlite, figure 5.4.9, and is likely to be due to the difference in ductility of the two phases with the pearlite being deformed away from the white etching layer which itself is not readily deformed. This second type of white etching layer is similar to that observed by Clayton and Allery[21] on rail removed from service, who found that cracks initiate at the surface on the WEL/pearlite interface, but it is not clear whether they continued to propagate along the interface or just near the interface within the pearlite. Other cracks were found by Clayton and Allery[21] to initiate within the white etching layer with the majority remaining within it but a few propagated below the boundary; the micrograph of these cracks imply that they propagate along proeutectoid ferrite within the WEL, like they do in WEL2 in this investigation.

The hardness profile of both white etching layers has been compared in figure 6.6 with data presented by Baumann et al.[16] for white etching layers present on grade 260 rail. The two hardness traces given by Baumann are similar to those discussed here. The first has a high hardness, but its depth is shallow, 20μm, with the hardness of the material below falling to the values expected for deformed pearlite; the second is harder to greater depths of up to 200μm. The difference between the two sets of samples is that grade 260

rail has a maximum hardness of 1300HV while grade 220 has a maximum of only 950HV with an average of 780HV. This can be accounted for by the difference in carbon contents of the two rails, grade 260 rail has a content of 0.6-0.8wt% compared with only 0.5-0.6wt% for 220 grade. The hardness of quenched martensite is directly proportional to the carbon content of steel; according to the ASM Metals Handbook the hardness of martensite for a 0.55wt%C steel is 850HV and that for a 0.7wt%C steel being 950HV[10]. The reason for the maximum values being harder than these is probably due to the nanocrystallisation of the martensite by plastic deformation, as has been proposed by Baumann *et al.*[16].

The comparison of shear strain for a section of rail exhibiting a WEL and one without, figure 5.4.12, demonstrates that a greater amount of plastic deformation is required for WEL formation. A shear strain of greater than 6 is required for its formation on rail. How much greater is unclear because the shear strain is only measured within the pearlite and not within the WEL. In comparison, the shear strain for the formation of WEL on discs, figure 5.3.10, shows a maximum of 2.8 at the interface with WEL and indicates the difference in the two situations under which WEL has formed. The sliding of discs is likely to result in much higher strains at the surface than the rolling/sliding contact of wheel on rail.

The second white etching layer is not continuous but present in patches on the surface of the rail. Therefore, the white etching layer cracks at the weak spots, relieving the tensile/shear stresses within it so they will not be strong enough to initiate cracks within the WEL. The thickness of the WEL will also have an effect on this, which is why WEL1 has not cracked at any obvious weak spots while WEL2 has. The subsurface pearlite of the thinner WEL2 will accommodate the stresses at the surface by plastic deformation of both the WEL and the pearlite, which the thicker WEL1 will not be able to accommodate and therefore cracks.

The varied properties and structures that have been reported in the literature (see chapter 2) indicate that there is more than one type of white etching layer formed on rail with differences depending on the conditions of formation and material properties of the rail. The presence of two types so close together on a railhead (within 50mm) show that the ever changing conditions between rail and wheel make it hard to form general conclusions on the formation of white etching layers.

The spot welded samples, even though their depth is much greater (2mm, equivalent to 43mm on rail), have allowed the effect of an interface between the WEL and the pearlite to be investigated. This is similar to that found to be present in WEL2 on rail which has been observed to initiate cracks. The continuous layer created by sliding one disc against another has allowed the effect of rolling and sliding a wheel disc against a very hard layer to be investigated. It has also allowed the effect of the initially deformed pearlite and that during rolling/sliding tests to be examined. The development of cracks, once they have

transferred from the WEL into the bulk material, can also be investigated. One difference between the white etching layers examined on rail, especially WEL2, and that found on rail discs after sliding, is the lack of proeutectoid ferrite at the surface, which is likely to have an effect on how cracks initiate within the white etching layer.

6.5   Rolling/Sliding Twin Disc Testing
6.5.1   Data Logging Results

The nominal Hertzian contact pressure for all tests has been 1500MPa. The reason this value has been used is because, as discussed in chapter 2, it is a common value found on the railhead[22]. This value has also been extensively used by other workers in twin disc testing thereby allowing a comparison with their results[23, 24]. The range in values around this nominal value has been within ±15MPa or ±1%; this is within the range of ±2% found by Fletcher during redevelopment of the machine[25].

The traction coefficient has been calculated from the normal and tangential forces which are data logged by the computer during the SUROS test. The general trend for all water lubricated tests is a rise to a maximum followed by a decrease until the end of the test. The initial rise is due to running in and the associated initial microstructural changes that occur with it, such as flattening of asperities[26]. The reason for the gradual decrease is that as wear and transverse deformation of both discs occur the diameters decrease, resulting in a decrease of the torque and consequently a decrease in the traction coefficient. During the initial dry cycles the traction coefficient reaches a maximum of between 0.25 and 0.38. These values are in accordance with that given by Stolarski and Tobe for dry rail[27]. The reason that these dry cycles were carried out was to plastically deform the pearlite and decrease the life of the test. After the initial tests had been carried out the test duration was deemed to be short enough, and to examine whether these cycles had any effect, the remainder of the tests on decarburised samples were carried out with water lubrication from the start. During the dry cycles, with a traction coefficient greater than 0.3, the maximum orthogonal shear stress is at the surface, therefore the maximum plastic strain will be at the surface. The effect of the wet phase is to reduce the traction coefficient to less than 0.2 and this results in the maximum orthogonal shear stress being subsurface and likewise the maximum strain[19]. This is reflected in the strain and hardness, and is discussed in the next section.

The traction coefficient values for the normal samples with water lubrication of 0.17-0.18 is in accordance with the values of 0.18-0.2 for a clean wet rail[27]. Twin disc testing is able to reproduce the traction conditions present on rail for both dry and water lubricated cycles. The average traction coefficient for water lubricated cycles has demonstrated that decarburised samples have lower values than the un-heat treated samples. One possible reason for this is the expected higher wear of the decarburised samples which would result in a greater decrease of the radius and hence in the traction coefficient. Examination of the

loss of radius for most decarburised tests shows that it is similar to normal samples, table 5.5.4.1; this hypothesis can also be discounted on examination of the maximum and end values, showing a very similar drop in the traction coefficient during the tests but starting from and ending with different values, table 5.5.1.1. It is therefore likely that the difference is due to the microstructural difference at the surface of the rail disc. It is possible that the softer ferrite means that asperities are removed or flattened faster than in pearlite and this results in the lower traction coefficient. If so, this would be expected to be reflected in the surface roughness after the test but the variance in results mean this is inconclusive. Even the two results after only 6600 cycles show very similar results, with the normal tests having a slightly lower surface roughness than the decarburised sample.

The traction coefficient results for the spot welded samples show typical values expected for rail and for standard grade 220 rail discs in wet and dry conditions. There appears to be little effect from the spot weld but this is probably due to their small area, compared with the surrounding pearlite.

The results for the sliding WEL experiments show that the average values are slightly higher than those for normal samples but only for the unidirectional test, the reversed tests are slightly lower. This indicates that the traction coefficient may be influenced by the ease of plastic deformation of the subsurface material. In the unidirectional tests the rate of plastic deformation decreases with each cycle as the material strain hardens, leading to the exhaustion of ductility, whereas in the reversed cycles initial plastic deformation is easy while it reverses that from the initial sliding[28]. This may also account for the decarburised samples having a lower traction coefficient because it is easier to deform the softer surface. The traction/friction coefficient has been found to be dependent on the hardness, grain size and texture[29]. It is therefore likely that the different traction coefficient values found are dependent on the surface microstructure of the rail disc. Although Beynon et al.[8] have investigated three different rail steels with a hardness that varied between 250 and 370HV and found no correlation between hardness and traction coefficient.

The traction coefficient of the two dry WEL tests show similar values to the dry cycles of the standard samples and the dry spot welded sample. Figure 5.5.1.13 for RA35 a sudden drop in the traction coefficient after 7000 cycles. It is unclear why but it may be caused by the initiation of cracks within the sample; several other samples show similar but less dramatic smaller drops but usually increase again back to the initial values.

6.5.2   Strain and Hardness

Shear strain and hardness have been measured to see the effect of the surface metallurgy on them, but as this is mainly in connection with the amount of strain required to initiate

cracks the majority of the discussion is carried out in the section on rolling contact fatigue, 6.7. This section ties together some general points about the results.

The maximum value of shear strain for water lubricated tests is subsurface, figure 5.5.2.1 *et seq.*, usually at a depth of around 200μm, which can be seen in figure 6.4 to be at the same depth as the maximum applied shear stress for water lubricated contact. There is also a large amount of deformation at the surface, which is due to the high contact stresses arising from asperity contact[19]. The difference between the lubricated and unlubricated samples can be seen in the figure for the spot welded samples, with the dry test having a maximum at the surface, figure 5.5.2.4. The method used to measure the shear strain is impossible to carry out at the surface because of the high degree of deformation; the flow lines become almost parallel to the surface. The use of a protractor allows angles to be measured within ±0.5°, which is an error of less than 1% of the strain value.

The reversed white etching layer tests show that the measurement of shear strain is difficult because it depends on the local conditions where it has been measured, figure 5.5.2.7. Two of the traverses on this graph show negative shear strains whereas the other two show only positive values but which are lower than a unidirectional test for the same number of cycles. These tests have also demonstrated the difference in the measurements of shear strain and hardness. Hardness is a measure of the total amount of plastic deformation which has occurred and appears not to be affected by its direction, as demonstrated by discs RA23 and RA28. These two tests have the same number of cycles but the former has the plastic deformation reversed; the hardness values for both are almost identical (RA23 = 326HV, RA28 = 333HV) but the shear strain values are completely different (RA23 = 1.01, RA28 = 2.85). Therefore if the direction of plastic deformation is reversed then hardness may not be an effective measure of whether a material is close to ductility exhaustion.

The results of shear strain rate (figure 5.5.2.10) for the decarburised sample show that as the depth was increased, the amount of strain that the material experiences at a depth of 200μm increases. The reason for this is that the decarburised layer of ferrite is softer and more ductile than pearlite; therefore, as there is a greater amount of ferrite at the surface it is able to undergo more deformation. This is even the case with the two samples that were run for only a few cycles but with a large amount of decarburisation, DP04 (13767 cycles) and DP05 (6619 cycles). DP05 had the largest strain rate and the lowest number of cycles of any test. This would indicate that the greatest amount of deformation at the surface occurs during the first few thousand cycles with the rate settling down to a lower steady state of strain accumulation. This is confirmed by test DP14 run for 6600 cycles with no decarburisation showing a strain rate of double that for those samples tested to failure. This initial deformation was found to be the case by Fletcher during unlubricated tests. He discovered that most of the deformation had occurred after 5000 cycles with only a slight increase in the amount of strain with subsequent cycles[19]. This process of a steady rate

of strain accumulation is associated with ratchetting, leading to the initiation of cracks by ductility exhaustion. It would therefore be expected that as the amount of decarburisation, and consequently the amount of ferrite increases, then the surface would be more ductile and as such able to undergo more shear strain than a surface without decarburisation. However, opposed to this is that a softer material means that more deformation per cycle is possible. Therefore, the overall result is that the ductility exhaustion will be reached at similar times for samples with and without decarburisation.

The results of the microhardness traverses and the percentage hardening (figure 5.5.2.19) of the rail disc show a similar trend to the shear strain measurements, increasing with depth of decarburisation. The hardness results for the samples with decarburisation, figures 5.5.2.14 and 5.5.2.15, show that the surface is softer than the bulk hardness of the rail disc but has increased from the initial value, demonstrated by the results from the reference samples. The greatest amount of hardening is subsurface at a depth of 225μm, very close to the value predicted by Hertzian contact theory as where the maximum shear stress would be for water lubricated contact, figure 6.4.

The shear strain for the unidirectional WEL tests demonstrates an increase with the number of rail discs cycles as would be expected for samples accumulating plastic strain with each cycle. The unidirectional samples show a similar trend to those without a WEL but with shear strain values that are slightly higher because of the initial strain required to form a WEL as exhibited in figure 5.5.2.12 by the sample with zero cycles. The two dry tests show much higher values of shear strain because of the higher contact stresses present when no lubricant is present. The reversed tests show a lower amount of shear strain, with a negative value after 30000 cycles. In contrast, the hardness at a depth of 200μm shows a gradual increase with rail disc cycles for all samples, figure 5.5.2.20. The only significant difference is the much higher hardness of the two dry tests but they also follow the same trend as the other samples. What is noticeable about these results is that the WEL samples have similar hardness values to those without, even though they have undergone more plastic strain to create the WEL, figure 5.5.2.20. The two samples, which have not had a rolling/sliding test carried out, give lower values than the samples tested to 2000 cycles. They also show that the majority of the strain hardening has occurred in the first few thousand cycles with only a gradual subsequent increase. This accounts for the similar hardness values for those samples with and without WEL under similar test conditions. Tyfour's study of wear behaviour with dry unidirectional tests showed that the majority of the hardness increase occurred at fewer than 5000 cycles with a subsequent increase in hardness of only 10% after the number of cycles is increased by 800% to 40000[30].

6.5.3   Surface roughness

The measurement of surface roughness, R_a, before the test was to ensure that for the normal and decarburised tests the machining had been sufficient to give a smooth surface

with an R_a of less than 1μm. With the sliding WEL this was not possible because machining would remove the layer from the surface. Therefore after the white etching layer had been created, the surface roughness of the disc was higher than before sliding, typically with an R_a of 1.5μm. This is due to the process of material transfer and deformation of the surface. Hill and Clayton have previously investigated the effect of surface roughness on the rolling contact fatigue life of grade 220 rail and found that between 0.6 and 1.6μm R_a there is little effect, but if the surface roughness is decreased below this range then the RCF life is reduced because of a greater true area of contact resulting in a higher friction coefficient [24]. It is therefore thought that the difference in surface roughness of the samples will have had little effect on the rolling contact fatigue performance of the samples. The measurement of the surface roughness after the test showed a decrease for all except those that spalled. The reason for this is that the plastic deformation and wear of the surface resulted in the flattening and removal of asperities; this is visually demonstrated in figures 5.5.3.1 and 5.5.3.2, where the original grinding channels have been removed.

Talyrond® profiles were carried out for each disc before the test to ensure that it was circular with the internal and external diameters being concentric. If the disc was found to be not within the standard required, it would be rejected as testing it might have caused vibration and damage to the testing rig. Profiles were carried out after the tests to see whether any uneven wear, such as corrugation, had occurred, figure 5.5.3.3b; an example of slight ovality can be seen in figure 5.5.3.3a. The profiles also demonstrate if spalling of the surface has occurred, as seen in figure 5.5.3.3b. The Talyrond profile of the spot welded sample, figure 5.5.3.4, demonstrates how the disc had worn unevenly and experienced plastic deformation of the pearlite around the spot weld; this figure will be discussed in section 6.7.

6.6   Wear
6.6.1   Decarburisation

The effect of decarburisation on the wear of the rail disc shows that as the depth of decarburisation increases, the total wear and the wear rate both increase. The wear rate is a more useful measure of wear because it eliminates the effect of the different number of cycles for each test. Increasing decarburisation results in greater amounts of softer ferrite at the surface, which is less resistant to wear than pearlite; ferrite has a hardness of 150HV (100g) compared to a hardness of between 222-272HV for the bulk of the samples. The wear is similar for samples with less than 300μm decarburisation to those without, because all have small amounts of ferrite at the surface along the grain boundaries, with increasing amounts as the depth of decarburisation increases. With this type of microstructure, wear resistance is dominated by the pearlite within the grains and not by the ferrite at the grain boundaries. Clayton and Danks found that for ferritic/pearlitic steels the wear resistance is

inversely related to the hardness of the sample[31], with a four-fold increase in the wear resistance of steel by doubling the amount of pearlite[32].

The depth of decarburisation is used on the graphs because it allows comparison with industrial practice. It is also possible to use the carbon content at the surface as another indicator of microstructure. Figure 6.7 shows that with increasing carbon content the wear of the rail decreases; this is because the lower the carbon content, the greater the amount of ferrite at the surface. Plotted in figure 6.7 is data taken from the literature: tests conducted by Tyfour[30] and Fletcher[25] on grade 220 rail steel show very similar results to tests without decarburisation, while those by Beynon *et al.*[8] on eutectoid rail steel show a very low wear rate similar to the lowest values found for grade 220 rail steel. As the carbon content is increased above 0.5wt%, the wear rates are very similar, suggesting that small amounts of proeutectoid ferrite have little effect on the wear of the steel.

The wear of rail is thought to be a combination of oxidation and flake formation due to micro-cracks, combined with abrasive wear from particles. With twin disc testing, the test duration and frequency of cycles would suppress oxidation as a wear mechanism, while the water lubrication removes the wear debris, therefore the dominant mechanism is most likely to be flake formation[33]. With a soft surface layer it is easier for cracks to grow and produce small flakes from the surface than it would be in a fully pearlitic steel. The maximum amount of radius lost by wear in this investigation was 12μm, which is very small compared to the depth of decarburisation, 612μm. It can therefore be seen in figure 5.6.2 that the ferrite does not wear away but deforms and work hardens, figure 5.5.2.15, until it is at a similar hardness to the non-decarburised samples and therefore more resistant to wear. The results from the samples run for 6600 cycles (RA06 and RA18) show that the rate of wear is much higher during the first few thousand cycles while the surface work hardens. Along with strain hardening, the presence of pearlite at the surface also decreases the wear rate with increasing cycles. The structure of pearlite, with alternate layers of ferrite and cementite, means that when it is deformed the original randomly orientated layers rotate to become parallel to the surface. The harder cementite is more resistant to wear than ferrite, which is consequently worn away leaving a higher percentage of cementite at the surface[7]; this self optimising structure can be seen in figure 5.6.2.6 where the plates are almost parallel to the surface.

The plot of wheel wear rate against the depth of decarburisation on the rail disc, figure 5.5.4.3, shows that there is no significant correlation between them. The wear of rail discs is higher than the wheel due to negative traction and the resultant higher contact stresses within the following surface than in the driving surface[34]. One of the wheel discs shows a gain in weight rather than a loss; this is likely to be due to contamination due to insufficient cleaning but may also be due to mass pick up from the rail disc, although this was not observed for any other tests. The wheel discs running against the decarburised rail samples show less wear than those without decarburisation, which may be due to the softer

initial surface of the rail doing less damage to the wheel. This would indicate that the majority of wheel wear occurs during the first few thousand cycles (especially for those with 200 dry cycles) before work hardening and the development of residual stresses occurs. The wheel disc wear, when tested against discs without decarburisation, are comparable but higher than those found by Fletcher[19] this may be a result of the slight differences in the wheel material used.

6.6.2   Spot Welds

The results for the water lubricated spot welded tests show that after 4000 cycles the wear of the rail disc is similar to that of samples without spot-welds, figure 5.5.4.4. This is because the majority of the surface is still pearlite with only a small amount of the harder martensitic phase; therefore wear would be expected to be similar to that of samples without the spot weld. In contrast, after 23000 cycles the wear is much greater because of the deformation of pearlite around the disc by the contact stresses, resulting in a pile up on the face of the spot weld which is exhibited by the Talyrond profile, figure 5.5.3.4. With extensive plastic deformation this pile up results in ductility exhaustion and crack formation, with the surface spalling off, figure 5.6.3.5. This is also the reason why the wear of the dry sample is higher than the wet sample after the same number of cycles. Dry contact results in higher contact stresses at the surface, figure 6.4, and consequently more plastic deformation. This pile up is demonstrated by the Vickers hardness results for the sample around the spot weld, figure 5.5.2.17. On the left hand side of this figure can be seen high hardness values (400HV) close to the interface. On the opposite interface the hardness is lower than is commonly found for plastically deformed pearlite at a depth of 0.2mm away from the weld, because the harder spot weld prevents the pearlite being deformed.

The wheel disc wear is higher for all spot welded samples than those without, figure 5.5.4.5, because of the high hardness of the martensite, combined with the uneven surface resulting from the pile up of the pearlite around the spot weld, figure 5.5.3.4. The wheel wear is especially higher for discs that have cracks present within the pearlite, indicating that the detachment of debris from one disc increases wear of the counter disc by producing third body abrasives.

6.6.3   Sliding White Etching Layer

The graph of wear rate against depth of the WEL is inconclusive because of the narrow range in depth of WEL, therefore to make the results clearer the total wear has been plotted against the number of rail cycles. The total wear of rail discs with white etching layer produced by sliding is much lower than for discs without, as long as the WEL has remained intact (figure 5.5.4.7). The lower wear of the white etching layer samples is because the surface is up to three times harder than the counter wheel disc; this is expected

if the wear follows an Archard type relationship[35]. The Archard wear equation is for sliding contact of surfaces and is for the complete system and not just one face, with the hardness used being that of the softer material[36]. As long as the white etching layer remains intact, the high hardness produces a low wear rate. If the WEL begins to spall off due to fatigue of the pearlite below, the loss of debris increases the wear of the rail disc to above that for a disc without WEL, figure 5.5.4.7. This increase in wear, due to the detachment of WEL, is in accordance with the results found by Millman *et al.*[37] who studied wear of WEL on railheads. The primary reason for wear under rolling/sliding conditions between two steel discs is the ratchetting of the surface and the formation of slivers of metal[38]. The hard undeformable WEL means that ratchetting does not occur at the surface but below, within the pearlite. Therefore the WEL does not wear like pearlitic rail, which creates debris from the surface, rather it spalls when the subsurface ductility has been exhausted and cracks have grown, see section 6.7.3.

The effect of the white etching layer on the wear of the wheel discs is severe, with the total wear being an order of magnitude greater than for those without, figure 5.5.4.8. This appears to be because the high hardness of the surface is combined with the cutting action by the edges of cracks present in the white etching layer of the rail disc. The cracks in the white etching layer are orientated so that they act as a cutting tool on the wheel disc, figure 5.6.3.17[39]. Some evidence for this cutting action can be found from the tests with and without a traction force after 2000 cycles; the sample without any cracks has wear similar to the samples without a WEL, whereas the sample with a traction force, and hence cracks, is almost double. Unfortunately, the test after 30000 cycles, with only perpendicular cracks, shows a much higher wear rate because of a problem with the testing equipment and hence is not shown in figure 5.5.4.8.

This cutting action, combined with the hard rail disc deforming the wheel disc surface more than for a disc running against a standard pearlitic disc, has resulted in the wheel disc spalling in several of the longer tests. This can be seen in figure 5.5.4.8 for disc WB27 with no traction force (0% slip ratio and run wet) after 24000 cycles. This behaviour is not in accordance with the wear normally experienced by wheel/rail contact, where an increase in the hardness of either surface decreases the total wear of the system[40]. This is because the higher hardness of one surface results in a lower wear rate and, therefore, less wear debris to act as third body abrasives on the opposing surface. With WEL this will not occur due to the presence of the hard surface cutting and deforming the softer surface, increasing the wear of the system.

6.6.4   Effect of Surface Metallurgy on Wear

A comparison between the two surface metallurgical features examined has been carried out by plotting the wear rate against the hardness of the surface, in figure 6.9 for rail and 6.10 for wheel discs. The wear rate plotted here has been converted to mass lost per metre

rolled per mm contact width to allow comparison with literature results. The results plotted from the literature are for grade 220[8, 19, 30, 41], grade 260 or equivalent[8, 42], BS11 head hardened[8] and the Infrastar coated rail[42]. The data of wheel wear taken from literature is for the same wheel steel used in this investigation tested against grade 220 rail[8, 25, 28].

The results for rail wear show a general trend of the rate decreasing with increasing hardness; this is in accordance with the Archard wear equation[35], where wear rate is inversely proportional to hardness of the surface. This is especially pronounced for the decarburised samples because of the greater amounts of ferrite along with softer pearlite at the surface; the samples with small amounts of decarburisation show similar values to those for normal grade 220 both from the results found in this investigation and those in the literature. For the other standard grades of rail and the Infrastar material, with increasing hardness there is a gradual decrease of wear rate. One of the Infrastar results is higher than the grade 220 rail samples but this demonstrates the spread of results possible with wear testing especially when different wear mechanisms occur. The spot welded samples show a similar wear rate to the grade 220 discs for the one sample that did not crack but much higher for the two that did. The sliding WEL samples show some of the lowest wear rates as long they did not spall, but if they did then the results are similar to the decarburised samples.

The results for the wheel discs show that as the hardness of the rail surface increases then the wear rate also increases. This is not in accordance with the theory held by the industry that as the hardness of one surface is increased then the wear of the other decreases[40]. In contrast, the results are in accordance with those found by Steele and Devine[43] who found that changing hardness of one component could increase or decrease the wear of the mating surface dependent on factors such as: the magnitude of the hardness change, the relative wear rates and the wear mechanism. The different contact conditions between twin disc testing and wheel/rail contact will also have an effect; the continuous lubrication will remove the majority of wear debris from the system instead of it acting as third body abrasives and little oxidation of the surface will occur because of the short times of the test.

6.7   Rolling Contact Fatigue
6.7.1   Decarburised Samples

The three measures of crack growth rate (figures 5.5.5.1-5.5.5.3) are the total values from the start to the end of the test and therefore include the time taken before cracks have initiated. Hence it is not an actual growth rate, but an average. A number of cycles are required to plastically deform the surface before cracks can initiate. It can be seen that for the average and maximum length crack growth rates there is a general trend of faster crack growth with increasing decarburisation. This is because ferrite is not as resistant to crack growth as pearlite, although this is dependent on the morphology and orientation of the

pearlite, for cracks running parallel to the lamellar structure the growth rate will be faster than for those running perpendicular to them, since the stronger cementite acts as a barrier to crack growth by deflecting the crack path. This leads to a second reason why crack growth at the surface is faster; pearlite with a lower carbon content has fewer cementite plates which are spaced at greater intervals and therefore fewer barriers to crack growth.

The crack growth results from literature compare well with the results for samples without decarburisation for all three measures of crack growth. Some samples do not follow this trend; one of these is RA09, which was seen to fail after 14000 cycles using the eddy current detector but was continued to run for a further 6000 cycles; this was the same as with the undecarburised samples with the shortest life of 20000 cycles. At the end of the test, the surface in one area had spalled away with large cracks of up to 4.4mm in length and 1.5mm deep, figure 5.6.2.7. No reason has been found for this but it is possible that a prior defect was present in the disc that had remained undetected, such as insufficient grinding to remove the oxide layer. Fletcher *et al.*[25] during initial testing of the SUROS machine after rebuilding, conducted a series of four tests with an average life of 48000 ±2000 cycles while a fifth test under the same conditions failed at 19100 cycles for unknown reasons. During the testing of the white etching layer a subsurface crack was found to be present that had no connection with the cracks at the surface; this can be seen in figure 5.6.3.42 where three cracks propagate from a central point. Examination of the centre of this crack in the SEM gave no sign of any defects where the crack could have initiated, such as oxide inclusions.

The best method of measuring the development of cracks is by calculating the maximum length crack growth rate. This is the measurement of the actual distance of crack growth per cycle and is the criterion used by industry for measuring growth rate within rail. The European standard EN 13674-1 specifies that grade 220 should have a maximum crack growth rate of 55nm.cycle^{-1} measured using a three point notched beam fatigue test[44]. The results for two of the samples without decarburisation are less than this figure whereas the majority of decarburised samples are similar or greater. A direct comparison is not possible because of the different loading conditions and the growth rates presented here include time to initiate. The average crack growth rate indicates the damage over a section of the sample, not just the longest crack, and indicates how severe the damage will be; this includes the probability of the surface spalling as many cracks in an area increases the likelihood that this will occur. The maximum crack depth growth rate is important because as cracks grow deeper into the rail, the more likely they are to cause transverse failure, driven by subsurface residual stresses.

Sample RA06, with a depth of decarburisation of 552μm, has a lower growth rate than any other samples with decarburisation. The reason for this is that it only ran for 6600 cycles because of problems with the equipment due to vibration from the loose running of the rail disc on the lathe shaft. To check how the strain and crack initiation were influenced at

short test durations a second test with no decarburisation was run, DP16. The decarburised sample, RA06, had twice as great a growth rate as that without, RA18, demonstrating that the ferrite at the surface increases the crack growth rate. The two tests at short durations have allowed an examination of the behaviour of discs before substantial cracks have formed. The results of crack growth rate show that they are much lower than for tests with greater numbers of cycles because of the time taken for the surface to plastically deform and for cracks to initiate.

The maximum depth crack growth rate, figure 5.5.5.2, shows a peak at a depth of around 300μm. As the material becomes softer to depths greater than 300μm, more deformation of the surface occurs and, since cracks grow preferentially along the flow lines, their depth is shallower even though their length is comparable. The shear strain is higher with increasing depth of decarburisation, as demonstrated by the graph at a depth of 200μm, figure 5.5.2.10. Therefore the cracks in the sample with the deepest decarburisation, RA17, were found to be long but shallow. This can be seen in figure 5.5.5.4, showing that the ratio of crack length/depth increases with the depth of decarburisation; this indicates that the cracks are penetrating to shallower depths but with similar lengths for those samples with greater amounts of decarburisation. It can also be seen on this graph that for tests of short duration the cracks are longer and shallower, giving a higher ratio, but with subsequent cycles the depth of the crack increases proportionately more than the length, bringing the ratio down to those values found for longer times. This demonstrates that cracks grow along the flow lines of the material; near the surface the strain is higher and therefore short cracks are much longer than they are deep. As the cracks grow to greater lengths the material is less deformed, so the cracks propagate more steeply towards greater depths, this can be seen in figure 5.6.2.5.

Under wholly water lubricated conditions, the maximum shear stress is subsurface (figure 6.4), therefore the ductility of the steel should first reach exhaustion below the surface, and consequently cracks would be expected to initiate subsurface. A number of cracks have been found in the rail disc that do not break the surface, but this is only one view through a crack and it may break the surface in front of or behind the plane of examination. The majority of cracks are found to reach the surface. If cracks did not break the surface then they would be unable to propagate by the fluid pressure mechanism, first proposed by Way[45] and described by, amongst others, Beynon and Kapoor[46]. In addition, cracks are also constrained from initiating subsurface by the material surrounding it and the compressive hydrostatic stresses. Even so, subsurface cracks have been found in rail that are not associated with material defects[18]. It is probable that cracks initiate at the surface after the ductility is exhausted by the high contact stresses arising from the asperity contact.

Surface cracks are seen to initiate at the interface between the proeutectoid ferrite and pearlite colonies, figure 5.6.2.6. The reason for this is that the work hardening of ferrite

and pearlite occur at different rates due to strain partitioning and their different characteristic hardening response. Deformation occurs first in the ferrite because of its lower strength, but consequently this is where ductility exhaustion occurs first, creating internal stresses between the proeutectoid ferrite and the pearlite which result in the material cracking[47]. In figures 5.6.2.3 and 5.6.2.4 it can be seen that cracks propagate along the lines of shear deformation. Cracks do not propagate along the easiest microstructural path, the softer ferrite on the grain boundaries, but instead propagate through the pearlite with occasional meanders into the ferrite. Other cracks have been found that show the crack propagating for some distance along a ferrite grain boundary but only when it is orientated along the lines of shear strain and at depths greater than 200μm. The crack in figure 5.6.2.3 terminates in a ferrite grain, showing that the crack propagation is not greatly increased in ferrite compared with pearlite. If ferrite were very weak in relation to crack propagation, the rate of growth would increase through the ferrite and it would be unlikely that cracks would be found to terminate within it. These observations of crack growth show that cracks under rolling contact fatigue are dominated by the applied stress system especially where they are high near the surface. The microstructural features of the sample also influence crack propagation, especially when the contact stresses are lower and the material is less plastically strained at depths of greater than 200μm. This is in accordance with observations of cracks on rail, which are dominated by the stresses at the surface but at depths of greater than 1mm are influenced by the microstructure[47].

6.7.2   Spot Welded Samples

There are two distinct types of cracks present within the spot welded samples. There are between one and three cracks in each of the spot welds close to the interface where the pearlite has been deformed away from the weld on the leading side, i.e. the interface that enters the contact first (the RHS of figure 5.6.3.2). Evidence for the pearlite being deformed away from the spot weld can be seen in the dip on the Talyrond® profile before each spot weld, with a magnitude of between 9 and 11μm, figure 5.5.3.4. This dip in the disc is responsible for the formation of cracks within the spot weld: the plastic deformation of the pearlite away from the spot weld results in a lack of support for the contact forces and therefore the cracks initiate within the spot weld. This has demonstrated that the interface is not inherently weak, with the broken section of the martensite remaining bonded to the pearlite. The maximum length and depth of these cracks are similar for all three samples whatever the test conditions or number of cycles, with the greatest being for the dry test after 4000 cycles. There is little point in comparing these cracks with normal samples as this is not crack initiation due to RCF but due to the movement of the pearlite away from the spot weld, resulting in cracks initiating because of the brittle nature of martensite. The longest of the cracks is furthest away from the interface and turns such that it is parallel to the surface once it has reached a depth of approximately 400μm. The turning of the crack is due to the much lower tensile stresses and the higher shear stresses away from the surface.

The second type of crack present within the spot welded samples arises due to the plastic deformation and ductility exhaustion within the pearlite at the interface with the white etching layer. This cracking occurs on the trailing interface after extensive deformation, which can be seen visually in the flow lines of the pearlite (figure 5.6.3.4) and by the increase in hardness, figure 5.5.2.17. The Talyrond® profile demonstrates how this deformation has resulted in the pile up of material, up to 20μm high, figure 5.5.3.4. After 4000 cycles of water lubricated running no cracks were found, figure 5.6.3.4, but after the same number of cycles with no lubrication small cracks, less than 150μm in length, were found. This can be explained by the difference in the contact stresses due to the higher traction coefficient, figure 6.4, resulting in the surface of the unlubricated sample being deformed at the surface more extensively. This is demonstrated in figure 5.5.2.11 where at a depth of 0.2mm the dry sample has a higher amount of strain than the lubricated sample. Figure 5.5.2.11 shows the increase in the strain of the pearlite remote from the spot welds; the actual values close to the spot weld in the piled up area are higher, as seen in figure 5.5.2.5, while the hardness is given in figure 5.5.2.17. The longer cracks and higher hardness found with the water lubricated sample after 23000 cycles are due to the accumulation of plastic strain with each cycle even though the stresses at the surface are lower than during dry running. The cracks within the pearlite in this sample were much longer than those in the spot weld, figure 5.5.5.5. Similar cracks have been found in aluminium based metal matrix alloys where the extensive deformation of the matrix is interrupted by the hard and undeformable reinforcing material resulting in easier initiation[48].

These experiments have shown that the presence of a discontinuous layer at the surface of a disc helps to initiate cracks, both within the harder and the softer phase due to different phenomena occurring, which depend on the local conditions. The depth of the spot welds is at least an order of magnitude larger than WEL found on rail and if the dimensions of the two contact situations are taken into account many orders of magnitude different. Therefore the propagation of cracks below the surface would not be expected to be the same as in actual rails because of the different contact stress fields. This was the main motivation for developing the sliding WEL samples.

6.7.3   Sliding WEL Samples

The results of twin disc testing on samples exhibiting WEL simulated by sliding have been split so that the first section concentrates on the crack morphologies while the second describes the numerical results. The development of different crack types are discussed before being related to the test series in which they were found to be present. The numerical results section discusses the results from each test series separately before drawing general conclusions.

6.7.3.1   Cracks within the WEL

The chevron cracks found on all WEL samples where a traction force was present are similar to single cracks found on discs made of martensitic bearing steel[49], while the close array of cracks of the same shape is similar to those on a SiC disc rolling and sliding against an alumina disc[50]. Similar cracks are present on the surface of a steel bar during hot rolling, where a very ductile bulk material with a hard undeformable surface layer (with a sharp interface)[51]. The cracks appear as a result of gross plastic deformation of the subsurface material while the top remains relatively static, cracking to accommodate the strain at the interface. With the rail disc samples the WEL cracks to accommodate the plastic strain of the subsurface pearlite, especially when this occurs in the transverse direction.

Sectioning of the discs has revealed two different types of cracks in the white etching layer during the early stages of rolling contact fatigue. The first is a single crack that propagates from the surface under a mixture of tensile and shear stresses, imposed on the surface by the traction from the wheel. The second type is the formation of a gap in the white etching layer.

6.7.3.1.1   *Single cracks*

An initial crack can be seen in figure 5.6.3.10 that has grown from the surface almost perpendicular to it. Cracks like this in the WEL were found after all tests, even those run for just 2000 cycles, where a creepage force was present; this is due to the mixed tensile and shear stresses present at the surface. The Hertzian contact model developed by Fletcher[19] for a line contact with a half width of 0.31mm, allows the calculation of tensile stresses at the surface where the stress is parallel with the movement of the wheel contact from right to left. Figure 6.12 shows the tensile stresses for a traction coefficient of 0.35 giving a maximum tensile stress of 720MPa at the leading edge of the contact followed by a compressive stress of 1800MPa. The ESDU publication 84017[52] gives equation 6.1 for the tensile failure of brittle materials under line contact loading where the friction is applied along the short dimension of the contact.

$$T_{Max} = 2p_o\mu \qquad\qquad\qquad (6.1)$$

where T_{max} is the critical value of tensile stress at the surface above which a brittle material may fail, p_o is the maximum Hertzian contact pressure and μ is the traction coefficient. Substituting a maximum Hertzian contact pressure of 1500MPa and a traction coefficient of 0.35, the tensile stress to cause cracking of the material will be 1050MPa. This critical tensile stress of failure is higher than the applied stress predicted by the model[19] of 720MPa, therefore the white etching layer would not be expected to crack solely due to tensile stresses with a perfectly smooth surface. Figure 5.6.3.10 demonstrates that the material is not perfectly flat but contains small notches or cracks in the surface, which can act as stress concentrations reducing the applied tensile stress required for cracks to

initiate. For the conditions in figure 6.13 for an edge crack of length, a, in a semi-infinite plate loaded by a uniform tensile stress, σ, the stress intensity factor is given by equation 6.2[53].

$$K_I = 1.1215\sigma\sqrt{\pi a} \tag{6.2}$$

The tensile stress present in the disc is not uniform but decreases with increasing depth therefore the model has also been run for depths of 40μm, the depth of the interface between the WEL and pearlite, and gives results that are lower than those at the surface by less than 0.1MPa on a value at the surface of 720 MPa. The size of a critical stress raising crack will be shorter than 40μm, therefore the tensile stress that the initial crack at the surface sees will be effectively uniform. The use of equation 6.2 is a simplification because the presence of two phases with different mechanical properties will alter the response of the material to the applied stresses. The equation also does not take into account the finite thickness and consequent edge effects of the material. The use of other calculations for stress intensity factor is possible but require the use of an a/w ratio (where w is the width of the material) and this makes evaluation of the equation very difficult.

It has been reported that white etching layer on rails has plasticity characteristics similar to ceramic materials[54], therefore it is possible to estimate fracture toughness using an equation given by Ashby for ceramics, equation 6.3[55].

$$K_{IC} = \sigma_y \sqrt{\pi d_y} \tag{6.3}$$

where σ_y is the tensile yield strength of the material and d_y is the size of the plasticity zone which for brittle materials has been found to be equal to the mean grain size. For a nanocrystalline structure the grain size is between 20-150nm and the yield strength is in the range 3-5GPa[56]; with selection of these values the maximum fracture toughness values is given by:

$$K_{IC} = 5 \times 10^9 \sqrt{\pi \times 20 \times 10^{-9}} = 1.3\text{MPa.m}^{\frac{1}{2}}$$

Rearranging equation 6.2 for crack length gives equation 6.4.

$$a_{crit} = \frac{(K_I)^2}{\pi(1.125\sigma)^2} \tag{6.4}$$

Substituting in the maximum applied tensile stress of 720MPa, given in figure 6.12, for a traction coefficient of 0.35 and a fracture toughness of $1.3\text{MPa.m}^{1/2}$ then the critical crack length is given by:

$$a_{crit} = \frac{\left(1.3 \times 10^6\right)^2}{\pi \left(1.1215 \times 720 \times 10^6\right)^2} = 0.8 \mu m$$

This is smaller than the cracks observed at the surface, figure 5.6.3.10, which have typical lengths of 1.5μm; therefore it would be expected that long cracks could initiate at the surface due to the concentration of stress around these initially small cracks. This calculation assumes that cracks are infinitely sharp whereas those seen are in fact quite rounded; this would explain why only some of the notches at the surface initiate cracks. This is combined with stress relaxation in the areas around a crack which has already propagated[57]. The problem with this calculation is that the estimated value of fracture toughness is very low and approximates to a Griffith material and would therefore behave in a highly brittle manner[58]. A value that has been measured for tempered martensite in a high speed steel has been given by Kim *et al.*[59] as 21.4MPa.m$^{1/2}$ using this value in equation 6.4 gives the following critical crack length:

$$a_{crit} = \frac{\left(21.4 \times 10^6\right)^2}{\pi \left(1.1215 \times 720 \times 10^6\right)^2} = 224 \mu m$$

This is much longer than the thickness of the white etching layer and therefore would have little effect on the cracking of it. The calculation of critical crack length is inconclusive because of the uncertainty in the estimation of fracture toughness values of white etching layer. Cracks could also initiate at the interface, figure 5.6.3.11, due to the bending stresses, combined with the deformation of the subsurface pearlite creating a strain between it and the WEL. It is unlikely that a significant number of cracks initiate subsurface because of the constraint of the surrounding material and the hydrostatic stresses; those that do are likely to be caused by a material weakness. Cracks are therefore expected to initiate at the surface, possibly associated with a material weakness in the WEL, and propagate towards the interface.

Once a crack has initiated in the white etching layer it will grow rapidly because of the brittle nature of martensite until it reaches the interface with the pearlite where the different microstructure deflects the crack and slows its propagation. This deflection is caused by the orientation of the cementite lamellae which are parallel to the surface; the crack would have to cross these lamellar if it were to continue to propagate vertically, therefore it turns and tends to propagate parallel to the lamellae along the flow lines of the pearlite[60], see section 6.7.3.2.2.

6.7.3.1.2   *Gap formation in WEL*

The second type of crack occurring in the WEL is in the form of gaps between 5 and 30μm wide. An example of such a gap is shown in figure 5.6.3.12, with subsurface deformation of the pearlite below it. There are several possible mechanisms by which these gaps could

form within the WEL. Once the gap has formed several other phenomena can occur which are also discussed.

a)   Angled cracks

An initial single crack grows at an angle to the surface, figure 5.6.3.13. As the contact patch approaches this crack it is deforming the WEL elastically both parallel and perpendicular to the surface by up to 5μm[19]. This is illustrated by the schematic in figure 6.14 where a gap has opened up, figure 6.14b, before being deflected downwards, figure 6.14c; once the contact passes to the left hand side of the crack it forces the faces together, figure 6.14d. The normal deformation then breaks the edges of the WEL adjacent to the crack, as seen in figures 5.6.3.14 and 5.6.3.15. The latter figure shows how a large section has broken off. With repeated cycles this would be broken up by the repeated passing of the contact patch leaving a gap in the WEL. The width of this gap will depend on the amount of material removed during deformation. If it is only the edges, as seen in the schematic in figure 6.14e, there will only be gaps at the surface and near the interface but in the centre of the white etching layer the crack faces will still be close together. Figure 5.6.3.16 shows a gap that has initially formed by this mechanism with the centre of both faces of the gap matching each other, but the edges have been removed allowing deformation of pearlite upwards into the gap.

b)   Two adjacent cracks in WEL

Another mechanism is where two cracks develop within the WEL close together; during subsequent cycles the movement of the faces of the two cracks break up the white etching layer in between, with fragments removed as wear debris. A schematic demonstrating the deformation of the surface and how the faces interact is given in figure 6.15. After the contact has passed over the cracks, the faces are forced towards each other. This, combined with the vertical movement, creates debris as the crack faces move against each other. Micrographs of gaps with some debris remaining in them can be seen in figures 5.6.3.15 and 5.6.3.17. The former figure shows that the WEL is still partly intact at the surface, preventing the debris from falling out, whereas the latter is being forced out by the deformation of the pearlite up into the gap. This mechanism would result in the faces not matching up after the test, of which many examples can be found, but the gaps opened up in this way will be small, less than 10μm wide, rather than the common size of 30μm found on the discs.

This mechanism requires two initial cracks within the WEL that are less than 10μm apart. Figure 6.12 predicts tensile stresses greater than 500MPa within 100μm of the front of the contact. The presence of one crack would reduce the tensile stresses within the WEL while the contact area is behind this crack because elastic deformation of the WEL to accommodate them will be easier; the presence of a second crack is therefore unlikely. Once the contact has passed over this first crack it will have little influence on the stresses with the exception that the crack will allow the WEL to be deformed more than when it

was continuous. This will increase the bending/shear stresses within the WEL close to and just in front of the first crack, resulting in the initiation of a second crack.

c)   *Movement of the WEL*

As the contact patch passes over the crack the elastic deformation of the WEL results in the plastic deformation of the pearlite along the surface, shown by the plastic strain seen in figure 5.6.3.16. This plastic deformation means that the WEL is continually moving circumferentially around the disc. With cracks present, any differences in the metallurgy, including orientation of the pearlite, may result in gaps opening up in the WEL. The downwards elastic deformation of the WEL results in the pearlite being deformed up towards and into the crack, as seen in the schematic, figure 6.16 and the micrograph 5.6.3.18. With repeated cycles this deformation can be large, as illustrated in figure 5.6.3.19, where cracks have formed to accommodate the plastic strain. This deformation of the pearlite forces the WEL behind the crack backwards but also prevents that in front of the crack moving backwards, thereby widening the gap. It is the movement of the white etching layer that results in the gaps discussed above being wider than expected.

If gaps open up by this mechanism then unless the white etching layer spalls off, it has to move somewhere else on the disc. One possibility is that the white etching layer moves towards the edges of the disc. Measurement after the tests showed that the width of the running track increased due to plastic deformation, in some case to over 11mm from the original 10mm. This would account for the numerous cracks present near the edges of the disc, as seen in figure 5.6.3.6, but is unlikely to account for the chevron cracks near the centre of the disc. Another option would be if the white etching layer was forced to overlap, which might occur in several ways. Figure 5.6.3.20 shows a section where the WEL has cracked in two places and has been deformed down into the pearlite. With greater amounts of deformation the WEL in front is deformed, along with the pearlite, over the detached segment, as is starting to occur in figure 5.6.3.21. With severe plastic deformation of the surface, such as during dry testing, the overlapping becomes severe, figure 5.6.3.22. It is also possible that the WEL is forced back into itself where extensive cracking occurs, as seen in figure 5.6.3.23, combined with the WEL being deformed down into the pearlite.

6.7.3.1.3   *Wear debris*

Several gaps in the WEL are filled with a substance that is thought to be wear debris; e.g. figures 5.6.3.20 and 5.6.3.24. This substance is in the form of thin slivers of material that are deformed and compacted into the gap. These slivers are created from the wheel disc rolling and sliding against the gaps in the WEL on the rail disc, whose edges act as a cutting tool removing material from the wheel surface. Also mixed in will be wear particles from the surface of the rail disc. This compacting of the debris appears to be aided by water lubrication, especially to the greater depths below the surface, since it was not found during dry tests.

Further evidence for this substance being wear debris has been provided by scanning electron microscopy (SEM) and energy dispersive spectroscopy (EDS) with the results summarised in figure 5.6.3.25. This has shown that the lighter coloured plates contain no oxygen, only iron, carbon and manganese, figure 5.6.3.26; the darker areas between do contain oxygen with iron, whereas there is none in the Bakelite mounting material, which is thus eliminated as a possible source of contamination. The white etching layer has also had an EDS trace taken and shows no oxide present within it, figure 5.6.3.27. Wear debris would be expected to oxidise at the surface, therefore the lighter areas are likely to be the centre of the steel plates from the wheel, whereas the dark areas are probably oxide films that have formed on the surface of the plates once they have been detached from the wheel.

Further evidence that this substance is wear debris is the slight increase in the mass of rail discs, samples RA28 and RA29, and the low wear rate for the other samples. A simple calculation for rail disc RA29 has been carried out to estimate the number and size of the cracks in the surface of the white etching layer and to compare this with the total amount of wear debris produced. Two gaps, A and B, filled with wear debris are shown in figure 6.17 with approximate dimensions. Sectioned sample RA29A with an arc length of 12.17mm was found to contain 4 type A and 5 type B cracks around the centre of the disc. Examination of figure 5.6.3.6 shows that the cracks around the centre had a maximum length of 7.5mm while those at the edge have a density of 28 cracks.(mm.arc)$^{-1}$ and an average length of 640μm. In RA29A the number of cracks at the edges is therefore $28 \times 12.17 \times 2 = 682$; the volume has been calculated assuming that half of the cracks are type A with the other half being type B. The volume of cracks within a section of the rail disc, V_S, is given by equation 6.5, where N is the number of cracks, CSA is the cross sectional area and L is the length of each type of cracks. Summation for each type of crack is carried out to give the total volume within the section of rail disc under examination.

$$V_S = \Sigma\, N \times CSA \times L \tag{6.5}$$

Volume of cracks in RA29A = $4{\times}7.5{\times}0.062{\times}0.046$ + $5{\times}7.5{\times}0.049{\times}0.007$ + $341{\times}0.64{\times}0.062{\times}0.046 + 341{\times}0.64{\times}0.049{\times}0.007 = 0.796$ mm^3

The volume of cracks, V, within a rail disc can be estimated from examination of one sectioned sample and is given by equation 6.6, where D is the diameter of the disc, V_S is calculated using equation 6.5 and Arc is the arc length of the rail disc section that has been examined.

$$V = \frac{\Sigma\, V_S}{Arc} \times \pi \times D \tag{6.6}$$

Volume of cracks in rail disc RA29 , V = $\dfrac{0.796}{12.17} \times \pi \times 47.01 = \underline{9.7\ \text{mm}^3}$

The volume of wear material can be calculated from the mass loss of both rail and wheel discs during the test from the density, ρ, which is assumed to be that of steel (7.85g.cm^{-3}). Any oxide will only be present in small amounts and therefore have little effect on the volume of wear debris.

	RA29	WB26		
Mass Before (g)	181.4744	181.1447		
Mass After (g)	181.4757	180.3668		
Total Mass Loss, m (mg)	- 1.3 +	777.9	=	776.6 mg

$$\text{Wear Volume} = \frac{m}{\rho} = \frac{0.7766}{7.85} = 98.9 \text{ mm}^3$$

$$98.9\text{mm}^3 > 9.7\text{mm}^3$$

$\therefore$ Wear Volume > Crack Volume

This simple calculation has demonstrated that there is an order of magnitude more wear debris produced during the test than the volume of cracks available to be filled. Therefore, sufficient wear debris is created during rolling/sliding to fill any gaps that are formed in the rail disc. There is also no external source of material that could fill the gaps in the disc in this way as the discs are cleaned in alcohol before testing and the lubrication used is fresh, clean, distilled water.

6.7.3.2   Crack propagation into the bulk pearlite

There have been several different crack morphologies observed in discs after twin disc testing.

1) Crack(s) that cross into the pearlite and propagate assisted by the liquid.
2) Crack(s) in the WEL that result in a gap leading to two cracks propagating in the direction of the flow lines.
3) Crack(s) in the WEL that result in a gap forming leading to two cracks propagating in opposite directions.

Figure 6.18 is a flow chart summarising how cracks grow and under what test conditions they occur.

6.7.3.2.1   *Fluid assisted crack propagation*

Some cracks are characterised by a single crack at the surface that is either vertical or slightly inclined to the surface. Once it has crossed the white etching layer it alters direction at the interface, figure 5.6.3.28, so that it propagates along the flow lines of the deformed pearlite. This propagation of cracks below the WEL is similar to the growth of cracks in standard samples without a WEL or in decarburised samples. The common

theory for the growth of these cracks is by the fluid pressure mechanism as described by Bower[61]. This requires a lubricant, such as water, that penetrates the crack and is pressurised by the contact from the wheel disc; this in turn requires the crack at the surface to be orientated so that it is sealed off when the contact is above it, allowing the fluid to be pressurised. Cracks of this type have been found to grow to lengths of over 2.5mm after 26000 cycles. These cracks also have a tendency to branch when they propagate below the surface, as seen in figure 5.6.3.29. A slight variation with these cracks is that some cracks do not cross the interface but actually propagate along it for some distance before turning down into the pearlite, figure 5.6.3.30. Only a few cracks are like this, the majority cross the interface, showing that it is not inherently weak when it is continuous below the surface.

6.7.3.2.2   *Two cracks propagating in the same direction*

The mechanism by which two cracks propagate from the white etching layer along the flow lines of the pearlite is shown schematically in figure 6.19. Once a gap has formed in the WEL it is possible for two cracks to start growing within the pearlite; an example is seen in figure 5.6.3.31. Immediately below the white etching layer the crack turns parallel to the surface in the area of high plastic deformation, not on the interface but within the pearlite. The results are in accordance with those by Nishida *et al.*[62] who used a full size wheel/rail testing rig and found that cracks grew more often near the interface within the pearlite and not along the interface. Once these cracks have started propagating, the pearlite in between starts moving up into the gap in the white etching layer, figure 5.6.3.32. This is because after the wheel has passed over the crack, the WEL is deformed downwards and forces the pearlite towards the surface, figure 6.19c. With increasing cycles the amount of subsurface deformation is increased and the pearlite is forced completely through the WEL until it is prominent above the surface, figure 5.6.3.33. This process results in two initial cracks extending to allow the deformation to occur, as well as the pearlite cracking further near the surface within the extrusion. The extrusion also results in the WEL in front being deformed downwards into the pearlite and subsequently cracking.

With a further increase in the number of cycles this deformation is continued but the action of the wheel disc results in the extrusion being chopped at the surface. This deformation of the pearlite in between the original cracks results in ductility exhaustion and the formation of many cracks, which are stained during etching and appear dark in the SEM micrographs, figure 5.6.3.34. The white etching layer in front of the crack is broken up and initiates further cracks within the pearlite. The numerous cracks and the deformation of the pearlite results in the formation of steps on the rail disc, figures 5.6.3.34 and 5.6.3.35. In the latter figure it can be seen that these steps on the surface lead to the growth of very long cracks, over 4.5mm after 36000 cycles. It is likely that these long cracks develop from the initial pair of cracks by the fluid pressure mechanism; it is unlikely that ductility exhaustion alone would cause them to grow to this length. Even with the numerous cracks present, it may still be possible for the fluid trapped in the crack to transfer stresses to the crack tip; once

the contact has passed over the crack mouth it will close up any cracks below it, pressurising the liquid present. Figure 5.6.3.35 shows that these cracks are much longer than their depth because of their tendency to grow along the flow lines of the material.

6.7.3.2.3   *Cracks propagating in opposite directions*

Once a gap has formed in the WEL it is possible that cracks can start propagating in opposite directions to each other, shown schematically in figure 6.20 with an example given in figure 5.6.3.12. The schematic shows that as the contact approaches the gap, the elastic deformation of the WEL is backwards (i.e. against the direction of movement of the counter disc) with the corner of the gap acting as a stress concentration initiating a crack, figure 6.20a. Once the contact has passed the gap, the elastic deformation of the WEL results in the deformation of the pearlite up towards the gap and the subsequent ductility exhaustion results in it cracking in the opposite direction to the first crack. As the number of cycles is increased, the pearlite is deformed to a greater extent with extension of the cracks to accommodate the strain, as seen in figure 5.6.3.19. This deformation of the pearlite results in it being completely deformed up into the crack and sealing the surface, removing any wear debris in the gap, figure 5.6.3.36. This plastic deformation of the pearlite demonstrates how the ductility of metals is increased because of the high hydrostatic stresses resulting from the constraint of surrounding material. The pearlite that fills the gap has to move from below the WEL, this can be seen in figure 5.6.3.16 with the cracks growing near the interface to accommodate the strain. This figure also demonstrates that the WEL behind the crack has moved slightly away from the gap, shown by the movement of the proeutectoid ferrite.

These cracks rarely appear on their own but are adjacent to other similar cracks, as demonstrated in figure 5.6.3.37. These cracks are more common above the longer type of cracks than away from them, figure 5.6.3.35. This suggests that the movement of the material above the long cracks creates bending forces in the WEL, promoting further crack growth. With these gaps being close together, the cracks growing from them join up. After the gaps have joined up the white etching layer will spall off because cracks grow in three dimensions, not just in the plane of the cross section, figure 5.6.3.38. Once the white etching layer has spalled off, the severe plastic deformation of the subsurface pearlite leads to further cracking and results in slivers of material being removed as wear debris, figure 5.6.3.39.

6.7.3.3   Crack growth within each test series
6.7.3.3.1   *Unidirectional tests*

The figures of maximum crack length and depth (figures 5.5.5.7 and 5.5.5.8) show that with fewer than 8000 unidirectional cycles cracks are larger for the WEL samples than for those without. This is because cracks are easy to initiate within the WEL because of its brittle nature. It is also easy for cracks to propagate within the WEL until they reach the interface with the pearlite where the different microstructure deflects a crack and slows its

propagation. This is demonstrated by the cracks in RA28, after 8000 cycles, which have only just propagated through the WEL and for a short distance into the pearlite. There is no direct evidence for the brittle behaviour of the white etching layer but, in general, steel with a high hardness, and therefore high UTS, behaves in a more brittle manner than steel with a lower hardness[1] and has been found in a previous investigation to behave like a ceramic[54].

For tests with more than 10000 cycles, cracks are larger for discs containing a white etching layer than for those without. With a large number of cycles, e.g. sample RA25 after 26000 cycles, very long cracks have grown, resulting in steps on the surface. There is also a proliferation of smaller cracks growing in opposite directions above the steps which have started to join up but have not yet spalled; other cracks are also present on sections of the disc away from the steps. With an increase to 36000 rail disc cycles, RA26, the white etching layer has completely spalled over large areas of the disc, with the maximum crack length increasing to over 5mm from 2.5mm for RA25. The reason for this being the large amount of plastic deformation of the pearlite below the white etching layer while it is being formed and during testing resulting in ductility exhaustion. The plastic strain is in the same direction therefore the total strain will be greater for the same number of SUROS cycles compared with those without a WEL, figure 5.5.2.12. This greater amount of plastic strain means that the cracks are longer but shallower after a greater number of cycles, figure 5.5.5.10, the opposite trend of samples without WEL. WEL-free samples have less deformation, therefore the flow lines are steeper and for the same crack length the depth is much greater, figure 5.5.5.8. The crack densities, figure 5.5.5.11, for the majority of the white etching layer tests are similar but lower than for tests without WEL. This is because samples without WEL have many weak spots at the surface, namely ferrite/pearlite boundaries, which allow the initiation of short crack that do not necessarily propagate[47]. The tests with WEL after 26000 and 37000 cycles show a higher density for the section of disc above the longer cracks than away from them because of the ability of the top face of the crack to bend, allowing further cracks to initiate within the WEL.

6.7.3.3.2   *Reversed tests*
The cracks present within the reversed test samples are of a similar length and depth as the unidirectional samples for tests with fewer then 8000 cycles. The crack lengths for rail discs RA20, with 2000 cycles, and RA23, with 8000 cycles, are greater than for tests without a white etching layer with a similar number of cycles. As the number of cycles is increased to 30000 (RA24) then both length and depth remained at similar magnitudes to the shorter reversed tests; the unidirectional tests and those without a WEL became much greater. Test disc RA20 with 2000 cycles demonstrates that the cracking of the white etching layer occurs after a small number of cycles whether the strain is unidirectional or in the reverse direction, but propagation depends on the strain history of the subsurface pearlite. The effect of the reversed plastic strain is that once cracks have propagated through the WEL they do not transfer very readily into the pearlite because the

deformation has not been in one direction, but occurs first one way and then the other, delaying ductility exhaustion. This is a demonstration of ratchetting, with the reversed tests showing much delayed ductility exhaustion, unlike the unidirectional tests. Tests employing reversed cycling have been carried out by Tyfour and Beynon[63] for the dry wear of discs, whose results show that the wear rate is decreased because of ratchetting in one direction followed by the other, delaying the attainment of the ductility limit and creation of wear particles. Further work by Tyfour and Beynon on RCF of discs found that a series of reversals was beneficial to rolling contact fatigue life for essentially the same reason[64]. The strain results show that the sample with 2000 cycles (RA20) is similar to RA31 where the WEL was created but no rolling/sliding test was carried out, in contrast the hardness values are higher as it includes the work hardening in both directions. Once the cracks have propagated through the WEL a gap is formed, which is commonly filled with pearlite and results in two cracks propagating in opposite directions to accommodate the strain, figure 5.6.3.22.

6.7.3.3.3   Dry tests

The consequence of running with no lubrication is in the maximum shear stress being at the surface rather than subsurface, as is the case with water lubricated contact. The stresses are also higher than for water lubricated contact, thus the amount of shear strain is much greater at a depth of 0.2mm than for the other samples; this is also the case with the increase in hardness. This greater amount of deformation at the surface can be seen in figure 5.6.3.40 where the white etching layer has been deformed over itself.

The lengths of cracks within dry samples is similar to water lubricated samples without a WEL, but are much shorter than the unidirectional tests, only 670μm after 32000 cycles. The depth of these cracks is less than in samples without WEL and similar to the reversed tests. A typical crack is seen in figure 5.6.3.40, propagating in one direction along the flow lines; the WEL has also been deformed up towards the surface. As these cracks only propagate in one direction they do not join up, therefore the white etching layer spalls by the exhaustion of ductility of the pearlite below the surface, figure 5.6.3.41, after 31000 cycles. The higher strain of the samples is responsible for a higher length-to-depth ratio than for samples without WEL with the cracks following the flow lines of the material. The difference in the length of dry cracks in comparison with the water lubricated unidirectional tests demonstrate that a lubricant is required to propagate the cracks to great lengths. This is because RCF cracks propagate under rolling/sliding conditions with the assistance of fluid, first discovered by Way[45] and described by Bower[61]. The fluid assists the crack growth by allowing the high contact stresses at the surface to be transferred to the crack tip by fluid pressure. A second reason is that fluid reduces the crack face friction, which increases the effective stress intensity at the tip by preventing the faces from touching and hence accelerating crack growth. This involves the water penetrating the crack with the contact from the wheel resulting in the pressurisation of the fluid and the transfer of tensile stresses to the crack tip[65]. The reason that cracks are of a

similar length to those in water-lubricated samples without a WEL are the much greater plastic strains that the surface has undergone; demonstrating that cracks are able to grow by ductility exhaustion of the material.

6.7.3.3.4   *Pure rolling tests*

These tests have shown that when no imposed traction was present between rail and wheel, i.e. pure rolling, no RCF cracks can form on the rail disc, demonstrated by the complete absence of cracks after 2000 cycles for RA27. The cracks found in disc RA30 after 23500 cycles (figure 5.6.3.8) are circumferential around the disc and are much shorter, less than 250µm in length. These cracks have two cracks propagating in opposite directions, figure 5.6.3.25 and as such are similar to those described in section 6.7.3.2.3 above. These cracks have formed because of the lateral subsurface deformation of the rail disc, figure 5.6.3.9, resulting in large tensile stresses within the white etching layer, which can not be accommodated and are therefore relieved by cracking. Measuring the width of the cracks in figure 5.6.3.9 and comparing with the change in width of the disc has demonstrated that up to 50% of the plastic deformation is accommodated by the cracks faces moving apart. The rest of the deformation will be accommodated by the pearlite at the edges where no WEL was present and by elastic strains within the intact white etching layer. The reason that the cracks are not parallel to the edge of the disc is because the deformation may result in some creep forces occurring at the edge of the contact width. It is the lack of a significant traction force between rail and wheel discs that results in the white etching layer remaining intact around the centre of the disc because the tensile or shear stresses are insufficient to create the initial crack in the WEL.

The depth of cracks is similar to those for the reversed series of tests, demonstrating that plastic flow of the subsurface pearlite is required to allow cracks to propagate below the interface, figure 5.5.5.8. Figure 5.5.2.12 shows that the strain is similar to that measured on RA31, therefore little plastic deformation has occurred, whereas figure 5.5.2.20 shows some hardening has occurred but less than for samples with an applied creep force.

6.7.4   Surface Metallurgy and Rolling Contact Fatigue: Twin Disc Tests

The two surface metallurgical features under investigation, decarburisation and white etching layer, differ in several ways but are also similar in some. Whichever treatment has been carried out, the surface of the disc is still made from steel with the same elastic properties; the only difference in chemical composition is the amount of carbon present in the decarburised samples. The obvious key feature is the difference in microstructure and consequently hardness of the two layers but this is not solely responsible for the different mechanisms of RCF. One aspect is the interface between the layer and the bulk material with the WEL showing an abrupt change, whereas decarburisation is a gradual change. The gradual change of the decarburisation means that the measurements of plastic strain up to the surface show no discontinuities, while the WEL has an abrupt change at the interface.

A comparison has been made between the growth of rolling contact fatigue cracks and the surface hardness of the rail disc. Figure 6.21 is the crack length growth rate and shows that there is a large spread of results for each test series; there is also no obvious correlation with the hardness. Therefore figure 6.22 has been plotted, although this does not take into account the different number of cycles that each test has undergone. This graph shows that, with the exception of the unidirectional WEL tests, the crack length is longer for decarburised samples than for WEL samples. One interesting graph is figure 6.23, which plots crack density against the hardness of the rail disc surface. This shows that the number of cracks present within the decarburised and normal samples is greater than in the WEL samples. These graphs demonstrate that different mechanisms are involved with RCF when the surface of the disc has been treated in different ways.

The effect of both surface metallurgical layers can be to reduce the lifetime of the discs through wear or rolling contact fatigue when compared with the normal samples. Decarburisation increases the crack growth and wear rate of the samples because there are more sites for initiation but also because the decarburised surface has lower resistance to crack growth. This is because of the lower carbon content at the surface, increasing the amount of ferrite but also increasing the interlamellar spacing of the pearlite and consequently reducing the hardness and strength of the material. In contrast, white etching layer with its much harder surface and abrupt interface also promotes RCF and wear but this depends on how the WEL has been formed. The spot welded samples demonstrate how a confined area of hard material at the surface promotes crack formation because of the difference in ductility, there are fewer cracks than in normal samples (figure 6.23) but they are longer and grow at a faster rate, figures 6.21 and 6.22. The behaviour of the sliding WEL samples depends on the strain history of the subsurface pearlite with the longest cracks observed when the strain was unidirectional. One consequence of the hard layer is to limit the number of cracks that grow compared with the normal and decarburised samples. This is probably due to the cracks within the WEL being initiated due to tensile stresses, which are relieved when several cracks are close to each other.

6.8 Decarburisation and Wheel/Rail Contact

The following two sections aim to relate the laboratory results discussed above to actual wheel/rail contact, but the complicated nature of the contact makes this difficult. The conditions used in the laboratory for twin disc testing are typical of those found on the railhead with stresses up to 1500MPa and a low slip ratio (or sliding velocity)[66]. Conditions at the gauge corner of the rail result in much higher creep ratios and much higher wear rates; therefore, the results from these tests can only be applied to contact between the wheel tread and the railhead and not flange/gauge corner contact. Scaling between twin disc testing and full size wheel/rail contact is possible using the maximum orthogonal shear stress shown in figures 6.4 and 6.5; the half space of line contact for twin

disc is 0.31mm and 6.6mm for wheel/rail contact. These contact stresses are predicted using a Hertzian contact analysis, which is only valid for elastic contacts. This is not strictly appropriate because ratchetting is a plastic deformation process but, after initial work hardening has occurred, the deformation per cycle is very small and therefore approximates to elastic contact conditions.

The decarburisation on a rail after manufacture has a maximum depth of 0.5mm, equivalent to 23.5µm on a rail disc. No tests have been conducted at such shallow depths because of the difficulty obtaining the correct depth during heat treatment and subsequent grinding of the disc. The test disc, RA16, with the lowest amount of decarburisation (93µm) shows that there is little difference from the samples without decarburisation in the crack growth rate, although there is a slight increase in the rail disc wear rate and a slight reduction in the wheel disc wear rate over those without decarburisation. This is because there is only slightly more ferrite at the surface for the decarburised test than for those without and the increase in pearlite interlamellar spacing will only be slight, demonstrated by the micrograph of the new rail, figure 5.4.1.

Decarburisation is going to have little effect on the ratchetting of rail because it will deform plastically to a depth of about 5mm compared to a depth of decarburisation of 0.5mm. A wheel/rail contact lubricated by rain (traction coefficient of 0.1-0.3[27]) has maximum shear stresses located subsurface, therefore the elastic shakedown will occur first below the surface, as well as at the surface due to the micro-scale stress field due to asperity contact. But when the rail is dry the traction coefficient will be greater than 0.3 and the shear stresses will be at a maximum at the surface. Rail in the temperate climate of the UK will undergo mixed cycles of lubricated and unlubricated contact over its lifetime; there will also be other contaminants on the surface such as oil, leaf mulch and Sandite (a compound added to increase traction). These variable conditions result in accumulation of strain in the railhead being gradual up to a depth of 5mm. It is likely that the high stresses arising from asperities will result in the ratchetting of the surface of the rail first. The decarburised surface found on rail, figure 5.4.1, shows only a slight increase in the amount of ferrite at the surface when compared to the bulk, therefore it is likely to strain harden like the bulk material; demonstrated by the rail disc samples with a depth of decarburisation of 93µm. The rail section shown in figure 5.4.2 shows a much greater amount of decarburisation and it is highly possible that some of this surface is removed by wear before a large amount of work hardening has occurred. Initial wear is also likely to be increased because of the uneven surface roughness and the oxide layer resulting from hot rolling increasing the shear stresses at the surface.

The increase in crack growth rate within the decarburised layer will only have an effect on wheel/rail contact during the early stages of crack growth. After the crack has initiated it may grow roughly twice as fast through the decarburised layer than it would in the non-decarburised metal (from figure 6.11 for the samples after 6600 cycles), but this difference

would cease when the crack reaches a depth of 0.5mm. In practice, it is probably less than this because of the gradient structure of the decarburised layer and the work hardening of this layer. This increase would mean that cracks will develop slightly faster during the initial stages but would have little long-term effect on the lifetime of the rail. It has been found that by the time a crack on the surface is visible to inspection it will have penetrated to a depth of at least 5mm below the railhead[67]. Therefore, in terms of maintenance, the rolling contact fatigue cracks may appear slightly earlier in rail with a decarburised layer, but this is only going to be one tenth less at the most than rail which had no decarburised layer. One other aspect of the decarburised surface is the greater number of initiation points for cracks, reflected in the higher density for some decarburised samples when compared to the normal samples, figure 6.23. A greater number of cracks initiating gives a higher probability of a crack propagating until the rail fails.

It has been demonstrated that the amount of material lost from the surface of the disc by wear is small compared to the depth of decarburisation. The crown of a railhead wears at a rate of 1mm for 50MGT of mixed passenger and freight traffic, therefore it will take at least 25MGT to wear the decarburised layer completely away, which for busy lines in the UK is approximately one year[68]. The wear of rail is a combination of wear particle formation and oxidation, whose wear particles will then act as third body particles increasing wear. It is therefore hard to relate the wear of rail to that during twin disc testing, because the continuous water lubrication used means that any wear debris is removed, combined with the short duration of the tests and the frequency of cycles limiting the amount of oxidation that can occur. The results from twin disc testing indicate that the effect of decarburisation will only increase the wear of rail slightly on the railhead. The higher creep forces at the gauge corner result in higher wear rates and a change in the mechanism[33] may be effected by the presence of a decarburised layer.

There is no evidence from this series of tests to show a delay in the observation of crack initiation which Rotthauser et al.[69] attributed to an increase in the amount of wear removing short cracks. A reason for this may be that the decarburised surface may have been able to remove the asperities faster than a rail without decarburisation because of the higher initial wear rate and ease of deformation. Therefore, the higher asperity contact stresses at the surface will only be present for shorter times and therefore ductility exhaustion will take longer. It is also possible that the wear rate with twin disc testing is lower than wheel/rail because of the absence of wear debris acting as a third body abrasive. Rotthauser et al.[69] also used a grade of rail with a eutectoid carbon concentration which is harder than the grade 220 used in these experiments and consequently does not have any ferrite in the bulk of the rail; consequently the difference in mechanical properties will be more severe. It is also difficult to tell from the micrographs what sort of gradient structure the decarburisation has which may have had an effect on the results. The results presented here are much more in accordance with Boulanger's finding of no noticeable difference in the effect of decarburisation on rolling contact fatigue[70].

With the maximum depth of decarburisation on rail being 0.5mm, the increased amount of ferrite at the surface, when compared to the bulk of grade 220 rail, is only small. Therefore there will be little increase in the wear rate of the rail. The wear of rail will initially be higher before it has had chance to strain harden and therefore any cracks that do initiate because of the greater amount of initiation sites will be worn away before they are able to propagate. The higher rate of crack propagation within the ferrite may decrease the life of rail slightly but this is unlikely to be significant over the life of the rail. In conclusion, the presence of decarburisation on rail is unlikely to have any noticeable effect on its total life.

6.9   WEL and Wheel/Rail Contact

The presence of a hard white etching layer on the railhead is likely to have a deleterious effect on the life of rail; this is the opposite of what is found by coating bearings with a hard surface layer[71]. Examination of the white etching layer found on a railhead shows that, unlike that produced by sliding on the disc, it is discontinuous and present in patches. There are therefore several ways that cracks can initiate at the surface. The spot welded samples showed that the presence of a hard layer when surrounded by a softer one leads to the initiation of cracks at the interface due to the difference in ductility; further evidence for this is given by the observations of rail, figure 5.4.9. The presence of proeutectoid ferrite at the surface has also been found to be responsible for initiating cracks, figure 5.4.10. Figure 5.4.6 shows that at the surface the WEL has been deformed by the wheels as demonstrated by the morphology of the proeutectoid ferrite. This may have been before the white etching layer has formed but has resulted in the proeutectoid ferrite being inclined to the surface. The ferrite has probably initiated the crack at 45° to the surface in figure 5.4.6, whereas the vertical crack has most likely been initiated by the tensile and/or shear stresses at the surface.

The high hardness of the WEL results in it being easier for cracks to initiate, especially when there is a stress concentration at the surface, as demonstrated by the greater length of cracks for WEL samples compared to those without at short test durations, figure 5.5.5.7. Once a crack has initiated and propagated up to the interface with the pearlite then it is possible for it to propagate into the bulk material. But the presence of a high hardness layer means that, once cracks have initiated, the stresses are relaxed resulting in fewer cracks at the surface than for samples without a WEL, figure 6.23. Crack growth to failure is a probabilistic process: the greater the number of cracks, the greater is the chance of one of them resulting in the failure of the rail. But the wear of rail without a WEL means that many cracks are removed before they can propagate. With a WEL the wear is much lower which, combined with the brittle behaviour, results in much longer cracks initially that are unlikely to be removed. The result is that when a WEL is present there are fewer cracks but each crack is more likely to propagate until failure of the rail than in standard rail samples.

Once a crack has initiated at the surface, either within the WEL or at an interface, it is possible that it can propagate into the bulk rail. This will depend on many variables but the most important is the strain history of the deformed pearlite. The presence of a WEL on the surface of rail will indicate that the pearlite has already been heavily deformed for the white etching layer to have formed. The WEL model, section 4.2, has demonstrated that a temperature rise alone is not sufficient for formation but a heavily deformed surface is also required. This deformation will be in the same direction when the WEL is formed and afterwards; in other words, it will be similar to the unidirectional twin disc tests with a WEL above the deformed pearlite. This deformation may make the pearlite susceptible to propagation of the cracks that have grown through the WEL and into it. The reason that rail does not behave like a coated bearing is that the bulk structure of the bearing is martensite with a hardness of around 500HV and consequently is much more resistant to plastic deformation. The plastic deformation of the subsurface does not occur and cracks rarely initiate. Furthermore, the coatings on industrial bearings are much more uniform than the rather uneven and unintentional white etching layers observed on rails.

Cracks that have propagated through the WEL can grow in two ways. The first may result in failure of the rail due to RCF crack growth, demonstrated by the unidirectional twin disc tests. This may occur after the rail has been in service many years where the pearlite has been heavily deformed resulting in easy propagation of the crack. The crack that has initiated on the right in figure 5.4.5 has resulted in the failure of the rail but it is impossible to know whether the WEL formed because of the crack or the crack formed because of the white etching layer. One key aspect of this type of crack is the orientation of the mouth at the surface, which has to be sealed when the wheel is above it to allow the crack to propagate by the fluid pressurisation mechanism. This is the reason that few cracks propagate to sufficient lengths for the rail to break under residual and bending stresses[72]. This has been demonstrated by the presence of only a few steps and long cracks, but with many more shorter cracks present in the WEL in figure 5.6.3.35.

The second type of crack grows along or near the interface of the white etching layer and pearlite but does not turn down into the bulk. Instead it may return to the surface or may join other cracks resulting in the WEL breaking away as wear debris[21]. These cracks may initiate at an interface or, like those in twin disc testing, in the continuous WEL. This will increase the wear rate of the surface because of the much larger particles being detached. Clayton has found that a major cause of rail wear is the formation of white etching layers that crack and spall off[73]. Twin disc testing has also shown that spalling of the WEL will leave behind a deformed surface that may have many cracks in it because of the plastic deformation which will either promote wear or may accelerate RCF cracks and rail failure.

The results from twin disc testing on samples with a simulated white etching layer have shown an increase in the rolling contact fatigue crack growth and the wear of the discs. It is

difficult to quantify the deleterious effect on rail life but the graphs of crack length, figure 5.5.5.7, and crack depth, figure 5.5.5.8, demonstrate for the unidirectional WEL tests that the rate of crack growth is between 1.5 and 5 times greater than for samples without a WEL. It is therefore expected that the life of the rail under rolling contact fatigue will be reduced by a factor that lies within this range, but this will depend on the crack being able to transfer from the WEL into the bulk of the rail. A secondary factor will be whether a rail experiences the same amount of plastic deformation that the unidirectional samples do. Although, the rail has to undergo initial cycles while the white etching layer is formed which will also plastically deform the subsurface layer, so that that the total amount of subsurface strain will be similar to that in the unidirectional samples.

The wear of pearlitic rail has been found to occur at a rate of 1mm for every 50 MGt [74] using the data for an average train, with a mass of 536t spread over 40 axles[75], this is equivalent to 3.7 million cycles and therefore a wear rate of 0.27nm/cycle. The number of cycles required for wear to remove a depth of 100μm, a typical depth of white etching layer, is 0.37 million cycles, which is equivalent to an average life in track of 8 weeks or 5MGt. Using the wear of the rail discs it is possible to estimate how much faster rail with a WEL will wear in comparison to that without. Figure 6.24 plots the wear of the rail discs against the number of cycles; the wear is the loss of radius, calculated using density from the mass loss, during the test. If the straight line through the standard sample is regarded as the wear of pearlite on rail then the point where it crosses a horizontal line, drawn at the level of the WEL samples, will approximate to 8 weeks of rail life. The higher wear of the WEL samples shows how much faster it would be to remove a layer of material 100μm thick if a WEL were present. For the sample, RA25, after 26000 cycles it would be 5.6 weeks and 2 weeks after 37000 cycles for RA26. It can therefore be seen that the results predict a reduction in the life of rail, at least for the first 100μm, by a factor between ¼ and ¾ if WEL were present. The reason for the range is that RA26 had much greater wear of the pearlite once the WEL had been removed than did RA25.

There are many complications to this prediction, the first being that the wear of pearlite is not constant but has a higher initial rate while the surface work hardens[7], which would result in a parabolic curve and lower wear rate at greater numbers of cycles and therefore a greater reduction in rail life for the WEL samples. White etching layer is only present at the surface up to a limiting depth, below this is pearlite that work hardens while the WEL is being removed. This may resist further wear once the WEL has been removed although the results from RA26 indicate that the wear will continue to increase because of spallation of the subsurface pearlite, figure 5.6.3.39. White etching layer has been found to take two weeks to start forming on the surface of the railhead[21] but it is unclear that once it has worn away whether it will form again in the same place. If it does not then the higher wear rate of the 100μm at the surface will have little effect on the total rail life as long as no cracks propagate into the bulk rail resulting in spalling of the pearlite.

It can therefore be seen, even if the quantitative estimations are inaccurate, that the consequence of having a white etching layer on the surface of a rail leads to some deterioration of rail life by promotion of rolling contact fatigue and/or wear of the rail.

6.10 References

1. Honeycombe, R. W. K. and Bhadeshia, H. K. D. H., Steels: Microstructure and Properties, 2nd Ed., Edward Arnold, London, UK, 1995
2. Bae, C. M., Nam, W. J. and Lee, C. S., Effect of microstructural features on ductility in hypo-eutectoid steels, Scripta Materialia, 41, (6), p605-610, 1999
3. Gray, G. T., Thompson, A. W. and Williams, J. C., Influence of microstructure on fatigue crack initiation in fully pearlitic steels, Metallurgical Transactions, 16A, (5), p753-760, 1985
4. Gray, G. T., Thompson, A. W., Williams, J. C. and Stone, D. H., The effect of microstructure on fatigue crack propagation in pearlitic eutectoid steels, Canadian Metallurgical Quarterly, 21, (1), p73-78, 1982
5. Hyzak, J. M. and Bernstein, I. M., The role of microstructure on the strength and toughness of fully pearlitic steel, Metallurgical Transactions, 7A, (8), p1217-1224, 1976
6. Kavishe, F. P. L. and Baker, T. J., Effect of prior austenite grain size and pearlite interlamellar spacing on strength and fracture toughness of a eutectoid rail steel, Materials Science and Technology, 2, (8), p816-822, 1986
7. Perez-Unzueta, A. J. and Beynon, J. H., Microstructure and wear resistance of pearlitic rail steel, Wear, 162-164, (1), p173-182, 1993
8. Beynon, J. H., Garnham, J. E. and Sawley, K. J., Rolling contact fatigue of three pearlitic rail steels, Wear, 192, (1-2), p94-111, 1996
9. Birks, N. and Meier, G. H., Introduction to High Temperature Oxidation of Metals, 1st Ed., 1983
10. Krauss, G., Microstructure, processing and properties of steels, in: Vol 1: Properties and Selection: Iron, Steel and High Performance Alloys, Metals Handbook, American Society of Metals, USA, p126-139, 1996
11. Clayton, P. and Jin, N., Unlubricated sliding and rolling/sliding wear behaviour of continuously cooled, low/medium carbon bainitic steels, Wear, 200, (1-2), p74-82, 1996
12. Mitao, S., Yokoyama, H., Yamamoto, S., Kataoka, Y. and Sugiyama, T., High strength bainitic steel rails for heavy haul railways with superior damage resistance, in: IHHA STS Conference on Wheel/Rail Interface, Moscow, Russia, p489-496, 1999
13. Williams, J. A., Engineering Tribology, 1st Ed., Oxford University Press, Oxford, UK, 1994
14. Lojkowski, W., Djahanbakhsh, M., Burkle, G., Gierlotka, S., Zielinski, W. and Fecht, H. J., Nanostructure formation on the surface of railway tracks, Materials Science and Engineering A, 303A, (1-2), p197-208, 2001
15. Newcomb, S. B. and Stobbs, W. M., A transmission electron microscopy study of the white etching layer on a railhead, Materials Science and Engineering, 66, (2), p195-204, 1984
16. Baumann, G., Fecht, H. J. and Liebelt, S., Formation of white etching layers on rail treads, Wear, 191, (1-2), p133-140, 1996
17. Heller, W., Schweitzer, R. and Weber, L., Modern developments in rail steel metallurgy and production, Canadian Metallurgical Quarterly, 21, (1), p3-15, 1982
18. D173, Report No. 1: Review of rolling contact fatigue in rails, Office for Research and Experiments of the International Union of Railways, Utrecht, The Netherlands, 1990
19. Fletcher, D. I., The influence of lubrication on the fatigue of pearlitic rail steel, PhD Thesis, Department of Mechanical Engineering, University of Sheffield, UK, 1999
20. Kapoor, A., Franklin, F. J., Wong, S. K. and Ishida, M., Surface roughness and plastic flow in rail wheel contact, Wear, 253, (2-3), p257-264, 2002
21. Clayton, P. and Allery, M. B. P., Metallurgical aspects of surface damage problems in rails, Canadian Metallurgical Quarterly, 21, (1), p31-46, 1982

22.   Olofsson, U. and Telliskivi, T., Wear, plastic deformation and friction of two rail steels: a full-scale test and a laboratory study, Wear, 254, (1-2), p80-93, 2003

23.   Fletcher, D. I. and Beynon, J. H., Equilibrium of crack growth and wear rates during unlubricated rolling/sliding contact of pearlitic rail steel, Proceedings of the I.Mech.E: Part F, Journal of Rail and Rapid Transit, 214, (2), p93-105, 2000

24.   Hill, D. N. and Clayton, P., The development of a laboratory rolling contact fatigue testing procedure, Report No: TM MF 32 / 263-384-32, British Rail Research, Derby, UK, 1982

25.   Fletcher, D. I. and Beynon, J. H., Development of a machine for closely controlled rolling contact fatigue and wear testing, Journal of Testing and Evaluation, 28, (4), p267-275, 2000

26.   Garbar, I. I., Microstructural changes in surface layers of metal during running-in friction processes, Meccanica, 36, (6), p631-639, 2002

27.   Stolarski, T. A. and Tobe, S., Rolling Contacts, 1st Ed., Professional Engineering Publishing Limited, Bury St Edmunds, UK, 2000

28.   Tyfour, W. R., Beynon, J. H. and Kapoor, A., The steady state wear behaviour of pearlitic rail steel under dry rolling/sliding conditions, Wear, 180, (1-2), p79-89, 1995

29.   Krause, H. and Lehna, H., Factors influencing the real trend of the coefficient of friction of two elastic bodies rolling over each other in the presence of dry friction, in: The Mechanics of Contact Between Deformable Bodies, Pater, A. D. and Kalker, J. J.(Ed's), Delft University Press, The Netherlands, p343-358, 1975

30.   Tyfour, W. R., Interaction between wear and rolling contact fatigue in pearlitic rail steels, PhD Thesis, Department of Engineering, University of Leicester, 1995

31.   Clayton, P. and Danks, D., Effect of interlamellar spacing on the wear resistance of eutectoid steels under rolling/sliding conditions, Wear, 135, (2), p369-389, 1990

32.   Clayton, P., The relation between wear behaviour and basic material properties for pearlitic steels, Wear, 60, (1), p75-93, 1980

33.   Bolton, P. J. and Clayton, P., Rolling/sliding wear damage in rail and tyre steels, Wear, 93, (2), p145-165, 1984

34.   Bohmer, H. J., Ertz, M. and Knothe, K., Shakedown limit of rail surfaces including material hardening and thermal stresses, Fatigue and Fracture of Engineering Materials and Structures, 26, (10), p985-998, 2003

35.   Archard, J. F., Contact and rubbing of flat surfaces, Journal of Applied Physics, 24, (8), p981-988, 1953

36.   Hutchings, I. M., Tribology: Friction and Wear of Engineering Materials, 1st Ed., Butterworth-Heineman, Oxford, UK, 1992

37.   Millman, Y. V., Grinkevych, K. E., Chugunova, S. I., Lojkowski, W., Djahanbakhsh, M. and Fecht, H. J., Tribological properties of the surface of railway tracks, studied by indentation technique, Wear, 258, (1-4), p77-82, 2005

38.   Kapoor, A., Wear by plastic ratchetting, Wear, 212, (1), p119-130, 1997

39.   Black, S. C., Chiles, V., Lissaman, A. J. and Martin, S. J., Principles of Engineering Manufacture, 3rd Ed., Arnold, London, UK, 1996

40.   Kalousek, J., Wheel/rail damage and its relationship to track curvature, in: Proceedings of the 6th International Conference on Contact Mechanics and Wear of Rail/Wheel Systems, Gothenburg, Sweden, Ekberg, A., Kabo, E. and Ringsberg, J. W.(Ed's), Chalmers University of Technology, Sweden, p1-16, 2003

41.   Garnham, J. E. and Beynon, J. H., Dry rolling/sliding wear of bainitic and pearlitic steels, Wear, 157, (1), p81-109, 1992

42.   Franklin, F. J., Weeda, G. J., Kapoor, A. and Hiensch, E. J. M., Rolling contact fatigue and wear behaviour of the Infrastar two material rail, in: Proceedings of the 6th International Conference on Contact Mechanics and Wear of Rail/Wheel Systems, Gothenburg, Sweden, Ekberg, A., Kabo, E. and Ringsberg, J. W.(Ed's), Chalmers University of Technology, Sweden, p559-566, 2003

43.   Steele, R. K. and Devine, T. J., Wear of rail/wheel systems, in: Proceedings of the 1st International Conference on Contact Mechanics and Wear of Rail/Wheel Systems, Vancouver, BC, Canada, p293-315, 1982

44.   BS EN 13674-1, Railway Track Applications - Rail - Part 1: Flat Bottom Symmetrical Rails 46kg/m and Above, British Standards Institution, London, UK, 2003

45.   Way, S., Pitting due to rolling contact, Journal Applied Mechanics, 57, pA49, 1935

46.   Beynon, J. H. and Kapoor, A., The interaction of wear and rolling contact fatigue, in: Reliability Assessment of Cyclically Loaded Engineering Structures, Smith, R. A.(Ed), Kluwer Academic Publishers, Dordrecht, The Netherlands, p1-26, 1997

47.   Eden, H. C., Garnham, J. E. and Davis, C. L., Influential microstructural changes on rolling contact fatigue crack initiation in pearlitic steels, Materials Science and Technology, 21, (6), p623-629, 2005

48.   Walker, J. C., Rainforth, W. M. and Jones, H., Lubricated sliding wear behaviour of aluminium alloy composites, Wear, 259, (577-589), 2005

49.   Soda, N. and Yamamoto, T., Effect of tangential traction and roughness on crack initiation/propagation during rolling contact, Transactions of the ASLE, 25, (2), p198-206, 1982

50.   Kudish, I. I. and Burris, K. W., Modern state of experimentation and modelling in contact fatigue phenomenon: Part I - Contact fatigue. Normal and tangential contact and residual stresses. Non metallic inclusions and lubricant contamination. Crack initiation and crack propagation. Surface and subsurface., Tribology Transactions, 43, (2), p187-196, 2000

51.   Li, Y. H. and Sellars, C. M., Behaviour of surface oxide scale before roll bite in hot rolling of steel, Materials Science and Technology, 17, (12), p1615-1623, 2001

52.   Anon., 84017 Contact Phenomena II: Stress fields and failure criterion in concentrated elastic contacts under combined normal and tangential loading, Engineering Science Data Unit (ESDU), Institute of Mechanical Engineers, London, UK, 1984

53.   Broek, D., Elementary engineering fracture mechanics, 4th Ed., Kluwer Academic Publishers, Dordrecht, The Netherlands, 1986

54.   Lojkowski, W., Millman, Y., Chugunova, S. I., Goncharova, I. V., Djahanbakhsh, M., Burkle, G. and Fecht, H. J., The mechanical properties of the nanocrystalline layer on the surface of railway tracks, Materials Science and Engineering A, 303, (1-2), p209-215, 2001

55.   Ashby, M. F., Materials selection in mechanical design, 1st Ed., Pergamon Press, 1992

56.   Ivanisenko, Y. V., Lojkowski, W., Valiev, R. Z. and Fecht, H. J., The mechanism of formation of nanostructure and dissolution of cementite in a pearlitic steel during high pressure torsion, Acta Materialia, 51, (18), p5555-5570, 2003

57.   Fletcher, D. I., Hyde, P. and Kapoor, A., Growth of multiple rolling contact fatigue cracks driven by rail bending modelled using a boundary element technique, Proceedings of the I.Mech.E: Part F, Journal of Rail and Rapid Transit, 218, (3), p243-253, 2004

58.   Tetelman, A. S. and McEvily, A. J., Fracture of Structural Materials, 1st Ed., John Wiley and Sons Inc., New York, USA, 1967

59.   Kim, C. K., Park, J. H., Lee, S., Kim, Y. C., Kim, N. J. and Yang, J. S., Effects of alloying elements on microstructure, hardness, and fracture toughness of centrifugally cast high-speed steel rolls, Metallurgical and Materials Transactions, 36A, (1), p87-97, 2005

60.   Aita, C. R. and Weertman, J., The effect of microstructure on fatigue crack propagation in iron - carbon alloys, Metallurgical Transactions, 10A, p535-544, 1979

61.   Bower, A. F., The influence of crack face friction and trapped fluid on surface initiated rolling contact fatigue cracks, Transactions of the ASME: Series F, Journal of Tribology:, 110, (10), p704-711, 1988

62.   Nishida, S. I., Sugino, K., Urashima, C. and Masumoto, H., Study on contact rolling fatigue of rails: II. Analysis by high speed rail testing machine, Bulletin Japanese Society of Mechanical Engineers, 28, (243), p1819-1824, 1985

63.   Tyfour, W. R. and Beynon, J. H., The effect of rolling direction reversal on the wear rate and wear mechanism of pearlitic rail steel, Tribology International, 27, (6), p401-412, 1994

64.   Tyfour, W. R. and Beynon, J. H., The effect of rolling direction reversal on fatigue crack morphology and propagation, Tribology International, 27, (4), p273-281, 1994

65.   Beynon, J. H., Brown, M. W. and Kapoor, A., Initiation, growth and branching of cracks in railway track, in: Engineering Against Fatigue, Sheffield, UK, Beynon, J. H., Brown, M. W., Smith, R. A., Lindley, T. C. and Tomkins, B.(Ed's), Balkema, Rotterdam, The Netherlands, p461-472, 1997

66.   Lewis, R. and Olofsson, U., Mapping rail wear regimes and transitions, Wear, 257, (7-8), p721-729, 2004

67.   Rolling contact fatigue in rails: a guide to current understanding and practice, RT/PWG/001, Railtrack, London, UK, 2001

68.   Purbrick, M. C., The use of rails on British Railways, in: 2nd International Heavy Haul Conference, Colorado Springs, USA, International Heavy Haul Association, Virginia Beech, Virginia, USA, p380-387, 1982

69.   Rotthauser, N., Muders, L. and Grohmann, H.-D., Influence of surface-decarburisation area of the rail on rolling contact fatigue, Eisenbahningenieur, 52, (3), p62-65, 2001

70.   Boulanger, D., Rail metallurgical developments to address the changing needs of railway, in: The World Congress on Railway Research, WCRR 2003, Edinburgh, Scotland, UK, Immediate Proceedings, Beccles, Suffolk, UK, p932-939, 2003

71.   Maurer, R. E., Friction, wear and corrosion control in rolling bearings through coatings and surface modification: A review, Journal of Vacuum Science Technology, 4, (6), p3002-3006, 1986

72.   Ringsberg, J. W., Shear mode growth of short surface-breaking RCF cracks, Wear, 258, (7-8), p955-963, 2005

73.   Clayton, P., Predicting the wear of rails on curves from laboratory data, Wear, 181-183, (1), p11-19, 1995

74.   Tolley, K. H., Rail wear and associated problems, in: Fourth R.I.A. Track Sector Course, p4.6.4/1-4.6.4/11, 1992

75.   Pritchard, R., Fox, P. and Hall, P., British Railways Locomotives & Coaching Stock 2005, Ed., Platform 5, Sheffield, UK, 2005

6.11 Figures
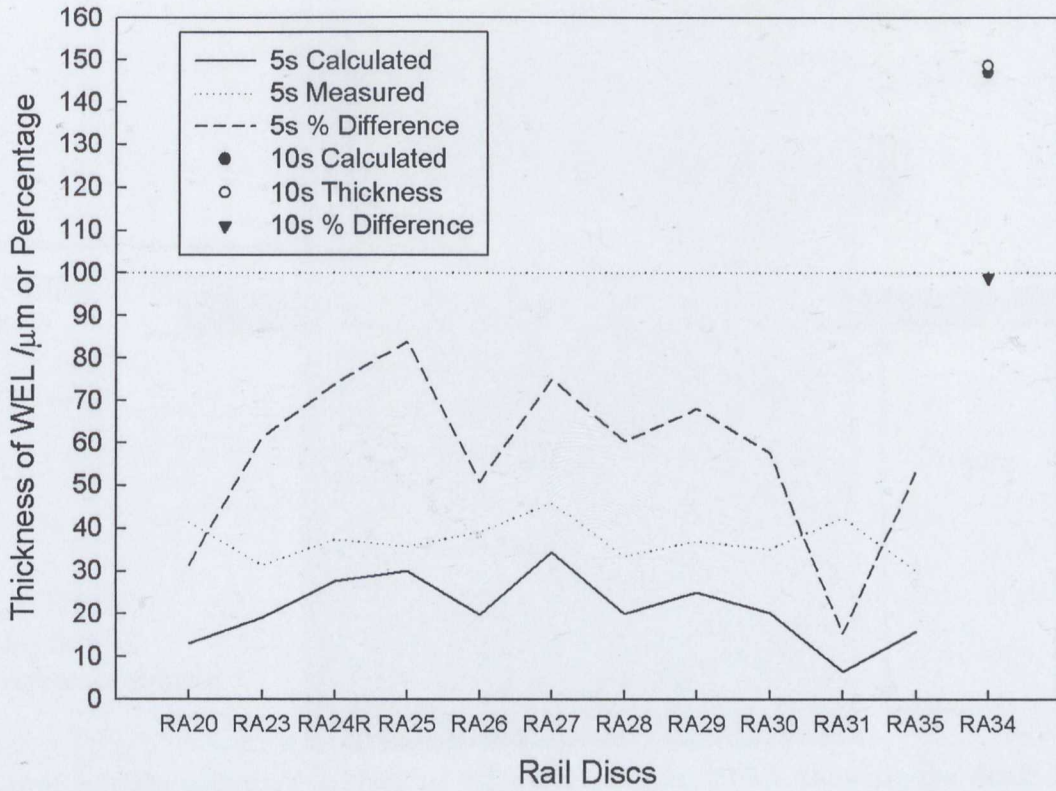
Figure 6.1: Comparison of calculated and observed thickness of WEL

Figure 6.2: Decarburisation of the corner of reference sample 10 demonstrating how depth of decarburisation of bloom is greatest at the corners
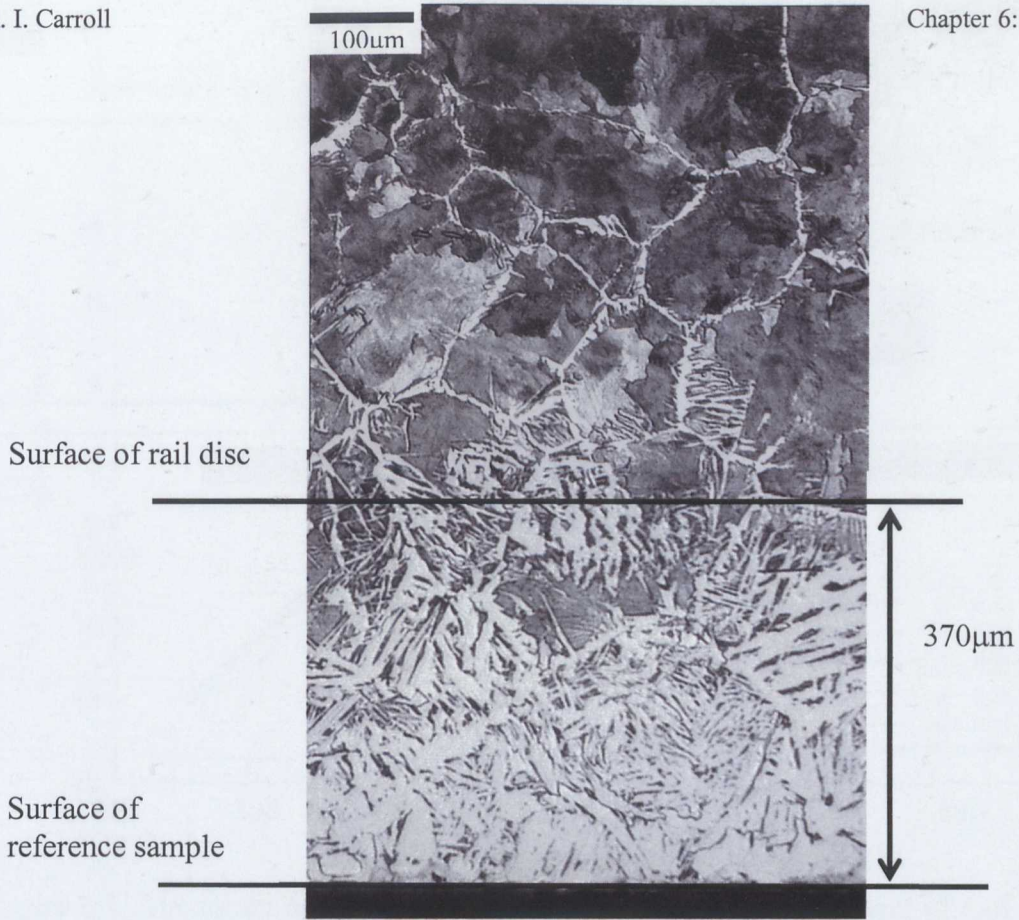
Figure 6.3: Decarburised surface of reference sample, DE38, showing the depth the rail disc, RA17, is ground to.
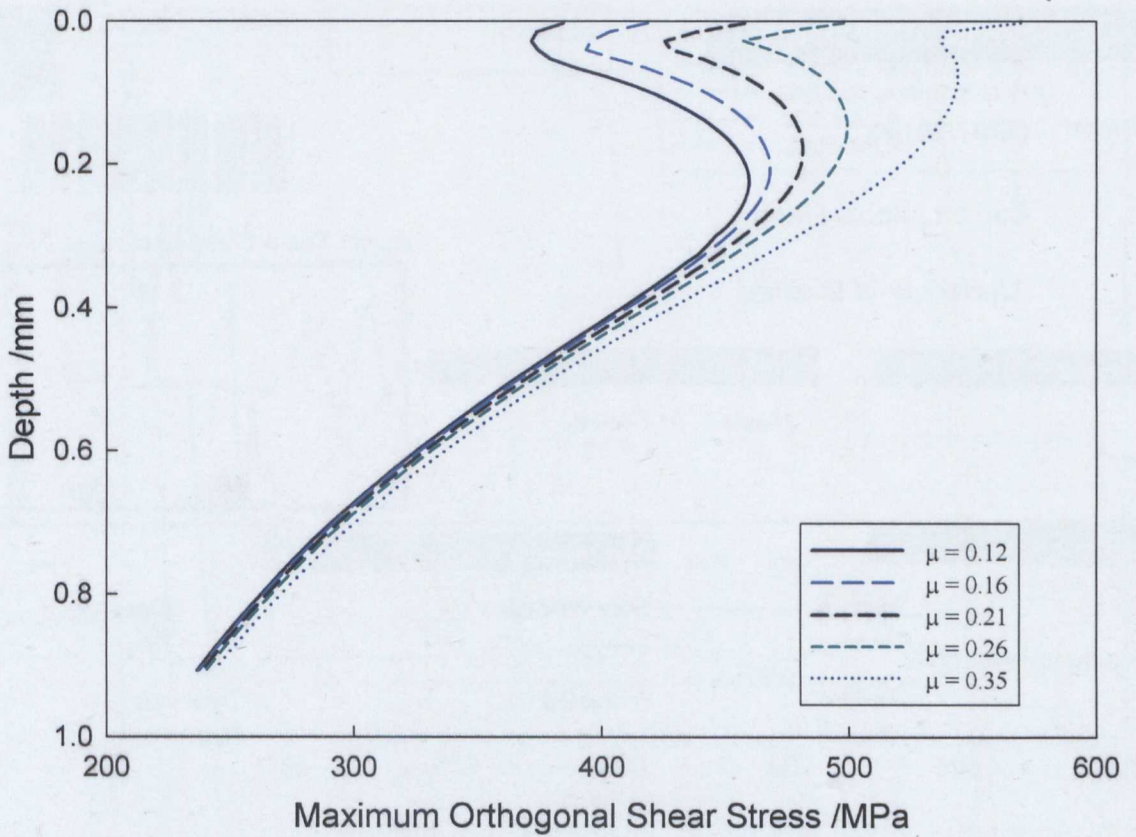
Figure 6.4: Maximum orthogonal shear stress below a twin disc testing contact of half width, a = 0.31mm (after Fletcher [19]).
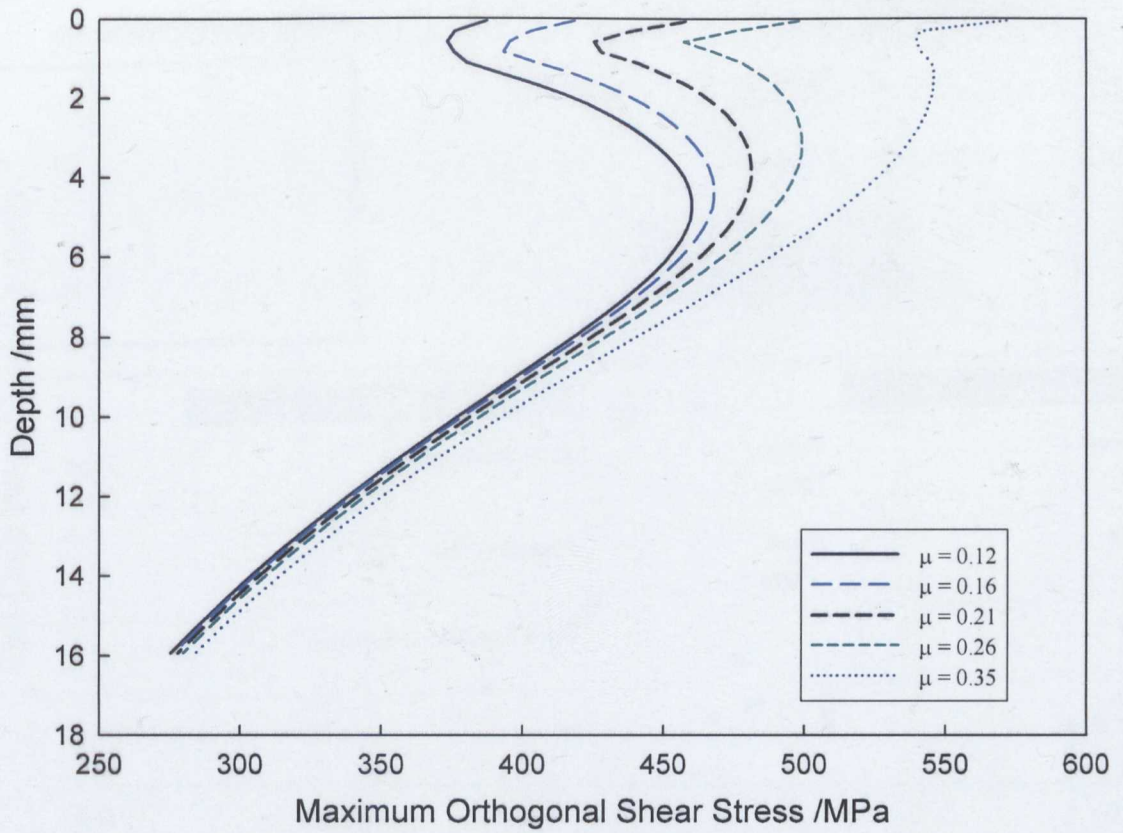
Figure 6.5: Maximum orthogonal shear stress below wheel/rail contact of half width, a = 6.6mm (after Fletcher [19]).
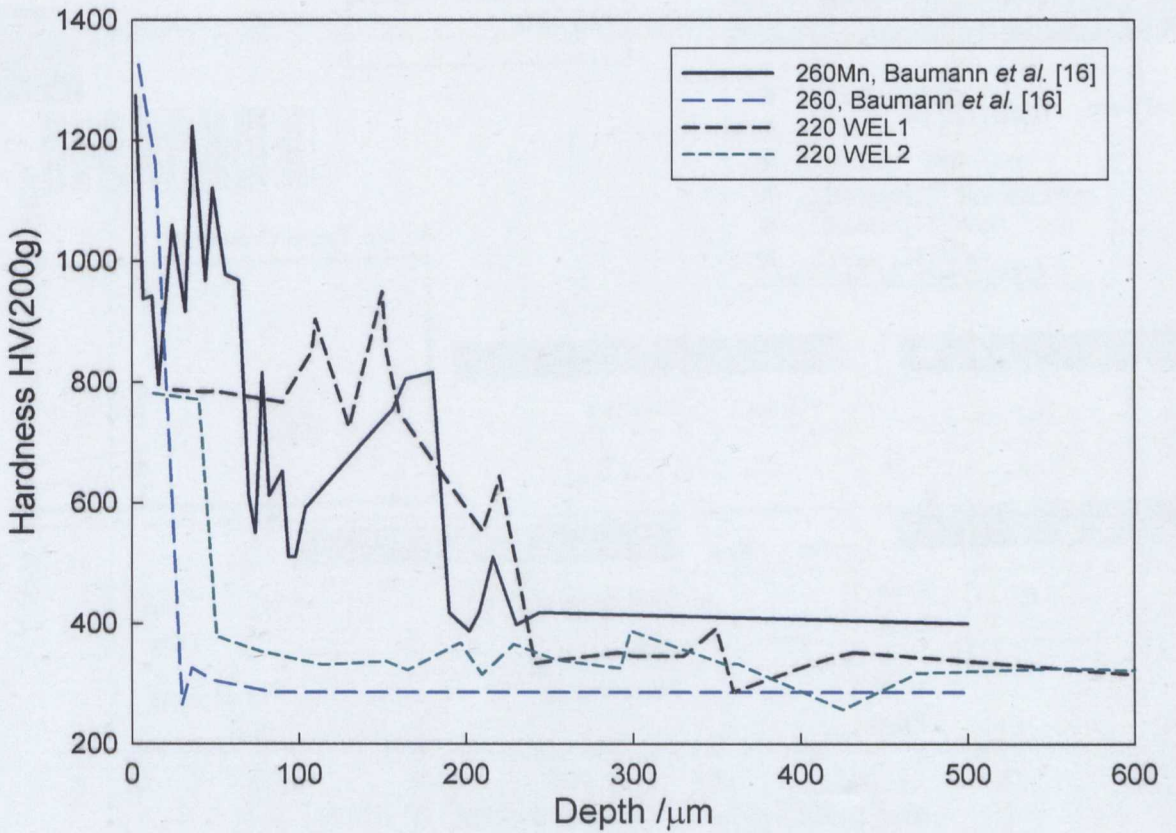
Figure 6.6: Microhardness traverse of WEL samples examined here and taken from Baumann et al.[16]
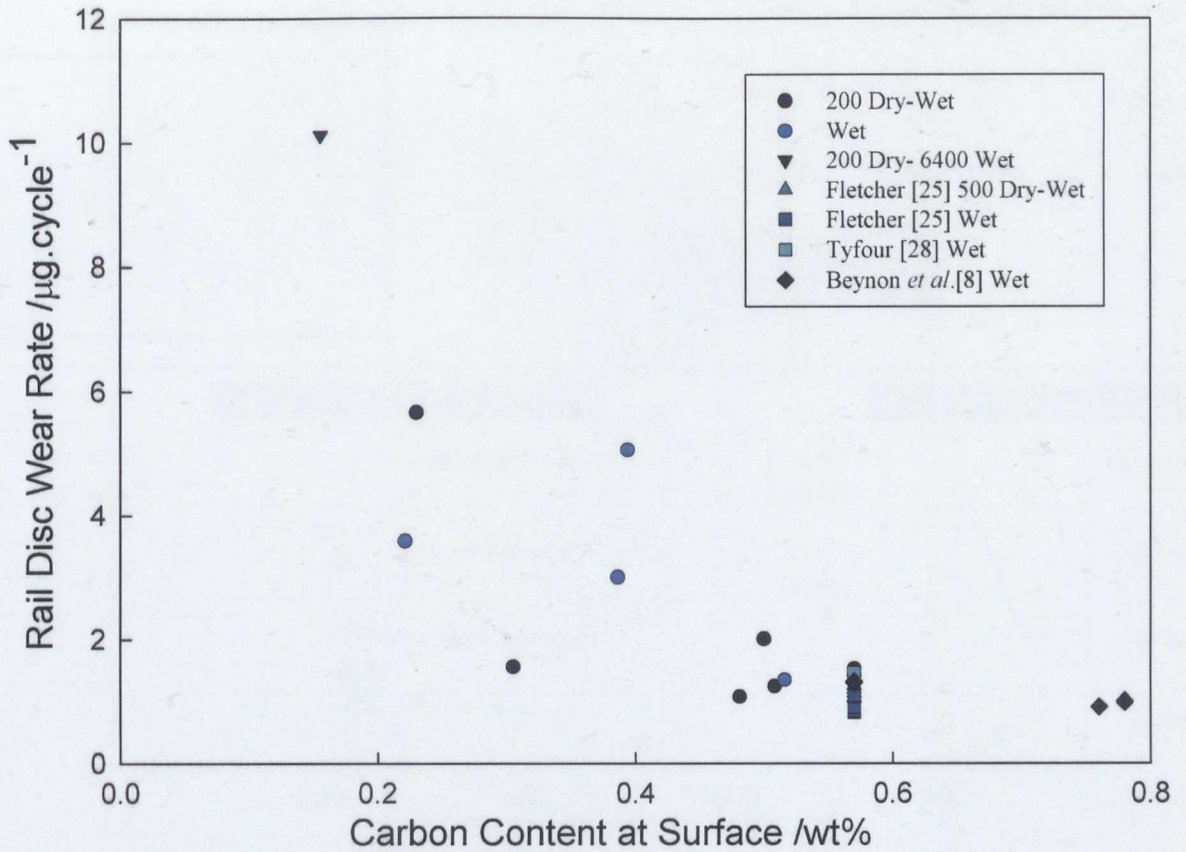
Figure 6.7: Effect of carbon content on the wear rate of rail disc sample with data from literature, (Beynon *et al.*[8], Fletcher *et al.*[25], Tyfour *et al.*[28])
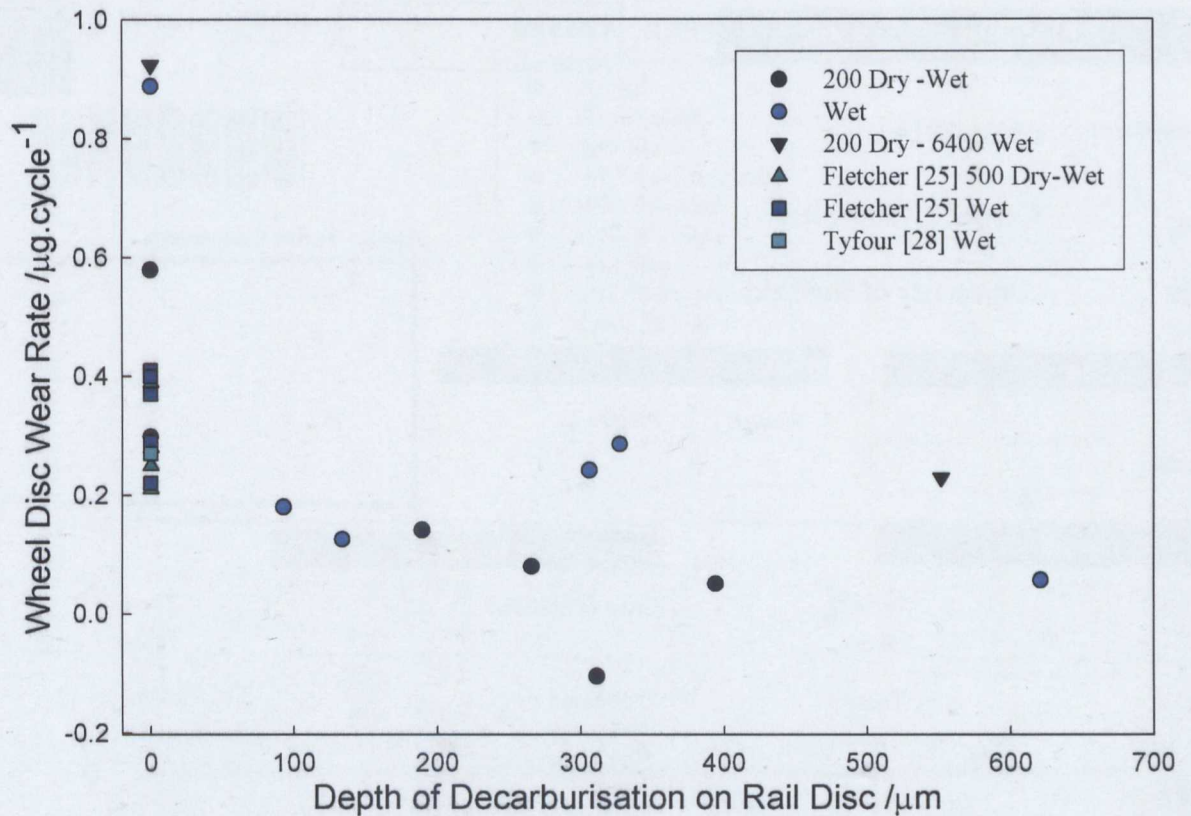
Figure 6.8: Wheel disc wear rate of sample with data from literature also plotted. (Fletcher *et al.*[25], Tyfour *et al.*[28])

237
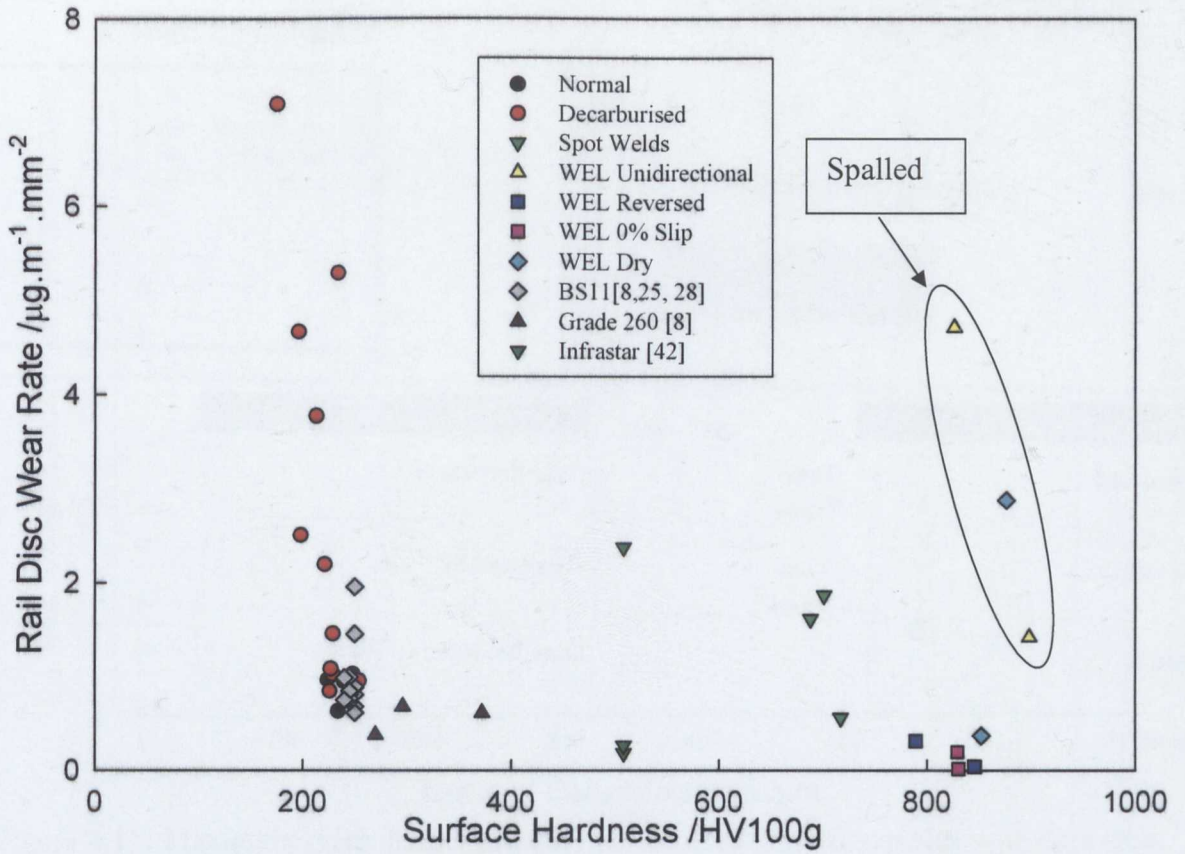
Figure 6.9: Comparisons of rail disc wear rates of decarburised and WEL samples
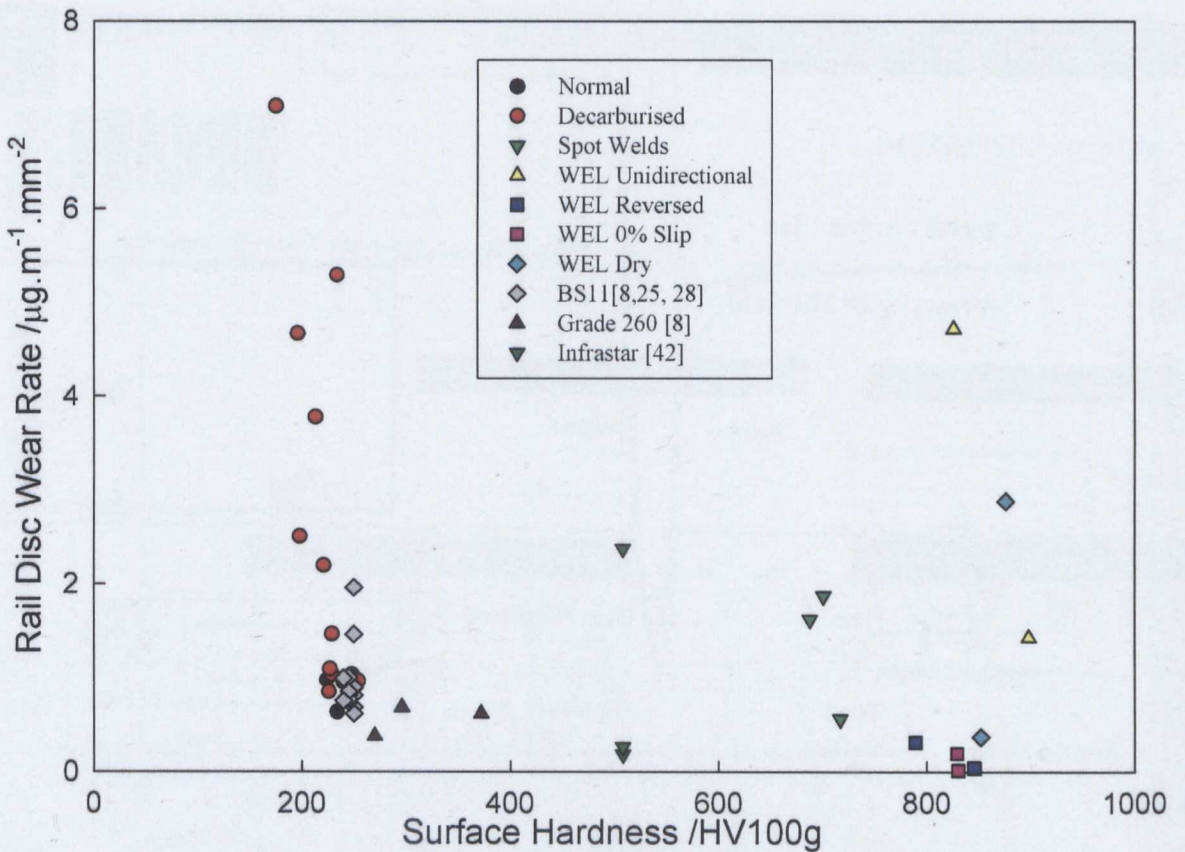
Figure 6.10: Comparisons of wheel disc wear rates of decarburised and WEL samples
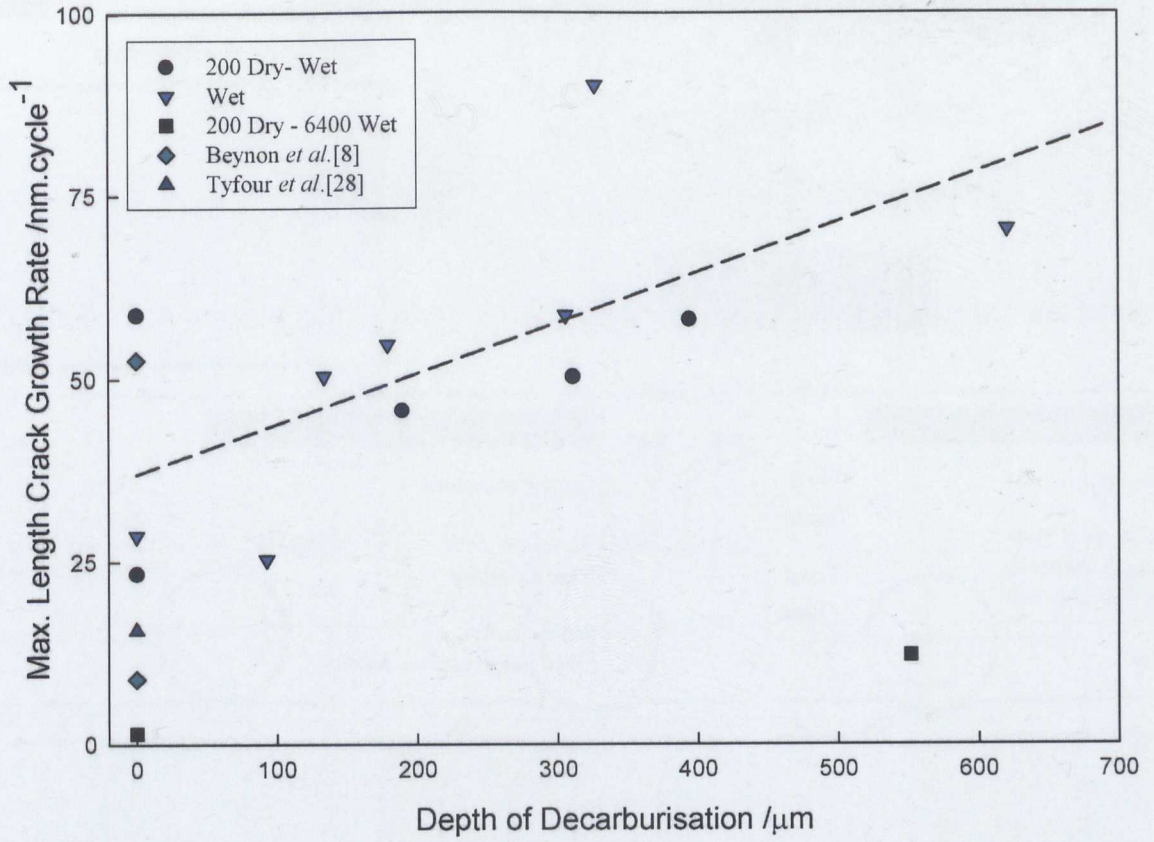
Figure 6.11: Maximum crack length growth rate for decarburised samples with data from literature for standard samples (Beynon *et al.*[8], Tyfour *et al.*[28])
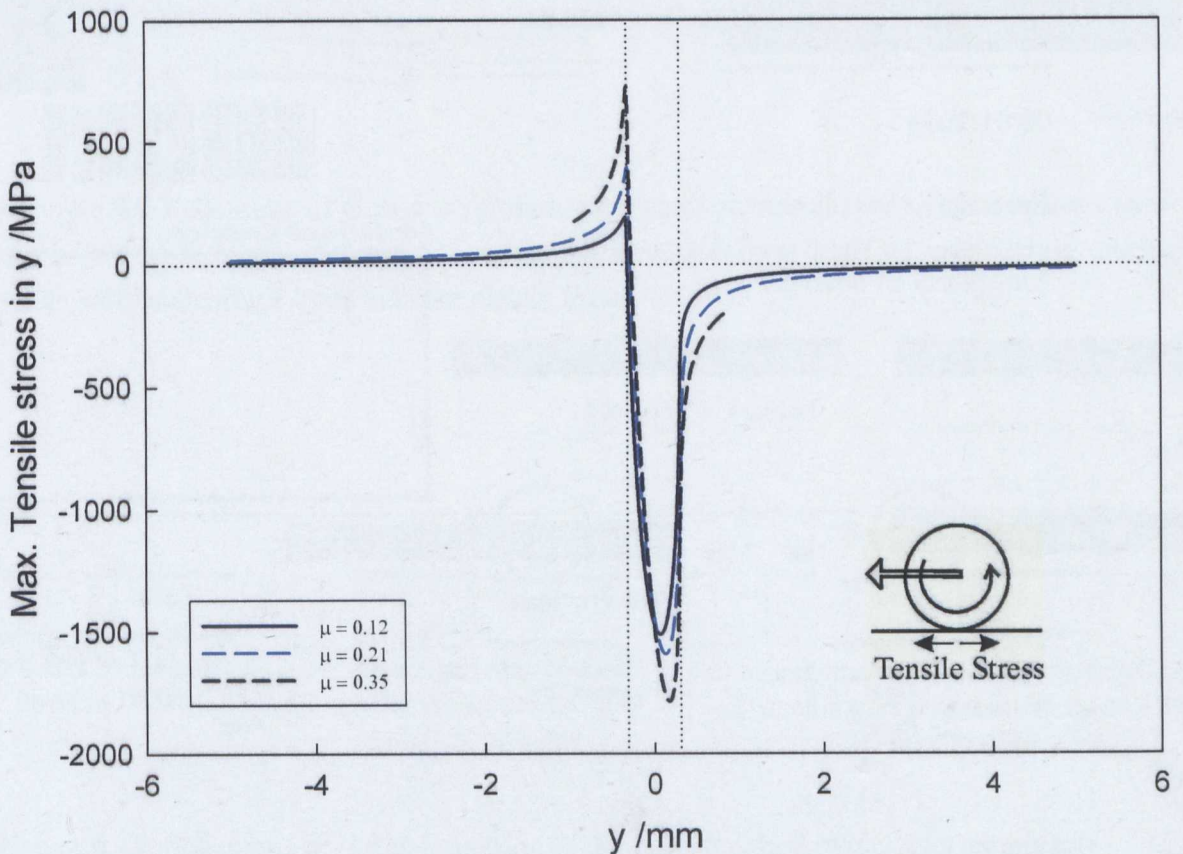
Figure 6.12: Maximum tensile stress at surface parallel to contact (after Fletcher [19])
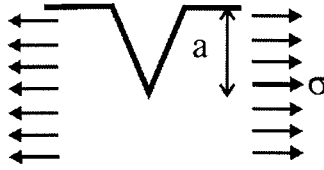
Figure 6.13: A semi-infinite plate with a surface crack of length, *a*, under a uniform tensile stress, σ
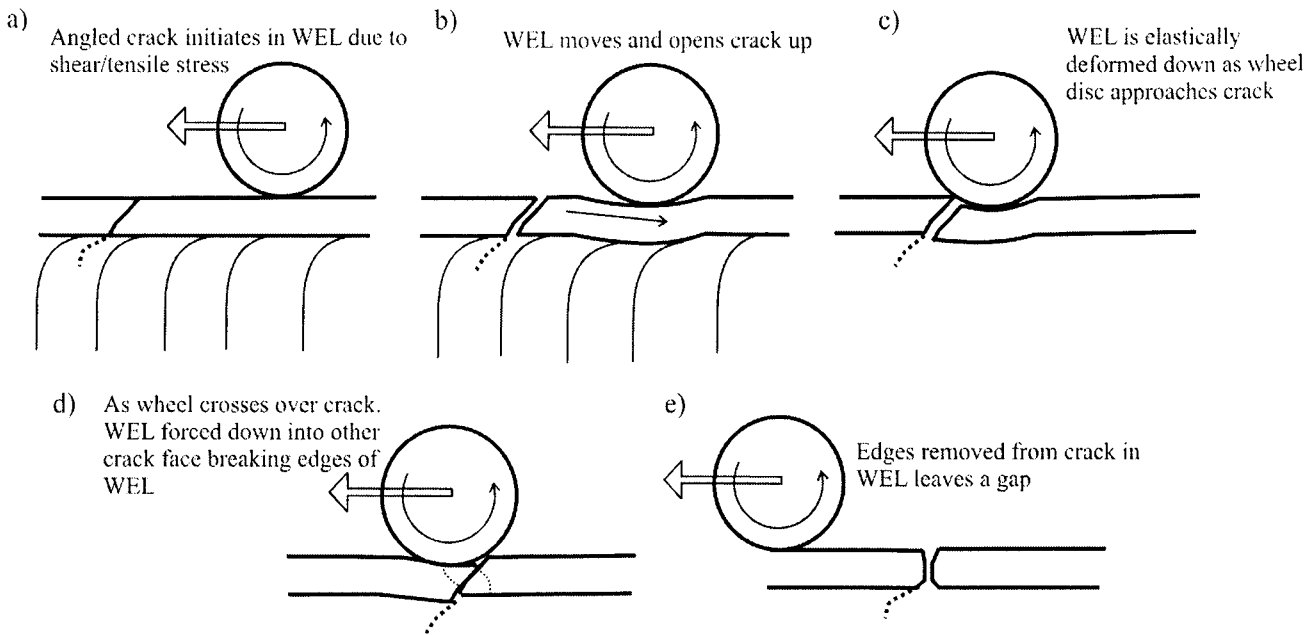
Figure 6.14: Schematic of elastic deformation of white etching layer as contact passes over crack (wheel disc scaled down for clarity). The dotted lines indicate propagating cracks while solid subsurface lines indicate plastic flow.
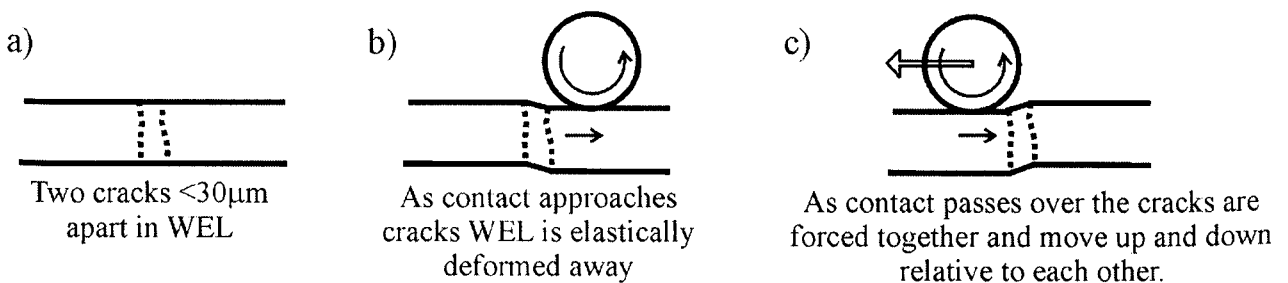
Figure 6.15: Schematic of the deformation of the pearlite when two cracks are present

As pearlite is deformed into gap
then it forces the WEL backwards
opening gap up

As wheel passes over gap pearlite below
WEL is plastically deformed up into gap
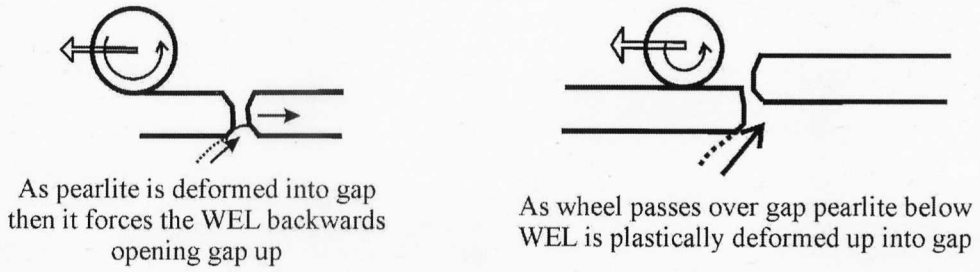
Figure 6.16: Schematic of deformation of pearlite into gasp in WEL

Gap A   Gap B

62μm   46μm   49μm   7μm
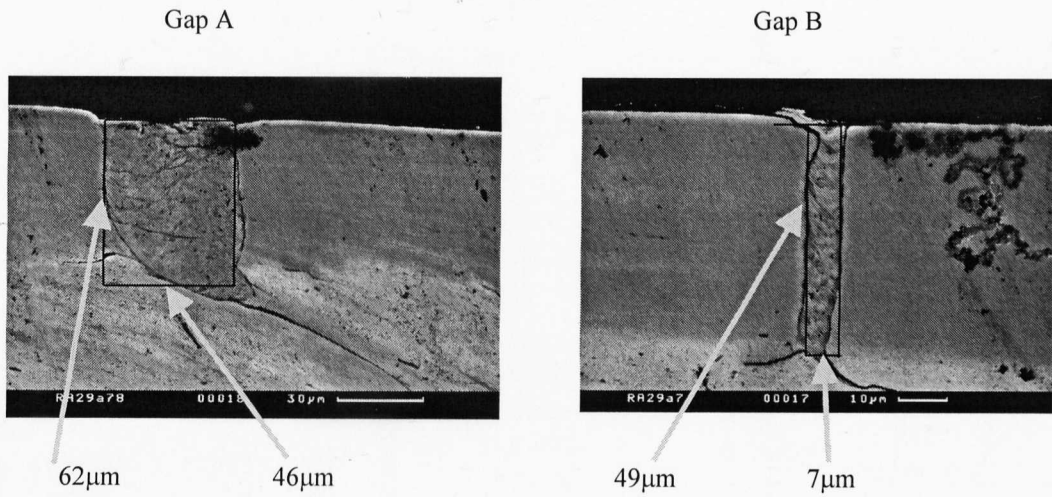
Figure 6.17: Approximation of size of gaps in WEL filled with wear debris
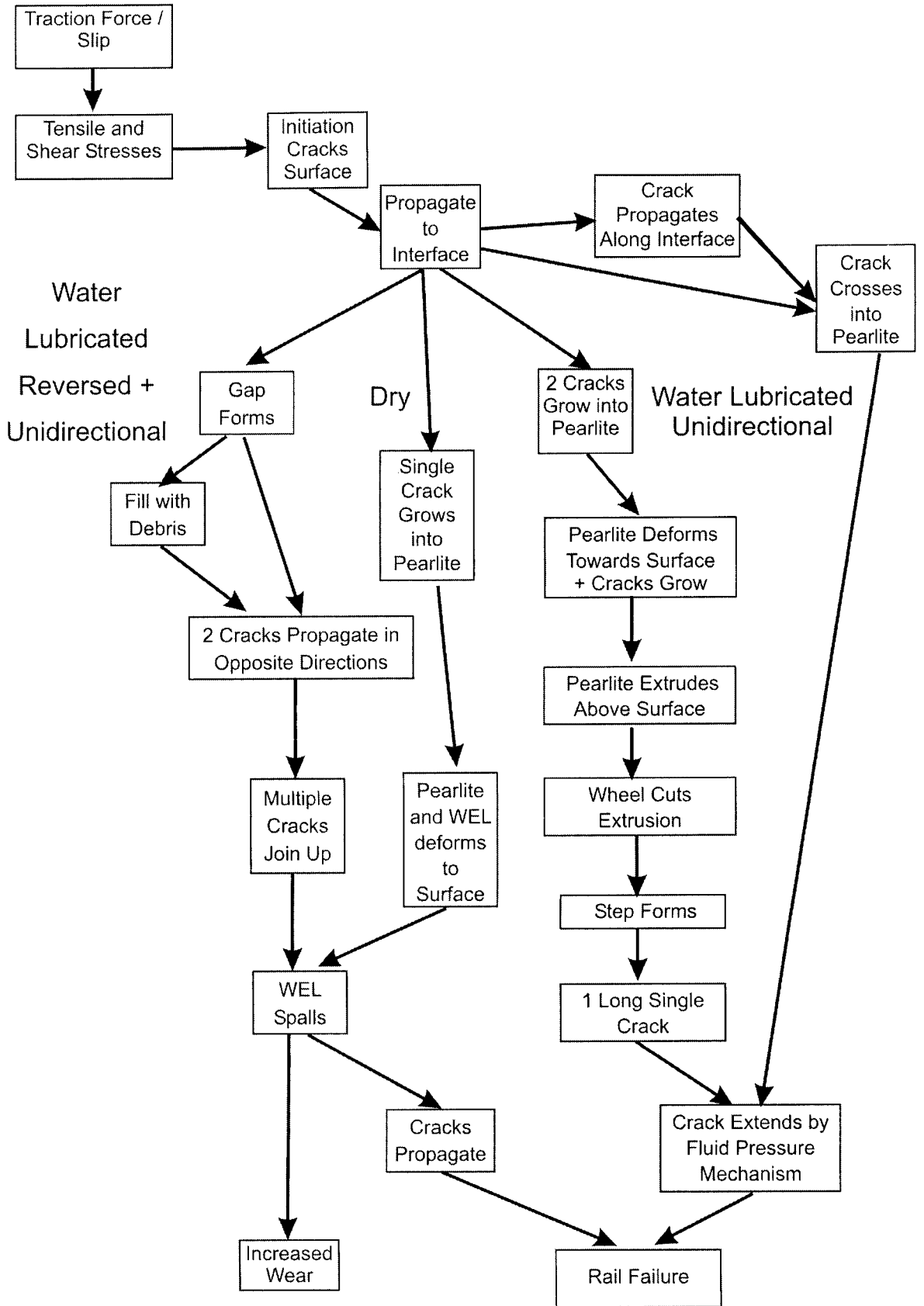
Figure 6.18: Flow chart summarising crack growth for WEL samples

a)

Two cracks in pearlite initiate from same crack in white layer

b)

c)

d)

e)

White layer cracks and is deformed below the extrusion, initiating further cracks in pearlite

f)

Wheel cuts extrusion and further plastic deformation results
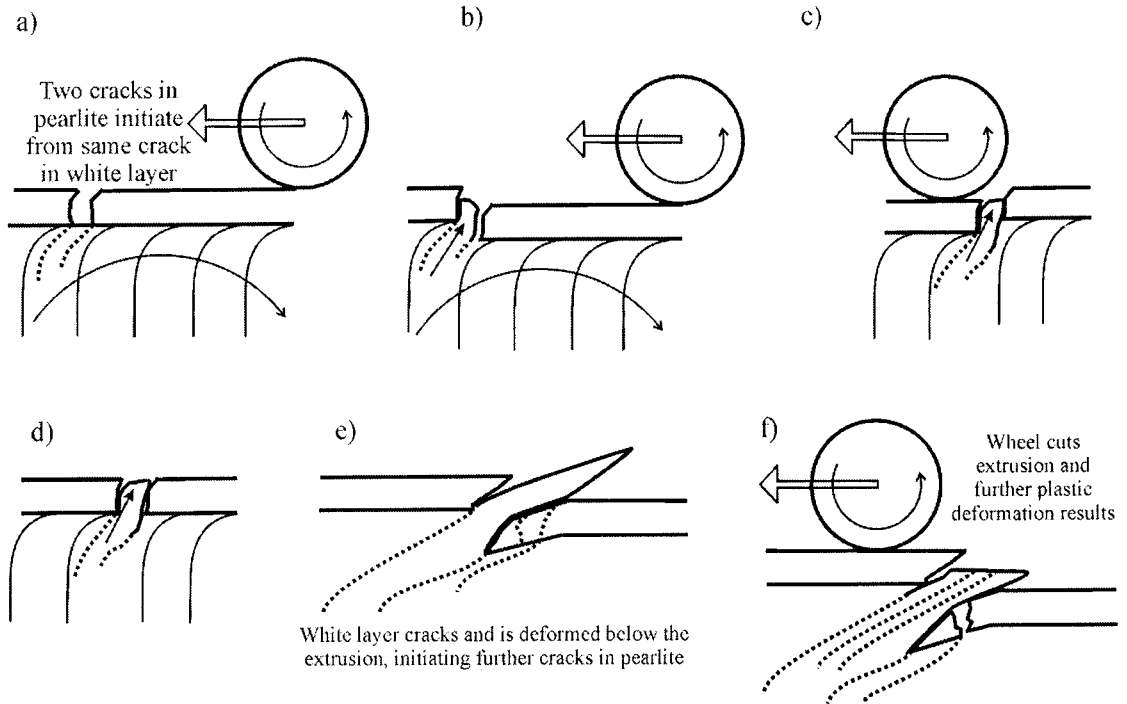
Figure 6.19: Schematic of the growth of two cracks into pearlite bulk material

a)

Elastic deformation leads to opening of crack by up to 7μm, combined with downwards plastic deformation of pearlite and cracking in opposite direction to plastic flow. To conserve volume then some pearlite has to be forced towards gap or under the buckle

b)

Elastic deformation of surface will close gap if it is not filled by pearlite. Pearlite is deformed towards surface through the gap once the contact patch has passed over it leading to propagation of cracks in the same direction as deformation

c)

Pearlite is deformed into crack

d)

Pearlite heals crack in WEL, deformation extends cracks

e)

Cracks join up and results in WEL spalling off.

f)

Cracks develop in the plastically deformed pearlite, creating slivers of wear debris

Figure 6.20: Schematic of cracks growing in opposite directions

243
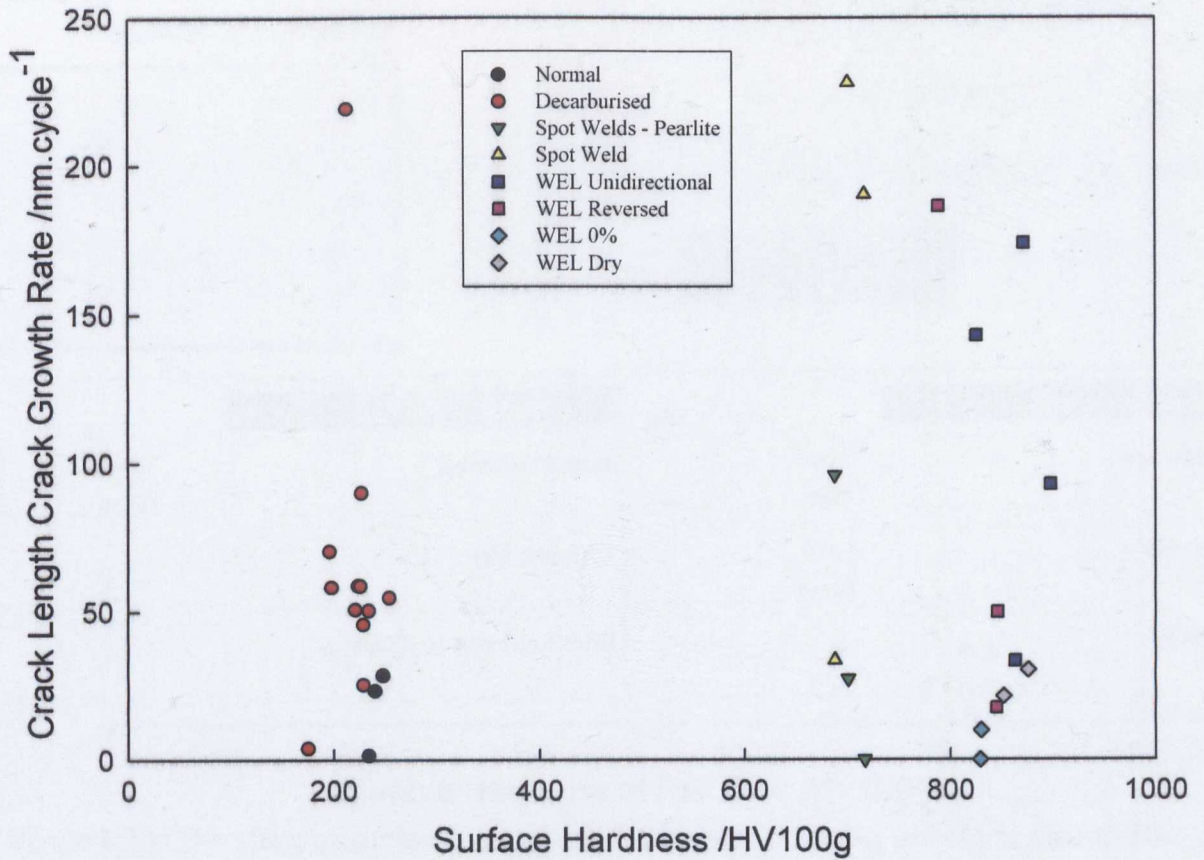
Figure 6.21: The effect of surface hardness on the crack length growth rate
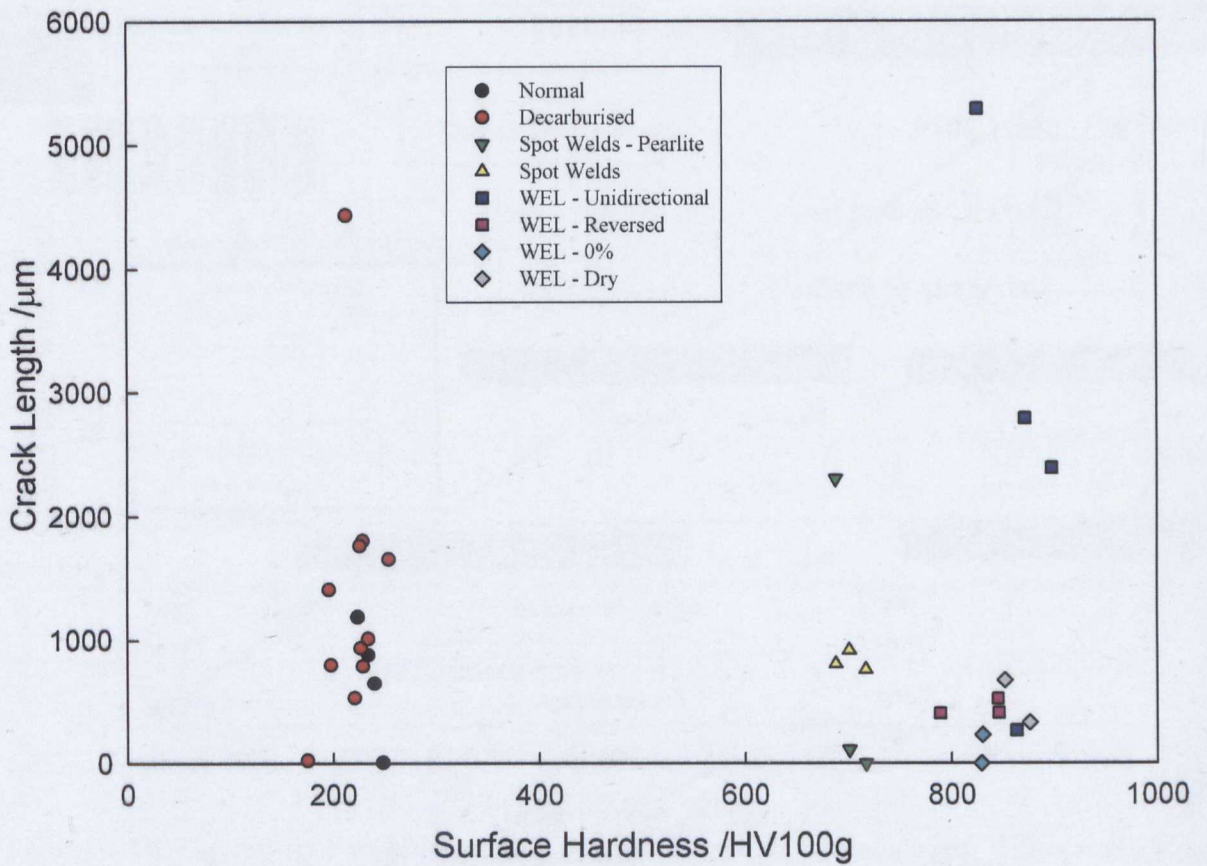
Figure 6.22: The effect of surface hardness on crack length
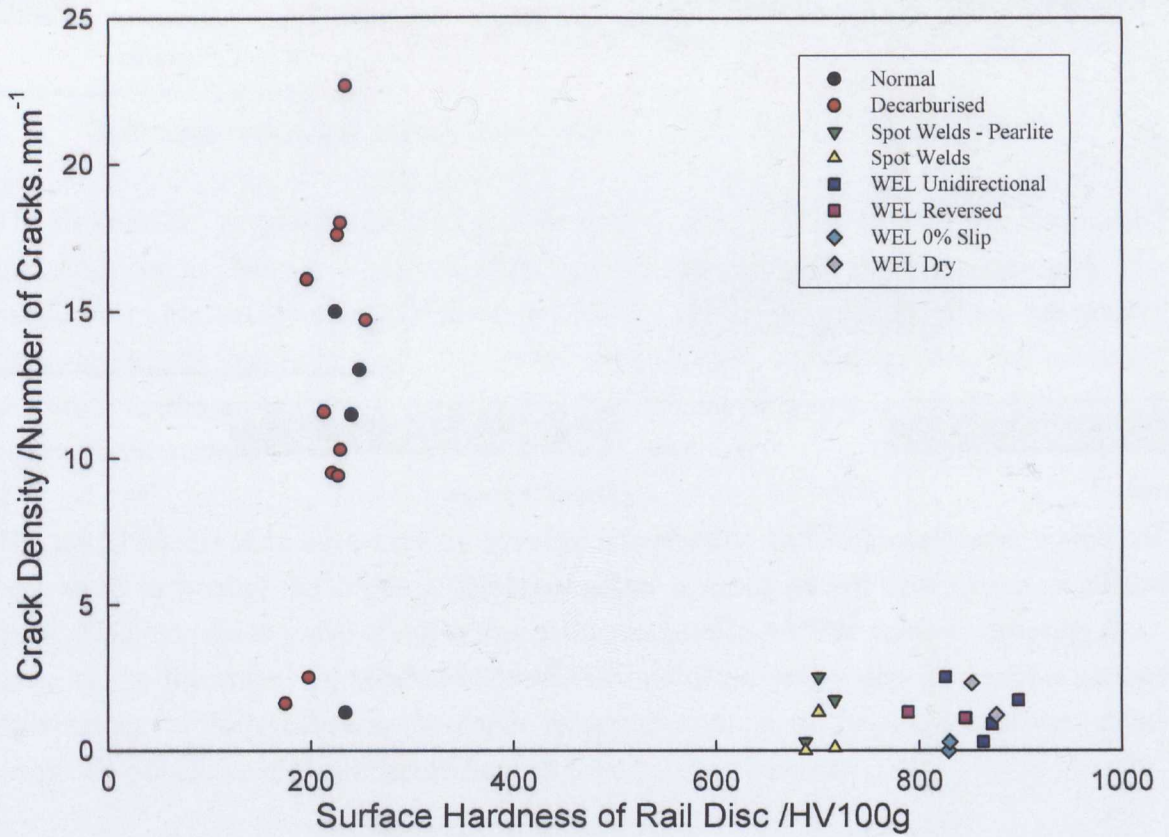
Figure 6.23: The effect of surface hardness on the number of cracks present in the rail disc sample
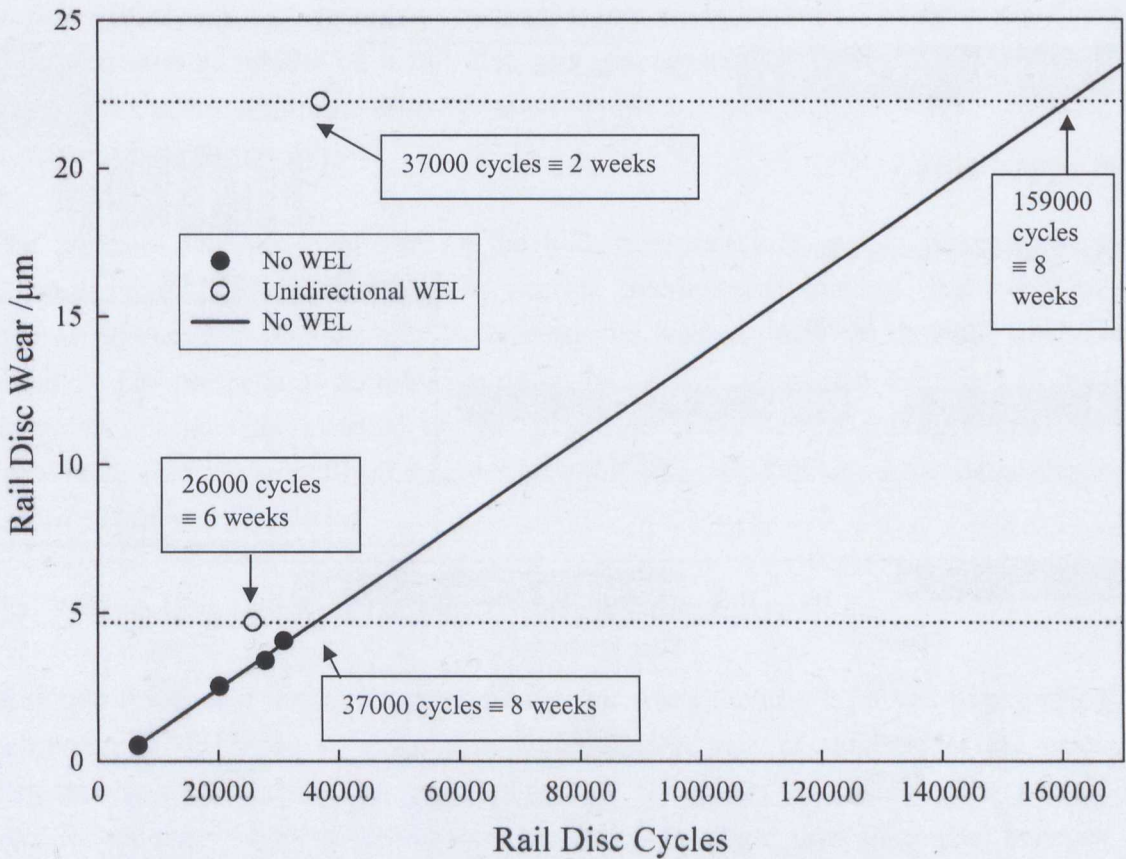
Figure 6.24: The rail disc wear in depth lost from the radius of the sliding WEL samples, calculated from the measurement of mass loss

Chapter 7: Conclusions

7.1   Diffusion Modelling of Decarburisation

The Birks model of decarburisation has been used to predict the depth obtained during heat treatment due to diffusion of carbon from the bulk to the surface of the steel sample. The results from the model using diffusion coefficients available in the literature are greater than the results observed from the initial experiments, indicating that the boundary condition used are invalid and therefore the rate determining step is not the diffusion of carbon to the surface.

The initial results have been used to calculate an effective diffusion coefficient which has been used to predict the depth of decarburisation attained during heat treatment of the discs. This calculated value is not a true diffusion coefficient, the value is different from those in the literature, but is a measure of the rate determining step of decarburisation. Comparison of the results for the depth of decarburisation of the discs with the model using this calculated diffusion coefficient showed good agreement.

7.2   Simulation of Decarburisation in the Laboratory

The decarburisation created by heat treatment of the rail disc resulted in ferrite at the surface with the amount decreasing with depth into the bulk metal. The minimum depth of decarburisation simulated on a rail disc was proportionately greater than the equivalent depth of the maximum that is allowed on rail by the European standard, as scaled using the contact half-width.

The effect of the heat treatment on the bulk microstructure was to increase the prior austenite grain size and decrease the pearlite interlamellar spacing. The effect of the refined interlamellar spacing was to increase the hardness and the strength of the bulk material. The presence of decarburisation at the surface means that the effect of the heat treatment on the bulk material would have little effect on the rolling contact fatigue behaviour. This is especially the case where the subsurface material has been plastically deformed and work hardened.

7.3   Modelling of the Formation of White Etching Layer

A simple theoretical model for the formation of white etching layer has been carried out involving the diffusion of carbon in austenite. As part of this model the effect of dislocations on diffusion has been examined, the effect of which is to reduce the temperature required for diffusion to occur during the short time of contact between the wheel and rail. The results indicate that high temperature diffusion cannot be responsible for the creation of white etching layer on the surface of railhead. This is because

transformation to austenite will only occur above a temperature of 620°C, whereas the maximum predicated, under normal conditions, between the wheel and rail is only 400°C.

7.4   Simulation of White Etching Layer in the Laboratory

White etching layer was simulated in the laboratory in two different ways, spot welding and gross sliding of the disc. Both techniques produced a hard layer at the surface with a distinct interface between it and the bulk material. The difference between the two is that spot welding produced a distinct area of WEL surrounded by pearlite, resulting in an interface between the two at the surface. In contrast, the WEL produced by sliding has a continuous interface below and parallel to the surface.

Spot welding locally heats the surface of the disc, resulting in the transformation of the original pearlite to austenite, followed by quenching, by the bulk material, to produce a martensitic layer. The mechanism of formation of the sliding WEL has been found to comprise material transfer from the wheel to the rail disc by adhesive wear combined with the severe deformation of both the transferred material and the original surface of the rail disc. The surface of the disc is severely plastically deformed so that the pearlite lamellar were broken up and dissolved into solution, combined with recrystallisation, resulting in the featureless appearance and high hardness of the white etching layer.

7.5   Twin Disc Testing of Decarburised Samples

Decarburisation has been created on rail discs with a wide range of depths between 93µm and 621µm. The results of the twin disc testing of artificially decarburised samples can be summarised as follows:
- As the depth of decarburisation is increased the amount of shear strain below the surface of the disc also increases.
- The wear rate of the rail steel increased because the surface of the decarburised disc is softer and less resistant to wear; the wear of the wheel disc decreased because of the softer surface of the rail disc.
- The rate of crack growth in the rail disc increased with depth of decarburisation, giving a rise of greater than double for a decarburised depth of 620µm. This is because pearlite with reduced amounts of carbon is less resistant to crack growth.
- The RCF crack growth under twin disc testing is driven by the contact stresses via the fluid pressure mechanism and influenced by the microstructure.

7.6   Twin Disc Testing of Samples with a White Etching Layer

The behaviour of white etching layer under rolling/sliding contact conditions has shown that cracks initiate within the WEL due to its brittle behaviour when a traction force is

present. Cracks have also been found to initiate where the soft pearlite meets the hard martensitic WEL due to the pile up and ductility exhaustion of the pearlite.

The propagation of cracks below the white etching layer have been found to be dependent on the ductility exhaustion of the subsurface pearlite. Cracks were also found to be much greater in length when water lubrication was used, demonstrating that water enhances crack growth.

The morphology of rolling contact fatigue cracks growing within the sample can be summarised as follows:

- Spot welded samples: cracks grow within the pearlite from the interface with the WEL due to plastic deformation and ductility exhaustion of the pearlite. Cracks also grow within the spot weld due to deformation of the surrounding pearlite resulting in the contact stresses being unsupported in the WEL.
- White etching layers created by sliding: cracks initiate at the surface due to tensile/shear stresses and propagate rapidly within the WEL but are deflected at the interface with the pearlite. Propagation below the WEL is dependant on the strain history of the subsurface pearlite and whether water lubrication is available.

The wear of WEL samples was found to be lower than for those without, but only if the WEL remained intact and did not spall off. If spallation occurred the wear of the rail samples was much higher than for samples without a WEL. This wear is due to the subsurface ductility exhaustion of the pearlite and subsequent growth of cracks. The wear of wheel samples is significantly greater than for samples run against normal discs because the edges of the cracks in the WEL effectively act as machining tools combined with heavy plastic deformation of the surface.

7.7   Surface Metallurgy and Twin Disc Testing

There is no general correlation between the hardness of the surface and the rolling contact fatigue performance and wear of the rail disc. Decarburisation and white etching layer both increased the crack growth rate of the disc, in comparison with a normal disc, by different mechanisms. Decarburisation reduces the hardness of the surface resulting in a lower resistance to crack propagation and hence a higher crack growth rate; it also increases the wear of the surface. White etching layer results in the ability of cracks to initiate more readily because of its hard brittle nature, combined with the subsurface ductility exhaustion resulting in long cracks; the presence of cracks also increases the wear.

7.8   Surface Metallurgy and Wheel/Rail Contact

The results from twin disc testing were related to wheel/rail contact. For simplification, a line contact model was used for both contact situations. This scaling between the two sets of contacting surfaces was conducted using different contact half-widths.

The maximum amount of decarburisation allowed on rail is 0.5mm, which scales, using the relative contact half width, to 23μm on a disc. The effect of such a small amount of decarburisation on rolling contact fatigue will be very small in practice because of its shallow depth and also the small amount of extra ferrite at the surface compared to the bulk material. Decarburisation would only be important if the amount of decarburisation on rail were increased to unrealistic levels.

White etching layer has been found to be detrimental to rail life through the promotion of both wear and crack propagation. The majority of cracks result in the WEL spalling off, increasing the wear rate of the steel. The cracks that manage to cross through the WEL and into the bulk, along with those that initiate at the interface between the pearlite/WEL, may lead to failure of the rail through rolling contact fatigue.

Chapter 8: Further Work

8.1   Decarburisation, White Etching Layer and Surface Metallurgy

The investigation of both decarburised and white etching layers using twin disc testing has only used conditions encountered on the railhead away from and not at the gauge corner. Decarburisation occurs all way around the rail and as such is present at the gauge corner, usually to greater depths. Therefore the higher slip ratios present at the corner[1] may influence the wear and rolling contact fatigue behaviour in a different way than under the conditions on the railhead employed in this investigation. Several tests could be carried out using a higher slip ratio with the results compared to those presented here.

Plastic deformation of a material proceeds by the introduction and movement of dislocations, when they become entangled their ability to move is reduced and the material hardens until its ductility is exhausted, resulting in the initiation of cracks[2, 3]. Dislocations can be observed using a transmission electron microscope (TEM) using a small foil sample. Removing such samples from twin disc test specimens used during this investigation would be possible by employing a focussed ion beam (FIB) microscope for subsequent examination in the TEM. The examination of rails removed from service could also be carried out in the vicinity of RCF cracks. At present there is little understanding of the microstructural underpinning of the ratchetting mechanism. Previous investigations have concentrated on the modelling of the hardening process[4, 5] with little validation through microstructural observations. The information on the location, density and distribution of dislocations gained in such an investigation would allow the prediction of the ratchetting behaviour of different materials to be predicted. The investigation would also give information into the proximity of dislocations to cracks and the reason why cracks only initiate in certain places. Through the knowledge gained it may be possible to optimise the surface metallurgy of rail, e.g. to enhance dislocation recovery, and to greatly reduce rolling contact fatigue and wear through the use of coatings.

The formation of white etching layers under both the sliding contact used in this investigation and under rolling/sliding conditions requires further investigation. There have been many investigations into the formation of WEL but none have been conclusive as to the mechanism by which it occurs[6, 7]. Investigation of the sliding WEL used in this investigation may allow further insight into the formation mechanism of white etching layers on rail and, because it is detrimental to rail life, may allow surface metallurgies to be developed that prevent its formation. This could be conducted by altering the conditions of the SUROS machine during sliding to see their effect on the formation of WEL. As part of this the effect of carbon composition on the formation of WEL can be investigated possibly including a test disc made from pure iron; the mechanisms of formation in the literature would indicate that the presence of carbon would be a key to the formation mechanism[7]. Other methods of deformation could also be investigated such as pin-on-disc wear testing

to study the conditions required for formation of WEL. White etching layers on rail are believed to form under rolling/sliding conditions[6], therefore using the SUROS test machine in this configuration and altering the test parameters may allow a WEL to be formed, giving further insight.

One of the problems with the theories of the formation of WEL is the prediction of temperatures lower than those required for transformation to austenite. In previous work theoretical modelling has been carried out because the measurement of the contact temperatures is difficult. With modern infrared cameras it may be possible to measure the contact temperature of the twin disc configuration; this could also be used during the sliding experiments to study the maximum rise and its effect on formation. This investigation could be related to that for the formation of white etching layer detailed above, as it would give further information into its mechanism.

As part of a further investigation into white etching layer, electron back scattered diffraction (EBSD) could be used to measure the crystallographic orientation (texture) of the near surface layers after testing. The effect of texture has been related to the friction coefficient[8] but such texture may also be different between the WEL and normal samples, indicating a reason for the formation of the WEL. This has previously been performed on a nanocrystalline layer of nickel created by deformation[9].

A fundamental part of the investigation into the formation of white etching layer will be to confirm that its structure is indeed nanocrystalline martensite. One possible way to do this will be to carry out tempering of the WEL to see whether it behaves in the same way as martensite produced by quenching.

In this investigation only one rail steel has been used. The results have demonstrated that the subsurface material is highly influential on the rolling contact fatigue and wear behaviour of rail. Therefore consideration should be given to further investigations of both decarburisation and white etching layer on other rail steels, particularly harder and more wear resistant materials such as head hardened rail and alloy steels.

In relation to the decarburisation model, further work is required to find the rate determining step which would allow an equation to be fitted to the carbon profile data. Such a model may be useful in industry to predict the oxidation and decarburisation during reheating and rolling. As such, further data measured using other techniques may be required; this could include thermogravimetric analysis (TGA) for oxidation data and electron probe microanalysis (EPMA) for the carbon profile.

8.2   Twin Disc Testing

In recent years there has been a trend for research into the coating of rails for greater wear and RCF resistance as an extension of using harder and stronger rails[10]. One of these has been through the use of a laser to modify the surface of the rail[11] through heating and may be similar to the white etching layer produced by sliding. A comparison of the behaviour under rolling/sliding twin disc testing of the two may lead to more information on the behaviour of surface layers under rolling/sliding conditions. There are also many different coatings used in other tribological applications and a review of these to find the most applicable to rail could be carried out with the most promising being investigated using twin disc testing.

Several different welding techniques are involved in the use and maintenance of rail: including thermite and flash butt welding to join sections together, along with electric arc welding to rebuild the profile (especially on austenitic manganese crossings)[12]. One feature apparent in the literature is that RCF cracks are commonly observed in the vicinity of these rail welds, this is not just in the weld material but also in the unheated material up to several metres away[13]. In spite of this very few investigations have been carried out on the behaviour of the weld material under rolling/sliding conditions especially under laboratory conditions. It may be possible for samples to be cut from the railhead through both flash butt and thermite welds to allow their testing. A problem arising from this will be a much greater area of weld during twin disc testing in relation to the size of the wheel and contact dimensions, than during actual wheel/rail contact. A possible way to overcome this would be to carry out welding on a smaller scale in the laboratory; comparisons could be made with rail to ensure that the weld material is similar.

Another fruitful area of research would be austenitic manganese (Hadfield) steel which is used for the manufacture of switches and crossings. This is another area of rail that is vulnerable to rolling contact fatigue because of the high stresses arising from the wheel impacting on the discontinuous rail[14]. Previously there has been little investigation of the behaviour of this highly work hardening steel under rolling/sliding conditions, with previous work having concentrated on the wear behaviour under sliding conditions.

8.3   References

1.   Olofsson, U. and Telliskivi, T., Wear, plastic deformation and friction of two rail steels: a full-scale test and a laboratory study, Wear, 254, (1-2), p80-93, 2003
2.   Hull, D., Introduction to dislocations, 2nd Ed., Pergamon Press, Oxford, UK, 1975
3.   Suresh, S., Fatigue of Materials, 2nd Ed., Cambridge University Press, 2003
4.   McDowell, D. L., Stress state dependence of cyclic ratchetting behaviour of two rail steels, International Journal of Plasticity, 11, (4), p397-421, 1995
5.   Johnson, K. L. and Jefferis, J. A., Plastic flow and residual stresses in rolling and sliding contact, in: Proceedings of the Symposium on Fatigue in Rolling Contact, Institution of Mechanical Engineers, London, 1963, pp. 54-65

6.   Baumann, G., Fecht, H. J. and Liebelt, S., Formation of white etching layers on rail treads, Wear, 191, (1-2), p133-140, 1996

7.   Newcomb, S. B. and Stobbs, W. M., A transmission electron microscopy study of the white etching layer on a railhead, Materials Science and Engineering, 66, (2), p195-204, 1984

8.   Krause, H. and Lehna, H., Factors influencing the real trend of the coefficient of friction of two elastic bodies rolling over each other in the presence of dry friction, in: The Mechanics of Contact Between Deformable Bodies, Pater, A. D. and Kalker, J. J., Delft University Press, 343-358, 1975

9.   Prasad, S. V., Micheal, J. R., Battaile, C., Kotula, P. G. and Majumdar, B. S., On the evolution of friction induced nanostructures in single crystal nickel, in: World Tribology Congress III, Washington DC, USA, American Society of Mechanical Engineers, 2005, pp. WTC2005-63577

10.   Hiensch, E. J. M., Two material rail combats rolling contact fatigue, Railway Gazette International, 159, (9), p587-590, 2003

11.   DiMelfi, R. J., Sanders, P. G., Hunter, B., Eastman, J. A., Sawley, K. J., Leong, K. H. and Kramer, J. M., Mitigation of subsurface crack propagation in railroad rails by laser surface modification, Surface and Coatings Technology, 106, (1), p30-43, 1998

12.   Shitara, H., Terashita, Y., Tatsumi, M., Fukado, Y. and Ueyama, K., Rail weld failures and non-destructive inspection methods for rail welds in Japan, in: Railway engineering 2002: 5th International Conference, London, 2002, pp.

13.   D173, Report No. 1: Review of rolling contact fatigue in rails, Office for Research and Experiments of the International Union of Railways, Utrecht, The Netherlands, 1990

14.   Sawley, K. J., Improvements to crossings, Proceedings of the Institution of Civil Engineers: Transport, 100, (11), p239-242, 1993